Space Science and Engineering Center
University of Wisconsin-Madison

The Technical Proceedings of

The Third International TOVS Study Conference

A REPORT from the

Cooperative Institute for Meteorological Satellite Studies

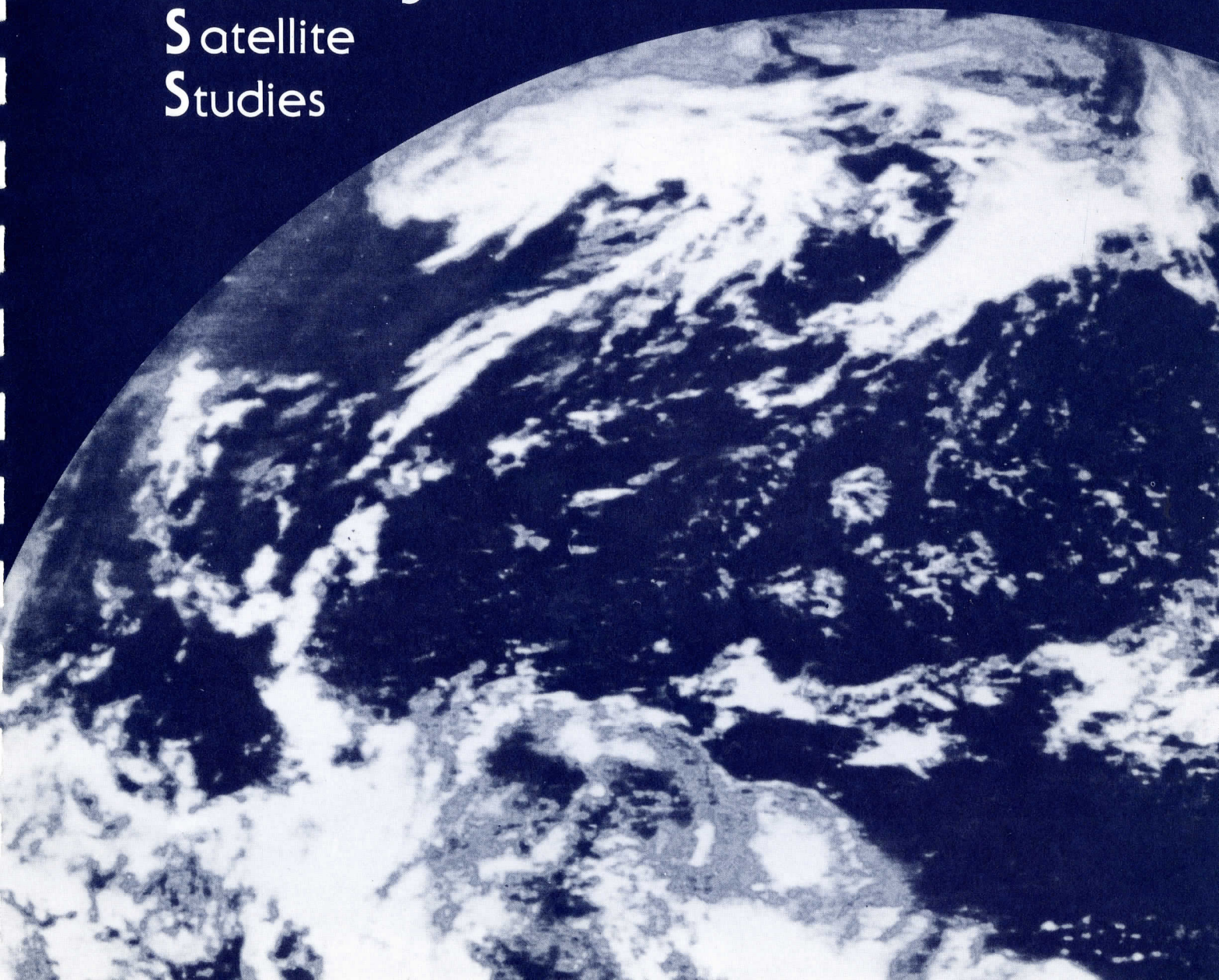

The Technical Proceedings of

The Third International TOVS Study Conference

Madison, Wisconsin

August 13 - 19, 1986

Edited by

W. P. Menzel

Cooperative Institute for Meteorological Satellite Studies
Space Science and Engineering Center
University of Wisconsin
1225 West Dayton Street
Madison, Wisconsin 53706
(608)262-0544

November 1986

FOREWORD

These technical proceedings detail the scientific presentations at the Third International TOVS Study Conference (ITSC-III) held in Madison, Wisconsin from 13-19 August 1986. A summary of conference objectives, conclusions, and plans for future action is contained in a separate document entitled "A Report on ITSC-III" available from the CIMSS, University of Wisconsin-Madison.

These technical proceedings focus on the retrieval of cloud parameters and the treatment of clouds in the TOVS sounding retrieval process. Methods are presented which make better use of existing TOVS radiances and which use ancillary data from the Advanced Very High Resolution Radiometer (AVHRR).

The proceedings contain additional papers dealing with constituent retrieval, in particular, water vapor and ozone. As with clouds, the papers indicate considerable progress in the retrieval of atmospheric constituent parameters which are important for weather forecasting and climate diagnosis.

Finally, the proceedings include a few shorter contributions dealing with TOVS navigation, personal computer applications, and future polar orbiting satellite sensors. Because of the diverse aspects of TOVS data processing and product applications covered, this report should be extremely useful to the international community of meteorological satellite measurement users and researchers.

William L. Smith, Chairman
Third International TOVS Study Conference

ACKNOWLEDGEMENTS

The publication of these proceedings has been possible through the financial support from the National Oceanic and Atmospheric Administration to the Cooperative Institute for Meteorological Satellite Studies in Madison, Wisconsin.

The careful retyping of several of the edited manuscripts was accomplished by Ms. Laura Beckett and the production was handled by Ms. Sue Pfefferkorn. We thank them for their quality work.

A special thank you goes to Dr. Guy Rochard of the Satellite Calibration Centre in Lannion, France. He has been an important catalyst in the attempt to specify accurate calibration and navigation techniques for the TOVS data. His efforts are helping to make the TOVS instrument more useful to the international satellite user community. His input to NOAA/NESDIS is most appreciated.

TABLE OF CONTENTS

Plans for TOVS in Portugal..... 1
Arlindo Arriaga

Recent Progress in the Determination of Meteorological Parameters from the Satellites of the TIROS-N Series..... 6
A. Chedin, N. A. Scott, C. Claud, J. F. Flobert, N. Husson, C. Levy, P. Moine, G. Rochard, J. Quere and T. Phulpin

New Developments in the French Mesoscale Analysis in the Use of Raw Satellite Data..... 45
Y. Durand and R. Juvanon du Vachat

TOVS Retrievals in the U.K.: Progress and Plans..... 60
J. R. Eyre, R. W. Pescod, P. D. Watts, P. E. Lloyd, W. Adams and R. J. Allam

Remote Sensing of Surface Air and Dew Point Temperature in Cloudy Atmospheres from Cloud Pattern-dependent Relationship..... 92
Louis Garand

The Application of TOVS Data to the Carolina Tornado Outbreak of 28 March 1984..... 102
D. W. Hillger, J. F. W. Purdom, T. H. Vonder Haar

An Extension of the Simultaneous TOVS Retrieval Algorithm - The Inclusion of Cloud Parameters..... 118
H.-L. A. Huang and W. L. Smith

The Operational and Research Processing of TOVS Data in the Australian Bureau of Meteorology..... 131
J. F. LeMarshall, G. A. Kelly, P. E. Powers and R. F. Davidson

Satellite Sounding Activities at the Western Australian Institute of Technology..... 146
M. J. Lynch

A Physical Model for Retrieving Total Ozone from the NOAA Satellite and Preliminary Results over China..... 151
Ma Xia-Lin and Zhang Feng-Ying

Some Modifications to the NESDIS Operational Clear Column Radiance Procedure..... 160
Larry M. McMillin and Andrew Nappi

Cloud Top Pressures and Amounts Using HIRS CO_2 Channel Radiances..... 173
W. P. Menzel

A Description of Prediction Errors Associated with the T-Bus-4 Navigation Message and a Corrective Procedure..... 186
Frederick W. Nagle

ESTHER Products for TOVS Processing Improvement..... 214
T. Phulpin

Observations of Tropical Cyclones in Western Australia Using Combined TOVS and AVHRR Radiances..... 222
A. J. Prata

Status Report on Calibration Problems..... 235
G. Rochard

Future NOAA POES Satellite and Sensors..... 243
James K. Sparkman, Jr.

Simultaneous Retrieval of Temperature and Relative Humidity Using Empirical Orthogonal Functions..... 259
J. D. Steenbergen, B. T. Greaves and T.-C. Yip

Estimating the Correct Degree of Smoothing in the Simultaneous Retrieval Method..... 276
Jan Svensson

Synthetic and Real Data Applications of the Typical Shape Function Simultaneous Physical Retrieval Algorithm..... 283
Michael J. Uddstrom

Validating a TOVS Cloud Clearing Scheme Using AVHRR Data..... 312
P. D. Watts and J. R. Eyre

A Preliminary Study of TOVS Retrieval in Taiwan, R.O.C..... 332
T.-C. Yen and J.-J. S. Wang

Abstract from Report on ITSC-III..... 339
Frederick Zbar

IBM PC Package for TOVS Processing and Display..... 344
Fengxian Zhou and Yanni Qu

Additional Papers Relevant to ITSC-III

Interactive Processing of Satellite Radiance Measurements..... 350
T. Achtor, H. Woolf, H. Maurer and F. Huang

WMO Issues for Discussion..... 353
J. Giraytys

Multivariate Analyses of ALPEX Satellite Retrievals..... 357
W. P. Menzel, G. A. Mills, A. J. Schreiner, C. M. Hayden, and W. L. Smith

Report of Phase 2 of the CIMO International Radiosonde Comparison Conducted From Wallops Island, Virginia, U.S.A..... 369
Francis J. Schmidlin and F. G. Finger

Comparisons of Relative Humidity Measurements from Phase I of the WMO International Radiosonde Comparison..... 375
J. Nash, M. Kitchen, and J. F. Ponting

PLANS FOR TOVS IN PORTUGAL

Arlindo Arriaga
Instituto Nacional de Meteorologia e Geofisica (INMG)
Rua C do Aeroporto
1700 Lisboa, Portugal

1. System Configuration and Current Capabilities

The National Institute of Meteorology and Geophysics, in Lisbon, is the government agency responsible for all operational and research activities in the fields of atmospheric sciences and physics of the solid Earth. The Meteorological Service is one of the main branches of this Institute.

The satellite receiving groundstation of the National Institute of Meteorology and Geophysics has been gradually expanded since 1978, and has capabilities to receive digital data from Meteosat, GOES and NOAA's satellites.

Original plans were revised by 1981, when it was decided to modify a stand-alone configuration for hardcopy images, and start with the implementation of an interactive system and data processing capabilities.

The present configuration (Figs. 1 and 2) must be intended as an intermediate stage, and its goal was to provide the Weather Forecasting Division of the Meteorological Service with the main operational means for manipulation and interpretation of images 24 hours a day. Priority has been given to the Meteosat data, and the basic software for Meteosat images was implemented in 1984.

The current capability for polar orbit satellites enables to receive HRPT transmissions:

- programmable tracking antenna (Scientific Atlanta)
- preamplifier, receiver and demodulator (Scientific Atlanta)
- bit synchronizer (EMR 720)
- frame synchronizer (EMR 814)
- image microprocessor (EMR 813)

The frame synchronizer is interfaced with a PDP 11/34 minicomputer, with 256 kB and a RSX-11M operating system. The acquisition software is the Televent package from EMR. Due to the priority given to the Meteosat PDUS, only a little investment was made to decode and process the AVHRR signal from polar orbiters.

The AVHRR images can be manipulated now in a Vision 1/20 interactive system from COMTAL, interfaced with the PDP 11/34, through a ZB driver, with four image and two graphic planes. Images can be sectorized, zoomed, combined, enhanced and analyzed with several algorithms. Data navigation and calibration cannot be applied as the actual frame synchronizer and acquisition software do not decode the necessary information.

The Weather Forecasting Division uses the AVHRR to monitor the activity and evolution of small scale perturbations, not identified by the large scale numerical model of the ECMWF: structure of frontal systems, early stages of cyclogenesis, convective areas and fog. The location of pixels is made with an algorithm based on the navigation data available in TBUS messages. Calibrated enhancements of the sea surface in coastal areas have been experimented, in cooperation with the Oceanographic Institute.

2. Future Plans for TOVS

The acquisition and use of TIP data is in our plans for the next three to five years:

a) Motivation

Portuguese meteorology is interested in the use of TOVS data, especially for the following reasons:

- retrieval of sea surface temperatures in coastal zones;
- improvement of hydrological and heat balances;
- support the implementation of mesoscale models;
- organize a regional cloud climatology data set;
- improvement of ozone observations.

b) Next Steps

- Some modifications in the hardware and acquisition software will be made to receive AVHRR ancillary information and TIP data.
- The interactive system will be expanded and complemented with other terminal, and interfaced with the computer center of the Institute.
- Implementation of software to handle the AVHRR as well as the implementation of the International TOVS Processing Package are expected to be made, after a plan of cooperation with the Cooperative Institute of Meteorological Satellite Studies be defined.

c) Scenario for Data Processing

- TOVS will be processed for operational and research purposes: operational routines will be run in the computer center, and research work will be based on minicomputers.
- Data will be used to analyze the mesoscale structure of the weather patterns, adjusting the long wave structures with the outputs from the ECMWF.
- Retrieving areas will be selected by interactive control (AVHRR), and optimum interpolation methods will be used to correct cloud effects.

- 3D adjustments will be made based on available observations and dynamical constraints of a mesoscale model.

Acknowledgements: The author expresses his gratitude to the CIMSS and SSEC for the collaboration, scientific information and technical support, which have important consequences for his present and future work in satellite data applications.

02/TOVS3/23

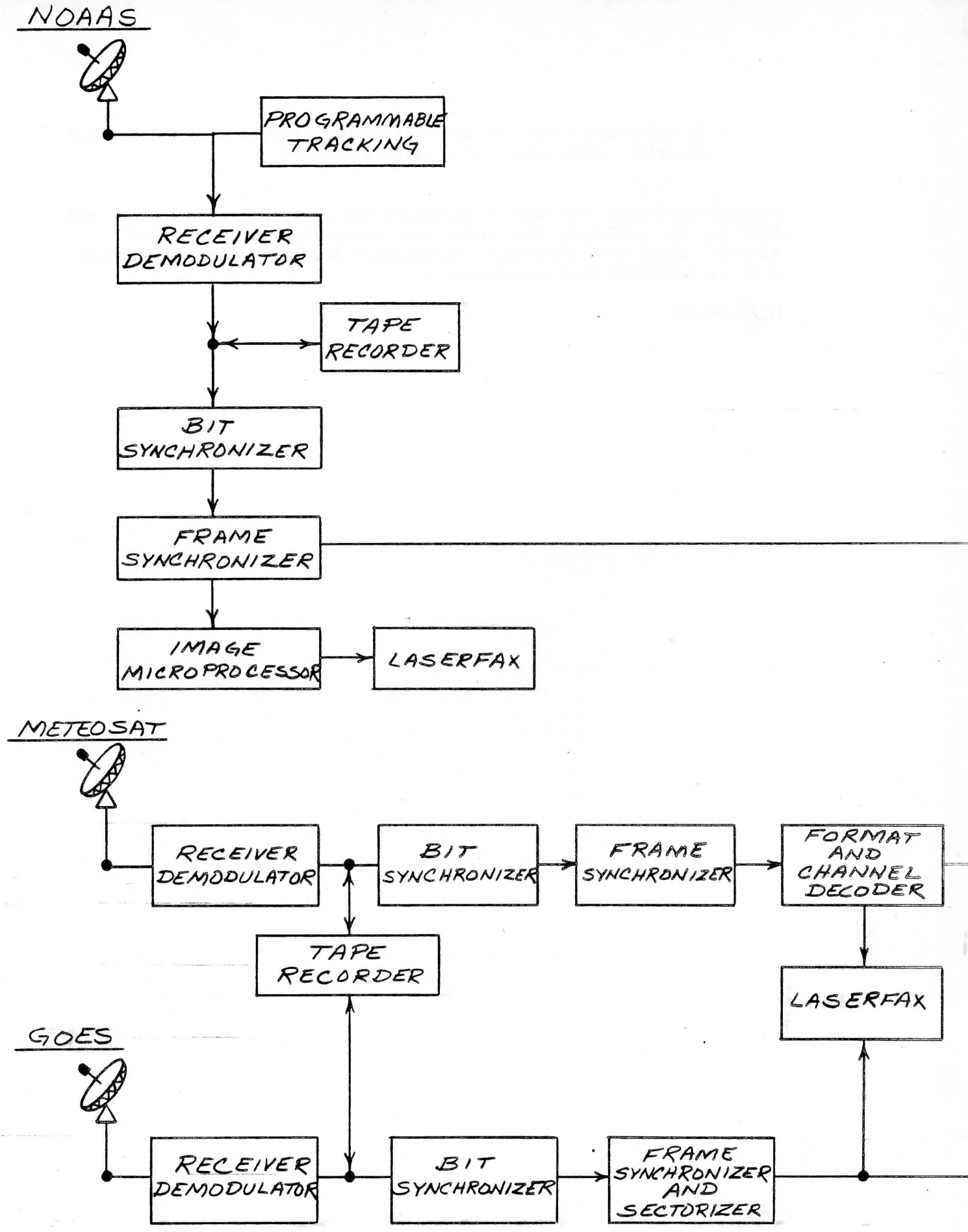
NOAAS
PROGRAMMABLE TRACKING
RECEIVER DEMODULATOR
TAPE RECORDER
BIT SYNCHRONIZER
FRAME SYNCHRONIZER
IMAGE MICROPROCESSOR
LASERFAX
METEOSAT
RECEIVER DEMODULATOR
BIT SYNCHRONIZER
FRAME SYNCHRONIZER
FORMAT AND CHANNEL DECODER
TAPE RECORDER
LASERFAX
GOES
RECEIVER DEMODULATOR
BIT SYNCHRONIZER
FRAME SYNCHRONIZER AND SECTORIZER

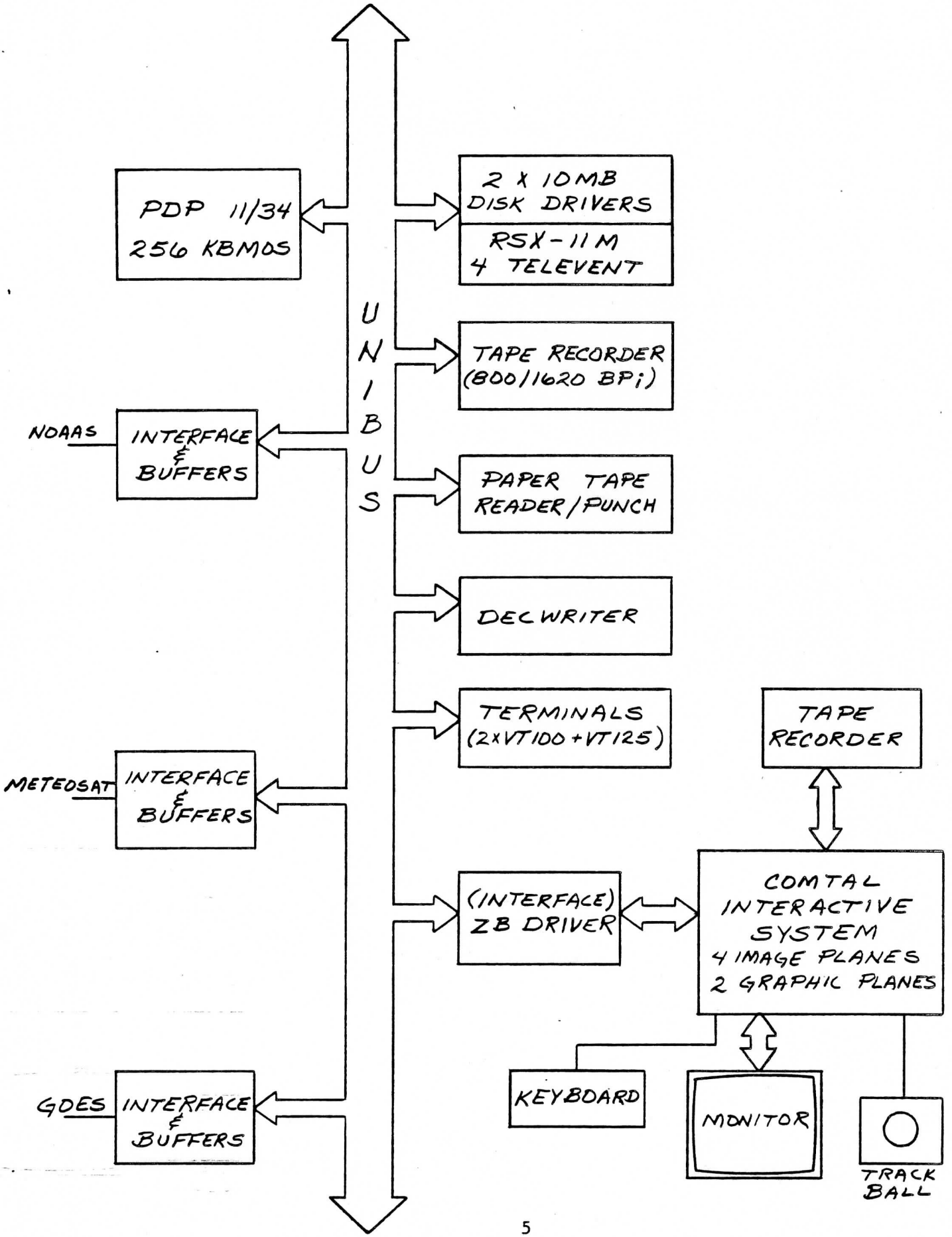
PDP 11/34
256 KBMOS
2 x 10MB
DISK DRIVERS
RSX-11M
4 TELEVENT
UNIBUS
TAPE RECORDER
(800/1620 BPi)
NOAAS
INTERFACE
&
BUFFERS
PAPER TAPE
READER/PUNCH
DECWRITER
TERMINALS
(2xVT100+VT125)
TAPE
RECORDER
METEOSAT
INTERFACE
&
BUFFERS
(INTERFACE)
ZB DRIVER
COMTAL
INTERACTIVE
SYSTEM
4 IMAGE PLANES
2 GRAPHIC PLANES
KEYBOARD
MONITOR
TRACK
BALL
GOES
INTERFACE
&
BUFFERS

RECENT PROGRESS IN THE DETERMINATION OF METEOROLOGICAL PARAMETERS FROM THE SATELLITES OF THE TIROS-N SERIES

A. Chedin,[1] N. A. Scott,[1] C. Cloud,[1] J. F. Flobert,[1]
N. Husson,[1] C. Levy,[1] P. Moine,[1]
G. Rochard,[2] J. Quere[2] and T. Phulpin[3]

[1]Laboratoire de Météorologie Dynamique du CNRS,
Ecole Polytechnique, 911 Palaiseau Cedex, France

[2]Centre de Météorologie Spatiale de Lannion,
P.O. Box 147, 22302 Lannion, France

[3]Centre National de Recherches Météorologiques / EERM,
42, avenue Coriolis, 31057 Toulouse Cedex, France

1. INTRODUCTION

The 3I (Improved Initialization Inversion) method has been designed for retrieving meteorological or climatic parameters from satellite vertical sounders and first applied to NOAA-7, the third of the Tiros-N operational weather satellites series. The 3I algorithm has already been described in some detail in several publications : Chedin and Scott (1984), Chedin et al. (1985), Scott et al. (1984), Wahiche et al. (1986). This approach to the radiative transfer equation problem directly pertains to pattern recognition theory as it has been shown by Chedin and Scott (1985). Recent developments and newer results have been presented at the last American Meteorological Society meetings held in Williamsburg (USA) in May 1986 : P. Moine et al. (1986), N.A. Scott et al. (1986), J.F. Flobert et al. (1986) and A. Chedin et al. (1986). Reference will be made to these papers throughout this article which main purpose is to review the latest developments that have occurred in the 3I code and to present results recently obtained.

2. RECENT IMPROVEMENTS IN THE CLOUD DETECTION ALGORITHM

Retrieving meteorological parameters (temperature profile, composition, ..) from satellite data requires a method of cloud detection to get the clear radiances used in the inversion of the radiative transfer equation. Alternately, that pollution of infrared radiance by

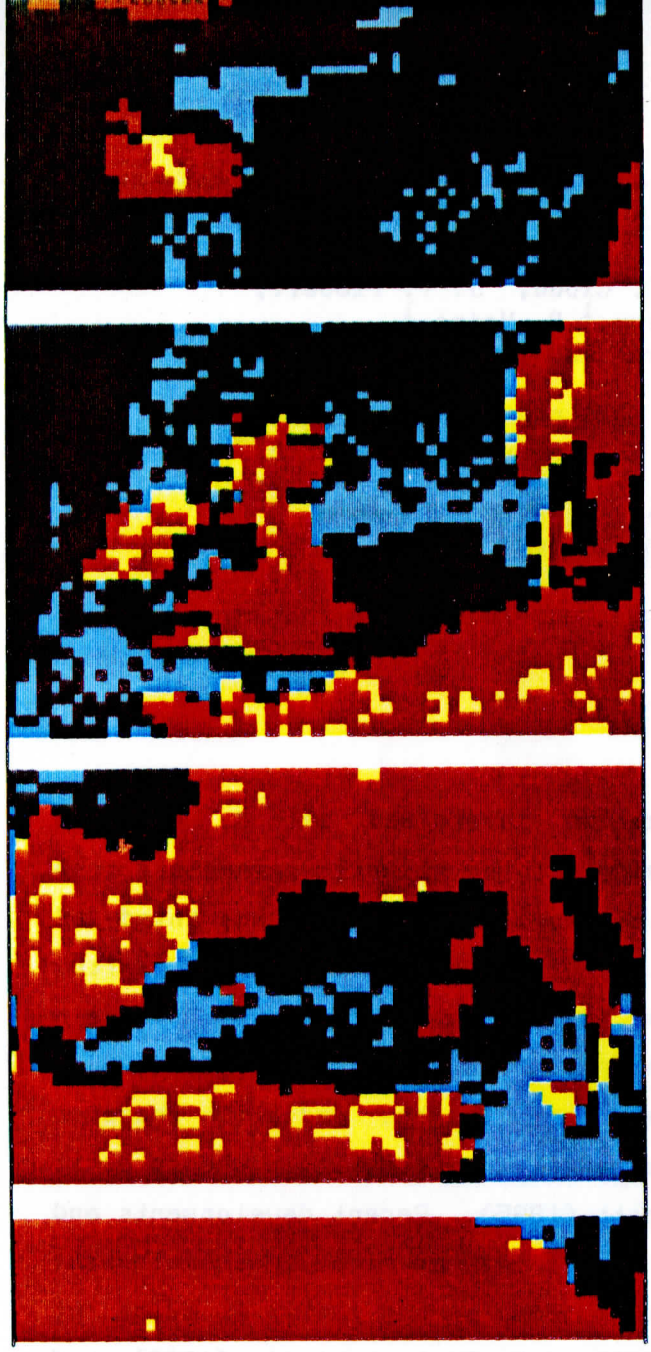

Results of the "old" cloud detection algorithm.

Dark blue : cloudy over sea.
Blue : clear over sea.
Red : cloudy over land.
Yellow : clear over land.

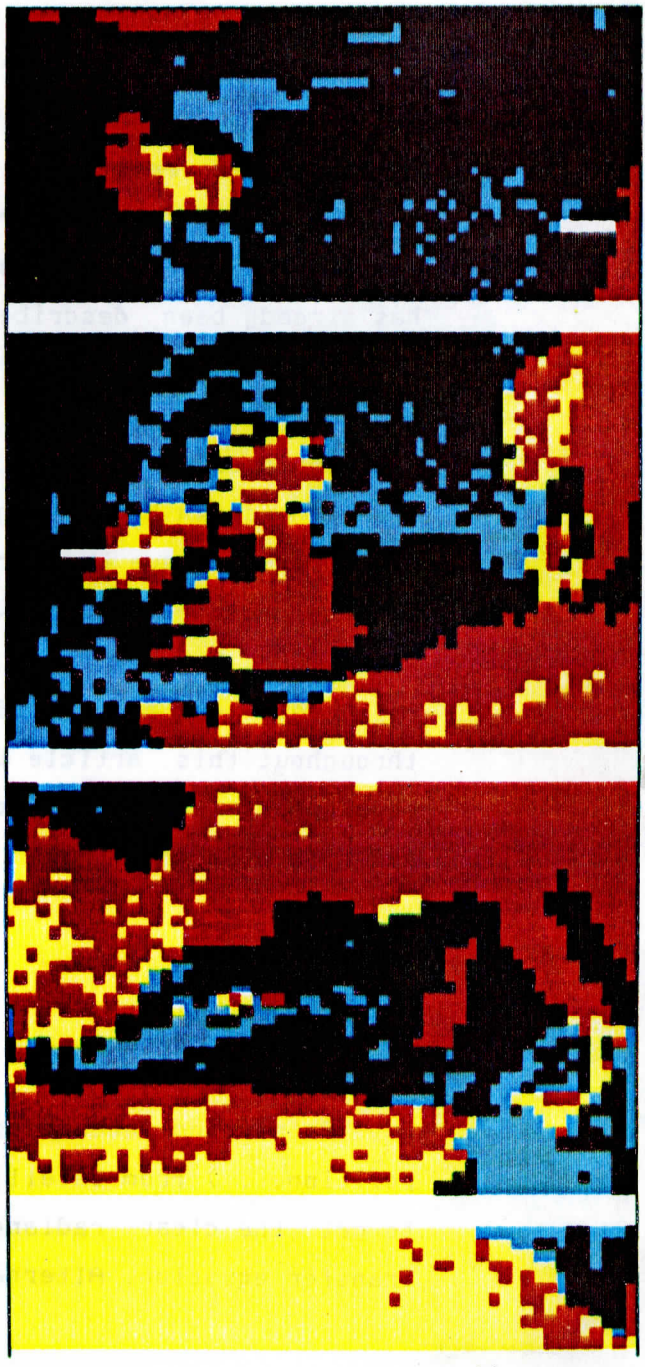

Results of the "new" cloud detection algorithm. Same legend as the figure above.

Figure 2.1

clouds makes it possible to determine some characteristics of the cloud cover, such as cloud top heights or cloud amounts, which are essential parameters in climate models.

In Wahiche et al. (1986), the problems of detecting clouds and of retrieving cloud parameters were approached through the use of the data from the satellites of the Tiros-N series, and more particularly from the two instruments HIRS/2 (19 infrared channels and one visible) and MSU (4 microwave channels). In this paper was presented an algorithm for cloud detection, essentially based upon that described by McMillin and Dean (1982), except that it applied to infrared radiances not corrected for the satellite viewing angle. The advantage of this method is to avoid the noise introduced by the "limb" correction, which is particularly critical under cloud conditions.

The purpose of this section is to review the (sometimes substantial) modifications that have been brought to the cloud detection algorithm as it is described in the reference above (Appendix 1). Seven tests were considered :

2.1 Frozen sea test : no modification

2.2 Adjacent spot tests.

Comparisons between the central spot and each adjacent spot are made only if the difference between the percentage of water in the two fields of view is smaller than 0.3 and if the difference between the mean elevations is smaller than 250 m. The central spot is declared cloudy if at least one of the adjacent spots is such that :

$$Ts_e \text{ (adjacent)} - TS_e \text{ (central)} > \ell$$

where TS_e is the estimated surface temperature and ℓ = 1.5 K over sea and ℓ = 3 K over land. The central spot will remain clear only if at least one adjacent spot is such that :

$$| TS_e \text{ (adjacent)} - TS_e \text{ (central)} | < \ell$$

It must be noticed that new regressions have been designed for estimating the surface temperature. They now exclude channel 10 of HIRS/2 which may be strongly contaminated by the so-called "restrahlen" effect over sand, resulting in an important decrease of the radiation measured.

2.3 Albedo test.

A spot is declared cloudy if A > 15 % over sea and A > 40 % over land. The latter limit has been adapted to desertic areas (sand), but still represents a problem for snow covered terrains (see Section 6).

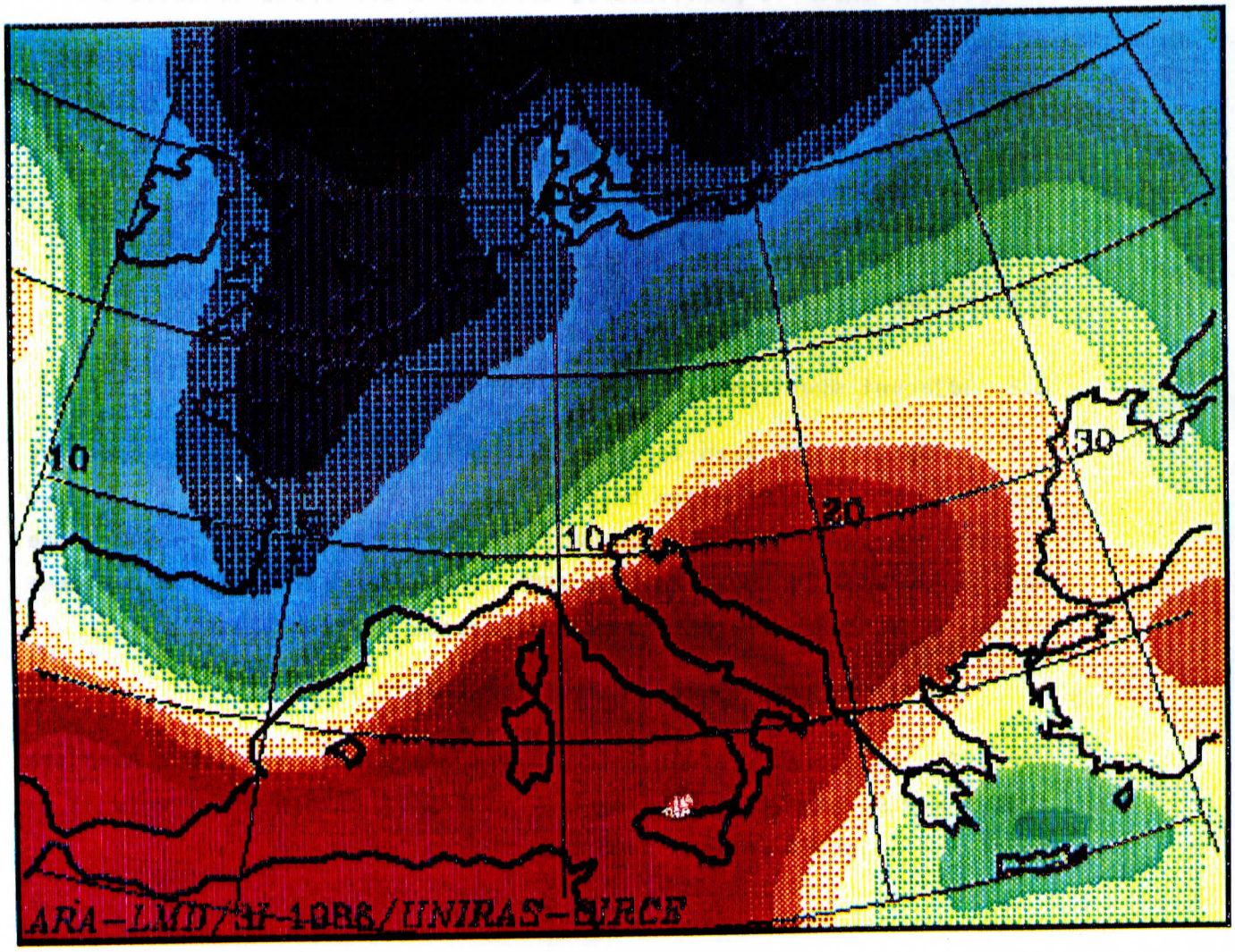

31 retrieved geopotential thicknesses for NOAA-7 observations during ALPEX. March 4, 1982. Orbits nb. 3586, 3587. Dark blue : below 524 dam. Mauve : above 550 dam. Step : 2 dam.

2.4 Window channels test.

No modification to Wahiche et al. (1986) at night. For day time observations, no modification over sea, but the test is skipped if the albedo is greater than 0.2 over land. This modification avoids declaring cloudy snow or sand covered areas.

2.5 Interchannel regression tests.

Five regressions are predicting HIRS/2 or MSU channels from other channels. In the three first regressions, channels HIRS/2 nb. 7, MSU 2 and MSU 3 are predicted from channels 13, 14, 15, 16. In the two last ones, channels MSU 2 and MSU 3 are predicted from channels 3, 4, 5, 6, 7, 8. Regression 1 has been maintained. Regressions 2 and 3 have been suppressed as useless or too sensitive to solar flux contamination. The test limits for regressions 4 and 5 have been made more severe over sea : 1.5 K instead of 2 K.

2.6 Surface temperature test.

No modification.

2.7 Maximum value test.

No modification.

2.8 Hot surface test.

This new test has been introduced over land in the case of hot surfaces. A spot which has been declared cloudy is changed to clear if the HIRS/2 channel 8 brightness temperature is greater or equal to 300 K.

The comparison between the "old" and the "new" cloud detection algorithm is illustrated by Figure 2.1 and is particularly spectacular over desertic areas for which the "old" code was erroneous (restrahlen phenomenon affecting channel 10, albedo limit too low).

3. AUTOMATIC CLASSIFICATION OF AIR MASS TYPES (POLAR, MIDDLE OR TROPICAL) FROM NOAA SATELLITES OBSERVATIONS.

Knowledge of the air mass type observed is essential to retrieval methods, physical as well as statistical, the average profile of temperature being very different in each case (tropical, mid or polar type air).

The major role of a priori information for the satellite retrieval problem is explained by the nature of the observed radiances which integrate the atmospheric thermal structure over relatively thick layers. The principal use of that kind of information is here to specify the initial guess in the "3I" (Improved Initialization Inversion) procedure as accurately as possible through a pattern recognition type approach. We present here a new approach for the searching of the closest element in the TIGR data set, which relies on an automatic classification of the air mass types using the measured brightness temperatures as descriptors. As in the former approach, the brightness temperatures are those of channels quite insensitive to clouds : HIRS/2 channels 1, 2, 3 and MSU channels 2, 3, 4.

In the former approach, the search for the closest element in the TIGR data set was made within the subset characterized (among other parameters such as angles of observations, surface elevations, surface emissivities) by the latitude of the satellite observations : three classes were considered : tropical $< +30°$; $30° <$ mid latitude $< 60°$; polar $> 60°$.

In case of incursions of "foreign" air masses within a given class of latitude (e.g. tropical (or polar) air masses into mid-latitude zones), this "latitude only" characterization of the sub-set turned out to be unsufficient. We thus developed a new approach based upon a more sophisticated clustering of the TIGR data set using the above brightness temperatures as descriptors.

The classification scheme we have adopted, is the "Dynamic Clusters Method" : its purpose is to separate the objects of a given set in disjoint classes - clusters - the elements of which have some given properties in common. It is based upon the notion of "strong patterns". The number of ending clusters which, in this method, has to be specified from the beginning, has been set to 5, in our case, featuring latitudes and seasons (winter, summer). For all the classification conditions - angle, surface pressure , .. - the same noteworthy results have been obtained : despite the pre-imposed number of 5 clusters, only 3 survived, corresponding exactly to the 3 initial groups of latitudes.

Results of this analysis have been applied to NOAA-7 observations over Europe of several relatively complex meteorological situations for which the forecast was particularly poor (see Moine et al., 1986) (Figure 3.1). With the purpose of experimentally validating the classification method described in the above reference, conventional analysis have been superposed on the maps obtained from the algorithm : surface or geopotential thicknesses (1000-500 mb) analyses. Figure 3.1 (top) illustrates these results for NOAA-7 orbit nb. 11664 of 09/27/1983. The map obtained from the classification shows an incursion of tropical air in an area including Spain, France and the south of Great-Britain : this can also be seen on the AVHRR picture (not shown here). On Figure 3.1 (bottom), NOAA-7 orbit nb. 12512, 11/26/1983, the classification gives, from North to South, an intrusion of polar type air mass down to 37°N followed by mid-latitude then tropical type air masses. With a low at 975 mb associated with cold fronts and 90 km/h winds, the analysis corroborates the presence of polar air masses as indicated by our algorithm.

This classification scheme is used to improve the initial guess retrieval procedure : the closest element(s) is searched within the cluster to which the input pattern belongs.

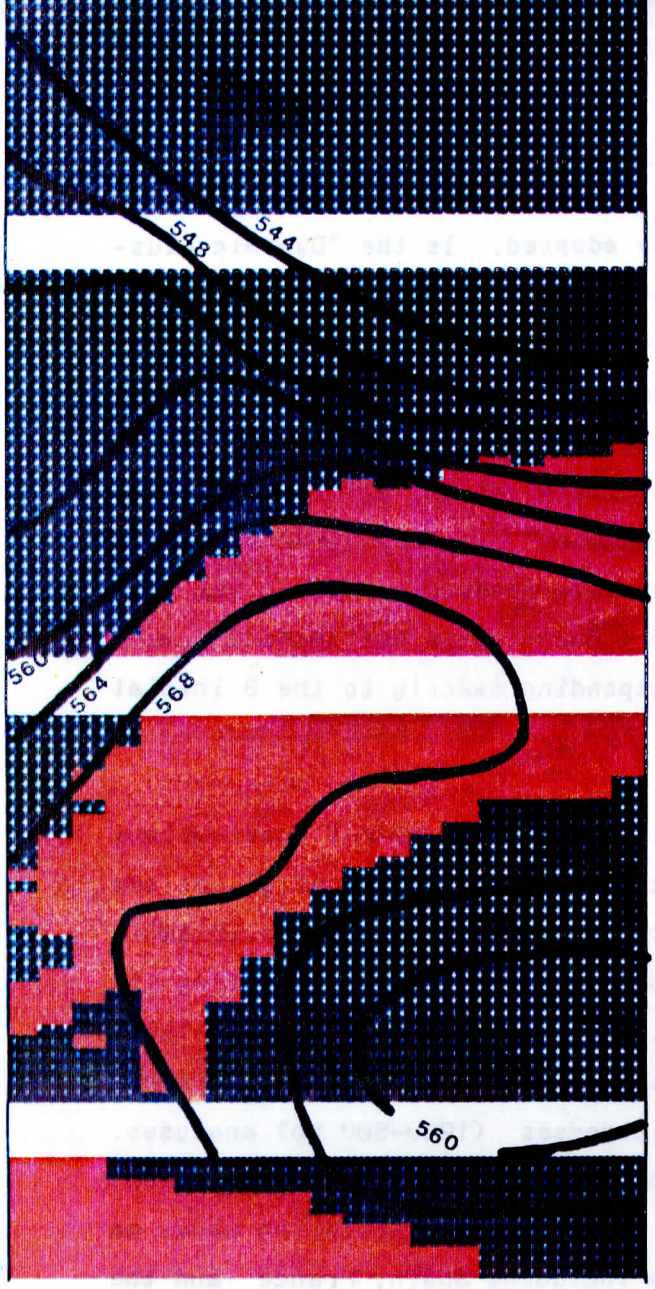

Results of the classification algorithm. NOAA-7 orbit nb. 11664, 27 September 1983, 14:35Z.

Blue : middle latitude type air masses (dark : land)

Red : tropical type air masses (dark : land)

1000-500 mb thicknesses analysis has been superimposed.

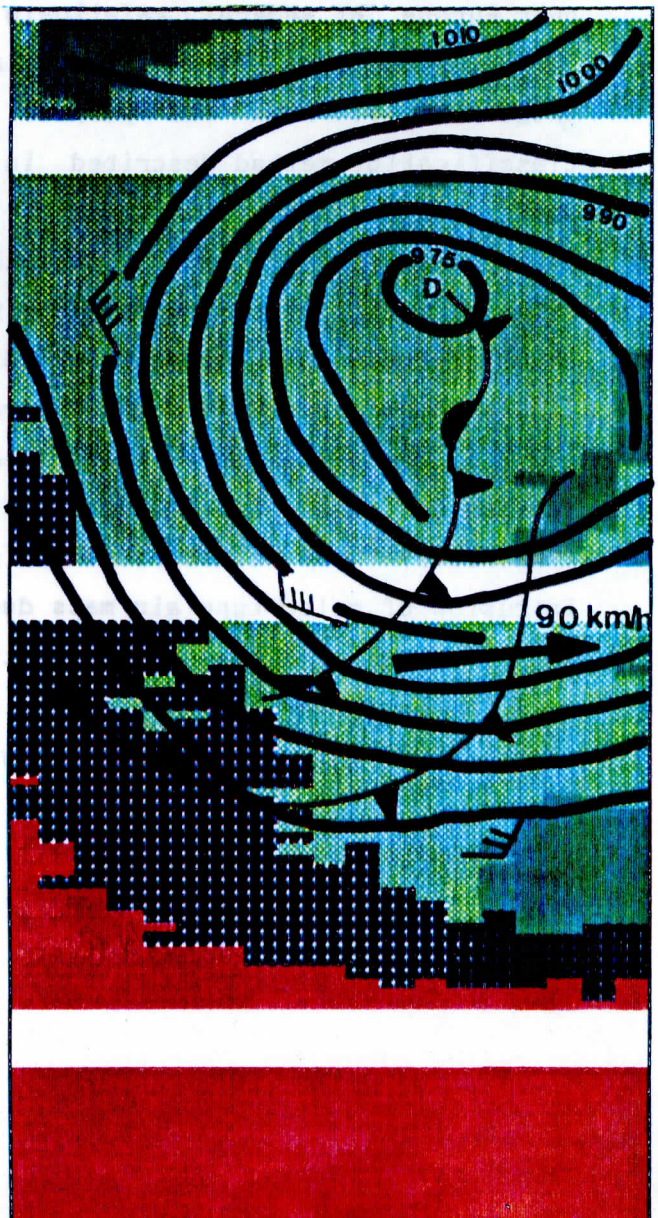

Results of the classification algorithm. NOAA-7 orbit nb. 12512, 26 November 1983, 14:47Z.

Green : polar type air masses.

Blue and Red : see figure above.

The surface analysis of 26 November at 18:00Z has been superimposed.

Figure 3.1

4. RECENT RESULTS IN THE RETRIEVAL OF ATMOSPHERIC OR SURFACE PARAMETERS FROM THE 3I CODE

The 3I retrieval algorithm explicitly takes into account the physical and statistical aspects of the phenomena involved and offers specific answers to the three following essential problems :

a) to enter the inversion process with an initial guess close to the final solution,
b) to acquire clear equivalent radiances through an appropriate cloud clearing algorithm , and
c) correlatively to derive high density retrievals even in case of heavy cloudiness.

Within the frame of the International TOVS Study Conference ITSC, I and II, held in Austria (August 1983, February 1985), the 3I method has already demonstrated its capability to produce accurate temperature soundings (Le Marshall, 1985). These first encouraging results must however be complemented by further systematic comparisons with either colocated radiosoundings data or operational analyses. Moreover, recent improvements brought to the 3I code (introduction of an air-mass classification scheme ; refinement of the initial guess retrieval procedure ; modification of the surface temperature estimation method ; review of the rejection tests, etc..) have led us to reassess its accuracy. This has been done, or is in progress, for several sets of observations, and, in particular for the "bench-mark" set made of NOAA-7 orbits of an ALPEX IOP (March 4-5, 1982).

4.1 Atmospheric temperatures and thicknesses

The basic statistics (mean, rms) generated from the atmospheric soundings are given : a) for temperatures at the standard levels ; b) for geopotential thicknesses obtained from the retrieved temperatures by vertical integration.

The observed sets are either RAOB data or analyses from ECMWF.

The colocations between RAOB and satellite soundings are accepted within the following constraints : (1°x1°) latitude longitude distance ; 2 hours in time ; measurement of temperature available up to 100 mb and of dew point temperature up to 400 mb. The colocations with the analyses are obtained through a spline interpolation procedure at the satellite sounding points.

A two step rejection procedure is applied to the 3I retrievals. The first step consists in analysing the differences between the satellite observations and the first guess solution resulting from the initialization through the TIGR data set. A concept of distance between the two situations, globally or channel by channel, is at the basis of this step. The second step consists of a simple 2-D "horizontal" filtering procedure. For a given pressure level, each retrieval, labeled (i,j), i being the scan line number and j being the box number along a scan line (ranging from 1 to 19 ; see Chedin et al., 1985a), is first compared to the mean of the "adjacent" retrievals comprised in an array (i±3, j±1). If the difference is larger than 1.8K (a value which has been empirically determined on the basis of various trials), the retrieval (i,j) is rejected. A second test concerns the number of available retrievals within the above array : if this number is smaller than 20, the test limit is changed from 1.8K to 1.3K. Each pass is explored twice : i and j increasing and i and j decreasing. As soon as a retrieval has been detected as "bad", it is no longer included in the process. Results are shown on Figure 4.1 and Table 4.1 (statistics in temperature) and Figure 4.2 (statistics in geopotential thicknesses).

Figure 4.1 is for the ALPEX orbit (daytime) nb. 3586 of March 4, 1982. For the standard levels between 1000 mb and 70 mb, this figure gives the biases and r.m.s. errors : (A) without filtering ; (B) with the 2-D filtering technique ; (C) no filtering, but rejection of any retrieval such that the difference between the retrieved temperature at a given pressure level and the corresponding ECMWF's analysis value is larger (smaller) than the mean over the sample plus (minus) two times the standard deviation (2σ procedure). The initial number of retrievals, prior to any rejection is 1236 giving a percentage of rejections of about 5 % for the case (B);

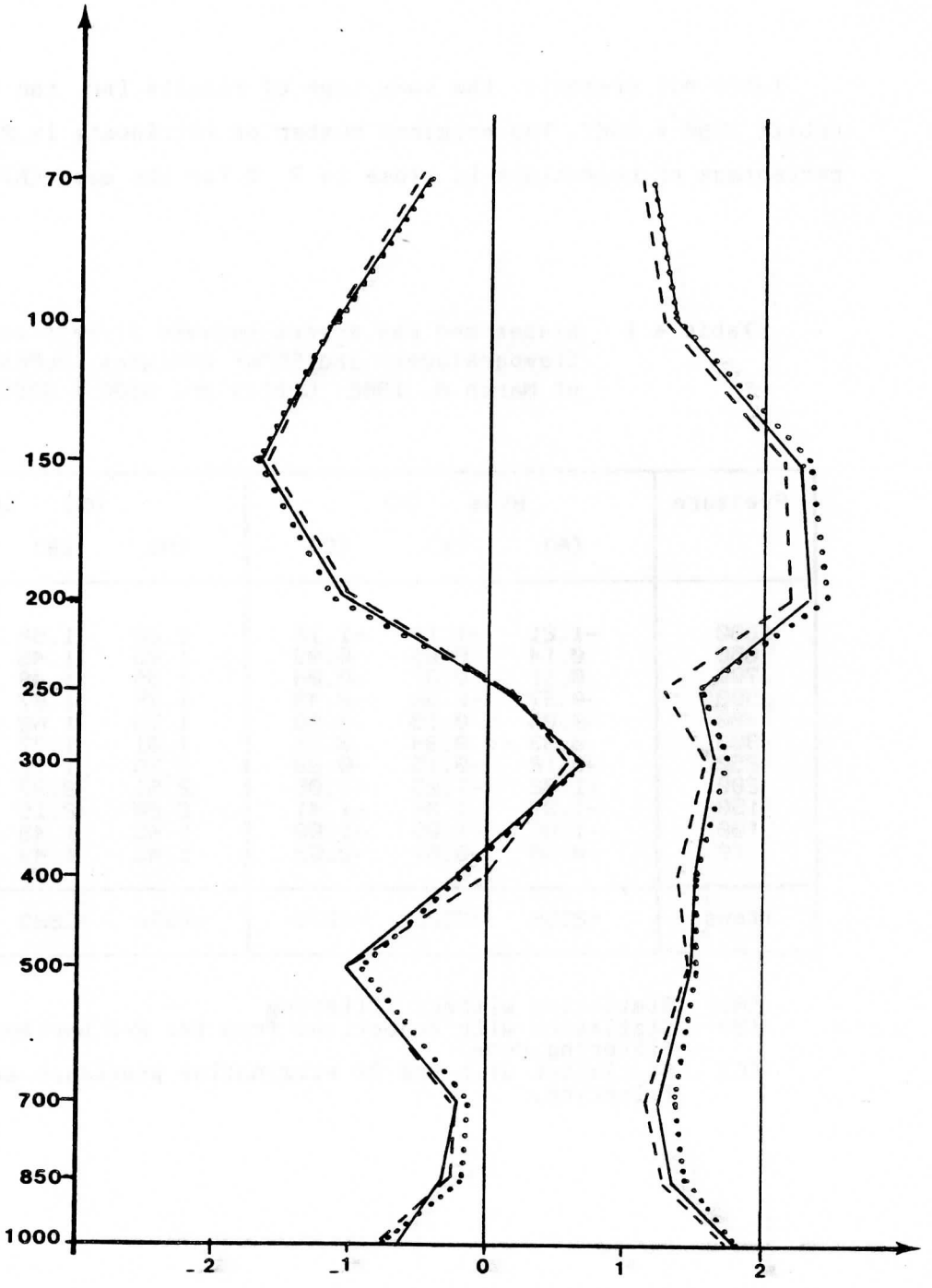

Figure 4.1 Biases and rms errors between the 3I retrievals and the ECMWF analysis.
ALPEX IOP ; March 4, 1982 ; orbit nb. 3586.
..... : no rejection ; ——— : 2-D filtering ;
------ : 2σ procedure.

Table 4.1 presents the same type of results for the two day-time orbits 3586 + 3587. The original number of retrievals is 2393 and the percentage of rejections is close to 7 % for the case (B).

Table 4.1 Biases and rms errors between 31 retrievals (temperatures) and ECMWF analyses. ALPEX IOP of March 4, 1982. Orbits nb. 3586 + 3587.

Pressure	Bias (K)			RMS (K)		
	(A)	(B)	(C)	(A)	(B)	(C)
1000	-1.21	-1.14	-1.12	2.02	1.92	1.90
850	0.14	0.05	0.03	1.65	1.45	1.33
700	0.11	0.07	-0.04	1.59	1.48	1.33
500	-0.37	-0.36	-0.43	1.75	1.67	1.58
400	-0.24	-0.19	-0.09	1.79	1.69	1.52
300	0.33	0.34	0.34	1.81	1.77	1.57
250	-0.12	-0.15	-0.23	1.75	1.71	1.48
200	-1.02	-1.03	-1.05	2.51	2.37	2.29
150	-1.37	-1.36	-1.41	2.20	2.15	2.06
100	-1.06	-1.05	-1.08	1.48	1.48	1.43
70	-0.58	-0.57	-0.63	1.49	1.49	1.38
Items	≈2386	≈2229	≈2270	≈2386	≈2229	≈2270

(A) Statistics without filtering
(B) Statistics with rejections from the 2-D horizontal filtering code.
(C) Statistics with the 2σ elimination procedure and no filtering.

Figure 4.2 illustrates the results for the thicknesses (statistics for the 1000-500 mb : bias : -1.02 dam ; rms = 2.38 dam ; std. dev. = 2.15 dam).

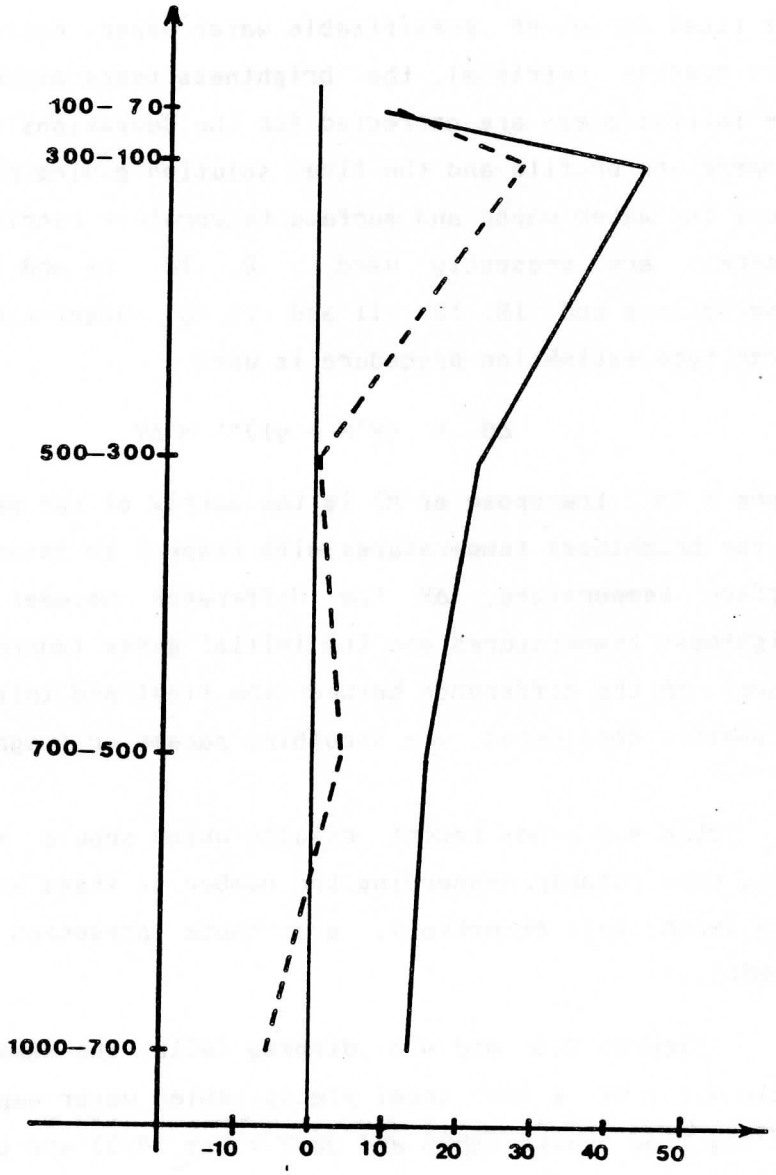

Figure 4.2 Biases and rms errors between 3I retrievals (thicknesses) and ECMWF analyses. ALPEX IOP, March 4, 1982 ; orbits nb. 3586 + 3587.

4.2 Water vapor fields and surface temperature

Retrievals of water vapor amounts are made for three layers delimited by the levels 1000 mb, 800 mb, 500 mb and 300 mb in addition to the total amount of precipitable water vapor. Following the temperature profile retrieval, the brightness temperatures associated with the initial guess are corrected for the deviations between the initial temperature profile and the final solution giving rise to the initial guess for water vapor and surface temperature retrievals. Four HIRS/2 channels are presently used : 8, 10, 11 and 12 for the day-time observations and 18, 10, 11 and 12 for night-time observations. A ridge type estimation procedure is used :

$$\Delta\beta = (X'X + \gamma I)^{-1} X'\Delta Y$$

where X (X', transpose of X) is the matrix of the partial derivatives of the brightness temperatures with respect to relative humidities and surface temperature, ΔY the difference between observed (cleared) brightness temperatures and the initial guess (corrected as explained above), $\Delta\beta$ the difference between the final and initial values of the parameters considered, γ a smoothing parameter (Lagrangian multiplier)

Table 4.2 gives recent results which show a significant improvement, particularly concerning the number of items entering the statistics (much less rejection), over those presented in Chedin et al. (1985b).

Figures 4.3 and 4.4 display (with the same limitation as for Table 4.2 : $N\varepsilon < 30\%$) total precipitable water vapor fields for the two day time orbits (3586 and 3587 : Fig. 4.3) and the two night time orbits (3594 and 3595 : Fig. 4.4).

Surface temperatures are physically retrieved simultaneously with water vapor. Comparisons have been made with in-situ measurements (ships of opportunity) for orbits 3587 (day) and 3595 (night) on one hand, and with AVHRR retrieved SST's for orbit 3587, on the other hand. Results are given in Table 4.3 for clear situations.

Table 4.2 3I retrieved humidities versus radiosonde data. Clear and partially cloudy areas (up to Nε ≤ 30%) are considered. March 4-5, 1982 ; NOAA-7 observations over Europe (4 passes).

Layer (mb)	Bias	Rms	Nb. of items
300 - 500 [1]	-0.03	0.21	79
500 - 800 [1]	-0.04	0.19	81
800 - 1000 [1]	-0.03	0.18	79
U_{TOT} [2]	0.05	0.20	78

[1] Relative humidity
[2] Total content in g cm^{-2}
Mean total content of the sample : 0.85 g cm^{-2}

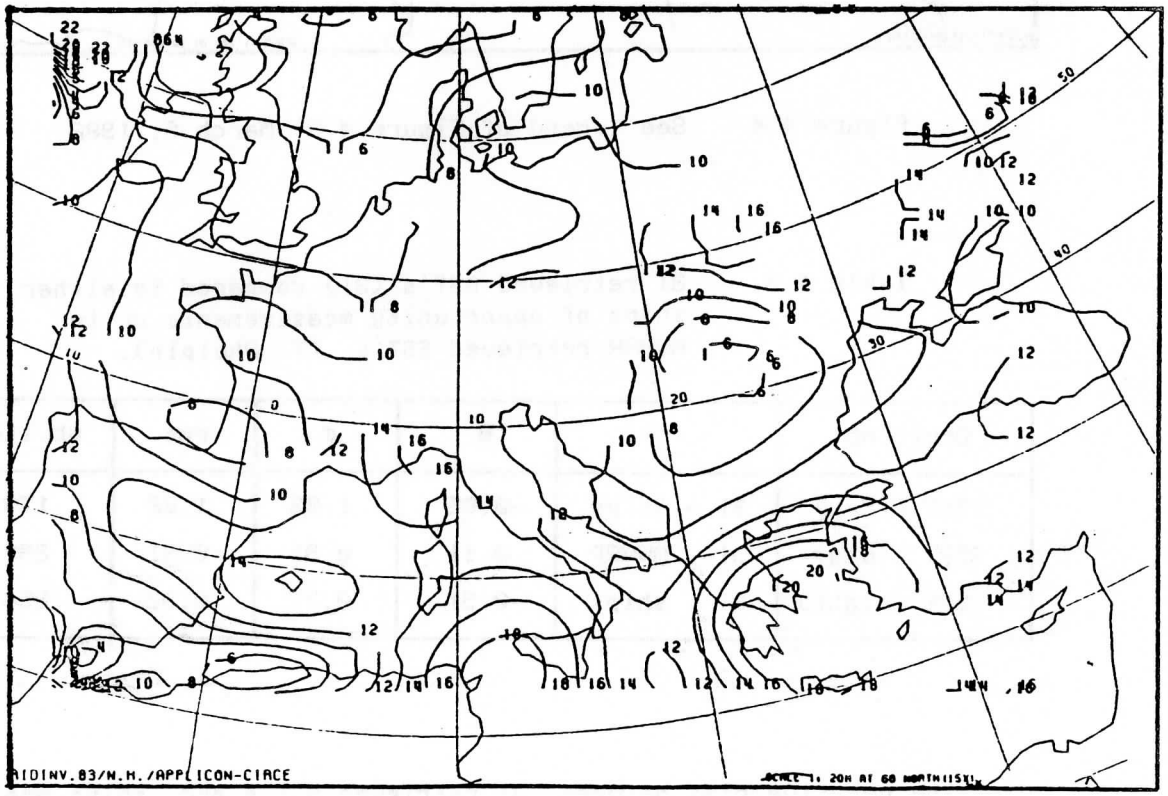

Figure 4.3 3I retrieved total precipitable water vapor above 1000 mb in mm for clear and partially cloudy areas (Nε ≤ 30 %). March 4, 1982.

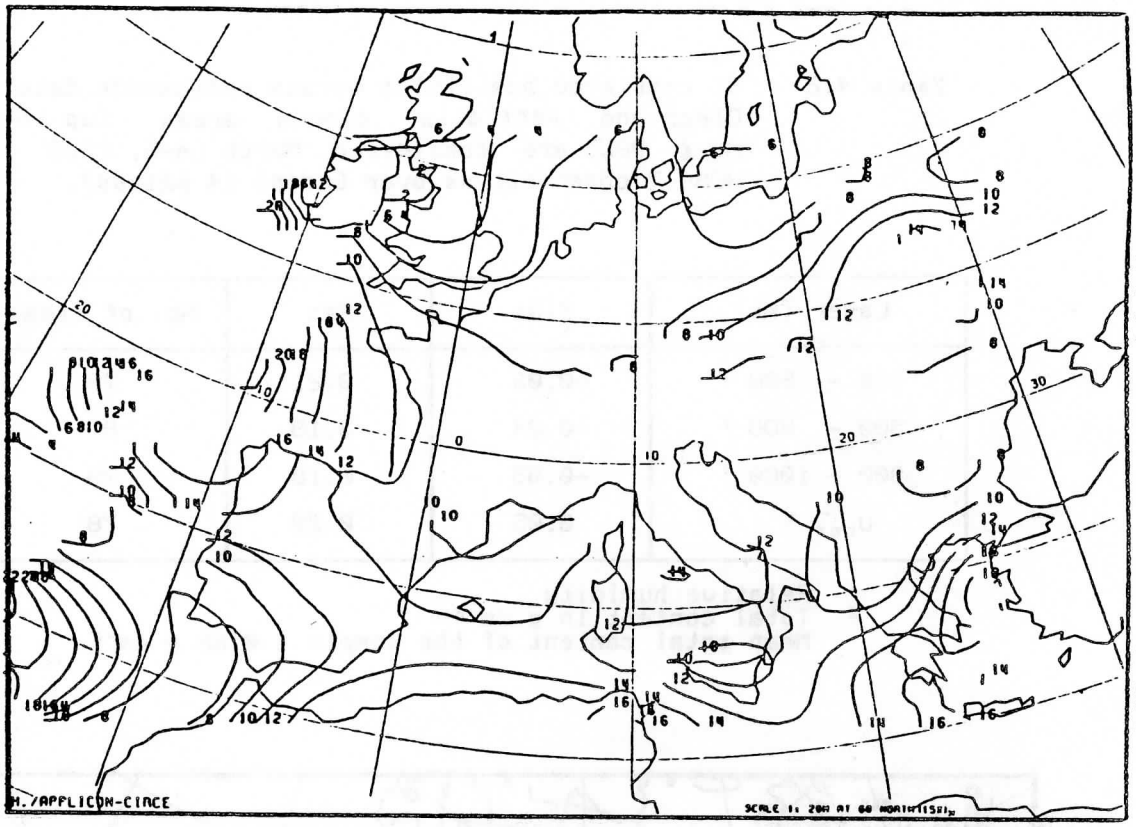

Figure 4.4 See legend of Figure 4.3. March 5, 1982.

Table 4.3 3I retrieved SST's (3I) compared to either ships of opportunity measurements or to AVHRR retrieved SST's (T. Phulpin).

Orbit nb.		$\bar{m}$	σ	rms	nb.items
3587 (day)	3I - ships	-0.65	1.03	1.22	173
3587 (day)	3I - AVHRR	0.11	0.91	0.91	289
3595 (night)	3I - ships	-0.51	0.77	0.92	256

The negative bias between 3I retrieved SST's and ships measurements has also been observed by other groups working on the same situation. Quantatively, these results are in agreement with other more extensive and less local (space and time) studies. TOVS SST's should probably be improved when HIRS-2 is equipped with a split window capability (NOAA-I).

5. EXTENSION OF THE RETRIEVALS TO THE UPPER STRATOSPHERE : PROCESSING OF THE SSU DATA

Rocket soundings and meteorolological or research satellites are the main sources of temperature data in the upper stratosphere. Rocket sounding give measurements of pressure and temperature up to about 80 km and allow good description of planetary waves perturbations and of sudden events like the stratospheric warmings to be derived. Temperature profiles, up to about 90 km, may also be derived from lidar measurements of the atmospheric density.

Satellite soundings instruments (aboard SME, NIMBUS, the TIROS-N series) produce atmospheric temperatures retrieved from radiance measurements in the 15 μm spectral region. On board the Tiros-N series, the Stratospheric Sounding Unit (SSU) allows retrieval of vertical temperature profiles to be accurately done between approximately 30 and 50 km. A twice daily global coverage is obtained from one platform.

Retrieving temperature in this altitude range is somewhat simpler than in the troposphere due to the absence of clouds, the extremely low amount of water vapor and the absence of surface contamination. This makes a purely statistical retrieval approach much more attractive than in the troposphere or lower stratosphere. This is the way we have chosen for processing the SSU data.

To establish the relation between satellite observations and atmospheric temperatures (or thicknesses), we have made use of data sets provided to us by the British Met. Office in Bracknell. Several days of observations have been selected for both NOAA-7 and NOAA-8 for the whole northern hemisphere. The predictors are the brightness temperatures of channels 1, 2, 3 of SSU ; 1, 2, 3 of HIRS/2 and 4 of MSU. The predictands are the geopotential thicknesses for the layers 100-20 mb, 100-10 mb, 100-5 mb and 100-1 mb issuing from the Bracknell's analysis at a relatively low spatial resolution (2 x 2 SSU spots ; see Figure 5.1).

The regressions allow the predictands to be accurately reproduced : no biases and the standard deviations are less than 0.3 % (in percentage) for tropical and mid-latitudes, less than 0.5 % for polar latitudes except for the layer 5-2 mb (obtained from 100-5 and 100-2) where it amounts to a maximum of 0.75 %.

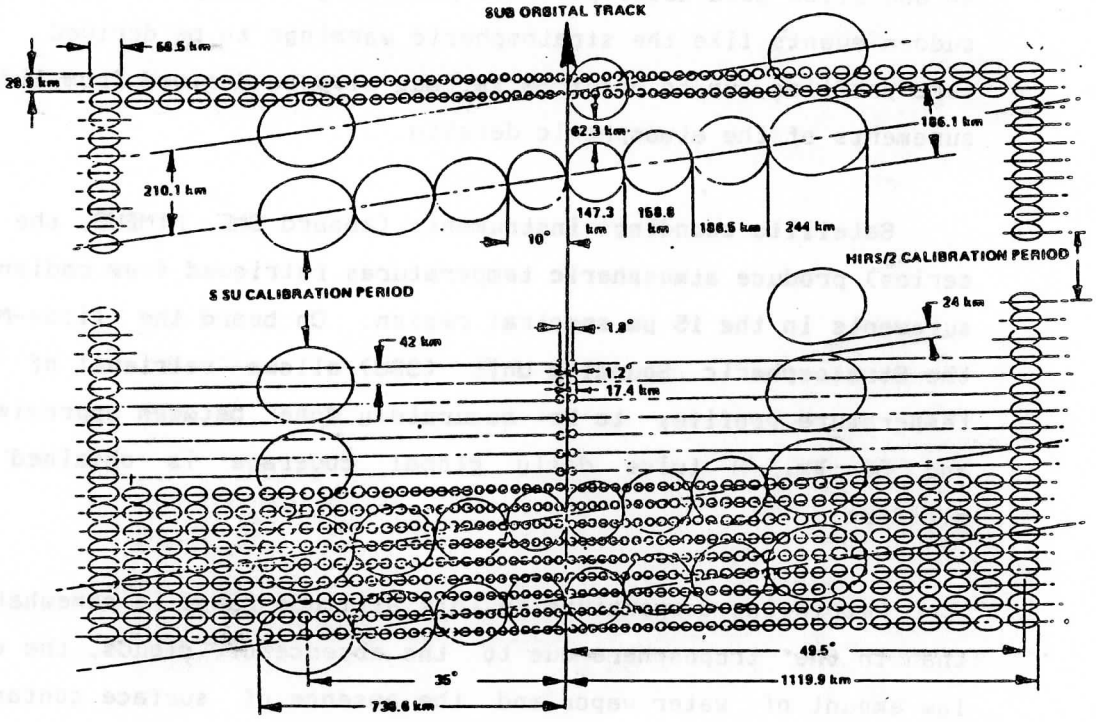

Figure 5.1 HIRS/2 and SSU scan patterns projected on earth.

5.1 Application to European scenes.

The statistical scheme described above has been applied to several passes of NOAA-7 over Europe, between September and December 1983. Figures 5.2 to 5.4 show the results obtained for the two successive passes on December 28 at 14:17Z and 15:58Z. They illustrate the thickness charts for the layer 20-10 mb (Figure 5.2), 10-5 mb (Figure 5.3) and 5-2 mb (Figure 5.4). Holes in those charts are due to the

Figure 5.5

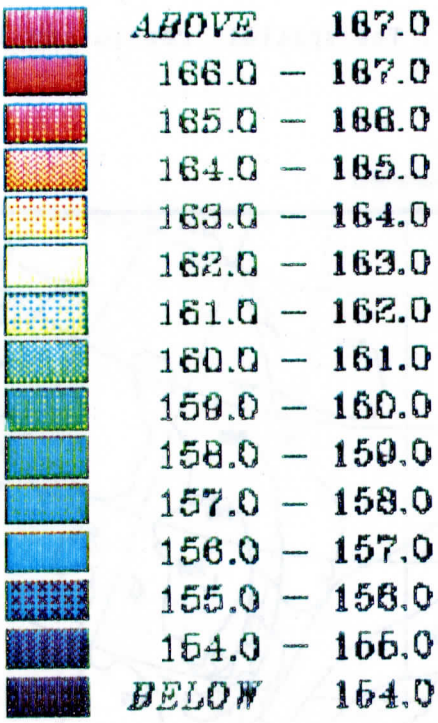

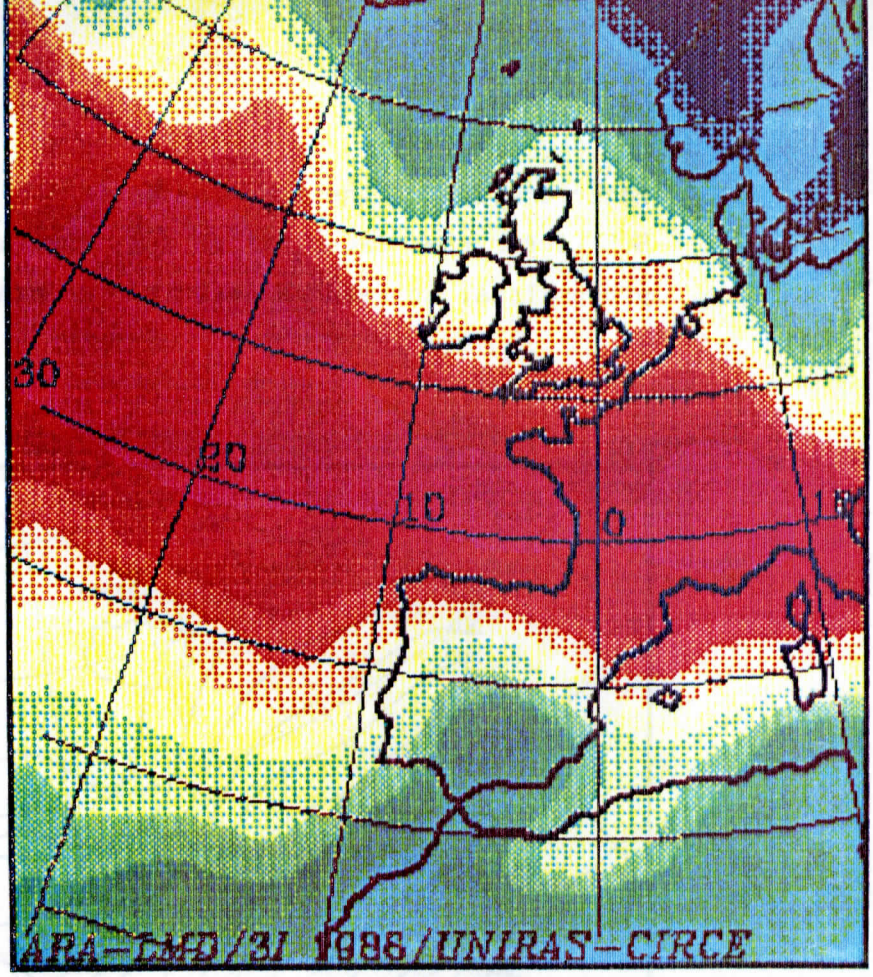

$TEMP(^{\circ}C)$

Figure 5.6

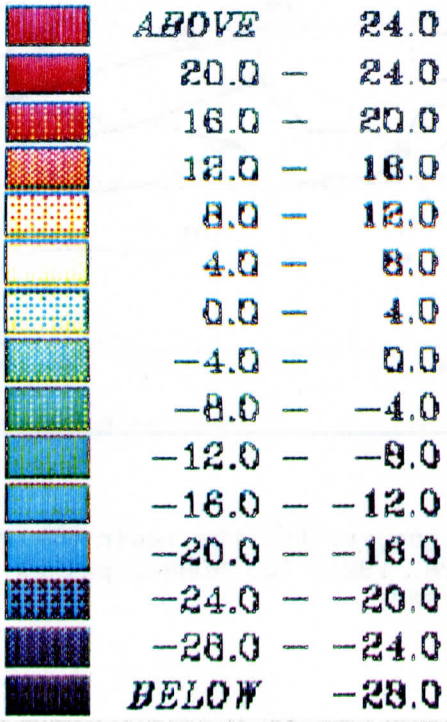

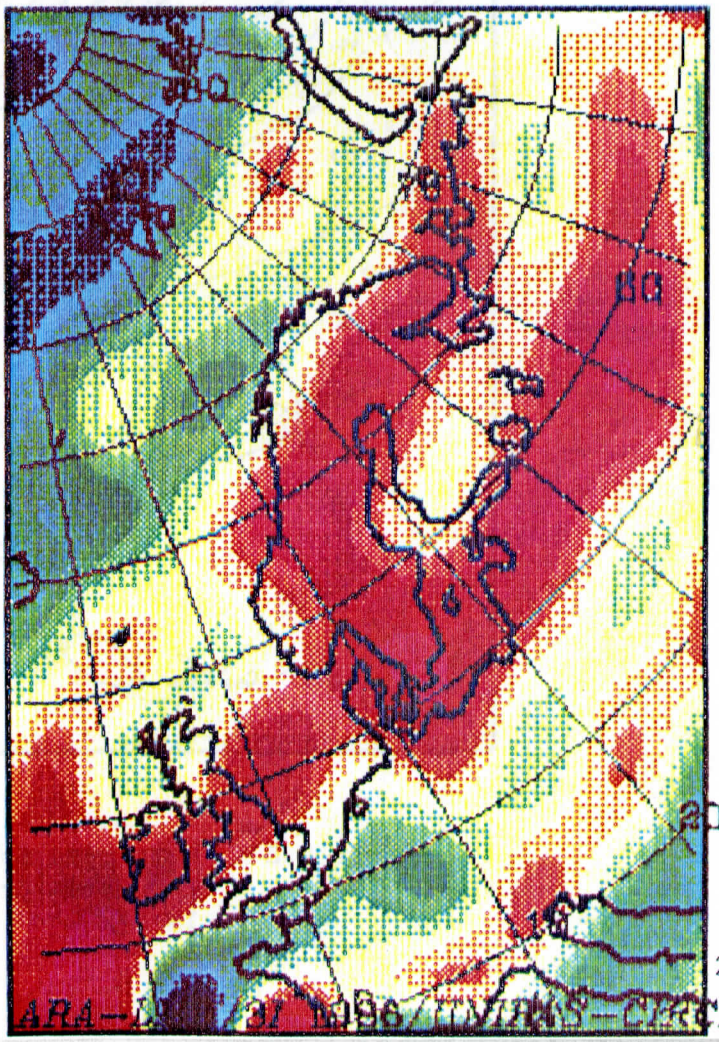

reduced width of the scanning pattern of SSU (see Figure 5.1). Figure 5.5 is for the layer 2-1 mb and displays the air density (inversely proportional to temperature) in 10^5 g/dm^3. The spatial resolution is

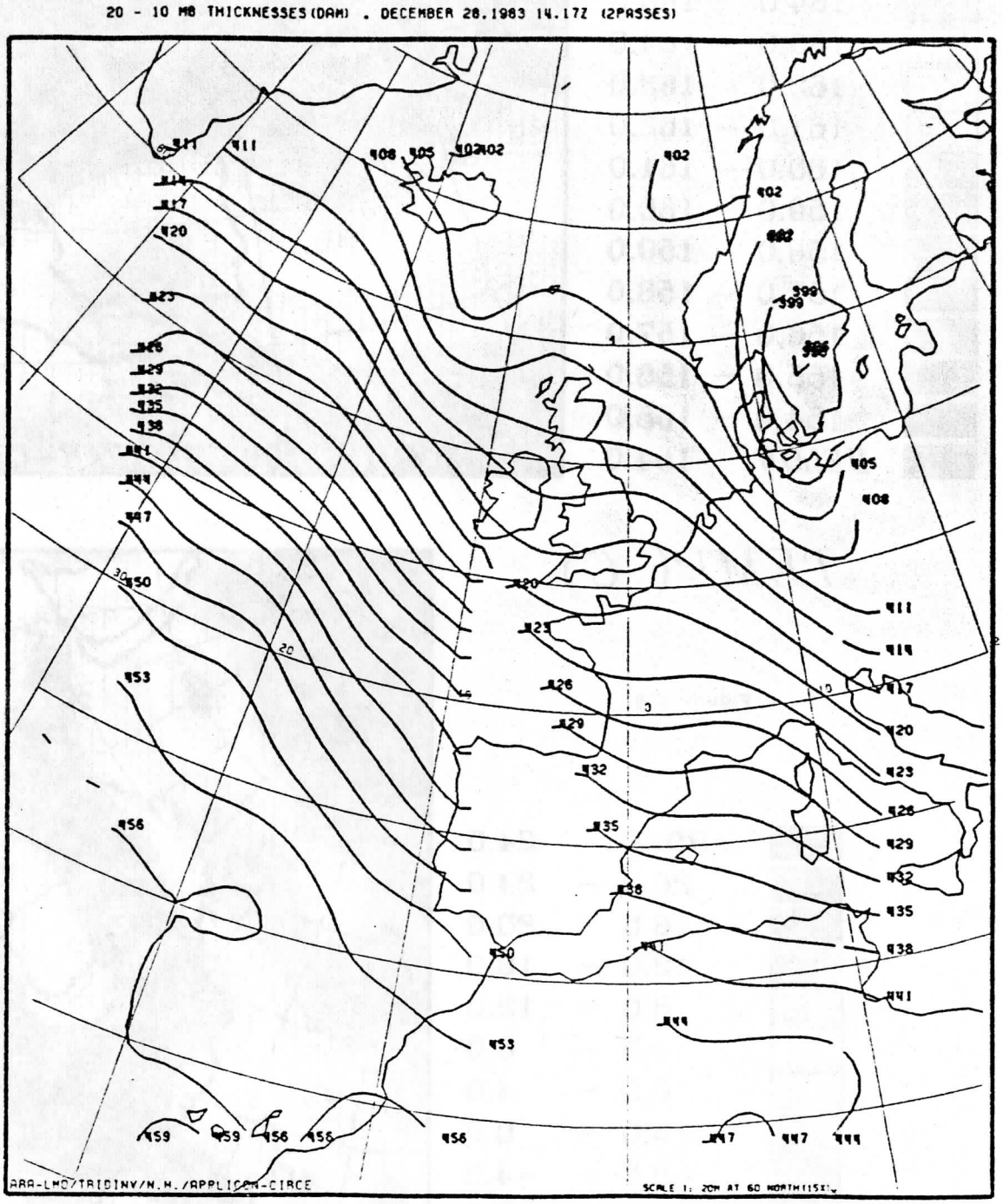

Figure 5.2 Retrieved thicknesses for the layer 20-10 mb for December 28, 1983. Two NOAA-7 passes at 14:17Z and 15:58Z.

that of the 31 boxes : 100 x 100 km², a number close to the SSU resolution. The figures show a rather disturbed situation for the highest layers, with strong undulations of the iso-lines. At the

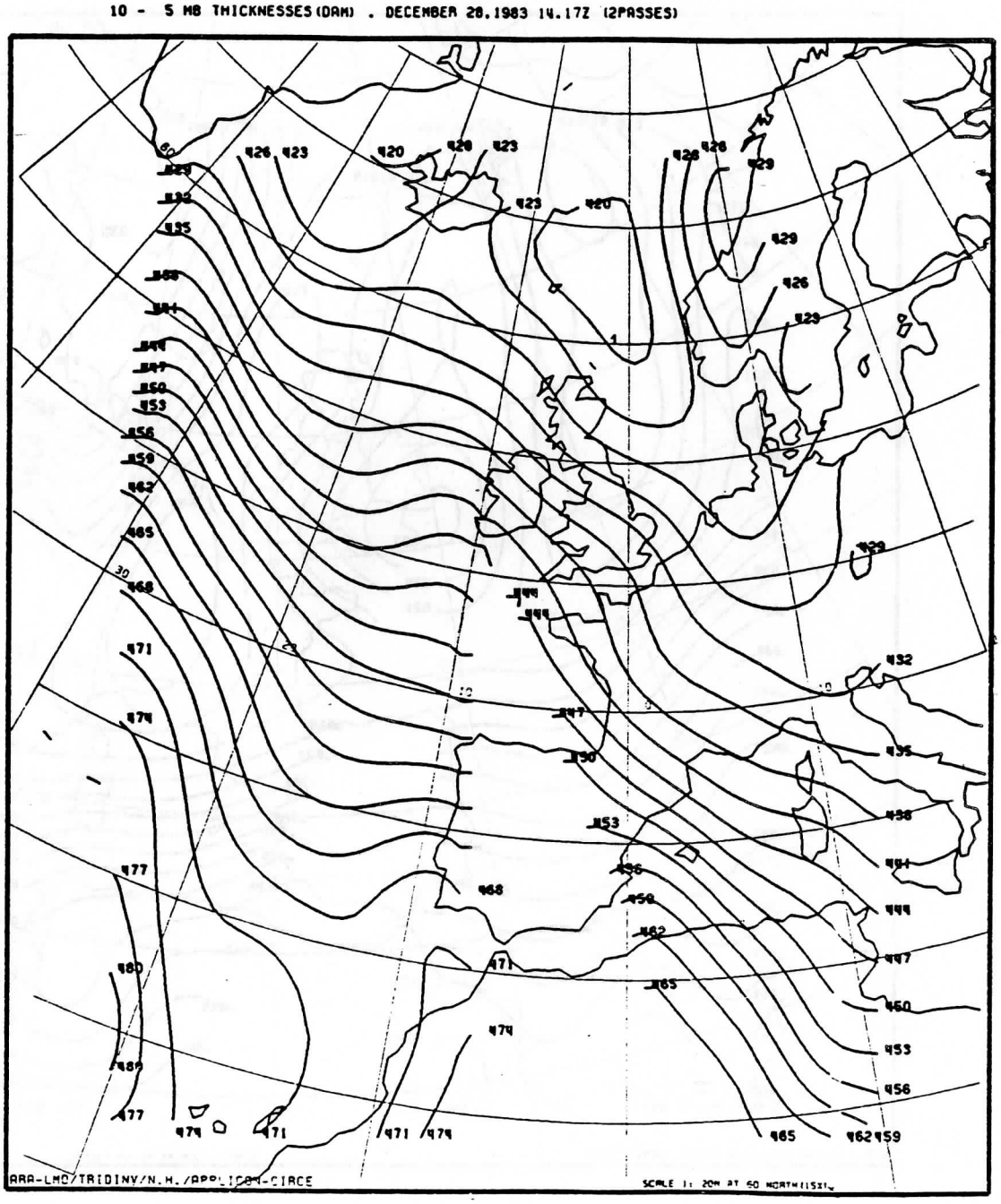

Figure 5.3 See legend of Figure 5.2. Layer 10-5 mb.

latitude of France, a cold area is apparent, extending northwest over Atlantic. For the two lowest layers, the situation is quieter with temperatures increasing from north to south.

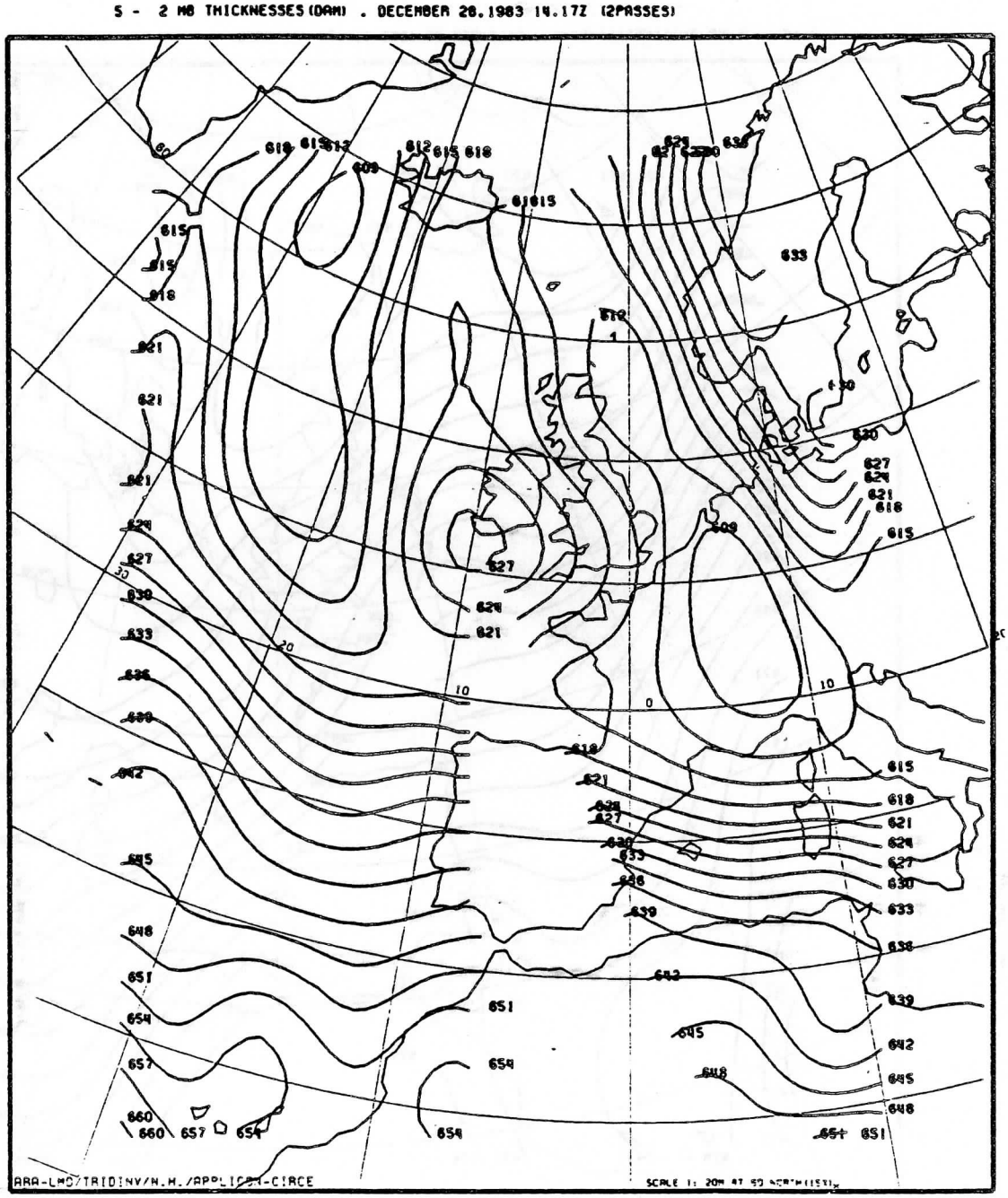

Figure 5.4 See legend of Figure 5.2. Layer 5-2 mb.

5.2 Application to a situation of "sudden stratospheric warming"

Applying the model to a rather unusual situation of strong sudden stratospheric warming (which may exceed an amplitude of 50°C) is a good way of testing its ability to retrieve out-of-statistics situations.

The major stratospheric warming of February 22-23, 1984 over Norway has been extensively studied during and after the WINE (Winter In Northern Europe) campaign. Corresponding NOAA-8 observations were provided to us by the British Met. Office (Bracknell). The most spectacular results are those concerning the highest layer, between 2 and 1 mb and are illustrated by Figure 5.6 which displays the mean layer temperatures in °C. Temperatures of 24°C are observed which are to be compared to a normal value of -30°C at the latitudes of Norway, for example. The warming also strongly affects lower layers. These results are in good agreement with the analysis, made by the Stratospheric Group in Berlin (K. Petzoldt ; private communication, 1986), which shows a strong warming on February 23rd over Andoya (north of Norway). Taking into account the fact that our study concerns the 22nd of February and that the warming was moving westward, the two analyses are in good concordance. The relatively high spatial resolution of the present analysis brings into evidence numerous interesting mesoscale features, sometimes curiously correlated (at least apparently) to features corresponding to much lower layers (see P. Moine, Thesis, for more details).

Very preliminary comparisons between SSU retrievals and either rocket or lidar soundings have shown a small negative bias (SSU minus sounding) of the order of 1-2°C and a standard deviation of 2-3°C.

Coupled with the 3I results, the SSU retrieved temperature profiles provide a continuous description of the atmospheric thermal structure from the surface to about 50 km.

6. 3I OVER POLAR LATITUDES THROUGH THE MIZEX (Marginal Ice Zone Experiment) CAMPAIGN

From May to August 1984, an international experiment, MIZEX, has been conducted in the Fram Strait, an area between Greenland and Spitzbard, aiming at a better understanding of the processes that govern the advance and retreat of the ice margin. A multidisciplinary team of over 200 scientists and technicians was supported by seven research ships, eight meteorological and remote sensing aircrafts, four helicopters. Numerous in-situ data are thus available in conjunction with satellite observations from NOAA-7 and NOAA-8, which may be used for studies of the interactions between sea ice and atmosphere.

As a starting point, three days of the MIZEX campaign have been selected : July 1st and 2nd, and August 5th, 1984, and NOAA-7 observations obtained from the Chr. Michelsen Institute (Norway). HIRS/2 and MSU data were calibrated and navigated by CMS Lannion.

Application of 3I to these latitudes requires that some modifications be made to the code, particularly concerning the cloud detection algorithm ; discrimination between sea ice and low clouds is a well known problem. We are approaching it through the coupling between HIRS/2 and MSU (mostly the window channel MSU-1) on the one hand and between HIRS/2 and AVHRR on the other. Knowledge of precise surface conditions from the MIZEX in-situ data base is of great importance for the validation of the algorithms retained.

Very preliminary results are presented on Figures 6.1 and 6.2. Figure 6.1 is a reproduction of AVHRR, channel 2, observations for August 5, 1984 (NOAA-7). Greenland is at the bottom left of the figure. For the same scene, Figure 6.2 displays the 3I retrieved 1000-500 mb thickness chart. Quantitatively, the numbers compare well with those of the European Meteorological Bulletin which, however,are much smoother than the 3I contours.

Figure 6.1 AVHRR channel 2 picture over Fram Strait, August 5, 1984 ; 12:38Z Bottom left : the Greenland coast.

This work will continue with the analysis of additional scenes from MIZEX and with NOAA-9 observations from the new international programme ARCTEMIZ (Arctic Experiment on Marginal Ice Zones).

This research is conducted in close cooperation with Laboratoire d'Océanographie Dynamique et Climatologie (Dr. J.C. Gascard) and with Laboratoire d'Optique Atmosphérique in Lille (Dr. C. Kergomard).

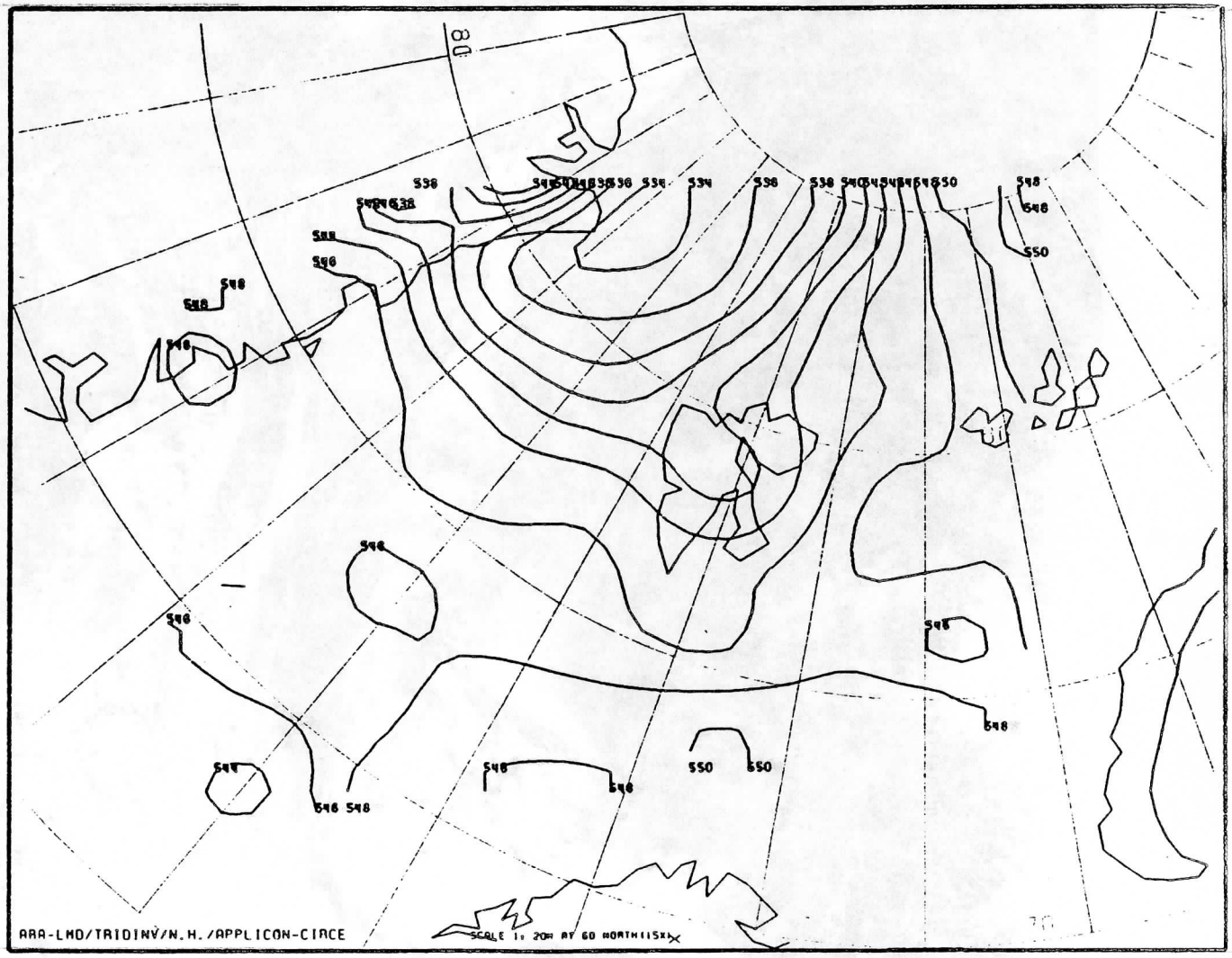

Figure 6.2 3I retrieved 1000-500 mb thicknesses for August 5, 1984 ; NOAA-7 observations over Fram Strait. Notice the low, east of Greenland.

7. PRELIMINARY RESULTS OF THE PROCESSING OF NOAA-7 OBSERVATIONS OVER EUROPE DURING ALPEX (March 16-17, 1982).

Within the frame of the activities of the International TOVS Working Group of the IRC (International Radiation Commission), NOAA-7 observations over Europe, during the IOP (Intensive Observing Period) of the international campaign ALPEX (ALPine EXperiment) of March 4-5, 1982, have served as a reference for intercomparing the results of retrieval algorithms from various groups. NOAA-8 observations over the Central United States and Gulf of Mexico have then been added to this "bench-mark", for an interesting pre-tornadic situation (June 7, 1984). A new series of NOAA-7 observations during ALPEX could possibly be of interest to the TOVS group, those of March 16-17, 1982, with an interesting low, north of Great-Britian.

igure 7.1 AVHRR, channels 2 and 3 pictures for March 1982. 3:00Z. NOAA-7

Figures 7.1 to 7.6 display the results we have obtained for three situations : orbit 3557 of March 16 at 14:43Z ; orbits 3763-3764 of March 17 at 3:00Z and orbit 3771 of March 17 at 14:32Z.

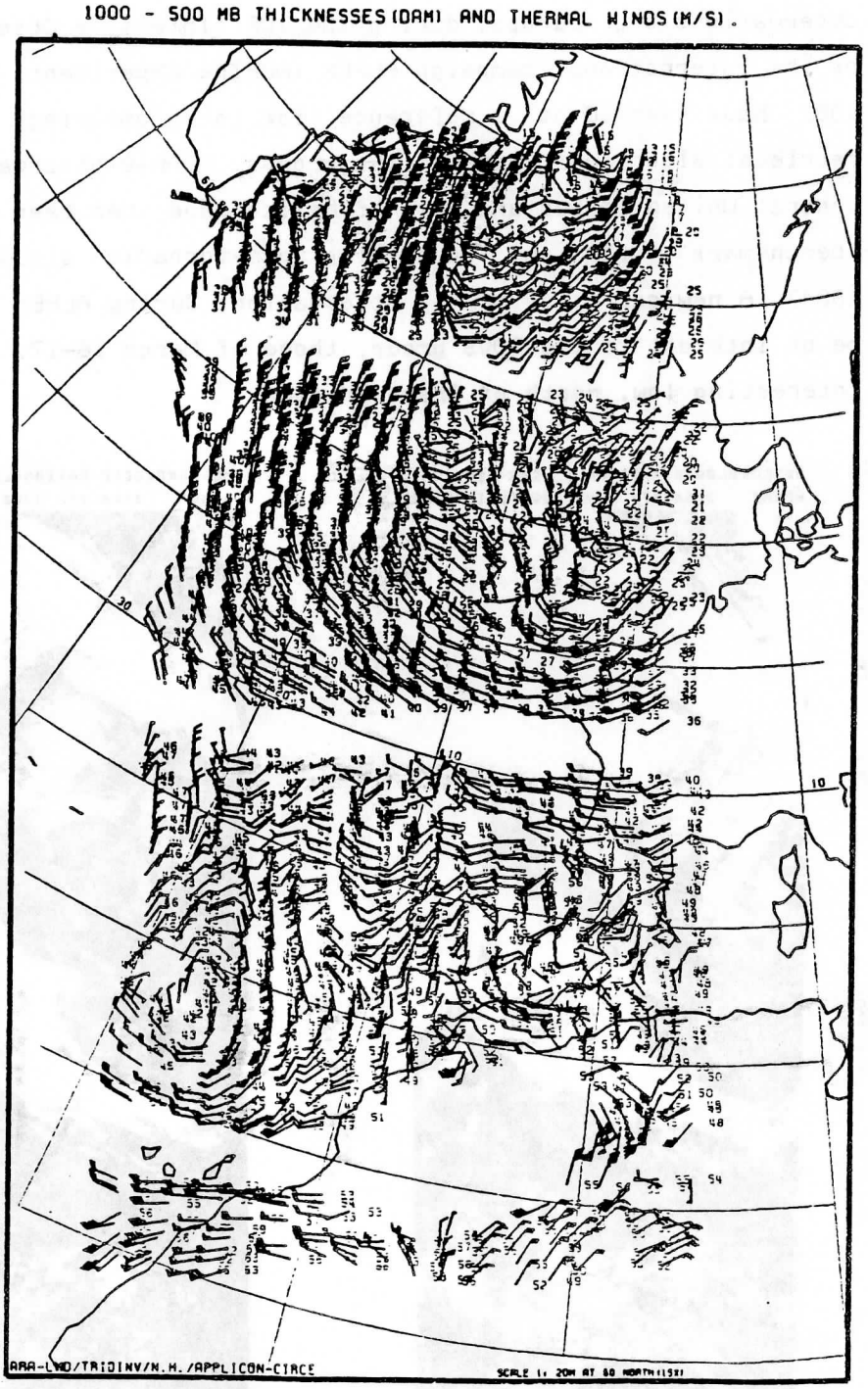

Figure 7.2 1000-500 mb thermal winds retrieved from the 3I algorithm. March 16, 182. 14:43Z. NOAA-7.

1000 - 500 MB THICKNESSES(DAM).

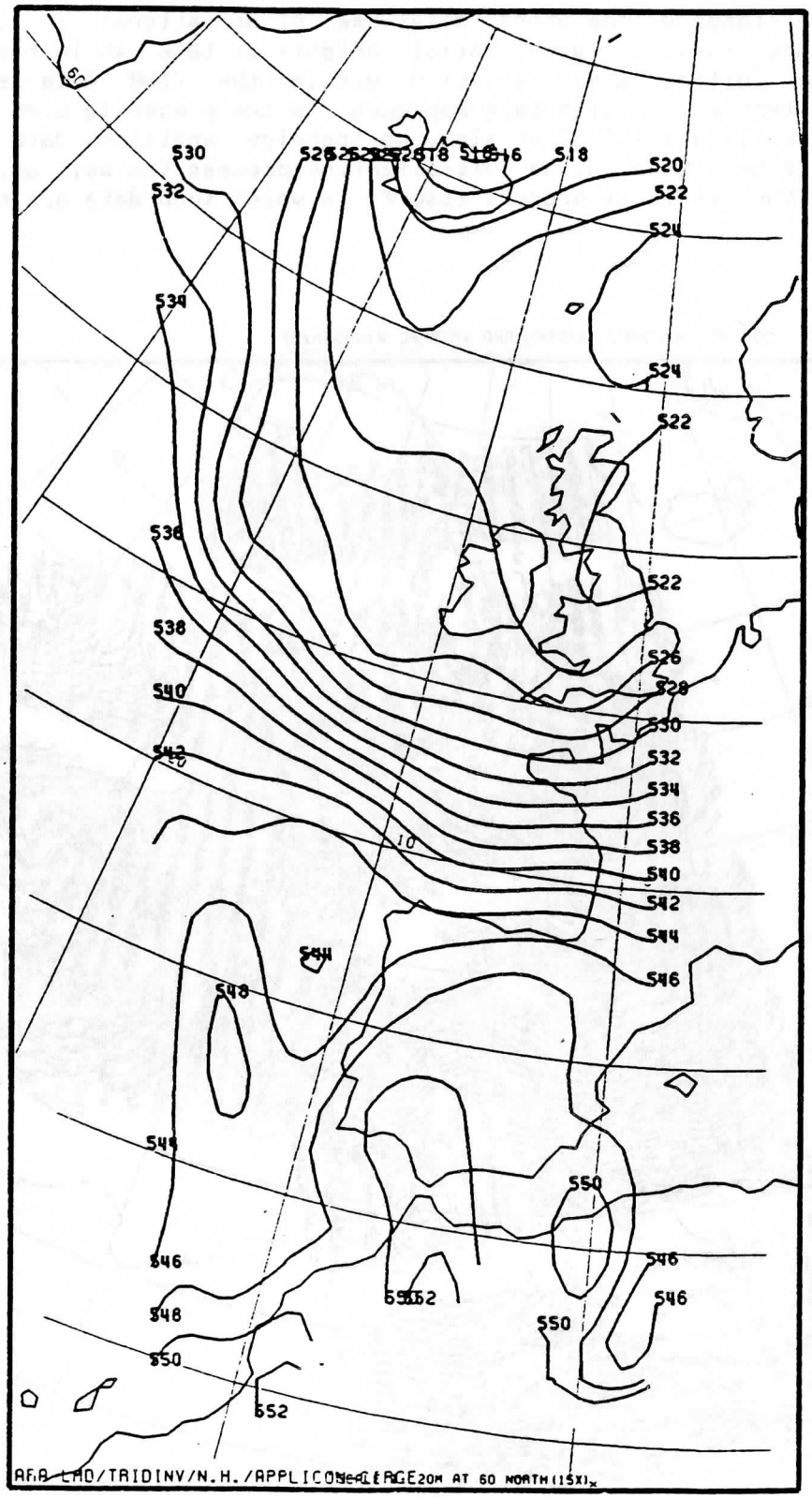

Figure 7.3 1000-500 mb retrieved thicknesses. March 16, 1982. 14:43Z. NOAA-7.

N.B. The retrieval algorithm used here is a slightly different version of the standard one which makes use of operational forecasts of the temperatures and geopotential heights at 1000 mb in the seeking of the initial guess solution within the TIGR data set, through a pattern recognition type approach. In the presently used version, the "satellite-only" 3I version, no "foreign" ancillary data of any kind have been used in the initialization process (as well as, a fortiori, in the retrieval process itself, in which such data are never used).

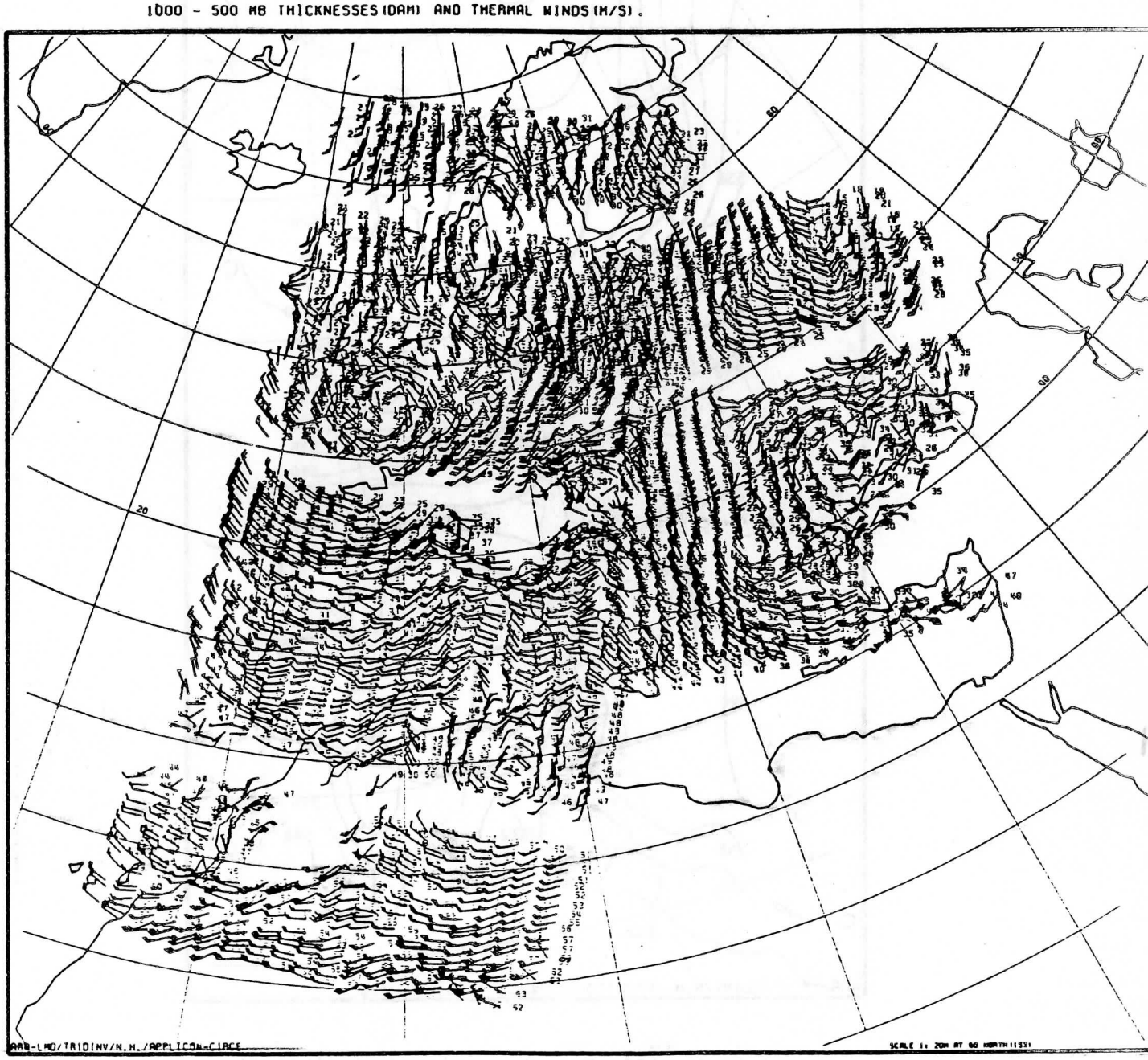

Figure 7.4 1000-500 mb thermal winds retrieved from the 3I algorithm. March 17, 1982. 3:00Z. NOAA-7. The restricted coverage by orbit 3763 (right) is due to a lack in the archives.

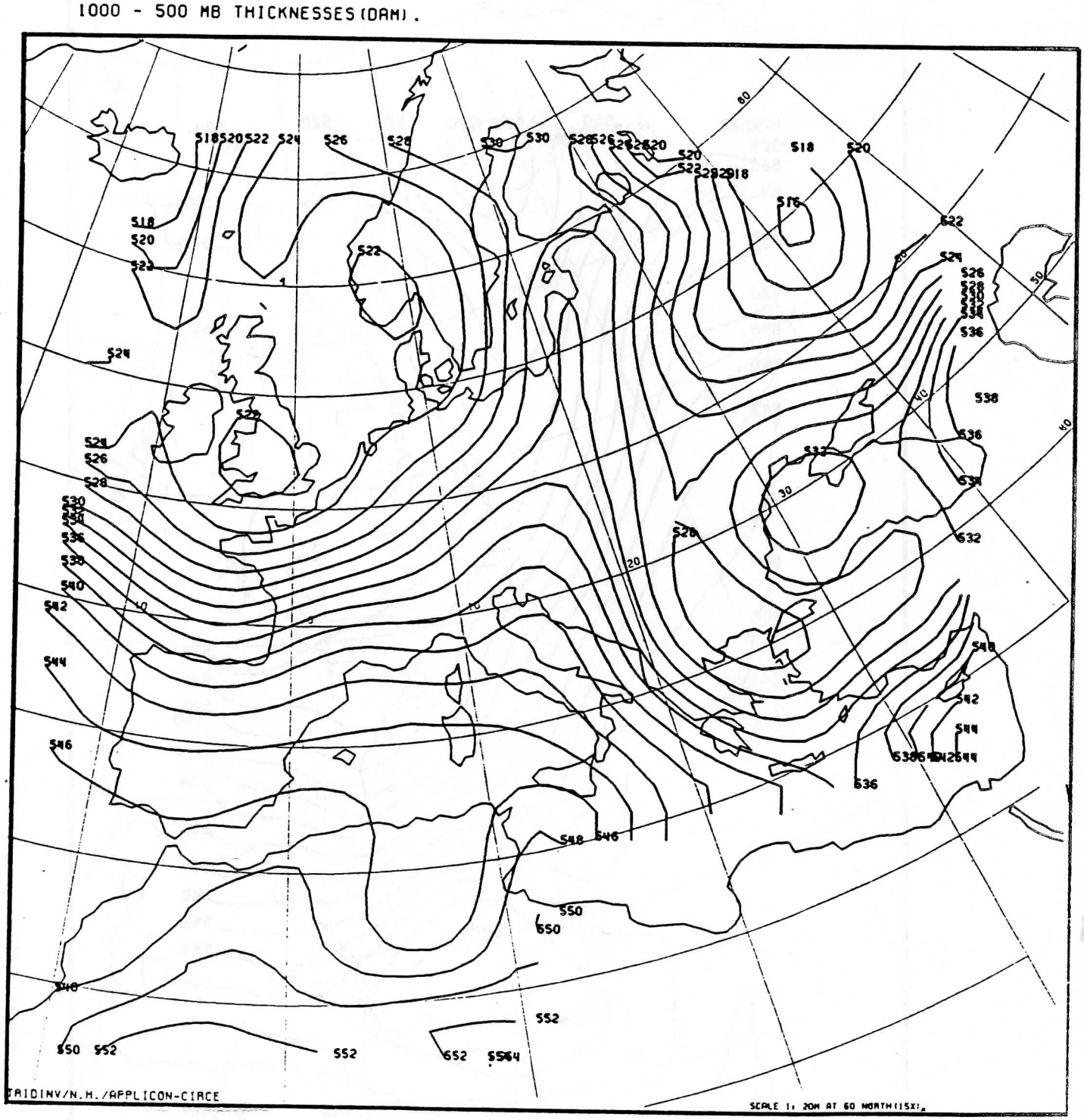

Figure 7.5 1000-500 mb 3I retrieved thicknesses.
March 17, 1982. 3:00Z. NOAA-7.

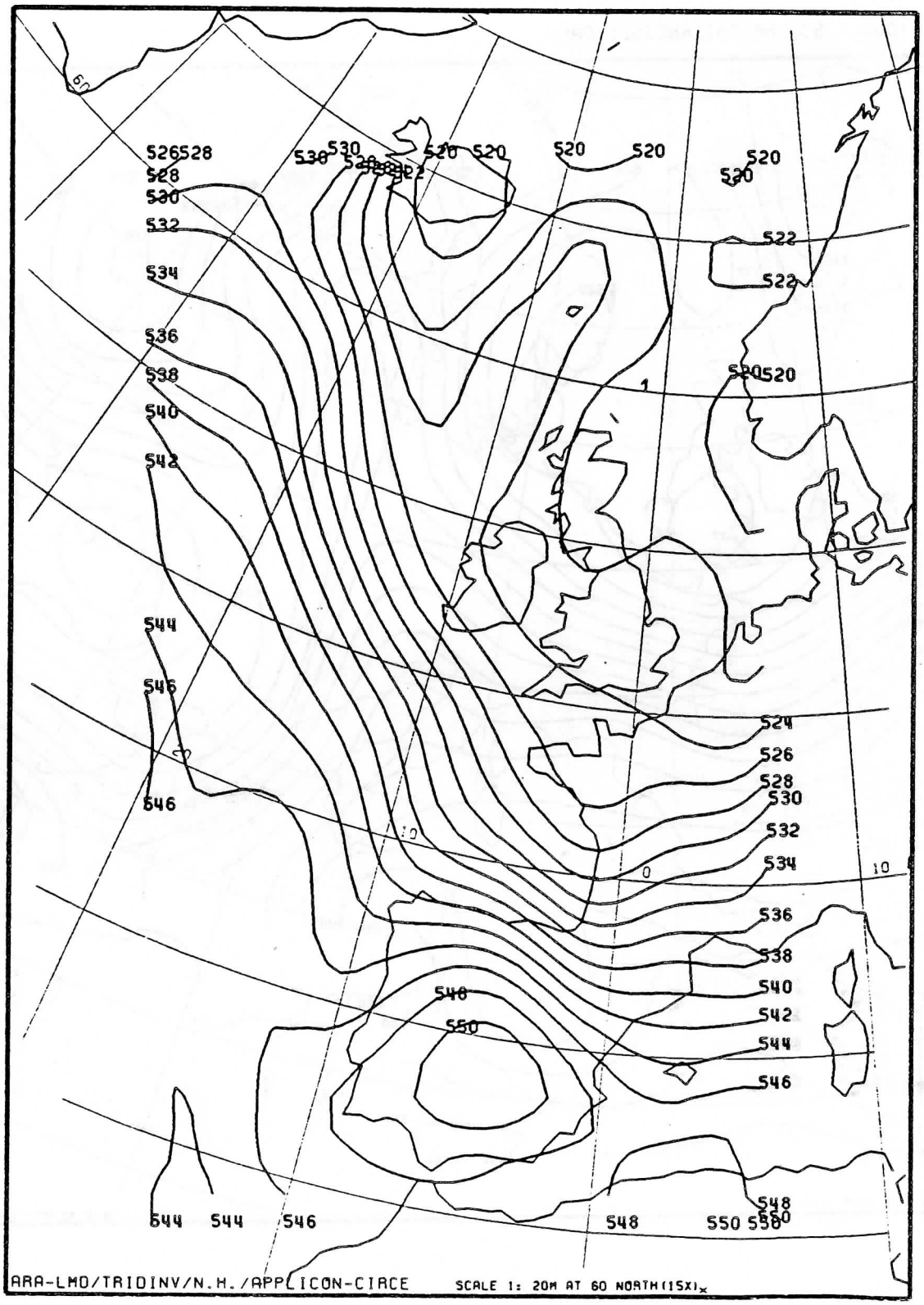

Figure 7.6 1000-500 mb 3I retrieved thicknesses. March 17, 1982. 14:322. NOAA-7.

Channel	Sea clear 147 items		Land clear 397 items		Cloudy 696 items	
	$\bar{m}$ (c-o)	σ	$\bar{m}$ (c-o)	σ	$\bar{m}$ (c-o)	σ
3	-0.78	1.02	-0.42	1.10	-0.09	1.13
4	-0.26	0.53	-0.01	0.52	0.11	0.45
5	0.11	0.63	0.66	0.57	0.30	0.58
6	0.15	0.67	0.93	0.67	0.33	0.56
13	0.42	0.43	-0.45	0.70	-	-
14	-0.10	0.43	-0.31	0.47	-0.41	0.40
15	-0.98	0.69	-0.86	0.72	0.17	0.61
MSU 2	0.46	0.51	0.91	0.78	0.23	0.42
MSU 3	0.06	0.11	0.02	0.20	0.09	0.12
MSU 4	0.04	0.23	-0.08	0.28	-0.20	0.32

Table 8.1 Statistics ($\bar{m}$ = mean ; σ : standard deviation) for the differences between TOVS observations (o) and corresponding brightness temperatures computed from 3I retrievals using the 3R code (c). ALPEX orbit nb. 3586, March 4, 1982 at 12:00Z.

Channel	Sea clear 313 items		Land clear 339 items		Cloudy 538 items	
	$\bar{m}$ (c-o)	σ	$\bar{m}$ (c-o)	σ	$\bar{m}$ (c-o)	σ
3	-0.40	1.05	-0.54	1.23	0.27	1.40
4	-0.12	0.42	-0.17	0.45	0.35	0.66
5	0.22	0.48	0.36	0.41	-0.08	0.62
6	0.39	0.60	0.52	0.51	-0.01	0.57
13	0.48	0.38	0.52	0.50	-	-
14	-0.01	0.42	-0.02	0.49	-0.09	0.37
15	-0.61	0.73	-1.10	1.20	-0.10	0.64
18	0.25	0.24	0.07	0.86	-	-
MSU 2	0.11	0.56	0.42	0.73	-0.18	0.43
MSU 3	0.08	0.14	0.12	0.15	0.16	0.14
MSU 4	0.02	0.38	-0.21	0.38	-0.07	0.34

Table 8.2 Same legend as Table 8.1. ALPEX orbit nb. 3595, March 5, 1982 at 03:45Z.

input and the initial guess are minimized through the use of the partial derivatives matrices also archived in TIGR. More details are given in Flobert et al. (1986). This reference also presents results of comparisons between the 4A and the 3R models when applied either to synthetic data from the TIGR data base or to real observations from files regularly archived by NOAA/NESDIS (the so-called DSDV files).

An interesting application of the 3R fast model consists in applying it to 3I retrievals of atmospheric profiles and to compare the results to the real TOVS observations. This has been done, in a first step, for those channels which are mostly sensitive to temperature and for two orbits of the ALPEX IOP of March 4-5, 1982 : nb. 3586 (day) and 3595 (night). The results are given in Tables 8.1 and 8.2 for 10 channels (11 at night since channel 18 for HIRS/2 is not contaminated by solar flux). The observations have been splitted into 3 categories : clear over sea, clear over land and cloudy. In the latter case, observations are replaced by the cloud-cleared values obtained through the ψ-method (see Chedin et al., 1985). A part from channel 3, for which retrievals do not extend high enough to cover the associated weighting function, the results are satisfactory. However, some of the biases are relatively large (channel 15 for example) and should be studied into more details.

This application of the 3R code is in progress and will be extended soon to water vapor sensitive channels. We also intend to include the 3R model in the automatic rejection procedure which removes "bad" retrievals from the final 3I products. A retrieval would be declared as bad if the differences between the observed brightness temperatures and those computed from the retrieved profiles using 3R exceed a certain limit value.

CONCLUSION

From the 1st International TOVS Study Conference (ITSC) held in Igls, Austria, 1983, the 3I method has demonstrated its capability to accurately derive atmospheric parameters. Quantitative intercomparisons studies using ECMWF analyses and colocated RAOB data have been made (J. Le Marshall, ITSC-II).

The 3I algorithm has been recently revised :

- optimization of the cloud detection algorithm, owing to, among other things, a better handling of the surface characteristics (quality of the terrain) ;
- improved specificity in the search for the closest element(s) in the TIGR data set owing to an optimized description of the air mass types ;
- optimization of the surface temperature estimation method ;
- optimization of the rejection tests based upon an improved filtering of the results :
- extension of the temperature profiles to the upper stratosphere owing to the use of the SSU data.

Newly derived results, using this revised version of the 3I code, have been submitted for comparisons studies (ITSC-III). They concern : temperature profiles, geopotential heights at standard pressure levels, cloud amounts, cloud-top pressure and temperature, H_2O content profiles, geostrophic winds.

The already demonstrated quality of the results (ITSC-II) has led us to extend the intercomparison studies to impact studies on the forecasts (Chedin et al., 1986a) and to the treatment of the satellite observations over polar regions.

Moreover, we have developed a very fast radiance calculation scheme (3R) to answer the effective utilization of satellite radiances directly in the numerical weather prediction schemes.

The ongoing development of this work is the combination of TOVS and AVHRR data and to prepare the processing of the coming AMSU data.

REFERENCES

Chedin A., and N.A. Scott, 1984 : Improved Initialization Inversion procedure. Proc. of the 1st TOVS Study Conference. Igls, Austria. August 1983. A report from the CIMSS, Ed. P. Menzel, p. 14-79.

Chedin A., and N.A. Scott, 1985 : Initialization of the radiative transfer equation inversion problem from a pattern recognition type approach. Applications to the satellite of the Tiros-N series. **Advances in Remote Sensing Retrieval Methods**, Academic Press, A. Deepak Ed. p. 495-515.

Chedin A., N.A. Scott, C. Wahiche and P. Moulinier, 1985a : The Improved Initialization Inversion method : a high resolution physical method for temperature retrievals from the Tiros-N series. **J. Clim. Appl. Meteor., 24**, 124-143.

Chedin A., N.A. Scott, C. Wahiche, P. Moulinier, N. Husson, G. Rochard, J. Quéré and M. Derrien, 1985b : The 3I procedure applied to the retrieval of meteorological parameters from NOAA-7 an NOAA-8. Proc. of the 2nd Int. TOVS Study Conference, Igls, Austria. February 1985. A report from CIMSS, Ed. P. Menzel, p. 11-38.

Chedin A., C. Levy, N.A. Scott and N. Husson, 1986 : High resolution retrievals from the satellites of the Tiros-N series. Proc. of the 2nd Conf. on Satellite Meteorology / Remote Sensing and Applications. Williamsburg, USA, p. 11-15.

Chedin A., N.A. Scott, J.F. Flobert, N. Husson, C. Levy, G. Rochard, J. Quéré, B. Bellec, J. Siméon, 1986a : Analyse de champs d'épaisseurs obtenus par la méthode 3I d'inversion des observations satellitaires du la série Tiros-N : Intérêt pour la prévision. To be published "La Météorologie".

Flobert J.F., N.A. Scott and A. Chedin, 1986 : A fast model for TOVS radiances computation. Proc. of the 6th Conference on Atmospheric Radiation. Williamsburg, USA, p. 186-189.

Le Marshall J.F., 1985 : An intercomparison of temperature and moisture fields from Tiros Operational Vertical Sounder data. The Technical Proceedings of the Second International TOVS Study Conference, Igls, Austria. Ed. W.P. Menzel, p. 106-161.

McMillin L.M. and Dean C., 1982 : Evaluation of a new operational technique for producing clear radiances. **J. Appl. Meteor., 21**, 1005-1014.

Moine P., C. Levy, N.A. Scott and G. Rochard, 1986 : Automatic air masses classification for satellite temperature retrievals. Proc. of the 2nd Conf. on Satellite Meteorology / Remote Sensing and Applications. Williamsburg, USA, p. 5-10.

Scott N.A. and A. Chedin, 1981 : A fast line-by-line method for atmospheric absorption computations : the Automatized Atmospheric Absorption Atlas. **J. Appl. Meteor., 20**, 802-812.

Scott N.A., A. Chedin, C. Wahiche and P. Moulinier, 1984a : Geopotential thicknesses and thermal winds retrieved from the satellites of the Tiros-N series through the "3I" method. In IRS'83 : Current Problems in Atmospheric Radiation, A. Deepak Pub., p. 304-307.

Scott N.A., N. Husson, A. Chedin, J.F. Flobert, G. Rochard and J. Quéré, 1986 : Comparisons between physically retrieved temperatures from NOAA-7 and NOAA-8 and conventional analyses or radiosonde data. Proc. of the 2nd Conf. on Satellite Meteorology / Remote Sensing and Applications. Williamsburg, USA, p. 126-130.

Petzoldt K., 1986. Private Communication.

Wahiche C., N.A. Scott and A. Chedin, 1986 : Cloud detection and cloud parameters retrieval from the satellites of the Tiros-N series. **Annales Geophysicae, 4B**, 207-222.

NEW DEVELOPMENTS IN THE FRENCH MESOSCALE ANALYSIS IN THE USE OF RAW SATELLITE DATA

Y. Durand and R. Juvanon du Vachat
Direction de la Meteorologie SCEM/EERM
2 Av Rapp 75007, Paris, France

I) Introduction

The mesoscale analysis system developed in the French Weather Service (mesh size=35 km,cf fig 1) as a part of the Peridot project (which includes also a forecast model and its corresponding initialisation) has been run operationally since the beginning of 1985 ; its results (and those of the model) are used daily by French meteorologists and provide interesting indications especially in short range forecasts of fields like rainfall,cloudiness,winds and temperature in low layers . In research we use these programs to study some particular meteorological cases or to test the practical impacts of some types of information as radiances or to tune the statistical model used . Since May 86 the analysis program has been used in an intermittent data assimilation 12 hour cycle (i.e. the guess-field comes from a 12 hour forecast of the forecast model) ,satellite data are only inserted at 00 Z (they will be inserted also at 12 Z in september 86) which allows a best four dimensional impact of treated orbits . The development of the whole system goes on and plans are made for a new version on the future Cray 2 .

The utilisation of satellite radiances has been described in refs a) and b) . The new improvements concern the use of HIRS cloudy radiances of NOAA 9 with indications from AVHRR radiometer (cf paragraph II) . The statistics concerning NOAA 9 errors have been produced (cf Tables 1,2,3,4 and paragraphs II and III) . An experiment with systematic comparisons of analysis with and without satellite data and the associated forecasts have been performed during Spring 85 , some results are summarized in paragraph IV.

II) Use of cloudy radiances.

The utilization of only clear radiances was the most severe limitation of our system . So we decided to use the experience of the CMS of Lannion in the treatment of AVHRR data . The constraints due to the limitation of computer time lead us to compute for each used HIRS pixel only a one-dimensional histogram with the AVHRR pixels values (channel 4) situated inside the HIRS pixel . So the number of points of each class gives an estimation of the fraction of cloudiness ; we know also the averaged radiative temperature of every class and its standard deviation which allows some rejection tests.

Using the guess-field profiles we compute the pressure value corresponding to the radiative temperature of each class . After that we can compute a synthetic radiance corresponding to the given histogram but using the profile values of the guess-field (temperature,humidity) by integrating the radiative transfer equation for each class from bottom conditions to the top of the atmosphere . For this purpose we use a NOAA program issued from the "TOVS Export Package" (cf ref d) . The result of each integration is weighted by the number of points of the class (RScy)(cf fig 2) . So we have continuity between the "clear" case (1 class with surface parameters) and the "cloudy" case (1 or more classes with different bottom conditions) .

We compute then a "clear" synthetic radiance (RScr) with surface parameters coming from AVHRR values (or from guess-field if the surface is not seen by the radiometer) and guess-fied profile in 1 integration .

We define the parameter a for every channel of each class :

a = RScy/RScr

We force 0.6<a<1. to keep the corresponding channel value .

All computations in the analysis program concern differences between each quantity of every type and the corresponding guess-field value . For radiances we shall study increments as :

IRcy = ROcy - RScy radiance increment in the "cloudy" case

IRcr = ROcr - RScr '' '' "clear " ''

(RO..= observed radiance in a channel)

But because of the continuity of the cloud model (a=1 : clear , a 1 : cloud) we shall note only IR , RS and RO for both cases when there is no ambiguity .

IR = (RO - a*RTcr) - (RS - a*RTcr)

(RTcr = true value of the clear radiance in this channel at this pixel)

IR = (RO - a*RTcr) - a*(RScr - RTcr)

The (RScr-RTcr) term is the synthetic radiance error wich comes from the errors of the parameters of the profile in the guess-field and from the internal errors of integration of RTE equation . We shall call it " eRScr " .

The (RO-a*RTcr) term takes into account the observation error and the errors due to the computation of "a" . Due to a lack of indication about its real value it will be approximated by the clear radiance observation error " eROcr " .

IR = eROcr - a*eRScr

It is the general form of a radiance increment . If a=1 it is clear otherwise it is cloudy .

In order to perform a linear regression between all increments we have to compute the covariances between increments of different channels at different locations . The method used is described in ref a) and b) . The only difference is that now all standard deviations of synthetic radiance error are multiplied by a factor "a" indicating the ratio of information which is in the corresponding increment . The cross correlations involving clear synthetic NOAA9 radiance errors (table 1,2,3) have been computed with the same way as used in ref b) . (by a Monte-Carlo method)

III) NOAA9 observation errors .

The knowledge of statistical properties concerning radiance observation errors is necessary for this kind of analysis program . Previous studies have been done by comparing observed radiances and collocated soundings . The low number of couples (..100) was not balanced by the interesting fact that sounding data errors are not spacially correlated . Nevertheless this kind of study allowed us to determine an estimate of the correlation matrix between channels (in the same location) concerning the sum of the observation error and the computation error of synthetic radiance (cf ref c) and table 4) .

Daily verifications of bias and variances of radiance increments are performed . They allow to tune the statistics used and to correct increments values if bias is too large .

A comparison experiment between observed radiances and synthetic ones computed with fine mesh analysis results (obtained without satellite information) has been performed over our area on about 55 situations (in collaboration with ECMWF) . The statistical structures of produced residuals has been studied . If we make the assumption that the analysed fields represent the truth we so obtain indications over statistical properties of the sum of the observation error and the computation one . In many channels the Gandin structure function allows to separate on the one hand an uncorrelated part on the other hand a correlated part with a variable radius of influence . (cf fig 3)

IV) Experiment of Spring 85 . (cf ref c)

Two analysis have been performed every day at 00 Z , one with clear radiances data the other one without , from April to June 85 . Both analyses used the same guess-field (the interpolated synoptic analysis) and the same conventional data . Some forecasts were made when we found some significant differences between the two runs .

IV.a) : Impact on analysis .

We can confirm that the correction implied by radiance data (used

alone = without conventional data) is compatible with the correction due to conventional data (used alone = without satellite data) : same sign but less amplitude . The major impact of radiances on the analysis is situated in levels with an amplitude of some degrees in temperature and few m/s in wind . In humidity analysis the conjugated impact of clear radiances and bogus data (build in case of complete cloud cover) gives high amplitude corections which have been judged very positive . A previous experiment showed already a clear positive impact without bogus data . Nevertheless the veracity of details in difference maps is always very difficult to appreciate ; some little features can be noise or an impact due to the presence or the absence of radiances. There is generally no other observation to give an opinion .

IV.b) Impact on forecasts .

The impacts in forecasts issued from the two sets of analysis appear only in "physical" fields : cloudiness , precipitation , humidity . In spite of the influence of boundary conditions which make the model forgetting quickly its initial conditions to the profit of lateral conditions , many cases of forecasted differences showed a positive impact of the run initialized by the analysis with radiances for these fields (cf fig 4) . In all cases the forecasts of geopotential , wind and tempertures were very similar although the analysis were showing differences .

V) Conclusion .

The experiment of insertion of radiance data directly in the analysis program goes on . We are now in a phase where results are used in an operational manner . It seems to be a viable method in our case where we need data very quickly over a small and consistent area and where we are sure of the quality of the used guess-field . In our future plans we think to use MSU data in case of fully cloud covered HIRS pixels by taking into account in the analysis program the difference of spacial scale . A comparison with the inversion method of the LMD is also planned . The increase of the area of analysis (especially over the Atlantic) will surely give some problems that we will have to solve .

This work is supported by the Institut National des Sciences de l'Univers (ATP - Recherches Atmospheriques - Contrat 1985 n 5622) and the computer time has been attributed by the Conseil Scientifique du Centre de Calcul Vectoriel pour la Recherche .

References .

a) Durand, Y ; Juvanon du Vachat, R : Mesoscale analysis using satellite information . Technical Proceedings of the First International TOVS Study Conference (Igls , September 1983) p. 80-93

b) Durand, Y ; Juvanon du Vachat, R : Developments of mesoscale analysis using raw satellite data . Technical Proceedings of the Second International TOVS Study Conference (Igls , February 1985) p. 39-57

c) Durand, Y : The use of satellite data in the French high resolution analysis . ECMWF Workshop on High Resolution Analysis . (Reading , June 1985) p. 89-128

d) Smith ,W.L and alii : The physical retrieval TOVS export package . Presented at the First International TOVS Study Conference (Igls , September 1983)

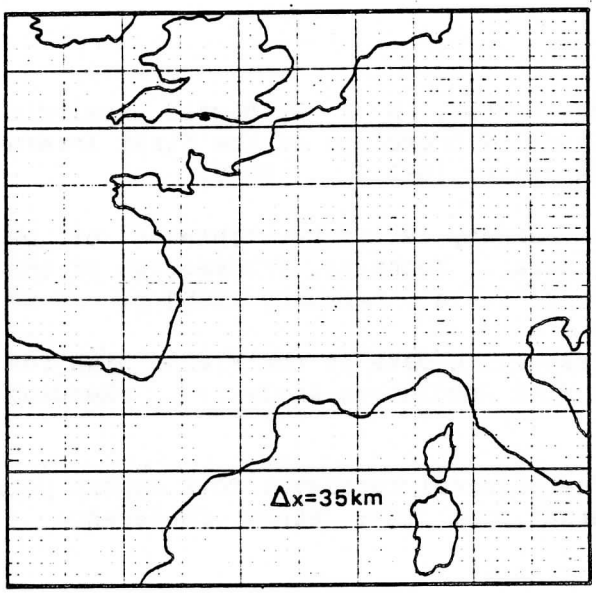

k	σ_k	p_k(mb)	Z_k(m)		$\bar{\sigma}_k$	$\bar{p}_k$(mb)	$\bar{Z}_k$(m)	k
0	0	0						
1	0,129	130	14500		0,064	65	18800	1
2	0,249	252	10300		0,189	191	12050	2
3	0,360	365	7830		0,340	308	8980	3
4	0,462	468	6050		0,411	417	6900	4
5	0,555	563	4690		0,509	516	5350	5
6	0,640	648	3610		0,598	606	4130	6
7	0,715	725	2730		0,678	687	3160	7
8	0,792	793	2020		0,749	759	2370	8
9	0,840	851	1450		0,811	822	1730	9
10	0,889	900	982		0,864	876	1210	10
11	0,929	941	618		0,909	921	789	11
12	0,960	973	343		0,944	957	480	12
13	0,982	995	151		0,971	984	247	13
14	0,995	1008	38		0,989	1002	94	14
15	1	1013,25	0		0,998	1011	19	15

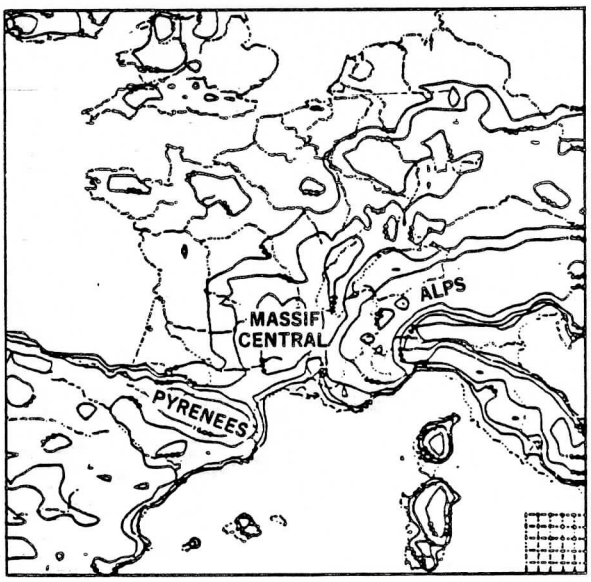

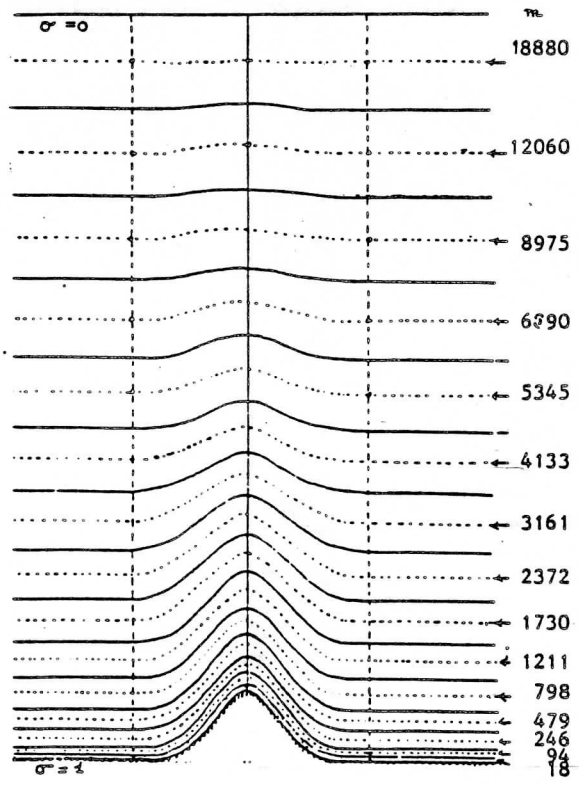

Fig. 1 Grid and levels used in the analysis.

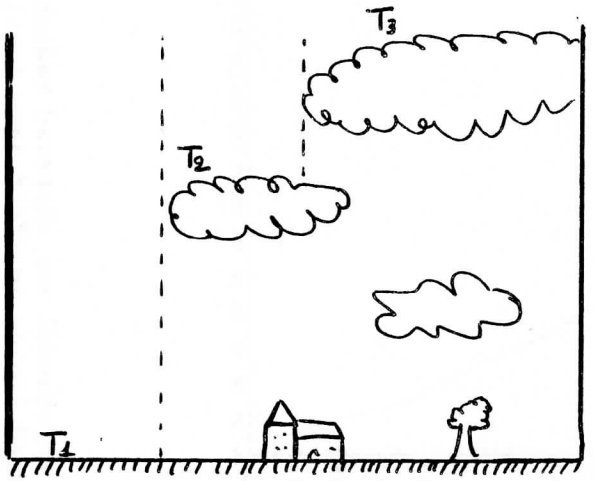

HIRS CLOUDY PIXEL

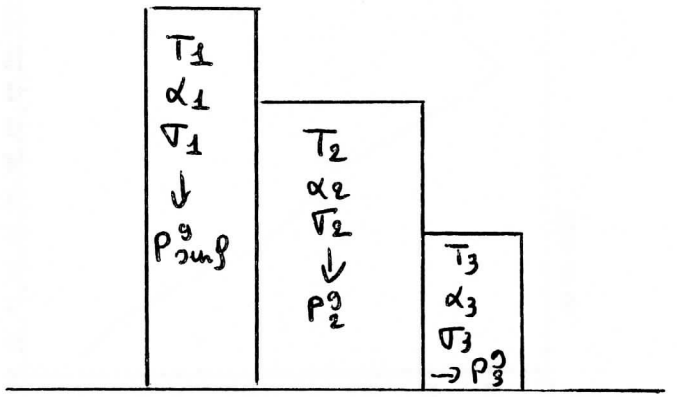

T_x = radiative temperature averaged
α_x = number of AVHRR points
∇_x = standard deviation in temperature
P^g_x = pressure in the guess-field corresponding to T_x

$$RS_{cy} = \sum_{i=1}^{3} \alpha_i \left[B(T_i, P_i^g) + \int_{P_i^g}^{0} B(T \ldots) \ldots \right]$$

Fig. 2: Cloudy pixel example.

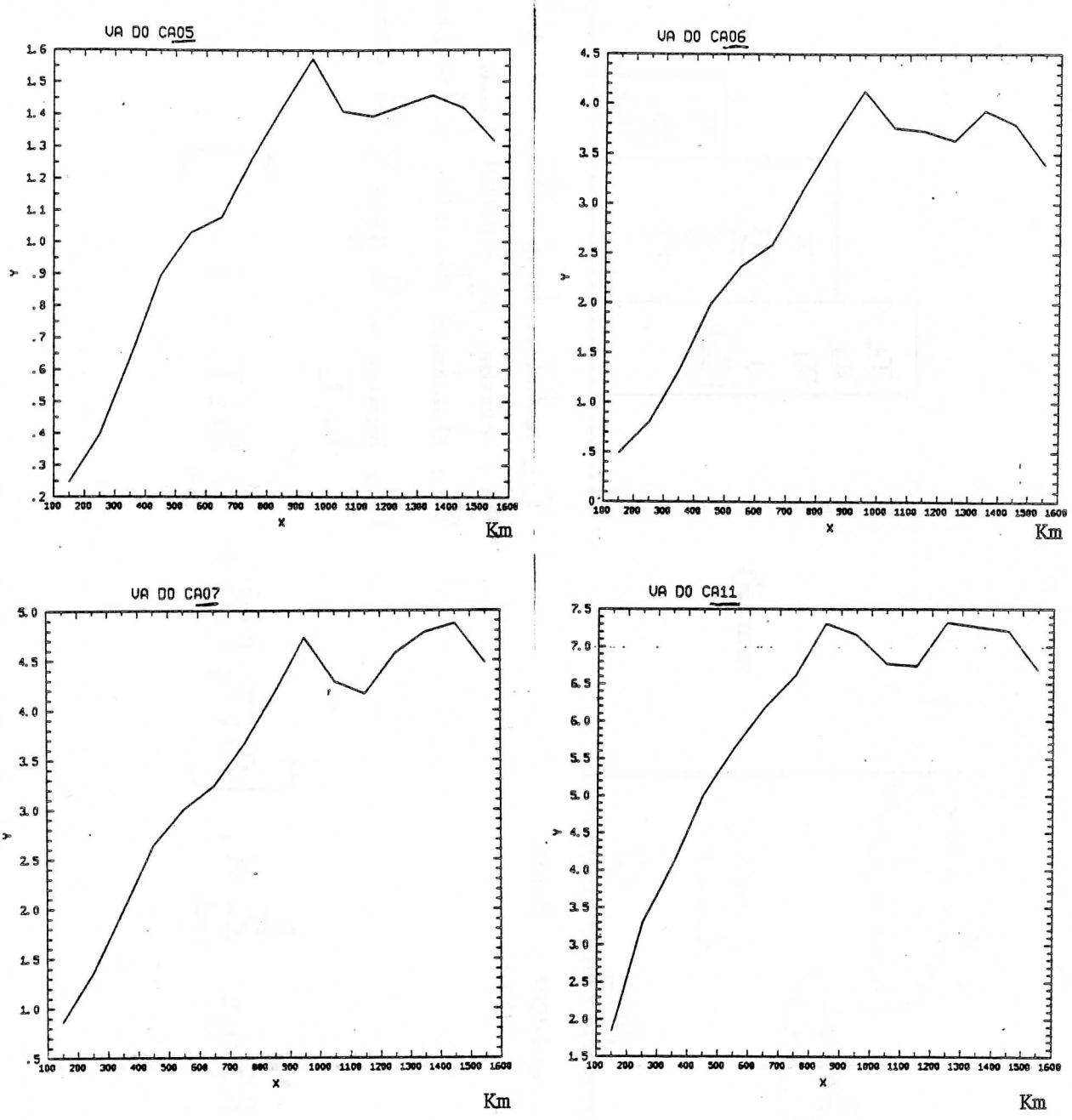

Fig. 3a: Gandin structure function of a given channel for observed radiance minus synthetic radiance computed with analyzed fields in $(°K)^2$ as a function of the distance in Km.

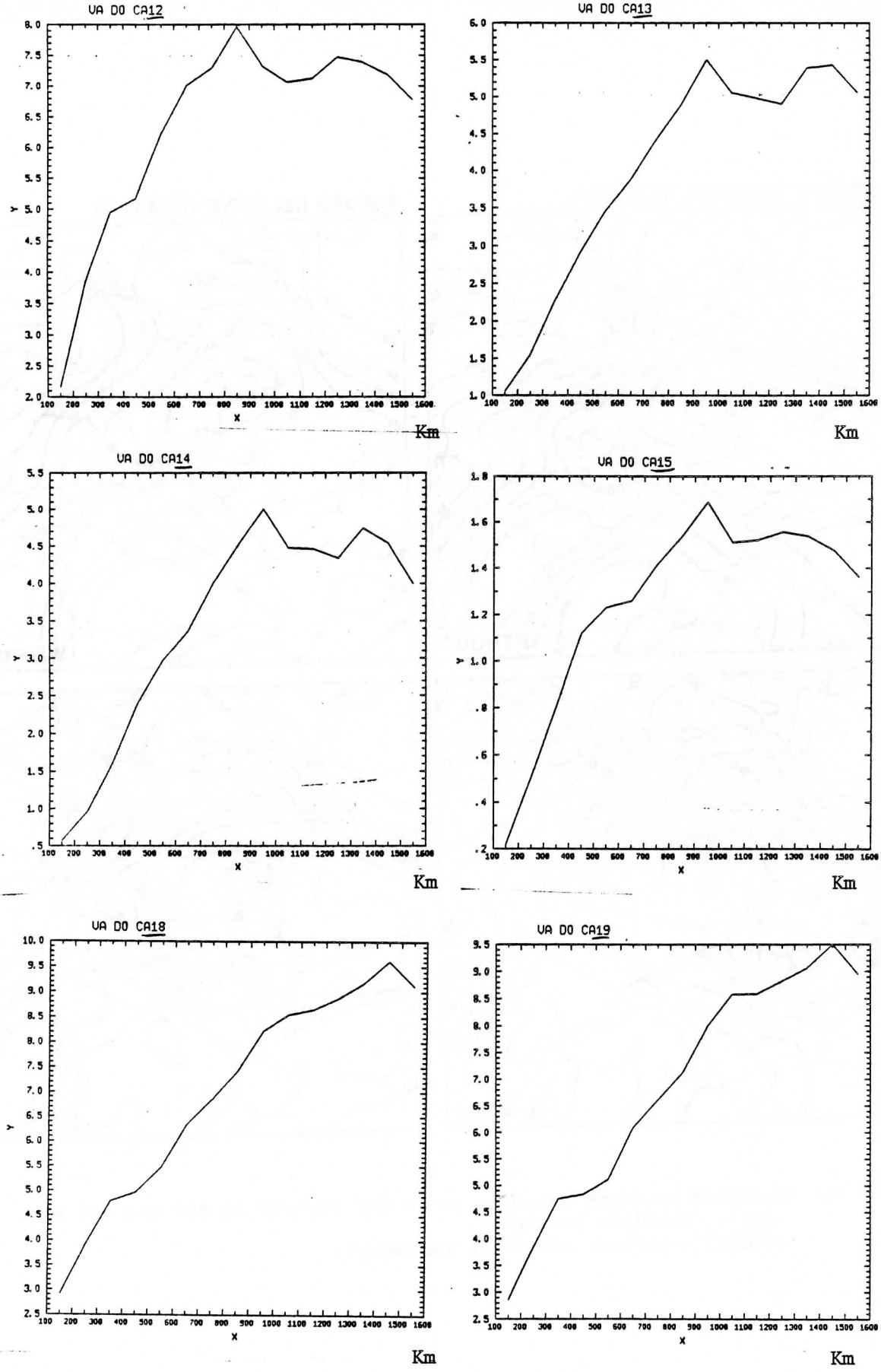

Fig. 3b: Same as Fig. 3a.

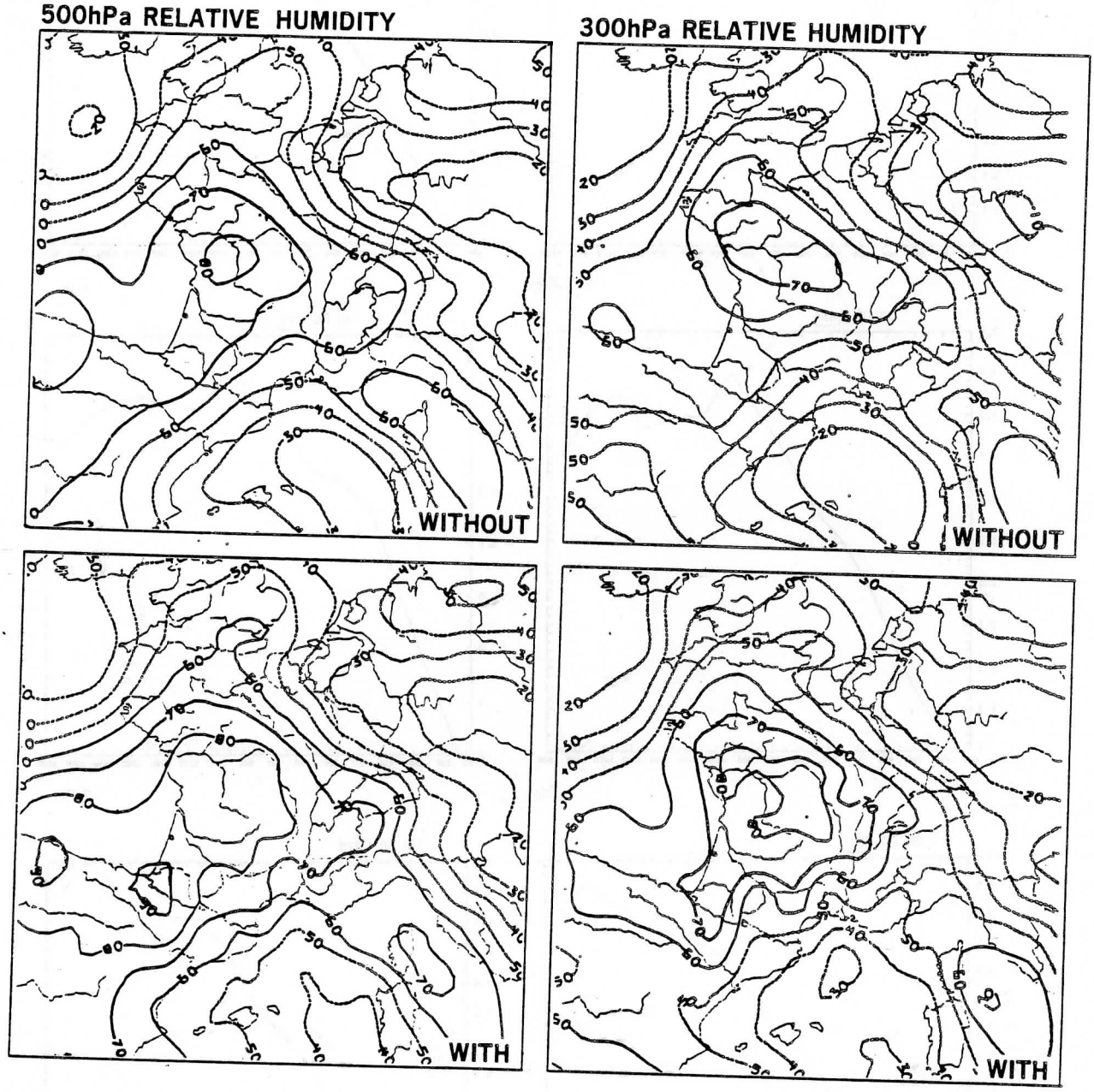

Fig. 4a: Analysed relative humidity at 00 GMT 22/4/85 at 500 and 300 hPa.
WITH = satellite radiances.
WITHOUT = without satellite radiances.

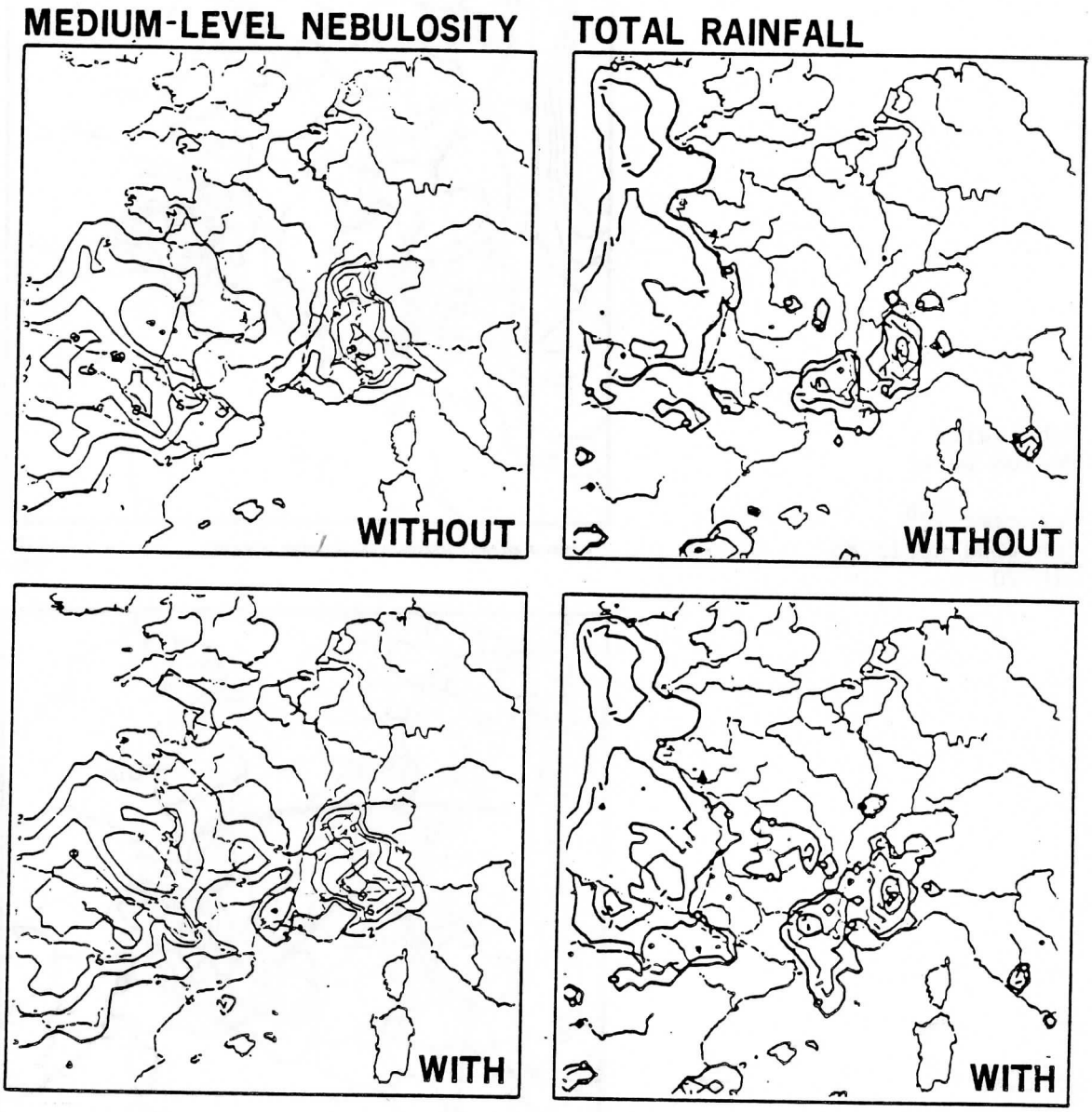

Fig.4b: 6 h forecast of medium level nebulosity and total rainfall valid 06 GMT 22/4/85.

Nebulosity
Medium Level

Forecast 12^h
for 22nd April 85
21^h TU

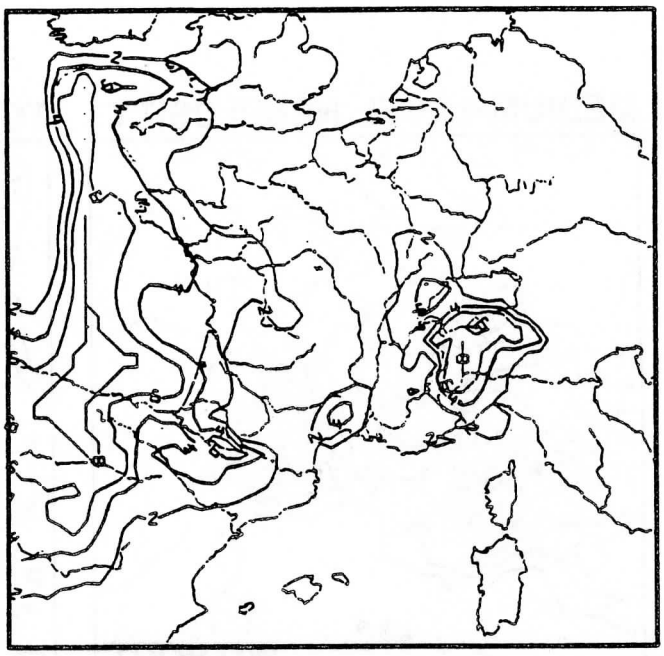

WITHOUT

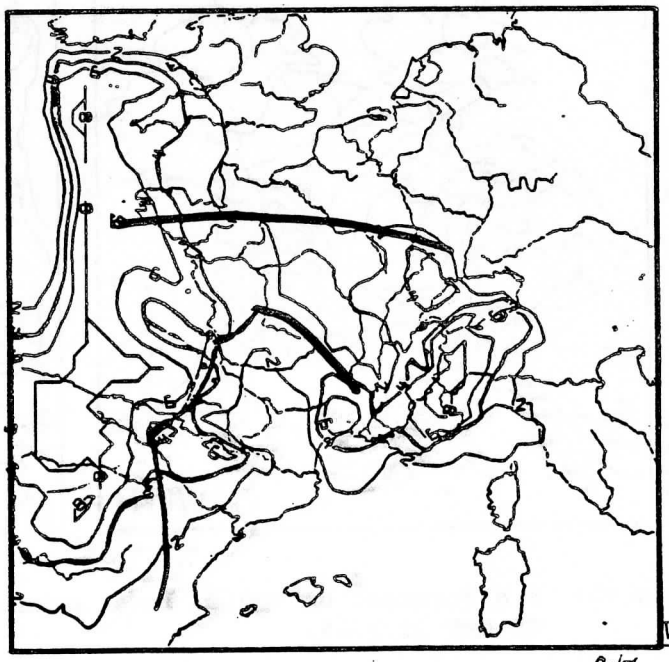

WITH

Fig. 4c

Standard deviation of synthetic radiance error (ρR^g) in °K

	1.6	1.3	1.15	.9	.8	.95	.9	.85	.9	.9	1.7	1.8	.9	.8	1.1	.9	1.3	.8	.8
	CORR T/RAD SUR 11 NIVEAUX $r(\rho T^g, \rho R^g)$																		
1000	-0.020	-0.040	-0.050	0.030	0.250	0.280	0.600	0.700	0.650	0.490	0.190	0.040	0.760	0.490	0.200	0.010	0.000	0.800	0.800
850	0.010	0.000	-0.020	0.100	0.450	0.350	0.450	0.290	0.230	0.330	0.100	-0.020	0.570	0.700	0.350	0.150	0.010	0.360	0.310
700	0.150	0.090	0.100	0.140	0.500	0.550	0.400	0.190	0.050	0.270	0.220	0.050	0.410	0.580	0.590	0.200	0.080	0.230	0.200
500	0.050	0.020	0.200	0.180	0.750	0.440	0.150	0.070	0.020	0.100	0.120	0.090	0.220	0.400	0.740	0.250	0.080	0.120	0.080
400	0.120	0.060	0.300	0.250	0.600	0.360	0.070	0.060	0.070	0.080	0.090	0.100	0.140	0.210	0.490	0.500	0.170	0.090	0.070
300	0.220	0.110	0.400	0.430	0.450	0.150	0.030	0.060	0.070	0.050	0.010	0.040	0.050	0.140	0.260	0.650	0.220	0.070	0.060
250	0.340	0.250	0.550	0.580	0.300	0.080	0.000	0.060	0.070	0.050	0.030	0.080	0.020	0.080	0.150	0.700	0.270	0.060	0.060
200	0.400	0.450	0.690	0.590	0.200	-0.010	-0.060	-0.020	-0.020	-0.030	-0.010	0.020	-0.070	-0.040	0.040	0.570	0.330	-0.030	-0.020
150	0.490	0.620	0.800	0.500	0.100	0.060	-0.040	-0.070	-0.080	-0.060	-0.020	0.000	-0.080	-0.030	0.090	0.500	0.390	-0.080	-0.070
100	0.650	0.800	0.860	0.450	0.050	0.150	-0.010	-0.110	-0.130	-0.090	-0.020	-0.010	-0.090	-0.020	0.190	0.400	0.460	-0.120	-0.120
50	0.750	0.720	0.650	0.400	0.030	0.220	0.080	-0.010	-0.010	0.000	0.000	0.000	0.000	0.050	0.200	0.270	0.590	-0.010	-0.010
	CORR Z/RAD SUR 11 NIVEAUX $r(\rho Z^g, \rho R^g)$																		
1000	-0.280	-0.220	-0.130	-0.300	-0.380	-0.270	-0.100	-0.040	-0.070	-0.010	-0.010	0.020	-0.190	-0.340	-0.470	-0.350	-0.290	-0.040	0.050
850	-0.200	-0.180	-0.140	-0.300	-0.310	-0.180	0.020	0.130	0.180	0.140	-0.020	-0.070	0.100	-0.120	-0.370	-0.400	-0.320	0.200	0.200
700	-0.170	-0.140	-0.180	-0.300	-0.200	-0.030	0.110	0.210	0.190	0.170	0.030	-0.010	0.240	0.070	-0.280	-0.390	-0.280	0.250	0.250
500	-0.160	-0.210	-0.260	-0.330	-0.020	0.130	0.260	0.160	0.170	0.150	0.080	0.060	0.390	0.310	0.050	-0.290	-0.250	0.260	0.230
400	-0.230	-0.260	-0.380	-0.370	0.030	0.300	0.170	0.150	0.150	0.140	0.060	0.040	0.290	0.320	0.130	-0.250	-0.200	0.210	0.190
300	-0.200	-0.350	-0.330	-0.140	0.120	0.310	0.130	0.080	0.100	0.080	0.030	0.010	0.210	0.330	0.320	-0.120	-0.160	0.130	0.100
250	-0.150	-0.320	-0.320	-0.080	0.150	0.250	0.060	0.020	0.070	0.020	0.010	0.020	0.130	0.350	0.330	-0.010	-0.130	0.090	0.050
200	-0.130	-0.270	-0.230	0.050	0.170	0.180	0.080	0.060	0.080	0.060	0.030	0.030	0.150	0.300	0.350	0.120	-0.100	0.110	0.080
150	-0.060	-0.220	-0.150	0.140	0.180	0.170	0.060	0.020	0.030	0.030	0.020	0.010	0.090	0.240	0.370	0.220	-0.090	0.040	0.030
100	0.050	-0.100	-0.010	0.260	0.220	0.170	0.030	-0.010	0.030	0.000	0.000	0.010	0.060	0.230	0.370	0.320	-0.080	0.040	0.020
50	0.160	0.300	0.370	0.470	0.320	0.200	0.040	-0.020	-0.020	0.000	0.020	0.030	0.030	0.200	0.380	0.550	0.080	-0.010	-0.020
	CORR ERR RAD SYNTH GUESS $r(\rho R^g, \rho R^g)$																		
1	1.00	0.95	0.96	0.81	0.44	0.08	-0.02	-0.05	-0.05	-0.05	0.03	-0.03	-0.05	-0.03	0.13	0.76	0.83	-0.05	-0.05
2	0.95	1.00	0.98	0.73	0.36	0.04	-0.02	-0.04	-0.04	-0.03	0.00	-0.05	-0.04	-0.05	0.03	0.62	0.62	0.01	0.01
3	0.96	0.98	1.00	0.82	0.37	0.00	0.00	0.00	0.00	0.00	0.00	0.00	0.00	0.00	0.00	0.75	0.73	0.00	0.00
4	0.81	0.73	0.82	1.00	0.67	0.13	0.00	0.00	0.00	0.00	0.15	0.16	0.00	0.00	0.33	0.97	0.77	0.00	0.00
5	0.44	0.36	0.37	0.67	1.00	0.87	0.72	0.62	0.59	0.65	0.43	0.24	0.65	0.73	0.91	0.50	0.43	0.60	0.61
6	0.08	0.04	0.00	0.13	0.87	1.00	0.96	0.89	0.84	0.92	0.42	0.20	0.91	0.95	0.88	0.07	0.11	0.86	0.87
7	-0.02	-0.02	0.00	0.00	0.72	0.96	1.00	0.97	0.93	0.98	0.32	0.14	0.98	0.97	0.77	-0.07	0.07	0.94	0.95
8	-0.05	-0.04	0.00	0.00	0.62	0.89	0.97	1.00	0.99	0.99	0.19	0.06	0.99	0.97	0.71	-0.09	-0.04	0.95	0.95
9	-0.05	-0.04	0.00	0.00	0.59	0.84	0.93	0.99	1.00	0.98	0.16	0.05	0.98	0.95	0.69	-0.08	-0.05	0.95	0.95
10	-0.05	-0.03	0.00	0.00	0.65	0.92	0.98	0.99	0.98	1.00	0.25	0.10	0.99	0.98	0.72	-0.09	-0.03	0.95	0.95
11	0.03	0.00	0.00	0.15	0.43	0.42	0.32	0.19	0.16	0.25	1.00	0.87	0.20	0.24	0.28	0.03	0.06	0.16	0.18
12	-0.03	-0.02	0.00	0.16	0.24	0.20	0.14	0.06	0.05	0.10	0.87	1.00	0.06	0.08	0.12	0.05	-0.01	0.05	0.06
13	-0.05	-0.04	0.00	0.00	0.65	0.91	0.98	0.99	0.98	0.99	0.20	0.06	1.00	0.99	0.75	-0.09	-0.04	0.99	0.99
14	-0.03	-0.05	0.00	0.00	0.73	0.95	0.97	0.97	0.95	0.98	0.24	0.08	0.99	1.00	0.83	-0.04	0.01	0.96	0.97
15	0.13	0.03	0.00	0.33	0.91	0.68	0.77	0.71	0.69	0.72	0.28	0.12	0.75	0.83	1.00	0.32	0.25	0.70	0.71
16	0.76	0.62	0.75	0.97	0.50	0.07	-0.07	-0.09	-0.08	-0.09	0.03	0.05	-0.09	-0.04	0.32	1.00	0.82	-0.09	-0.09
17	0.83	0.62	0.73	0.77	0.43	0.11	0.07	-0.04	-0.05	-0.03	0.06	-0.01	-0.04	0.01	0.25	0.82	1.00	-0.04	-0.04
18	-0.05	-0.01	0.00	0.00	0.60	0.86	0.94	0.95	0.95	0.95	0.16	0.05	0.99	0.96	0.70	-0.09	-0.04	1.00	0.95
19	-0.05	-0.01	0.00	0.00	0.61	0.87	0.95	0.95	0.95	0.95	0.18	0.06	0.99	0.97	0.71	-0.09	-0.04	0.95	1.00
	1	2	3	4	5	6	7	8	9	10	11	12	13	14	15	16	17	18	19

NOAA 9 **Synthetic radiance errors based on the 6 h forecasts.**

ρT^g = error in T
ρZ^g = error in Z
ρR^g = error in synthetic radiance

Tables 1, 2 and 3

MAT DE CORR D ERREUR D OBS DE RADIANCE

1	1.00	.72	.73	-.51	-.51	-.51	-.50	-.47	-.08	-.42	-.55	-.59	-.35	-.38	-.27	.69	.74	-.08	.27
2	.72	1.00	.74	-.54	-.52	-.52	-.50	-.45	-.14	-.43	-.57	-.60	-.35	-.39	-.35	.62	.69	-.05	.26
3	.73	.74	1.00	-.49	-.44	-.44	-.41	-.35	.02	-.32	-.53	-.58	-.24	-.28	-.23	.65	.70	.01	.25
4	-.51	-.54	-.49	1.00	.75	.74	.73	.71	.66	.71	.73	.64	.70	.71	.70	-.39	-.49	.52	-.01
5	-.51	-.52	-.44	.75	1.00	.75	.74	.73	.67	.73	.73	.62	.72	.73	.70	-.40	-.49	.55	.03
6	-.51	-.52	-.44	.74	.75	1.00	.75	.73	.67	.73	.73	.62	.72	.73	.69	-.42	-.50	.56	.04
7	-.50	-.50	-.41	.73	.74	.75	1.00	.75	.68	.74	.72	.59	.73	.73	.67	-.44	-.50	.58	.07
8	-.47	-.45	-.35	.71	.73	.73	.75	1.00	.68	.75	.70	.55	.74	.72	.65	-.44	-.47	.61	.11
9	-.08	-.14	.02	.66	.67	.67	.68	.68	1.00	.70	.62	.43	.71	.70	.67	-.04	-.06	.62	.31
10	-.42	-.43	-.32	.71	.73	.73	.74	.75	.70	1.00	.71	.57	.75	.73	.68	-.34	-.40	.61	.13
11	-.55	-.57	-.53	.72	.73	.73	.72	.70	.62	.71	1.00	.69	.69	.70	.68	-.43	-.53	.53	.02
12	-.59	-.60	-.58	.64	.62	.62	.59	.56	.43	.57	.69	1.00	.55	.58	.60	-.44	-.58	.33	-.07
13	-.35	-.35	-.24	.70	.72	.72	.73	.74	.71	.75	.69	.55	1.00	.74	.69	-.28	-.34	.24	.22
14	-.38	-.39	-.28	.71	.73	.73	.73	.72	.70	.73	.70	.58	.74	1.00	.73	-.27	-.36	.62	.18
15	-.27	-.35	-.23	.70	.70	.69	.67	.65	.67	.68	.68	.60	.69	.73	1.00	-.07	-.22	.57	.19
16	.69	.62	.65	-.39	-.40	-.42	-.44	-.44	-.04	-.34	-.43	-.44	-.28	-.27	-.07	1.00	.72	-.08	.26
17	.74	.69	.70	-.49	-.49	-.50	-.50	-.47	-.06	-.40	-.53	-.58	-.34	-.36	-.22	.72	1.00	-.07	.30
18	-.08	-.05	.01	.52	.55	.56	.58	.61	.62	.61	.53	.33	.24	.62	.57	-.08	-.07	1.00	.62
19	.27	.26	.25	-.01	.03	.04	.07	.11	.31	.13	.02	-.07	.22	.18	.19	.26	.30	.62	1.00
	1	2	3	4	5	6	7	8	9	10	11	12	13	14	15	16	17	18	19

Observation error correlation between channels.

Table 4a

Observation error variances (including synthetic radiance computation error) in $(°K)^2$
(var of the correlated part , var of the uncorrelated part)

(0.6,4.8),(1.1,0.6),(1.2,0.5),(0.4,0.3),(1.0,0.2),(2.2,0.4),(2.8,0.7),(2.5,2.2)
(6.0,6.0),(3.2,1.5),(3.8,1.5),(4.1,1.8),(3.7,1.8),(3.0,0.5),(1.0,0.2),(9.9,1.0)
(2.1,0.2),(2.8,2.3),(2.8,2.3)

Radius of influence of correlations between observation radiance error (in Km)
300. 800. 800. 500. 500. 500. 600. 300. 700. 400. 400. 500. 800. 800. 500. 500.
500. 100. 100.

Table 4b

TOVS RETRIEVALS IN THE U.K.: PROGRESS AND PLANS

J.R.Eyre, R.W.Pescod, P.D.Watts,
(Meteorological Office Unit, Hooke Institute for Atmospheric Research, Clarendon Laboratory, Oxford, U.K.)

P.E.Lloyd,
(Dept. of Atmospheric Physics, Hooke Institute for Atmospheric Research, Clarendon Laboratory, Oxford, U.K.)

W.Adams and R.J.Allam
(Meteorological Office, London Road, Bracknell, U.K.)

1. INTRODUCTION

The Satellite Meteorology branch of the Meteorological Office at Bracknell runs a processing scheme called LASS (Local Area Sounding System) to provide retrievals from locally-received TOVS (TIROS Operational Vertical Sounder) data in real-time for use in operational weather forecasting and in particular for inclusion in the data assimilation of the regional forecast model (Bell 1986). At the Hooke Institute for Atmospheric Research in Oxford, activities include research on improved methods for processing TOVS data which, if successful, are introduced into the operational system at Bracknell. The original software for the TOVS processing scheme was obtained from the Co-operative Institute for Meteorological Satellite Studies (CIMSS), Madison, in 1980 and is commonly known as "Export Package I". This system has already been modified in many respects and continued modifications are planned, some of them constituting fundamental changes to the original retrieval methods.

The main features of the LASS scheme have been described by Eyre (1984a) and by Turner et al (1985). Developments to this system up to the end of 1984 are reviewed by Eyre et al (1985). In this paper we review developments to the operational system since the Second International TOVS Study Conference (TOVS-II) and discuss aspects of research which are currently underway or planned. These include the development of a new TOVS cloud-clearing scheme and the investigation of AVHRR (Advanced Very High Resolution Radiometer) data both to validate the new cloud-clearing scheme and to extract parameters for improving this scheme. The inversion scheme used operationally is still a regression method but now uses regression coefficients generated locally rather than those obtained from NESDIS. Research continues on a new inversion scheme which retrieves simultaneously all atmospheric variables of interest and uses a forecast first-guess profile and its error covariance to constrain the inversion. Some preliminary results are presented. Also, plans for a new scheme to pre-process MSU data are described.

2. OPERATIONAL DEVELOPMENTS

2.1 Locally-generated retrieval coefficients

In July 1985, LASS was modified to use locally-generated retrieval coefficients in place of the operational NESDIS coefficients. A data set of 9600 radiosonde profiles from a 7-year period for the European/N.Atlantic area (800 profiles for each month) has been constructed (Pescod and Eyre 1983). A fast radiative transfer model (Eyre 1984b) is used to calculate the corresponding TOVS brightness temperatures for the appropriate monthly sub-set. Regression coefficients are then computed from coefficients of a truncated eigenvector representation of the profile and brightness temperature covariance matrices in the manner described by Smith and Woolf (1976). TOVS channels used in the inversion for NOAA-9 are HIRS (High-resolution Infra-red Radiation Sounder) channels 1-8 and 10-15 and MSU (Microwave Sounding Unit) channels 2-4. A full description of the scheme for calculating the retrieval coefficients and the inter-channel regression coefficients used in the cloud-clearing is given by Watts (1984).

This change represents a transition from a purely statistical inversion scheme (as used operationally by NESDIS -- see Smith et al, 1979) to a physical-statistical scheme, since radiative transfer calculations are required in the computation of the retrieval coefficients.

2.2 Bias corrections

In any inversion scheme which includes radiative transfer calculations it is necessary to make provision for empirical corrections to minimise differences between measured and theoretically computed radiances. We have followed the approach adopted by many other groups, in which calculated atmospheric transmittances for channel i are raised to the power γ_i and brightness temperatures calculated using these adjusted transmittances are further corrected by a bias term, δ_i. The γ-values employed are those calculated and supplied by CIMSS, and those currently used for NOAA-9 are given in Table 1.

δ-values are calculated locally. As part of LASS, all radiosonde profiles which collocate with TOVS retrievals to within 150 km and 3 hours are captured and archived. Every day the brightness temperatures corresponding to the radiosonde profiles are calculated, and the mean and standard deviation of their difference from collocated measured brightness temperatures are computed using the scheme described by Eyre (1983). Daily values are later combined to give monthly statistics. In these radiative transfer calculations the CIMSS γ-values are used but δ is set to zero. The mean difference

between measured and calculated brightness temperatures can then be used to assess the appropriate δ-values to apply in the retrieval scheme.

Recently we have made several improvements to the brightness temperature collocation scheme. The quality control on radiosonde profiles has been improved in several respects. At heights above the reported radiosonde special levels, a temperature profile is extrapolated using regression relations on temperatures at lower levels. Errors, both systematic and random, are inherent in this extrapolation which complicates the interpretation of the subsequent difference statistics for those TOVS channels with stratospheric weighting functions. We have alleviated this problem to some extent by insisting that an acceptable radiosonde ascent must reach 15 mb or higher (rather than 50 mb as previously) and by including the extra pressure levels (30, 25, 20 and 15 mb) in the extrapolation procedure for higher levels. Nevertheless problems in assessing the radiative transfer model for the stratospheric channels remain. Problems also exist for the channels which sense the surface, since radiosonde reports do not in general include a value for the surface "skin" temperature. We currently set this equal to the surface air temperature and, in the quality control, insist that measured and computed values of HIRS-8 brightness temperature are within 5K. Even so, examination of the difference statistics indicates that values for the window channels (and to a lesser extent channels sounding the lower troposphere) are significantly affected by residual cloud contamination. The monthly values obtained for all channels since the above improvements were introduced are shown in Fig.1.

The δ-values assessed with the aid of these statistics are applied in the calculation of retrieval coefficients and are updated only infrequently. They correspond to bias corrections of brightness temperatures. In addition to these, we are currently applying biases to the retrieved products on the basis of the mean differences between retrieved temperatures/dew-points and those of collocated radiosondes. These "product biases" are monitored daily and updated every few days as necessary. The aim of these corrections is to maintain a satellite sounding product which is unbiased with respect to other observing systems. These biases will include components from a number of sources: any mean errors in calculated brightness temperatures inadequately corrected by the γ-δ scheme, residual cloud contamination errors, any mean radiosonde errors and others. However they also include significant biases from a source which has received little attention until recently -- a mean error which arises because, for any limited area and/or period, the mean "first guess" used in the inversion process is different from the mean atmospheric state. This effect is discussed further in section 3.4. In the case of our current operational retrieval scheme, the first guess implicit in the inversion is the climatological mean profile for the European/N.Atlantic area in the appropriate month.

2.3 New cloud-clearing scheme

A new approach to the HIRS cloud-clearing problem has been outlined previously (Eyre et al 1985). Briefly, at each HIRS field-of-view (FOV) for each channel an estimate of the clear column brightness temperature and its error is obtained by some method: the measured brightness temperature may be passed as cloud-free, or it may be cleared using the N* method, or it may be obtained by regression from the MSU data. A two-dimensional sequential estimation filter is then applied to this field of estimates (and their estimated errors) to obtain improved values at every HIRS FOV. A detailed description of this scheme is given by Eyre and Watts (1986). Further discussion of some aspects of the scheme, particularly those relevant to its validation, is presented in a companion paper (Watts and Eyre 1986).

The new cloud-clearing scheme has been validated successfully in research mode and is currently undergoing operational trials.

2.4 Other developments

Some other minor changes to the operational scheme have been implemented since TOVS-II. The new HIRS calibration scheme made available by CIMSS with "Export Package III" has been introduced. This removes discontinuities in the calibrated radiance fields by allowing the calibration coefficients to vary linearly in time between HIRS calibration frames.

Further work has been done on the scan-dependent errors in calibrated MSU brightness temperatures. Corrections for this effect are supplied by CIMSS but there is evidence that they do not compensate fully for the observed effects in the European area. We therefore calculated "residual scan-dependent corrections" which are applied in addition to the CIMSS values (Eyre and Pescod 1985). The values currently used for NOAA-9 are given in Table 2. These corrections are applied after all brightness temperatures have been corrected to nadir, and it should be noted that they compensate not only for any residual instrument anomalies but also for any mean errors in the MSU "limb corrections".

The diagnostic software of LASS has been enhanced in a number of ways. A system of flags has been added to identify the reason for a retrieval failure (e.g. data not available, cloud-clearing failure, surface elevation too high). With appropriate display software, this gives a more effective means of monitoring problems and finding their causes. Prior to sending the operational retrievals for use in the numerical forecast suite, these flags are examined and unreliable data suppressed. This system is also used to trap other classes of retrieval which are known through experience to be unreliable. For example, acting on the statistical evaluation of differences between

retrievals and collocated radiosondes partitioned according to scan angle, we are currently suppressing all retrievals in the outermost 4 HIRS FOVs on each side of the swath. This particular problem is discussed further in sections 3.2 and 5.1.

3. FORECAST FIRST-GUESS INVERSIONS

3.1 Theory and implementation

At TOVS-II, plans were outlined for an inversion scheme which uses a forecast profile as first guess and the forecast error covariance as a constraint on the inversion (Eyre et al 1985). Since then, such a scheme has been developed and its theoretical characteristics examined. It has recently been used in trials with real data. Plans have also been made for the incorporation of these retrievals into the forecast model assimilation scheme (Lorenc et al 1985).

The work is motivated by the conviction that TOVS retrievals should not be treated as an end in themselves, but rather as part of the process whereby information from satellite-measured radiances are assimilated into numerical weather prediction models. Indeed the scheme under development, although it retains a separate "retrieval" stage, is almost mathematically identical to an optimal interpolation scheme (in the vertical) for including cloud-cleared brightness temperatures directly in a multi-variate analysis of model temperature. It has been recognised that the common current practice of assimilating satellite sounding data as though they were poor quality radiosondes is unsatisfactory and often degrades the analysis. This arises principally because the retrieved profiles necessarily contain some components from the first guess used in the inversion (see section 3.4), and the data assimilation should be performed in such a way that this first guess dependence is recognised and compensated for. The problem is most acute with retrieval schemes which use a climatological first guess, which can often be very different from the true atmospheric state. In order to compensate correctly for this first-guess dependence, the assimilation scheme should be presented with both the retrieved profile AND the first guess on which it was based. Effectively, it is the difference between the retrieval and its first guess which contains the new information from the radiances which the model should attempt to assimilate.

The forecast first-guess inversion takes the following form: we retrieve a "profile vector" which should include simultaneously all the variables of interest. At present it contains temperature and humidity profiles and surface temperature but it could be extended to include total ozone, microwave surface emissivity or any other variable which has a significant effect on TOVS radiances. The

retrieved profile vector, $\hat{\underset{\sim}{x}}$, is obtained using the relation

$$\hat{\underset{\sim}{x}} = \underset{\sim}{x}_0 + (\underset{\sim}{K}\cdot\underset{\sim}{C})^T \cdot (\underset{\sim}{K}\cdot\underset{\sim}{C}\cdot\underset{\sim}{K}^T + \underset{\sim}{E})^{-1} \cdot (\underset{\sim}{y}_m - \underset{\sim}{y}_c(\underset{\sim}{x}_0)), \qquad (1)$$

where $\underset{\sim}{x}_0$ is the first guess for the profile vector obtained from the forecast model,
$\underset{\sim}{C}$ is the covariance of the first guess error,
$\underset{\sim}{y}_m$ is the vector of measured (pre-processed, cloud-cleared) brightness temperatures,
$\underset{\sim}{E}$ is the error covariance of $\underset{\sim}{y}_m$,
$\underset{\sim}{y}_c(\underset{\sim}{x}_0)$ is the brightness temperature vector calculated from the first guess,
and $\underset{\sim}{K}$ is a matrix containing the partial derivatives of the elements of $\underset{\sim}{y}$ with respect to the elements of $\underset{\sim}{x}$ (ideally evaluated at $\underset{\sim}{x} = \underset{\sim}{x}_0$).

This leads to a statistically optimal retrieval if $\underset{\sim}{y}_m$ and $\underset{\sim}{x}_0$ have Gaussian error statistics and the problem remains linear to the perturbations of $\underset{\sim}{x}$ about $\underset{\sim}{x}_0$ which are encountered in practice (see, for example, Rodgers 1976).

$\underset{\sim}{x}_0$ is obtained for the location of the sounding from forecast fields of the Meteorological Office's "fine-mesh" (regional) forecast model which has a horizontal resolution of about 75 km. To date, we have used forecasts of about 12 hours -- forecast fields for T+6, T+12 and T+18 hours have been interpolated linearly to the time of the satellite data. Forecast fields are available interpolated to standard pressure levels and we have made use of fields of temperature (skin, 1.5 m and standard levels from 1000 to 50 mb), relative humidity (1.5 m and standard levels from 1000 to 300 mb) and surface pressure.

$\underset{\sim}{C}$ has been evaluated by diagnostic experiments on forecast model output. The differences between 12-hour forecasts and subsequent analyses valid for the same time have been calculated for a large number of cases for the appropriate month. The standard deviation of difference at each level and the inter-level correlations of these differences have been calculated. It is recognised that these represent an under-estimate of forecast model error because analysis and forecast errors are positively correlated. Previous work using forecast-radiosonde differences has suggested that true forecast errors have a standard deviation of about 1.4 times the standard deviation of forecast-analysis difference. We have therefore applied this factor to obtain the forecast error at all levels but have preserved the same coefficients for the inter-level correlation of error in the computation of the forecast error covariance matrix. Further work remains to be done to assess whether these assumptions are appropriate and to what extent one matrix is adequate to characterise the forecast error. Table 3 gives the values used in this study.

At levels above 50 mb, values of $\underset{\sim}{x_o}$ are extrapolated by regression on values at lower levels (using regression coefficients computed from a set of radiosonde/rocket-sonde profiles extending to 0.1 mb). Corresponding elements of $\underset{\sim}{C}$ are calculated taking account of the errors in those lower levels used in the extrapolation, their amplification by the regression coefficients and the residual error in the regression relation.

$\underset{\sim}{y_m}$ is a vector of TOVS brightness temperature obtained at the output of the cloud-clearing stage (either the original version or the new scheme discussed in section 2.3). HIRS channels 1-8 and 10-15 and MSU channels 2-4 are used for NOAA-9. $\underset{\sim}{E}$ is the error covariance of $\underset{\sim}{y_m}$ and to date we have assumed a diagonal matrix (equivalent to errors uncorrelated between channels). The diagonal elements have been estimated in an ad hoc manner but are constrained to lie between the radiometric noise and the standard deviation of measured-calculated brightness temperature differences discussed in section 2.2. Strictly, $\underset{\sim}{E}$ should also allow for any uncompensated error in $\underset{\sim}{y_c}(\underset{\sim}{x_o})$. Table 4 gives the values used in this study.

$\underset{\sim}{K}$ has been computed by a perturbation experiment. For a given atmospheric profile, vector $\underset{\sim}{x}$, the corresponding brightness temperatures are calculated. Then one element only of $\underset{\sim}{x}$ is perturbed by 1 unit (1K for temperature, 1% for relative humidity) and the brightness temperatures re-calculated. This is repeated for all other elements of $\underset{\sim}{x}$ in turn, and the differences between the brightness temperatures for the perturbed profiles and the unperturbed profile then yield all the elements of $\underset{\sim}{K}$. To date, when processing data for a given month, we have used just one K-matrix, obtained from the mean matrix for 100 representative profiles. The sensitivity of the method to changes in $\underset{\sim}{K}$ and the need for a number of such matrices has yet to be explored.

If the first guess and measurement errors have Gaussian statistics it can be shown that the probability that the measured brightness temperature vector belongs to the population described by the first-guess brightness temperature vector and its error covariance is given by

$$P \propto \exp\left\{-\tfrac{1}{2}\,(\underset{\sim}{y_m} - \underset{\sim}{y_c}\{\underset{\sim}{x_o}\})^T \cdot (\underset{\sim}{K}\cdot\underset{\sim}{C}\cdot\underset{\sim}{K}^T + \underset{\sim}{E})^{-1} \cdot (\underset{\sim}{y_m} - \underset{\sim}{y_c}\{\underset{\sim}{x_o}\})\right\}, \quad (2)$$

or $(-2 \ln P + \text{constant}) =$

$$(\underset{\sim}{y_m} - \underset{\sim}{y_c}\{\underset{\sim}{x_o}\})^T \cdot (\underset{\sim}{K}\cdot\underset{\sim}{C}\cdot\underset{\sim}{K}^T + \underset{\sim}{E})^{-1} \cdot (\underset{\sim}{y_m} - \underset{\sim}{y_c}\{\underset{\sim}{x_o}\}) . \quad (3)$$

This suggests a method of quality control: for each measurement $\underset{\sim}{y_m}$ and first guess $\underset{\sim}{x_g}$, the right hand side of Equ.3 is evaluated. It can be shown that the expected value of the quantity is equal to the number of channels used, N, and that values greater than (say) 3N are improbable for truly Gaussian statistics. When such values occur they can be interpreted as values of either brightness temperature vector

or forecast profile vector which lie beyond their normal error bounds. Experience so far suggests that many of the soundings rejected by this test correspond to gross cloud-clearing errors, although further investigation of the behaviour of this quality control procedure is necessary.

The new inversion scheme is intended to run with a forecast first guess but can also be applied using a climatological first guess. In this case an appropriate C-matrix is the covariance of a set of radiosonde profiles representative of climatology, with their mean profile as $\underset{\sim}{x}_0$. This mode could be useful operationally as a "fall-back" option if, for some reason, an appropriate forecast were not available.

3.2 Case study

As a preliminary evaluation of the new inversion scheme, it was applied to the 6 passes of NOAA-9 data received by LASS on 25 January 1986. These data have been processed using both the current operational (regression) inversion scheme and the new forecast first-guess scheme. In each case, input data from both the operational cloud-clearing scheme and the new scheme (see section 2.3) have been used. In addition, those operational cloud-cleared brightness temperatures which collocated with radiosonde profiles have been re-processed with the forecast first-guess inversion scheme, and statistics of differences between retrievals and radiosondes produced for both schemes. These experiments have yielded interesting insights into the performance of the new inversion scheme and have also provided a data base for assimilation experiments. Only a small selection of the results obtained are presented here to illustrate some of the major findings so far.

As stated above, optimal assimilation of retrievals requires access to the first guess used in the inversion. For this reason we output them both and have also found it useful to retain both measured and first-guess brightness temperatures. This permits examination of difference fields of either retrieved minus first-guess values or measured minus first-guess brightness temperatures. Fig.2 shows for one pass the field of retrieved minus first-guess surface temperature. Soundings for which Equ.3 gives values greater than 3N have been excluded. As expected, this is found to be very similar to the pattern for measured minus first-guess brightness temperature in HIRS channel 8. These difference fields are expected to be very sensitive to any deficiencies in the cloud-clearing scheme and some areas of negative values are thought to be a result of this. Indeed, the cloud-clearing schemes (both old and new) performed significantly worse on this particular day than is usual. Examination of the problem showed that the inter-channel regression relations used in the cloud-clearing did not hold to within their usual tolerances. This

feature has prompted further improvements to the cloud-clearing scheme. Nevertheless there are other areas in Fig.3, particularly where the surface temperature difference is positive, in which measurements appear to be identifying real errors in the first-guess field.

Fig.3 is a difference field for measured minus first-guess MSU channel 2. It confirms that, for a mid-tropospheric sounding channel in which cloud-clearing problems are negligible, the differences (and hence the first-guess errors themselves) are small. It also reveals the "tram-line" effect resulting from systematic limb correction errors and confirms the findings of LeMarshall and Schreiner (1985). It is clear in this case that the limb correction error is of a magnitude comparable to the first-guess error we are attempting to correct and confirms the need to move to a retrieval method which obviates the limb correction step as soon as possible.

Comparisons with collocated radiosondes have given some interesting results. Fig.4 shows the standard deviation of the difference between retrievals and collocated radiosondes for one pass using a number of retrieval approaches. The values shown represent "differences" and not purely retrieval errors, since they contain contributions from radiosonde errors and "collocation errors". However, if these are uncorrelated with the errors in the satellite data, the difference statistics provide a useful guide to the relative errors in retrievals by different methods. The new scheme, when used with a climatological first guess and constraint, is seen to give very similar results to those from the operational regression retrieval. This is expected since the two methods are mathematically identical in the linear limit. The retrievals with a forecast first guess are significantly better at most levels, demonstrating the sensitivity to an improved first-guess. The correspondence with radiosondes is improved a little further by screening out those soundings for which the measured and first-guess brightness temperatures are inconsistent (i.e. right-hand side of Equ.3 greater than 3N). However at most levels the best agreement with radiosondes is found with the first-guess alone, showing that the retrievals have not produced an overall improvement on the first guess. Results for other passes differ in detail but yield the same general conclusions.

3.3 Discussion

The above results are disappointing, and it should be remembered that this is the first full trial of the scheme. Several improvements to the scheme are possible (e.g. in the way the stratosphere is extrapolated above the forecast model first guess) and this case study may not be typical. Also the validation is biased towards land, where most of the radiosondes are located and where the short-range forecast errors are expected to be lower. However, some insight into the

reason why overall improvements on the first guess are difficult to achieve can be obtaining by examining the matrix $\underset{\sim}{K}.\underset{\sim}{C}.\underset{\sim}{K}^T$. This is the forecast error covariance mapped into brightness temperature space, i.e. the covariance of first-guess brightness temperature error. The square roots of its diagonal element give a measure of the "first guess error" in each channel. These are given in Table 4 along with the assumed measurement errors (i.e. the square roots of the diagonal elements of $\underset{\sim}{E}$). The first-guess brightness temperature errors are seen to be quite small and comparable with the assumed measurement errors. This arises because:

- the forecast profile error itself is quite small, which is not surprising for a 12-hour forecast in northern hemisphere mid-latitudes,

- the weighting functions of TOVS are broad, and

- the inter-level correlations of forecast error are quite weak.

These factors limit the ability of TOVS data to make large overall improvements to the first guess but are not sufficient to explain why they should degrade it. This leads us to conclude that, at present, the errors in the measurements after pre-processing and cloud-clearing are larger than those assumed and that the quality control of the brightness temperatures used in the inversion is not adequate. Furthermore, these results suggest that it is essential to perform the pre-processing, cloud-clearing and quality-control with extreme care if TOVS measurements are to have a positive impact on the first guess.

3.4 A theoretical study of systematic errors in satellite sounding products

The development of a forecast first-guess inversion scheme and the importance of an appropriate first guess resulted in a parallel theoretical study of the role of the first guess and an analysis of the systematic retrieval errors which it can produce. This study is described in detail by Eyre (1987).

To summarise, Equ.1 can be re-written as

$$\underset{\sim}{\hat{x}} - \underset{\sim}{x_0} = \underset{\sim}{W} . (\underset{\sim}{y_m} - \underset{\sim}{y_c}\{\underset{\sim}{x_0}\}) . \qquad (4)$$

$\underset{\sim}{W}$ is the "inverse matrix" and in our case takes the particular form for a minimum variance inversion. However Equ.4 is a general expression relevant to any linear inversion algorithm for a general inverse matrix, $\underset{\sim}{W}$, and a general first guess, $\underset{\sim}{x_0}$. Also, the "forward" problem can be written in general as:

$$\underset{\sim}{y_m} - \underset{\sim}{y_c}\{\underset{\sim}{x_0}\} = \underset{\sim}{K} . (\underset{\sim}{x_T} - \underset{\sim}{x_0}) + \underset{\sim}{\epsilon_m} , \qquad (5)$$

where $\underset{\sim}{x}_T$ is the true atmospheric profile and $\underset{\sim}{\epsilon}_m$ is the measurement error. Substituting Equ.5 into Equ.4 gives

$$\hat{\underset{\sim}{x}} - \underset{\sim}{x}_0 = \underset{\sim}{W} \cdot \underset{\sim}{K} \cdot (\underset{\sim}{x}_T - \underset{\sim}{x}_0) + \underset{\sim}{W} \cdot \underset{\sim}{\epsilon}_m , \qquad (6)$$

and re-arranging:

$$\hat{\underset{\sim}{x}} - \underset{\sim}{x}_T = (\underset{\sim}{I} - \underset{\sim}{W} \cdot \underset{\sim}{K}) \cdot (\underset{\sim}{x}_0 - \underset{\sim}{x}_T) + \underset{\sim}{W} \cdot \underset{\sim}{\epsilon}_m , \qquad (7)$$

where $\underset{\sim}{I}$ is an identity matrix. This is an equation for retrieval error which states that it is composed of two parts: measurement error, mapped into retrieval error through matrix $\underset{\sim}{W}$, and first guess error, mapped into retrieval error though matrix $(\underset{\sim}{I}-\underset{\sim}{W}.\underset{\sim}{K})$. In general $\underset{\sim}{W}.\underset{\sim}{K} \neq \underset{\sim}{I}$, and so the retrieval error is sensitive to the first-guess error. Moreover, for a particular retrieval in which $\underset{\sim}{W}$ and $\underset{\sim}{K}$ are known, this dependence can be quantified for the linear case. Iterative methods are often applied in an attempt to handle the non-linear aspects of the inversion, but it can be shown that the problem of first-guess dependence is not significantly reduced by iteration.

For climate studies we are often interested in observations averaged in time and space. If satellite soundings are averaged in this manner (and assuming that the measurement errors are unbiased and the problem remains linear), Equ.7 yields

$$\overline{\hat{\underset{\sim}{x}} - \underset{\sim}{x}_T} = (\underset{\sim}{I} - \underset{\sim}{W} \cdot \underset{\sim}{K}) \cdot \overline{\underset{\sim}{x}_0 - \underset{\sim}{x}_T} + \underset{\sim}{W} \cdot \overline{\underset{\sim}{\epsilon}_m} . \qquad (8)$$

On averaging over many retrievals, the component due to measurement error will become negligible. Then we see that the mean retrieval error is determined by the mean first-guess error and the matrix, $(\underset{\sim}{I}-\underset{\sim}{W}.\underset{\sim}{K})$. This result may have important implications for the use of satellite sounding products in climate studies, particularly if a zonal or global mean first guess is used in the inversion, which is presently the case for NESDIS operational retrievals of both temperature/humidity profiles from TOVS (Smith et al 1979) and sea surface temperature from AVHRR (McClain et al 1983).

4. INVESTIGATIONS OF AVHRR AND TOVS DATA

AVHRR data are being used to improve the exploitation of TOVS data in two ways. They are being employed as a diagnostic tool to evaluate and improve the new TOVS-only cloud-clearing scheme. This work is described separately (Watts and Eyre 1986). Also they are being investigated as part of a TOVS+AVHRR cloud-clearing scheme. Initial work in this area was described by Lloyd et al (1985).

Validation of the TOVS-only scheme using AVHRR data has demonstrated an improved performance compared with the old scheme but has highlighted a number of weaknesses which are difficult to correct with any TOVS-only scheme. Firstly, in some HIRS FOVs flagged as clear, residual cloud contamination remains a problem -- the weighting function of MSU channel 2 peaks too high to be used with HIRS as a sensitive indicator of low cloud. Secondly, although the N* algorithm is used with some gross quality checks, no explicit tests are made to establish whether the cloud and surface conditions assumed by the N* algorithm are actually obeyed. Thirdly, HIRS data estimated from MSU data give particular problems in the window and low-level HIRS channels for which MSU channels 2-4 are relatively poor predictors. All these aspects may be improved with the help of information extracted from AVHRR data.

The processing scheme applied to the group of AVHRR pixels within each HIRS FOV is outlined in Fig.5. A series of cloud detection tests is used at the pixel level. They are similar to those described by Saunders (1986). In addition, a test on the difference between brightness temperatures in AVHRR channels 4 and 5 is applied: cloud is detected if

$$T_4 - T_5 > c \cdot T_5 - d \quad , \qquad (9)$$

where T_4 and T_5 are in K, and c and d are respectively 0.065 and 17.255 K over sea and 0.094 and 25.11 K over land. The coefficients have been determined empirically (J.N. Roozekrans, private communication), and the test is a useful check particularly for thin, high-level cloud. Over the sea (and over land at night when shortwave checks cannot be used), a spatial coherence check is applied in addition -- the standard deviation of each 3x3 box of pixels for cloud-free conditions must not exceed 0.2 K over sea and 1 K over land in AVHRR channel 4. From the pixels which pass all the cloud tests applied, the mean cloud-free radiance is calculated. If all pixels are judged cloud-free then the HIRS data can be used directly. Otherwise an analysis of the type of cloud contamination is made. The histogram of local mean against local standard deviation of brightness temperature in AVHRR channel 4 is analysed in a manner similar to that described by Coakley and Bretherton (1982) as a test for single-layer cloud. If a HIRS FOV passes this test it becomes a candidate for the N* algorithm. In coastal areas, and elsewhere if the single-layer test fails, the measured HIRS data are rejected and cloud-cleared HIRS values are estimated by regression from MSU data. However, if clear brightness temperature estimates are available from AVHRR channels 4 and 5, these are used to calculate the clear-column brightness temperature in HIRS channel 8 through a regression relation. This is then used with the MSU data as a predictor for the other HIRS channels.

The above tests lead to each HIRS pixel being labelled as in one of 4 categories. For the candidate N* category it is necessary also to check that "N* conditions" hold between the HIRS FOV and one of its neighbours. We require that the neighbour is colder and that the AVHRR mean clear brightness temperatures in the 2 fields of view are within 0.5 K of each other and the mean cloudy brightness temperatures within 1 K. If this test fails for all neighbouring FOVs, then we revert to estimating HIRS values by regression on MSU and AVHRR data. In other respects, the TOVS+AVHRR cloud-clearing scheme follows the approach of the TOVS-only scheme discussed in section 2.3.

Fig.6 illustrates the cloud-clearing routes taken in both schemes for each FOV on the same 48 scan lines of HIRS data over western Europe. Clear areas are identified in the same general regions, but the details of the processing show marked differences. The TOVS+AVHRR scheme identifies fewer clear FOVs. This arises primarily because the detection of low cloud and small amounts of cloud is more successful with AVHRR data. However the number flagged as clear depends somewhat on the levels of various empirical thresholds used in the cloud detection, and there is scope for further work to determine the optimum values for these. The number of N* FOVs is also considerably reduced with AVHRR data, principally because a much more stringent test for good N* conditions is now available. This results in a greater proportion of FOVs for which HIRS data are rejected, and we have not yet established a successful procedure for recovering any information from tropospheric HIRS channels in these regions. However in many cases we are able to improve on HIRS estimates obtained from MSU by the addition of a HIRS channel 8 value constructed from cloud-free AVHRR data.

Validation of the TOVS+AVHRR scheme presents a problem since we are no longer able to use AVHRR data as independent information. We have recently turned to brightness temperatures computed from forecast fields (as described in section 3.1) as an independent standard against which the two cloud-clearing schemes may be compared. With this approach we do not assume that the forecast values approximate to the truth but only require that their errors are uncorrelated with the errors in either cloud-clearing scheme. Then the r.m.s. differences between forecast brightness temperatures and cloud-cleared brightness temperatures, obtained for the same FOVs by different methods, provide measures of the relative performances of the methods. Fig.7 illustrates preliminary results from this method of comparison; all HIRS channel 8 brightness temperatures obtained from MSU+AVHRR with the TOVS+AVHRR scheme are shown, together with the results for the same FOVs (processed by various routes) for the TOVS-only scheme. The comparison here is made prior to the sequential estimation filtering, so that the changes made in the initial cloud-clearing are not obscured. This study is currently incomplete, and Fig.7 serves only as an illustration of the validation approach.

5. FUTURE PLANS

5.1 General

It is evident from recent work on the forecast first-guess inversion scheme (section 3) that the measurements used at the inversion stage must be of very high quality if TOVS data are to provide a useful input to regional, short-range forecasting systems in the northern hemisphere. For data to have a significant positive impact on the forecast model, the brightness temperature errors assumed in the inversion must approximate to those of the data, and these must be comparable or lower than the brightness temperature errors corresponding to typical forecast model errors. This means that the cloud-clearing and other pre-processing must be accurate and that quality control within these processes is very demanding. There is strong evidence for significant deficiencies in current operational LASS pre-processing algorithms which render the retrievals of marginal value for their intended application. Consequently, it is proposed to develop new pre-processing procedures to address these problems.

One obvious deficiency is in the limb correction. This problem can be ameliorated by removing the limb correction for both HIRS and MSU data and applying the brightness temperatures at their angle of measurement. Improvements should be greatest for the MSU channels (for which the current regression limb-corrections are most deficient), but these data also play a crucial role in HIRS cloud-clearing. It is also planned to remove the MSU surface emissivity correction and to treat emissivity as a free parameter of the inversion (with suitable constraints).

We are currently investigating a new approach to those aspects of MSU pre-processing which remain, namely the antenna pattern correction and the mapping of MSU data to HIRS FOVs. This method is outlined in section 5.2. Transition to such a scheme will necessitate the re-assessment of MSU scan-dependent corrections, and this will probably be performed most effectively by assessing the mean difference (for a large number of passes) between measured and forecast first-guess brightness temperatures at each angle of measurement.

The calibrated HIRS brightness temperature will undergo minimal pre-processing prior to cloud-clearing; only data quality checks will be performed. The new HIRS cloud-clearing scheme will then need to be adapted to run on non-limb-corrected data. However it will be preferable to retain a local limb correction (i.e. for each 3x3 box to which the N* algorithm is applied) and, for this purpose only, to make a surface emissivity correction to MSU channel 2. We also plan to adapt the forecast first-guess inversion scheme to use brightness temperatures at the angle of measurement. It is anticipated that this will involve calculation of the necessary inverse matrices by interpolation between matrices at a (small) number of zenith angles

(rather than just one matrix for nadir, as at present).

Work will continue to improve the cloud-clearing scheme; a number of possibilities have already been identified for the TOVS-only scheme (see Watts and Eyre 1986). In addition, when the products of AVHRR become available to LASS in real time, further improvements will be possible as demonstrated in section 4.

5.2 A new approach to MSU pre-processing

Although HIRS is the primary instrument within TOVS, MSU is highly complementary. It permits retrievals in cloudy areas, considerably enhances the yield of retrievals in partly cloudy areas and is used widely in the identification of HIRS FOVs which are truly cloud-free. For this reason it is important that the limited amount of MSU data should be used as effectively as possible. The current LASS scheme has a number of deficiencies which render the MSU data of reduced quality, particularly at the edge of the swath where the footprint on the ground is largest (and covers the greatest range of zenith angles) and where the limb and antenna pattern correction problems are most acute. We propose here a new method which treats the MSU pre-processing as an "analysis problem", i.e. we seek the best estimates of the MSU brightness temperature field on some regular grid (in our case, the HIRS FOVs) given relatively sparse measurements of MSU antenna temperature. This approach combines the antenna pattern correction and the mapping to HIRS FOVs into one process.

"Antenna temperature" is the quantity obtained directly from the MSU calibration. It is a measurement of radiation received from a range of incident angles weighted according to the antenna gain pattern of the radiometer. "Brightness temperature" is the radiative temperature of a point in the scene, and so the antenna temperature field is a convolution of the brightness temperature field with the antenna gain pattern. For a scene which is not uniform over angles of significant antenna gain, it is desirable to de-convolve (or otherwise correct) the discrete measurements of antenna temperature to estimate brightness temperatures either as a continuous field or on some discrete grid.

It is proposed to estimate values of the variable brightness temperature field x at grid points i (HIRS FOV centres) from measurements y of measured MSU antenna temperature centred at points k. It is assumed that x and y are related through the antenna gain pattern in a known way. x is a brightness temperature field in one MSU channel as it would be measured by a satellite instrument with a very narrow angular response. The effect of brightness temperature changing with surface zenith angle is therefore present in the across-track direction.

Let x_i^a refer to the analysed value of brightness temperature, and let us assume a background field x_i^b (discussed below). Now let y_k^o and y_k^b be, respectively, the observed antenna temperature and the corresponding value appropriate to the background field. The analysed field can be obtaining by computing increments to the background field which are weighted averages of the observation increments:

$$x_i^a = x_i^b + \frac{\sum_k W_{ki} (y_k^o - y_k^b)}{W_i^b + \sum_k W_{ki}} \qquad (10)$$

W_{ki} is the weight (discussed below) of the kth observation at the ith grid point. Non-zero values of W_i^b imply that the background field values themselves are given some weight in the process.

y_k^o is not a point measurement but on average over the antenna gain pattern, and y_k^b must be calculated accordingly. The brightness temperature field can be expressed in polar co-ordinates referenced to the axis of an MSU sounding as $x(\theta,\phi)$. Similarly the antenna gain pattern is $f(\theta,\phi)$. The antenna temperature calculated from the brightness temperature background field is then

$$y^b = \frac{\int_0^{2\pi}\int_0^{\pi/2} x^b(\theta,\phi)\, f(\theta,\phi)\, \theta\, d\theta\, d\phi}{\int_0^{2\pi}\int_0^{\pi/2} f(\theta,\phi)\, \theta\, d\theta\, d\phi} \qquad (11)$$

If we approximate the continuous field by a field of contiguous rectangular "tiles" of uniform brightness temperature centred on HIRS FOVs, then Equ.11 may be written for measurement k as:

$$y_k^b = \frac{(1 - F_k) \sum_i x_i^b\, f(\theta_{ki}, \phi_{ki})\, G_{ki}}{\sum_i f(\theta_{ki}, \phi_{ki})\, G_{ki}} \qquad (12)$$

$f(\theta_{ki}, \phi_{ki})$ is the value of relative antenna gain at angular displacement (θ_{ki}, ϕ_{ki}) of HIRS tile i with respect to MSU FOV k. G_{ki} is a function representing the relative solid angles subtended by different HIRS tiles when viewed from a fixed satellite position. F_k is the fraction of the antenna gain pattern which "sees" space. In practice F_k will be small even for the outermost MSU FOV but it should be noted that a 1% response from space will lead to a 1% error in brightness temperature if not properly accounted for. The summations in Equ.12 are in principle over all HIRS tiles for which $f(\theta_{ki}, \phi_{ki})$ is non-zero. In practice the summation will be over all points i for which $\theta_{ki} < \theta_{max}$. θ_{max} in the range 10 to 20 degrees should be adequate, but this requires investigation. The HIRS swath contains 56 FOVs with a maximum nadir angle of 49.5 degrees. For the purposes of this analysis, a field must be defined outside this limit to allow an accurate estimation of y_k^b for the outermost MSU FOVs. An extra 6 "HIRS tiles" will be required at each side of the swath.

The weights required in Equ.10 may be found be several methods. A successive correction method, employing an empirical formula for W_{ki}, may prove to be the best, e.g.

$$W_{ki} = A \cdot \exp\{-\theta_{ki}^2 / \theta_o^2\}, \quad (13)$$

where A and θ_o are constants, or a similar expression. A successive correction scheme will use a number of iterations in which the analysed field for one step acts as the background field for the next. If so, θ_o may be reduced at each iteration in order to analyse the larger scales in the field first. The iteration may proceed either for a fixed number of steps (determined empirically) or until the differences between y_k^o and y_k^b are of the order of the MSU noise.

An initial background field is required, and it provides a means of imposing a priori aspects of the brightness temperature field which are not well observed. The more accurate is the background field, the faster will be the convergence of the iteration. It practice it will be necessary to trade off accuracy in the initial field against the ease and speed with which it can be obtained. A simple initial brightness temperature field which may be adequate would be one corresponding to a fixed atmospheric profile and surface temperature but including the limb effect and discontinuities corresponding to changes of emissivity at land-sea boundaries. Beyond the edge of the Earth the field should be initialised, and held constant, as a 3K black body. With such an initial field the treatment of MSU data at the edges of the swath should be improved considerably.

5.3 The effects of ozone on HIRS longwave channels

The radiative transfer model used to simulate TOVS brightness temperatures for given atmospheric profiles includes the effects of ozone on the temperature sounding channels, HIRS 1-7. (It does not at present contain an algorithm for the "ozone" channel, HIRS-9). However, to date we have used a constant ozone total column amount of 347 Dobson Units (DU). Indeed, for many applications of the model (e.g. computation of brightness temperatures from radiosonde or forecast profiles), co-incident measurements of total ozone are not available. The sensitivity to this problem has been assessed by varying the total ozone amount. Fig.8 illustrates the change in brightness temperature for the most sensitive channel, HIRS-5. Values shown are for monthly mean total ozone at 20°N, 50°N and 80°N (taken from Houghton 1977) as differences from the value for 350 DU. Changes in this channel, and also for HIRS channels 4, 6 and 7, are found to be small but not negligible; they probably account for some of the seasonal variation in mean differences between measured and calculated HIRS brightness temperatures (see Fig.1). Also, if an incorrect total ozone amount is used in the forward model of a physical inversion scheme, then changes in brightness temperature which are really caused

by ozone variations may be falsely interpreted as temperature changes. The current practice of using a constant ozone amount may be improved significantly by using a value appropriate to the month and latitude. However, in mid-latitudes day-to-day variations of over 50 DU may occur -- equivalent to about 0.2K in HIRS channel 5. A better approach would be to include HIRS channel 9 among the channels used in the inversion and to add total ozone amount to the variables to be retrieved simultaneously, e.g. through Equ.1. This would effectively correct the temperature sounding channels for ozone changes and also provide retrievals of total ozone optimally corrected for temperature variations.

6. SUMMARY

In this paper we have provided an update to developments on the Meteorological Office's Local Area Sounding System (LASS) with a description of the changes made since the TOVS-II Conference. We have also outlined improvements to the cloud-clearing and inversion procedures which are currently underway. Research on inversions using a forecast first-guess has yielded valuable insights into the true potential and limitations of TOVS data for contributing to improved numerical analyses and has highlighted the problems still to be overcome. Evidence from a number of sources indicates that deficiencies in the pre-processing and remaining weaknesses in the cloud-clearing of the current LASS degrade the measured TOVS brightness temperatures such that they will not provide consistent improvements to numerical analyses over data-dense areas such as Europe. Plans for a new approach to the pre-processing to alleviate these deficiencies have been presented and a method for improving the cloud-clearing through the use of AVHRR data has been outlined.

Research on forecast first-guess retrievals has also led to a theoretical analysis of those systematic errors in satellite sounding products which originate in the inversion process itself. Such error characteristics must be properly understood and allowed for, if the products are to be used optimally in numerical weather prediction or climate studies.

ACKNOWLEDGEMENTS

We have been assisted in this work by the co-operation, assistance and comments of a number of people at both Oxford and Bracknell. We note particularly the contributions of Roger Saunders, Andrew Lorenc, John Turner and David Chapman (Meteorological Office), John Barnett and Charles Warner (Oxford University), and Hans Roozekrans (KNMI, visiting scientist at the Hooke Institute). One of us (PEL) is supported in this work by a studentship of the

Natural Environment Research Council. Finally, we remain indebted to CIMSS for their continued support in the provision of software.

REFERENCES

Bell R.S. 1986
The Meteorological Office fine-mesh data assimilation scheme.
Meteorological Magazine, 115, 161-177.

Coakley J.A., Bretherton F.P. 1982
Cloud cover from high-resolution scanner data: detecting and allowing for partially filled fields of view.
J. Geophys. Res., 87C7, 4917-4932.

Eyre J.R. 1983
Comparisons between measured and simulated TOVS brightness temperatures.
Meteorological Office, Met.O.19 Branch Memo 68.

Eyre J.R. 1984a
High-resolution temperature retrievals at the U.K. Meteorological Office.
Tech. Proc. 1st Int. TOVS Study Conf.; 29 August - 2 Sept 1983; Igls, Austria; CIMSS Report, 94-100.

Eyre J.R. 1984b
User guide to TOVSRAD: a program for calculating synthetic HIRS-2 and MSU equivalent black body temperatures.
Meteorological Office, Met.O.19 Branch Memo 75.

Eyre J.R. 1987
On systematic errors in satellite sounding products and their climatological mean values.
To appear in Quart. J. Roy. Met. Soc.

Eyre J.R., Pescod R.W. 1985
Residual scan-dependent corrections for the Microwave Sounding Unit.
Meteorological Office, Met.O.19 Branch Memo 78.

Eyre J.R., Watts P.D. 1986
A sequential estimation approach to cloud-clearing for satellite temperature sounding.
Submitted to Quart. J. Roy. Met. Soc.

Eyre J.R., Watts P.D., Turner J., Lorenc A.C. 1985
Research and development on TOVS retrievals in the U.K.
Tech. Proc. 2nd Int. TOVS Study Conf., 18-22 February 1985; Igls,

Austria; CIMSS Report, 58-74.

Houghton J.T. 1977
Cambridge University Press.
The physics of atmospheres.

LeMarshall J.F., Schreiner A.J. 1985
Limb effects in satellite temperature sounding.
J. Clim. Appl. Meteor, 24, 287-290.

Lloyd P.E., Barnett J.J., Eyre J.R. 1985
Investigations of AVHRR data to improve TOVS retrievals.
Tech. Proc. 2nd Int. TOVS Study Conf; 18-22 February 1985; Igls, Austria; CIMSS Report, 162-176.

Lorenc A.C., Adams W., Eyre J.R. 1985
The analysis of high resolution satellite data in the Met. Office.
Proc. Workshop on "High resolution analysis"; Reading, U.K.; 24-26 June 1985; ECMWF report, 69-87.

McClain E.P., Pichel W.G., Walton C.C., Ahmad Z., Sutton J. 1983
Multichannel improvement to satellite-derived sea surface temperatures.
Advances in Space Research, 2, 43-47.

Pescod R.W., Eyre J.R. 1983
Accumulation of a set of radiosonde profiles for use with satellite sounding data from the European and N.Atlantic areas.
Meteorological Office, Met.O.19 Branch Memo 71.

Rodgers C.D. 1976
Retrieval of atmospheric temperature and composition profiles from remote measurements of thermal radiation.
Rev. Geophys. Space Phys., 14, 609-624.

Saunders R.W. 1986
An automated scheme for the removal of cloud contamination from AVHRR radiances over Western Europe.
To appear in Int. J. Remote Sensing.

Smith W.L., Woolf H.M. 1976
The use of eigenvectors of statistical covariance matrices for interpreting satellite sounding radiometer observations.
J. Atmos. Sci., 33, 1127-1140.

Smith W.L., Woolf H.M., Hayden C.M., Wark D.Q., McMillin L.M. 1979
The TIROS-N Operational Vertical Sounder.
Bull. Amer. Meteor. Soc., 60, 1177-1187.

Turner J., Eyre J.R., Jerrett D., McCallum E. 1985
The HERMES system.

Meteorological Magazine, 114, 161-173.

Watts P.D. 1984
A study of local area synthetic coefficients for use in the "LASS" system.
Meteorological Office, Met.O.19 Branch Memo 76.

Watts P.D., Eyre J.R. 1986
Validating a TOVS cloud-clearing scheme using AVHRR data.
To be presented at 3rd Int. TOVS Study Conf., 13-19 August 1986; Madison, Wisconsin.

TABLE 1.

Transmittance correction factors, γ, used for NOAA-9

HIRS-1	0.943	HIRS-11	1.015	MSU-1	-
-2	0.971	-12	1.041	-2	1.063
-3	1.156	-13	0.992	-3	1.052
-4	1.049	-14	0.970	-4	0.936
-5	0.944	-15	0.947		
-6	0.971	-16	-		
-7	0.953	-17	-		
-8	1.000	-18	-		
-9	-	-19	-		
-10	1.042	-20	-		

TABLE 2

MSU "ASYMMETRY CORRECTIONS" for NOAA-9 from CIMSS (in K) .

	MSU scan position										
	1	2	3	4	5	6	7	8	9	10	11
MSU-2	-0.093	0.118	0.104	0.075	-0.037	0.000	0.098	0.275	0.543	0.694	1.043
MSU-3	0.385	0.247	0.087	0.049	0.008	0.000	0.047	0.108	0.222	0.420	0.906
MSU-4	-0.302	-0.068	-0.003	-0.005	0.005	0.000	0.010	-0.003	0.001	-0.084	-0.369

MSU "RESIDUAL SCAN-DEPENDENT CORRECTIONS" FOR NOAA-9 (in K)

	MSU scan position										
	1	2	3	4	5	6	7	8	9	10	11
MSU-2	0.69	0.25	0.09	0.01	0.04	0.00	0.01	0.03	0.15	0.37	0.74
MSU-3	0.31	0.13	0.08	0.04	0.01	0.00	0.01	0.04	0.09	0.16	0.29
MSU-4	1.76	0.98	0.50	0.20	0.04	0.00	0.07	0.22	0.53	0.98	1.63

MODIFIED MSU "ASYMMETRY CORRECTIONS" for NOAA-9 (in K) .

	MSU scan position										
	1	2	3	4	5	6	7	8	9	10	11
MSU-2	-0.783	-0.132	0.014	0.065	-0.077	0.000	0.088	0.245	0.393	0.324	0.303
MSU-3	0.075	0.117	0.007	0.009	0.002	0.000	0.037	0.068	0.132	0.260	0.616
MSU-4	-2.062	-1.048	-0.503	-0.205	-0.035	0.000	-0.060	-0.233	-0.529	-1.064	-1.999

Table 3

Assumed forecast errors and inter-level correlations of error

Inter-level correlation coefficients																								Error	Level
temperature at level (mb)														relative humdity at level (mb)							temp	T*	p		
1000	950	850	700	500	400	300	250	200	150	100	70	50	1000	950	850	700	500	400	300	1.5m		msl		
1.00	0.85	0.49	0.17	0.02	-0.01	-0.02	-0.03	-0.02	0.02	0.04	0.06	0.06	-0.04	-0.06	0.01	0.03	0.01	0.00	0.00	0.76	0.19	-0.25	3.58	T-1000
0.85	1.00	0.57	0.18	0.01	-0.03	-0.04	-0.04	-0.02	0.04	0.07	0.08	0.07	0.06	-0.16	0.02	0.05	0.02	0.01	0.01	0.64	0.14	-0.27	3.53	T-950
0.49	0.57	1.00	0.31	0.01	-0.06	-0.07	-0.06	-0.03	0.06	0.10	0.11	0.10	0.13	0.03	-0.16	0.07	0.01	0.01	0.00	0.36	0.02	-0.28	3.04	T-850
0.17	0.18	0.31	1.00	0.15	-0.01	-0.07	-0.09	-0.07	0.02	0.09	0.08	0.07	0.04	0.03	0.00	-0.19	0.01	0.01	0.03	0.12	-0.03	-0.26	2.69	T-700
0.02	0.01	0.01	0.15	1.00	0.33	0.01	-0.18	-0.24	-0.20	-0.09	-0.01	0.01	-0.01	0.01	0.03	0.00	-0.06	0.06	0.06	0.01	-0.01	-0.16	2.48	T-500
-0.01	-0.03	-0.06	-0.01	0.33	1.00	0.17	-0.15	-0.30	-0.33	-0.24	-0.14	-0.11	-0.01	0.01	0.01	0.01	-0.01	0.00	0.07	-0.01	0.05	-0.14	2.87	T-400
-0.02	-0.04	-0.07	-0.07	0.01	0.17	1.00	0.37	-0.13	-0.27	-0.20	-0.12	-0.10	0.02	0.03	0.01	0.02	-0.02	-0.05	0.00	-0.01	0.04	-0.11	2.69	T-300
-0.03	-0.04	-0.06	-0.09	-0.18	-0.15	0.37	1.00	0.28	-0.01	-0.01	-0.04	-0.02	0.00	0.01	-0.01	-0.01	-0.06	-0.11	-0.15	-0.03	-0.01	-0.03	3.80	T-250
-0.02	-0.02	-0.03	-0.07	-0.24	-0.30	-0.13	0.28	1.00	0.50	0.04	0.09	0.10	0.01	0.01	0.00	-0.02	-0.03	-0.08	-0.14	-0.03	-0.04	-0.01	2.81	T-200
0.02	0.04	0.06	0.02	-0.20	-0.33	-0.27	-0.01	0.50	1.00	0.74	0.26	0.23	-0.03	-0.05	-0.01	-0.02	-0.01	-0.02	-0.04	-0.02	-0.11	-0.01	2.43	T-150
0.04	0.07	0.10	0.09	-0.09	-0.24	-0.20	-0.01	0.04	0.74	1.00	0.61	0.51	-0.04	-0.06	-0.01	-0.01	-0.01	0.00	0.01	0.00	-0.14	-0.01	2.69	T-100
0.06	0.08	0.11	0.08	-0.01	-0.14	-0.12	-0.04	0.09	0.26	0.61	1.00	0.88	-0.03	-0.05	-0.01	0.00	-0.03	-0.01	0.00	0.03	-0.09	0.00	2.95	T-70
0.06	0.07	0.10	0.07	0.01	-0.11	-0.10	-0.02	0.10	0.23	0.51	0.88	1.00	-0.02	-0.04	-0.02	-0.01	-0.03	-0.03	0.00	0.04	-0.08	0.03	2.87	T-50
-0.04	0.06	0.13	0.04	-0.01	-0.01	0.02	0.00	0.01	-0.03	-0.04	-0.03	-0.02	1.00	0.56	0.24	0.15	0.06	0.04	0.01	-0.02	0.03	-0.07	22.57	RH-1000
-0.06	-0.16	0.03	0.03	0.01	0.01	0.03	0.01	0.01	-0.05	-0.06	-0.05	-0.04	0.56	1.00	0.34	0.15	0.05	0.04	0.02	0.02	0.06	-0.07	28.59	RH-950
0.01	0.02	-0.16	0.00	0.03	0.01	0.01	-0.01	0.00	-0.01	-0.01	-0.01	-0.02	0.24	0.34	1.00	0.28	0.08	0.06	0.03	0.05	0.06	-0.06	35.20	RH-850
0.03	0.05	0.07	-0.19	0.00	0.01	0.02	-0.01	-0.02	-0.02	-0.01	0.00	-0.01	0.15	0.15	0.28	1.00	0.21	0.11	0.04	0.05	0.04	-0.03	46.08	RH-700
0.01	0.02	0.01	0.01	-0.06	-0.01	-0.02	-0.06	-0.03	-0.01	-0.01	-0.03	-0.03	0.06	0.05	0.08	0.21	1.00	0.45	0.16	0.02	0.03	-0.03	51.61	RH-500
0.00	0.01	0.01	0.01	0.06	0.00	-0.05	-0.11	-0.08	-0.02	0.00	-0.01	-0.03	0.04	0.04	0.06	0.11	0.45	1.00	0.38	0.01	0.02	-0.03	56.44	RH-400
0.00	0.01	0.00	0.03	0.06	0.07	0.00	-0.15	-0.14	-0.04	0.01	0.00	0.00	0.01	0.02	0.03	0.04	0.16	0.38	1.00	0.01	0.01	-0.03	51.48	RH-300
0.76	0.64	0.36	0.12	0.01	-0.01	-0.01	-0.03	-0.03	-0.02	0.00	0.03	0.04	-0.02	0.02	0.05	0.05	0.02	0.01	0.01	1.00	0.43	-0.16	3.31	T-1.5m
0.19	0.14	0.02	-0.03	-0.01	0.05	0.04	-0.01	-0.04	-0.11	-0.14	-0.09	-0.08	0.03	0.06	0.06	0.04	0.03	0.02	0.01	0.43	1.00	-0.09	2.46	T*
-0.25	-0.27	-0.28	-0.26	-0.16	-0.14	-0.11	-0.03	-0.01	-0.01	-0.01	0.00	0.03	-0.07	-0.07	-0.06	-0.03	-0.03	-0.03	-0.03	-0.16	-0.09	1.00	4.83	pmsl

Units: temperature in K
relative humidity in %
pressure in mb

T-1.5m = temperature at 1.5m height
T* = physical surface temperature
pmsl = mean sea level pressure

TABLE 4.

TOVS brightness temperature errors

For NOAA-9.

Channel	Assumed errors in measured brightness temps (K)	Equivalent errors in first-guess brightness temps (K)
HIRS-1	2.7	4.7
-2	1.1	2.6
-3	1.0	2.1
-4	0.5	1.0
-5	0.4	0.8
-6	0.4	0.7
-7	0.4	0.9
-8	0.9	1.6
-9	-	-
-10	0.7	1.4
-11	0.7	3.4
-12	0.9	5.0
-13	0.7	1.1
-14	0.5	0.8
-15	0.4	0.8
-16	-	-
-17	-	-
-18	-	-
-19	-	-
MSU-1	-	-
-2	0.4	0.6
-3	0.5	0.8
-4	0.7	1.7

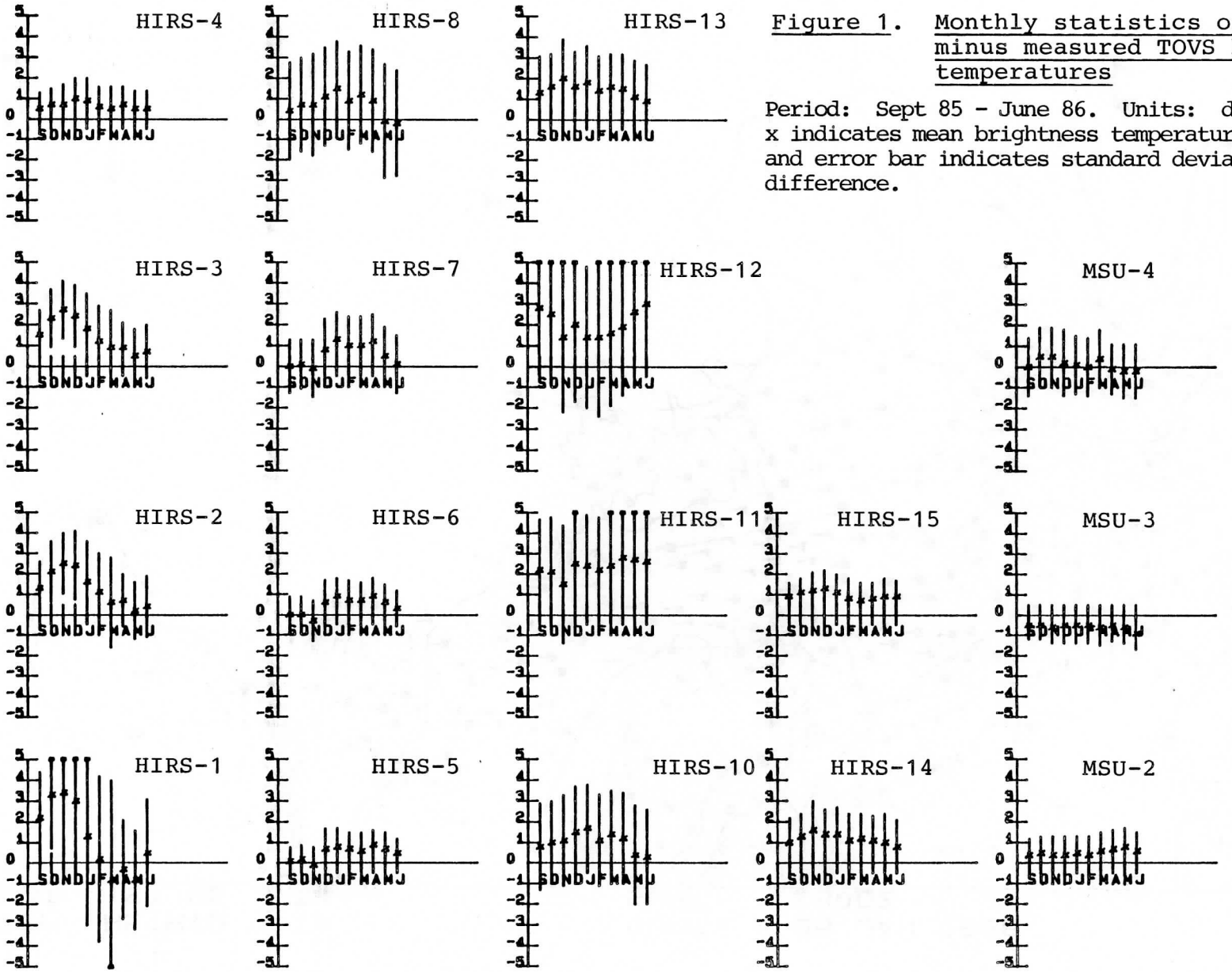

Figure 1. Monthly statistics of calculated minus measured TOVS brightness temperatures

Period: Sept 85 - June 86. Units: deg K.
x indicates mean brightness temperature difference and error bar indicates standard deviation of difference.

Figure 2. Retrieved minus first-guess surface brightness temperature (T*)

NOAA-9. 25 January 1986. 1300Z.

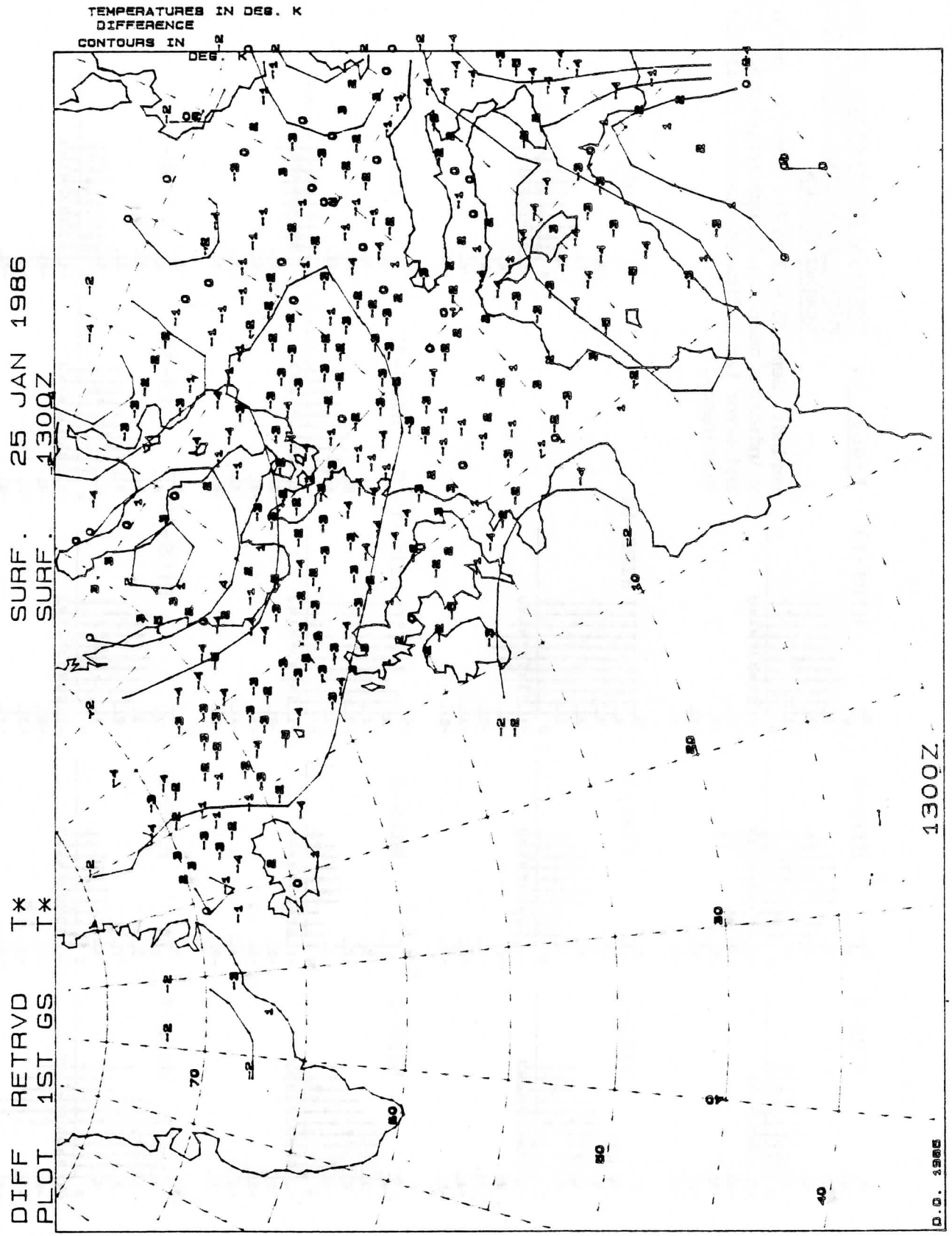

Figure 3. Measured minus first-guess MSU channel 2 brightness temperature

NOAA-9. 25 January 1986. 0310Z.

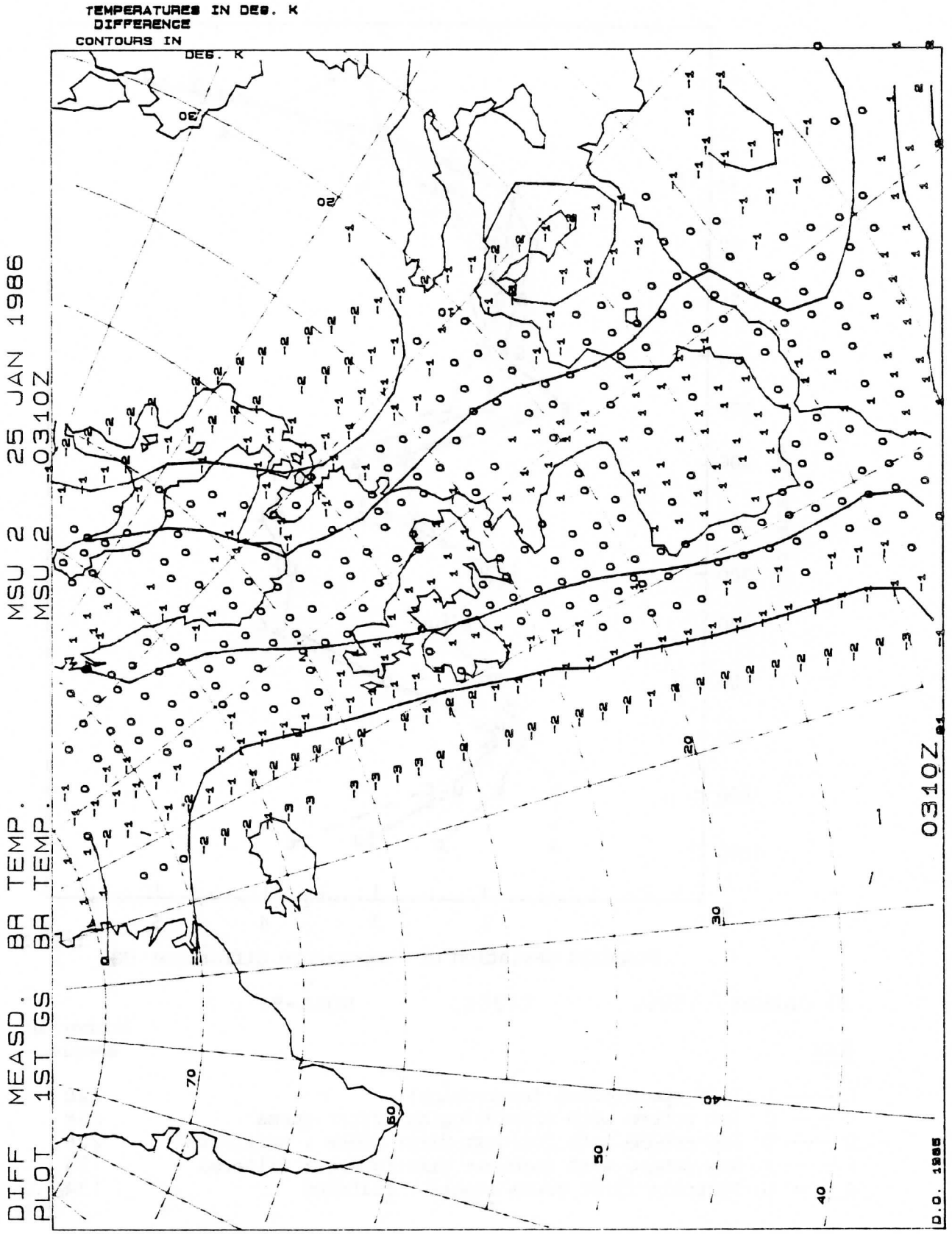

Figure 4. Standard deviation of difference between retrieval (or first guess) and radiosonde

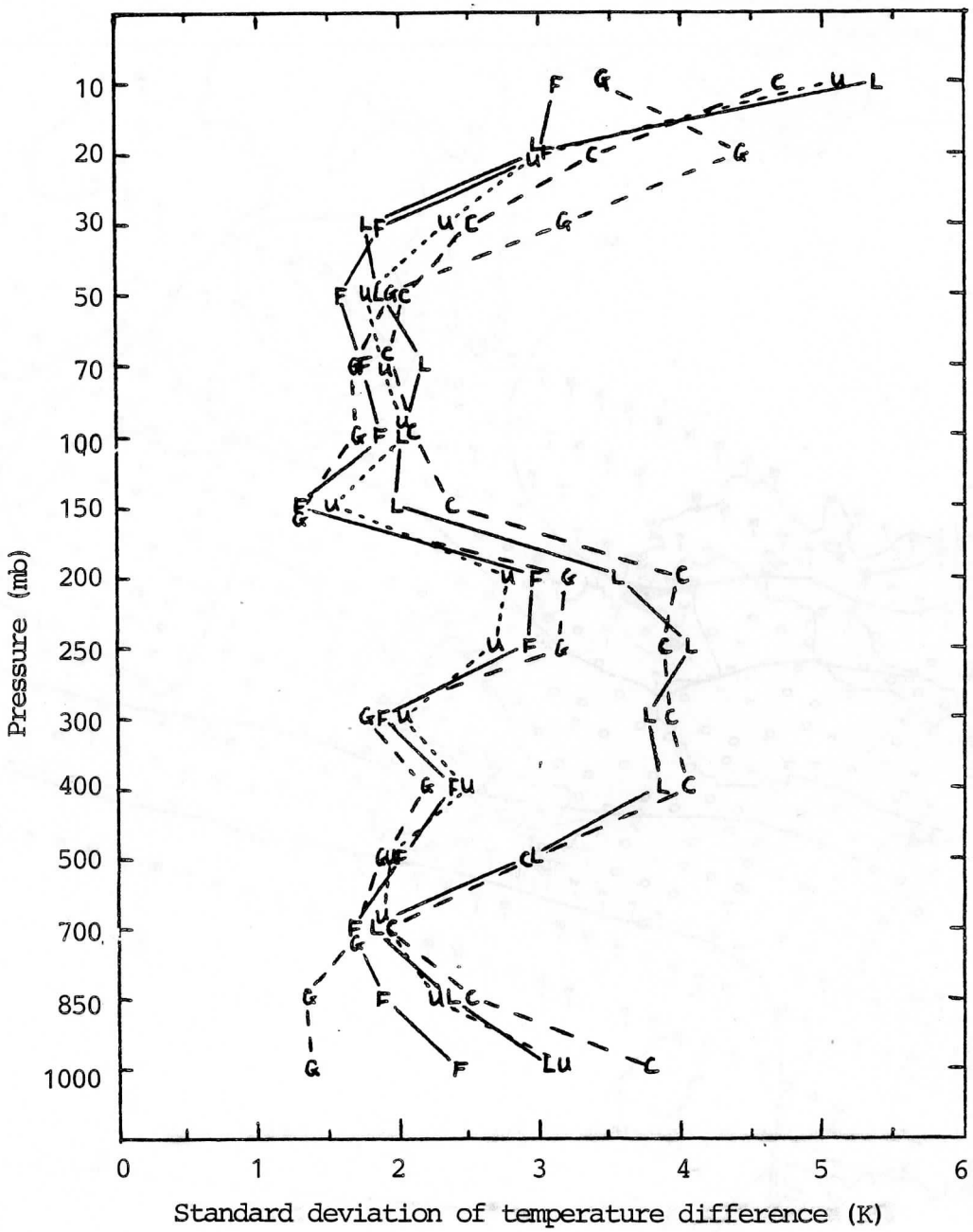

25 January 1986. 0130Z. NOAA-9.

KEY		Number in sample
L —— L	LASS operational (regression)	228
C – – C	New scheme with climatological first guess	228
U ---- U	New scheme with forecast first guess : unfiltered	228
F —— F	New scheme with forecast first guess : filtered	134
G – – G	Forecast first guess itself : filtered	134

Figure 5. AVHRR processing scheme for each HIRS spot

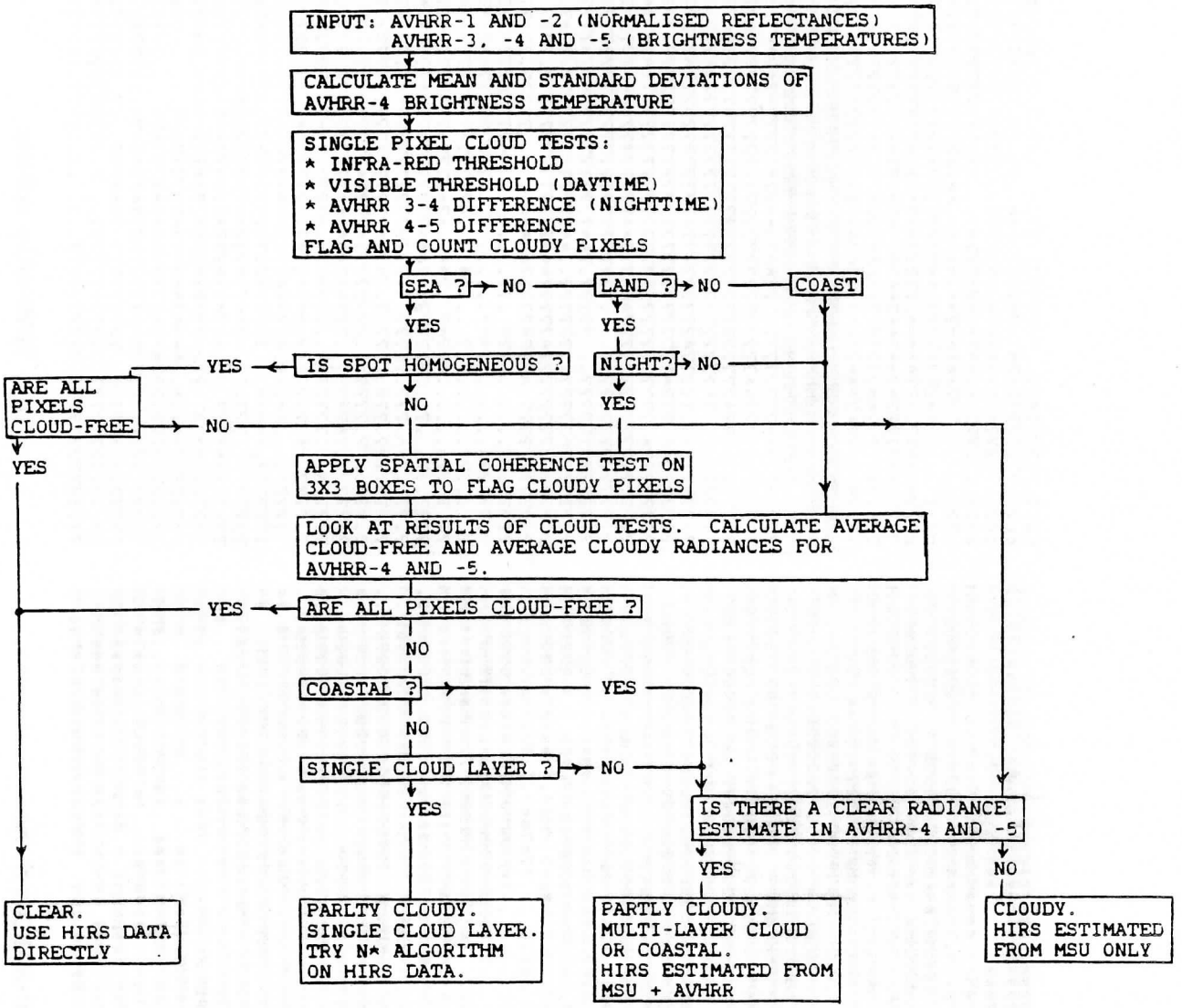

(a) TOVS+AVHRR scheme

(b) TOVS-only scheme

KEY TO CLOUD CLEARING ROUTES

. Clear

* N* successful

? N* failed, use regression on:

(a) MSU+AVHRR
(b) MSU-only

\# Regression on MSU + AVHRR

M Regression on MSU - only

c Search neighbouring FOVs

C Climatology

Figure 6. Cloud-clearing route maps for TOVS+AVHRR and TOVS-only schemes

NOAA-9. 25 January 1986. 1307Z. Same 48 lines of HIRS data in each case.

Figure 7.

Forecast versus measured brightness temperatures in HIRS channel 8. For all FOVs process by the MSU+AVHRR regression route in the TOVS+AVHRR scheme and the same FOVs in the TOVS-only scheme. NOAA-9. 25 January 1986. 1307Z.

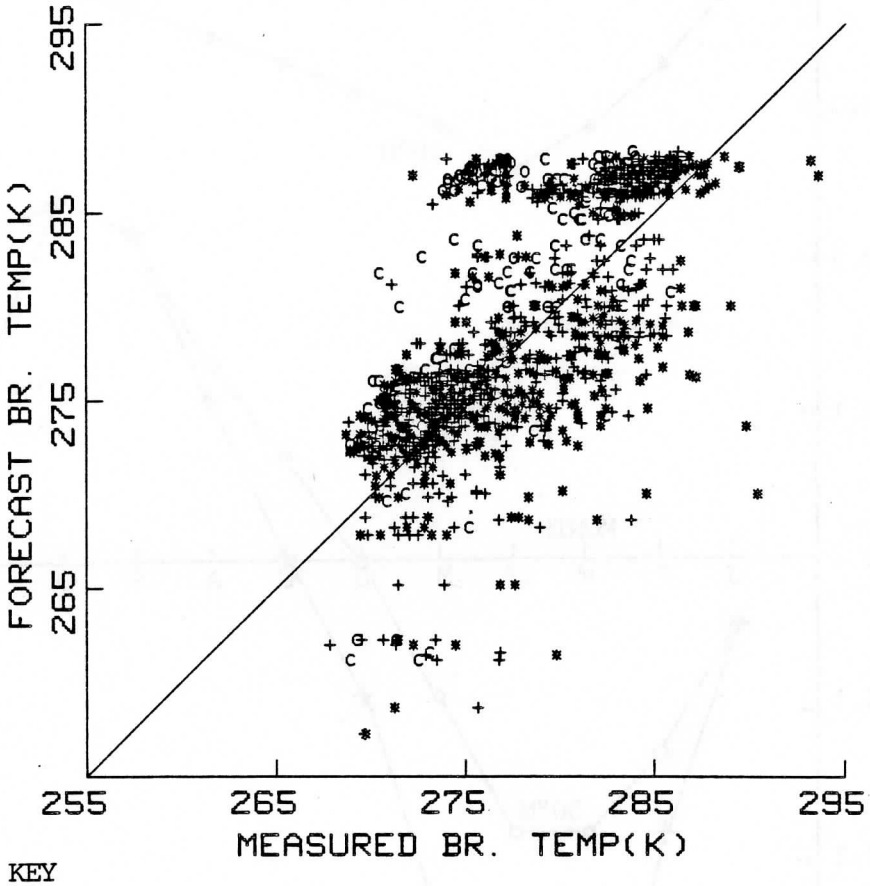

KEY

	CLOUD-CLEARING ROUTE	SCHEME
+	MSU + AVHRR	TOVS+AVHRR
C * O	CLEAR N* REGRESSION	TOVS - ONLY

STATISTICAL SUMMARY (of measured-minus-forecast differences)

	TOVS - ONLY	TOVS+AVHRR
MEAN	-1.58 K	-0.47 K
STANDARD DEVIATION	5.20 K	3.47 K

Figure 8. Changes in HIRS channel 5 brightness temperature caused by seasonal and latitudinal changes in total ozone

(expressed as differences from the value corresponding to 350 Dobson Units)

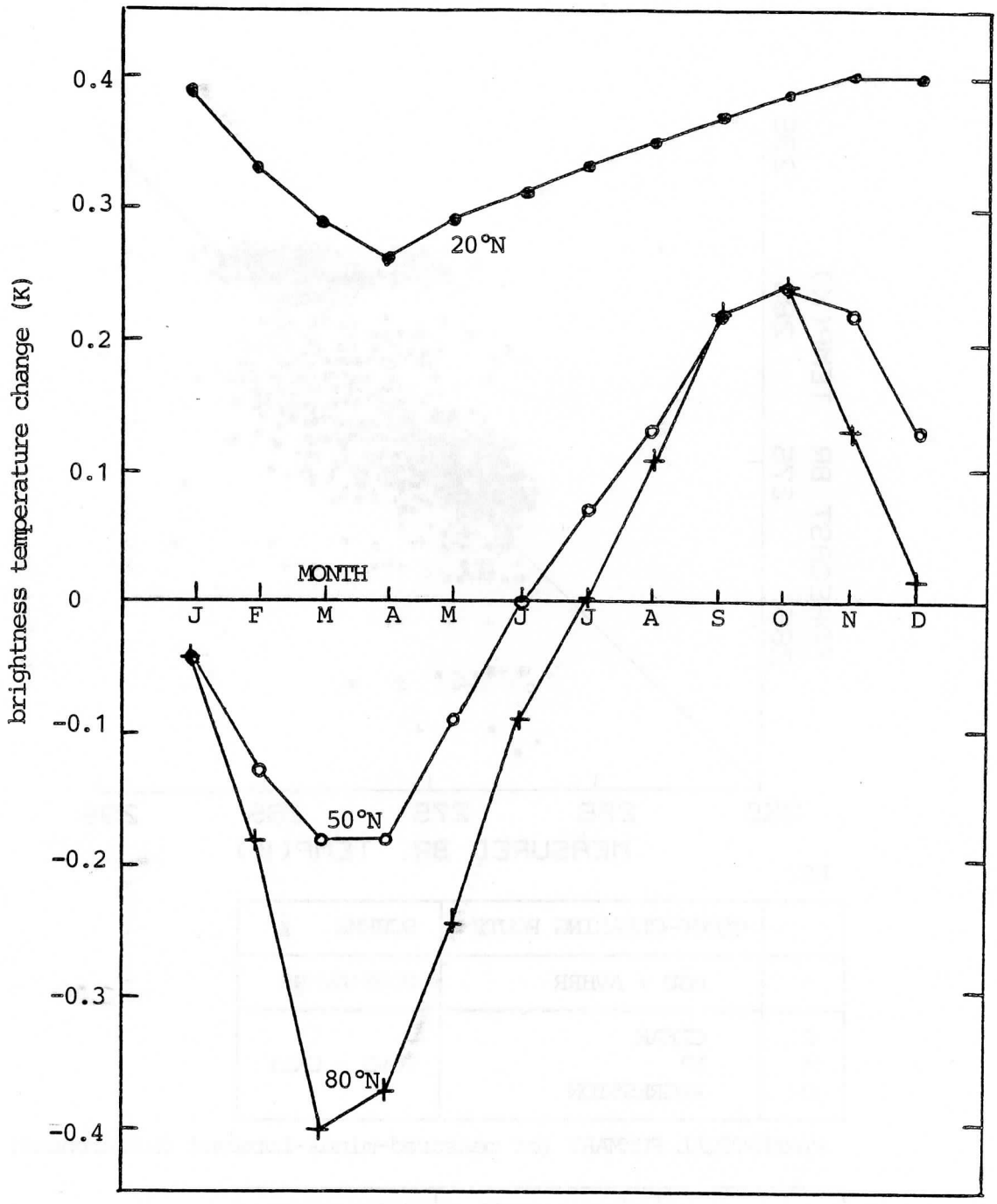

REMOTE SENSING OF SURFACE AIR AND DEW POINT TEMPERATURE IN CLOUDY ATMOSPHERES FROM CLOUD PATTERN-DEPENDENT RELATIONSHIPS

Louis Garand
Recherche en Prevision Numerique
Dorval, Quebec, Canada

1. Introduction

A new method is proposed for the remote sensing of surface meteorological parameters over the ocean and under all weather conditions. Its originality resides in its use of cloud patterns as indicators of the physical state of the atmosphere. The method utilizes ordinary visible and infrared (11μm) imagery from GOES and is consequently applicable to most meteorological satellites. We shall demonstrate that reasonable estimates of surface air (Ta) and dew point (TD) temperature can be obtained from cloud pattern-dependent relationships. Thus, vertical temperature and humidity retrievals may be improved as well since it is known that the first guess on the lower boundary condition strongly influences the solution to the inversion of the radiative transfer equation.

2. Cloud classification

Garand (1986) designed a twenty-class scheme for oceanic areas. The classes are defined in Table 1. A novel aspect is the attention given to mesoscale cellular patterns (7 to 10). To the author's knowledge, this is the first scheme that recognizes directional patterns (rolls, streets). Multilayered clouds, thin cirrus and cumulonimbus are also recognized specifically. The classifier was developed from a training set of 2000 samples taken in February 1984 over the North-Western Atlantic (Fig. 1). The scale of analysis is 128 X 128km. The visible image has 64 X 64 pixels at 2km resolution whereas the infrared image has 32 X 32 pixels at 4km resolution. A set of thirteen features are used in a simple maximum likelihood classifier that assumes multivariate normal distributions. The features describe the height, albedo, shape and multilayering characteristics of the cloud field.

Three nephanalists were assigned the task of inferring the accuracy of the scheme from 1020 independent samples (5 images with 204 samples in each). The consensus of two out of three agreeing or not with the machine result gave an overall accuracy of 79% on a strict basis with the machine result at least second best among 20 classes 89% of the time. Twelve out of twenty classes scored above 90% including the directional classes (class 7, 92% from 78 samples and class 8, 94% from 79 samples) and all high level classes (16 to 20) scored above 97%. Less successful results were obtained for class 10 (64%, 56 samples) and 14 (63%,

30 samples). Fig. 1 provides an example of classification for the 8th of January at 18GMT. The contiguous boxes can be classified at the rate of 2.5s per box. Confident in the reliability of the classifier, the next task was to study the physical attributes of the objectively defined classes.

3. Retrieval of Ta and TD

As many as 2130 cloud fields were classified with nearly perfect colocation with ship or buoy reports at 18GMT for the sixty consecutive days of January and February 1984. The machine result was accepted as such: no editing was made. The means and standard deviations of the various meteorological parameters reported by the ships and buoys were computed for each class. Garand (1986) showed, for example, that the probability of precipitation varies from 0% (classes 1 and 16) to 73% (class 20) depending on the class; similarly, the mean sensible heat flux varies from - 3W/m^2 (class 2, 38 samples) to 177W/m^2 (class 8, 60 samples) whereas the mean latent heat flux varies from 33W/m^2 (class 2) to 433 W/m^2 for class 8 and 436W/m^2 for class 9. These numbers are cited here only to convince the reader of the relevancy of the classification in terms of sorting different physical processes occurring in the atmosphere.

For, Ta and TD, we found that the within class variance could be lowered substantially from multiple linear regression (MLR) involving satellite features that were extracted to classify the samples. In short, class-dependent relationships were established between Ta or TD observed at the surface and satellite-retrieved quantities. The MLR equations are shown in Appendix A. The features used in those relationships are briefly described below. Their dynamic range is 0-1 except for the first three features.

HT: the height of the uppermost cloud layer (0-14km).

Tb: the apparent cloud base temperature (K) defined as the temperature threshold corresponding to the cloud fraction. It will be shown shortly that this is the most important predictor of Ta and TD.

DT: the difference between the sea surface temperature, Ts, and Tb, Ts - Tb, is also an important predictor; it is a measure related to the thickness of the boundary layer.

AL: the mean albedo of the cloudy pixels in the visible image.

LR: the fraction of cloudy pixels below 25% reflectance.

BC: background connectivity: the median background size in pixels divided by the total number of cloud-free pixels; BC is low for open cells.

CC: cloud connectivity: the median size of the clouds in pixels divided by the total number of cloudy pixels, a measure of the fragmentation of the cloud field (CC is low for cumulus, high for stratus).

CF: total cloud fraction.
ML: multilayer index: the fraction of cloudy pixels between the coldest pixel and 2km lower than HT (near unity for single layered cloud fields, low for multilayered ones).
ST: streakiness factor: the correlation coefficient taken on the two-dimensional power spectrum, an essential feature for the detection of directional patterns
SE: the fraction of spectral intensity in the power spectrum corresponding to wavelengths 20-40km, a measure detecting open cells since their typical size is 30km (SE higher for open cells than for other cloud fields). Features ST and SE were first proposed by Garand and Weinman (1986).

Tables 2a,b show the means and standard deviations of Ta and TD before and after MLR involving the features just described. Examination of these tables immediately show that:
1) Tb is the most important predictor; it is used in all Ta equations. Second in importance is DT.
2) the standard deviations (SD) are about halved as compared with the class climatological value. SD's on Ta lower from 6 to 8K to 2.5-4K whereas SD's on TD lower from 6 to 8K to 3-5K.

No regression is attempted when CF=1 or CF=0 as Tb and DT lack physical meaning in these cases. This explains the lower number of samples for some classes after MLR. Figs. 2a,b illustrate the very strong relationship of Ta and TD with Tb for a particular class (8, rolls). Note that the relationship is strong over the entire dynamic range of 30K. We consider this a major finding since Ta and TD are derived directly in all weather conditions from measures easily retrievable from space (provided one has a good algorithm for cloud fraction). A surprising and comforting result is that the SD's can be lowered for all classes. This results from our scale of analysis (128 X 128km) which is large enough to retrieve Tb and DT in all cases except, as noted, when CF=0 or CF=1 exactly. This argument, among others pertaining to the necessary minimum spatial scale for pattern recognition of cloud fields, speaks in favor of box by box methods as opposed to pixel by pixel methods.

The output of this technique for real time retrievals is further depicted in Figs. 3a,b which show maps of Ta and Td for January 8, 1984 at 18GMT (matching Fig.1). Boldfaced numbers are surface observations. Typical errors are in the range 2-4K except for some cases above 5K, particularly in clear air. By its nature, it is admitted that the present method will not work well in clear air as well as in nearly overcast conditions (at the scale of 128 X 128km), that is, in cases where Tb and DT are difficult to measure. The reader will notice that the contours are naturally smooth; yet, strong gradients such as in the north-east portion of the domain are well captured. These plots were produced from the 204 contiguous retrievals shown in Fig.1, using

the relationships of Appendix A.

Finally, we show in Fig.4 a time series of retrieved and observed values of Ta at a fixed point (a buoy) for the 60 days of January and February 1984. The vigorous cold air outbreaks centered on Julian days 8, 32 and 38 are fairly well captured as well as the rapid warming that followed those events. Since different cloud patterns occurred during those two months, it appears that the method is skilful in all weather conditions. Only four retrievals out of fifty had errors larger than 4.5K, including an 8K error on the 4th. We argue that those errors, especially the largest ones, could be lowered considerably upon considering temporal and spatial consistency, in other words from the retrievals made in the recent past and at neighboring sites. This is the logical next step for the improvement of the method presented herein. At seasonal time scales (data for January and February, observed and retrieved, pooled together at 32 grid points), the standard deviations for Ta and TD were 1.45K and 1.70K respectively.

4. Conclusion

A new method is proposed for the retrieval of Ta and TD in cloudy atmospheres. Standard deviations are halved with respect to climatological values, thus providing economical retrievals possibly every half hour. The method utilizes ordinary visible and infrared sensors onboard all meteorological satellites. Since a first guess, substantially better than a climatological estimate, can be obtained in regions devoid of in situ data, improved vertical retrievals are expected, in addition to improved surface fields of air temperature and humidity for initialization of numerical weather prediction models.

Acknowledgments

The author thanks Dr. J. A. Weinman for many discussions and suggestions concerning this work and Mr. Chris Moeller for programming assistance.

References

Garand, L. and J. A. Weinman, 1986: A structural-stochastic model for the analysis and synthesis of cloud images, J. Appl. Meteor, 25, 1052-1068.

Garand, L., 1986: Automated recognition of oceanic cloud patterns and its application to remote sensing of meteorological parameters, Ph.D. dissertation, U. of Wisconsin-Madison, 225pp.

A.1 Air temperature (Ta, in K)

Ta(1) = 4.860 HT + .78611 Tb + 60.05
Ta(2) = .5889 DT + .69376 Tb + 85.24
Ta(3) = .8318 DT + 1.0970 Tb - 27.09
Ta(5) = 1.240 DT + 1.1429 Tb - 42.86
Ta(6) = T(4) = -40.52 AL + .81633 Tb + 80.17
Ta(7) = 1.1622 Tb - 40.88
Ta(8) = .87653 Tb + 41.25
Ta(9) = 2.670 BC + .65181 Tb +104.26
Ta(10) = - 12.16 LR + .85161 Tb + 49.40
Ta(11) = .8081 DT + .81991 Tb + 49.48
Ta(12) = .5151 DT + .87085 Tb + 37.57
Ta(13) = - 18.51 LR + .67906 Tb - 23.00 AL + 114.67
Ta(14) = .89507 Tb + .8691 DT + 30.11
Ta(15) = .82853 Tb + .7597 DT + 48.44
T(16) = .8427 HT + .79249 Tb + .4850 DT + 59.88
Ta(17) = .62398 Tb + .3576 DT - 8.076 LR + 115.49
Ta(18) = 2.018 HT + .63850 Tb + .3110 DT + 91.66
Ta(19) = 1.710 HT + .36407 Tb + 37.91 ML + 145.30
Ta(20) = 3.607 HT + .21160 Tb + 195.71

A.2 Dew point temperature (TD, in K)

TD(1) = 26.13 SE + 5.735 BC + .34172 Tb + 182.51
TD(2) = -3.824 CF + .70317 Tb + 86.34
TD(3) = .99306 Tb + .71564 DT - 1.93
TD(5) = 3.5147 HT + .87370 Tb + 30.36
TD(6) = TD(4) = .53353 Tb - 43.86 AL + 156.91
TD(7) = 6.221 ST +1.0193 Tb - 9.89
TD(8) = 12.69 CF + .76293 Tb + 56.42
TD(9) = 3.976 BC + .60961 Tb + 109.85
TD(10) = 35.61 BC + .69277 Tb - 12.11 LR + 86.19
TD(11) = .70378 Tb + .6560 DT + 78.26
TD(12) = .72834 Tb + .3667 DT + 75.16
TD(13) = .57229 Tb - 16.97 LR - 22.94 AL + 138.84
TD(14) = .79650 Tb + .6814 DT + 55.57
TD(15) = .70156 Tb + .8513 DT + 77.92
TD(16) = .9266 HT + .60381 Tb + 113.94
TD(17) = .59016 Tb - 7.697 LR + .3212 DT + 121.29
TD(18) = 1.628 HT + .53592 Tb + .2149 DT + 121.69
TD(19) = 126.0 CC + .8018 AL + 160.90
TD(20) = 2.609 HT + .34304 Tb + 169.13

Table 1 List of the cloud classes

1. Clear
2. Stratus
3. Scattered cumulus
4. Broken cumulus
5. Scattered stratocumulus
6. Broken stratocumulus
7. Cloud streets
8. Rolls
9. Polygonal open cells
10. Strongly convective open cells
11. Bright closed cells
12. Nimbostratus
13. Altocumulus
14. Altocumulus with cumulus
15. Altocumulus with stratocumulus
16. Thin cirrus
17. Multilayers with cirrus
18. Bright multilayers with cirrus/cumulonimbus
19. Dense cirrostratus
20. Overcast cumulonimbus

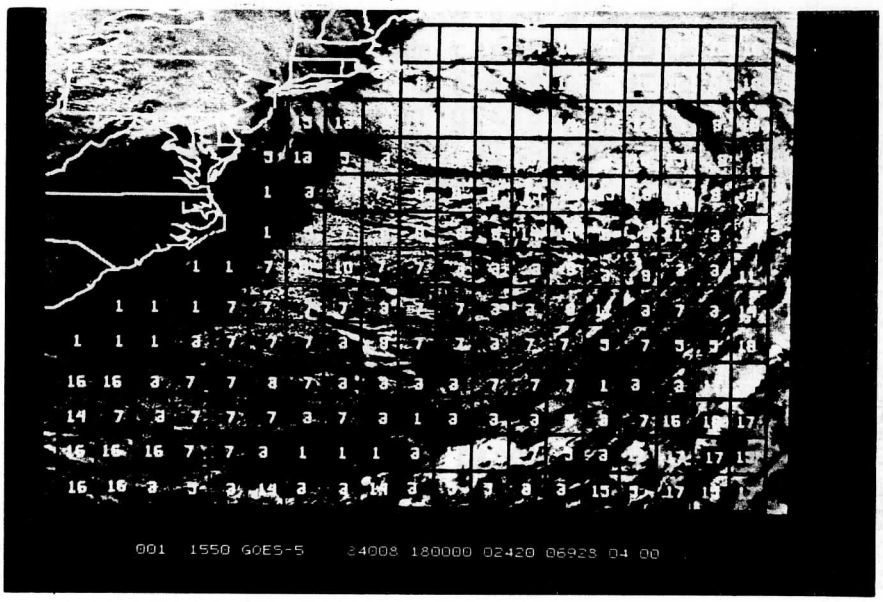

Fig. 1 Example of automated cloud classification for January 8, 1984 at 18GMT, overlaying visible image. Region and grid of analysis are shown (128 X 128km) with the machine class number in the middle of each of the 204 contiguous areas.

Table 2a Means (m) and standard deviations (SD) for each cloud class of the surface air temperature (K) before and after use of multiple linear regressions (MLR). MLR predictors shown with sign of correlation. Missing values for N, m after MLR same as N, m before regression.

	Before MLR			After MLR			
Class	N	m	SD	N	m	SD	Predictors
1	108	287.7	8.73	45	289.5	3.87	Tb,HT
2	54	280.6	5.61	37	281.1	3.65	Tb,DT
3	215	290.7	7.34			3.65	Tb,DT
5	103	289.0	7.82			3.09	Tb,DT
4,6	33	288.7	6.27			3.33	Tb,-AL
7	77	288.1	7.69			4.13	Tb
8	64	280.6	7.72			2.88	Tb
9	34	288.6	3.83			2.49	Tb,BC
10	32	283.1	7.00			3.22	Tb,-LR
11	115	282.7	7.86			4.02	Tb,DT
12	133	281.3	6.22	88	281.8	3.50	Tb,DT
13	76	286.5	8.93			4.51	Tb,-LR,-AL
14	64	287.8	7.89			4.27	Tb,DT
15	59	286.0	8.25	58	286.1	3.82	Tb,DT
16	128	291.3	6.94			3.85	Tb,DT,HT
17	229	290.3	7.03			4.21	Tb,DT,-LR
18	295	285.3	7.66	194	286.3	4.20	Tb,DT,HT
19	57	292.3	5.16	47	293.2	3.18	Tb,HT,ML
20	183	287.7	6.42	30	286.7	4.12	Tb,HT

Table 2b Same as 2a but for dew point temperature (K).

	Before MLR			After MLR			
Class	N	m	SD	N	m	SD	Predictors
1	77	282.7	8.30	37	285.3	5.55	Tb,SE,BC
2	33	278.7	5.44	25	278.5	3.30	Tb,-CF
3	156	285.9	7.34			5.06	Tb,DT
5	82	284.3	8.26			5.30	Tb,HT
4,6	26	285.1	5.15			3.45	Tb,-AL
7	52	282.2	7.52			4.56	Tb,AL
8	48	276.0	7.79			3.30	Tb,CF
9	30	283.0	4.11			2.86	Tb,BC
10	25	278.4	5.89			2.71	Tb,BC,-LR
11	88	278.3	7.47			4.92	Tb,DT
12	89	278.7	5.79	58	278.6	3.43	Tb,DT
13	56	281.3	8.47			4.43	Tb,-AL,-LR
14	48	284.5	7.94			5.41	Tb,DT
15	42	281.7	7.90			4.60	Tb,DT
16	95	287.4	6.98			5.04	Tb,HT
17	178	286.6	7.14			4.94	Tb,-LR,DT
18	193	283.0	7.28	119	284.0	4.67	Tb,HT,DT
19	44	290.1	4.01	37	290.9	2.39	CC,AL
20	133	286.0	6.37	21	283.4	5.56	Tb,HT

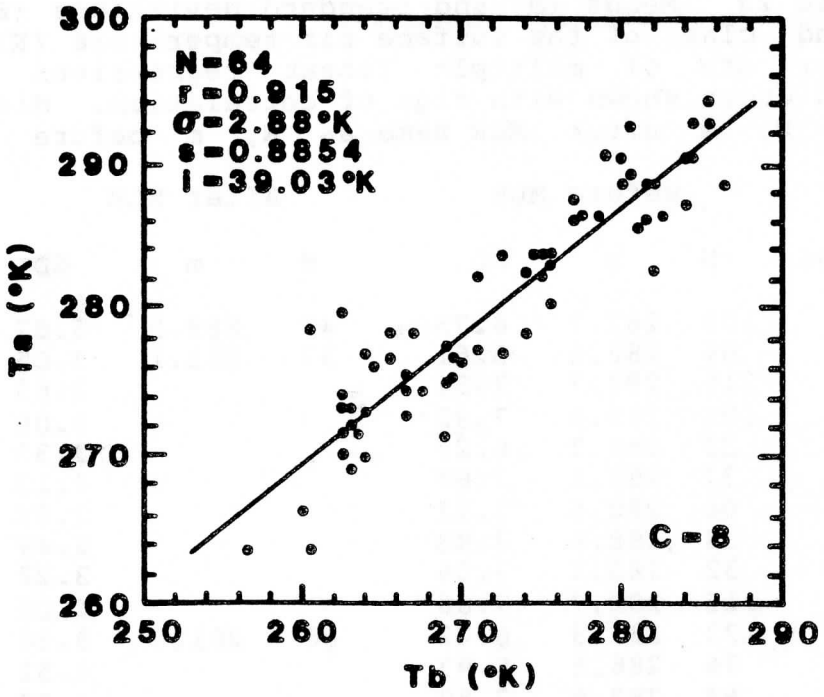

Fig. 2a Observed surface air temperature, Ta, versus Tb for class 8. Best fit line and parameters shown.

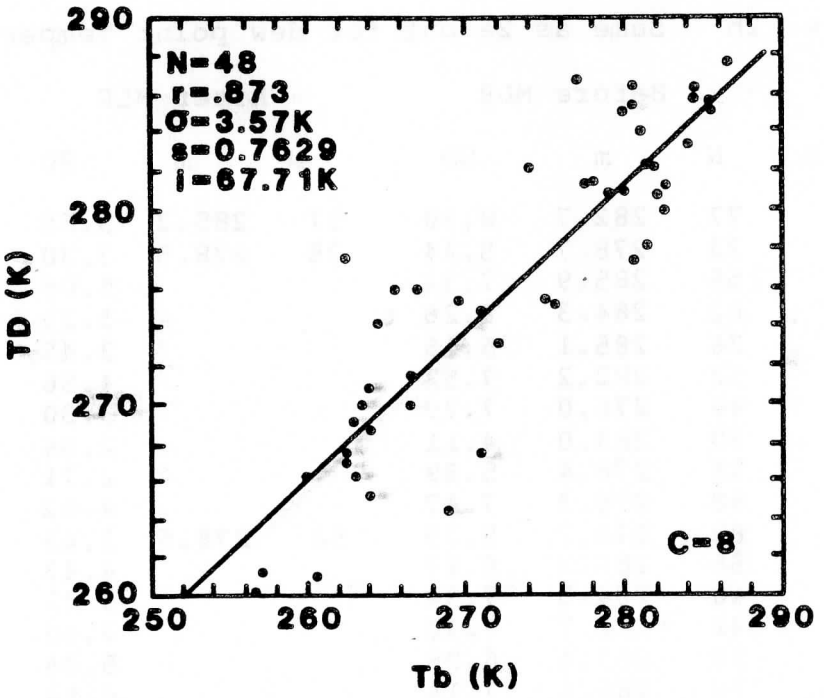

Fig. 2b Observed surface dew point temperature, TD, versus Tb for class 8. Best fit line and parameters shown.

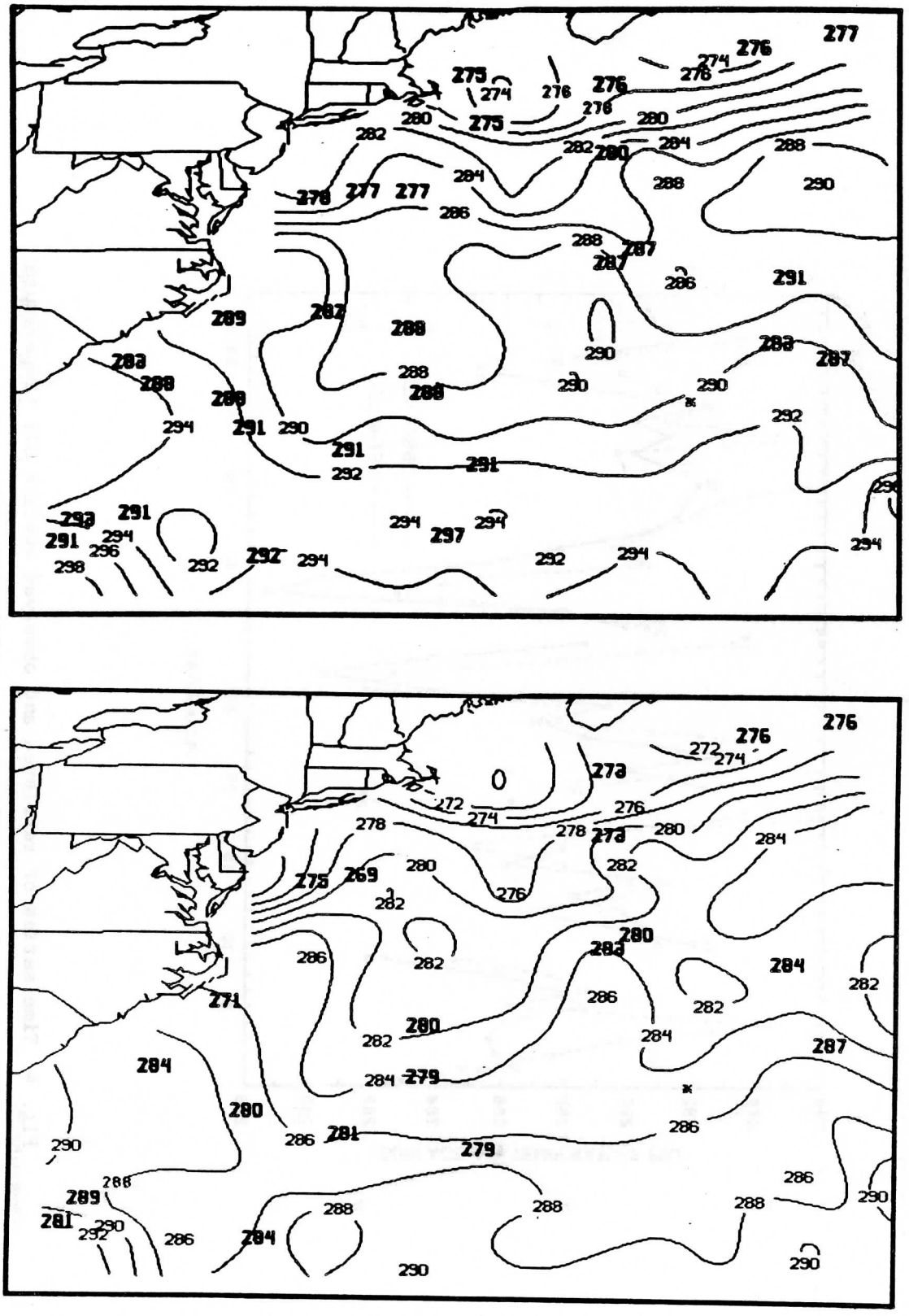

Fig. 3 Retrieved surface air temperature (a) and dew point (b) for January 8, 1984 at 18GMT (degrees K). Boldfaced numbers are surface observations.

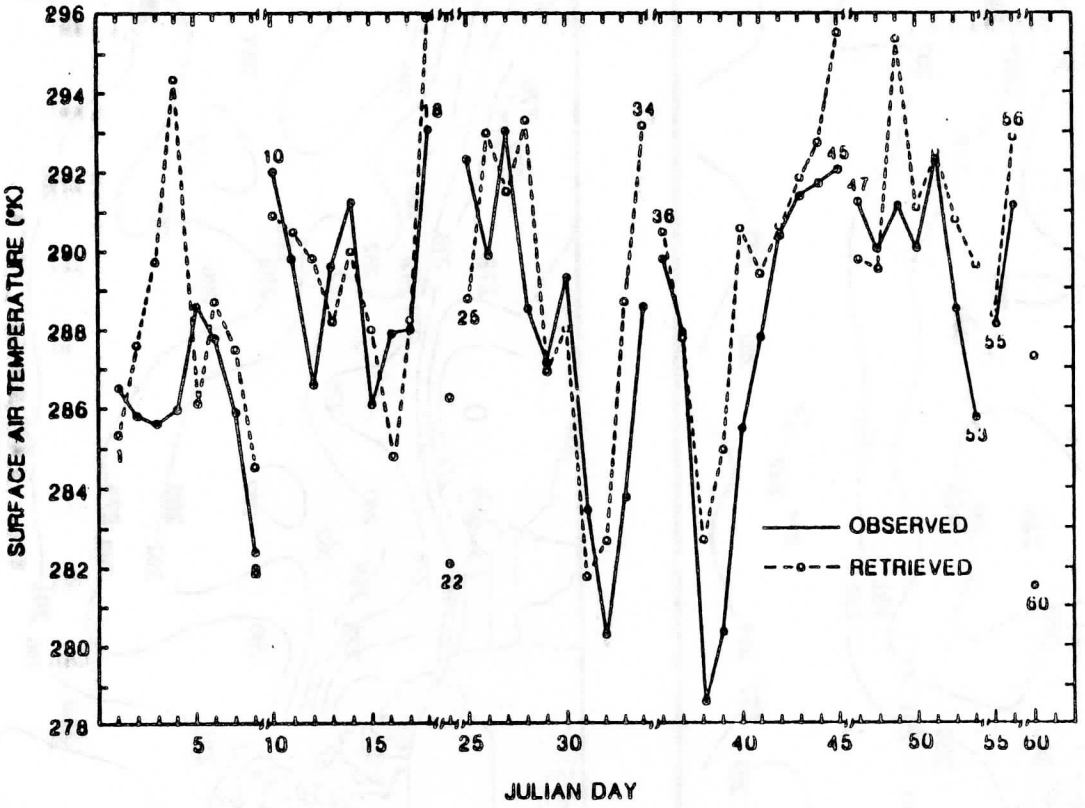

Fig. 4 Time series of retrieved and observed surface air temperature for Julian days 1-60 in 1984 at buoy 41001 (34N, 72W). Numbers on the plot are Julian days.

THE APPLICATION OF TOVS DATA TO THE CAROLINA TORNADO OUTBREAK OF 28 MARCH 1984.

D.W. Hillger[1], J.F.W. Purdom[1,2], and T.H. Vonder Haar[1]

[1]Cooperative Institute for Research in the Atmosphere (CIRA)
Colorado State University
Fort Collins, CO 80523

[2]Regional and Mesoscale Meteorology Branch, Development Laboratory
NOAA/NESDIS
Fort Collins, CO 80523

ABSTRACT

An analysis of satellite-derived soundings is presented for the 28 March 1984 Carolina Tornado Outbreak. The ability of the TIROS Operational Vertical Sounder (TOVS) to detect significant differences in water vapor profiles over small horizontal distances is shown. Temperature and water vapor profiles were retrieved in cloud-free areas at single field-of-view resolution of approximately 35 km without the aid of surface observations or other ancillary data. Significant differences in resultant profiles occur over horizontal distances of less than 200 km.

Besides temperature and mixing ratio profiles, various sounding parameters such as stability indices and buoyant energies were computed. These parameters help accentuate the differences in the profiles retrieved in the various air masses surrounding the tornado outbreak area.

1.0 INTRODUCTION

The ability of satellite-derived soundings to detect significant differences in water vapor profiles over small horizontal distances will be shown. The case study day under analysis was the Carolina tornado outbreak of 28 March 1984. This tornado outbreak case is especially significant because the air mass characteristics (in particular, water vapor and stability) were directly related to the location of developing severe weather (tornadoes and severe downbursts).

Satellite sounding radiances from the NOAA-7 TIROS Operational Vertical Sounder (TOVS) are used to retrieve water vapor and temperature profiles at single fields-of-view (FOVs). Examples of vertical water vapor and temperature profiles are given for selected areas which are identified as being different air masses. At each FOV various water vapor and stability parameters are computed and then related to the potential for the development of severe weather. Horizontal analyses of these parameters

show regions for preferred development of severe storms. This analysis is based solely on the satellite data, without the use of surface observations or other ancillary data.

2.0 SATELLITE DATA

The TIROS Operations Vertical Sounder (TOVS) operates on board NOAA polar-orbiting satellites which normally view a region of the earth at 12-hour intervals (twice-a-day). Data from the infrared and microwave sensors were used in this study to derive water vapor and temperature profiles at a single FOV resolution of about 35 km. The characteristics of the TOVS infrared channels which were used in this study are listed in Table 1. Not all channels were employed actively (used to modify the temperature or water vapor profile), only the tropospheric channels, since emphasis was placed on lower-tropospheric results. This was justified due to lack of mesoscale variations in the upper channels and for computational expediency. Of special concern were the lower tropospheric water vapor profiles. The weighting functions for the water vapor channels, which describe where the majority of the radiance contribution for these channels originates, are shown in Figure 1.

The horizontal coverage and resolution of the TOVS measurements is indicated in Figure 2, which is the channel 20 (0.7 μm) relative reflected radiance for approximately 21 UTC (Coordinated Universal Time) on 28 March 1984. The TOVS retrievals were attempted only in the clear or mostly clear regions as indicated by the FOVs plotted. The data-rich regions in Figure 2 compare closely with the clear regions in the NOAA-7 Advanced Very High Resolution Radiometer (AVHRR) image in Figure 3 at 1-km resolution.

3.0 TOVS RETRIEVALS

The iterative retrieval method for the TOVS data employs techniques similar to those described by Smith (1983) and Smith and Zhou (1982) for the VISSR Atmospheric Sounder (VAS). However, before the retrievals were performed the reflected solar component of the TOVS radiances was subtracted off (Hayden, et. al., 1981). Care also had to be taken to avoid cloud contaminated FOVs. However, oversight of cloud avoidance may be recognizable in resultant soundings with saturated or unrealistic water vapor profiles. An alternate means of cloud detection, besides a reflected radiance threshold, is to use a threshold value of the difference in brightness temperature between the 3.7 and 11 μm window channels (Hillger, 1984). In this study both a brightness temperature difference threshold of 12 K and a 0.7 μm reflected threshold of 2.0 were used.

A single smoothed composite RAOB sounding was used as the initial guess profile for all retrievals. The result is that differences between the retrievals at various FOVs were due to the satellite data alone and were not due to an objectively analyzed initial guess field. Likewise, no surface observations were used in the retrieval process. The microwave data were used in one iterative step as an adjustment to the initial guess temperature profile. After this initial adjustment the infrared data were used exclusively.

Table 1
Selected TOVS Channels

TOVS Channel Number	Central Wavelength (μm)	Principal Absorbing Constituent	Approximate Peak Pressure (kPa)
8	11.1	window	surface
19	3.7	window	surface
10	8.3	H_2O	90
11	7.3	H_2O	70
12	6.7	H_2O	50
4	14.2	CO_2	40
5	14.0	CO_2	60
6	13.7	CO_2/H_2O	80
7	13.4	CO_2/H_2O	90
13	4.57	N_2O	100
14	4.52	N_2O	95
15	4.26	CO_2/N_2O	70
16	4.40	CO_2/N_2O	40
20	0.7	window	reflected

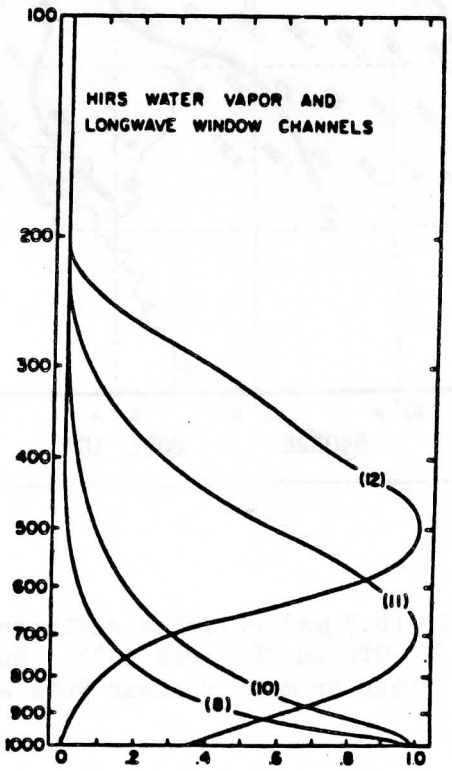

Figure 1. TOVS H_2O channel weighting functions.

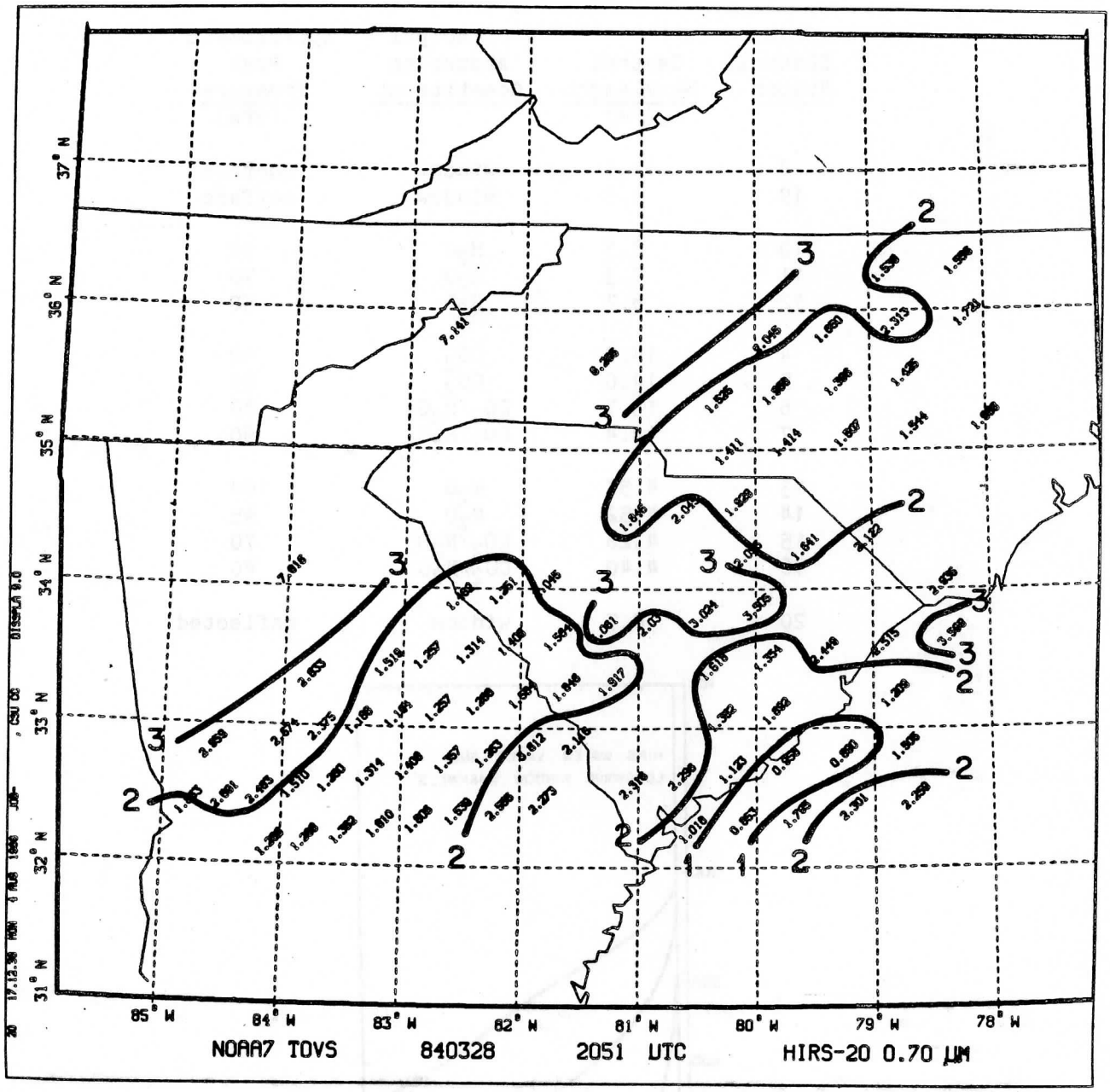

Figure 2. TOVS channel 20 (0.7 μm) relative reflected radiances for approximately 21 UTC on 28 March 1984. Numbers show single FOV values. Only clear or mostly clear FOVs are shown.

Figure 3. AVHRR 1-km resolution visible image for same area as in Figure 2. Letters A, B, C, and D denote regions where satellite soundings were retrieved.

Once the retrievals were performed several water vapor and stability parameters were calculated for each sounding. Hillger and Vonder Haar (1981) showed that these parameters, as derived from satellite soundings, can be useful in the prediction of convection based on the pre-convective environment. In that study local maxima of low-level water vapor and instability were linked to later convective activity for several case study days.

4.0 RESULTS FOR 28 MARCH 1984

Figure 4 (Storm Data, 1984) shows the paths of the tornadoes and severe downbursts during this Carolina tornado outbreak. The major activity was confined to one long and nearly continuous corridor. A large storm developed in northeast Georgia and tracked east-northeast along a thunderstorm outflow boundary across South Carolina and into North Carolina. This boundary was a result of outflow from early morning convection to the northwest of this line (Purdom, 1985).

The holes between the cloudy regions allowed the use of satellite-derived soundings to analyze the pre-storm environment surrounding this boundary. Figure 5 shows the positions of selected soundings in each of four clear regions labeled A, B, C, and D. These 4 clear regions upon examination show contrasting differences in the retrieved soundings, especially the water vapor profiles. The numbers in each enclosed rectangle are the line and element numbers for single FOVs. Only the clear or mostly clear FOVs are shown, based on a 12 K window-channel brightness temperature difference threshold. The cloudy regions with no plotted data show where the satellite soundings are located with respect to the cloud field.

The 4 clear regions, chosen by examination of the AVHRR imagery and surface observations and labeled in Figure 5 can be categorized as:

Region A - Dry region on the west edge of the clear tongue extending up into Georgia. This dry air is ahead of the frontal boundary stretching northeast to southwest across Georgia.

Region B - Moist air mass over coastal south Carolina. This air is probably of oceanic origin.

Region C - Warm sector air for the mesolow region where the tornadic storm first developed on the South Carolina-Georgia border.

Region D - Outflow air to the north of the outflow boundary on the North Carolina-South Carolina border.

For each of these regions retrievals were performed at the selected TOVS locations. Examples of the vertical temperature and water vapor profiles in each region are given in Figures 6a through 6d. The profiles are shown on skew-T log-p backgrounds. Each type of sounding shown is confirmed by a similar sounding at an adjacent location and is not a singular example.

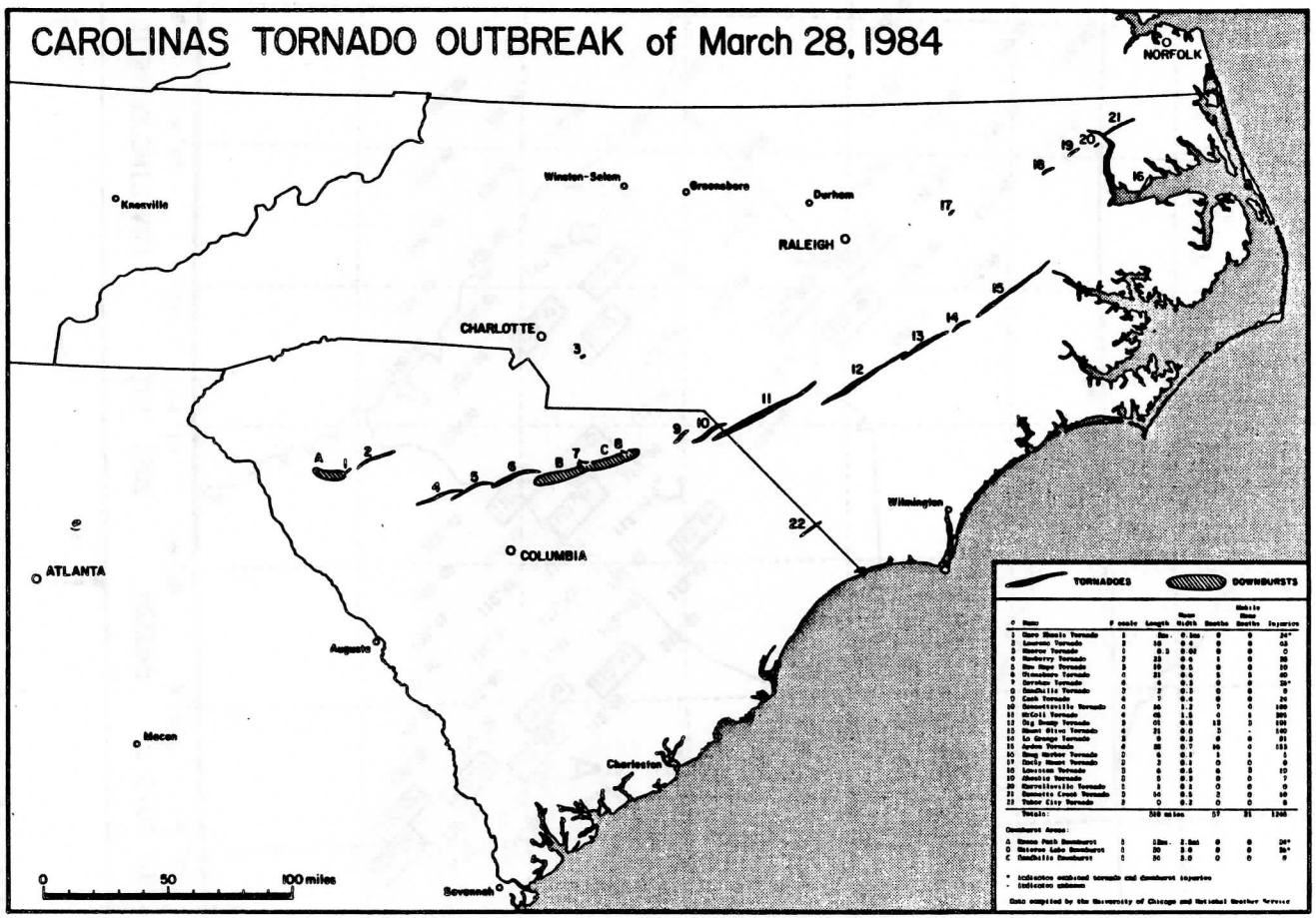

Figure 4. Line of tornadoes and severe downbursts during the 28 March 1984 Carolina tornado outbreak. (Storm Data, 1984)

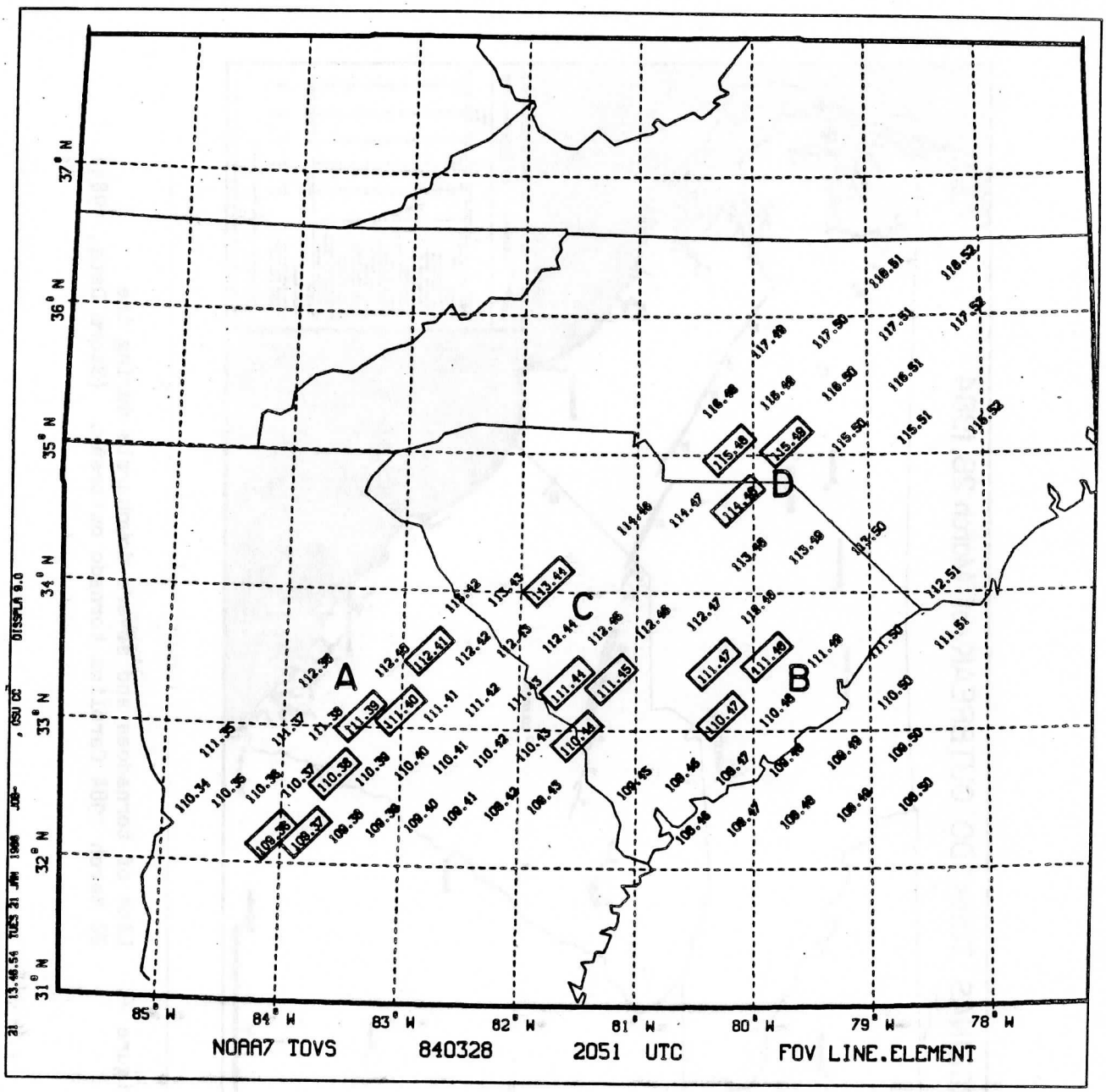

Figure 5. Locations of selected soundings in areas which have different air mass characteristics. Region letters and line and element numbers are used for identification purposes. Only FOVs with a -channel window brightness temperature difference of 12 K or less are shown.

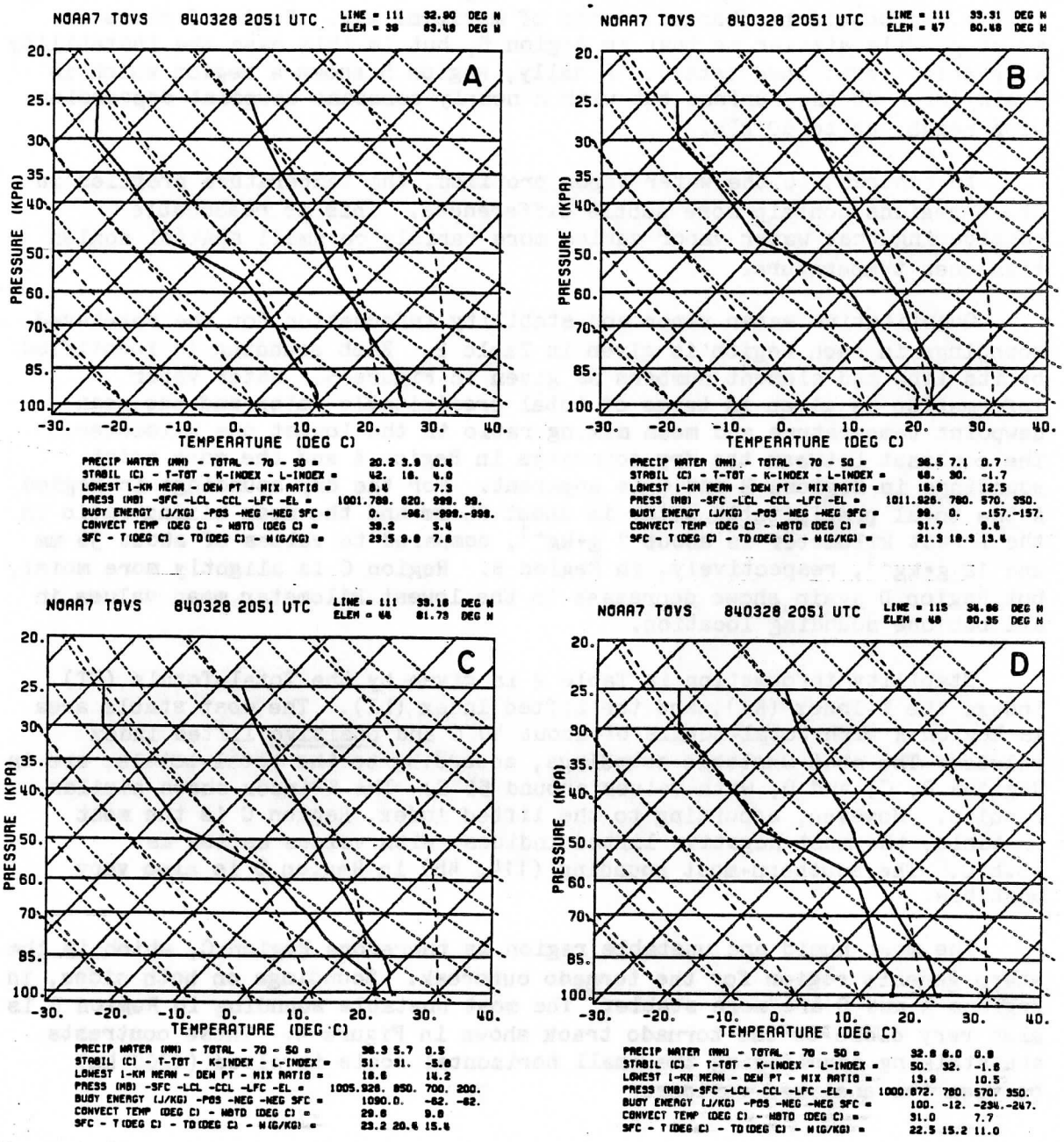

Figure 6. One TOVS retrieved sounding (plotted on a skew T-log p background) from each of the 4 regions in Figure 5. (See text for details).

By examining the 4 soundings in Figure 6 (one for each region) the contrast in the water vapor profiles is apparent. Region A consists of a dry sounding from the surface upward. Region B is much more moist in lower levels, as should be characteristic of maritime air. Region C shows a moist profile similar to that in Region B, but in this case the instability is greater (explained later). Finally, Region D shows a region which is again drier at the surface but with a nearly constant dewpoint depression with height up to 60 kPa.

In contrast to the water vapor profiles, the temperature profiles in the 4 regions contain more subtle differences. This is reasonable considering that water vapor varies more rapidly on small spatial scales than does temperature.

Quantitative water vapor and stability information for the retrieved soundings in each region is given in Table 2. Each sounding is identified by its line and element numbers as given in Figure 5. Water vapor information is given in terms of total precipitable water and the mean dewpoint temperature and mean mixing ratio in the lowest one kilometer. The contrast between the dry soundings in Region A and the more moist soundings in Regions B and C is apparent. For the dry soundings in Region A the total precipitable water is about 20 mm and the mean mixing ratio in the lowest kilometer is about 7 $g \cdot kg^{-1}$, compared to values of about 36 mm and 12 $g \cdot kg^{-1}$, respectively, in Region B. Region C is slightly more moist, but Region D again shows decreases in the lowest kilometer mean values in all but one sounding location.

Stability information in Table 2 is given by the Total-Totals (TT) index, the K-Index (KI), and the Lifted Index (LI). The most stable area is Region A with total-totals of about 40°C and positive lifted index values. The most unstable soundings, according to the total-totals, are in Regions B, C, and D, with values around 50°C. The K-index shows similar results. However, according to the lifted index, Region C is the most unstable, the most negative lifted indices, with values as low as -5.8°C. The southern-most sounding (114, 48) in Region D is also very unstable.

The most humid and unstable region is therefore Region C, which is the storm genesis region for the tornado outbreak. Soundings on both sides, in Regions A and B are more stable. The most unstable sounding in Region D is also very close to the tornado track shown in Figure 4. These contrasts are striking considering the small horizontal scale involved (<200 km) between the analyzed regions.

4.1 Horizontal Fields of Stability and Energy

In order to show the extent and variability of various air masses, some horizontal plots of stability indices and energy calculations are given in Figure 7a, b, and c. Figure 7a shows the lifted index for all satellite-derived soundings in the area. The largest region of unstable air (most negative lifted indices) crosses South Carolina in the same

Table 2

Precipitable Water and Stability
for Selected Satellite Soundings

Region	Line and Element	Total PW(mm)	Stability*(°C) TT	KI	LI	Lowest 1-km Mean T (°C)	W(g•kg^{-1})	Energy (J•kg^{-1}) Pos	Neg
A	109 36	19	39	12	5.5	7.9	7.0	0	-999
A	109 37	21	41	15	4.4	9.6	7.9	0	-999
A	110 38	21	41	15	5.0	8.5	7.3	0	-999
A	111 39**	20	42	16	4.0	8.4	7.3	0	-999
A	111 40	19	42	15	4.6	6.7	6.4	0	-999
A	112 41	20	42	17	3.6	8.4	7.3	0	-999
B	110 47	35	47	28	-1.0	16.1	12.2	23	-215
B	111 47**	36	48	30	-1.7	16.6	12.5	99	-157
B	111 48	38	47	30	-1.7	17.1	12.9	81	-137
C	110 44	39	48	32	-2.8	17.9	13.6	268	- 88
C	111 44**	36	51	31	-5.8	18.6	14.2	1090	- 62
C	111 45	37	48	31	-2.2	17.0	12.9	165	-139
C	113 44	32	49	28	-4.3	17.3	13.1	693	- 52
D	114 48	44	55	41	-5.3	18.5	14.2	924	0
D	115 48**	33	50	32	-1.6	13.9	10.5	100	-247
D	115 49	34	50	33	-2.1	14.5	10.9	183	-204

*TT=Total Totals, KI= K-Index, LI= Lifted-Index

**denotes soundings shown in Fig. 5

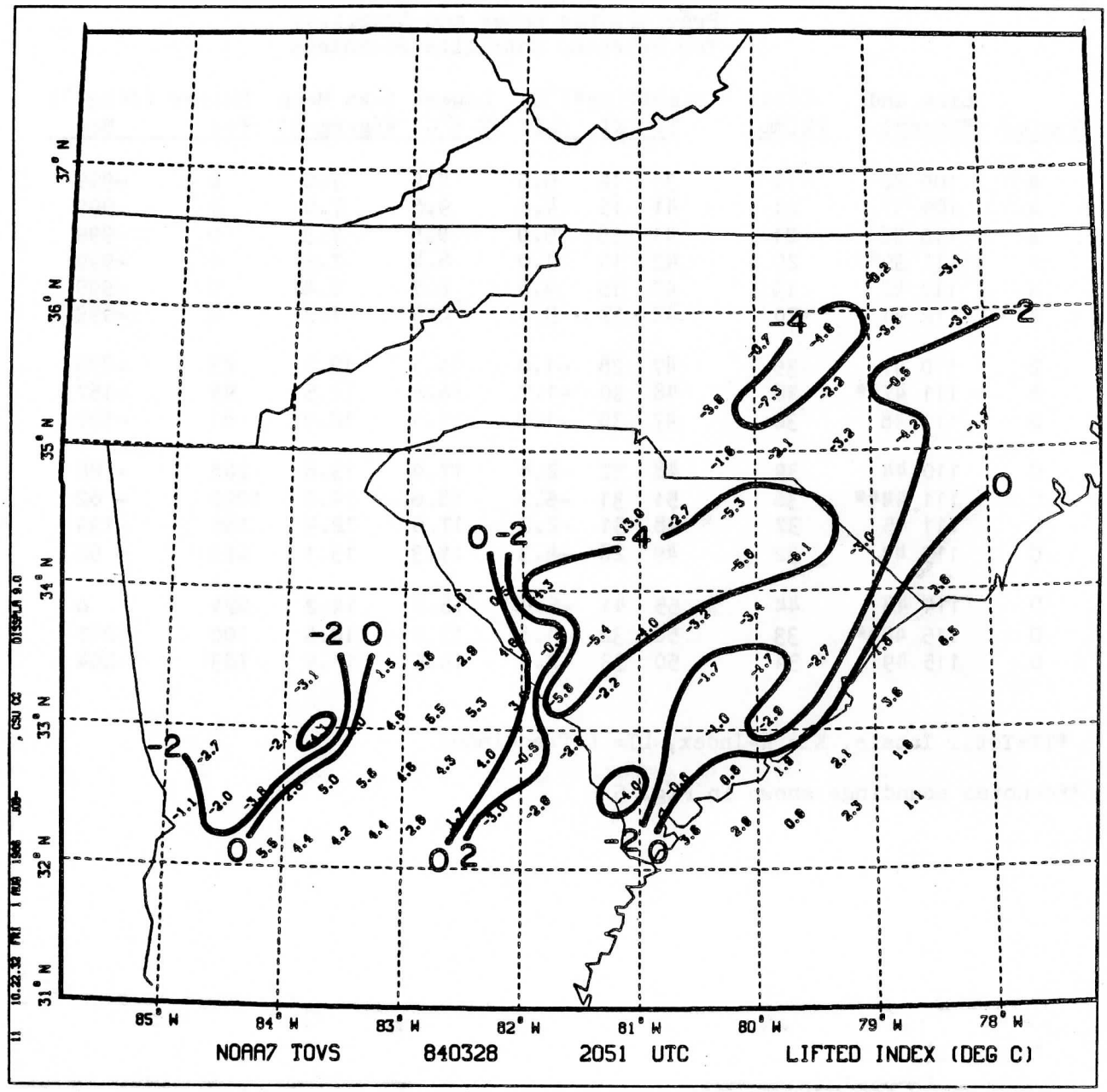

Figure 7a. Horizontal field of lifted index stability computed from the satellite soundings over the area under study.

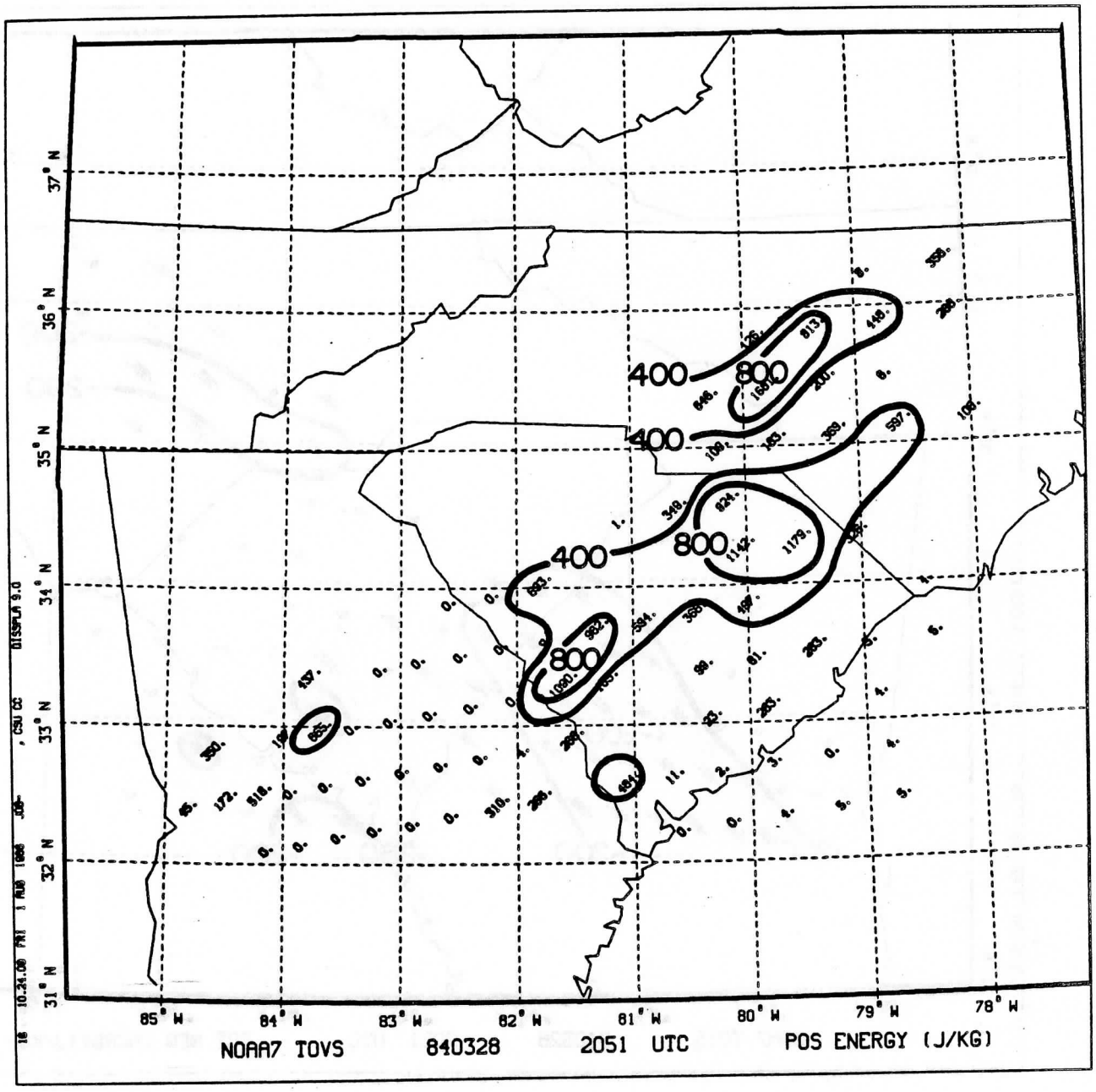

Figure 7b. Horizontal field of positive buoyant energy computed from the satellite soundings over the area under study.

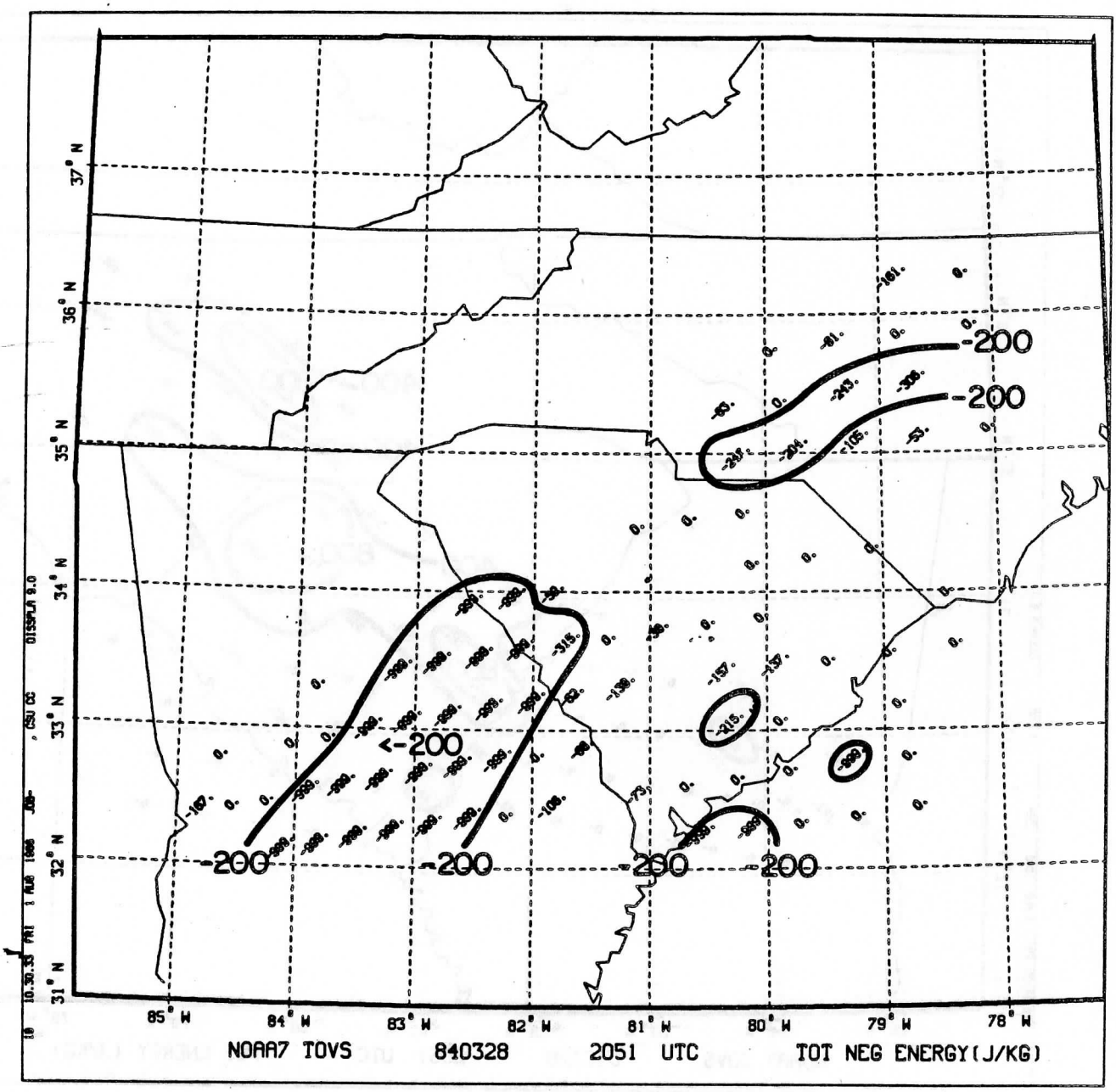

Figure 7c. Horizontal field of negative buoyant energy computed from the satellite soundings over the area under study.

orientation as the storm track in Figure 5. A second area of unstable air lies in North Carolina. However, it is thought that this is anomalous due to cirrus contamination undetected by the TOVS channels.

Two buoyant energy fields are also shown. The positive energy in Figure 7b has a pattern similar to that of the lifted index just shown. The positive buoyancy is the energy available once convection starts. However, negative buoyant energy in the lower levels must be overcome. Figure 7c shown the negative buoyant energy as maximum in Georgia. A secondary maximum occurs in North Carolina, partially offsetting the potential positive buoyant energy in that region. The areas where there is positive buoyant energy with little negative buoyant energy to be overcome is a preferred region for convection. That area happens to be northern South Carolina along the tornado track. The air both to the north and south is more stable due to the negative buoyancy capping those regions.

One caution in using these figures is to beware of relying too much on a sounding derived from a single FOV. Because of possible cloud contamination some individual soundings may be in error. This confirms the need for reproducibility in adjacent soundings before an individual sounding can be relied upon. An alternate means would be to include more than one FOV in each retrieval and produce soundings at lower resolution. But in that case some small scale features may be lost in the averaging. By grouping soundings by their characteristics there is increased reliability in the individual soundings in the group.

5.0 SUMMARY AND CONCLUSIONS

Satellite sounding data were used to produce soundings at single FOV locations on 28 March 1984, the Carolina tornado outbreak. The TOVs measurements at high horizontal resolution (35 km) have the ability to detect small-scale features which are undetectable by the standard coarse radiosonde network. Only surface observations are available at a similar high resolution, but they contain no information on vertical temperature or water vapor structure. The satellite soundings for this study were produced without the aid of surface observations in the retrieval process.

On this case study day, satellite soundings were examined in selected regions around a tornado genesis area. The retrieved soundings showed a wide range of water vapor profiles over a relatively small horizontal scale (<200 km). Total precipitable water and mean dewpoints and mixing ratios in the lowest one kilometer show contrasts. However, the primary indicators of the best region of severe weather potential are the lifted index and buoyant energies computed from the soundings.

ACKNOWLEDGEMENTS

The TOVS data used in this study were obtained from the NOAA/NESDIS Development Laboratory at the University of Wisconsin. This research was supported through NOAA grants NA84AA-D-00017 and NA84AA-H-00020.

REFERENCES

Hayden, C.M., W.L. Smith and H.M. Woolf, 1981: Determination of moisture from NOAA polar-orbiting satellite sounding radiances. J. Appl. Meteor., 20, 450-466.

Hillger, D.W. and T.H. Vonder Haar, 1981: Retrieval and use of high-resolution moisture and stability fields from Nimbus-6 HIRS radiances in pre-convective situations. Mon. Wea. Rev., 109, 1788-1806.

Hillger, D.W., 1984: Spatial and temporal variations in mesoscale water vapor retrieved from TOVS infrared radiances in a nocturnal inversion situation. J. Climate Appl. Meteor., 23, 704-723.

Purdom, J.F.W., 1985: The application of satellite sounding and image data to the Carolina tornado outbreak of 28 March 1984. Proceedings, 14th Conference on Severe Local Storms, AMS, 29 Oct - 1 Nov, Indianapolis, IN, 276-279

Smith, W.L., 1983: The retrieval of atmospheric profiles from VAS geostationary radiance observations. J. Atmos. Sci., 40, 2025-2035.

Smith, W.L. and F.X. Zhou, 1982: Rapid extraction of layer relative humidity, geopotential thickness, and atmospheric stability from satellite sounding radiometer data. Appl. Opt., 21, 924-928.

Storm Data, 1984: Vol. 26, No. 3, March, NOAA/NESDIS/NCDC, 5-12.

AN EXTENSION OF THE SIMULTANEOUS TOVS RETRIEVAL ALGORITHM - THE INCLUSION OF CLOUD PARAMETERS

Huang, Hung-Lung Allen
Satellite Ground Station, Central Weather Bureau
Taipei, Taiwan, Republic of China

W. L. Smith
Cooperative Institute for Meteorological Satellite Studies
University of Wisconsin
Madison, Wisconsin 53706

1. INTRODUCTION

A direct simultaneous solution of the radiative transfer equation for temperature, water vapor and surface skin temperature (Smith, et al., 1984) is used by Cooperative Institute for Meteorological Satellite Studies (CIMSS) at the University of Wisconsin-Madison for routine processing of VAS and TOVS data. An evaluation of retrieval results from VAS and TOVS data indicate significant improvements in the water vapor profile and small, but significant improvements for temperature profiling (Jedlovec, 1985; Smith et al., 1985). Despite these recent improvements, retrieval quality still suffers from the contamination of the sounding radiances by cloud (Susskind et al., 1982; Wielicki and Coakley, 1981). Hence an extension of the simultaneous retrieval algorithm to include cloud parameters is formulated to improve the retrieval of temperature and water vapor profiles, and surface skin temperature in cloudy situations. The extension enables the simultaneous retrieval of cloud amount and cloud top temperature with the atmospheric profiles from polar orbiting satellite TIROS Operational Vertical Sounder (TOVS) spectral radiance observations.

The results have been compared with those of the original simultaneous retrieval algorithm for the ALPine EXperiment (ALPEX) orbits (March 4 and 5, 1982). The comparison between the retrieval results and European Center for Medium Range Weather Forecasting (ECMWF) analyses of radiosonde data indicate significant improvements of temperature profile accuracy for both regression and climatology based guess for all weather conditions. The results of this extended algorithm using a regression guess show a very large improvement for moderate and heavy cloud conditions.

2. EXTENDED SIMULTANEOUS PHYSICAL RETRIEVAL SOLUTION

The radiative transfer equation for the cloudy FOV can be expressed by,

$$I = (1-N)[B_s\tau_s - \int_o^{p_s} B\frac{d\tau}{dp}dp] + N[B_c\tau_c - \int_o^{p_c} B\frac{d\tau}{dp}dp] \qquad (1)$$

where the cloud pressure is p_c, the effective cloud amount is N, the cloud top temperature is T_c, transmittance at cloud level is τ_c, and the temperature and transmittance at the surface is T_s and τ_s, respectively (Fig. 1).

The dependence on wavelength of Eq.(1) and the pressure dependence of all integrand variables are to be understood. Equation (2) is written in perturbation form,

$$\delta T^* = [(1-N)\tau_s \frac{(\partial B_s/\partial T_s)}{(\partial B/\partial T^*)} \delta T_s] + [N\tau_c \frac{(\partial B_c/\partial T_c)}{(\partial B/\partial T^*)} \partial T_c]$$

$$+ [N \int_{P_c}^{P_s} \delta T \frac{\partial \tau}{\partial P} \frac{(\partial B/\partial T)}{(\partial B/\partial T^*)} dP - \int_{o}^{P_s} \delta T \frac{\partial \tau}{\partial P} \frac{(\partial B/\partial T)}{(\partial B/\partial T^*)} dP]$$

$$+ [\int_{o}^{P_s} \delta U \frac{\partial \tau}{\partial U} \frac{\partial T}{\partial P} \frac{(\partial B/\partial T)}{(\partial B/\partial T^*)} dP - N \int_{P_c}^{P_s} \delta U \frac{\partial \tau}{\partial U} \frac{\partial T}{\partial P} \frac{(\partial B/\partial T)}{(\partial B/\partial T^*)} dP]$$

$$+ [B_c \tau_c \frac{1}{(\partial B/\partial T^*)} - B_s \tau_s \frac{1}{(\partial B/\partial T^*)} + \int_{P_c}^{P_s} B \frac{\partial \tau}{\partial P} \frac{1}{(\partial B/\partial T^*)} dP] \delta N \qquad (2)$$

Here it has been assumed that the cloud pressure is prescribed, however, cloud pressure is to be updated through its relation to cloud top temperature.

The unknowns of Eq.(2) are δT_s, the perturbation of surface temperature, δT_c, the perturbation of cloud top temperature, δT, the perturbation of temperature profile, δU, the perturbation of precipitable water profile, and δN, the perturbation of effective cloud amount. Since the unknown δT and δU are too numerous to be solved for directly, a small set of basis functions is assumed to represent the profiles. The basis functions are

$$\delta U(P) = \sum_{i=1}^{3} \alpha_i \int_{o}^{P} q_o(P) \frac{\partial \tau}{\partial \ln P} dP \qquad (3a)$$

$$\delta T(P) = \sum_{i=4}^{9} \alpha_i \frac{\partial \tau}{\partial \ln P} dP \qquad (3b)$$

$$\delta T_s = \alpha_i \; ; \; i = 10 \qquad (3c)$$

$$\delta N = \alpha_i \; ; \; i = 11 \qquad (3d)$$

$$\delta T_c = \alpha_i \; ; \; i = 12 \qquad (3e)$$

where the zero subscript indicates the a priori condition. Substituting equation 3(a-e) into equation (2), yields for each spectral radiance observation, δT^*_j, for a set of K spectral channels and k+1 and k+2 ancillary surface temperature and mixing ratio data.

$$\delta T_j^* = \sum_{i=1}^{12} \alpha_i \Phi_{ij} \quad ; \; j = 1, 2, \ldots K, K+1, K+2 \tag{4}$$

The α_i's are the explicit coefficients which need to be solved for to achieve the solution, K is the number of spectral channels used, and K+1, K+2 refer to ancillary surface temperature and water vapor data included to improve the retrieval results.

In Eq.(4), $\Phi_{i,j}$ are given by,

$$\Phi_{ij} = \int_o^{P_s} \left(\int_o^{P} q_o(P) \left(\frac{\partial \tau_i}{\partial \ln p} \right) dp \right) \frac{\partial \tau_j}{\partial U} \frac{\partial T}{\partial P} \frac{\partial B_j / \partial T)}{(\partial B_j / \partial T_j^*)} dp$$

$$-N \int_{P_c}^{P_s} \left(\int_o^{P} q_o(P) \left(\frac{\partial \tau_i}{\partial \ln p} \right) dp \right) \frac{\partial \tau_j}{\partial U} \frac{\partial T}{\partial P} \frac{\partial B_j / \partial T)}{(\partial B_j / \partial T_j^*)} dp \quad ; \quad 1 \leq i \leq 3 \tag{4a}$$

$$\Phi_{ij} = \int_o^{P_s} \left(\frac{\partial \tau_i}{\partial \ln p} \frac{\partial \tau_j}{\partial P} \frac{\partial B_j / \partial T)}{\partial B_j / \partial T^*} \right) dp - N \int_{P_c}^{P_s} \left(\frac{\partial \tau_i}{\partial \ln p} \right) \frac{\partial \tau_j}{\partial P} \left(\frac{\partial B_j / \partial T}{\partial B_j / \partial T_j^*} \right) dp \tag{4b}$$

$$; \quad 4 \leq i \leq 9$$

$$\Phi_{ij} = (1-N) \tau_{sj} \frac{(\partial B_{sj} / \partial T_s)}{(\partial B_{sj} / \partial T_j^*)} \quad ; \quad i=10 \tag{4c}$$

$$\Phi_{ij} = B_{cj} \, \tau_{cj} \frac{1}{(\partial B_j / \partial T_j^*)} - B_{sj} \, \tau_{sj} \frac{1}{(\partial B_j / \partial T_j^*)}$$

$$+ \int_{P_c}^{P_s} B_j \frac{\partial \tau_j}{\partial P} \frac{1}{(\partial B_j / \partial T_j^*)} dp \quad ; \; i=11 \tag{4d}$$

$$\Phi_{ij} = N \tau_{cj} \frac{(\partial B_{cj} / \partial T_c)}{(\partial B_{cj} / \partial T_j^*)} \quad ; \; i=12 \tag{4e}$$

In Eq.(4), the quantities $\Phi_{i,j}$ are calculated from the a priori estimates or mean profile conditions.

In solving Eq.(4), the conditional least squares solution is used,

$$[\alpha]_{12} \cong ([\Phi]^T [\Phi] + r[I])^{-1} [\Phi]^T [\delta T^*] \; . \tag{5}$$

where $[\ ]^T$ indicates matrix transposition, and $(\ )^{-1}$ indicates matrix inversion. Letter r is a scalar (0.1 is used for the clear condition, and 1.0 is used for the cloudy condition). [I] is the identity matrix, r[I] is incorporated to stabilize the matrix inversion. Once $[\alpha]_{12}$ is determined, $\delta U(p)$, $\delta T(p)$, δT_s, δN and δT_c can be calculated and added to the a priori estimates to yield the final solution.

3. RETRIEVAL LOGISTICS

The simultaneous retrieval method has been used at CIMSS for routine processing of both Polar Orbiting (TOVS) and Geostationary (VAS) satellite soundings since 1984. Since then, related papers and reports have been presented at two International TOVS study conferences and detailed descriptions of the retrieval algorithm and logistics have been published (Smith et al., 1984, Smith, Woolf, 1984, Smith et al., 1985). In this study, only the retrieval procedures which differ from the CIMSS's operation package are discussed.

Figure 2 shows the flow diagram for the extended (modified) simultaneous retrieval procedure. After HIRS and MSU data are amalgamated and one set of retrieval radiances have been calculated from the 3 by 3 HIRS FOVs, the CO_2 slicing method (Smith and Platt, 1978, Menzel et al., 1983) is performed and cloud parameters for the initial guess are determined. The extended simultaneous retrieval will then conduct the "step 1" retrieval procedure. The perturbation of cloud top temperature δT_c is checked to see that the cloud height determination does not deviate greatly from the "prescribed" value. If it is too large, "step 1" is repeated to obtain a better first estimate. The "step 2" retrieval is performed to reach the final solution.

For the achievement of the final sounding profiles and parameters, the perturbation of cloud top temperature, δT_c, has to be small to terminate the retrieval process. If δT_c is not small, the "step 2" retrieval is iterated until the convergence criterion is satisfied. The cloud top pressure is obtained by comparing the cloud top temperature with the final temperature profile. The cloud pressure level where the atmospheric temperature is best matched to the retrieval cloud top temperature.

4. RESULTS

To study the impact of the extended simultaneous retrieval algorithm, two sets of retrievals were achieved using two independent initial guess profile procedures; (a) statistical regression guess, and (b) climatology guess. The original simultaneous retrieval algorithm and the extended simultaneous retrievals were compared with conventional analyses of radiosonde data for the March 4, 5, 1982 ALPEX data sets.

Root mean square deviation (RMSD) between TOVS retrievals and ECMWF analyses were produced for the March 4, 5, 1982 cases. Figure 3 shows the RMSD comparison of the original simultaneous and the extended simultaneous methods for the regression guess condition. Improvement is shown at all levels with significant improvement displayed for the 850 mb to 400 mb region and the 250 mb level. Figure 4 displays the same comparison except for climatology first guess condition showing significant temperature

improvement below 600 mb. In order to explore the cause of the improvements displayed for the extended (modified) simultaneous retrieval, different sets of statistics have been produced. These statistics are the temperature RMSD values for the three different cloud conditions. Namely, (1) clear or low cloud conditions, (i.e., brightness temperature of HIRS/2 channel 8 TB(8) larger than 270 K), (2) moderate cloudy conditions, (i.e., TB(8) between 250 to 270 K), and (3) heavy cloudy conditions, (i.e., TB(8) smaller than 250 K). Figures 5-7 show the improvements in these three conditions. Clearly, the most significant improvements in the temperature profile retrieval using the extended simultaneous retrieval method are in the cloudy regions.

5. SUMMARY AND CONCLUSIONS

An extended (modified) simultaneous TOVS sounding profile retrieval algorithm has been developed to simultaneously account for the effects of the clouds. The results show significant improvement for retrievals of temperature for the ALPEX data sets of March 4 and 5, 1982. Classification of the statistics reveal the temperature retrieval improvements in different cloud conditions; a) clear or low cloud, small improvement, b) moderate cloudiness, large improvement, and c) heavy cloudiness, very large improvement. As a result of the improvements displayed here the UW-CIMSS is planning to incorporate this method of simultaneously accounting for cloud effects in it's International TOVS Processing Package (ITPP), used by direct readout satellite data producers on a world-wide basis.

6. REFERENCES

Jedlovec, G. J., 1985: "An Evaluation and Comparison of Vertical Profile Data from the VISSR Atmospheric Sounder (VAS)". J. of Atmos. and Oceanic Tech., 2, pp.559-581.

Menzel, W. P., W. L. Smith, T. R. Stewart, 1983: "Improved Cloud Motion Wind Vector and Altitude Assignment Using VAS". J. of Climate and Appl. Meteor., 22, pp.377-384.

Smith, W. L. and C. M. R. Platt, 1978: "Comparison of Satellite-Deduced Cloud Heights with Indications from Radiosonde and Ground-Based Laser Measurements". J. of Appl. Meteor., 17, pp. 1796-1902.

Smith, W. L., 1983: "The Retrieval of Atmospheric Profiles from VAS Geostational Radiance Observations". J. of Atmos. Sci., 40, pp.2025-2035.

Smith, W. L., H. M. Woolf, C. M. Hayden, A. J. Schreiner and J. M. LeMarshall, 1983: "The Physical Retrieval TOVS Export Package". The Tech. Proc. of the First International TOVS Study Conf., W.P. Menzel, Editor, pp.227-278.

Smith, W. L. and H. M. Woolf, 1984: "Improved Vertical Soundings from an Amalgamation of Polar and Geostationary Radiance Observations". Preprint Volume: Conference on Satellite Meteorology/Remote Sensing and Applications, June 25-29, 1984, Clearwater Beach, FL. Published by Amer. Met. Soc., Boston, MA, pp.45-48.

Smith, W. L., H. E. Revercomb, H. B. Howell and H. M. Woolf, 1984: "Recent Advancement in Satellite Remote Sounding". Presented at International Radiation Symposium 1984, Perugia, Italy, 21-29 August 1984.

Smith, W. L., H. M. Woolf, C. M. Hayden, and A. J. Schreiner, 1985: "The Simultaneous Retrieval Export Package". The Technical Proceedings of the Second International TOVS Study Conference, W. P. Menzel, Editor, pp.224-253.

Susskind, J., J. Rosenfield, D. Reuter and M. T. Chahine, 1982: "The GLAS Physical Inversion Method for Analysis of HIRS/MSU Sounding Data". NASA Tech. Memo. TM 84936, pp.1-101.

Wielicki, B. A. and J. A. Coakley, Jr., 1981: "Cloud Retrieval Using Infrared Sounder Data: Error Analysis". J. of Appl. Met., 20, pp.157-169.

4/3TOVS3/01

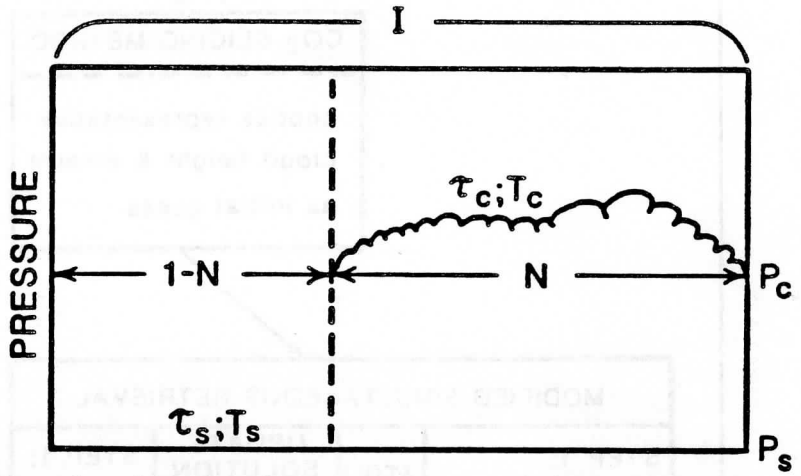

Vertical cross section of FOV as seen from the satellite with one layer of cloud.

Figure 1

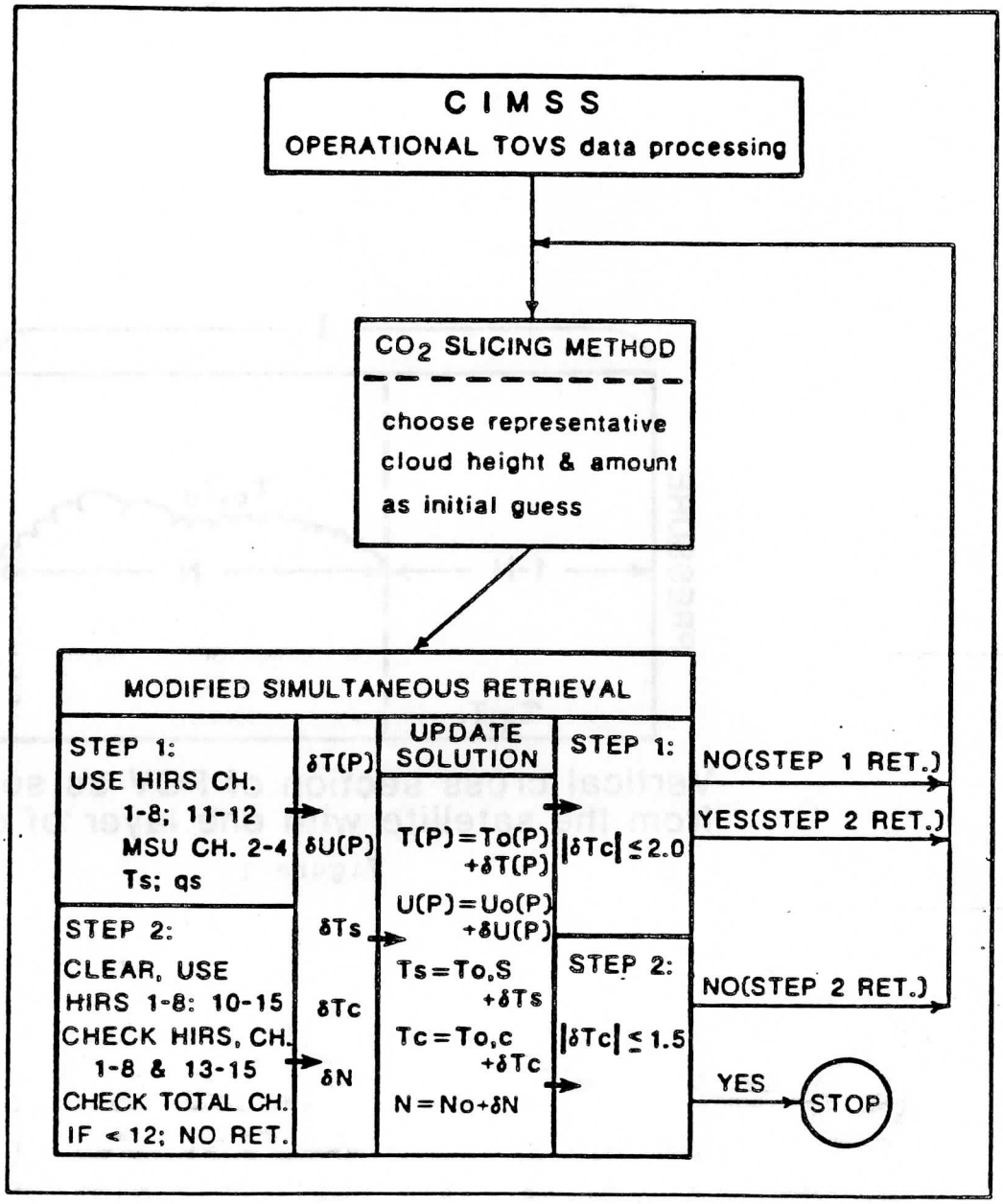

Flow diagram for the modified simultaneous retrieval

Figure 2

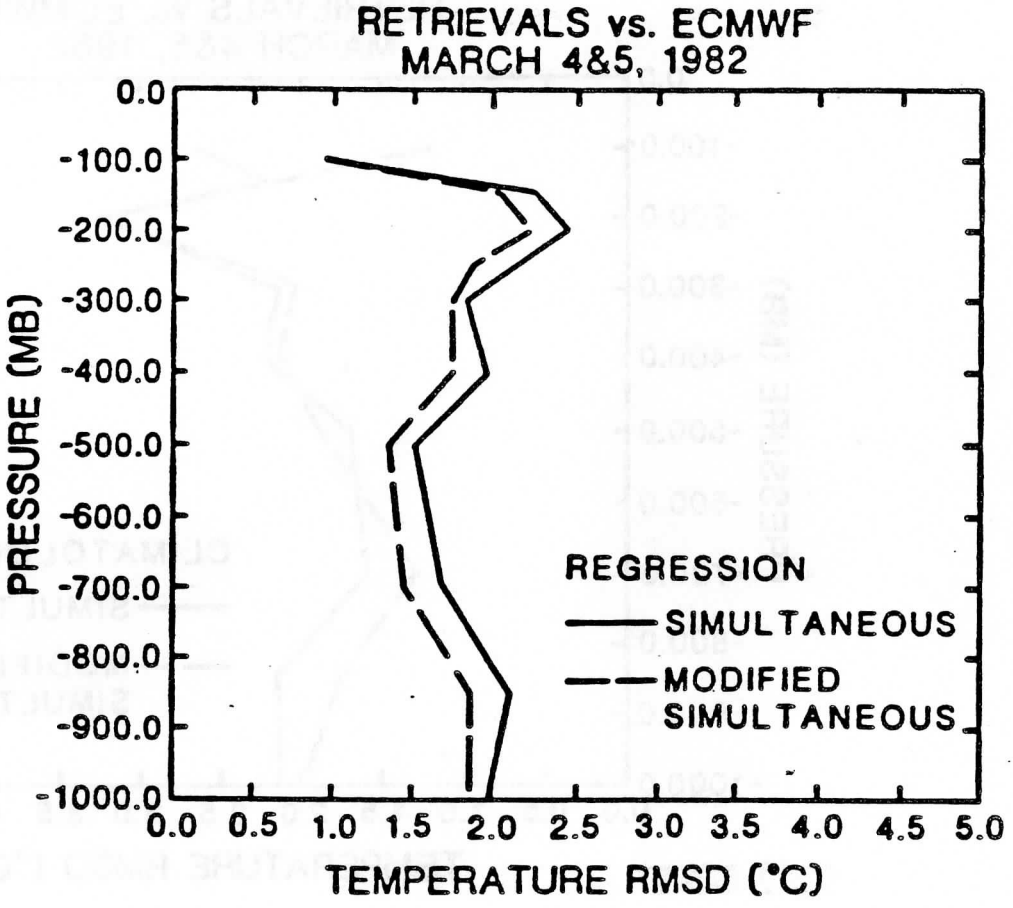
RETRIEVALS vs. ECMWF
MARCH 4&5, 1982
PRESSURE (MB)
0.0
-100.0
-200.0
-300.0
-400.0
-500.0
-600.0
-700.0
-800.0
-900.0
-1000.0
0.0 0.5 1.0 1.5 2.0 2.5 3.0 3.5 4.0 4.5 5.0
TEMPERATURE RMSD (°C)
REGRESSION
SIMULTANEOUS
MODIFIED
SIMULTANEOUS

Figure 3

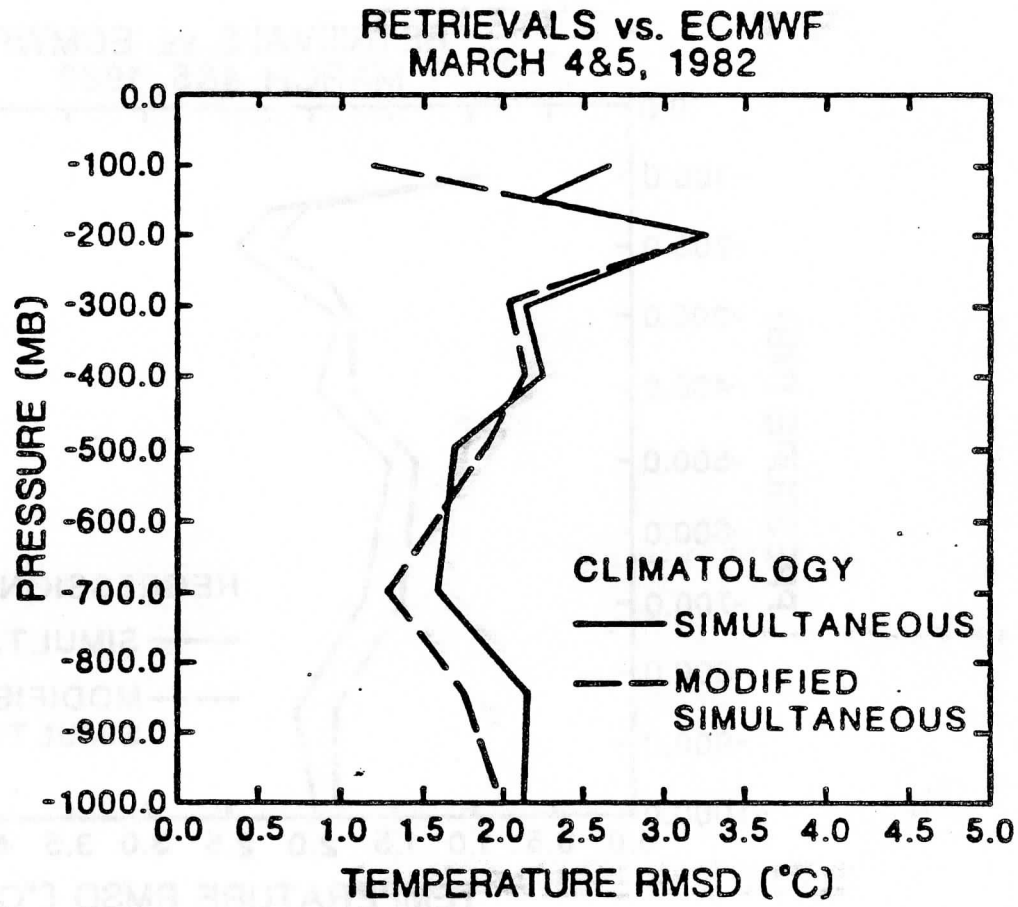
RETRIEVALS vs. ECMWF
MARCH 4&5, 1982
PRESSURE (MB)
0.0
-100.0
-200.0
-300.0
-400.0
-500.0
-600.0
-700.0
-800.0
-900.0
-1000.0
0.0 0.5 1.0 1.5 2.0 2.5 3.0 3.5 4.0 4.5 5.0
TEMPERATURE RMSD (°C)
CLIMATOLOGY
SIMULTANEOUS
MODIFIED SIMULTANEOUS

Figure 4

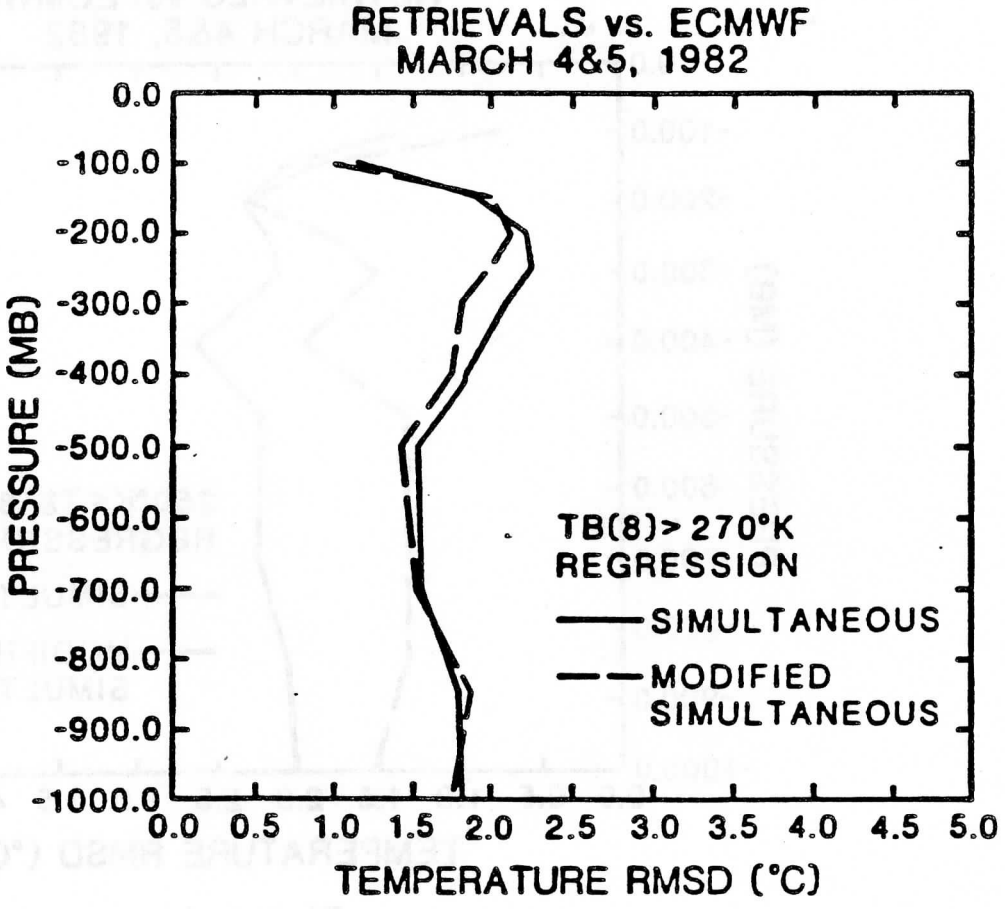
RETRIEVALS vs. ECMWF
MARCH 4&5, 1982
PRESSURE (MB)
0.0
-100.0
-200.0
-300.0
-400.0
-500.0
-600.0
-700.0
-800.0
-900.0
-1000.0
0.0 0.5 1.0 1.5 2.0 2.5 3.0 3.5 4.0 4.5 5.0
TEMPERATURE RMSD (°C)
TB(8)> 270°K
REGRESSION
SIMULTANEOUS
MODIFIED
SIMULTANEOUS

Figure 5

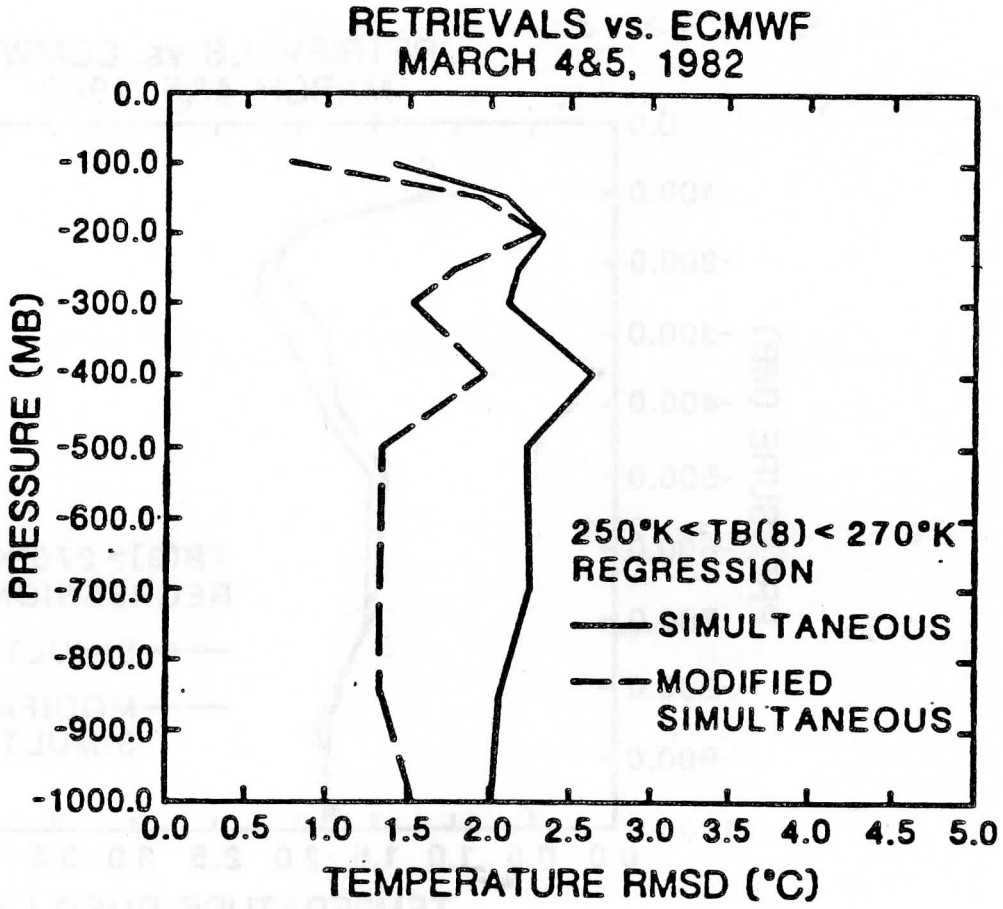
RETRIEVALS vs. ECMWF
MARCH 4&5, 1982
PRESSURE (MB)
0.0
-100.0
-200.0
-300.0
-400.0
-500.0
-600.0
-700.0
-800.0
-900.0
-1000.0
0.0 0.5 1.0 1.5 2.0 2.5 3.0 3.5 4.0 4.5 5.0
TEMPERATURE RMSD (°C)
250°K<TB(8)<270°K
REGRESSION
SIMULTANEOUS
MODIFIED
SIMULTANEOUS

Figure 6

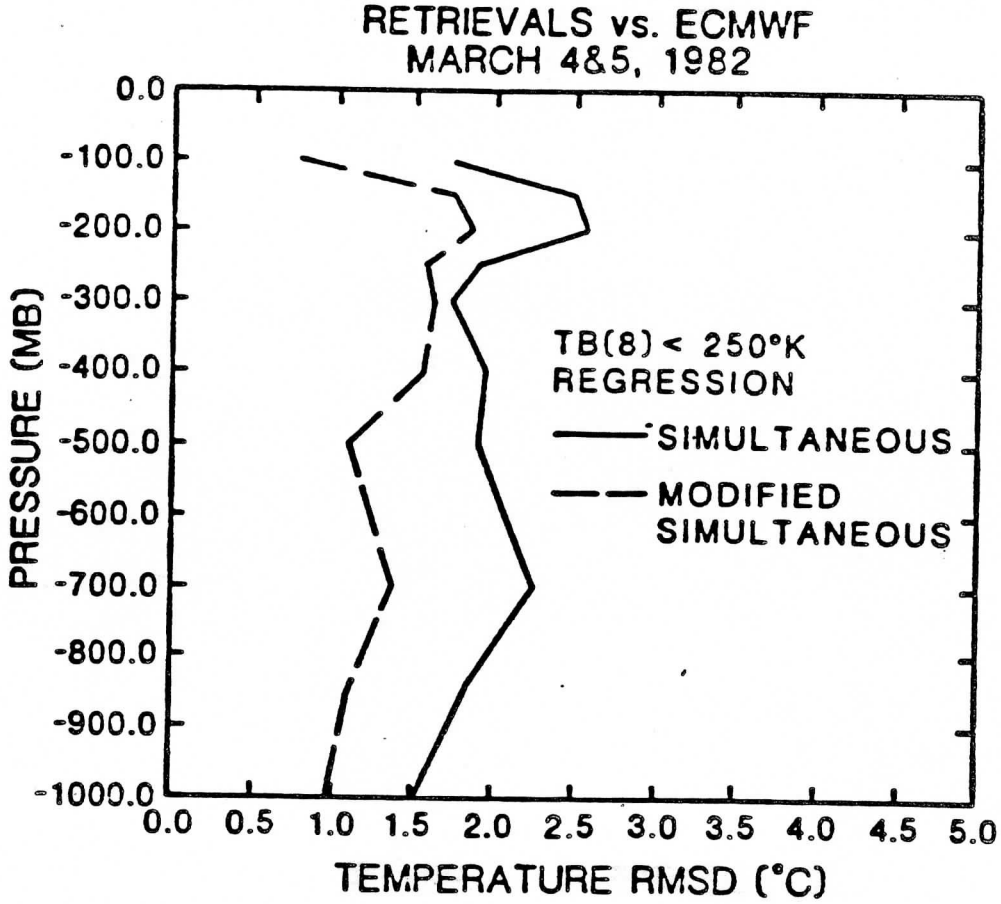
RETRIEVALS vs. ECMWF
MARCH 4&5, 1982
PRESSURE (MB)
0.0
-100.0
-200.0
-300.0
-400.0
-500.0
-600.0
-700.0
-800.0
-900.0
-1000.0
0.0 0.5 1.0 1.5 2.0 2.5 3.0 3.5 4.0 4.5 5.0
TEMPERATURE RMSD (°C)
TB(8) < 250°K
REGRESSION
SIMULTANEOUS
MODIFIED
SIMULTANEOUS

Figure 7

THE OPERATIONAL AND RESEARCH PROCESSING OF TOVS DATA IN THE AUSTRALIAN BUREAU OF METEOROLOGY.

J.F. Le Marshall, G.A. Kelly, P.E. Powers and R.F. Davidson.

Bureau of Meteorology
Melbourne, Australia

ABSTRACT

Since the launching of the TIROS-N Series satellites in 1978 the Bureau of Meteorology in Australia has used data generated from the second generation sounders on these spacecraft. In the Australian Region this data is received and processed locally. This paper describes the present operational TOVS direct readout processing system used by the Bureau of Meteorology. It briefly describes the recently implemented ARM (Australian Region McIDAS) system, which has facilitated the interactive processing of TOVS data. It also briefly details the statistical and physical retrieval systems incorporated into this system which are now the basis of a significant amount of operational development and research. This research and development work is also summarised in the paper.

1. INTRODUCTION

The sparsity of conventional data in the Southern Hemisphere and even in large parts of the Australian Region illustrates the importance of satellite data to Australian meteorology.

Satellite imagery was first received in the Bureau on Christmas day in 1964 and satellite picture interpretation (Guymer, 1978) has been used since then in the analysis process in the National Meteorological Centre (NMC), Melbourne. It is still used both in the Regional and Hemispheric numerical analyses, giving an initial estimate of mean sea level pressure and also the 1000 to 500mb thickness. The pseudo-observations generated by this cloud picture interpretation process are distributed by the Global Telecommunications System (GTS).

Vertical Temperature Profile Radiometer (VTPR) Data from the initial NOAA operational satellites gave an early chance to further quantify satellite based estimates of 1000 to 500mb thickness. Thickness data available in real time in NMC Melbourne, from the National Environment Satellite Service (NESS), via the GTS, were followed after 1976 by locally derived temperature and moisture profiles (Kelly et al., 1976) which were calculated from NESS clear radiances, arriving over the GTS.

The importance of satellite sounding data in analysis and prediction in the middle latitudes (Kelly et al., 1976 and Bourke et al., 1983) and low latitudes (Velden et al., 1984 and Le Marshall et al., 1985) has resulted in the Bureau of Meteorology (BoM) establishing and continuing to enhance facilities for direct readout and processing of second generation satellite data. From May 1980 the BoM has had the capacity to receive, process and utilize data from the TIROS-N/NOAA A series of satellites. This data is used in the Australian Region, to augment the less dense global data received from the National Environmental Satellite and Data Information Service (NESDIS) via the GTS. These GTS data are in the form of geopotential thickness and layer mean precipitable water and have a density of near one observation per 5 degree latitude by 5 degree longitude block, which is less than the optimum density required by both the NMC's regional and hemispheric analyses. This paper describes the operational system presently used by the BoM to provide higher density soundings for these numerical analyses and other forecast applications.

Recently to enable meteorologists to properly utilize the burgeoning data base, composed largely of satellite data, and amongst other things, to improve the operational and research environment for TOVS processing, the BoM has implemented the Australian Region McIDAS (ARM), (Le Marshall et al., 1986). This system was implemented in the Bureau of Meteorology Research Centre (BMRC) in September 1985 and in NMC in July 1986. The ARM system provides an excellent vehicle for interactive TOVS processing and also allows the production of cloud drift winds which are complementary to the sounding data in the analysis process (Le Marshall et al., 1985).

The statistical and physical retrieval schemes incorporated into the ARM system are also described. These systems are the subject of most of the present operational development and research endeavours and have many characteristics which render them suitable as an operational system, as well as making them a reliable research processing system.

2. THE OPERATIONAL SYSTEM

2.1 RECEPTION

Raw TOVS data in their TIROS-N Information Processor(TIP) form are acquired directly by reception and processing of the VHF Beacon Direct Sounder Broadcast from the TIROS-N satellites. Reception is via aerials in Melbourne (31'31S, 144'57E) and Perth (31'55S, 115'58E). A detailed description of the reception facilities and data ingest is given by Kelly and Le Marshall (1983). It is appropriate to note that the data received using the VHF system for the most recent satellites in the TIROS-N/NOAA A Series is far noisier than that from the original spacecraft.

2.2 PROCESSING

An overview of the present operational TOVS processing system is given in Figure 1. An ensemble of 11 programs is used to process the data completely, using eighteen fixed reference files to produce four main production files. The preprocessing and retrieval procedure is described below.

PREPROCESSING - The scheduling program automatically initiates processing for all reasonable orbits received. The data is initially decoded, earth located and calibrated. The resultant radiances are then corrected for limb or slant path effects, while certain of the channels are corrected for water vapour absorption, emissivity, fluorescence and reflected sunlight (Smith et al., 1979). After this the Microwave Sounding Unit (MSU) data are mapped onto the High Resolution Infrared Radiation Sounder (HIRS) data using a successive correction technique (Cressman, 1959). Hence at each of the 56 HIRS spots there is a value of latitude, longitude and interpolated MSU channels.

A rainfall check is subsequently performed on the microwave data (Phillips, 1980). The MSU data is then edited using synthetic microwave data generated from the output fields of the operational Australian Region Primitive Equation (ARPE) model for the orbit time and a file of MSU retrievals is generated.

The HIRS and MSU data are then used to generate IMAGE (horizontal fields) and SOUNDER (vertical profile fields) files. The latitude and longitude associated with the retrievals are then smoothed to allow for noisy data.

RETRIEVAL - The first step in the retrieval process involves the selection of cloud free fields of view or the correction of partly cloudy radiances to produce "clear column" radiances using the N* technique (Smith et al., 1976).

Once a clear radiance is obtained, it is possible to express temperature and moisture as a linear function of satellite measured brightness temperatures (Smith et al., 1970), however one set of regression equations relating these variables is insufficient to cover the range of temperature and moisture profiles observed in the Australian Region. To overcome this problem regression coefficients can be selected according to the latitude of observation, but this approach clearly has shortcomings, when for example polar air intrudes into the mid-latitudes. To resolve this problem, the operational scheme uses discriminant analysis (Anderson, 1958) to categorize the air mass type from three MSU channels, and hence to select the regression coefficients to be used in the retrieval process.

The discriminant function is calculated using MSU

channels 2,3 and 4. The groups are determined using a TOVS/radiosonde match data set for the Australian Region which is initially sorted into eight equal groups based on MSU channel 2 brightness temperature. Eight group probabilities are calculated for each observation and the groups are readjusted for misclassifications. New discriminant functions are then calculated for the eight groups and the data again readjusted. Following several iterations the probability of misclassification of an observation is usually less than 0.1.

These final groups are then used to calculate the regression equations for predicting both temperature and moisture. The effectiveness of this grouping approach can be gauged by examining Fig. 2(a), which shows the mean temperature sounding for each of the groups used operationally for NOAA-9. It shows a separation of the observed brightness temperatures into groups whose mean temperature traces illustrate the range of temperature profiles sampled in the Australian Region. It is interesting to note both the tropical and middle tropopause levels have been defined by these groups. It should also be noted these groups were generated from data, received on the VHF beacon.

The differences between radiosonde measured and NOAA-9 TOVS derived temperatures in the Australian Region, for these eight discriminant groups, using MSU, HIRS and MSU plus HIRS data is seen in Figure 2(b). Space and time separation for the radiosonde and satellite did not exceed 60 km and 3 hours respectively.

After the retrieval process the soundings are checked for internal consistency and also against the temperatures generated by the operational ARPE forecast model. They are then enhanced by MSU based retrievals in areas where no infrared retrievals are available. Finally these data are again checked for internal consistency and redundancy and the derived geopotential height is used to calculate winds.

An example of the output from the operational system is seen in Figure 3(a), which shows the cold pool over Eastern Australia which was responsible for the recent heavy rain and floods in the Sydney area. The figure shows the 250mb height and geostrophic winds from NOAA-9 data at 0458Z on the 6 August, 1986. An independent manual working chart from NMC produced from conventional data, cloud drift winds, aircraft observations and cloud imagery is seen in figure 3(b). It shows good agreement with TOVS analysis.

3. SYSTEM DEVELOPMENT

3.1 PREAMBLE

Research and Development processing of TOVS data in the BoM is now largely centred around the one step simultaneous

physical retrieval scheme (Smith et al., 1985). This algorithm permits the simultaneous retrieval of surface-skin (or cloud) temperature, and atmospheric temperature and moisture profiles. The advantages of this technique are well established. It solves for surface skin temperature and atmospheric temperature and moisture profiles simultaneously, directly taking in account the dependence of the radiances on surface temperature, and atmospheric temperature and moisture. Because it gives a solution for all parameters with one matrix inversion, it is very efficient and its form makes it easy to use ancillary data. In theoretical simulations and practice it is found to produce high quality moisture retrievals when compared to many of the present retrieval schemes (Smith and Woolf, 1984, and Le Marshall, 1985).

3.2 THE ARM SYSTEM

Recently the ARM (Australian Region McIDAS) system has been implemented in the BoM (Le Marshall et al., 1986). It provides for the user access to a very extensive and integrated historical and real time meteorological data base. It also permits the user to generate further derived data such as cloud drift winds from the basic data set, which includes for example polar orbiting and geosynchronous satellite radiance observations. Just as importantly the system enables use of the data for a range of research and forecasting tasks by providing an extensive number of application programs. These range from meteorological data analysis, stability analysis, three dimensional and time lapsed image display, to both the generation and display of Numerical Weather Prediction (NWP) forecast fields.

As a result of these characteristics the system provides an excellent vehicle for the interactive processing of TOVS data and the majority of TOVS development work in the Bureau is now being done on this system. In particular the system makes available for use by the TOVS processing system, real time conventional data, satellite imagery and gridded analyses and forecasts in an easily accessible way. In addition it also provides a powerful real time validation and editing facility.

3.3 TOVS PROCESSING SYSTEM DEVELOPMENT

Most of development work on the TOVS system has been centred around the simultaneous retrieval scheme, which can be used both in batch and interactive mode on the ARM system.

In the preprocessing stage, the Cressman analysis scheme used in the operational system, has been replaced by a Generalised Cross Validation (GCV) Analysis (Hutchinson, 1984) to map the low resolution and occasionally noisy MSU channels data onto the high resolution HIRS data.

In the retrieval step itself, the very important first

guess surface conditions are provided by a univariate Barnes analysis (Barnes, 1973) of surface temperature, moisture and pressure, or by the regional optimum interpolation surface analysis scheme of Keenan et al., (1986) which provides surface temperature, moisture and pressure. This latter scheme uses a modelled diurnal cycle to provide a first guess for the surface fields in consecutive analyses, which are performed every three hours. Cloud clearing using the N* technique can also be performed early in the processing to increase the retrieval yield.

The first guess for the retrieval scheme is provided by climatology, the Australian Region Primitive Equation Model, the Hemispheric Assimilation Model or regression.

Significant development work has been performed on the regression retieval scheme, not only to provide a good first guess for the physical retrieval scheme, but because of its operational significance, where the simplicity, efficiency and the high quality of the retrievals from the scheme are important. The regression scheme is similar to the operational scheme, however a version using regressions calculated for each of the different limb viewing angles, is being developed. It is hoped to reduce the problems associated with the usual statistical limb correction techniques (Le Marshall and Schreiner, 1984) using this approach. In addition some variation in the grouping techniques for the discriminant analysis has also been used, although to date only modest improvements in skill over the present classification scheme have been seen.

3.4 AN EXAMPLE.

In February this year conventional, radar and satellite image and sounding data was collected as TC "Winifred" crossed the Queensland Coast. Temperatures derived from these data using the simultaneous retrieval scheme are seen in Figure 4. It shows the TOVS data based 500mb temperatures around TC "Winifred" at 0436Z on the 1 February, 1986. The temperatures are plotted over 03Z GMS-3 infrared image, and are seen to be consistent with the NMC analyses and the small amount of radiosonde data available for 00Z on that day.

A further example of interactive retrievals for this situation, produced on the ARM is seen in Figure 5. It shows a set of 250mb temperatures, derived from the TOVS MSU channels, using an iterative physical retrieval scheme (Smith et al., 1983). These are plotted over the 04Z GMS-3 visible image. Some indication of tropospheric warming in the general area of the cylcone can be seen. The magnitude of this warming is close to that expected from an average decaying cyclone in the Southwest Pacific (Holland, 1983) and may be related to its intensity (Velden et al., 1984). Further information about the storm may also be inferred from the

TOVS data by examination of other levels for instance a strong warm anomaly also appears at 150mb (Figure 6).

Relating this to temperature anomaly fields for a 'composite' axisymmetric cyclone for the Southwest Pacific (Merrill, 1985) suggests a decaying tropical cyclone. Stronger statements about these features await further examination of the soundings for rainfall effects, using among other things radar data, and also an examination of several more cyclones.

3.5 FUTURE DEVELOPMENTS

Future development work will be directed into several areas. The provision of TOVS based estimates of cloud height and amount, which can be used to assign cloud heights to cloud drift winds, in modelling applications and by operational forecasters is an important task.

A continuation of present work looking at different grouping procedures for the discriminant analysis scheme, different limb correction techniques and examining of the impact of ancillary data on the simultaneous physical retrieval scheme will also be pursued.

Data impact studies in both the mid and low latitudes will also be continued, using both TOVS temperature and moisture soundings and cloud drift winds in both the regional and hemispheric numerical analysis and prognosis systems.

In 1987, S-band antennae will be installed in Melbourne and Perth and will provide higher quality TOVS and AVHRR data in real time. It is intended that both these data will be used in the TOVS retrieval scheme.

In the longer term a proposal has been prepared by the BoM and CSIRO Office of Space Science Applications for a geostationary sounding instrument in the Australian Region and studies in support of this are now underway.

4. CONCLUSION

A statistical retrieval scheme, using a discriminant analysis procedure is being used operationally in the Australian Region. As a result of interfacing the scheme to the operational analysis and prognosis system in NMC, it is quite a robust operational system, if one neglects the problems attributable to the poor data quality provided by VHF reception. This problem is being partially overcome at the moment by receiving some TIP data in real time from the CSIRO Division of Atmospheric Research, S-band antenna at Aspendale, Victoria. A satisfactory solution of the problem awaits the Bureau's installation of S-band reception facilities in 1987 in Melbourne and Perth.

With regard to the future development of the operational

system, the ARM is now used operationally in NMC and the implementation of an operational interactive TOVS processing scheme using this system is underway. Initially this processing system will be an enhanced version of the operational statistical scheme. It is intended however that the simultaneous retrieval scheme, using data from the real time analysis and prognosis system and with some refinements now under development will be the basis of the next operational system.

ACKNOWLEDGEMENTS.

Many thanks are due to Ross Bouchier and Paul Hambleton for their help in preparing this paper.

REFERENCES

Anderson, T.W., 1958. Introduction to multi-variate statistical analysis. John Wiley publisher.

Bourke, W., Puri, K., Seaman, R., 1982. Numerical weather prediction studies from the FGGE southern hemisphere data base. Mon. Wea. Rev., 110, 1787-1800.

Barnes, S.L., 1973. Mesoscale objective analysis using weighted time series observations. NOAA. Tech. Memo. ERL NESSL-62, National Severe Storm Laboratory 1313 Halley Circle, Norman, OK 73069, 60pp.

Cressman, G.P., 1959. An operational objective analysis system. Mon. Wea. Rev., 87, 367-374.

Guymer, L., 1978. Operational application of satellite imagery to synoptic analysis in the southern hemisphere. Tech. Rep. 29, Bureau of Meteorology, Melbourne, Australia.

Holland, G., and Gray, W., 1983. Tropical cyclones in the Australian/Southwest Pacific Region. Atmospheric science paper 363, Department of Atmospheric Science, Colorado State University, Fort Collins, Colorado. Rept. No. CSU ATS-363.

Hutchinson, M.F., 1984. A summary of some surface fitting and contouring programs for noisy data. CSIRO Division of Mathematics and Statistics, Consulting Report Act 84/6

Keenan, D.W., Davidson, N.E., Kelly, G.A., 1986. Surface analysis of temperature and dewpoint in the Australian region. To be submitted to Aust. Meteor. Mag.

Kelly, G.A., Powers, P.E. and Gauntlett, F.J., 1976. Temperature and water vapour retrievals from the NOAA-4 satellite in the southern hemisphere. Proceedings of the symposium on meteorological observations from space: Their contribution to the First GARP Global Experiment, June 8-10, 1976, Philadelphia, Penna., USA, COSPAR, 77-84.

Kelly, G.A., Mills, G.A., and Smith, W.L., 1978. Impact of Nimbus-6 temperature soundings on Australian Region forecasts. Bull. Amer. Meteor. Soc. 59, 393-405.

Kelly, G.A., and Le Marshall, J.F., 1983. The Australian operational direct read out and TOVS processing system and its application to the Tasman Sea Intercomparison study. The technical proceedings of the first international TOVS study conference, Igls, Austria, 29 August - 2 September 1983. A report from the CIMSS, SSEC, University of Wisconsin, Madison, Wisconsin 53706, 111-131.

Le Marshall, J.F., 1985. An intercomparison of temperature and moisture fields retrieved from TIROS Operational Vertical Sounder Data. The technical proceedings of the second international TOVS study conference, Igls, Austria, 18-22 February. A report from the CIMSS, SSEC, University of Wisconsin, Madison, Wisconsin 53706, 106-161.

Le Marshall, J.F., and Schreiner, A., 1985. Limb effect in satellite temperature sounding. J. Clim. and Appl. Meteor. 24, 287-290

Le Marshall, J., Smith, W. and Callan, G., 1985. Hurricane Debby - An illustration of the complementary nature of VAS soundings and cloud and water vapour drift winds. Bull. Amer. Meteor. Soc., 66, 258-263.

Le Marshall, J.F., Stirling, L.J., Davidson, R.F., and Hasset, M. 1986. The ARM system - An integrated meteorological data base and data utilization system for research and operations in the Australian Region. To be submitted to Aust. Meteor. Mag.

Merrill, T. 1985. Environmental influence on hurricane intensification. Atmospheric Science, Colorado State University, Fort Collins, Colorado. Rept. No. CSU ATS-394

Phillips, N. 1980. Two examples of satellite temperature retrievals in the North Pacific. Bull. Amer. Meteor. Soc., 62, 712-717.

Smith, W.L., Woolf, H.M., and Jacob, W.J., 1970. A regression method for obtaining real time temperature and geopotential height profiles from satellite spectrometer measurements and its application to Nimbus 3 "SIRS" observations, Mon. Wea. Rev. 98,582-603.

Smith, W.L., and Woolf, H.M. 1976. The use of eigenvectors of statistical covariance matrices for interpreting satellite sounding radiometer observations. J. Atmos. Sci., 33, 1127-1140.

Smith, W.L., Woolf, H.M., Hayden, C.M., and Wark, D.,

1979. The TIROS-N operational vertical sounder. Bull. Amer. Meteor. Soc., 60,1177-1187.

Smith, W.L., Woolf, H.M., Hayden, C.M., Schreiner, A.J., and Le Marshall, J.F., 1983. The physical retrieval TOVS export package. The technical proceedings of the first international TOVS study conference, Igls, Austria, 29 August-2 September 1983. A report from the CIMSS, SSEC, University of Wisconsin, Madison, Wisconsin 53706, 111-131.

Smith, W.L., and Woolf, H.M. 1984. Improved vertical soundings from an amalgamation of polar and geostationary radiance observations. Preprint volume: Conference on satellite meteorology/remote sensing and applications. June 25-29, 1984. Clearwater Beach, Florida. Published by Amer. Meteor. Soc., Boston, Massachusetts.

Smith, W.L., Woolf, H.M., Hayden, C.M. and Schreiner, A.J., 1985. The simulataneous retrieval export package. The technical proceedings of the second international TOVS study conference, Iglis, Austria, 18-22 February. A report from the CIMSS, SSEC, University of Wisconsin, Madison, Wisconsin 53706, 224-273.

Velden, C.S, Smith, W.L., and Mayfield, M., 1984. Applications of VAS and TOVS to tropical cyclones. Bull. Amer. Meteor. Soc., 65, 1059-1067.

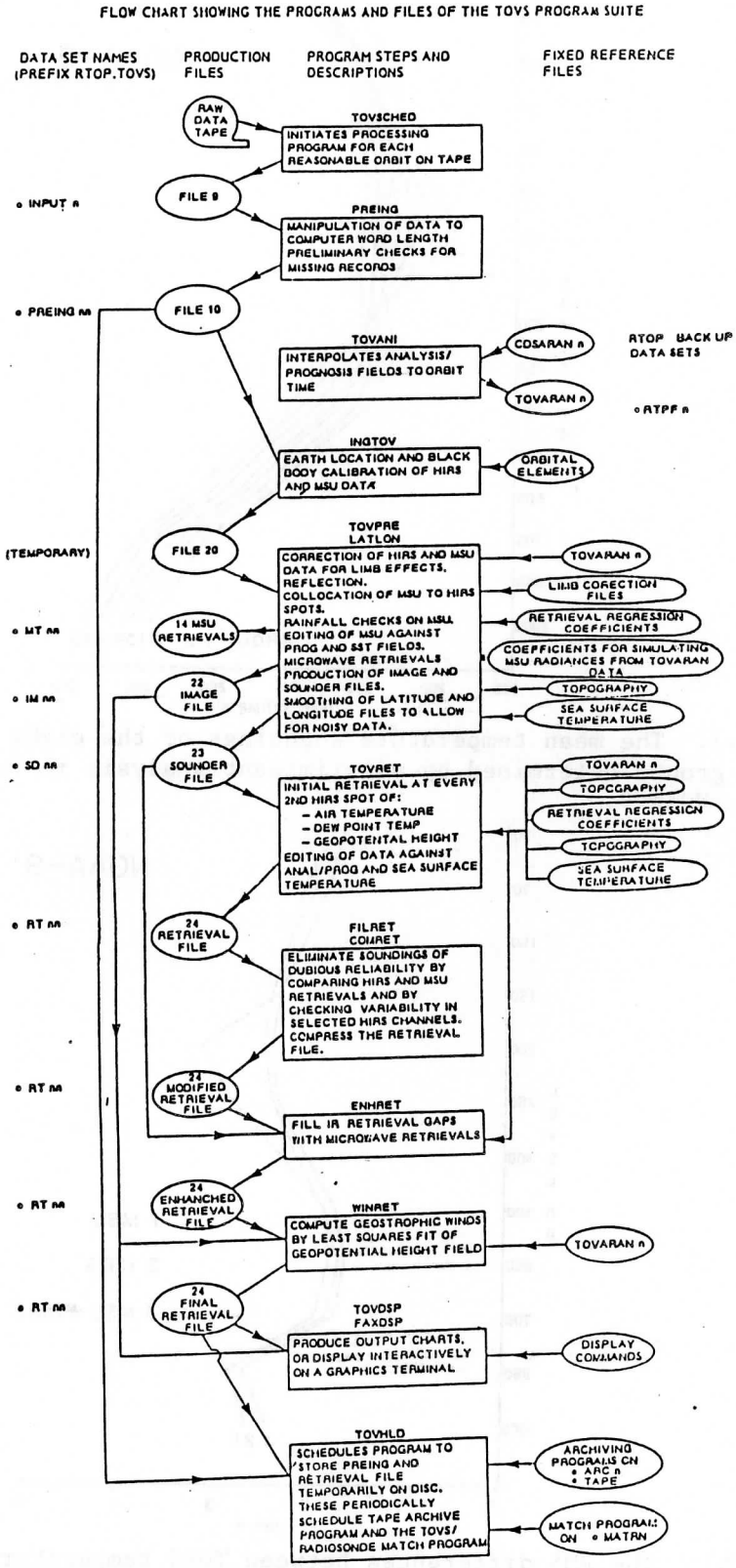

Figure 1: Flow chart illustrating the programs and files of the operational TOVS processing system

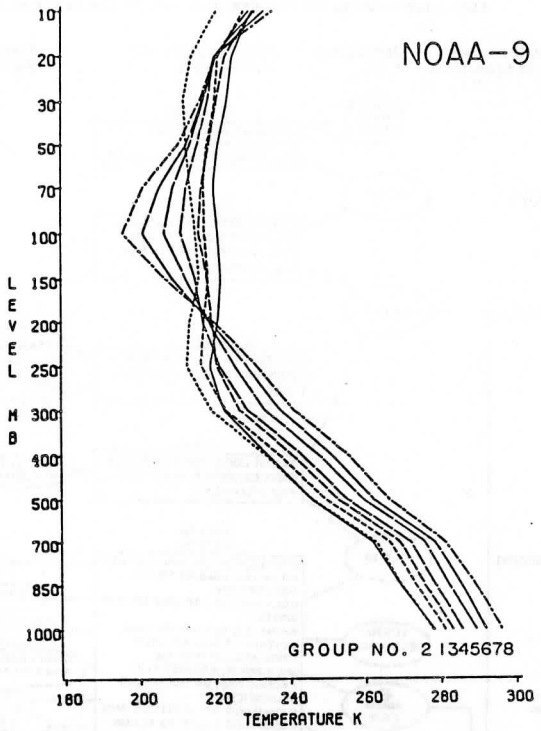

Figure 2(a): The mean temperature soundings of the eight operational retrieval groups determined by discriminant analysis in the Australian Region for NOAA-9.

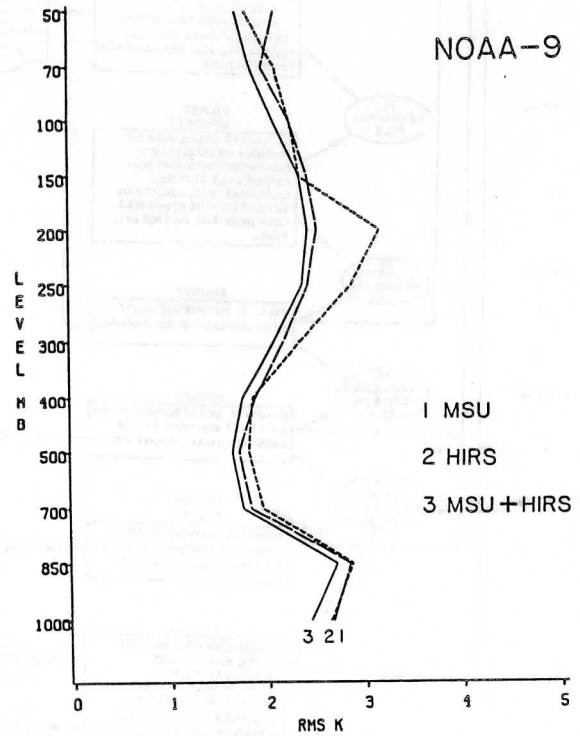

Figure 2(b): The RMS differences between TOVS temperature soundings and radiosonde data in the Australian region, for eight discriminant groups using MSU, HIRS and MSU plus HIRS data.

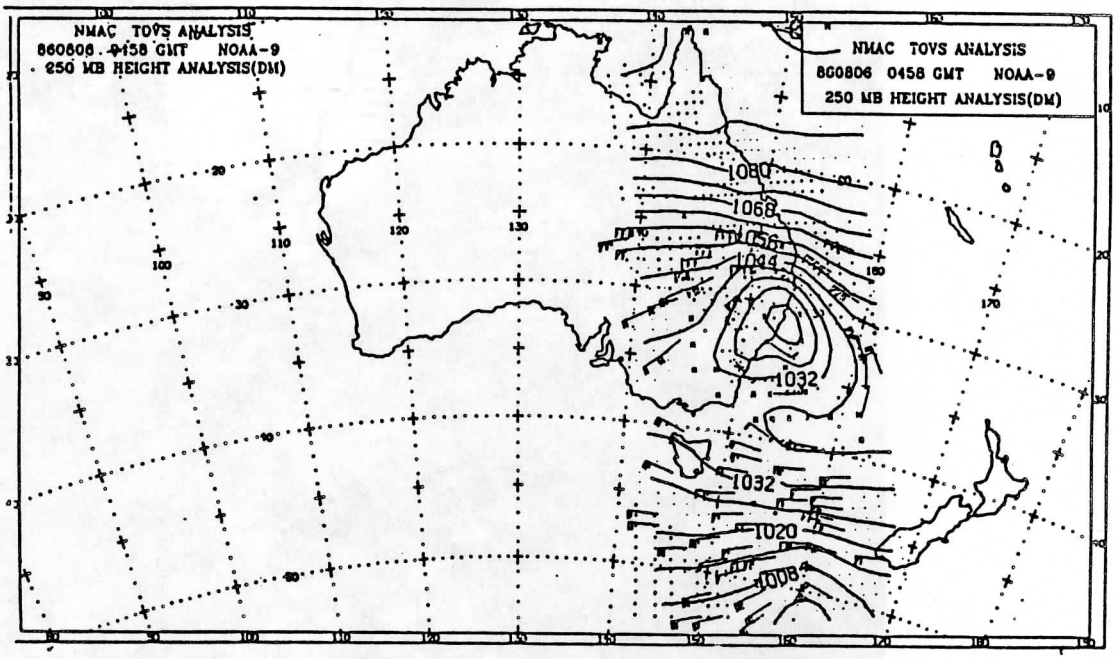

Figure 3(a). The operational TOVS 250 mb height analysis and geostrophic winds from NOAA-9 at 0458Z on 6 August 1986.

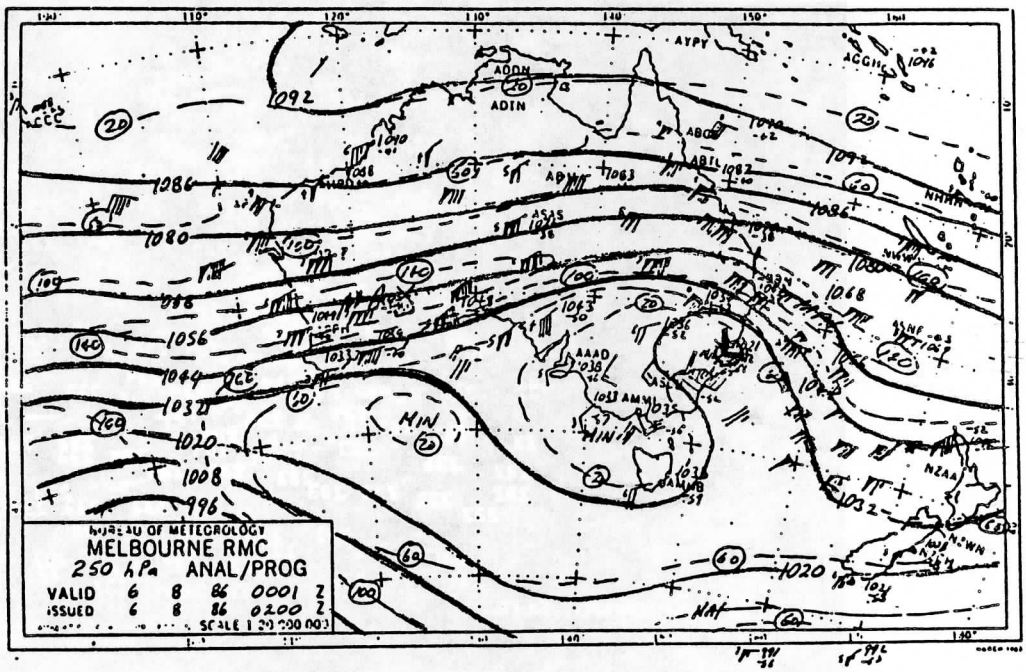

Figure 3(b). A manually analysed 250 mb height chart from NMC, produced from conventional data, aircraft observations, cloud drift winds and cloud imagery.

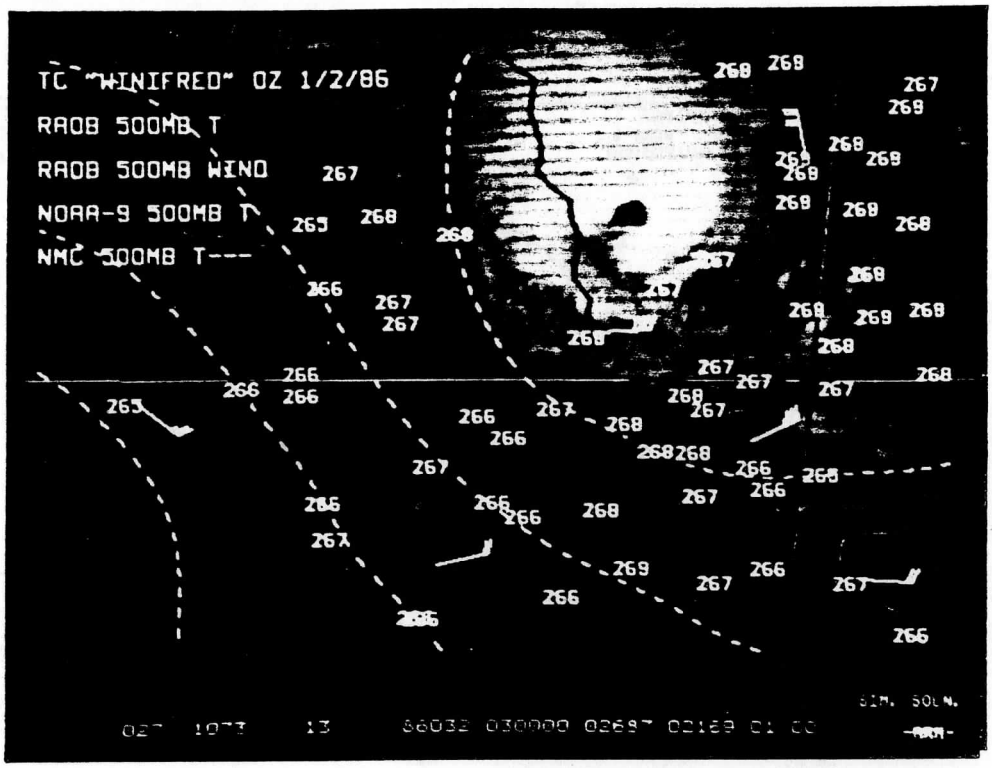

Figure 4: TOVS derived 500mb temperatures plotted over a GMS-3 IR image with the radiosondes and the NMC operational analysis shown.

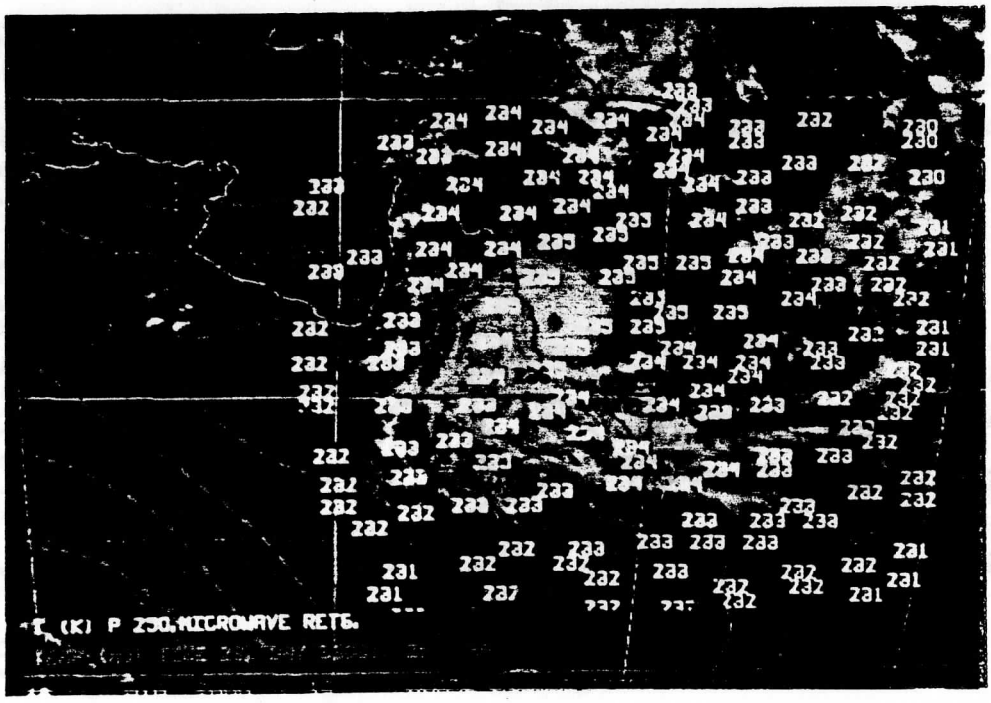

Figure 5: As above for 250 mb and with the TOVS temperatures based on microwave data.

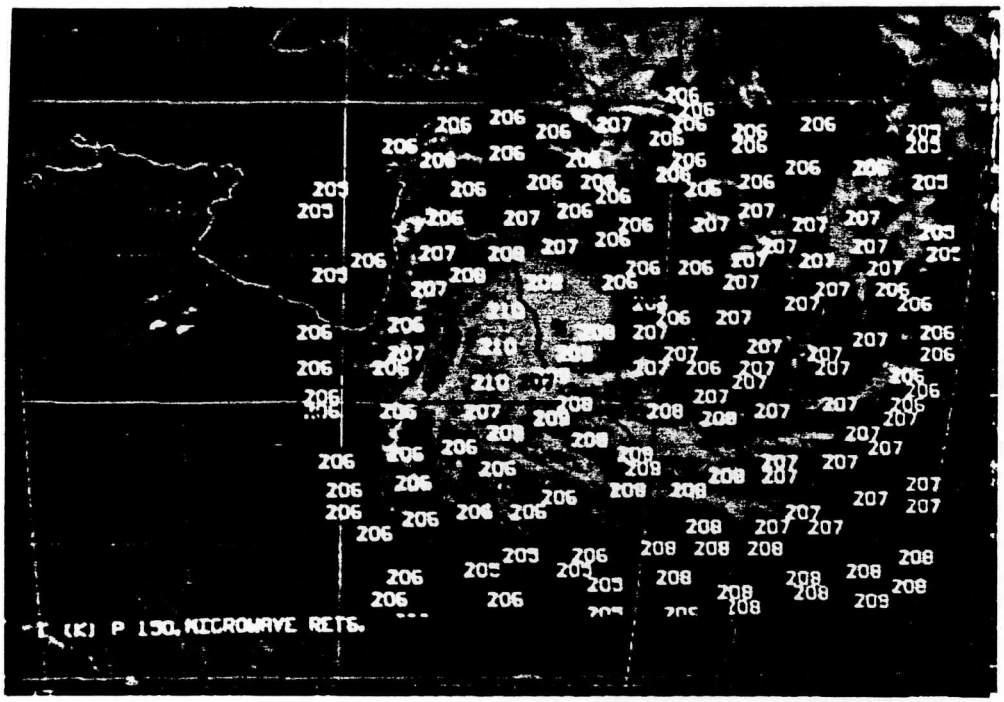

Figure 6: As above for 150 mb and with the TOVS temperatures based on microwave data.

SATELLITE SOUNDING ACTIVITIES AT THE WESTERN AUSTRALIAN INSTITUTE OF TECHNOLOGY

M. J. Lynch

School of Physics and Geosciences
Western Australian Institute of Technology
Bentley, Western Australia

1. INTRODUCTION

This presentation outlines the scope and progress achieved on a number of satellite sounding projects at the Western Australian Institute of Technology in Perth.

2. TROPICAL CYCLONE RESEARCH

The application of TOVS data to the study of tropical cyclones off the NW coast has been in progress for the last 3 years. The MSU channels are used to study the upper level warming. HIRS channels are employed to define the environment away from the cyclone. The AVHRR channels provide cloud top temperatures and identify regions of high sea surface temperature. The latter and the associated high moisture flux are important precursors for tropical cyclone intensification over the ocean.

This work which is conducted jointly with Dr. A. J. Prata of the CSIRO Division of Groundwater Research and is described in more detail in a companion paper in this volume.

The efforts contributed by Mr. R. Hille and Mr. L. van Burgel to this project are gratefully acknowledged.

3. VAX-BASED TOVS PROCESSING

The ITPP version III has been installed on VAX750. Apart from temperature and moisture profiling we have been providing data to permit the production of atmospheric refractive index fluctuations. These are employed in microwave ray tracing and in studying radar beam propagation.

Some of this work has been conducted over the Southern Ocean where in situ surface data are non-existent. It is important to reinforce the conclusions of Smith et al. (1985) that the physical retrieval scheme in ITPP-III will produce large RMS errors if surface data (in situ or first guess fields) are not employed. Errors of some 4°C at the surface may affect the temperature profile up to the 300mB region.

In Figure 1 we provide an example of a profile retrieved without surface data from NOAA-9 orbit 6331 over Garden Island (33°S, 115°.7E) near Perth, Western Australia on March 6, 1986. The retrieval (at

0720 GMT) is compared to a radiosonde released at Garden Island at 0650 GMT. Serious problems are evident in the retrieval.

The afternoon pass in a coastal environment in summertime-like conditions poses particular problems. For example, the land/sea mix, possible afternoon sea breeze (depth $\sim$ 500m), a temperature inversion above the sea breeze, possible superadiabatic lapse rates in the boundary layer over the land surface, and warm offshore flow of dry continental air overlaying the sea breeze cell, and finally convection and production of small cumulus cells in the coastal region.

The assistance of Mr. J. E. Davies in processing of TOVS data is greatly appreciated.

4. OCEAN CRUISE DATA

In March-April, 1985 an ocean cruise was undertaken from Perth to Broome to Indonesia and return.

Data recorded on this cruise included supporting sets of sea surface temperature (SST) measurements from a radiometer, bucket samples and a towed thermistor string. Additionally we have processed AVHRR data over the accessible cruise legs for SST's.

Ship meteorological data included air temperature, dew point temperature and surface winds. Radiosondes were releases from the ship and were selected to be as near as possible coincident with satellite overpass times.

Presently, we are using the AVHRR SST's as surface data input to the ITPP III to recover improved temperature profiles for comparison with sonde data.

An additional objective is verification of the performance of SST algorithms in the high water vapour regimes in the tropics.

This work is being undertaken jointly with Dr. J. Penrose, WAIT.

5. CLOUD TOP HEIGHTS

Mid-1986 we commenced a programme of cloud top height verification using the TOVS multispectral CO_2 technique and the WAIT Nd:YAG LIDAR.

The emphasis of this work is directed at thin cirrus in that these heights are frequently underestimated due to transmitted upwelling radiation indicating an apparently warmer cloud than its true temperature.

A LIDAR is able to detect cirrus cloud heights with an accuracy of order 7 meters. If the cirrus is thin, it is possible without difficulty to detect multiple layers.

This work is being undertaken jointly with Dr. S. Young, WAIT.

6. OZONE MEASUREMENTS

WAIT is one of the stations in the Global Aerosol Network established by the WMO. Dobson measurements taken at Perth are corrected for aerosol extinction as measured with the WAIT stratospheric LIDAR.

Using the ITPP III, we intend routinely producing regional ozone estimates from the 9.6 micron channel and calibrating these products against the corrected Dobson measurements taken at Perth.

Shortly, we plan to produce superior ozone measurements from the SBUV instrument on the NOAA platform.

Apart from studying ozone fluctuations on a synoptic scale, we have been studying ozone anomalies arising from tropospheric folding events associated with frontal systems. These events are identified from warming in the troposphere coupled with an anomalously high ozone burden brought down from the stratosphere.

The LIDAR aerosol measurements are undertaken as a joint project with Dr. S. Young, WAIT.

7. PC-BASED PROCESSING

WAIT and the CSIRO Division of Groundwater Research have initiated a joint programme in the development of PC-based processing of satellite data.

Activities embrace TOVS processing, application of MSU to tropical cyclones and AVHRR processing. Transmitting data to remote users is an additional target.

Products from the above work will be used in a training programme in satellite meteorology also being developed on PC systems.

8. THE WESTERN AUSTRALIAN SATELLITE TECHNOLOGY AND APPLICATIONS CONSORTIUM (WASTAC)

Since 1980, HRPT data has been received on the WAIT campus using a facility developed jointly by WAIT and CSIRO. This installation is to be upgraded in early 1987 by installation of new reception equipment.

The new facility is being purchased and managed by a Consortium comprising WAIT, CSIRO Division of Groundwater Research, the Bureau of Meteorology and the WA Department of Land Administration. Data from the facility will be put into a permanent archive along with HRPT data archived on the older-facility.

9. AN AUSTRALIAN GEOSTATIONARY MET. AND OCEAN INSTRUMENT

In 1985 Australia's first geostationary satellites went into orbit. These were essentially communication satellites. Consideration of new platform (AUSSAT-II) for the mid-1990's is in progress.

Present plans have considered both imaging and sounding capabilities. A 0.6 meter diameter mirror, 35 spectral channels with a 1-2 km footprint are being evaluated.

Products derivable from the instrument which have been suggested include:

- temperature and moisture soundings;
- cloud height/cloud drift winds;
- low level water vapour/water vapour drift winds;
- ozone;
- near surface temperature and moisture soundings from superwindow channels;
- vegetation/land applications;
- multichannel SST's;
- ocean colour;
- high resolution interferometric soundings.

Development is at an early stage and it might be that international collaboration will be desirable and necessary if such a project is to eventuate.

10. CONCLUSIONS AND ACKNOWLEDGEMENTS

A range of projects underway are at WAIT using TOVS data have been described. Some of these activities benefit from using other data sources including AVHRR, LIDAR, etc. Much of this work has progressed only through the excellent efforts of colleagues with whom I have collaborated.

Support for this research has come from a number of sources including WAIT, the Marine Sciences and Technologies Grants Scheme, the Defense Research Centre (South Australia) and the Bureau of Meteorology.

The HRPT data used has been recorded by the Satellite Technology Unit within the WAIT Satellite Technology and Remote Sensing Centre. The efforts of Dr. D. Myers, Head of the Satellite Technology Unit are appreciated.

11. REFERENCES

Smith, W. L. (1985): The Simultaneous Retrieval in the International TOVS Processing Package. Technical Proceedings of the Second International TOVS Study Conference, Igls, Australia (Feb 18-23, 1985). CIMSS Report, University of Wisconsin, Madison.

04/ITSC/03

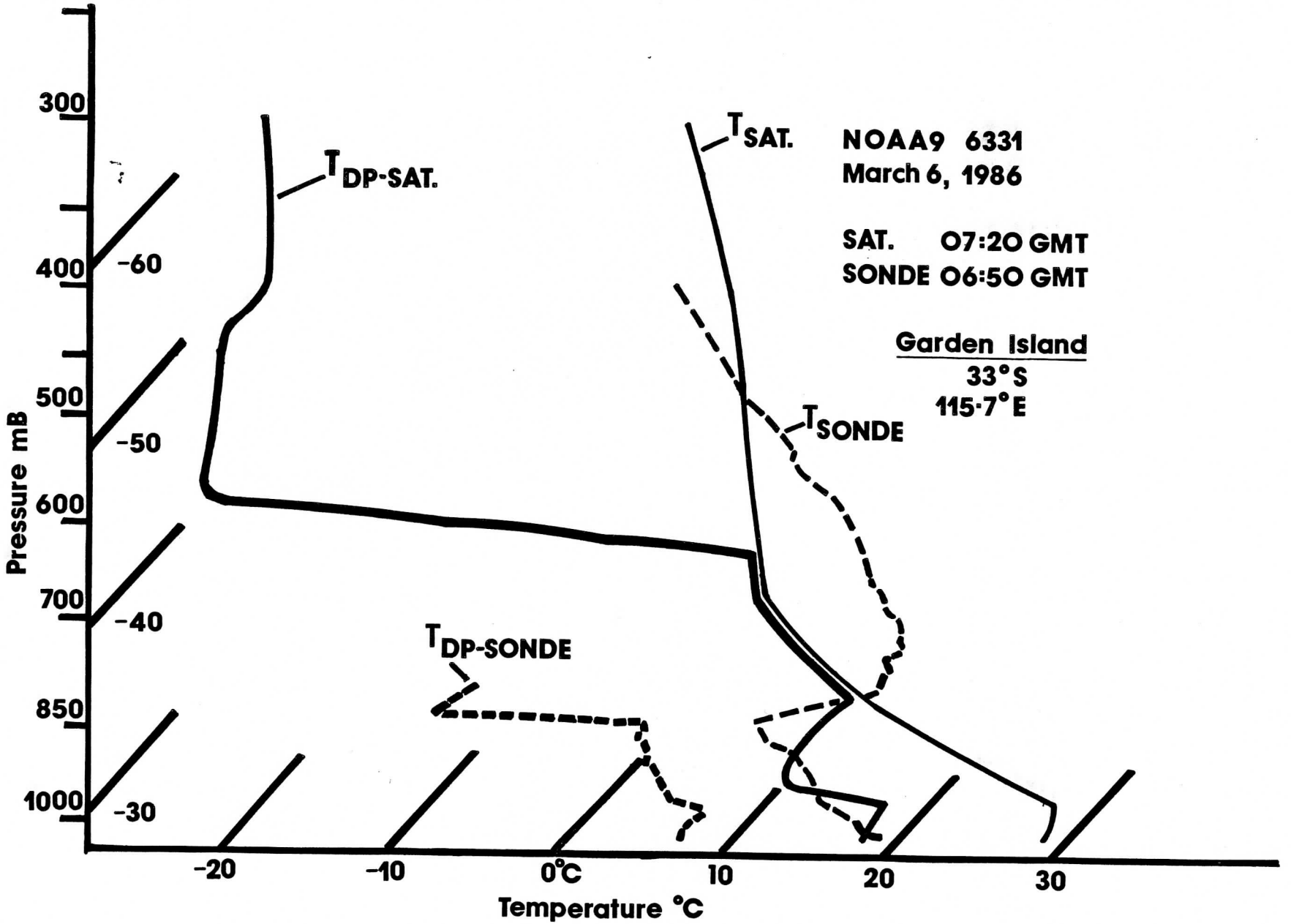

Figure 1. Satellite and radiosonde retrievals of temperature and dew point for a coastal environment in summer-like conditions. Problems with the retrieval are evident.

A PHYSICAL MODEL FOR RETRIEVING TOTAL OZONE FROM THE NOAA SATELLITE AND PRELIMINARY RESULTS OVER CHINA

Ma Xia-Lin and Zhang Feng-Ying
Satellite Meteorology Center
State Meteorological Administration
Beijing, People's Republic of China

ABSTRACT

A physical model is presented for calculating the total ozone amount from HIRS radiance measurements on the TIROS-N/NOAA satellites. The total ozone distribution charts are obtained according to this physical model calculation over China. Comparisons of analyses are presented for real time physical ozone retrievals versus analyses of conventional sounding total ozone data at Beijing and Kunming. These comparisons show that the total ozone amount can be retrieved with an accuracy of better than 3%. Also, this paper reveals that high (or low) values of total ozone usually correspond to the low (or high) 500 hpa heights.

1. INTRODUCTION

The physical retrieval TOVS export package has been implemented on the computer system at the Satellite Meteorology Center (SMC), PRC. A total ozone retrieval model developed by Smith, Woolf and Ma is a part of the software package. This paper introduces the total ozone retrieval technique and presents some preliminary results over China.

2. MATHEMATICS OF THE METHOD

Assuming a nonscattering atmosphere in local thermodynamic equilibrium, the radiative transfer equation can be expressed as

$$R(\nu, \Theta) = B(\nu, T_s)\,\tau(\nu, \Theta, P_s) - \int_o^{P_s} B(\nu, T)\frac{\partial \tau(\nu,\Theta,p)}{dp} \qquad (1)$$

where $R(\nu, \Theta)$ is the radiance at particular wavenumber ν for a zenith angle of observation Θ, $B(\nu, T)$ is the Planck function of temperature, and $\tau(\nu, \Theta, P)$ is the transmittance from the pressure level P to the top of the atmosphere along the observation angle Θ. The subscript s denotes surface values, either ground or cloud. Equation (1) is used to estimate the distribution of the total ozone in the atmosphere from HIRS radiance measurements in the 9.6μm spectral channel.

In equation (1), ozone concentration is related to the radiance $R(\nu, \Theta)$ through the transmittance $\tau(\nu, \Theta, P)$. Thus, the changes in the radiance measurements indirectly reflect the ozone concentration increase or decrease in the atmosphere. In order to calculate the total ozone, it is necessary to make a mathematical transformation to equation (1). Using a first order Taylor expansion of the Planck function in terms of temperature and integrating equation (1) by parts, it can be expressed as

$$T(\nu, \Theta) - T^n(\nu, \Theta) = \int_o^{P_s}[\tau(\nu,\Theta,P) - \tau^n(\nu,\Theta,P)]\,Q(\nu,\Theta,P)\,\frac{dp}{p} \qquad (2)$$

where $T_B(\nu,\Theta)$ is the measured brightness temperature, $T_B^n(\nu,\Theta)$ is the brightness temperature calculated for the n-th estimate of the ozone profile whose corresponding transmittance profile is $\tau^n(\nu,\Theta,p)$; and

$$Q(\nu,\Theta,p) = \left(\frac{\partial B(\nu,\Theta,T)/\partial T}{\partial B(\nu,\Theta,T_B)/\partial T}\right)\left(\frac{\partial T}{\partial \ln p}\right)$$

Using the mathematical derivation of Smith (1970, 1983) for water vapor retrieval the brightness temperature measured by HIRS in the 9.6μm ozone band can be related to the ozone concentration u(p) in the following manner:

$$T_B(\nu,\Theta) - T_B^n(\nu,\Theta) = \int_o^{P_s} \ln \frac{u(p)}{u^n(p)} \; W^n(\nu,\Theta,p) \; \frac{dp}{p} \,, \tag{3}$$

where

$$W^n(\nu,\Theta,p) = \left(\frac{\partial B(\nu,\Theta,T)/\partial T}{\partial B(\nu,\Theta,T_B)/\partial T}\right)\left(\frac{\partial T}{\partial \ln p}\right)\left(\frac{\partial \tau(\nu,\Theta,p)}{\partial \ln u^n(p)}\right) ,$$

and the superscript n denotes a n-th estimate. For every pressure level (0.1, 0.2, 0.5, 1.0, 1.5, 2., 3., 4., 5., 7., 10., 15., 20., 25., 30., 50., 60., 70., 85., 100., 115., 135., 150., 200., 250., 300., 350., 400., 430., 475., 500., 570., 620., 670., 700., 780., 850., 920., 950., and 1000. hpa) an estimate of the true ozone concentration profile is obtained using

$$u^{n+1}(pj) = u^n(p_j)\; r^n(\nu) \;, \quad j=1, 2, \ldots, 40.$$

Thus, according to equation (3), assuming that the true ozone profile is proportional to the n-th etimate by the scaler $r^n(\nu)$,

$$r^n(\nu) = \frac{u(p)}{u^n(p)} = \exp\left\{\frac{T_B(\nu) - T_B^n(\nu)}{\int_o^{P_s} W^n(\nu,p)\,\frac{dp}{p}}\right\} .$$

Equation (4) is iterated until $r^n(\nu) \doteq 1.0$, and thus $u(p) \doteq u^n(p)$. In other words, the iteration is terminated as soon as the difference between the measured ozone brightness temperature and that calculated is less than the measurement noise level (approximately 0.2°C). The total ozone amount is obtained by vertical integration of the mixing ratio profile.

3. DETERMINATION AND ADJUSTMENT OF THE FIRST GUESS OZONE PROFILE

In order to perform the iterations according to equation (4), the first guess ozone profile should be constructed at the beginning of iteration. The basic principle of constructing such a guess ozone profile is based upon the physical fact that the dynamic processes which cause warm and cold stratospheric air also cause maxima and minima of total ozone. The brightness temperature observed in the HIRS carbon dioxide

channels 1-4 reflect the thermal structure in this region. Therefore, there are excellent correlations between the ozone concentration and the brightness temperatures measured by HIRS channels 1-4. In test cases, we have found correlations to be .90 or higher. Using these regression equations, the first ozone guess profile can be obtained according to the measured brightness temperatures of HIRS channels 1-4. The regression coefficients are derived from a set of conventional ozone and temperature profiles (452 samples), and radiances synthesized from them, covering all seasons of the year over the Northern Hemisphere. Since the total ozone distribution changes rapidly with latitude across a transition zone around 30N (Prabhakara et al., 1973), two sets of regression coefficients are generated to separate mid-latitude structure from low-latitude structures. Furthermore, because ozone and temperature sounding data yield good statistics only up to 10 hpa (30 km), the ozone and temperature profiles are extrapolated using standard atmospheric lapse rates between 10 and 1.0 hpa (up to 50 km), since the contribution to the outgoing radiation by ozone above the ten hpa level is only a few percent of the total radiance measured. Above 50 km, the ozone contribution to the outgoing radiation is negligible.

When the regression equations are used to construct a first ozone guess profile, it is found that the profile shape and vertical position of the peak ozone mixing ratio corresponding to the ozone guess profile are crucial to obtaining a satisfactory retrieval, because only one ozone channel radiance in the 9.6μm band is available. During the procedure of iteration, the shape and the vertical position of the ozone peak cannot be changed. In other words, the true ozone profile is assumed to have the same shape and position as the first guess. If the position of the ozone peak mixing ratio is higher or lower than the true situation in the atmosphere, a large error will result in the total ozone calculation. Therefore, in order to make the guess profile sufficiently accurate in both shape and position of the ozone peak mixing ratio, it is necessary to make an adjustment to the vertical position of the first guess ozone peak mixing ratio. Specifically, the ozone mixing ratio profile is moved up or down δN levels according to the following equations:

$$\delta N = 0.5 + 1.4\ (T^{cal} - T^{obs}) \tag{5}$$

for low latitudes and

$$\delta N = -0.2 + 1.8\ (T^{cal} - T^{obs}) \tag{6}$$

for middle latitudes, where T^{cal} and T^{obs} are the brightness temperatures calculated from the ozone guess profile and observed in the ozone 9.6μm band, respectively. The coefficients of equations (5) and (6) are obtained by linear regeression between δN and $(T^{cal} - T^{obs})$ from an independent set of conventional sounding data (382 samples). The adjustment factor δN can be determined from equations (5) or (6). After the ozone guess profile is adjusted by δN levels, the accuracy of total ozone retrieval can be greatly improved.

4. RESULTS AND DISCUSSION

The total ozone calculation in our model is based upon the TOVS export software package which was developed by the Cooperative Institute for Meteorological Satellite Studies (CIMSS), Madison, Wisconsin (Smith et al., 1983). This software package yields temperature and water vapor profiles with a spatial resolution of 75 km from a statistical or physical iteration model. Using the methods introduced in sections 2 and 3, a first ozone guess profile can be determined. Furthermore, the HIRS 9.6μm ozone band transmittance, corresponding to the guess profile, is estimated in the manner described by Ma et al. (1984). Finally, the measured ozone radiance is used in the iterative equation (4) to achieve a final estimate of the total ozone amount with a spatial resolution of 75 km.

At the Beijing Meteorological Satellite Ground Station, TIROS-N/NOAA satellite measurements can be received and processed. Figures 1-4 show the retrieved total ozone amount which is obtained from our physical model using HIRS measurements. The curves in the figures represent the isolines of retrieved ozone amount (Dobson units, where 1000 Dobson = 1 cm STP/km). In order to assess the accuracy of HIRS total ozone measurements, it is necessary to compare calculated total ozone amount with matched (both time and location) conventional total ozone measurements.

Our physical model was tested against TOMS (Total Ozone Mapping Spectrophotometer) data and the comparison results were satisfactory (Ma et al., 1984). In China, there are only two conventional ozone observation stations. One is in Beijing, the other in Kunming. Table 1 presents the comparison of physical retrievals from HIRS observations with conventional total ozone measurements.

The retrieved total amount from our physical model has an absolute mean error of less than 3%. Figures 1-4 also show the distributions of total ozone measurements. From these figures, the ozone amount decreases towards the equator and changes rapidly with time. Figure 5 shows the 500 hpa height at 00:00 GMT on February 25, 1984. Comparisons of Figure 2 with Figure 5 indicate that the ridge (trough) region at 500 hpa corresponds to low (high) values region of total ozone amount and high (low) center coincides with minimum (maximum) region of total ozone amount. This coincides with the study performed by Reiter (1982). As for interaction between the total ozone distribution and some weather phenomena, it remains for future research to explore this relationship.

5. SUMMARY

In summary, a physical model for calculating total ozone from HIRS radiances has been presented. Using this model, the total ozone distribution with a resolution of 75 km can be obtained over China. Comparisons of retrieved results with conventional sounding ozone data indicate that absolute mean errors are less than 3%. In addition, a correlation between the minimum (maximum) region of total ozone amount and high (low) center at 500 hpa height has been presented.

REFERENCES

Ma, X.-L., W. L. Smith and H. M. Woolf, 1984: Total ozone from NOAA satellites--a physical model for obtaining measurements with high spatial resolution. J. Clim. Appl. Meteor., 23, 1309-1314.

Prabhakara, C., E. B. Rodgers and V. V. Salomonson, 1973: Remote sensing of the global distribution of total ozone and the infrared upper tropospheric circulation from Nimbus IRIS experiments. Pure Appl. Geophys., 106-108, 1226-1237.

Reiter, E. R., and D.-Y. Gao, 1982: Heating of the Tibet plateau and movements of the South Asian high during spring. Mon. Wea. Rev., 110, 1694-1711.

Smith, W. L., 1970: Interactive solution of the radiative transfer equation for temperature and absorbing as profiles of an atmosphere. Appl. Opt., 9, 1993-1999.

Smith, W. L., 1983: The retrieval of atmospheric profiles from VAS geostationary radiance observations. J. Atmos. Sci., 40, 2025-2035.

Smith, W. L., H. M. Woolf, C. M. Hayden, A. J. Schreiner and J. M. LeMarshall, 1983: The physical retrieval TOVS export package. Technical Proceedings of the First International TOVS Study Conference, Igls, Austria.

Table 1. Total ozone accuracy comparison

location	time	total ozone amounts (Units: Dobson)	
		satellite meas.	conventional meas.
Beijing	Feb. 13, 1984	404	406
	Feb. 15, 1984	375	379
Kunming	Feb. 18, 1984	278	262
	Feb. 19, 1984	268	260

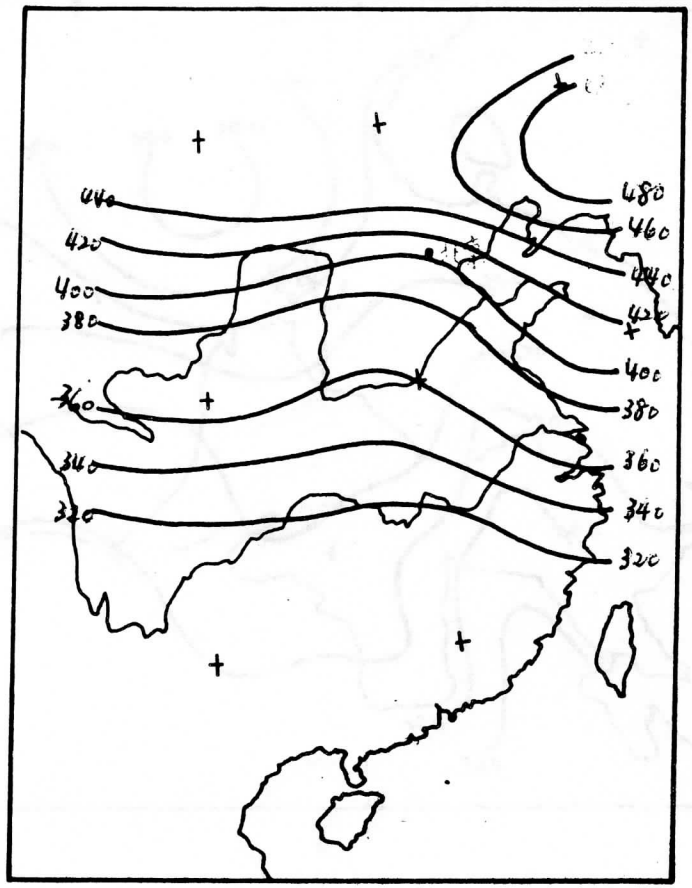

Fig. 1: Distribution of total ozone amount for 20:23 GMT February 13, 1984.

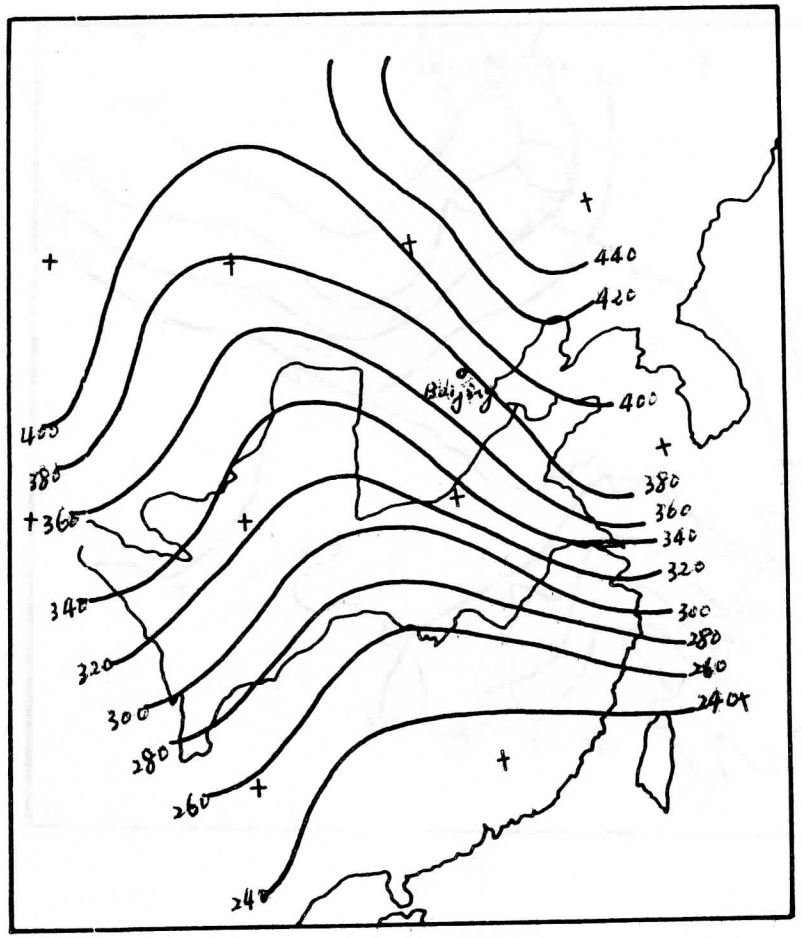

Fig. 2: As in Fig. 1, but for 7:32 GMT February 15, 1984.

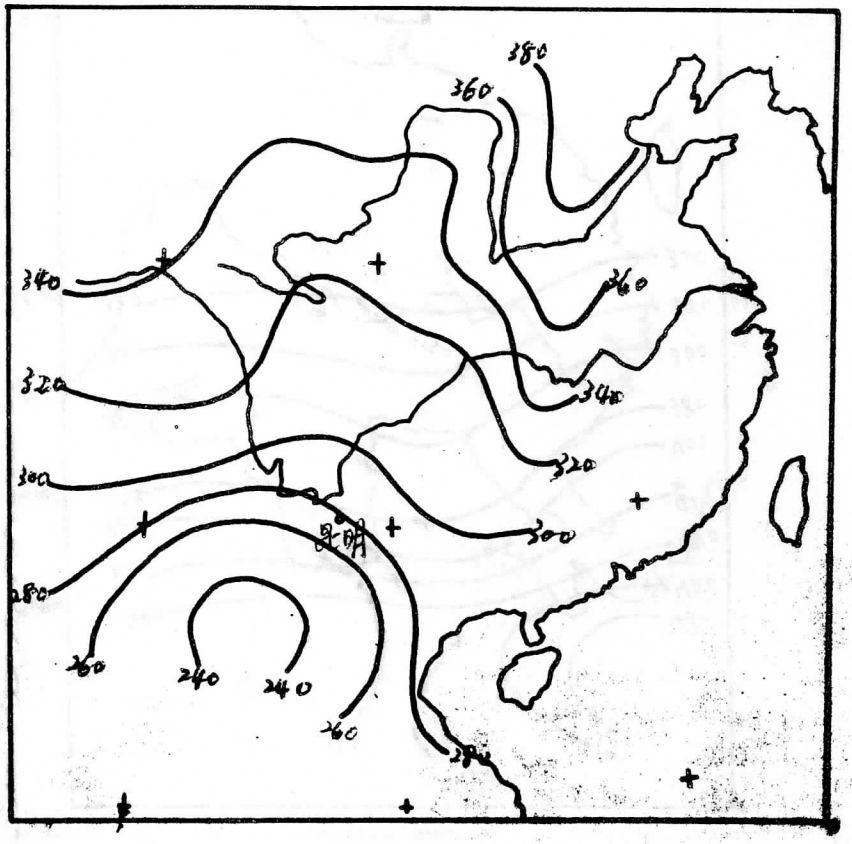

Fig. 3: As in Fig. 1, but for 20:59 GMT February 18, 1984.

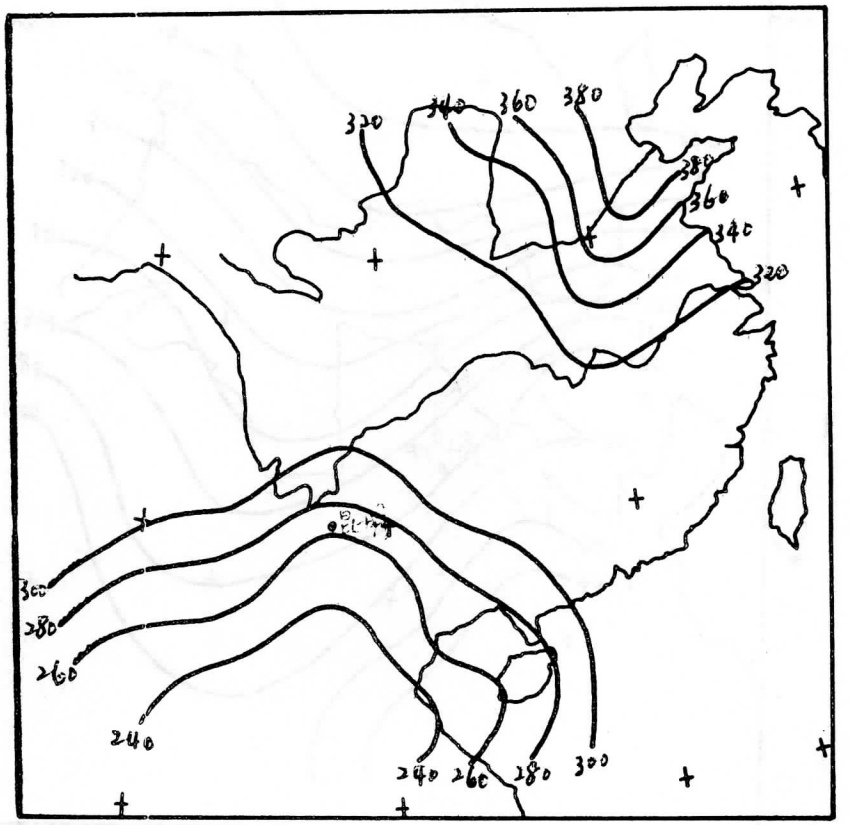

Fig. 4: As in Fig. 1, but for 20:46 GMT February 19, 1984.

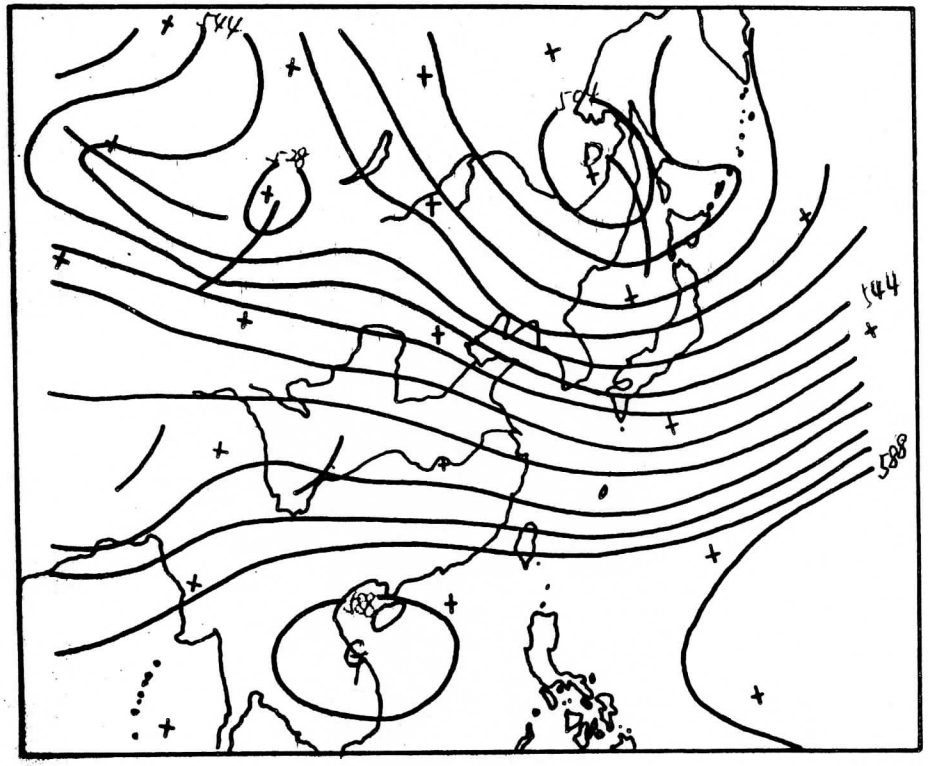

Fig. 5: 500 hpa height for 0:00 GMT February 15, 1984.

Some Modifications to the NESDIS Operational Clear Column Radiance Procedure

Larry M. McMillin

National Oceanic and Atmospheric Administration
National Environmental Satellite, Data, and Information Service
Washington, D.C. 20233

Andrew Nappi

SASC Technologies
4400 Forbes Boulevard
Lanham, Maryland 20706

1. INTRODUCTION AND REVIEW

It is difficult to know what to report on at this conference because there are so many interesting new results. For example, the classification approach is making substantial improvements in accuracy over the current operational procedure (see McMillin, 1985a), and a method of using satellite measurements to obtain biases between radiosonde types shows excellent agreement with conventional comparisons as well as providing some revealing facts about radiosondes (see McMillin, 1985b). While these results are being reported in other forums, there have been incremental changes in the operational clear radiance procedure which are not being reported elsewhere. In addition, the cloud clearing approach used by the National Environmental Data and Information Service (NESDIS) is unique in its emphasis on deleting multiple level clouds. Because of this uniqueness, a discussion of the approach is appropriate for this forum.

The present operational cloud clearing approach used by NESDIS evolved from ideas presented by W. L. Smith in several papers in the late 60's and early 70's (Smith 1967, Smith 1968, and Fritz et al. 1970). In 1967, Smith introduced the concept of N^*, defined as

$$N^* = \frac{I(\nu,1) - I(\nu,c)}{I(\nu,2) - I(\nu,c)} \qquad (1)$$

where $I(\nu,c)$ is the clear radiance at wavenumber ν, $I(\nu,1)$ was defined as the average of all the radiances in the total area of observation and $I(\nu,2)$ was defined as the average of all radiances less than the total average. In 1968, Smith modified the definitions of $I(\nu,1)$ and $I(\nu,2)$ to be two adjacent measurements within the total area. The change in definitions was made because the first definition required all spots within the area to have the same cloud height, an unlikely event for most situations. In (Fritz et al. 1970), Smith discussed the idea of using wavelength differences to

obtain a solution when no single channel could be regarded as clear.

An essential element of the solution is an assumption that N^* is a constant that is independent of channel. Unfortunately, this has been frequently justified by assuming that emissivity is independent of wavelength and, as a result of this justification, it has often been assumed (incorrectly) that the method will not work if emissivity is wavelength dependent. While this assumption was not bad for some early instruments which had all the sounding channels in a single band, it is questionable for instrument systems such as the Tiros Operational Vertical Sounder (TOVS) which have channels at very different wavelengths. Fortunately, the clear column radiance procedure does not depend on this assumption because the assumption that cloud emissivities are equal for the two observations, rather than as a function of wavelength, leads to the same result. To see the alternative, note that $I(\underline{\nu},1)$ can be defined as

$$I(\nu,1) = (1-n(1)*\epsilon(\nu,1))*I(\nu,c) + n(1)*\epsilon(\nu,1)*I(\nu,o) \qquad (2)$$

where $n(1)$ is the fraction of spot 1 covered by cloud, $\epsilon(\nu,1)$ is the cloud emissivity for spot 1, and $I(\nu,o)$ is the radiance from the overcast regions in spot 1. A similar equation can be written for spot 2 to yield

$$I(\nu,2) = (1-n(2)*\epsilon(\nu,2))*I(\nu,c) + n(2)*\epsilon(\nu,2)*I(\nu,o). \qquad (3)$$

To obtain a solution with either assumption, it is necessary to require that $I(\nu,c)$ is the same for both spots. Effectively, this means that the cloud tops in both spots are equal. Given that the cloud heights are equal, if the cloud bases and densities are also equal then the cloud emissivities are also equal and $\epsilon(\nu,1)$ is equal to $\epsilon(\nu,2)$. Since cloud tops are more likely to vary than cloud bases, and because clouds with the same bases and tops in the same area are very likely to have the same densities, the assumption that cloud emissivities are equal is only slightly more restrictive than the assumption that the cloud tops are equal. Eq. (2) can be written as

$$I(\nu,1)-I(\nu,c) = n(1)*\epsilon(\nu,1)*[I(\nu,o)-I(\nu,c)]. \qquad (4)$$

Writing a similar equation for eq. (3) and dividing into Eq. (4) gives

$$\frac{I(\nu,1)-I(\nu,c)}{I(\nu,2)-I(\nu,c)} = \frac{n(1)}{n(2)} = N^* \qquad (5)$$

since the emissivities are equal and the other terms cancel. As Smith showed, once N^* is determined for one channel, it can be used to solve eq. (5) for $I(\nu,c)$, giving values of $I(\nu,c)$ for the other channels from the relationship

$$I(\nu,c) = [N^*I(\nu,2) - I(\nu,1)]/(N^*-1). \qquad (6)$$

Although the N* approach provides clear radiances for all channels once a value is determined for any single one, it is necessary to obtain a value for at least one channel by some other method. One way is to use Eq. (5) with both clear and partly cloudy radiances for at least one channel. Appropriate values have been determined in several ways. Vertical Temperature Profile Radiometer (VTPR) data (see McMillin et al. 1973) were processed over oceans using the ocean surface temperature and a forecast to calculate a radiance for the window channel, since the atmospheric absorption for the window channel is minimal. If the forecast is in error, the solution can be iterated. McMillin (1971) suggested using a "split window" to remove the atmospheric effect and thus eliminate the dependence on an atmospheric forecast. Susskind et al. (1984) couple the cloud clearing process and the retrieval step. Approaches that depend on forecasts are followed by other countries, most notably Britain (Eyre et al. 1985), and to some extent, France (Chedin et al. 1985). Japan and New Zealand (Aoki et al. 1985 ,Taylor et al. 1985, and Hayden et al. 1985) have done work involving the use of higher resolution Advanced High Resolution Radiometer (AVHRR) to determine a clear value for the window channel which provides a clear estimate for the window channel on the TIROS Operational Vertical Sounder (TOVS).

There is an appeal to using a method that does not depend on a forecast. The AVHRR approach has this appeal, but presently AVHRR data are not available at NESDIS for real time processing. Iterative methods produce a retrieval for physical parameters and then calculate a radiance from the physical parameters. This is the actual method used by Susskind et al. (1984). However, an equivalent alternative is to use some channels to retrieve directly for another, thus bypassing the physical parameter retrieval and radiance calculation steps for the purpose of cloud clearing. This separates the cloud clearing and retrieval steps and greatly simplifies the maintenance of an operational system which must be periodically improved while minimizing the occurrence of catastrophic errors in the retrieval system. There are also potential advantages from an accuracy standpoint, since the retrieval for another channel radiance from channels with very similar weighting functions is inherently more accurate than a retrieval for a parameter with a very different weighting function such as temperature. In addition, errors caused by differences between calculated and observed quantities are avoided.

To be fair, these potential advantages are balanced, at least in the minds of people who prefer physical retrievals over regression methods, by the fact that a retrieval for another channel can only be done by regression. However, a correction for many regression errors can be made when a first guess is available by simulating radiances for both wavelength regions and applying the regression coefficients to the calculated values as well as the measured ones. For the calculated radiances, the simulated clear as well as the simulated cloudy radiances are known, so the error in the cloud clearing method for the local condition in question can be immediately determined. If the first guess is reasonable, then errors in the regression error due to errors in the first guess become second order errors in the final radiances. Application of this correction would allow

separation of the cloud clearing and retrieval steps while providing results equivalent to those provided by the full iteration process since there is no doubt that radiance calculation errors far exceed the second order errors that would result from this approach. However, the results of this correction, as well as of the full iteration, are dependent on the accuracy of the radiance calculations. Any systematic difference in radiance calculation errors between channels could easily negate any potential advantage that this step could provide. Because of doubts that radiance calculations have reached the accuracy level required for this step to prove to be beneficial, this potential correction is not employed by NESDIS.

The approach used at NESDIS is based on regression relationships between channels which are described in detail in McMillin and Dean (1982). One relationship can be thought of as using microwave brightness temperatures to predict a clear brightness temperature for a 15 μm. channel to be converted to a clear radiance, which is then combined with the observed cloudy radiances for the same channel to calculate N^*. This is the way the solution would be done on an Advanced Microwave Sounding Unit (AMSU) with numerous microwave channels. However, TOVS has only three microwave channels and it is more accurate, but less straightforward, to calculate a cloudy microwave pseudo radiance, I(6,22), for channel 22, (MSU channel 2), scaled to a typical radiance in the 15 μm. region (channel 6) from the relationship

$$I(6,22)=C(0) + \sum_{c=5}^{8} C(c)*I(c) \qquad (7)$$

where C(c) are the regression coefficients for channel c and I(c) are the observed cloud contaminated radiances for channel c. Values of C(c) are obtained from a sample that has been screened to contain only clear cases. The scaling to the channel 6 wavelength is similar to converting radiances to brightness temperatures when retrieving temperatures, and is done for the same reason, to minimize the nonlinear effects introduced by the Planck relationship. It differs from the brightness temperature approach in that instead of stopping with the brightness temperature, the brightness temperatures are used to calculate radiances at the desired wavelength which differs from the one at which the original measurement was obtained. At the same time, the scaling in eq.7 is done in a way that preserves the linear relationship between cloud amount and radiance that is present in the observed values, I(c), and creates the same relationship in the predicted value, I(6,22). Although the values of C(c) in eq.(7) are derived from clear values, when the values of I(c) are cloudy, eq.(7) provides the cloudy values required for the N* determination. Clear values are obtained by converting measured radiances observed the frequency of channel 22 in the microwave region to equivalent radiances at the wavelength of channel 6 in the infrared region. When these steps are completed, both clear and partly cloudy radiances for the pseudo channel I(6,22) are available and can be used to calculate a value of N^*. Of course the method is dependent

on the assumption that the microwave measurements are not attenuated by clouds.

A second solution can be obtained from a regression relating radiances at 15 μm. to a channel in the 4.3 μm. region. This solution is an evolution of an idea presented by Smith in Fritz et al. (1972). Again, the regression coefficients are obtained from clear data. In this approach, neither observation is independent of clouds, but due to the highly nonlinear nature of the Planck function, they respond differently to clouds that differ in temperature from the surface. Because the method is dependent on sufficient contrast between the clouds and the surface, it works much better for high clouds in the tropics than for low clouds or clouds in polar atmospheres. The solution is both lengthy and iterative, and is given in the appendix of McMillin and Dean (1982). As explained by McMillin and Dean (1982), both methods are used in the operational processing and a consistency check is preformed when both results are available.

2. MULTIPLE LEVEL CLOUD PROBLEMS AND SOME SOLUTIONS

The entire cloud clearing approach is dependent on the assumption that the clear and overcast radiances are uniform over the area covered by the spots used to obtain a solution. If the spots are close to each other and small, the assumption that the clear radiances are uniform is usually valid. However, cloud top heights vary rapidly over small areas and the overcast radiance is strongly related to the cloud top height. In addition, errors in cloud-cleared radiances due to mixed cloud heights are biased rather than random, an effect that is expected when cloud amount and cloud height are correlated rather than random. McMillin and Dean (1982) demonstrated that for a typical cloud shape, there is a significant correlation between cloud amount and cloud height. This correlation between height and amount in a field of view makes it even more difficult to find spots with different cloud amounts while still having similar cloud top heights. To avoid errors, some screening method is essential and much of NESDIS's effort has been devoted to assuring similar cloud heights in the measurements actually used in the cloud clearing process.

McMillin (1978) describes the major approach that has been used at NESDIS for screening observations for cloud heights. This approach has been supplemented by an additional test. When measurements for a partly cloudy area are plotted on a figure with radiances for one channel as one axis and radiances for a second channel as the other axis, the points fall into a roughly triangular area with one side determined by the points for the highest cloud in the area, another side determined by the points for the lowest cloud in the area, and a third side formed by a curve defined by the points completely overcast clouds at all heights. A typical case is shown in fig.1.

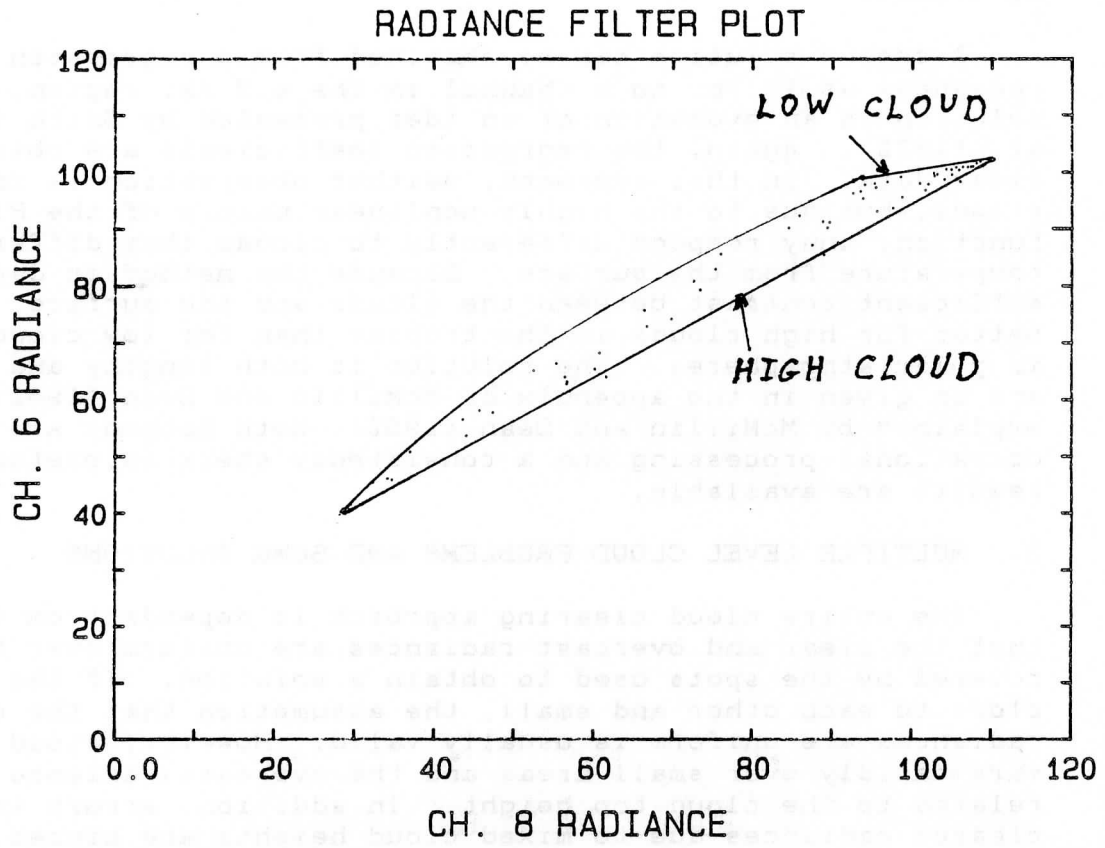

Fig. 1 Measured radiances for mixed clouds. Lines representing the high and low clouds are shown. Individual measurements are shown by points. Points between the lines are from mixed clouds.

Although the angle between the second and third sides is often small making the separation of the sides difficult to observe, the first side is usually clearly defined. An approximation to the first side can be obtained from a collection of observations by selecting only those points along the lower edge that form a monotonic progression from coldest to warmest. This is accomplished by ordering the observations according to the radiance values for one channel from lowest (coldest) to highest (warmest). Radiances for the second channel are then examined. If a given point is not ordered in the second channel, then one or more of the previous points is from a lower cloud and the previous point is discarded. The last point and the new previous point are then examined to see if they are monotonic. If they are not, the new previous point is discarded and the process is repeated until all the multiple cloud points have been eliminated. Figs. 2 and 3 illustrate the approach for a typical example. Fig. 2 contains all the points for a typical case and Fig. 3 shows the points that remain after screening. This procedure has demonstrated a capability to detect some cases of multiple level

clouds that were escaping detection by the tests described by McMillin and Dean (1982), and has been added to the string of tests.

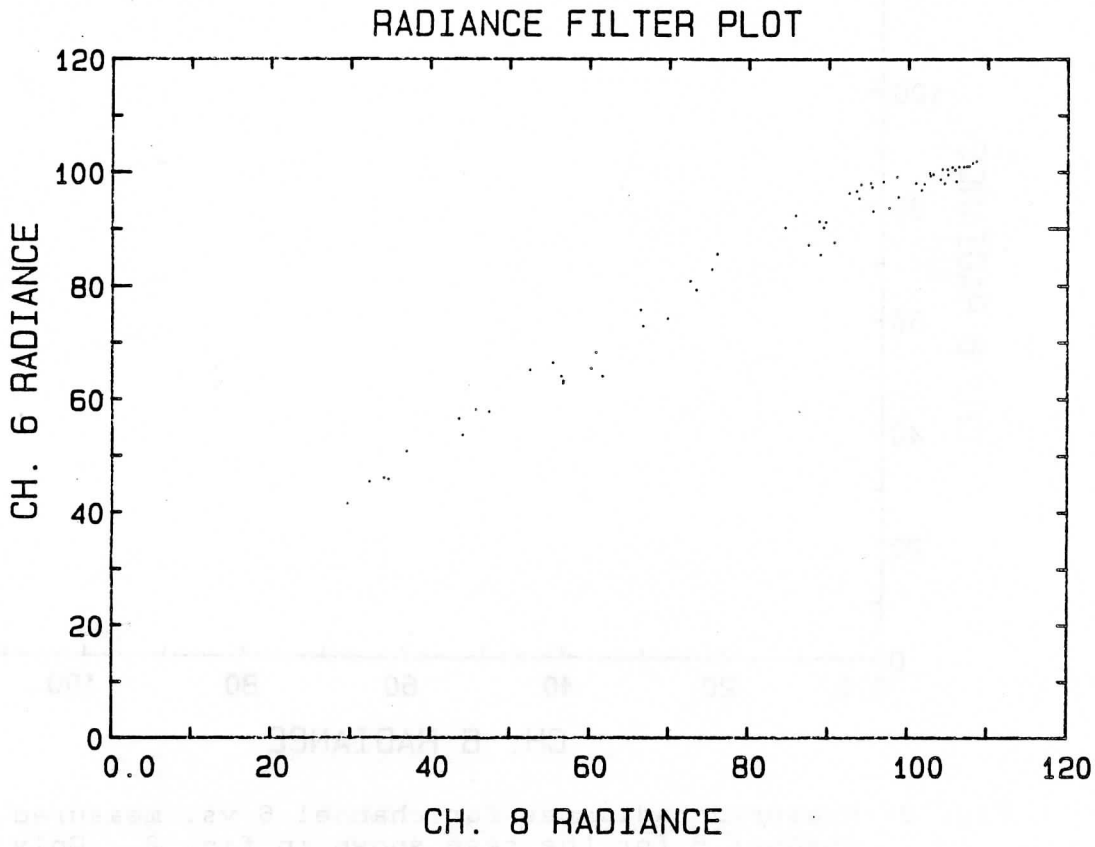

Fig. 2 Measured radiances for channel 6 vs. measured radiances for channel 8 for a case of mixed cloud heights. All points are shown.

Recent evaluations have shown that the best cloud clearing algorithm is level dependent in that more averaging is better at higher levels where multiple level cloud effects are minimal, while more screening is better at lower levels where multiple level could effects are present. The reason for this can be seen from eq. 6. When it is written as

$$I(\nu,c) = I(\nu,2) + [I(\nu,2)-I(\nu,1)]/(N^*-1), \qquad (8)$$

it becomes obvious that any noise in the quantity $[I(\nu,2)-I(\nu,1)]$ is multiplied by the ratio $N^*/(N^*-1)$. Since N^* is usually close to 1.0, any noise is amplified. Near the ground, radiances are affected by both high and low level clouds, and cloud effects are larger than any noise. However, at higher levels, radiances are affected only by the highest clouds and effectively only one cloud level is present, and at still higher levels, cloud effects go to zero and noise

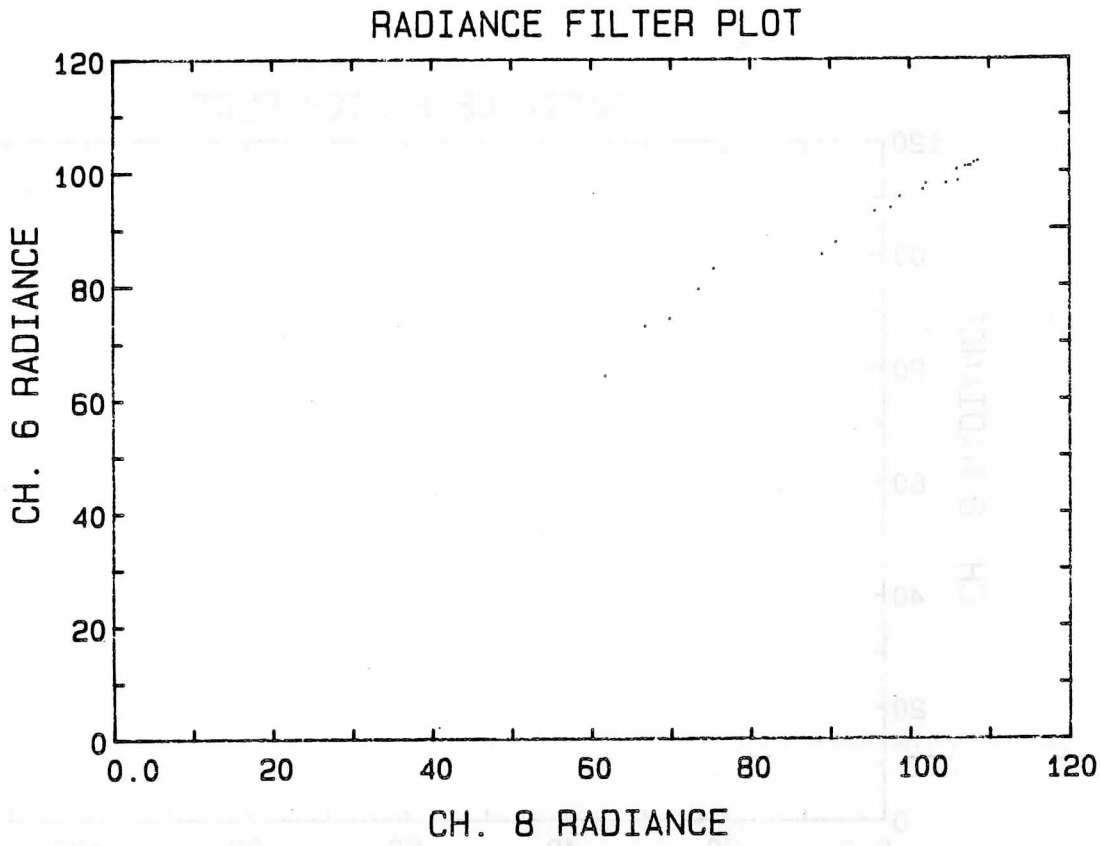

Fig. 3 Measured radiances for channel 6 vs. measured radiances for channel 8 for the case shown in fig. 2. Only measurements passing the monotonic filter for a single cloud level are shown.

amplification becomes the dominant error source. At these levels, it would be better to follow the original approach (Smith 1967) of using differences of averages rather than the later approach (Smith 1968) of averages of differences of adjacent pairs because the method based on averages is correct for single level clouds, and produces errors where multiple cloud levels are present, while the method based on adjacent pairs minimizes errors at these levels. These effects are clearly evident in the results of the Second International TOVS Study Conference (ITSC-II) where the comparisons presented by LeMarshall (1985) show that model using the averaging approach (Susskind et al. 1984) produced some of the most accurate results of all the methods in the upper troposphere while an approach based on the adjacent pair approach (McMillin 1982) produced some of the most accurate results of all the methods in the lower troposphere.

It is desirable to devise a method that has both advantages. In an attempt to do so, all the spots which are monotonic are used to produce a least squares line for two channels. The differences between the points and the line are screened for outliers which are

rejected. Points that remain are used to derive least squares lines for all channels relative to the channel for which a clear radiance is known. This slope is used for all spots within the area from which the sample was collected. Typically, the area required to produce a sample large enough for the slope procedure to work is larger than is desirable for a single sounding. If the intercept were also fixed, all the soundings in the larger area would be identical. To avoid this, a separate intercept is derived for each sounding based on the subset of screened points that lie within that particular sounding area. In this new approach, it is anticipated that the least squares procedure will provide some of the noise reduction of the averaging at high levels while allowing for the screening of multiple level clouds to minimize cloud clearing errors at lower levels.

3. CLOUD RETRIEVALS

On July,2 1984 the TOVS adopted a new method for retrieving cloud parameters. It is based on the radiance slope method described by McCleese and Wilson (1976) and evaluated by Wielicki and Coakley (1981). That approach is based on the relationship between the slope of a line connecting two or more spots with different cloud amounts on a plot with radiances for two channels as the axis. However our new approach has a significant difference in the way the overcast radiance is obtained. In the old version, cloudy radiances were obtained by calculating radiances from the retrieved profile. In the new version, it is noted that a curve exists on a plot of radiance of one channel versus radiance for a second channel that is the locus of all the points for which both radiances have the same brightness temperature. The intersection of a line connecting radiances for two spots with this curve is taken as the first estimate of the cloudy radiance. Because the atmosphere above the clouds has some attenuation, the curve defined by the locus of points is shifted to account for the attenuation at the point of intersection and the new point of intersection is found. For programming ease, use is made of the fact that a shift of the line formed by the two measurements is equivalent to a shift of the curve formed by the locus of points since the point of intersection is determined by the relative positions of the two curves. After an evaluation of possible corrections for the attenuation, a correction of the form

$$Tbn(i) = Tbm(i)+C(i,0,k)+\Sigma[C(j,k,i)*Tbo(j) + C(j,k,i)*Tbc(j)] \quad (9)$$

was applied to the two channels forming the straight line, where Tbn(i) is the corrected (new) radiance for channel i, Tbm(i) is the measured radiance, C(j,k,i) are the regression coefficients to predict the correction for channel i from measurements from channel j for overcast condition k (clear or overcast), Tbo(j) are the overcast estimates of brightness temperature for channel j from the first iteration, and Tbc(j) are the clear radiances for channel j. In practice, it was found that the correction could be produced from a single channel, (channel 8) and that addition of other channels increases the size of the regression coefficients while producing a minimal improvement in accuracy. This approach has the advantage of

making the retrieval for cloud amount and cloud top temperature a single step that can be incorporated as part of the cloud clearing process, separate from the retrieval step. Cloud top height can be obtained at a later step by finding the level in the profile with th same temperature as the cloud top temperature.

As usual, the implementation of the cloud retrieval is more complex than indicated by the description in the previous paragraph. Cloud retrievals are processed by one of four selections of channels given here in order of decreasing accuracy, depending on the situation. The most accurate results are obtained by using HIRS channels 8 and 18. However, channel 18 is subject to contamination by solar radiation and can be used only at night. In daylight, channel 18 is replaced by channel 6. Another problem occurs in completely overcast areas where the required estimate of the clear column radiance is not available. In these areas, the solution must be obtained from microwave channels. Over oceans, an estimate of th surface skin temperature is available for channel 8 and can be used with eq. 7 and measurements of MSU 2 and HIRS channel 8. Estimates for cloudy cases over land are derived by using MSU channels 2,3, an 4 to predict HIRS channels 6 and 7 using normal regression procedures. Ofcourse the last method can be applied everywhere that microwave measurements are available, but is the least accurate.

For a single point, an initial estimate of the cloud top radianc is obtained by solving for the intersection of the straight line and the line defined by the locus of all points with the same brightness temperature. Figure 4 illustrates the method. It shows the locus o points of equal temperature as a curve, and several pairs of clear and observed points as straight lines connecting the two points. These lines can be extended to find the intersection with the curve. Since the line defining the locus of points with the same brightness temperature is a curve, in practice, the Newton-Rapsilon method is used to find the intersection.

4. SUMMARY

Several incremental improvements to the cloud clearing algorithm have been presented, as well a modified method to obtain cloud amounts and heights. The improvements stem from the recognition that many cloud fields consist of clouds for which cloud amount and cloud height are correlated. This lack of independence causes a bias rather than a random error in derived clear column radiances, and methods that rely only on statistical approaches such as averaging to remove the errors will be affected by the bias. To remove the bias, some means of filtering is needed, and the NESDIS procedure is designed to filter out cases of mixed cloud heights. After filtering, many of the statistical procedures are useful as additional steps.

The new cloud algorithm has been implemented into the operation. In doing so, the definition of the TOVS cloud height and amounts have been changed. When the present processing system was designed, there was interest in a dynamic indicator of retrieval accuracy for retrievals derived from clear column radiances. Cloud amount and

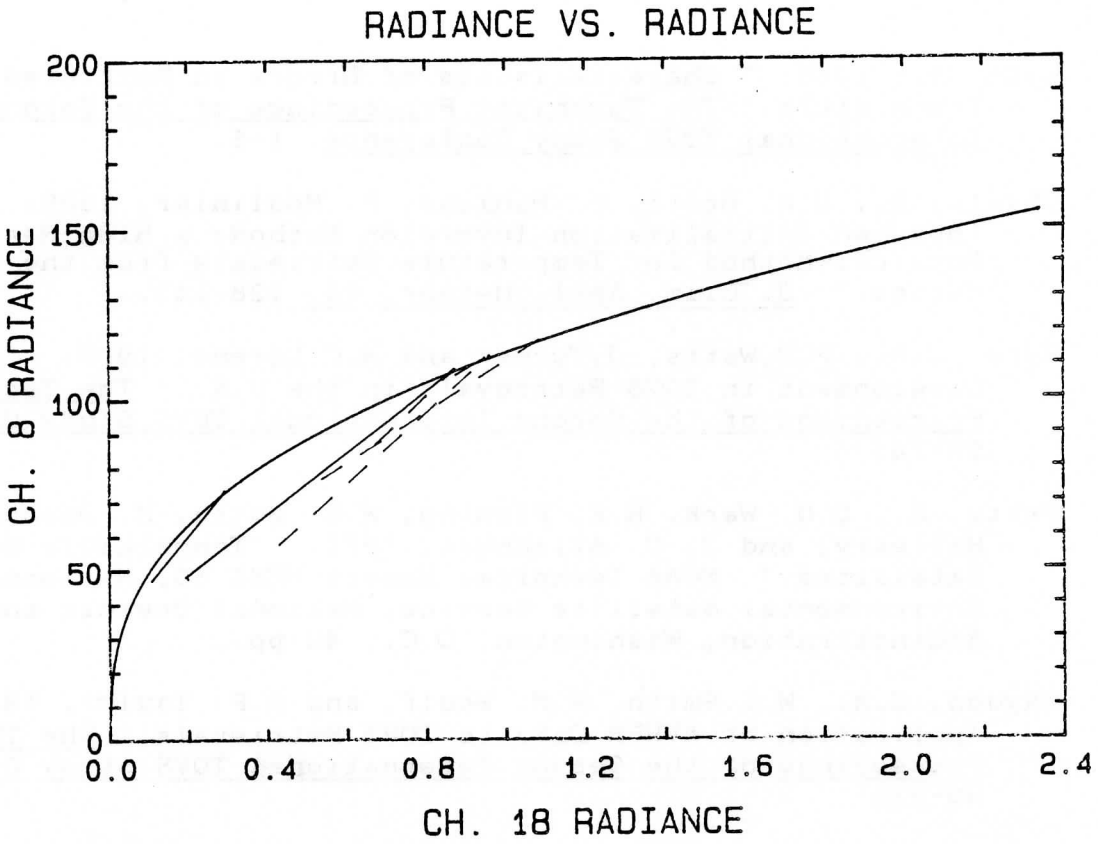

Fig.4 Channel 8 radiance vs. channel 18 radiance showing the curve formed by the locus of points with the same brightness temperature. Extrapolation of the lines to the left to intersect the curve provides the overcast radiances. Straight lines on the figure connect clear and observed radiances for several examples. Lines nearly tangent to the curve and short lines lead to larger uncertainties in the derived cloud top temperature.

height for the spots going into the retrieval provide some limited information about the reliability of the resulting retrievals. Since that time, we know of no user who has used these quantities as accuracy indicators, and there has been considerable interest in cloud amounts and heights. For these reasons, these parameters have been modified to represent the average of all the spots in a retrieval box, rather than just the spots used in deriving clear column radiances. As a result, the current cloud amounts and heights being produced by NESDIS provide useful meteorological information and are better agreement with conventional measurements of these quantities.

5. REFERENCES

Aoki, T., 1985: " Characteristics of Errors in Retrieved Vertical Temperature," The Technical Proceedings of the Second International TOVS Study Conference, 1-5.

Chedin, A., N.A. Scott, C. Wahiche, P. Moulinier, 1985: "The improved Initialization Inversion Method: a High Resolution Physical Method for Temperature Retrievals from the TIROS-N series." J. Clim. Appl. Meteor. 24, 128-143.

Eyre, J.R., P.D.Watts, J.Turner and A.C.Lorenc, 1985: "Research and Development in TOVS Retrievals in the U.K.," The Technical Proceedings of the Second International TOVS Study Conference, 58-74.

Fritz, S., D.Q. Wark, H.E. Fleming, W.L. Smith, H. Jacobowitz, D.T. Hilleary, and J. C. Alishouse, 1972: "Temperature Sounding from Satellites," NOAA Technical Report NESS 59, National Environmental Satellite Service, National Oceanic and Atmospheric Administration, Washington, D.C., 49 pp.

Hayden, C.M., W.L.Smith, H.M. Woolf, and B.F. Taylor, 1985: "An Application of AVHRR Data to TOVS Retrievals," The Technical Proceedings of the Second International TOVS Study Conference, 88-93.

LeMarshall, J.F., 1985: "An Intercomparison of Temperature and Moisture Fields Retrieved from TIROS Operational Vertical Sounder Data," The Technical Proceedings of the Second International TOVS Study Conference, 106-161.

McCleese, D.J., and L.S. Wilson, 1976: Cloud Top Heights from Temperature Sounding Instruments." Quart. J. Roy. Meteor. Soc., 102, 781-790.

McMillin, L.M., 1985a: "The Use of Classification Procedures to Improve the Accuracy of Satellite Soundings of Temperature and Moisture," Preprint Volume: Second Conference on Satellite Meteorology/Remote Sensing and Applications. Williamsburg Va., 1-4.

McMillin, L.M., 1985b: "The Use of Satellite Measurements to Evaluate Biases Between Radiosonde Types," to be presented at the Second International Conference on Southern Hemisphere Meteorology. Wellington, New Zealand.

McMillin, L.M., and C. Dean, 1982: "Evaluation of a New Operational Technique for Producing Clear Radiances," J. Appl. Meteor.,21, 1005-1014.

McMillin, L.M., 1978: "An Improved Technique for Obtaining Clear Column Radiances from Cloud-contaminated Radiances, Mon. Wea. Rev., 106, 1590-1597.

McMillin, L.M., D.Q. Wark, J.M. Siomkajlo, P.G. Abel, A. Werbowetzki, L.A. Lauritson, J.A. Pritchard, D.S. Crosby, H.M. Woolf, R.C. Luebbe, M.P. Weinreb, H.E. Fleming, F.E. Bittner and C.M. Hayden, "Satellite Infrared Soundings from NOAA Spacecraft," Department of Commerce, National Oceanic and Atmospheric Administration, NOAA Technical Report NESS 65, 112 p, September 1973.

McMillin, L.M., "A Method of Determining Surface Temperature from Measurements of Spectral Radiance at Two Wavelengths," Thesis for Degree of Doctor of Philosophy, Iowa State University, November 1971.

Smith, W.L., 1968: "An Improved Method for Calculating Tropospheric Temperature and Moisture from Satellite Radiometer Measurements." Mon. Wea. Rev., 96, 387-396.

Smith, W.L., 1967: "An Iterative Method for deducing Tropospheric Temperature and Moisture Profiles from Satellite Radiation Measurements," Mon. Wea. Rev., 95, 363-369.

Susskind, J., J.Rosenfield, D.Reuter, and M.T.Chahine, 1984: "Remote Sensing of Weather and Climate Parameters form HIRS/MSU on TIROS-N. J. Geophys. Res., 89, 4677-4697.

Taylor,B.F., C.M.Hayden, and W.L.Smith, 1985: "The Determination of HIRS Scene Temperatures from AVHRR DATA," The Technical Proceedings of the Second International TOVS Study Conference, 308-311.

Wielicki, B.A., J.A. Coakley, 1981: "Cloud Retrieval Using Infrared Sounder Data: Error Analysis," J. Appl. Meteor., 20, 157-169.

CLOUD TOP PRESSURES AND AMOUNTS USING HIRS CO_2 CHANNEL RADIANCES

W. Paul Menzel, Don Wylie and Allen H. L. Huang

Cooperative Institute for Meteorological Satellite Studies
Madison, Wisconsin 53706

1. INTRODUCTION

The determination of cloud heights and amounts is important for cloud climatologics and atmospheric circulation studies using cloud tracers. Several methods for determining cloud heights using satellite data are currently available. (a) The IR window method compares the IR window channel brightness temperature with an in situ vertical temperature profile to infer the height of the cloud. Assuming the cloud is opaque and fills the satellite field of view, this method provides good heights for dense stratoforms of cloud (see Figure 1). However, it is inaccurate for semi-transparent cirrus clouds and small element cumulus clouds. (b) The bi-spectral method improves the IR window channel estimate of a cloud top height by allowing for fractional cloud cover and by determining the cloud emissivity from visible reflectance data. Using a multiple scattering model, the visible brightness of the cloud is used to calculate the optical thickness, from which the infrared emissivity of the cloud can be computed (Mosher, 1976; Reynolds and Vonder Haar, 1977). Nonetheless, the bi-spectral method is till inaccurate for semi-transparent cirrus clouds. (c) The CO_2 method combines IR window channel data with CO_2 absorption channel data to specify a cloud height. As derived from the radiative transfer equation, cloud pressure is determined from the ratio of the deviations in cloud produced radiances and the corresponding clear air values for two or more spectral channels (Smith and Platt, 1978). This multispectral CO_2 absorption method does not suffer from any of the previous assumptions and thus, in principle, works on all cloud types. In addition, cloud amounts (emissivities) are a by-product of the calculation.

The CO_2 technique for deriving cloud top altitudes using radiances observed by the VISSR Atmospheric Sounder (VAS) was developed by Menzel (1983). It has also been adapted to the polar orbiting High-resolution Infrared Radiometer Sounder (HIRS). The technique takes advantage of infrared channels with partial CO_2 absorption where the different channels are sensitive to different levels in the atmosphere. Thus, clouds appear on each channel in proportion to their level in the atmosphere. Low clouds will not appear at all on the high level channels, while high clouds appear on all channels. By modelling the upwelling infrared radiation from the earth atmosphere system in several VAS or HIRS channels simultaneously, it is possible to infer the cloud top height independent of radiative transmissivity of the cloud. This gives the CO_2 technique the ability to distinguish thin cirrus clouds that would normally be missed by other techniques due to the transmission of terrestrial radiation through the cirrus. The frequency of cirrus clouds usually has been underestimated in cloud population studies. The IR window and bi-spectral methods of analyzing cloud cover often mistake cirrus clouds for lower level clouds or completely miss

them, because their infrared brightness temperatures are warmer than the temperature associated with their true altitudes. Thin cirrus are especially hard to identify on visible satellite images because they reflect little solar radiation and appear as dark or broken cloud fields. With the multi-spectral infrared sensor on the GOES-VAS or the NOAA-HIRS the identification of most cirrus is now possible.

The CO_2 technique has been installed on the Man-computer Interactive Data Access System (McIDAS) at the University of Wisconsin-Madison. It has been run operationally using the GOES-VAS imagery starting in October 1985. Statistics on cloud cover and especially cirrus cloud cover are being gathered for the continental United States and its bordering oceans. Since August 1986, cloud parameters are being calculated using the NOAA-HIRS radiances also, with a software module that has been appended to the International TOVS Processing Package (version 3). This paper describes the technique and presents the cloud statistics for 4-5 March 1982 of ALPEX using the HIRS data. The ALPEX has been used as the test bed for TOVS retrieval algorithms by the International TOVS Working Group.

2. CO_2 METHOD USING HIRS

The HIRS radiometer detects infrared radiation in eighteen spectral bands that lie between 3.9 and 15 microns at 25 to 40 km resolution (depending on viewing angle) in addition to visible reflections at the same resolution. The 15 micron CO_2 band channels provide a good sensitivity to the temperature of relatively cold regions of the atmosphere. A demonstration of the vertical resolution of the four relevant CO_2 channels is given by the temperature profile weighting function shown in Figure 2a. Each curve in the figure shows the sensitivity of the radiance observe in the spectral interval of the indicated channel to local variations in atmospheric temperature. Figure 2b shows the atmospheric transmission of radiance to space as a function of the emitting level. As may be seen, only clouds above the 400 mb level will have strong contributions to the radiance to space observed by the 14.2 micron band (HIRS channel 4), while the 14.0 micron band (HIRS channel 5) senses down to 600 mb the 13.7 micron band (HIRS channel 6) senses to 800 mb, and the 13.4 micron band (HIRS channel 7) senses down near the surface of the earth.

To assign a cloud top pressure to a given cloud element, the ratio of the deviations in cloud produced radiances, $I(\nu)$, and the corresponding clear air radiances, $I_{cl}(\nu)$, for two spectral channels of frequency ν_1 and ν_2 viewing the same field-of-view is written as

$$\frac{I(\nu_1) - I_{cl}(\nu_1)}{I(\nu_2) - I_{cl}(\nu_2)} = \frac{\varepsilon_1 \int_{P_s}^{P_c} \tau(\nu_1, p) \frac{dB[\nu_1, T(p)]}{dp} dp}{\varepsilon_2 \int_{P_s}^{P_c} \tau(\nu_2, p) \frac{dB[\nu_2, T(p)]}{dp} dp} . \quad (1)$$

In this equation ε is the cloud emittance, P_s the surface pressure, P_c the cloud pressure, $\tau(\nu, p)$ the fractional transmittance of radiation of frequency ν emitted from the atmospheric pressure level (p) arriving at the top of the atmosphere (p = 0), and $B[\nu,T(p)]$ is the Planck radiance of frequency ν for temperature T(p). If the frequencies are close enough together, then $\varepsilon_1 \cong \varepsilon_2$, and one has an expression by which the pressure of the cloud top within the field-of-view (FOV) can be specified. The observed cloud attenuation on the left side of equation (1) is determined from the HIRS observed radiances and clear air radiances provided from spatial analyses of HIRS clear-sky radiance observations or calculated from an in situ temperature and moisture profile. The calculated cloud attenuation on the right side of equation (1) is calculated from a temperature profile and the profiles of atmospheric transmittance for the spectral channels as a function of P_c, the cloud top pressure (discrete values at ∿50 mb intervals spanning 1000 to 100 mb are used). The optimum cloud top pressure is determined when the absolute difference $|\text{right } (\nu_1, \nu_2) - \text{left } (\nu_1, \nu_2, P_c)|$ is a minimum.

Once a cloud height has been determined, an effective cloud amount can be evaluated from the infrared window channel data using the relation

$$N\varepsilon = \frac{I(w) - I_{c1}(w)}{B[w, T(P_c)] - I_{c1}(w)} \qquad (2)$$

Here N is the fractional cloud cover within the FOV, $N\varepsilon$ is the effective cloud amount, w represents the window channel frequency, and $B[w, T(p_c)]$ is the opaque cloud radiance.

Using the ratios of radiances of the four CO_2 spectral channels, four separate cloud top pressures can be determined (14.2/14.0, 14.0/13.7, 13.7/13.4 and 14.0/13.4). If $(I - I_{c1})$ is within the noise response of the instrument (~ 1 mW/m^2/sr^1/cm^{-1}) the resulting P_c is rejected. Using the infrared window and the four cloud top pressures, four effective cloud amount determinations are made. As described by Menzel (1983), the most representative cloud height and amount are those that best satisfy the radiative transfer equation for the four CO_2 channels.

If no ratio of radiances can be reliably calculated because $(I - I_{c1})$ is within the instrument noise level, then a cloud top pressure is calculated directly from the HIRS observed 11.2 micron infrared-window channel brightness temperature and the temperature profile via the infrared window method. In this way all clouds are assigned a cloud top pressure either by CO_2 or infrared-window calculations.

The CO_2 technique is independent of the fractional cloud cover; heights and effective cloud amounts can be determined for partially cloudy FOVs. However, the CO_2 technique sees only the highest cloud and cannot resolve multi-layer clouds. Because the HIRS FOV resolution is very coarse, small element clouds are difficult to detect. Also, because the weighting functions for the HIRS channels are broad, there is an inherent lack of vertical resolution in the measurements. Nonetheless, reliable cloud parameters can be calculated with appropriate application of the technique.

3. VERIFICATION OF METHOD

Quantitative comparisons of CO_2 (or infrared window where necessary for low clouds) cloud top pressures have been made with determinations from radiosonde and radar echoes (Menzel, 1978). Radiosonde temperature and dew point temperature profiles can be used to infer cloud top pressures by noting that the dew point temperature profile becomes much drier as it emerges from the cloud. For about twenty different cloud forms, the HIRS CO_2 cloud top pressures were found to be within 50 millibars of the radar and radiosonde determinations. Comparable results have been achieved for the VAS CO_2 determinations (Menzel, 1983). These comparisons did not include cirrus clouds, as neither radiosonde or radar could provide reliable determinations.

A relative confirmation of the CO_2 cloud top pressure within cirrus clouds can be seen in Fig. 3. This figure shows the CO_2 and bi-spectral cloud top pressures plotted versus the position along the cirrus anvil emanating from a dense cumulus center. Moving from the dense cumulus clouds towards the thin cirrus, the CO_2 method maintains the height of the anvil while the bi-spectral method often underestimates the height. In the bi-spectral method, the IR window is sensing radiation from within and below the thin cirrus and therefore the brightness temperature is warmer than the cloud temperature causing the height miscalculation. The CO_2 method is independent of the fractional cloud cover and cloud emissivity, and thus provides a relatively consistent determination of the cirrus anvil height. Validation of the cirrus heights is currently being attempted with lidar intercomparisons.

VAS and HIRS CO_2 cloud parameters have been determined on several days from radiance observation within 30 minutes of one another. The intercomparison showed results within the estimated accuracy of the cloud top pressure, 50 mb, and the cloud amount, 20%. These good VAS and HIRS comparisons are very reassuring; two different radiometers in different earth orbits are yielding comparable determinations using the CO_2 method.

4. ALPEX RESULTS

THE CO_2 technique has been applied to the HIRS data from the NOAA-7 overpasses of the ALPEX region on 4-5 March 1982. The processing was accomplished as follows. For every box of 3 by 3 FOV, the clearest FOV was selected and a temperature profile was calculated from the HIRS radiance using the simultaneous physical retrieval (Smith et al., 1985). The ALPEX surface observations were used to adjust the profile; topography was also incorporated. Transmittances were determined from line-by-line calculations with the spectral response functions for the appropriate HIRS channels. HIRS clear FOV radiances were then calculated from the temperature profile for the four CO_2 channels and the infrared window. The cloud top pressure and amount were determined for the center and the four corner FOVs of each box resulting in roughly 70 km spacing.

Figure 4a shows the cloud top pressures (in centibars) over the ALPEX region from 0200 GMT March 4, 1982 superimposed on the infrared window image (only a sampling of the 356 determinations are shown).

Clear areas are designated at 100 centibars, regardless of topography. Sometimes the infrared window method mistates the surface pressure in clear areas. This occurs when there is a low level inversion and the surface temperature is identical to the temperature at 700 or 800 mb. The 700 mb reports in southern Italy and the 780 mb reports in Greece and Bulgaria are examples of this. A schema using the two infrared windows to screen low level inversions is being implemented (four micron must be somewhat colder than 11 micron for nocturnal inversions).

Figure 4b shows the corresponding cloud amounts. Cloud amounts greater than 100% are computationally possible when the opaque cloud radiance is calculated to be less than the observed radiance in the window channel; values within 5% of total cloud should be interpreted as total cloud.

Table 1 shows the statistics of the cloud observations during this overpass for ten intervals of cloud top pressure and for five intervals of effective cloud amount. The left column gives the frequency of cloud reports by pressure regardless of the cloud amount/emissivity. The next five columns show the distribution of cloud reports for five intervals of cloud amount or emissivity. The low cloud amount/emissivities (center columns) indicate thin or cirrus clouds which were partially transmitting infrared radiation, while the right column summarizes the reports of opaque clouds that did not transmit upwelling radiation. The sum of the five right columns should account for all of the cloud reports (100%). The most immediate finding is that 32% (summing columns 2 thru 5 less the clear sky percentage) of the area was covered with thin or cirrus clouds (emissivities less than .8); approximately 48% was covered with thick opaque clouds and truly clear sky conditions occurred about 20% of the time. The cloud top pressures were distributed with 8% above 400 mb, 24% between 400 and 600 mb, 30% between 600 and 800 mb, 18% between 800 and 1000 mb, and 20% at the surface (clear sky conditions). The thin clouds were mostly above 600 mb.

Table 2 shows the combined statistics for the four overpasses at 0200 and 0300 GMT on 4 and 5 March. Again, transmissive thin clouds are found to occur at roughly one-third of all observations.

5. CONCLUSION

The CO_2 method for calculating cloud top pressures and effective cloud amounts is producing good results with HIRS radiances. Cloud parameter determinations have been found to be reliable in all cloud types, including thin cirrus clouds where other techniques have been inconsistent. Cloud parameter determinations from the VAS and HIRS have been intercompared and have been found to agree within the accuracy of the CO_2 method. Observations from HIRS during 4-5 March 1982 of ALPEX reveal that roughly 30% of Europe was covered with thin clouds (radiative attenuation less than 80%), 50% was covered with thick opaque clouds, and 20% had clear sky conditions.

The most obvious finding in this work is the high occurrence of transparent or thin cirrus clouds. Since cirrus clouds have a large

impact on the radiative balance of the earth, the ISCCP global cloud climatology studies must include reliable cirrus detection schemas.

6. REFERENCES

Menzel, W. P., W. L. Smith and H. M. Woolf, 1978: A man interactive technique for specifying cloud heights from sounding radiance data. Third Conference on Atmospheric Radiation, June 18-20, 1978, Davis, CA, 154-157.

Menzel, W. P., W. L. Smith, and T. R. Stewart, 1983: Improved cloud motion wind vector and altitude assignment using VAS. J. Clim. and Appl. Meteor., 22, 377-384.

Mosher, F. R., 1976: Cloud height determination. COSPAR Proceedings of the Symposium on Meteorological Observations from Space: Their Contribution to the First Garp Global Experiment, 201-204.

Reynolds, D. and T. Vonder Haar, 1977: A bi-spectral method for cloud parameter determination. Mon. Wea. Rev., 105, 446-457.

Smith, W. L., and C. M. R. Platt, 1978: Comparison of satellite-deduced cloud heights with indications from radiosonde and ground-based laser measurements. J. Appl. Meteor., 17, 1796-1802.

TABLE 1. Cloud statistics for 356 observations over the European region (shown in Figure 4) on 4 March 1982 at 0200 GMT.

Level	All Cloud OBS	Cloud Amount 0.0-0.2	0.2-0.4	0.4-0.6	0.6-0.8	0.8-1.0
100 to 199 mb	0 %	0 %	0 %	0 %	0 %	0 %
200 to 299 mb	3	2	1	0	0	0
300 to 399 mb	5	0	0	1	1	3
400 to 499 mb	12	3	3	1	1	4
500 to 599 mb	12	1	2	3	3	3
600 to 699 mb	13	0	1	2	2	8
700 to 799 mb	17	0	0	1	2	14
800 to 899 mb	13	0	0	1	1	11
900 to 999 mb	5	0	0	0	0	5
1000 to 1099 mb	20	20	0	0	0	0
Total	100 %	26 %	7 %	9 %	10%	48 %
		20% Clear		32% Cirrus		48% Cloudy

TABLE 2. Cloud statistics for 1472 observations over the extended European region on 4-5 March 1982 at 0200 and 0300 GMT (four overpasses in all).

Level	All Cloud OBS	Cloud Amount 0.0-0.2	0.2-0.4	0.4-0.6	0.6-0.8	0.8-1.0
100 to 199 mb	0 %	0 %	0 %	0 %	0 %	0 %
200 to 299 mb	3	2	1	0	0	0
300 to 399 mb	6	1	1	1	1	2
400 to 499 mb	12	2	3	1	1	5
500 to 599 mb	11	0	2	3	2	4
600 to 699 mb	12	0	1	2	3	6
700 to 799 mb	17	0	1	2	2	12
800 to 899 mb	8	0	0	0	0	8
900 to 999 mb	8	0	0	0	0	8
1000 to 1099 mb	23	23	0	0	0	0
Total	100 %	28 %	9 %	9 %	9%	45 %
		23% Clear		32% Cirrus		45% Cloudy

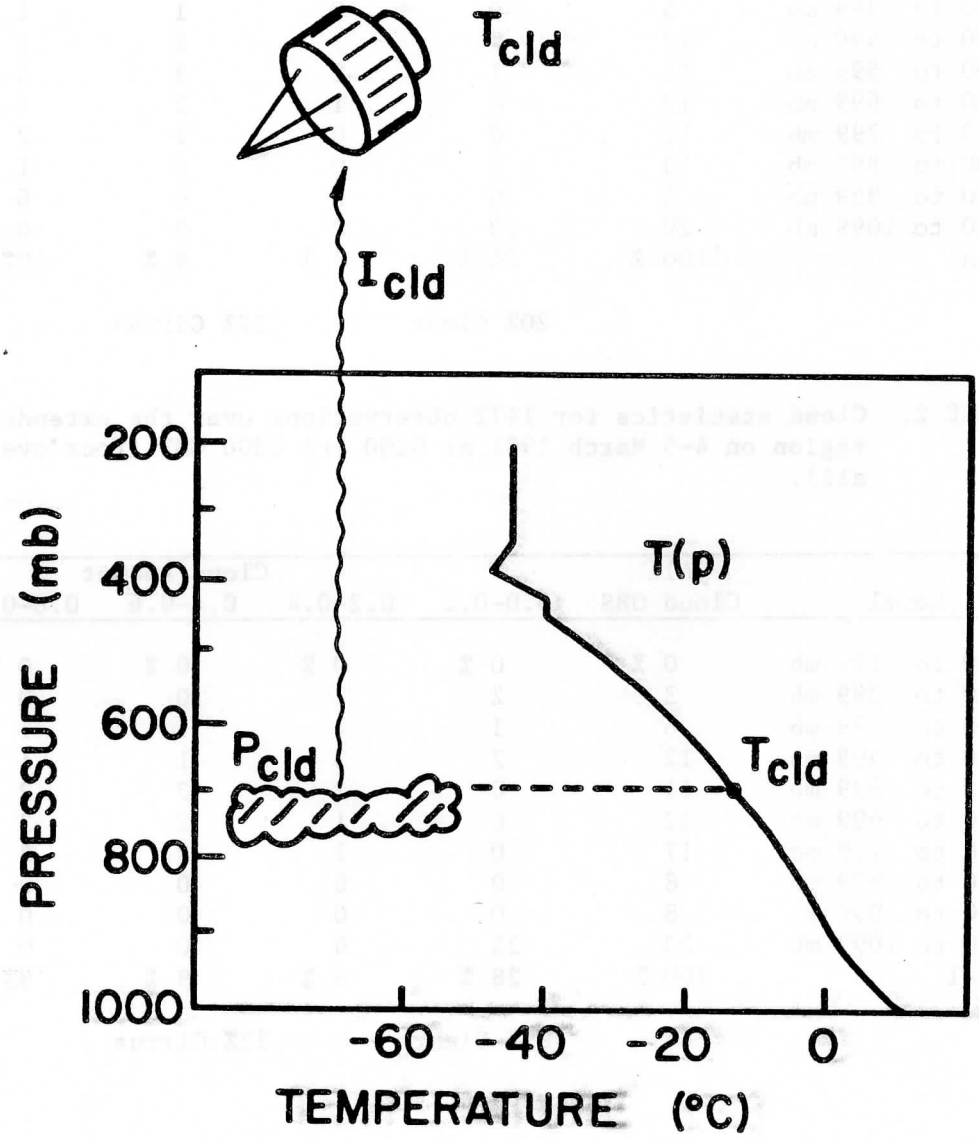

Figure 1. A schematic of the infrared window method where the satellite observed brightness temperature, T_{cld}, is used in conjunction with an in situ temperature profile to infer the cloud top pressure, P_c.

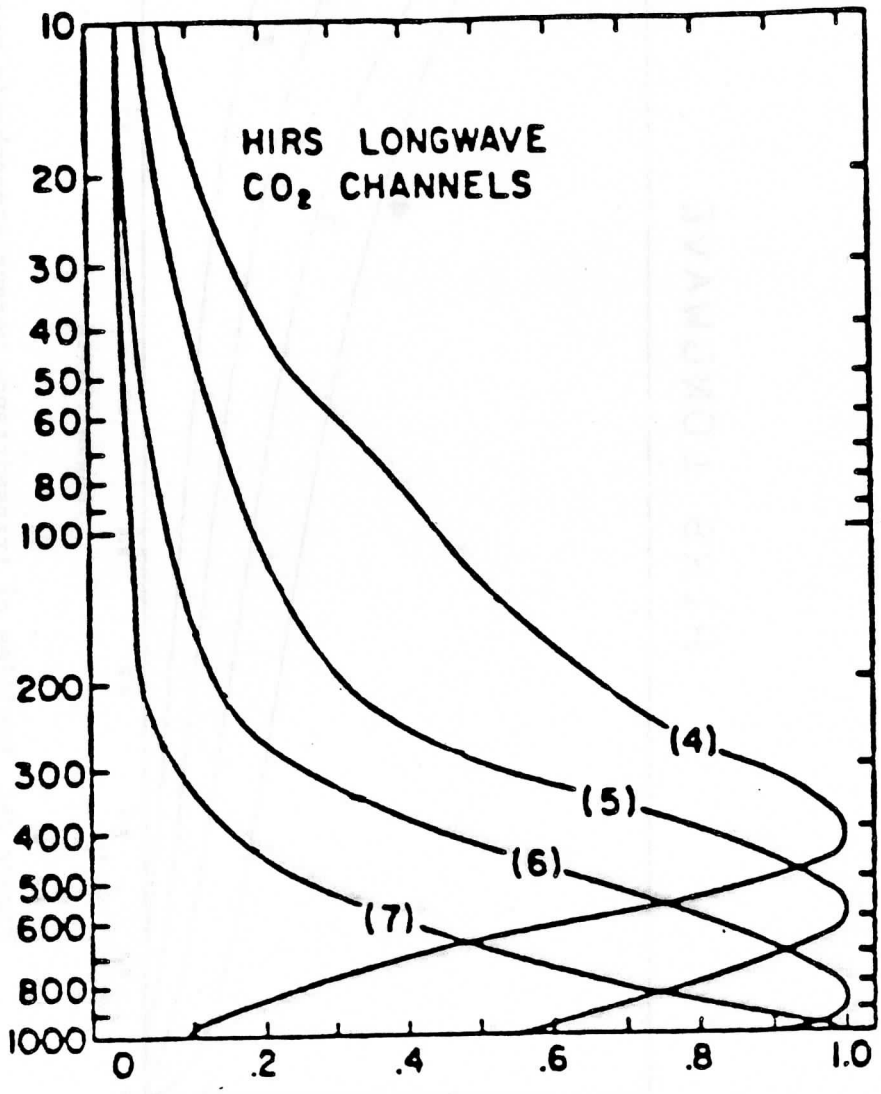

Figure 2a. Weighting functions for HIRS channels 4-7 centered at 14.2, 14.0, 13.7, and 13.4 microns.

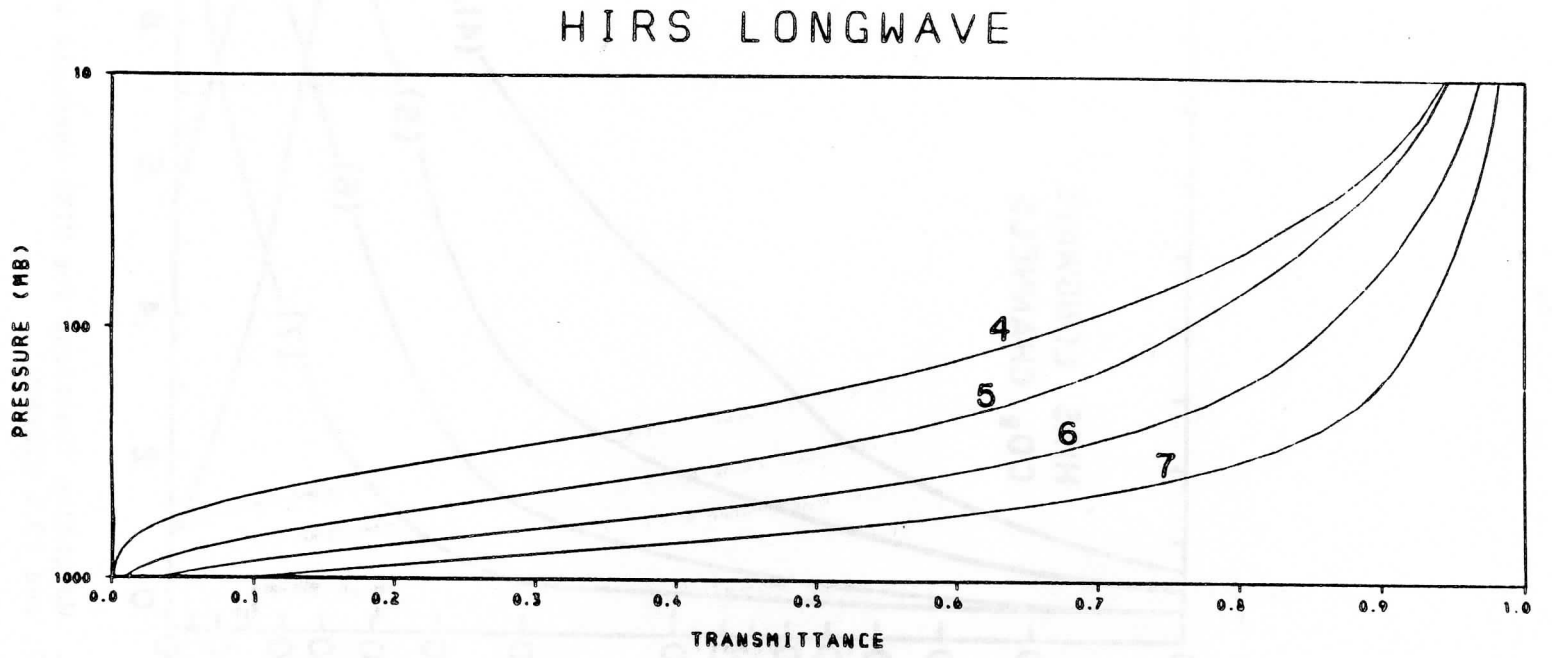

Figure 2b. Profiles of transmittance versus atmospheric pressure for HIRS channels 4-7.

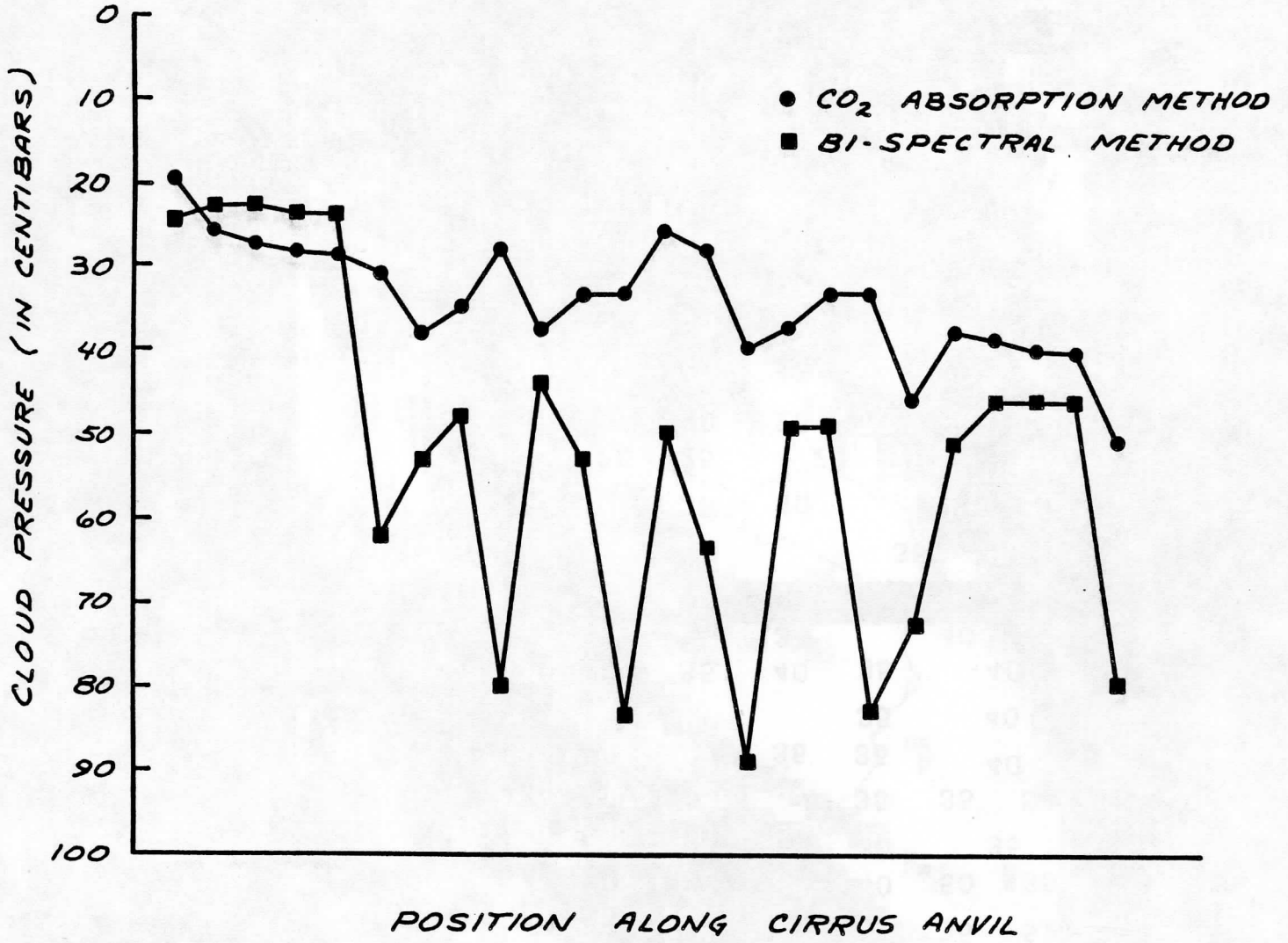

Figure 3. Cloud top pressures (in centibars) plotted versus the position along the cirrus anvil emanating from the dense cumulus center.

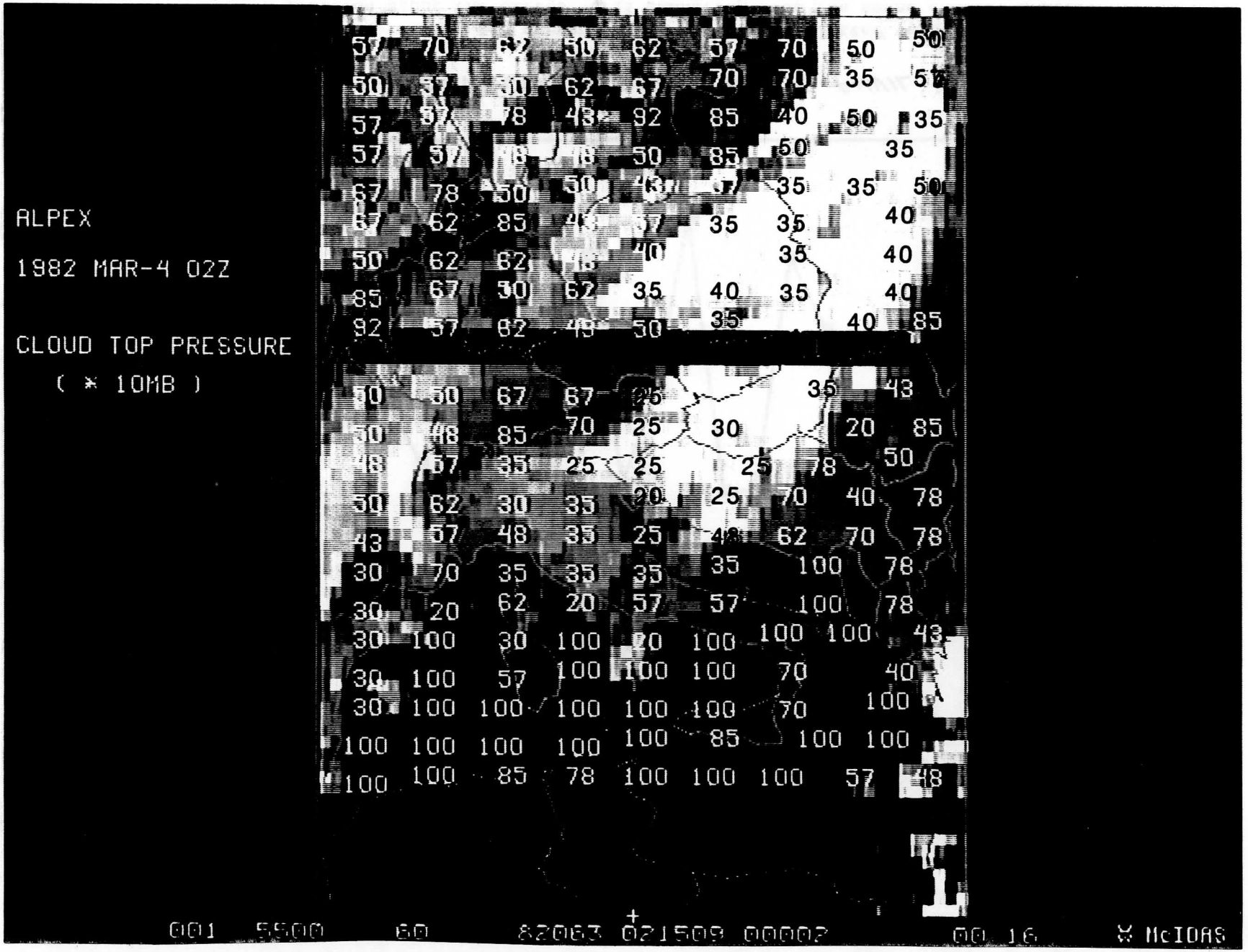

Figure 4a. Cloud top pressures, in centibars, superimposed on the HIRS infrared window image for 200 GMT March 4, 1982 over central Europe.

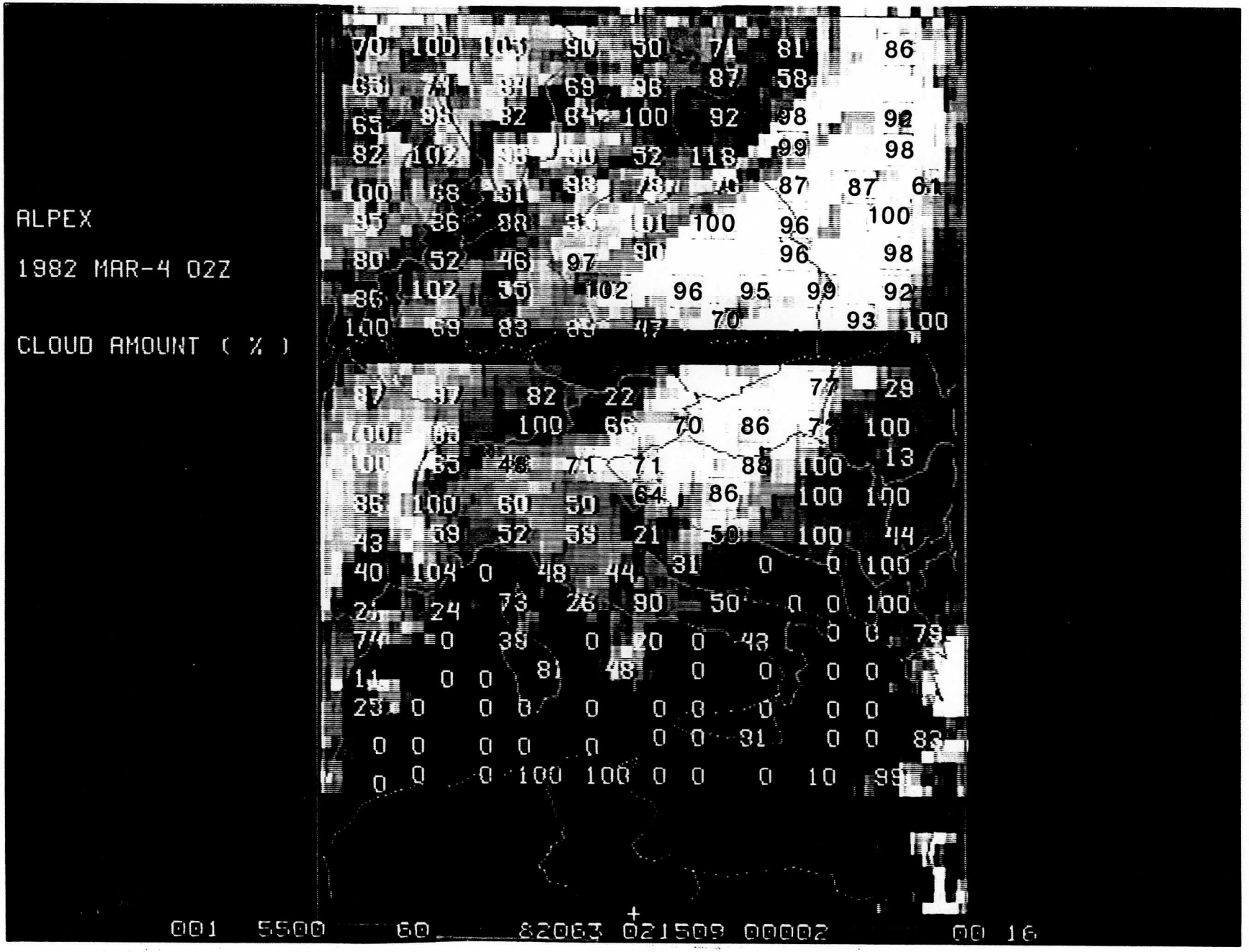

Figure 4b. Effective cloud amounts, fractional cloud cover times emissivity, for 200 GMT March 4, 1982 over central Europe.

A DESCRIPTION OF PREDICTION ERRORS ASSOCIATED WITH THE T-BUS-4 NAVIGATION MESSAGE AND A CORRECTIVE PROCEDURE

Frederick W. Nagle

NOAA/NESDIS Satellite Applications Laboratory
Systems Design and Applications Branch

1. INTRODUCTION

During his visit to the United States in 1985 spent at CIMSS, Madison, Wisconsin, Dr. Brian Taylor of the New Zealand Meteorological Service, complained of navigational errors in the predicted position of the NOAA-9 satellite when using orbital parameters obtained from Part IV of the T-Bus message (sample attached) provided to international users of NOAA data. The existence of the errors was confirmed by other members of the International TOVS Study Conference (ITSC) held at Igls, Austria during February 1985; an action item was recommended to ascertain the nature of the problem, and to report possible remedial action at the next ITSC meeting to be held in Madison, Wisconsin in the summer of 1986. This report addresses the investigation accomplished at CIMSS.

2. DESCRIPTION OF PROBLEM

For this investigation, orbital parameters obtained from three sources were used. The first set was obtained from NOAA/NESDIS, Orbital Mechanics Branch, Suitland, Maryland, using the subroutine PSCEAR installed on the NAS 9000 system in Suitland. Definitive (not predicted) parameters were gathered daily over a period of several weeks from December 1985 through February 1986. Satellite positions obtained from the most recent PSCEAR parameters were considered the best available approximation to the truth, and were the standard against which the predicted positions were compared. The definitive parameters were usually used within one day of their epoch, and never more than three. A second set of parameters was obtained approximately daily from the T-Bus Part IV message received on the McIDAS system at Madison. This is the same set available to Dr. Taylor and others.

The T-Bus orbital parameters have the somewhat unusual property that their epoch is the time of an ascending Equator crossing. Presumably, a number of users around the world use a satellite prediction system predicated on the assumption that the parameters are valid at the instant of an Equator crossing. However, this involves a possibly suspect interpolation since primary navigation parameters are not provided in this way, and this question has been considered by generating a third set of "pseudo" T-Bus parameters at SDAB, Madison, for comparison with the T-Bus parameters cited above. These pseudo-parameters were obtained from a program which extrapolates a set of definitive parameters (our "truth") forward to the next ascending Equator crossing. The short program which performs this extrapolation is shown in the appendix below.

The basic element of the study is the prediction of satellite positions from either the actual or pseudo T-Bus, and the comparison of this prediction with the position obtained from definitive parameters. The subroutine used to predict satellite positions from a given set of orbital parameters was obtained from OMB/NESDIS, in order to use standardized software. The subroutine is known as BROLYD on the NAS 9000, and appears in the present study as the vector-valued function VBLMOD (Vector Brouwer-Lyddane Model). A complete listing of the routine on the SSEC McIDAS IBM 4381 is given below.

Figure 1 illustrates the problem of which Dr. Taylor has complained. The y axis is the epoch of whatever set of parameters is used to make the prediction. The abscissa represents the time of a prediction after the epoch of the prediction, each tick mark delineating one day, the entire range being 27 days. The ordinate represents the along-track error of the prediction with the horizontal lines positioned at ±100 kilometers. The strings of semi-continuous dots depict the navigation error as the T-Bus ages, and the continuous line is a quadratic fit to these errors. Several points can be noted. Firstly, there is an overall tendency toward degradation in that the predicted positions generally fall further and further behind with time. Secondly, the degradation occurs at a rate which is by no means uniform, for certain sets of parameters tend to produce strings of predicted positions which degrade much more rapidly than other strings produced by other sets. Thirdly, the prediction error for any given epoch is not continuous. The discontinuities are obvious and occasionally very large as evidenced by the scattering of individual dots. Finally, the error is frequently non-trivial even at the time of epoch (the origin). It should be recalled that this navigation is being used to locate the AVHRR data where an error of even a few kilometers is objectionable.

Figure 2 is similar to Figure 1, but is derived from the pseudo T-Bus parameters produced in Madison. In some ways, there is an improvement. The short term error is reduced and it appears that there is somewhat less long-term bias. However, the scatter of the predicted positions is worse, with some sets of parameters producing positive, and others negative errors, which become rapidly worse with time. Hence, for long-term predictions, neither set is acceptable.

3. A METHOD OF REDUCING THE ERROR

We have not been successful in locating the source of the error in the predictions from the T-Bus. Its elimination appears to involve an in-depth study of the orbital prediction model which is clearly beyond the scope of our effort. However, we can offer a palliative which will generally make the navigation suitable over periods of up to a week.

The fact that large along-track errors occur using either set of T-Bus parameters suggests that for whatever reason, the mean orbital period is badly predicted. Yet, the true orbital period is rather well-known, for it can be obtained from the known times of satellite equator crossings found in either the true or pseudo T-Bus parameters.

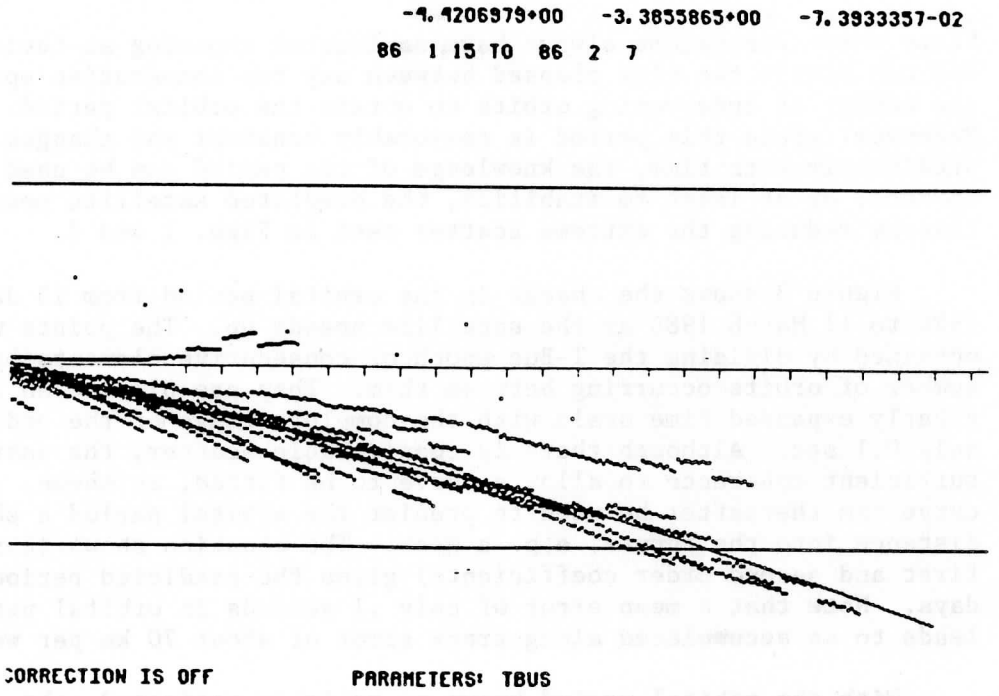

Figure 1. Prediction errors from standard T-Bus parameters; no periodic stabilization.

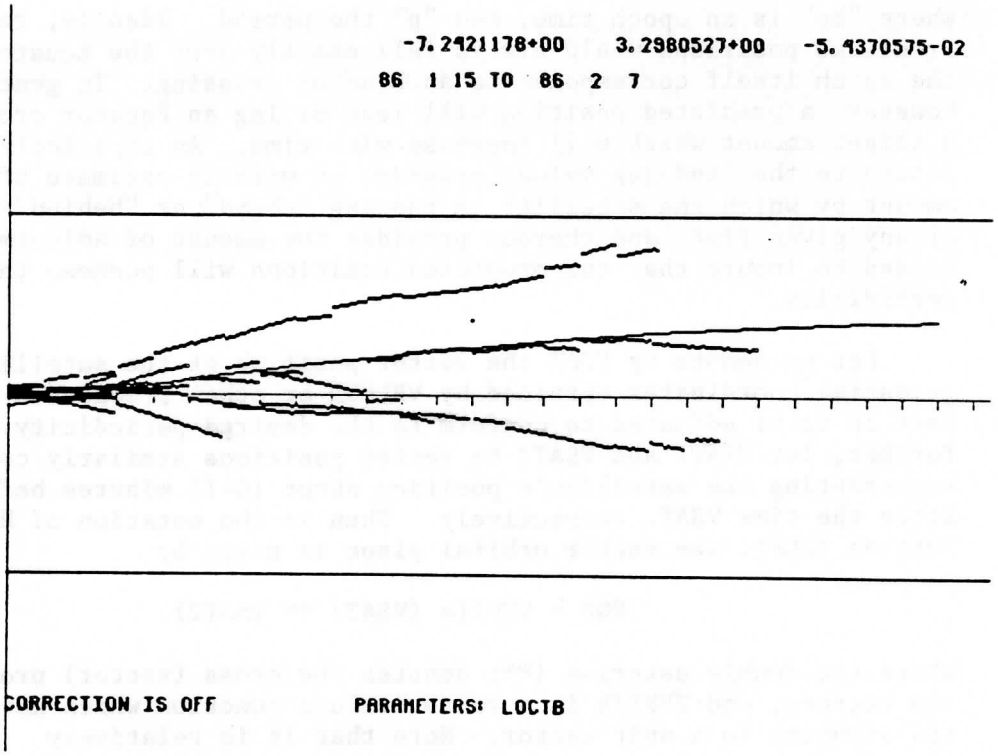

Figure 2. Prediction errors from CIMSS-generated pseudo-T-Bus parameters; no periodic stabilization.

Since these parameters always have an Equator crossing as their epoch, one can divide the time elapsed between any two consecutive epochs by the number of intervening orbits to obtain the orbital period. Moreover, since this period is reasonably constant and changes predictably with time, the knowledge of the period can be used to correct, or at least to stabilize, the predicted satellite positions, thereby reducing the extreme scatter seen in Figs. 1 and 2.

Figure 3 shows the change in the orbital period from 15 January 1986 to 11 March 1986 as the satellite speeds up. The points were obtained by dividing the T-Bus epoch of consecutive elements by the number of orbits occurring between them. They are plotted on a greatly expanded time scale with the complete range of the ordinate only 0.1 sec. Although there is considerable scatter, the pattern has sufficient coherence to allow a curve to be fitted, as shown, and this curve can thereafter be used to predict the orbital period a short distance into the future, e.g. a week. The equation shown (constant, first and second order coefficients) gives the predicted period in days. Note that a mean error of only .1 seconds in orbital period leads to an accumulated along-track error of about 70 km per week.

With the orbital period known or reliably estimated, the predicted satellite positions can be much stabilized as follows. Beginning at the epoch of a given set of parameters, satellite positions are predicted at every tenth orbital period thereafter, at the times

$$ep,\ ep + 10*p,\ ep + 20*p,\ ep + 30p,\ \text{etc.}$$

where "ep" is an epoch time, and "p" the period. Ideally, the predicted positions would always fall exactly over the Equator, since the epoch itself corresponds to an Equator crossing. In general, however, a predicted position will lead or lag an Equator crossing by a slight amount which will increase with time. An empirical curve fitted to the lead/lag values provides us with an estimate of the amount by which the satellite is running "ahead" or "behind" schedule at any given time, and thereby provides the amount of adjustment needed to insure that the predicted positions will possess the desired periodicity.

Let us denote by VSAT the vector position of the satellite in celestial coordinates obtained by VBLMOD or other prediction program. This is to be adjusted to conform to the desired periodicity. Further, let VSAT1 and VSAT2 be vector positions similarly computed representing the satellite's position about 10-15 minutes before and after the time VSAT, respectively. Then in the notation of High-Level Fortran (HLF), the vector orbital plane is given by

```
VOP = VUNIT4 (VSAT1 ** VSAT2)
```

where the double asterisk (**) denotes the cross (vector) product of two vectors, and VUNIT4 is a vector-valued function which normalizes its argument to a unit vector. Note that it is relatively

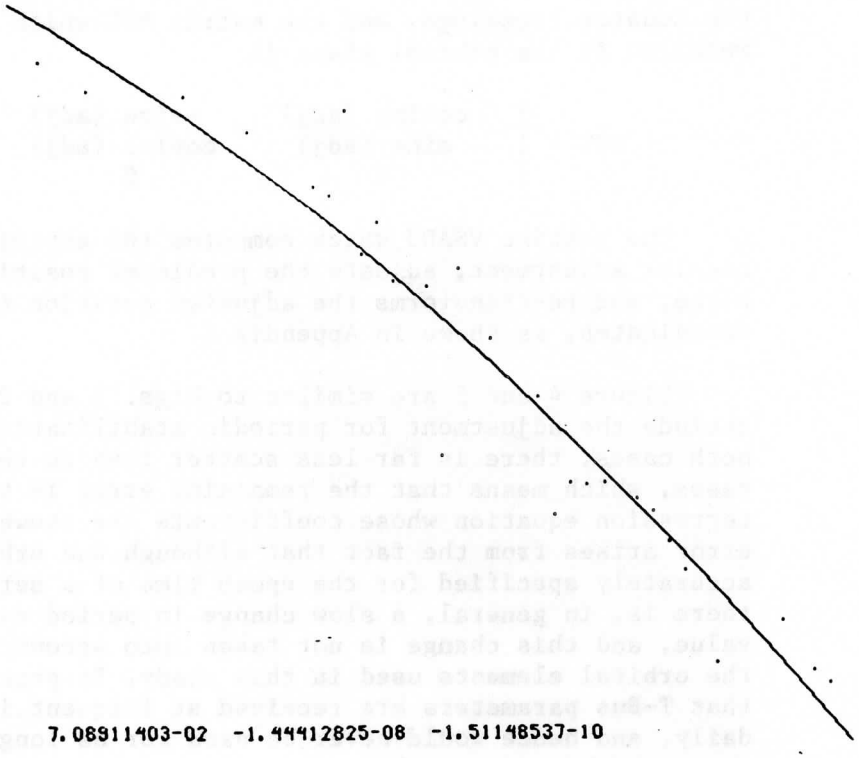

Figure 3. Change in NOAA-7 orbital period 15 January 1986 to 11 March 1986. The entire range is only about .1 second.

unimportant if the two positions VSAT1 and VSAT2 contain slight along-track errors, since the vector orbital plane precesses only very slowly, about one-fourteenth of a degree per orbit.

The vector orbital plane VOP is one of three orthonormal vectors which constitute a dextral coordinate set attached to the plane of the orbit. VOP is normal to the plane of the orbit, and two other orthonormal vectors in this plane can easily be found, as follows. Let VEQ by the projection of VOP onto the plane of the Equator. Then the cross-product VX = VEQ**VOP is a vector lying along the intersection of the orbital and equatorial planes. Finally, VY = VOP**VX points from the center of the earth, in the orbital plane, toward the point of maximum satellite latitude. For example,

```
VEQ = VEC4 (vop(1), vop(2), 0.)
VX  = VUNIT4 (VEQ ** VOP)
VY  = VOP ** VX
```

The vector-valued function VEC4 returns a vector whose three components are its three arguments. The three unit vectors thus found (VOP, VX, VY) may themselves be regarded as the columns of a 3x3 orthogonal matrix MXR which transforms an arbitrary vector from the basis of the orbital plane to the celestial basis. Moreover, its inverse is also its transpose, and transforms a vector from the celestial to the orbital basis. The angular adjustment "adj" to be made to the satellite's position is known from the lead/lag values in

the Equator crossings, and the matrix ROT which accomplishes this rotation in the orbital plane is

$$ROT = \begin{vmatrix} \text{cosine (adj)} & \text{-sine (adj)} & 0 \\ \text{sine (adj)} & \text{cosine (adj)} & 0 \\ 0 & 0 & 1 \end{vmatrix}$$

The routine VSADJ which computes the empirical equation for angular adjustment, adjusts the predicted position in the orbital plane, and re-transforms the adjusted position to celestial coordinates, is shown in Appendix C.

Figure 4 and 5 are similar to Figs. 1 and 2, respectively, but include the adjustment for periodic stabilization described above. In both cases, there is far less scatter than in the two unstabilized cases, which means that the remaining error is better described by a regression equation whose coefficients are shown. This remaining error arises from the fact that although the orbital period can be accurately specified for the epoch time of a set of orbital elements, there is, in general, a slow change in period even from this estimated value, and this change is not taken into account over the lifetime of the orbital elements used in this study. In practice, it is assumed that T-Bus parameters are received at frequent intervals, perhaps daily, and hence would never be used for as long as three weeks (as shown in these figures).

4. CONCLUSIONS AND RECOMMENDATIONS

It appears feasible even with imperfect orbital elements and imperfect prediction programs to upgrade significantly the quality of NOAA-9 (or other) satellite positions by making use of the orbital period, which can be reliably estimated. To achieve this end, the following general approach can be used, although its precise application by any user will depend on the resources available at his site.

(a) An archive of recent T-Bus orbital elements must be available. The fact that their epoch coincides with an Equator crossing is desirable, because Equator-crossing is a moment of the orbit at which orbital periods can be easily measured. If no T-Bus elements are available, but definitive elements are known, the former can be obtained from the latter using, for example, a routine such as shown in Appendix A.

(b) With T-Bus or pseudo T-Bus elements available, a program like that in Appendix B can be used to obtain a regression equation for predicting orbital periods in the near future.

(c) With an accurate estimate of period now available for any orbit, the known periodicity can be applied to stabilize the orbital position in order to remove both bias and scatter from the predicted positions. A routine like that shown in Appendix C can be used.

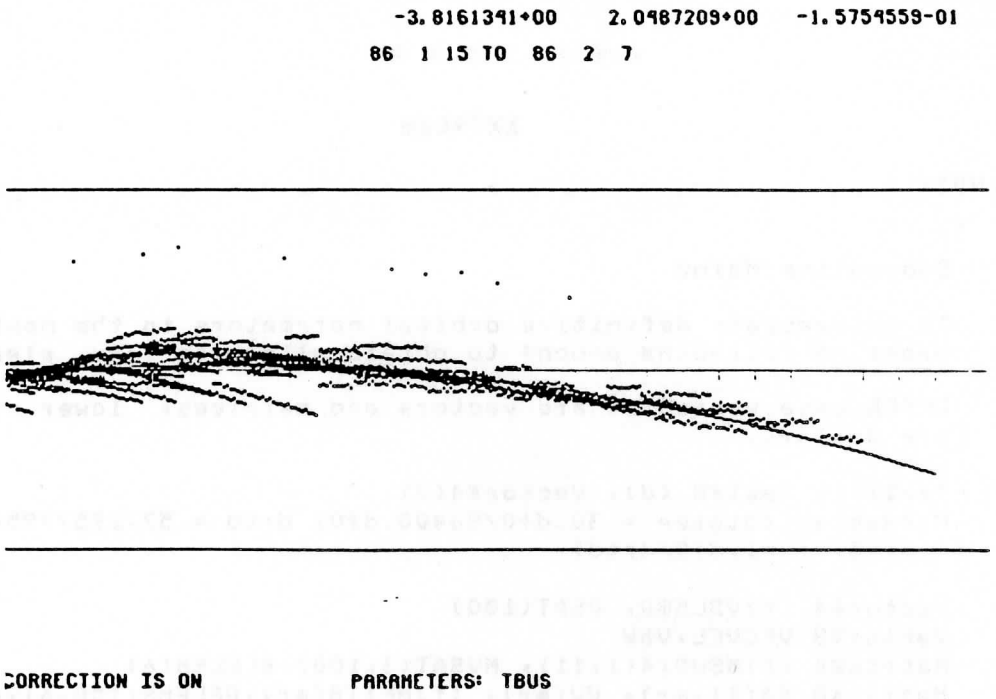

Figure 4. Prediction errors from standard T-Bus parameters using periodic stabilization.

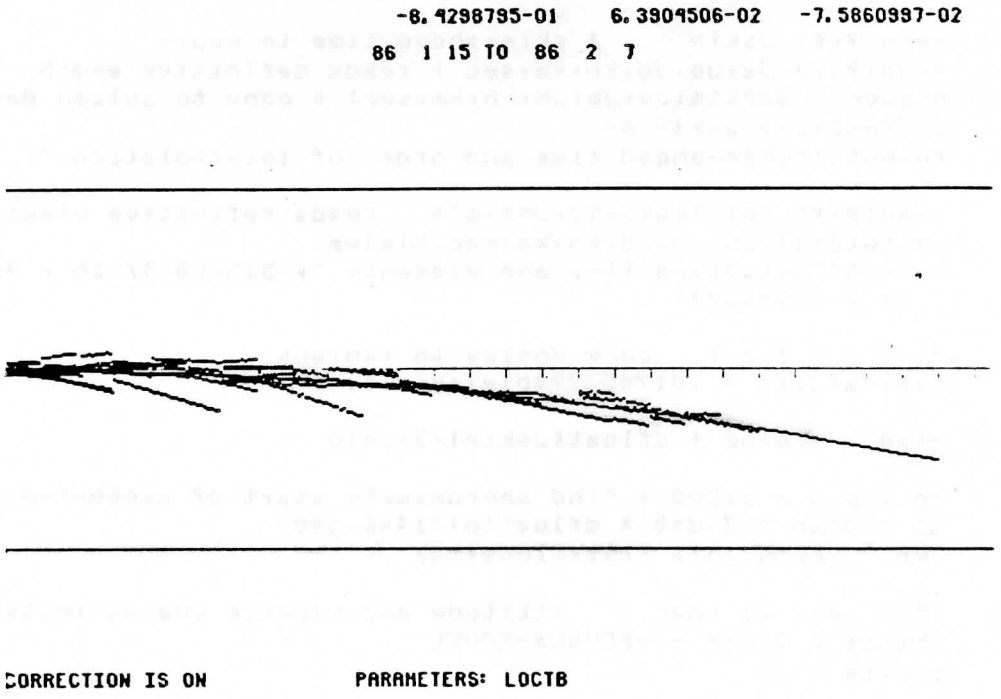

Figure 5. Prediction erros from pseudo-T-Bus parameters using periodic stabilization.

APPENDIX A

```
*
      Subroutine Main0
*
*     To extrapolate definitive orbital parameters to the next Equator
*     crossing following epoch; to obtain alternate T-Bus elements.
*
*     UPPER case variables are vectors and matrices;  lower case
*     are scalars.
*
      Implicit real*8 (d), Vector*4(V)
      Parameter (dtstep = 30.d+0/86400.d+0, drtd = 57.2957795d+0,
     1  mr=5, rx=1.d+0/drtd)
c
      Vector*4 (f)VBLMOD, VSAT(100)
      Vector*8 VECVEL,VBW
      Matrix*4 (f)MSUBI4(1,11), MVSAT(3,100),BLELEM(6)
      Matrix*8 AA(11,mr), VV(mr), (f)MFIT8(mr),DELEMS(100,6),UPDELS(6),
     1  MX(11),MCOEFS(mr,1),(f)MSUBI8(11,6),MSUB(11,6),
     2  DTT(100),(f)MALL8(100),DINELS(6)
*
      common/blxtra/dtprep,UPDELS,VECVEL ; Updated BL elements
      common/vbl/ dtepoc,BLELEM
*
      equivalence( VSAT(1), MVSAT)
*
c     ccccccccccccccccccccccccccccccccccccccccccccccccccccccccc
c
      read(9,*) jskip      ; skip-ahead time in hours
      read(9,*) jy,jm,jd,kh,km,sec ; reads definitive epoch
      dtepoc = dabtim(jy,jm,jd,kh,km,sec) ; conv to Julian Day Number
      write(6,17) jskip,mr
17    format('0skip-ahead time and order of interpolation ', 2i6/)
*
      read(9,*) (blelem(j,1),j=1,6);   reads definitive elements
      write(6,1) jy,jm,jd,kh,km,sec,blelem
1     format('0starting time and elements ', 5i3,f8.3/ 1h , 3e16.6/
     1  1h , 3e16.6/)
c
      do 2 j = 3,6 ;   conv angles to radians
2     blelem(j,1) = .01745329*blelem(j,1)
c
      dtgo = dtepoc + dfloat(jskip)/24.d+0
c
      do 100 n = 1,200 ; find approximate start of ascending pass
      dt = dtgo + 3.d+0 * dfloat(n)/1440.d+0
      VWB = VBLMOD(dt, flat,flong,cd)
*
      if(n .eq. 1) then ;   altitude and kinetic energy initially
      dkinet = 1.d+6 * VECVEL*VECVEL
      dzorig = cd
```

```
      dsfa = 9.8d+0 * (6371.d+0 / dzoris)**2
      write(6,91) cd,dkinet
91    format('0Initial altitude and energy ', f9.1,2x,d18.7/)
*
      else
      dk = 1.d+6 * VECVEL*VECVEL
      dp = 1000.d+0 *dsfa * (dble(cd) - dzoris)
      dtot= dp + dk
      write(6,93) n,dk,dp,dtot
93    format(4x, i6, 3d18.8)
      end if
*
      if(flat .lt. -75.) go to 102 ;    close to mimumum latitude
100   continue
c
102   do 110 n = 1,100;  search northward in small steps
      dtt(n,1) = dt + dtstep * dfloat(n)
      VSAT(n) = VBLMOD(dtt(n,1), flat,flong,cd)
c     VBLMOD also returns updated BL elements thru common/blxtra/
110   DELEMS(n,$) = UPDELS
c
      lit = litsch(MVSAT(3,$), 100) ; search for smallest z-component
*     Litsch searches an array for the smallest absolute value.
*     The 3rd row of MVSAT is the z-components of position vectors.
*
      jso = lit - 5;  choose 5 points on either side near Equator
      jstop = lit + 5
      MX = MSUBI4( MVSAT,3,100, 3,3,1, jso,jstop,1)
      MCOEFS = MFIT8(MX, DTT(jso,1), 11, mr,   VV, AA)
*
*     We just obtained mr coefficients fitting time as a function
*     of z-component near Equator crossing.  The constant term
*     (the approximation when z=0) is the crossing time.
c
      dtx = mcoefs(1,1) ;     interpolated crossing time
      call tinver( dtx,  ny,nm,nd,kh,km,ks, nth)
*     Tinver converts Julian Day Number back to civil date/time.
      write(6,11) ny,nm,nd,kh,km,ks
11    format('0approximate crossing time ', 6i3/)
c
c     Extract the sub-matrix of orbital parameters straddling Equator
      MSUB = MSUBI8( DELEMS,100,6, jso,jstop,1, 1,6,1) ; 11x6
      DTT = DTT - MALL8( dtx, 100,1);  subtract dtx from all times
*     DTT times are now relative to Equator crossing.
c
      do 150 j = 1,6  ;  interpolate each of 6 elements to dtx
      MCOEFS = MFIT8(DTT(jso,1),MSUB($,j),11,mr, VV,AA)
150   dinels(j,1) = mcoefs(1,1)
*
c     convert parameters to McIdas storage format
      ecc = dinels(2,1)
      ap = drtd*dinels(5,1)
```

```
      ra = drtd*dinels(4,1)
      fincl = drtd*dinels(3,1)
      sma = dinels(1,1)
      fma = drtd*dinels(6,1)
*
      call tinver(dtx, jy,jm,jd,kh,km,ks, nth)
      frac = 86400.d+0 * (dtx - dabtim(jy,jm,jd,kh,km,ks))
      sec = float(ks) + frac
      write(6,77) jy,jm,jd,kh,km,sec, sma,ecc,fincl,ra,ap,fma
77    format(1h ,5i3,f6.2, f8.2, f9.6, f7.3, 3f8.3/)
*
*     Compute energies using the definitive elements, and also using
*     the pseudo-TBUS elements just computed.
*
      VX = VBLMOD(dtx, flat,flong,cd)
      dkin = 1.d+6 * VECVEL*VECVEL
      dpot = 1000.d+0 * dsfa * (dble(cd) - dzorig)
      dtot = dkin + dpot
      write(6,79) flat,flong,dkin,dpot,dtot
79    format('0definitive lat/long at epoch, kinetic, potential, total'/
     1  1h , 2f9.2/1h , 3d18.8)
*
      dtepoc = dtx
      BLELEM = DINELS  ;  insert pseudo-elements just computed.
      VSUDO = VBLMOD(dtx, flat,flong,cd)
      dkin = 1.d+6 * VECVEL*VECVEL
      dpot = 1000.d+0 * dsfa * (dble(cd) - dzorig)
      dtot = dkin + dpot
      write(6,83) flat,flong,dkin,dpot,dtot
83    format('0using pseudo-tbus parameters ', 2f9.1/1h , 3d18.7/)
*
      call mfstak(0)
      return
      end
c
*     ***************************************************************
      Matrix Function MFIT8*8 (x,y,n,m,  v,aa)
c
c     UPPER case symbols are matrices; lower case are scalars.
c     To obtain the m coefficients (m,1) for a least-squares fit to
c     n  x,y pairs of data.  See p. 278 on 'Approximation' in Froberg.
C     The functional value returned by this routine is the (m,1)
c     matrix of real*8 fitting coefficients, in ascending powers.
C     If this routine is called from a conventional Fortran program,
c     the call is...
C
c     This routine is similar to MATFIT, but has REAL*8 inputs.
c
C     CALL MFIT8( XLIST, YLIST, NPAIRS, MORDER,  V,AA,  COEFS)
C                    8      8       I4      I4   8  8      8
c
      Matrix*8 MFIT8(m),AA(n,m), (f)MTRAN8(m,n), (f)MSYMVT(m,m),
```

```
     1  V(m),X(n),Y(n)
c
      V = 0.
C
      do 10 i = 1,n
      aa(i,1) = 1.d+0
10    v(1,1) = v(1,1) + y(i,1)
c
      do 20 k = 2,m
      do 20 i = 1,n
      aa(i,k) = x(i,1) * aa(i,k-1)
20    v(k,1) = v(k,1) + aa(i,k) * y(i,1)
c
      MFIT8 = MSYMVT( MTRAN8(AA,n,m)*AA, m) * V
      return
      end
```

```
    1   APPENDIX B:
    2
    3   *
    4         Subroutine Main0
    5   *
    6   C ?   y1 m1 d1 y2 m2 d2 cfile(loctb)
    7   *
    8   *     To obtain coefficients for the regression equation for
    9   *     predicting orbital periods
   10   *
   11         Implicit real*8 (d)
   12         character*8 cfile,cpp
   13         Matrix*8 (f)MFIT8(3), MCOFS(3), AA(200,3),VV(3,3)
   14         dimension dpers(200),dts(200)
   15   *
   16         common/vbl/dtepoc,elems(6)
   17         common/tab/tabuf(33)
   18   *
   19   *     xxxxxxxxxxxxxxxxxxxxxxxxxxxxxxxxxxxxxxxxxxxxxxxxxxxxxxxxxxxxxxx
   20         call encode( '(132x, t1,
   21        1  'Entering period on initiator ',i3/)', tabuf, luc(-23))
   22         dtgo = dabtim(ipp(1,86), ipp(2,1), ipp(3,1), 0,0,0)
   23         dtstop = dabtim(ipp(4,1),ipp(5,1),ipp(6,1),0,0,0)
   24         cfile = cpp(7, 'loctb   ')
   25         call encode( '('  file: ', a8/)', tabuf, cfile)
   26         jp = 0
   27         call getble(cfile, dtgo)
   28         if(dtgo .lt. dtepoc) dtgo = dtepoc + .01d+0
   29         dper = 1.701361111d+0/24.d+0
   30         dtlast = dtepoc
   31         dt = dtgo
   32         dpmin = 1.d+20
   33         dpmax = -dpmin
   34   *
   35         do 100 n = 1,1000000
   36         if(dt .gt. dtstop) go to 102
   37         call getble( cfile, dt)
   38         if(dtepoc .lt. 0.d+0) go to 102
   39         if(dtepoc .le. dtlast) go to 100
   40   *
   41         dlapse = dtepoc - dtlast
   42         norbs = dlapse/dper + .5d+0
   43         jp = jp + 1
   44         dpers(jp) = dlapse/dfloat(norbs)
   45         if(dpers(jp) .gt. dpmax) dpmax = dpers(jp)
   46         if(dpers(jp) .lt. dpmin) dpmin = dpers(jp)
   47         dts(jp) = dtepoc - dtgo
   48         dtlast = dtepoc
   49   100   dt = dt + 1.d+0
   50   *
   51   102   dymean = .5d+0 * (dpmax + dpmin)
   52         call initpl(0,0)
```

```
      xscale = 500.d+0 / (dtepoc - dtso)
      yscale = 400.d+0 / (dpmax - dpmin)
*
      do 110 j = 1,jp
      jyp = 250. - yscale*(dpers(j) - dymean)
      jxp = 50. + xscale*dts(j)
      call plot( jyp,jxp,0)
110   call plot(jyp-1, jxp, 3)
*
      do 112 j = 1,jp
112   call encode( '( i6, 1h., 4x, d20.10, d16.8/)', tabuf,
     1  j, dts(j), dpers(j))
*
      MCOFS = MFIT8(dts, dpers, jp, 3,  VV,AA)
*     The matrix MCOFS contains the desired coefficients.
      kf = 0
*
*     Plot the resulting curve over the scatter.
      do 120 j = 1,20
      jxp = 50. + 25.*float(j-1)
      dpx = float(jxp - 50)/xscale
      dpy = MCOFS(1,1) + dpx*(MCOFS(2,1) + dpx*MCOFS(3,1))
      jyp = 250. - yscale*(dpy - dymean)
      call plot(jyp,jxp,kf)
120   kf = 3
*
      call encode( '( *3d16.8)', tabuf, MCOFS)
      call wrtext( 420, 50, 7, tabuf, 48, 3)
      call encode( '(/)', tabuf)
      call endplt
      call mfstak(0)
      return
      end
```

```
APPENDIX C:


      VECTOR FUNCTION VSADJ*4 (dt,dtorig,dcp,correc)
*
*     To compute predicted satellite positions, maing adjustment for
*     gradual changes in orbital period
*
      Implicit real*8 (d), VECTOR*4(V)
      Parameter( halfpi = .5 * 3.141593)
*
      character*8 correc
      MATRIX*8 (f)MFIT8(3), VV(3,3), AA(35,3), MADCOF(3)
      MATRIX*4 (f)MTRAN4(3,3),ROT(3,3),MXR(3,3)
      VECTOR*4 (f)VEC4,(f)VUNIT4,(f)VBLMOD
      dimension dangs(35),dxs(35),dcp(3)
*
      common/vbl/ dtepoc, elems(6)
      common/tab/tabuf(33)
*
      equivalence(vx(1),mxr(1,1)),(vy(1),mxr(1,2)),(vop(1),mxr(1,3))
*
      data dt1,dt2/ 2 * 0.d+0/, delast/0.d+0/, ROT/ 8*0., 1./
c     xxxxxxxxxxxxxxxxxxxxxxxxxxxxxxxxxxxxxxxxxxxxxxxxxxxxxxxxxxxxxxx
      if(correc .eq. 'off') go to 30
      dx = dt - dtepoc
      dx2 = dx*dx
      if( delast .eq. dtepoc) go to 30
*
*     Get a new estimate of orbital period.
      dtx = dtepoc - dtorig
      if(dtx .lt. 0.d+0) dtx = 0.d+0
      dper = dcp(1) + dtx*(dcp(2) + dtx*dcp(3))  !  estimated period
      call tinver(dtepoc, jy,jm,jd,kh,km,ks,nth)
*
c     Compute lead or lag in future Equator crossings
      do 26 j = 1,35
      dtx = dtepoc + 10.d+0 * dper * dfloat(j-1)
      VBLX = VBLMOD(dtx, slat,slong,cd)  !  Sat pos near Eq crossing
      VOP = VBLX ** VBLMOD(dtx+.01d+0, slat1,slong,cd)
      VEQ = VEC4( vop(1), vop(2), 0.)
      VX = VEQ ** VOP * sign(1., elems(3)-halfpi)
      dxs(j) = dtx - dtepoc  !  times after epoch
26    dangs(j) = angbtw( VX,VBLX) * sign(1., vblx(3))
*
*     ...and get regression coefficients to estimate them.
      MADCOF = -MFIT8( dxs,dangs,35,3,  VV,AA)
*     call encode( '( 6i3, d16.8, d12.4, 2f9.1/ 1h , *3d16.8/)',
*    1  tabuf, jy,jm,jd,kh,km,ks,dper,dangs(35),slat,vblx(3),
*    2  MADCOF)
*
30    VSAT = VBLMOD(dt, slat,slong,cd)  !   unadjusted position
```

XXN

```
53    *
54
55    *       if(correc .eq. 'on') then
56
57            if(dt.lt.dt1 .or. dt.gt.dt2) then  ;  recompute vector orbit
58            dt1 = dt
59            dt2 = dt + .02d+0
60            VOP = VUNIT4( VBLMOD(dt1, slat1,slons1,cd1) **
61           1  VBLMOD(dt2, slat2,slons2,cd2))  ;  unit vector orbital plane
62    *       end if
63
64    *       adj = madcof(1,1) + dx*(madcof(2,1) + dx*madcof(3,1))
65            Angular adjustment which must be made to satellite position
66            VEQ = VEC4( vop(1), vop(2), 0.)
67            VX = VUNIT4( VEQ ** VOP) * sign(1., elems(3)-halfpi)
68    *       VY = VOP ** VX  ;  the matrix MXR is now defined by equivalence
69            MXR converts a vector from celestial to orbital plane coords
70            adj = dx2*adj/(dx2 + 6.d+0)  ;  weights the adjustment
71            rot(1,1) = cosine(adj)
72            rot(2,1) = sine(adj)
73            rot(1,2) = -rot(2,1)
74            rot(2,2) = rot(1,1)
75    *       VADJPO = ROT * MTRAN4(MXR,3,3) * VSAT
76            Adjusted position vector in the plane of the orbit
77    *       VSADJ = MXR * VADJPO  ;  rotate back to celestial coords
78
79            else
80            VSADJ = VSAT
81    *       end if
82
83            delast = dtepoc
84            return
85            end
```

```
//VBLM55RP JOB CLASS=B,MSGLEVEL=(0,0)
//* TRVBLMOD N     03/13/86; MOVED IMPLICIT IN BROLYD
//* TRVBLMOD N     03/06/86; NSC
//* (N)    THIS PROGRAM IS IN THE PUBLIC DOMAIN
//*
//A EXEC MFSUB,OPT=2,COND.EDIT=(0,LT),LANGLVL=77
//FORT.SYSPRINT DD SYSOUT=A
//FORT.SYSIN DD *
C
C      VECTOR SATELLITE POSITION BY BROUWER-LYDDANE MODEL
C
C      VECTOR FUNCTION VBLMOD*4 (DTIME,   FLAT,FLONG,CD)
       SUBROUTINE VBLMOD(DTIME, FLAT,FLONG,CD,   VEC)
C
C      'DTIME' IS THE TIME FOR WHICH A SATELLITE POSITION IS DESIRED,
C      EXPRESSED IN JULIAN DAY NUMBER, WHICH IS NOT, REPEAT, IS NOT
C      THE DAY OF THE YEAR.  'DTIME' MAY BE OBTAINED FROM ORDINARY
C      TIME UNITS (YEAR,MONTH,DAY,HOUR,MINUTE,SECOND) USING THE
C      REAL*8 FUNCTION 'DABTIM'.
C
*      FOR A DEFINITION OF 'JULIAN DAY NUMBER' SEE BOWDITCH,
*     'AMERICAN PRACTICAL NAVIGATOR', PUBLICATION NO. 9,  VOL II,
*      P. 469, (DEFENSE MAPPING AGENCY)
*
C      THE RETURNED VALUES ARE GEOCENTRIC LATITUDE, LONGITUDE,
C      CENTRAL DISTANCE (I.E. FROM CENTER OF EARTH TO SATELLITE,
C      IN KILOMETERS), AND THE CELESTIAL POSITION VECTOR.  THE LATTER
C      IS RETURNED THRU THE FUNCTION NAME IF THIS ROUTINE IS CALLED
C      AS A METEFOR VECTOR-VALUED FUNCTION.
C
C      THE COMMON BLOCK /BLXTRA/ RETURNS THE B-L ELEMENTS UPDATED
C      TO THE GIVEN INPUT TIME.
C
C      THE ORBITAL PARAMETERS MUST ALREADY HAVE BEEN PUT INTO THE
C      COMMON BLOCK /VBL/ BY SOME OTHER ROUTINE, SUCH AS 'VBLSET'
C      OR 'GETBLE'.
C
C      THIS ROUTINE USES THE SAME ORBITAL PREDICTION SOFTWARE USED BY
C      NOAA/NESDIS, AND HENCE CANNOT FAIL TO BE UTTERLY CORRECT.
C
C      DDDDDDDDDDDDDDDDDDDDDDDDDDDDDDDDDDDDDDDDDDDDDDDDDDDDDDDDDDDD
C
       PARAMETER ( DTR = 6.28318530717958D+0/360.D+0)
C
       IMPLICIT REAL*8 (A-H,O-Z)
       REAL*4 GIVENS,VEC(3),VLL(3),FLAT,FLONG,CD
C
       DIMENSION  BLLAST(6), OSCUL(6),AUX(5),
      1  VECPOS(3)
C
       COMMON/BLCNST/ DTSECS,CENDIS,RADEAR,GRAV, DARGS(7)
       COMMON/VBL/ DTEPOC, GIVENS(6)
```

```
      COMMON/BLXTRA/ DTPREP,DBLPRE(6),VECVEL(3)
C
      DATA DTLAST, BLLAST/ -1.D+0, 6*0.D+0/, ANOM/-99999./
C     XXXXXXXXXXXXXXXXXXXXXXXXXXXXXXXXXXXXXXXXXXXXXXXXXXXXXXXXXXXXXXXXXXXXXXX
C
      IF(DTIME .LT. DTEPOC) GO TO 900
C
      DO 10 J = 1,6
10    BLLAST(J) = GIVENS(J)
C
      DTSECS = 86400.D+0 * (DTIME - DTEPOC)
      IF(GIVENS(6).NE.ANOM) CALL BROLYD( OSCUL, BLLAST, 0, 1, 1, AUX)
C     RE-INITIALIZES PREDICTION SOFTWARE IF WE HAVE CHANGED ORBITAL
C     PARAMETERS SINCE THE PRECEDING CALL.
C
      ANOM = GIVENS(6)
      CALL BROLYD( OSCUL, BLLAST, 2, 2, 1, AUX)
C     BROLYD COMPUTES OSCULATING KEPLERIAN VALUES VALID AT TIME
C     DTIME FROM B-L ELEMENTS VALID AT EPOCH 'DTEPOC'.
C
C     RETURN UPDATED B-L ELEMS THRU COMMON /BLXTRA/
      DO 20 J = 1,6
20    DBLPRE(J) = BLLAST(J)
C
      DTPREP = DTIME
C     EPOCH OF PREDICTED PARAMETERS
C
      CALL CELEM(OSCUL, GRAV, VECPOS, VECVEL)
C     CELEM CONVERTS OSCULATING TO CELESTIAL
C
      DO 30 J = 1,3
30    VEC(J) = VECPOS(J)
C
      CALL VCOORD( DTIME,  VEC,  'CLL ',  VLL)
      CD = CENDIS
      FLAT = VLL(1)
      FLONG = VLL(2)
      RETURN
C
900   FLAT = -999999.
      CD = 0.
      VEC(1) = 0.
      VEC(2) = 0.
      VEC(3) = 0.
      RETURN
      END
C     RRRRRRRRRRRRRRRRRRRRRRRRRRRRRRRRRRRRRRRRRRRRRRRRRRRRRRRRRRRRRRRRRRRRRRRR
C
      SUBROUTINE BROLYD
     1 (OSCELE,DPELE,IPERT,IPASS,IDMEAN,OPBEL)
C*****************************************************************************
C*  REF. '' BROUWER-LYDDANE ORBIT GENERATOR ROUTINE''                        *
```

```
C*                    (X-553-70-223)                                    *
C*                 BY E.A. GALBREATH 1970                               *
C*-------------------------------------------------------------------------*
C*  MODIFIED 7/31/74 VIONA BROWN AND R.A. GORDON TO INTERFACE WITH GTDS*
C     FURTHER MODIFIED 11 DEC 85 BY F W NAGLE, NOAA/NESDIS, TO
C     PARAMETERIZE THE FRACTIONAL CONSTANTS FOR GREATER SPEED.
C*************************************************************************
      IMPLICIT REAL*8(A-H,O-Z)
C
      PARAMETER(
     X  F3D8=3.0D0/8.0D0,
     X  F1D2=1.0D0/2.0D0,
     X  F3D2=3.0D0/2.0D0,
     X  F1D4=1.0D0/4.0D0,
     X  F5D4=5.0D0/4.0D0,
     X  F1D8=1.0D0/8.0D0,
     X  F5D12=5.0D0/12.0D0,
     X  F1D16=1.0D0/16.0D0,
     X  F15D16=15.0D0/16.0D0,
     X  F5D24=5.0D0/24.0D0,
     X  F3D32=3.0D0/32.0D0,
     X  F15D32=15.0D0/32.0D0,
     X  F5D64=5.0D0/64.0D0,
     X  F35384=35.0D0/384.0D0,
     X  F35576=35.0D0/576.0D0,
     X  F35D52=35.0D0/1152.0D0,
     X  F1D3=1.0D0/3.0D0,
     X  F5D16=5.0D0/16.0D0)
C
C
      DIMENSION OSCELE(6),DPELE(6),ORBEL(5)
      COMMON /BLCNST/ TTO,R,AE,GM,BJ2,BJ3,BJ4,BJ5,FLTINV,XKE,ESQ
C
      DATA BMU, RE/1.0D+0, 1.0D+0/, BKSUBC/0.01D+0/
      DATA PI2/6.2831853071795860+0/
C
C     XXXXXXXXXXXXXXXXXXXXXXXXXXXXXXXXXXXXXXXXXXXXXXXXXXXXXXXXXXXXXXXXXX
      EK = DSQRT(GM/AE**3)
      DELT = EK*TTO
      GO TO (10,111 ), IPASS
CI-----------------------------I
CI EPOCH ELEMENTS AT EPOCH TIME I
CI-----------------------------I
   10 ADP = DPELE(1)/AE
      EDP = DPELE(2)
      BIDP = DPELE(3)
      HDP = DPELE(4)
      GDP = DPELE(5)
      BLDP = DPELE(6)
      A0 = ADP
      E0 = EDP
      BI0 = BIDP
```

```
      HO = HDP
      GO = GDP
      BLO = BLDP
      IFLG = 0
C----------------------I
C COMPUTE MEAN MOTION I
C----------------------I
      ANU=DSQRT(BMU/AO**3)
C--------------------I
C COMPUTE FRACTIONS I
C--------------------I
      BK2 = -F1D2*(BJ2*RE*RE)
      BK3 = BJ3*RE**3
      BK4 = F3D8*(BJ4*RE**4)
      BK5 = BJ5*RE**5
      GO TO 153
C
111   IF(IPERT.EQ.0)GO TO 7
C
      IF(IDMEAN.NE.0) GO TO 202
C
      ADP = DPELE(1)/AE
      EDP = DPELE(2)
      BIDP = DPELE(3)
      HDP = DPELE(4)
      GDP = DPELE(5)
      BLDP = DPELE(6)
C
153   EDP2=EDP*EDP
      CN2=1.0-EDP2
      CN23 = CN2*CN2*CN2
      CN=DSQRT(CN2)
      GM2=BK2/ADP**2
      GMP2=GM2/(CN2*CN2)
      GM4=BK4/ADP**4
      GMP4=GM4/CN**8
      THETA=DCOS(BIDP)
      THETA2=THETA*THETA
      THETA4=THETA2*THETA2
C
202   IF(IDMEAN.EQ.0)GO TO 155
      IF ( IPASS.EQ.2 ) GO TO 150
C------------------------I
C COMPUTE LDOT,GDOT,HDOT I
C------------------------I
157   BLDOT=CN*ANU*(GMP2*(F3D2*(3.0*THETA2-1)+GMP2*F3D32*(THETA2
     1*(-96.0*CN+30.0-90.0*CN2)+(16.0*CN+25.0*CN2-15.0)+THETA4
     2*(144.0*CN+25.0*CN2+105.0)))+EDP2*GMP4*F15D16*(3.0+35.0*THETA4
     3-30.0*THETA2))
      GDOT=ANU*(F5D16*GMP4*((THETA2*(126.0*CN2-270.0)+THETA4*(385.0
     1-189.0*CN2))-9.0*CN2+21.0)+GMP2*(F3D32*GMP2*(THETA4*(45.0*CN2
     2+360.0*CN+385.0)+THETA2*(90.0-192.0*CN-126.0*CN2)+(24.0*CN
```

```
     3*25.0*CN2-35))+F3D2*(5*THETA2-1)))
      HDOT=ANU*(GMP4*F5D4*THETA*(3.0-7.0*THETA2)*(5.0-3.0*CN2)+GMP2
     1*(GMP2*F3D8*(THETA*(12.0*CN+9.0*CN2-5.0)-THETA*THETA2*(5.0*CN2
     2+36.0*CN+35.0))-3*THETA))
 155 IF(IFLG.EQ.1)GO TO 19
CI-----------------------------------------I
CI COMPUTE ISUBC TO TEST CRITICAL INCLINATION I
CI-----------------------------------------I
      BISUBC=((1.0-5.0*THETA2)**(-2))*((25.0*THETA4*THETA)*(GMP2*EDP2))
      IFLG=1
CI-------------------------------------I
CI FIRST CHECK FOR CRITICAL INCLINATION I
CI-------------------------------------I
      IF(BISUBC.GT.BKSUBC)GO TO 158
      ASSIGN 163 TO ID8
      GO TO 159
C-------------------------------I
C IS THERE CRITICAL INCLINATION I
C-------------------------------I
  19 IF(BISUBC.GT.BKSUBC)GO TO 150
 159 IF(IPERT.EQ.1)GO TO 150
      GM3=BK3/ADP**3
C     GMP3=GM3/(CN2*CN2*CN2)
      GMP3=GM3/CN23
      GM5=BK5/ADP**5
      GMP5=GM5/CN**10
      G3DG2=GMP3/GMP2
      G4DG2=GMP4/GMP2
      G5DG2=GMP5/GMP2
CI---------------I
CI COMPUTE A1-A8 I
CI---------------I
      A1=(F1D8*GMP2*CN2)*(1.0-11.0*THETA2-((40.0*THETA4)/(1.0-5.0*THETA2
     1)))
      A2=(F5D12*G4DG2*CN2)*(1.0-((8.0*THETA4)/(1.0-5.0*THETA2))-3.0
     1*THETA2)
      A3=G5DG2*((3.0*EDP2)+4.0)
      A4=G5DG2*(1.0-(24.0*THETA4)/(1.0-5.0*THETA2)-9.0*THETA2)
      A5=(G5DG2*(3.0*EDP2+4.0))*(1.0-(24.0*THETA4)/(1.0-5.0*THETA2)-9.0
     1*THETA2)
      A6=G3DG2*F1D4
      SINI=DSIN(BIDP)
      A10=CN2*SINI
      A7=A6*A10
      A8P=G5DG2*EDP*(1.0-(16.0*THETA4)/(1.0-5.0*THETA2)-5.0*THETA2)
      A8=A8P*EDP
C
C     COMPUTE B13-B15
C
      B13=EDP*(A1-A2)
      B14=A7+F5D64*A5*A10
      B15=A8*A10*F35384
```

```
C
C    COMPUTE A11-A27
C
      A11=2.0*EDP2
      A12=3.0*EDP2+2.0
      A13=THETA2*A12
      A14=(5.0*EDP2+2.0)*(THETA4/(1.0-5.0*THETA2))
      A17=THETA4/((1.0-5.0*THETA2)*(1.0-5.0*THETA2))
      A15=(EDP2*THETA4*THETA2)/((1.0-5.0*THETA2)*(1.0-5.0*THETA2))
      A16=THETA2/(1.0-5.0*THETA2)
      A18=EDP*SINI
      A19=A18/(1.0+CN)
      A21=EDP*THETA
      A22=EDP2*THETA
      SINI2=DSIN(BIDP/2.0)
      COSI2=DCOS(BIDP/2.0)
      TANI2=DTAN(BIDP/2.0)
      A26=16.0*A16+40.0*A17+3.0
      A27=A22*F1D8*(11.0+200.0*A17+80.0*A16)
CI----------------I
CI COMPUTE B1-B12 I
CI----------------I
      B1=CN*(A1-A2)-((A11-400.0*A15-40.0*A14-11.0*A13)*F1D16+(11.0+200.0
     1*A17+80.0*A16)*A22*F1D8)*GMP2+((-80.0*A15-8.0*A14-3.0*A13+A11)
     2*F5D24+F5D12*A26*A22)*G4DG2
      B2=A6*A19*(2.0+CN-EDP2)+F5D64*A5*A19*CN2-F15D32*A4*A18*CN*CN2
     1+(F5D64*A5+A6)*A21*TANI2+(9.0*EDP2+26.0)*F5D64*A4*A18+F15D32*A3
     2*A21*A26*SINI*(1.0-THETA)
      B3=((80.0*A17+5.0+32.0*A16)*A22*SINI*(THETA-1.0)*F35576*G5DG2*EDP)
     1-((A22*TANI2+(2.0*EDP2+3.0*(1.0-CN2*CN))*SINI)*F35D52*A8P)
      B4=CN*EDP*(A1-A2)
      B5=((9.0*EDP2+4.0)*A10*A4*F5D64+A7)*CN
      B6=F35384*A8*CN2*CN*SINI
      B7=((CN2*A18)/(1.0-5.0*THETA2))*(F1D8*GMP2*(1.0-15.0*THETA2)+(1.0
     1-7.0*THETA2)*G4DG2*(-F5D12))
      B8=F5D64*(A3*CN2*(1.0-9.0*THETA2-(24.0*THETA4/(1.0-5.0*THETA2))))
     1+A6*CN2
      B9=A8*F35384*CN2
      B10=SINI*(A22*A26*G4DG2*F5D12-A27*GMP2)
      B11=A21*(A5*F5D64+A6+A3*A26*F15D32*SINI*SINI)
      B12=-((80.0*A17+32.0*A16+5.0)*(A22*EDP*SINI*SINI*F35576*G5DG2)+(A8
     1*A21*F35D52))
  150 IF(IPERT.EQ.0)GO TO 7
      IF(IDMEAN.EQ.0)GO TO 4
C-----------------------I
C COMPUTE SECULAR TERMS I
C-----------------------I
CI-----------------------I
CI **MEAN** MEAN ANOMALY I
CI-----------------------I
      BLDP = ANU*DELT + BLDOT*DELT + BL0
      BLDP = DMOD(BLDP,PI2)
```

```
      IF(BLDP.LT.0.0D0)BLDP = BLDP + PI2
CI----------------------------I
CI  MEAN ARGUMENT OF PERIGEE I
CI----------------------------I
      GDP = GDOT*DELT  + G0
      GDP = DMOD(GDP,PI2)
      IF(GDP.LT.0.0D0)GDP = GDP + PI2
C    MEAN LONGITUDE OF ASCENDING NODE
      HDP = HDOT*DELT + H0
      HDP = DMOD(HDP,PI2)
      IF(HDP.LT.0.0D0)HDP = HDP + PI2
C
    4 DO 33 NN=1,6
   33 OSCELE(NN) = DPELE(NN)
C
      A = ADP
      E = EDP
      BI = BIDP
      H = HDP
      G = GDP
      BL = BLDP
CI-------------------------------------I
CI COMPUTE TRUE ANOMALY(DOUBLE PRIMED) I
CI-------------------------------------I
      EADP = DKEPLR(BLDP,EDP)
      SINDE= DSIN(EADP)
      COSDE= DCOS(EADP)
      SINFD= CN*SINDE
      COSFD= COSDE - EDP
      FDP = DATAN0(SINFD,COSFD)
      IF(IPERT.EQ.1) GO TO 7
C
C     DADR=(1.0-EDP*COSDE)**(-1)
      DADR = 1.D+0 / (1.D+0 - EDP*COSDE)
      SINFD=SINFD*DADR
      COSFD=COSFD*DADR
      CS2GFD=DCOS(2.0*GDP+2.0*FDP)
      DADR2=DADR*DADR
      DADR3=DADR2*DADR
      COSFD2=COSFD*COSFD
CI---------------------------I
CI COMPUTE A(SEMI-MAJOR AXIS) I
CI---------------------------I
      A=ADP*(1.0+GM2*((3.0*THETA2-1.0)*(EDP2/CN23)*(CN+(1.0/(1.
     1+CN)))+((3.0*THETA2-1.0)/CN23)*(EDP*COSFD)*(3.0+3.0*EDP
     2*COSFD+EDP2*COSFD2)+3.0*(1.0-THETA2)*DADR3*CS2GFD))
      SN2GFD=DSIN(2.0*GDP+2.0*FDP)
      SNF2GD=DSIN(2.0*GDP+FDP)
      CSF2GD=DCOS(2.0*GDP+FDP)
      SN2GD=DSIN(2.0*GDP)
      CS2GD=DCOS(2.0*GDP)
      SN3GD=DSIN(3.0*GDP)
```

```
      CS3GD=DCOS(3.0*GDP)
      SN3FGD=DSIN(3.0*FDP+2.0*GDP)
      CS3FGD=DCOS(3.0*FDP+2.0*GDP)
      SINGD=DSIN(GDP)
      COSGD=DCOS(GDP)
      GO TO ID8,(163,164)
  163 DLT1E=B14*SINGD+B13*CS2GD-B15*SN3GD
CI-------------------------I
CI COMPUTE (L+G+H) PRIMED I
CI-------------------------I
      BLGHP=HDP+GDP+BLDP+B3*CS3GD+B1*SN2GD+B2*COSGD
      BLGHP=DMOD(BLGHP,PI2)
      IF(BLGHP.LT.0.0D0)BLGHP=BLGHP+PI2
      EDPDL=B4*SN2GD-B5*COSGD+B6*CS3GD-F1D4*CN2*CN*GMP2*(2.0*(3.0*THETA2
     1-1.0)*(DADR2*CN2+DADR+1.0)*SINFD+3.0*(1.0-THETA2)*((-DADR2*CN2
     2-DADR+1.0)*SNF2GD+(DADR2*CN2+DADR+F1D3)*SN3FGD))
      DLTI=F1D2*THETA*GMP2*SINI*(EDP*CS3FGD+3.0*(EDP*CSF2GD+CS2GFD))
     1-(A21/CN2)*(B8*SINGD+B7*CS2GD-B9*SN3GD)
      SINDH=(1.0/COSI2)*(F1D2*(B12*CS3GD+B11*COSGD+B10*SN2GD-(F1D2*GMP2
     1*THETA*SINI*(6.0*(EDP*SINFD-BLDP+FDP)-(3.0*(SN2GFD+EDP*SNF2GD)+EDP
     2*SN3FGD)))))
CI-----------------I
CI COMPUTE (L+G+H) I
CI-----------------I
  164 BLGH=BLGHP+((1.0/(CN+1.0))*F1D4*EDP*GMP2*CN2*(3.0*(1.0-THETA2)*
     1(SN3FGD*(F1D3+DADR2*CN2+DADR)+SNF2GD*(1.0-(DADR2*CN2+DADR)))+2.0*
     2SINFD*(3.0*THETA2-1.0)*(DADR2*CN2+DADR+1.0)))+GMP2*F3D2*((-2.0*
     3THETA-1.0+5.0*THETA2)*(EDP*SINFD+FDP-BLDP))+(3.0+2.0*THETA-5.0*
     4THETA2)*(GMP2*F1D4*(EDP*SN3FGD+3.0*(SN2GFD+EDP*SNF2GD)))
      BLGH=DMOD(BLGH,PI2)
      IF(BLGH.LT.0.0D0)BLGH=BLGH+PI2
      DLTE=DLT1E+(F1D2*CN2*((3.0*(1.0/CN23)*GM2*(1.0-THETA2)
     1*CS2GFD*(3.0*EDP*COSFD2+3.0*COSFD+EDP2*COSFD*COSFD2+EDP))-(GMP2
     2*(1.0-THETA2)*(3.0*CSF2GD+CS3FGD))+(3.0*THETA2-1.0)*GM2*(1.0/
     3CN23)*(EDP*CN+(EDP/(1.0+CN))+3.0*EDP*COSFD2+3.0*COSFD+
     4EDP2*COSFD*COSFD2)))
      EDPDL2=EDPDL*EDPDL
      EDPDE2=(EDP+DLTE)*(EDP+DLTE)
CI-------------------------I
CI COMPUTE E(ECCENTRICITY) I
CI-------------------------I
      E=DSQRT(EDPDL2+EDPDE2)
      SINDH2=SINDH*SINDH
      SQUAR=(DLTI*COSI2*F1D2+SINI2)*(DLTI*COSI2*F1D2+SINI2)
      SQRI=DSQRT(SINDH2+SQUAR)
CI-------------------------I
CI COMPUTE BI (INCLINATION) I
CI-------------------------I
      BI=DARSIN(SQRI)
      BI=2.0*BI
      BI=DMOD(BI,PI2)
      IF(BI.LT.0.0D0)BI=BI+PI2
```

```
417   CI-----------------------------I
418   CI CHECK FOR E(ECCENTRICITY)=0 I
419   CI-----------------------------I
420         IF(E.NE.0.0) GO TO 168
421         BL=0.0
422   CI-----------------------------I
423   CI CHECK FOR BI(INCLINATION)=0 I
424   CI-----------------------------I
425     145 IF(BI.NE.0.0) GO TO 169
426         H=0.0
427   CI---------------------------------I
428   CI COMPUTE G(ARGUMENT  OF PERIGEE) I
429   CI---------------------------------I
430     146 G=BLGH-BL-H
431         G=DMOD(G,PI2)
432         IF(G.LT.0.0D0)G=G+PI2
433   CI----------------------I
434   CI COMPUTE TRUE ANOMALY I
435   CI----------------------I
436         EA    = DKEPLR(BL,E)
437         ARG1 = DSIN(EA) * DSQRT(1.0-E**2)
438         ARG2 = DCOS(EA) - E
439         F = DATAN0(ARG1,ARG2)
440   C
441         OSCELE(1) = A*AE
442         OSCELE(2) = E
443         OSCELE(3) = BI
444         OSCELE(4) = H
445         OSCELE(5) = G
446         OSCELE(6) = BL
447   C
448   7     DPELE(1) = ADP*AE
449         DPELE(2) = EDP
450         DPELE(3) = BIDP
451         DPELE(4) = HDP
452         DPELE(5) = GDP
453         DPELE(6) = BLDP
454         IF(IPERT.EQ.0)BL = DMOD(ANU*DELT,PI2)
455         ORBEL(1) = EADP
456         ORBEL(2) = GDP + FDP
457         ORBEL(3) = GDP
458         ORBEL(4) = EK*(ANU + BLDOT)
459         ORBEL(5) = FDP
460         R = A*AE*(1.0D0 - E*DCOS(EA))
461         GO TO 45
462   CI-----------------------------------------I
463   CI MODIFICATIONS FOR CRITICAL INCLINATION I
464   CI-----------------------------------------I
465     158 DLT1E=0.0
466         BLGHP=0.0
467         EDPDL=0.0
468         DLTI=0.0
```

```
      SINDH=0.0
      ASSIGN 164 TO ID8
      GO TO 150
  168 SINLDP=DSIN(BLDP)
      COSLDP=DCOS(BLDP)
      SINHDP=DSIN(HDP)
      COSHDP=DCOS(HDP)
CI-------------------------I
CI COMPUTE L(MEAN ANOMALY) I
CI-------------------------I
      ARG1=EDPDL*COSLDP+(EDP+DLTE)*SINLDP
      ARG2=(EDP+DLTE)*COSLDP-(EDPDL*SINLDP)
      BL=DATAN2(ARG1,ARG2)
      BL=DMOD(BL,PI2)
      IF(BL.LT.0.0D0)BL=BL+PI2
      GO TO 145
CI-------------------------------------I
CI COMPUTE H(LONGITUDE OF ASCENDING NODE) I
CI-------------------------------------I
  169 ARG1=SINDH*COSHDP+SINHDP*(F1D2*DLTI*COSI2+SINI2)
      ARG2=COSHDP*(F1D2*DLTI*COSI2+SINI2)-(SINDH*SINHDP)
      H=DATAN2(ARG1,ARG2)
      H=DMOD(H,PI2)
      IF(H.LT.0.0D0)H=H+PI2
      GO TO 146
   45 CONTINUE
      RETURN
      END
C
C     RRRRRRRRRRRRRRRRRRRRRRRRRRRRRRRRRRRRRRRRRRRRRRRRRRRRRRRRRRRRRRRR
      SUBROUTINE CELEM (ORBEL,GMC,PV,VV)
C   ORIGINAL VERSION ...1/22/71....CHARLES K. CAPPS
C   PURPOSE:
C       THIS ROUTINE CONVERTS CLASSICAL OSCULATING ORBITAL ELEMENTS
C       TO CARTESIAN ELEMENTS.
C   CALLING SEQUENCE:
C       CALL CELEM(ORBEL,GMC,PV,VV)
C   INPUT THRU ARGUMENT LIST:
C       ORBEL(1) = SEMI-MAJOR AXIS,A  (OSCULATING ELEMENTS)
C       ORBEL(2) = ECCENTRICITY, E
C       ORBEL(3) = INCLINATION, I
C       ORBEL(4) = LONGITUDE OF ASCENDING NODE, CAP OMEGA
C       ORBEL(5) = ARGUMENT OF PERIFOCUS, OMEGA
C       ORBEL(6) = MEAN ANOMALY, M
C       GMC = GRAVITATIONAL CONSTANT
C   OUTPUT THRU ARGUMENT LIST:
C       PV = CARTESIAN POSITION VECTOR
C       VV = CARTESIAN VELOCITY VECTOR
C   METHOD:
C       USES MILES STANDISH ITERATIVE SCHEME FOR SOLN TO KEPLERS EQN.
C   REFERENCES:
C       GTDS TASK SPEC FOR CELEM, C.E. VELEZ, 13 JANUARY 1971
```

```
C       DOOS SYSTEM DESCRIPTION, SUBROUTINE KEPLR1
C       P. EXCOBAL-"METHODS OF ORBIT DETERMINATION"
C       X-552-67-421,"COMPARISON FO ITERATIVE TECHNIQUES FOR THE
C       SOLUTION OF KEPLERS EQUATION", I.COLE AND R. BORCHERS
C   PROGRAMMER:
C       CHARLES K. CAPPS,  CODE 553.2.  GSFC
C
        IMPLICIT REAL*8(A-H,O-Z)
C
        DATA MAX /10/
        DIMENSION PV(3),VV(3),ORBEL(6)
        DATA TOL /+0.5D-16/
C
        ITER = 0
C       FIND IF THIS IS ELLIPTIC OR HYPERBOLIC ORBIT
        IF (ORBEL(1).LE.0.0D0.AND.ORBEL(2).GT.1.0D0) GO TO 50
C
C       ELLIPTIC ORBIT TAKES THIS ROUTE.
C       FIRST FIND ECCENTRIC ANOMALY VIA NEWTONS (MILES STANDISH VERSION)
        E1 = ORBEL(6)
   10   F = E1 - (ORBEL(2) * DSIN(E1)) - ORBEL(6)
        D = 1.0D0 - (ORBEL(2) * DCOS(E1 - 0.5D0 * F))
        E2 = E1 - (F / D)
        IF (DABS (E1-E2)-TOL )40,40,20
   20   ITER = ITER + 1
        E1 = E2
        IF(ITER - MAX) 10,10,30
C       SET UP ERROR CODE TO RETURN FROM SUBROUTINE
   30   NERR = 13
C       ECCENTRIC ANOMALY CONVERGED, NOW GET XO, YO, R
   40   COSE = DCOS(E2)
        SINE = DSIN (E2)
        TEMP = 1.0D0 - ORBEL(2) * ORBEL(2)
        XO = ORBEL(1) * (COSE - ORBEL(2))
        YO = ORBEL(1) * (DSQRT(TEMP)* SINE)
        R = ORBEL(1) * (1.0D0 - ORBEL(2) * COSE)
        XOD = (-DSQRT(GMC* ORBEL(1))* SINE)/R
        YOD = (DSQRT(GMC*ORBEL(1)*(TEMP))*COSE) / R
        GO TO 100
C
C       HYPERBOLIC ORBITS TAKE THIS ROUTE
   50   E1 = ORBEL(6) / 2.0D0
   60   F = ORBEL(2) * DSINH(E1) - E1 - ORBEL(6)
        D = ORBEL(2) * DCOSH(E1 - 0.5D0 * F ) - 1.0D0
        E2 = E1 - (F / D)
        IF (DABS (E1-E2)-TOL )90,90,70
   70   ITER = ITER + 1
        E1 = E2
        IF (ITER - MAX) 60,60,80
C        SET UP ERROR CODE FOR NON-CONVERGENCE PRIOR TO EXIT.
   80   NERR = 14
C       ECCENTRIC ANOMALY COMPUTED, NOW GET XO,YO,R
```

```
      90 COSE = DCOSH (E2)
         SINE = DSINH(E2)
         TEMP = ORBEL(2) * ORBEL(2) - 1.0D0
         XO = ORBEL(1)*(COSE- ORBEL(2))
         YO = - ORBEL (1)*DSQRT (TEMP) * SINE
         R = ORBEL(1)*(1.0D0 - ORBEL(2) * COSE)
         XOD = (-DSQRT(-GMC*ORBEL(1))*SINE)/R
         YOD = (DSQRT(-GMC*ORBEL(1)*TEMP)*COSE) / R
     100 COSO = DCOS(ORBEL(5))
         SINO = DSIN (ORBEL(5))
         COSOM = DCOS (ORBEL(4))
         SINOM = DSIN (ORBEL(4))
         COSI = DCOS(ORBEL(3))
         SINI = DSIN (ORBEL(3))
         B11 = COSO * COSOM - SINO * SINOM * COSI
         B21 = COSO * SINOM + SINO * COSOM * COSI
         B31 = SINO * SINI
         B12 = -SINO * COSOM - COSO * SINOM * COSI
         B22 = -SINO * SINOM + COSO * COSOM * COSI
         B32 = COSO * SINI
C        NOW MULTIPLY 3 X 2 MARTIX BY 2 X 1 VECTORS FOR POSITION, VELOCITY.
         PV(1) = B11 * XO + B12 * YO
         PV(2) = B21 * XO + B22 * YO
         PV(3) = B31 * XO + B32 * YO
         VV (1) = B11*XOD + B12 * YOD
         VV(2) = B21 * XOD + B22 * YOD
         VV(3) = B31 * XOD + B32 * YOD
     999 RETURN
         END
C
C        RRRRRRRRRRRRRRRRRRRRRRRRRRRRRRRRRRRRRRRRRRRRRRRRRRRRRRRR
         BLOCK DATA
         IMPLICIT REAL*8 (A-H,O-Z)
C
C    NAME- BLCNST
C
C    LANGUAGE- FORTHXP      TYPE- PROGRAM
C
C    THIS COMMON BLOCK WAS UPDATED MARCH 28, 1984 TO INCLUDE XKE AND ESQ
C     BY E. HARROD S/SP12
C    THIS BLOCK DATA IS COMPILED WITH THE ROUTINE PSCEAR, ANY PROGRAM
C     USING PSCEAR DOES NOT NEED TO RECOMPILE THIS BLOCK DATA
C
C*****************************************************************************
C
         COMMON/BLCNST/ TTO,R,AE,GM,BJ2,BJ3,BJ4,BJ5,FLTINV,XKE,ESQ
C
         DATA TTO,R,GM,AE,BJ2,BJ3,BJ4,BJ5,FLTINV,XKE,ESQ/2*0.D0,
        * 398600.8D0,6378.135D0,-0.10826158D-02,0.25388100D-05,
        * 0.16559700D-05,0.21848266D-06,298.25D0,0.743669161D-01,
        * 0.6994317778266721D-02/
         END
```

```
      C
      C     XXXXXXXXXXXXXXXXXXXXXXXXXXXXXXXXXXXXXXXXXXXXXXXXXX
            REAL FUNCTION DATAN0*8 (DA,DB)
            IMPLICIT REAL*8 (A-H,0-Z)
      C
            DATA PI2/6.2831853071795860+0/
      C
            DA = DATAN2(DA,DB)
            IF(DA .LT. 0.D+0) DA = DA + PI2
            DATANC = DA
            RETURN
            END
      C     RRRRRRRRRRRRRRRRRRRRRRRRRRRRRRRRRRRRRRRRRRRRRRRRRRRRRRRRR
      C
            FUNCTION DKEPLR(M,E)
            IMPLICIT REAL*8(A-H,0-Z)
            REAL*8 M,PI2/6.283185307179586D0/,TOL/0.5D-15/
      C
      C           SUBROUTINE TO SOLVE KEPLER'S EQ.
      C  KEPLER'S EQ.,RELATES GEOMETRY OR POSITION IN ORBIT PLANE TO TIME.
      C
      C M - MEAN ANOMALY (0<M<2PI)
      C E - ECCENTRICITY
      C EA- ECCENTRIC ANOMALY
      C
            EA=0
            IF(M)1,2,1
          1 EA=M + E*DSIN(M)
            DO 22 I=1,12
            OLDEA=EA
            FE=EA-E*DSIN(EA)-M
            EA=EA-FE/(1-E*DCOS(EA-0.5D0*FE))
      C TEST FOR CONVERGENCE
            DELEA=DABS(EA-OLDEA)
            IF(DELEA.LE.TOL)GO TO 2
         22 CONTINUE
          2 EA=DMOD(EA,PI2)
            DKEPLR=EA
            RETURN
            END
      /*
      //EDIT.SYSPRINT DD SYSOUT=A
      //EDIT.SYSIN DD *
       NAME VBLMOD(R)
      /*
      //
```

ESTHER PRODUCTS FOR TOVS PROCESSING IMPROVEMENT

T. Phulpin

Centre National de Recherches Meteorologiques
42 avenue G. Coriolis
31057 Toulouse , FRANCE

1. INTRODUCTION

The aim of this work is to show the interest of AVHRR products in inversion scheme improvement and particularly for the 3I method developed by Chedin et al.(1985). The AVHRR high resolution imagery can be used to give a description of the different surfaces within each HIRS footprint and products like surface temperature, relative percentage of land and sea, total cloudiness and spectral cloud features should improve the reliability of the satellite profiles.
An improved version of ESTHER (Phulpin et al.,1983) has been applied to the AVHRR data within HIRS ellipses for the Alpex orbit NOAA 7 3587.
In the first part we examine the results and show the necessity to screen them to get reliable products. In a second part we discuss the reasons for erroneous classifications in ESTHER and propose some tests to filter the results . In the last part we give a way ESTHER products can be used to improve the 3I method.

2. ESTHER RESULTS

The principles of the method has been described in Phulpin et al. (1983). In the new version, instead of rectangles of 33 pixels by 38 lines, the arrays are made of the AVHRR pixels registered in the HIRS field of view (Rochard,1985). As these sets are 2 to 3 times smaller, the thresholds used in the procedure have been modified. Furthermore, the number of outputs has been changed to provide a better description of all the clusters and the unsorted pixels as well. Some outputs are displayed in Figure 1.
In some cases, along the coasts, cloud clusters temperature is warmer than sea surface temperature, indicating an error in the atlas index. For some "sea" arrays the sea surface temperatures are obviously colder than in the surrounding arrays, showing a misclassification of the observed surfaces. At least, over the land, cloudfree, partly cloudy and overcast HIRS spots have to be clearly identified. To summerize, ESTHER outputs have to be screened before being used in an inversion procedure.

3. ESTHER CORRECTIONS

3.1 Atlas index correction

The atlas index has been recomputed using the following rules :

- Land spots which are very homogeneous and exhibit an averaged reflectance lower than 8% are reclassified as "sea" spots;
- Sea spots where a cluster is characterized by a high reflectance and a temperature warmer than for the "sea" cluster are

reclassified as "coast" spots if the averaged reflectance in channel 2 is higher than in channel 1. The final map of coast contours is shown in Figure 2. The shift between the initial and the final contour is due to the navigation error and to the way of using the atlas.

3.2 Screening of cloudy "sea" spots

The comparison with the results of the previous version of ESTHER applied to the same data indicates that the number of erroneous classifications has been strongly increased mainly in cirrus and small clouds areas since the array size has been reduced. The reason is that in ESTHER, as with most stastistical methods, the warmest and blackest surface is "a priori" considered as the sea. In fact this is only valuable in large arrays where the probability to meet cloudfree pixels is high. In the HIRS FOV, if there are no cloudfree pixels, cirrus covered pixels which have a very low reflectance are considered as clear.
To reject the erroneous results a threshold method has been preferred to any smoothing method. Some of the thresholds have been set constant (for $T_{11} - T_{12}$ and for N the total cloudiness). A test with $T_{3.7} - T_{12}$ has proven to be very efficient to reject cirrus covered pixels (e.g Liljas,1986). In this situation with a large sunglint area, the threshold can't be a constant, but neither can be simulated. Indeed, high 3.7 µm reflectances are observed in the southeast of the image where the simulation gives low reflectance values. This is probably due to the scattering of the clouds. The thresholds are finally given by this method :

i) A map of well classified spots is drawn. It is made of absolutely clear spots which are very homogeneous and have a low reflectance and partly cloudy spots where the cloud clusters characteristics are very different from those of the surface.
ii)The maximum value of $T_{3.7} - T_{12}$ for the well-classified spots in a large box of 20 HIRS lines and 8 columns is used to fix the threshold. The map of thresholds is given in Figure 3.

The final map of the clear and partly cloudy "sea" spots is displayed in Figure 4. The total number of these spots appears somewhat small when looking at the image. A careful comparison with the results of a visual analysis of the images indicates a slight overestimation of the cloudiness which is preferable to an underestimation which could not be avoided otherwise. A real improvement will result from applying ESTHER to larger sets of data, classifying the different observed surfaces, and associating each AVHRR pixel in a HIRS spot to the closest cluster.

3.3 Cloud clearing over land

The warmest cluster in a spot is assumed to correspond to the cloudfree part of the spot. The overcast spots are screened by using thresholds on $T_{35} = (T_{3.7} - T_{12})/\cos\theta_s$ and PVI which is a pseudo vegetation index computed with the averaged reflectance in channels 1 and 2. The thresholds used for PVI depend on the latitude and those for T_{35} depend on the vegetation as well.

Shadow areas exhibit low values for PVI and $T_{3.5}$ but are identified thanks to their very low reflectance. The final map of land brightness temperatures is illustrated in Figure 5.

4 . ESTHER PRODUCTS IN THE INVERSION

Some ESTHER products can be used in the 3I method to improve the research of the closest profile in the TIGR data set. They can also be used to control 3I results. The most useful ESTHER products would be :

i) surface brightness temperature and moreover the actual surface temperature and the surface spectral emissivity;
ii) total cloudiness (the number of contaminated AVHRR pixels) or the effective cloudiness N' when possible;
iii) cloud type : cirriform clouds, one layer clouds,cumuliform clouds, cumulonimbus and precipitation areas;
iv)the atlas localisation ,i.e the relative percentage of land and sea and so on.

On the other hand ESTHER products can be used to retrieve the clear column radiances. This will be studied in the next months.

5 . CONCLUSION

The main conclusions concern first the array size required to get reliable results with a two dimensional method like ESTHER. It has been shown that this method should preferably be applied to large arrays (e.g 200 by 200 pixels) and the pixels within a HIRS FOV must be classified using an automatic classification method. The second conclusion concerns the usefulness of the channel 3 to discern the cirrus or thin aerosol contaminated spots. It has been shown that thresholds applied to $T_{3.7} - T_{12}$ cannot be accurately simulated and that they have to be derived from the values obtained in the well-classified spots.

6 . REFERENCES

A. Chedin, N. A. Scott, C. Wahiche, P. Moulinier, 1985 : The Improved Initialization Inversion Method : A High Resolution Physical Method for Temperature Retrievals from Satellites of the TIROS N Series, J. Climate Appl. Meteor.,**24**, 128-143

E. Liljas, 1986 : Use of AVHRR 3.7 micrometer Channel in Multispectral Cloud Classification, SMHI Promis Rapporter, Norkopping Sweden

T. Phulpin, M. Derrien, A. Brard, 1983 : A Two Dimensional Histogram Procedure to Analyze Cloud Cover from NOAA Satellite High Resolution Imagery, J. Climate Appl. Meteor.,**22**, 1332-1345

G. Rochard, 1985 : Personal Communication

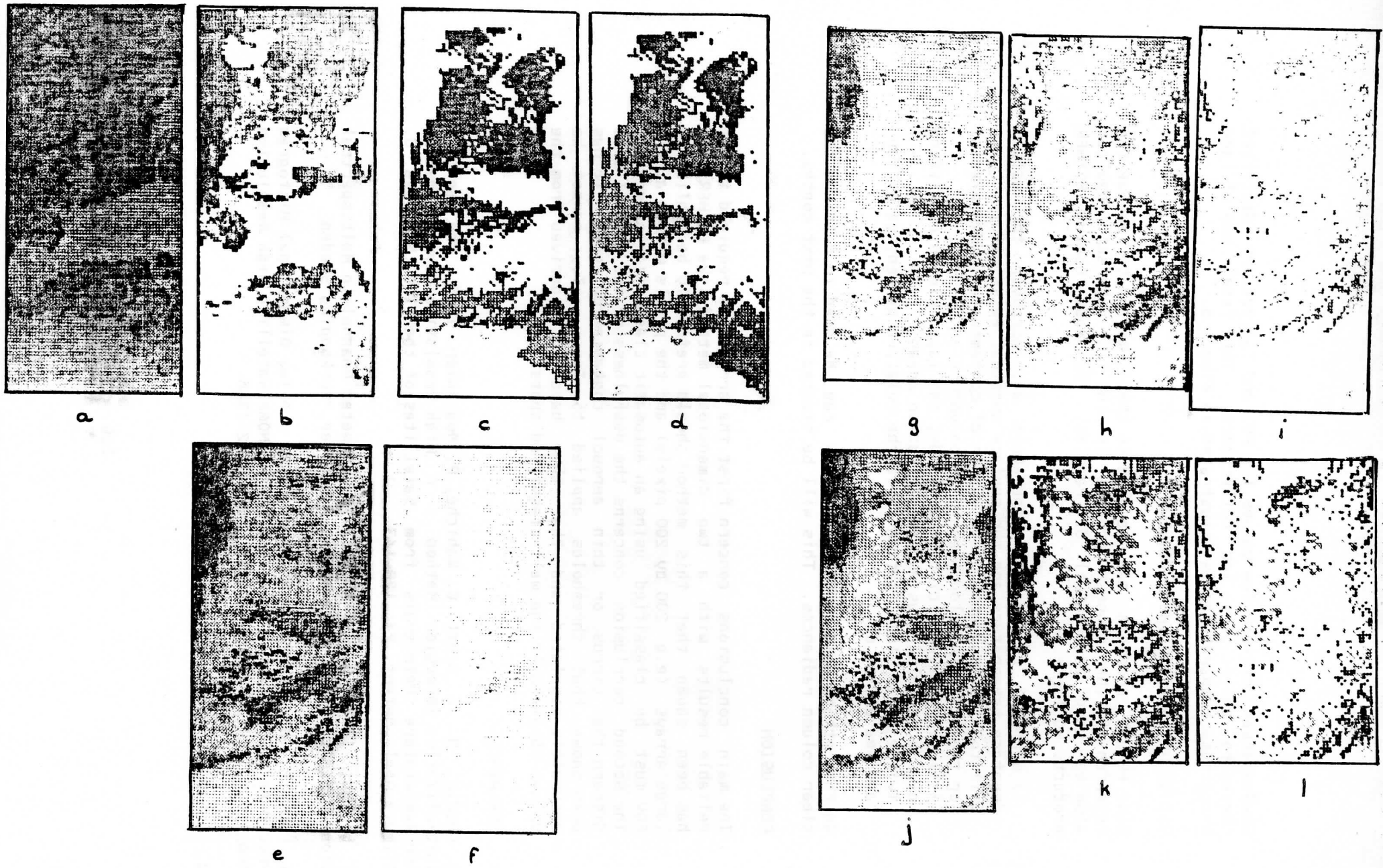

Fig. 1: Some ESTHER outputs (N7-3587). (a) Atlas index; (b) total cloudiness; (c) surface temp. (ch. 4); (d) (ch. 3); (e) HIRS ch. 8; (f) HIRS ch. 19; (g) 11μm cloud temp (level 1); (h) (level 2); (i) (level 3); (j) 3.7μm cloud temp (level 1); (k) (level 2); (l) (level 3).

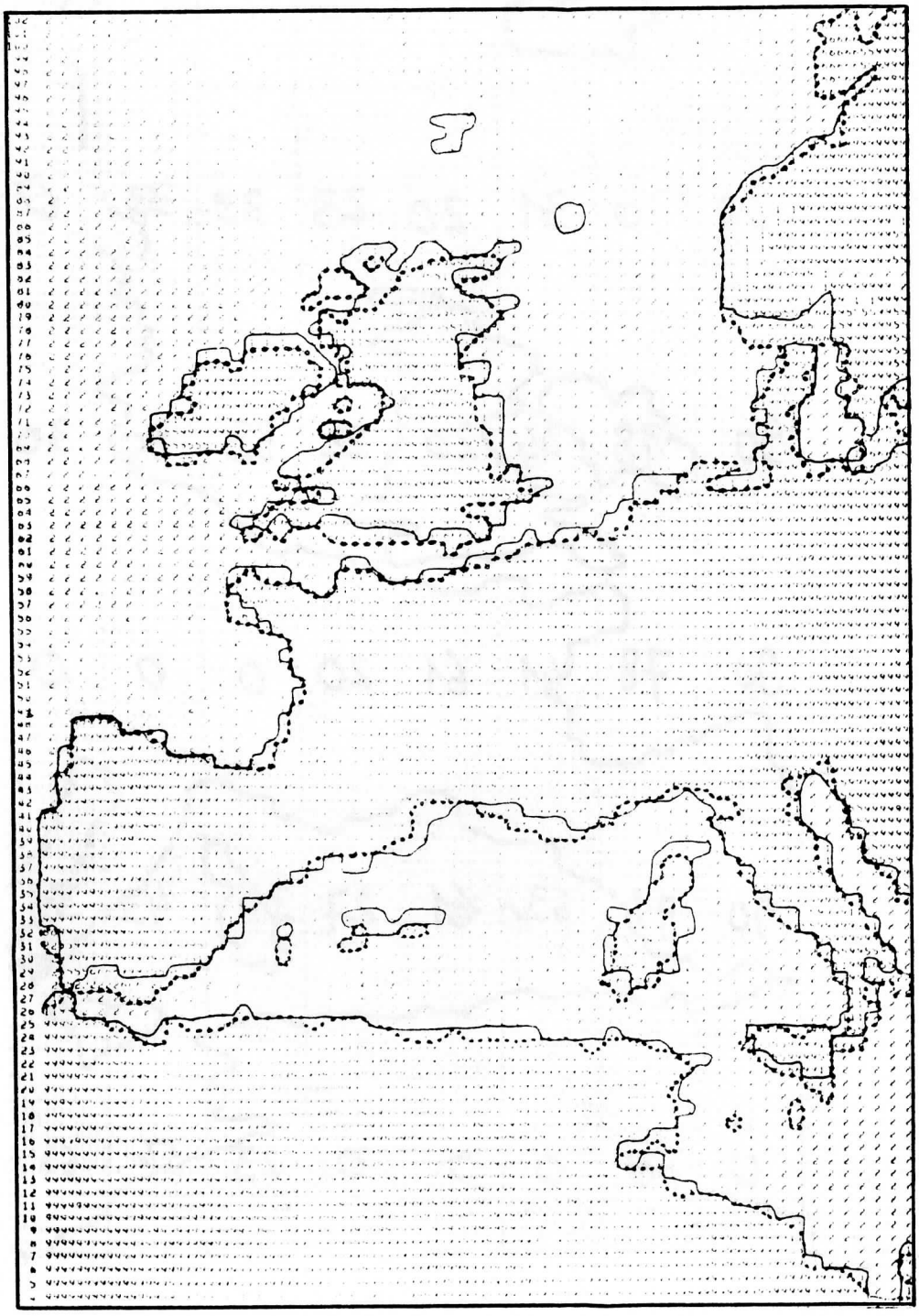

Fig. 2: Coast Contours —— initial (from orbit parameters and Atlas)
.... final (from ESTHER)

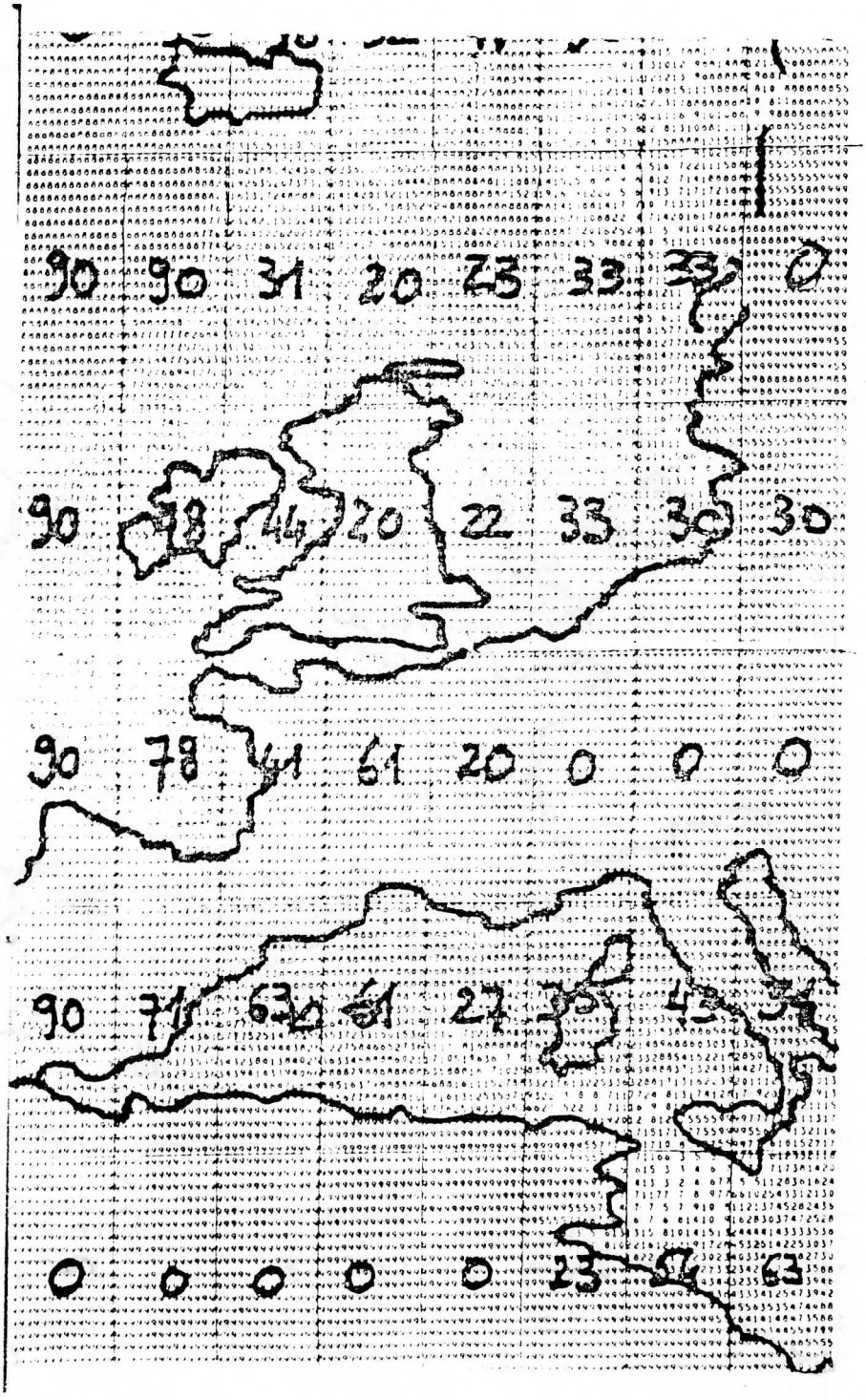

Fig. 3: $T_{3.7} - T_{12}$ thresholds for N7-3587.

Fig. 4: ESTHER final results -- clear or partly cloudy "sea" spots (■).

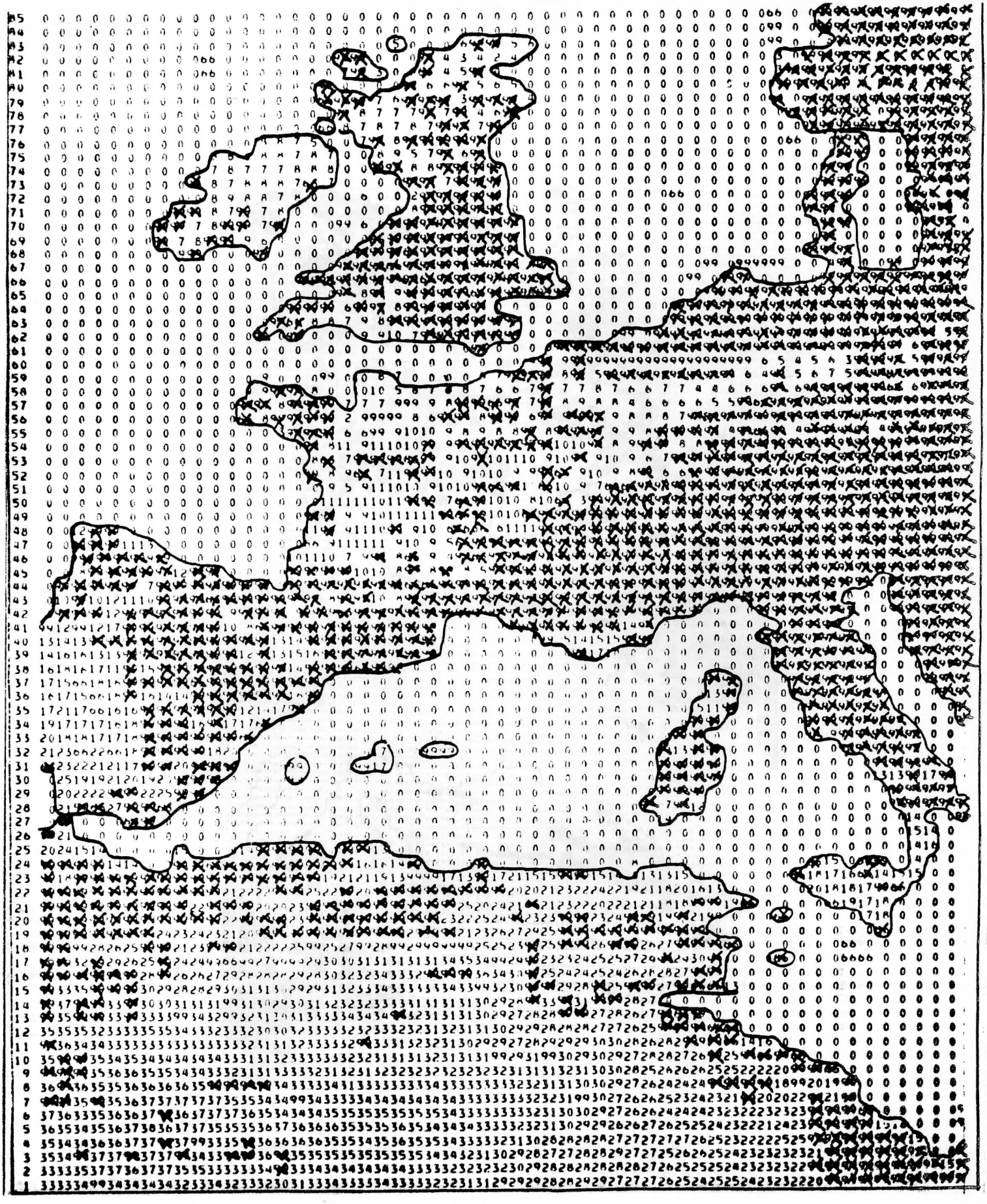

Fig. 5: Overcast "land" spots (x) and surface brightness temperatures.

OBSERVATIONS OF TROPICAL CYCLONES IN WESTERN AUSTRALIA USING COMBINED TOVS AND AVHRR RADIANCES.

By

A J Prata*, M J Lynch+, R Hille and L Van Burgel

*CSIRO, Division of Groundwater Research, Perth, WA
+Western Australian Institute of Technology, Perth, WA
Bureau of Meteorology, Perth, WA

1 Introduction

This paper discusses the use of measurements from the Microwave Sounding Unit (MSU) and the Advanced Very High Resolution Radiometer (AVHRR) for monitoring tropical cyclones off the Northwest coast of Western Australia. Previous studies (Rosenkranz et al,1977, Kidder,1979, Veldon & Smith,1983, Prata & Lynch, 1985) have shown that passsive microwave meassurements of the warming observed in mature hurricanes and tropical cyclones are correlated with the surface pressure drop in the eye of the storm. Although some encouraging results have been obtained, the large size of the MSU footprint (110 km at nadir), inadequate corrections for limb effects and the effects of the antenna gain pattern remain a problem. We show in this paper, how these problems affect the microwave brightness temperature and present some results for West Australian tropical cyclones.

The AVHRR measurements are used to locate the centre of the storms, estimate cloud top temperature and to provide information for correcting the MSU brightness temperatures.

2 Determination of Surface Pressure.

Assuming hydrostatic balance it can be shown that (eg Kidder, 1979)

$$\Delta TB_i = - A \, \Delta Ln\,(P_s) \qquad (1)$$

where ΔTB_i is the difference in brightness temperature between the warm anomaly and the environment $\Delta Ln(P_s)$ is the difference between the natural logarithm of the surface pressure in the vicinity of the warming and the natural logarithm of the environmental surface pressure and

$$A = \frac{g}{R} \int_0^H \frac{\hat{T}(z)}{T_E^2(z)} dz \left[\int_0^H K_i(z)\, \hat{T}(z) dz \right]^{-1} \qquad (2)$$

K_i is the weighting function for channel i

$\hat{T}$ is the anomolous temperature profile

T_E is the environmental temperature profile

Kidder has shown that for the 55.45 GHz channel of the SCAMS instrument and for a mean typhoon profile, A may be assumed constant. In this derivation no account was taken of the effects of the limb and the antenna gain pattern.

For the storms used in Kidders' study (8 typhoons), the value of A was found to be $-0.0178\ K^{-1}$ which corresponds roughly to a temperature difference of 0.6 K for a 10 mb pressure drop. Veldon and Smith (1983) used MSU measurements for 3 hurricanes in the North Atlantic and found the average sensitivity to be about 0.5 K difference in MSU brightness temperature per 10 mb pressure drop.

The data we have used consists of 5 Western Australian tropical cyclones. The scatter plot of the natural logarithm of the pressure near the eye, estimated by the Dvorak technique versus MSU-3 brightness temperature difference (eye-environment) is shown in figure 1. Excluding the two points (TC Frank and one of TC Victor), the intercept and slope of the regression line were found to be 1001 mb and $-0.03124\ K^{-1}$. This corresponds to a sensitivity of about 0.3 K per 10 mb pressure drop. The reasons for omitting the two outliers will be discussed later.

The sensitivity reported by Kidder for typhoons, Veldon and Smith for hurricanes and our result for WA cyclones differ markedly from what might be expected from a theoretical calculation. Veldon and Smith showed that a sensitivity of 1.8 K per 10 mb should be expected simply by integrating the hydrostatic equation and inserting typical values. Kidder used anomaly profiles and obtained a value of 1 K per 10 mb. The lower sensitivities found in practice are due to the large FOV size and the effect of limited vertical resolution. Whereas the low spatial resolution of the measurement cannot be overcome with the present instrument, other problems such as limb effects, the effects of horizontal and vertical misalignment and the effect of the antenna gain pattern can be estimated and to a large extent corrected.

3 Microwave Antenna Temperature

The temperature T_A measured at the antenna of the microwave radiometer may be written

$$T_A = \frac{\int_z \iint_\Omega T(z,\theta)\, K(z,\theta)\, F(\alpha,\theta,\phi)\, dz\, d\Omega}{\int_z \iint_\Omega F(\alpha,\theta,\phi)\, K(z,\theta)\, dz\, d\Omega} \qquad (3)$$

where α, θ, ϕ are angles defined in figure 2; Ω is the solid angle and $F(\alpha, \theta, \phi)$ is the normalised antenna radiation pattern. The angle α corresponds to the scan angle of the MSU.

To assess the importance of the various factors on the antenna temperature, we have integrated equation (2), assuming the following:-

(1) Temperature Distribution. The anomaly and mean storm profiles for Australian cyclones were taken from the data of Keenan and Templeton (1983) and those for hurricanes and typhoons from Nunez and Gray (1977). Figure 3 shows the mean storm profiles and figure 4 shows the anomaly profiles. The horizontal distribution of the temperature field was taken as a Gaussian of the form,

$$T(\theta_o) = \exp\left\{-\left(\frac{h \tan\theta_o}{R_o}\right)^2\right\} \qquad (4)$$

where θ_o is defined in figure 1., h is the height of the satellite and R_o is a measure of the width of the Gaussian. The temperature distribution as a function of θ_o is shown in figure 5 for three values of R_o.

(2) Weighting Functions. These have been calculated for the storm profiles and anomalies using the methods supplied with the TOVS software.

(3) Antenna Gain Pattern. The radiation pattern was assumed the same for all channels and all scan angles. Figure 6 shows the radiation pattern used, taken from the data supplied in SUBROUTINE ANGAIN of the TOVS software. To further assess the importance of the radiation pattern, a symmetric pattern of the form (Ulaby et al., 1981):

$$F(\alpha,\theta,\phi) = F(\alpha,\theta) = \left(\frac{1+\cos\theta}{1+\cos\alpha}\right)^2 \mathrm{sinc}^2\left[\frac{a}{\lambda}(\sin\theta - \sin\alpha)\right] \qquad (5)$$

was used. The aperture size is a, λ is the wavelength and α is the scan angle. Scan angle dependence is only significant at large scan angles ($> 60^o$). Results using this pattern were very similar to the pattern shown in figure 6.

4 Results

(i) Limb Effects. There are two major effects associated with scan angle: (a) the lifting of the weighting function peak and consequent sensing of a layer of atmosphere higher up and (b) the larger volume of atmosphere sensed as scan angle increases. A third, smaller effect, is associated with the change in the shape of the radiation pattern as the scan angle changes (e.g. see

equation 3). Figures 7(a) and 7(b) show the effects of scan angle on the MSU-3 and MSU-4 brightness temperature differences (eye-environment) for cyclones, typhoons and hurricanes. For MSU-3 the expected decrease in difference with increasing scan angle is evident for all storms profiles. However the magnitude for typhoons is almost twice as great as that for cyclones and hurricanes. More significant differences are found for MSU-4. The stronger cooling above the warming associated with Australian cyclones leads to much greater differences for cyclones. The differences increase with increasing scan angle, except for hurricanes which show a slight increase at large scan angles.

(ii) Eye-Size. The size of the warming in the horizontal varies from storm to storm. When the warming is large and completely fills the MSU field of view (FOV), we should expect to observe a greater signal than when the warming is small and partially fills the FOV. We expect qualitatively that the size of the eye be correlated with the size of the warming. To assess this effect we have calculated the MSU-3 temperature difference (DT3) as a function of the parameter R_o, for nadir and for the extreme scan angle (figure 8). As R_o increases, DT3 increases rapidly at first and then smoothly up to a constant value. Once the warming has completely filled the FOV, no further increase in DT3 is expected. For small warmings (small storms), the magnitude of the warming may be considerably underestimated from an MSU-3 measurement.

(iii) Horizontal Misalignment. Non-centering of the storm with respect to the centre of the FOV will lead to an underestimate of DT3. Figure 9 shows the effect of non-centering on DT3 for nadir and the extreme scan angle. The ordinate is measured in degrees; θ_o defined in figure 2. For a satellite height of 850 km, 1 degree corresponds to approximately 15 km.

(iv) Vertical Misalignment. The maximum warming has been observed to occur roughly at 250 mb. Changes in the shape of the anomaly will affect the observed temperatures in MSU-3 and MSU-4. In particular, strong cooling above the warming could lead to an underestimate of the strength of the warming. To compensate for this effect we have suggested using a combination of MSU-3 and MSU-4 channels (Prata and Lynch, 1985). The anomaly profile for cyclones has been multiplied by a factor F, varying from 0.0 to 3.8 and plotted against DT3 and DT4 (figure 10). The strength of the anomaly is defined as

$$AS = \int_o^H |\hat{T}(z)|\, dz \qquad (6)$$

Both DT3 and DT4 are linear functions of the anomaly strength, suggesting a two parameter equation of the form

$$AS = a\,DT3 + b\,DT4 \qquad (7)$$

For F=1.0, AS=1.12 K for cyclones, AS=0.86 K for hurricanes and AS=1.09 K for typhoons. This leads to the following equations for 0^{o} scan angle:

Australian Cyclones	AS = 0.510*DT3 - 0.438*DT4
Atlantic Hurricanes	AS = 0.382*DT3 - 0.577*DT4
Pacific Typhoons	AS = 0.253*DT3 - 2.780*DT4

These results are specific to the type of anomaly profiles used here. For a sample of many different profiles we expect a large scatter and a mulitiple regression on DT3 and DT4 should lead to more appropriate coefficients.

5 Conclusions

Simulations involving typical storm profiles for Australian cyclones, Atlantic hurricanes and Pacific typhoons reveal that several important corrections should be made to the MSU brightness temperature differences (eye-environment) if a reliable estimate of the warming is to be made from these measurements. These corrections involve allowing for non-centering of the eye with the FOV, vertical misalignment of the warming with the MSU weighting function peak, limb effects and warming size. In a practical situation these effects can be accounted for by utilising the AVHRR data. The visible, near infra-red and thermal channels of the AVHRR provide information on eye location and eye-size. Colocated MSU/AVHRR FOV's (Prata, 1986) can be used to estimate the degree of overlap between the eye of the storm and the MSU FOV and the AVHRR alone can be used to assess the size of the eye. Vertical misalignment can be accounted for using an equation involving both MSU-3 and MSU-4 channels and a correction for the limb and antenna gain pattern added to each channel. These corrections may be of the order of the observed values of DT3 and are therefore highly significant.

With reference to figure 1., the reason for omitting the two outlying points may be explained because one was for an MSU FOV at the extreme scan angle and the other was for a storm of very small size (TC Frank). The next step in this work will be to apply the corrections to the existing data and plot these new values. At this time the corrections involving the AVHRR data have not been completed and a method for relating the observed eye-size to the size of the warming is still under development.

6 References

Keenan, T D and J I Templeton (1983) A Comparison of Tropical Cyclone, Hurricane and Typhoon Mass and Moisture Structure. Mon. Wea. Rev., 11, 320-327.

Kidder, S Q (1979) Determination of Tropical Cyclone Surface Pressure and Winds from Satellite Microwave Data. Atmos. Sci. Paper No. 307, Colorado State University.

Nunez, E and W M Gray (1977) A Comparison between West Indies Hurricanes and Pacific Typhoons. Preprints 11th Tech. Conf. on Hurricanes and Tropical Meteorology, Miami Beach, Amer. Met. Soc., 528-534.

Prata, A J and M J Lynch (1985) Satellite Radiance Measurements of Tropical Cyclones, Proc. of the 2nd Australian Conf. on Tropical Meteorology, Perth, Australia.

Prata, A J (1986) Colocation of AVHRR/HIRS/MSU Fields of View and Image Display Geometry. CSIRO, Division of Groundwater Research Tech. Memo 86/1, Perth, Western Australia.

Rosenkranz, P W, D H Staelin and N C Grody (1978) Typhoon June (1975) Viewed by a Scanning Microwave Spectrometer. J. Geophys. Res., 83, 1857-1868.

Ulaby, F T, R K Moore and A K Fung (1981) Microwave Remote Sensing Vol I., Addison-Wesley Publ. Co. Inc., 456 pp.

Veldon, C S and W L Smith (1983) Monitoring Tropical Cyclone Evolution with NOAA Satellite Microwave Observations. J. Clim. and Appl. Meteor., 22(5), 714-724.

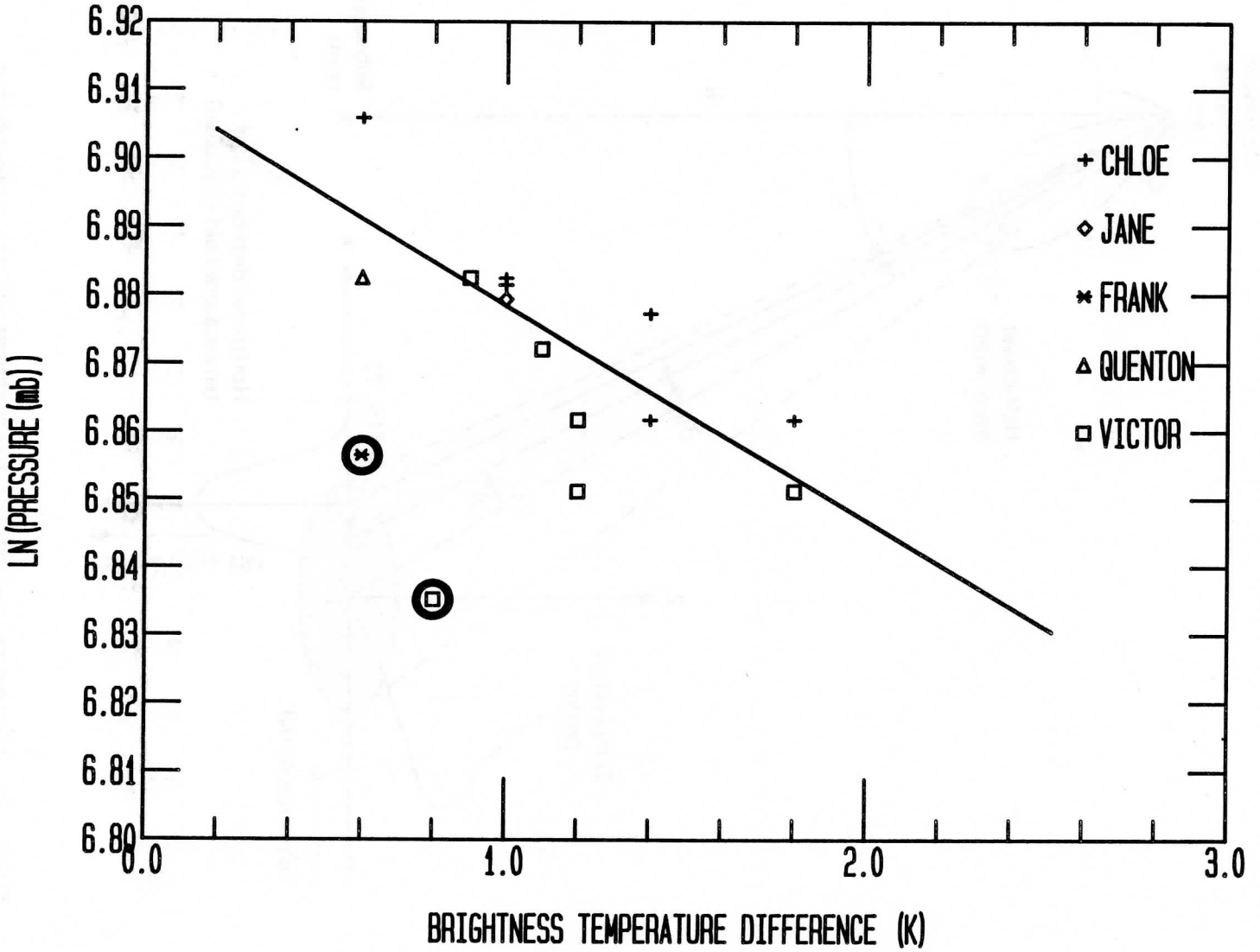

FIGURE 1: MSU channel 3 brightness temperature difference versus logarithm of pressure. The two points circled have not been included in the calculation of the regression line.

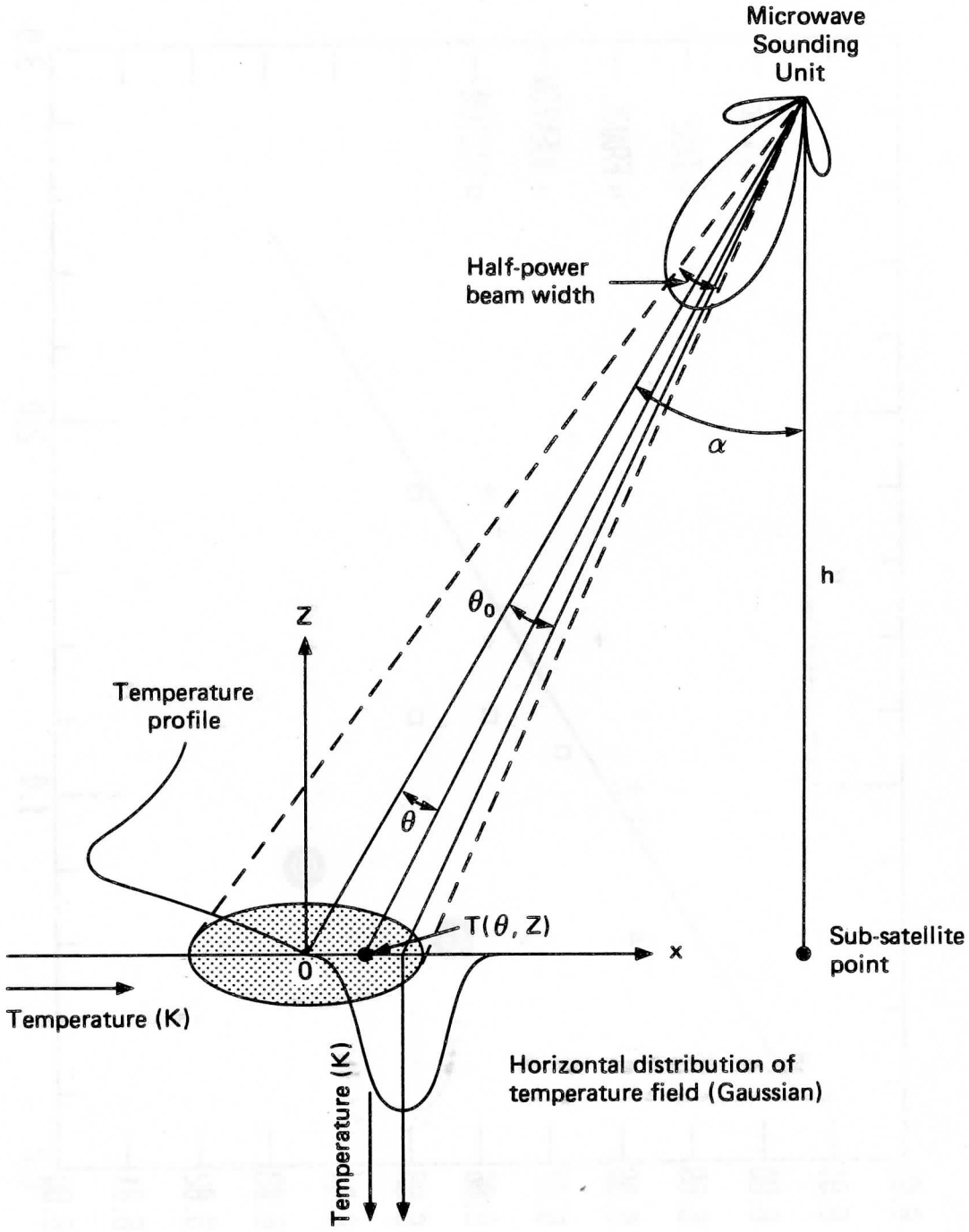

FIGURE 2: Microwave radiometer measurement of the atmospheric temperature field.

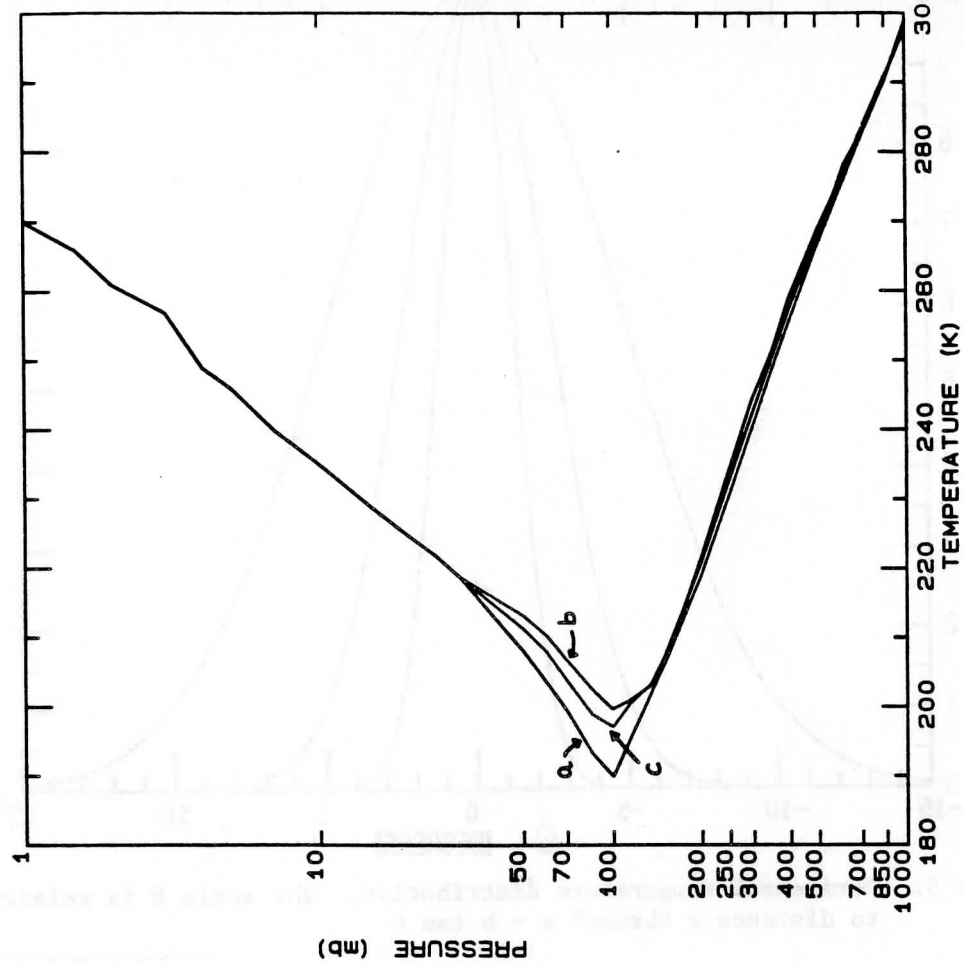

FIGURE 3: Mean storm profiles for (a) Australian tropical cyclones, (b) Atlantic hurricanes and (c) Pacific typhoons.

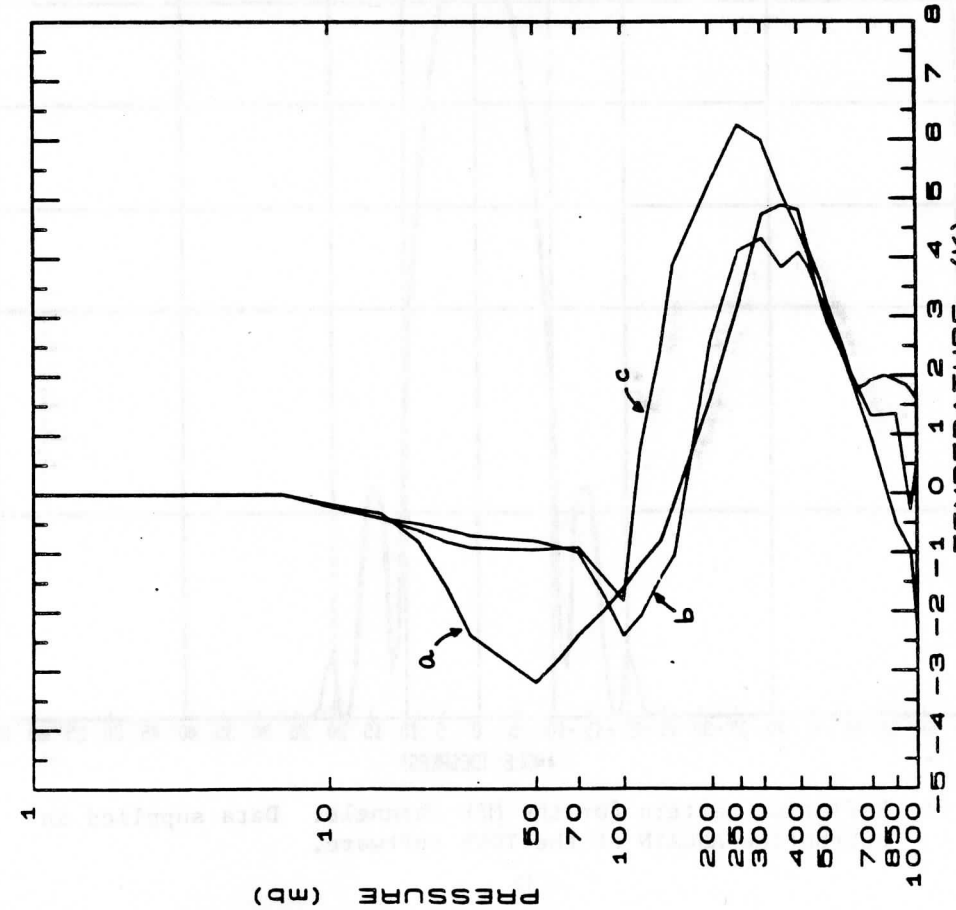

FIGURE 4: Anomaly profiles for (a) Australian tropical cyclones, (b) Atlantic hurricanes and (c) Pacific typhoons.

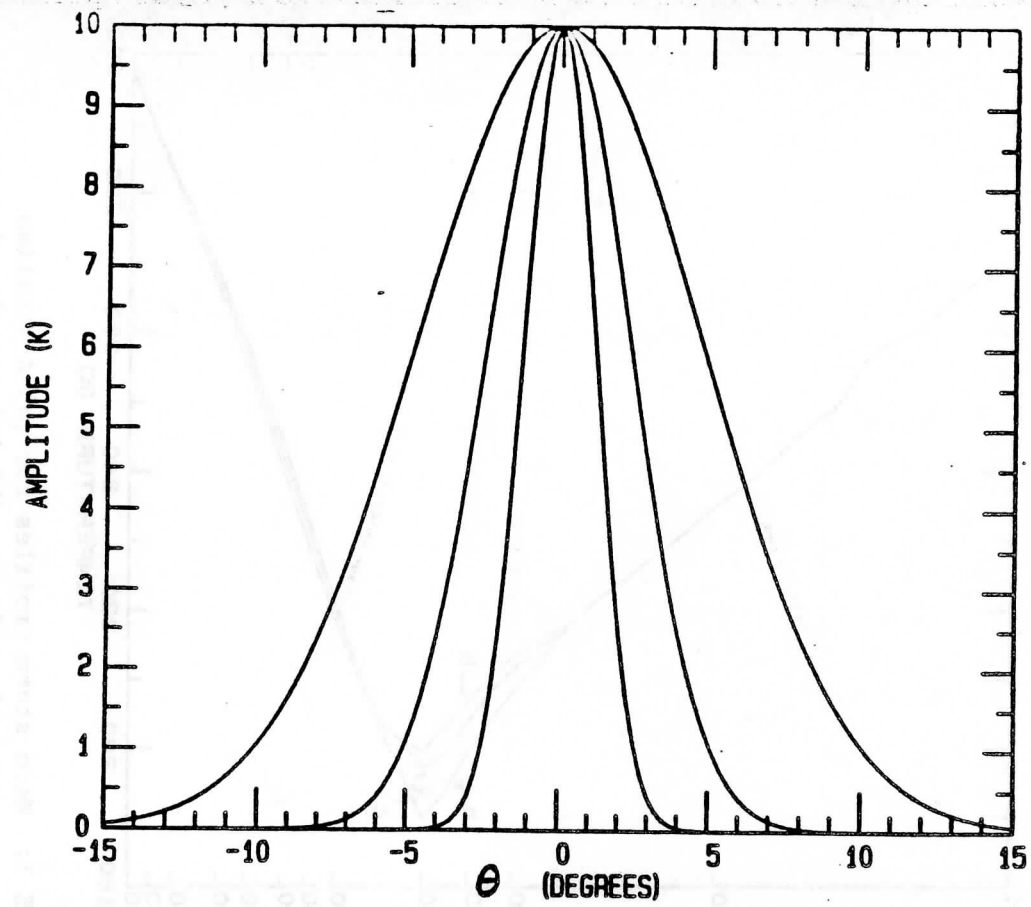

FIGURE 5: Horizontal temperature distribution. The angle θ is related to distance x through x = h tan θ

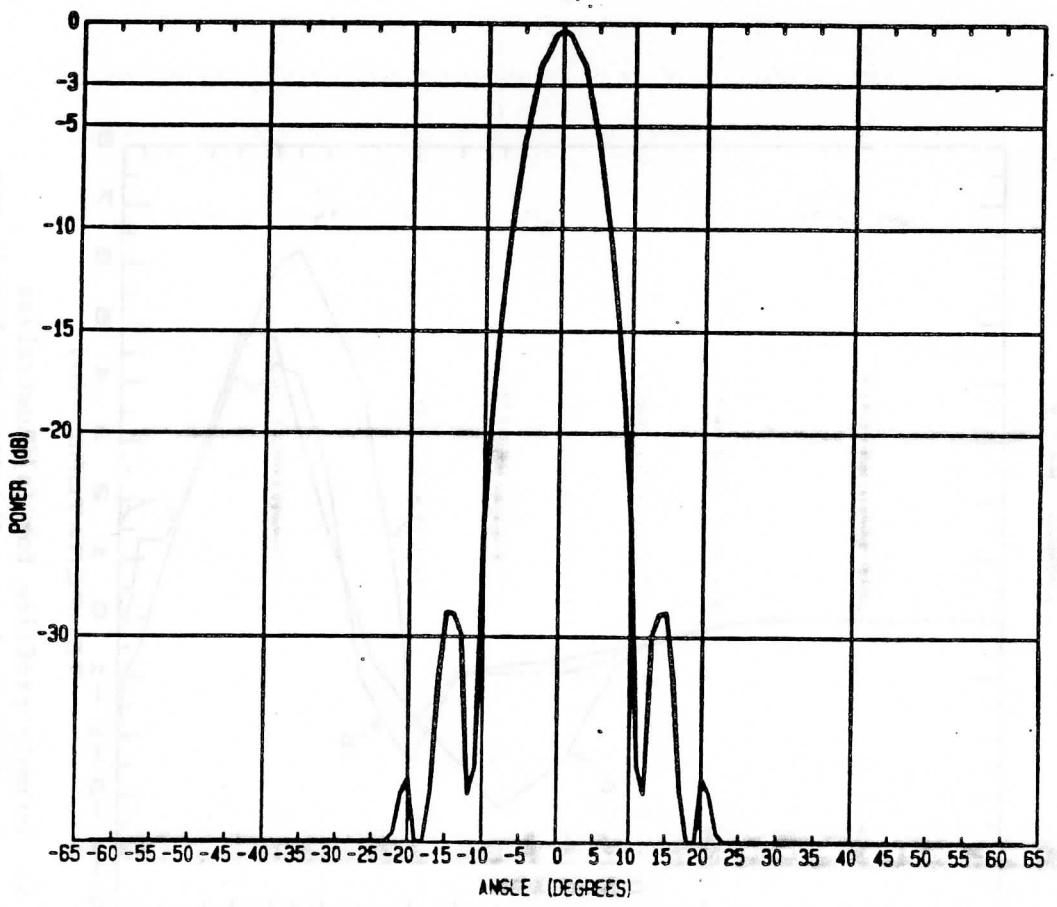

FIGURE 6: Radiation pattern for the MSU channels. Data supplied in subroutine ANGAIN of the TOVS software.

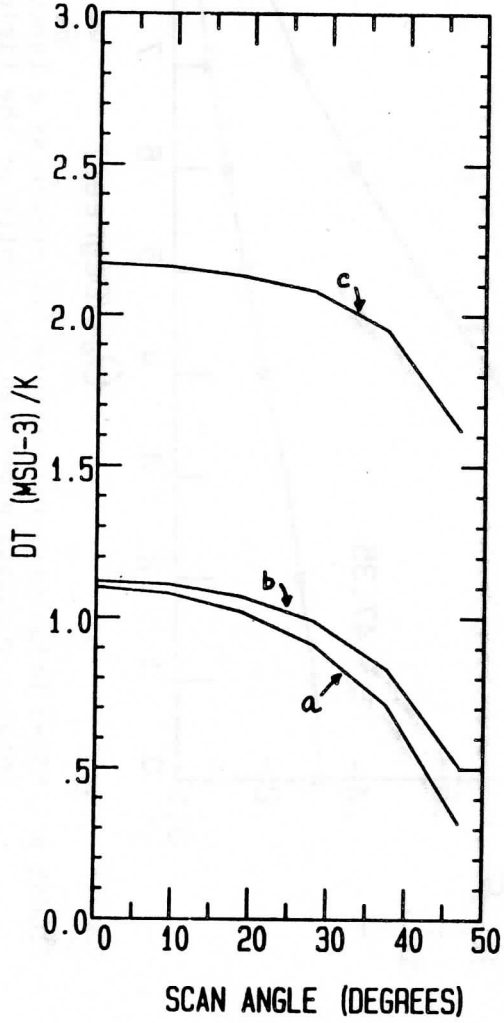

FIGURE 7(a): MSU-3 brightness temperature difference versus scan angle for (a) Australian tropical cyclones, (b) Atlantic hurricanes and (c) Pacific typhoons.

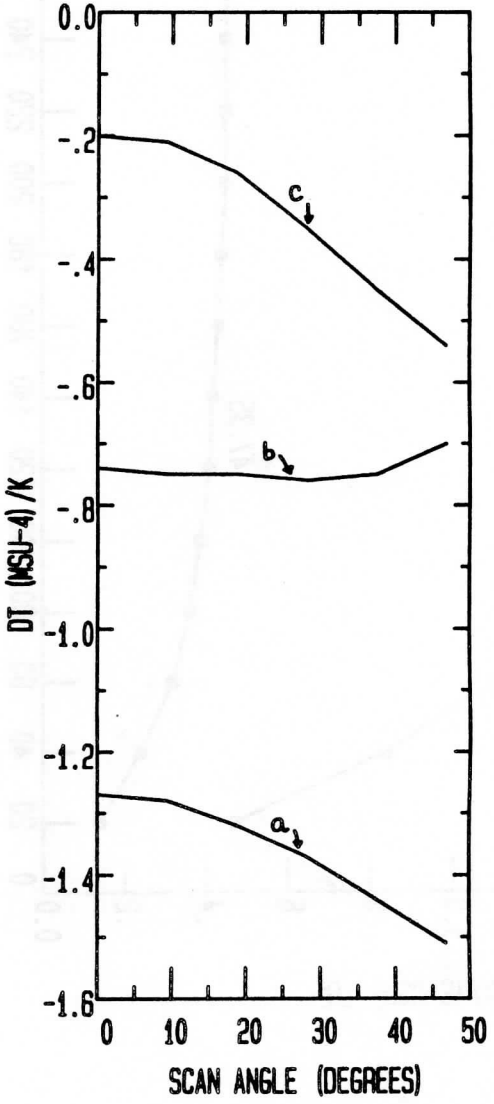

FIGURE 7(b): MSU-4 brightness temperature difference versus scan angle for (a) Australian tropical cyclones, (b) Atlantic hurricanes and (c) Pacific typhoons.

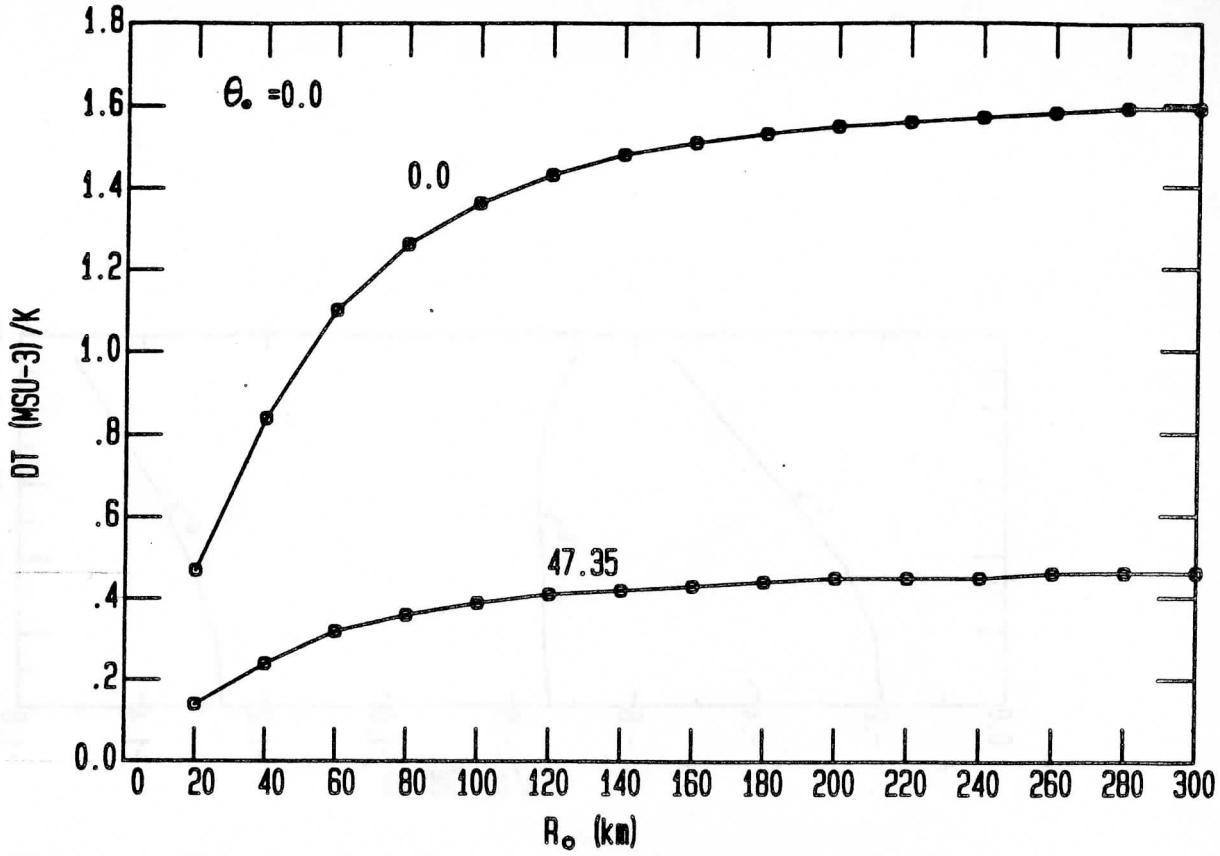

FIGURE 8: MSU-3 brightness temperature difference versus horizontal size of anomaly, for nadir and the extreme scan angle.

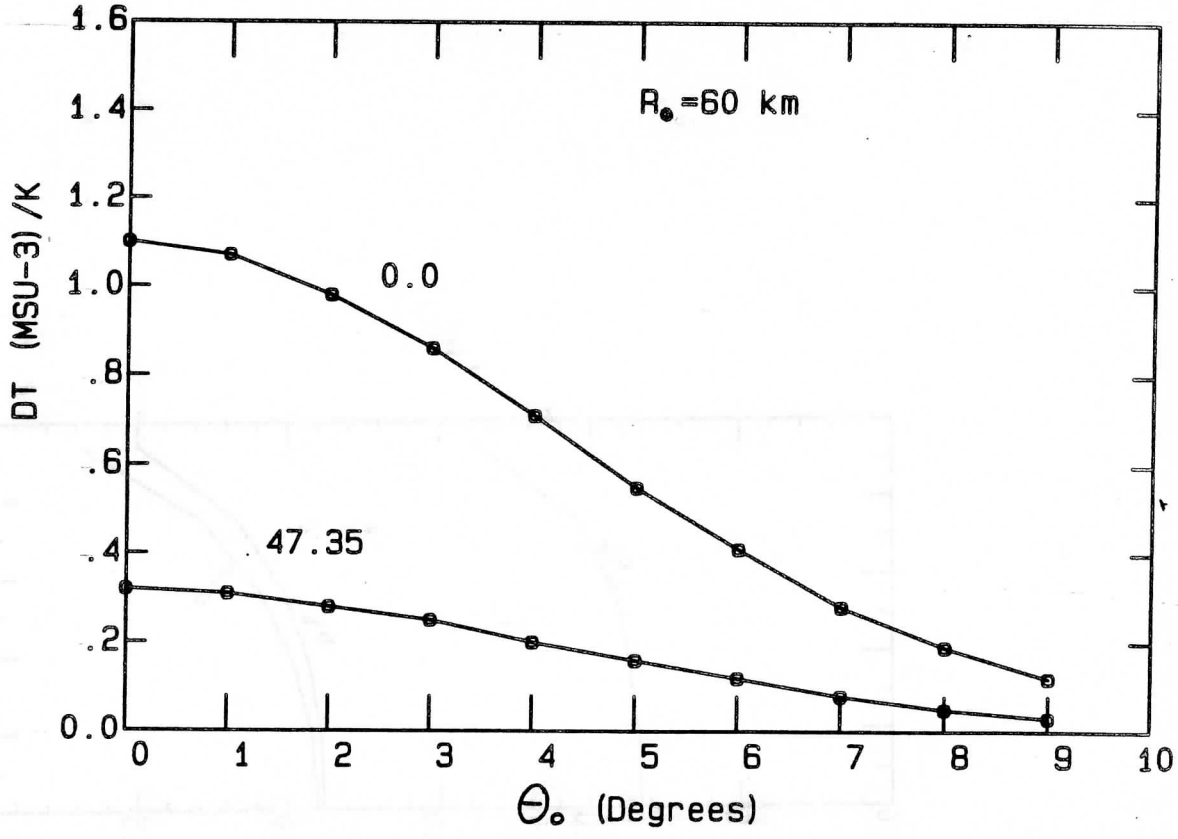

FIGURE 9: MSU-3 brightness temperature difference as a function of the angular separation between the centre of the field of view and the centre of the storm. Two scan angles are shown.

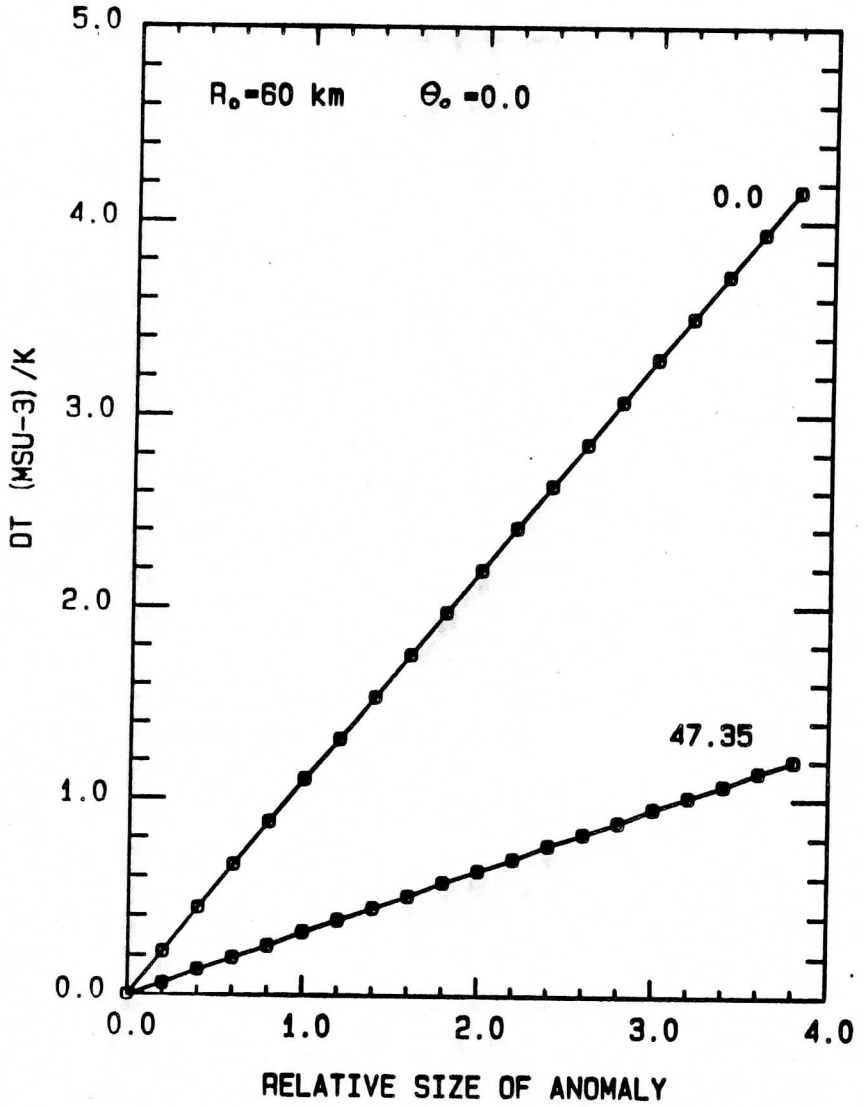

FIGURE 10(a): MSU-3 brightness temperature difference as a function of relative magnitude of the anomaly for Australian tropical cyclones.

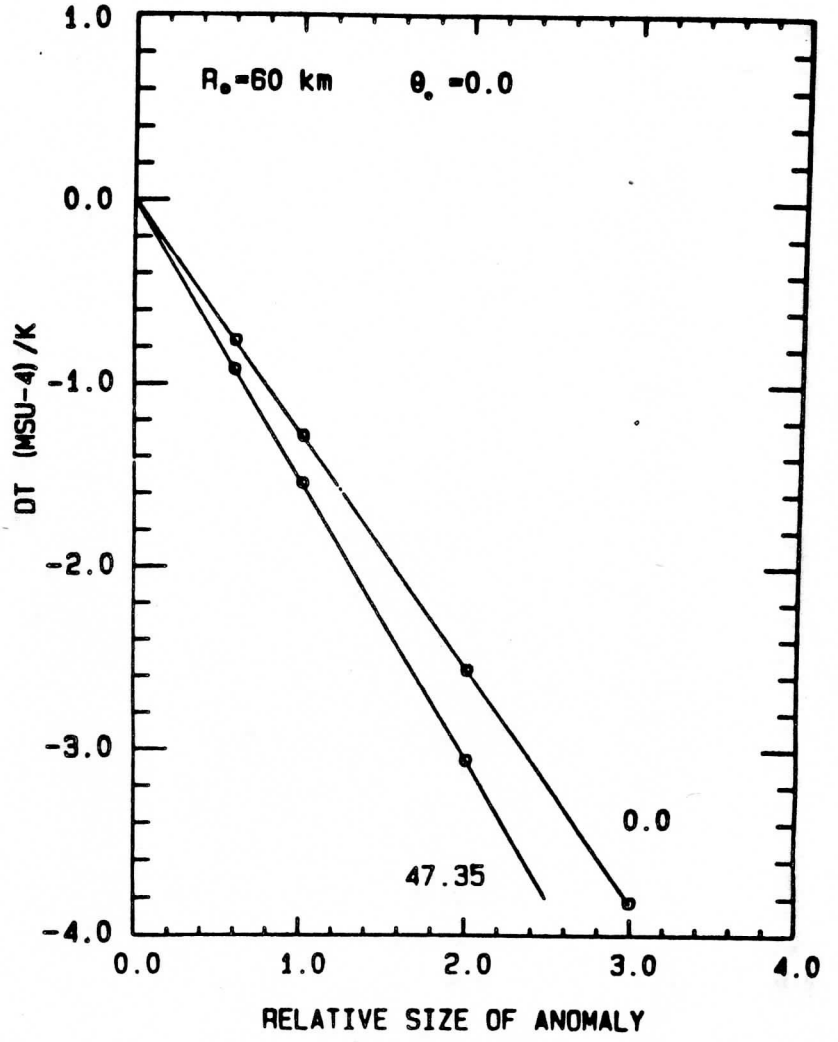

FIGURE 10(b): MSU-4 brightness temperature difference as a function of relative magnitude of the anomaly for Australian tropical cyclones.

STATUS REPORT ON CALIBRATION PROBLEMS

Guy Rochard

Centre de Meteorologie Spatiale
Lannion, France

1. INTRODUCTION

During ITSC-III it was recommended that a detailed report concerning calibration should be produced (see Report on ITSC-III, page 25).
However, after the First International AVHRR Conference last October, it became evident that a joint effort must be undertaken between the calibration working group of the TOVS conference the the corresponding one of the AVHRR conference (Prata, Rochard, et al.).

Furthermore, several important questions about the AVHRR nonlinearity correction and MSU have not yet been answered. Therefore, this paper will summarize the available information and a more complete report will be forthcoming in March 1987 to take into account new developments arising from action items initiated at the AVHRR conference.

2. MISCELLANEOUS INFORMATION ABOUT AVHRR

a. There is no ambiguity about the clock; the time clock update is explained in the Electronic Bulletin Board.

b. AVHRR is digitized at 39936 samples per second, thus the AVHRR scan (center point 1, center point 2048) is 110.769 degrees. The HIRS2 scan (center IFOV 1, center IFOV 56) is 49.43 degrees.

c. The current AVHRR blackbody temperature is given by the formula

$$\overline{T} = \sum_{i=1} b_i T_i$$

(NESS Technical Report 107, p. 45). Sometimes, T_4 is 1 or 2°K colder than T_2 due to gradients across the internal warm blackbody and this can cause errors up to 0.1°K.

d. At SCC/Lannion, using the calibration procedures outlined in NESS 107, AVHRR channel 1 has been found to be more brilliant than HIRS2 channel 20:

for NOAA-6 : AVHRR channel 1 ≅ 0.8 x HIRS2 channel 20
NOAA-7 : AVHRR channel 1 ≅ 0.75 x HIRS2 channel 20
NOAA-8 : AVHRR channel 1 ≅ 0.8 x HIRS2 channel 20
NOAA-9 : AVHRR channel 1 ≅ 0.85 x HIRS2 channel 20

Comparing NOAA-7 and NOAA-9 with the visible channel of Meteosat and GMS, it also appears that AVHRR channel 1 for NOAA-9 is 10% more brilliant than AVHRR channel 1 for NOAA-7.

3. AVHRR NONLINEARITY CORRECTIONS (OLD METHOD)

The true AVHRR brightness temperature is given by a two point linear fit plus a ΔT correction as described in Appendix B of the NESS 107 Technical Report.

a. For TIROS N (Appendix B of NESS 107, November 1979); NOAA-6 (Appendix B, Lauritson, January 21, 1980); NOAA-7 (Appendix B, Robel, October 19, 1981), the AVHRR nonlinearity error tables giving ΔT have been established (using NSP=0 where NSP is defined as the radiance of space in NESS 107, p. 46). However, users have found it necessary to use negative NSP. For example:

- 1.151 for TIROS-N channel 4
- 2.182 for NOAA-6 channel 4
- 1.176 for NOAA-7 channel 4

b. For NOAA-7, a table of ΔT corresponding with NSP$\neq$0 has been published.

Target Temperature (°K)	Error (°K)	
	10.5 micron	11.5 micron
305	+.80	+.40
295	+.36	+.18
285	0	0
275	-.25	-.08
255	-.20	-.12
235	+.20	+.02
225	+.61	+.38
205	+1.88	+1.20

The difference with the table using NSP=0 is for example 0.35°K for a target temperature 305°K in channel 4.

c. For NOAA-8, the table of ΔT (Appendix B, Wrublewski and Turotich, May 3, 1983, p. B-38) is probably given for NSP$\neq$0, but this must be confirmed.

d. For NOAA-9, the table (Appendix B, October 29, 1984) is confused. The corrected Appendix B disseminated in February 1985 gave both the table with NSP=0 and the table with NSP$\neq$0.

4. AVHRR NONLINEARITY CORRECTIONS (NEW METHOD)

a. Appendix B, March 3, 1986 contains coefficients for NOAA-10 and changes for NOAA-9 nonlinearity corrections wherein a new algorithm is proposed and new nonlinearity table is given for both NOAA-9 and NOAA-10.

However, the paper of Brown et al. (Journal of Geophysical Research, November 20, 1985, Vol. 90) raises some questions concerning these new tables. With the same new algorithm, Brown finds the table for NOAA-9 to be different. For example, differences are found to be 0.8°K for channel 4 and 20°C for the SST. This issue is not resolved.
At the moment, SCC/Lannion is still using the table from Appendix B.

5. HIRS2 INFORMATION

a. In NESS 107, p. 39, Table 4-7, the text should read

$$\Delta\text{Time HIRS2} = 0.05 \ .$$

b. For NOAA-7, a first draft of Appendix B was available early 1981, but the official NOAA-7 Appendix B is from Robel, October 19, 1981. Between those two versions, filters of HIRS channels 6, 9, 10 and 13 have been changed. However, the 15 other channels still have problems.

(i) The central wavelengths and band correction coefficients (Appendix B for NOAA-9, October 19, 1981, page 36), are correct (b for channel 6 is -0.081).

(ii) The filters given on pages 32 to 35, are incorrect (except channels 6, 9, 10 and 13). For example, the real filter for channel 16 (obtained from ITT) has two maxima (2277 cm^{-1} and 2266 cm^{-1}) and the wrong one (page 32 in Appendix B) has only one maximum at 2261 cm^{-1}. Using those wrong filters produces an error on the computed temperature of about 1°K for channel 16, .5°K for channel 19, 0.3°K for channel 12, etc.

(iii) The correct filters for NOAA-7 are available at SCC/Lannion.

c. The IFOV of HIRS2 is given in NESS 107 on page 4 as 1.25° and on page 41 as 1.2°. In fact, from matching AVHRR and HIRS2, it seems better to use about 1.4°.

d. On NOAA-9, HIRS2 channel 16 is unusable because the wrong filter was installed.

e. On NOAA-9, the central wavelength of HIRS2 channel 7 is given as 808.7 cm^{-1} (Appendix B, February 1985). The value seems wrong. The central wavelength corresponding to the filter is near 750 cm^{-1}.

6. MATCHING AVHRR AND HIRS2

T. Aoki from Japan, P. Lloyd from the United Kingdom, and G. Rochard from France have obtained comparable results for matching AVHRR and HIRS. The principle of the method is given in the Technical Proceedings of the Second TOVS Study Conference on pages 349 to 367 (particularly, the definitions of ΔI, ΔJ, ΘAH an ΘA). For example, the for NOAA-8 and NOAA-9 were found to be:

NOAA-8	ΔI	ΔJ	ΘAH
Aoki	-1.14	+4.87	-0.062
Lloyd	-2.17	+4.95	?
Rochard	-1	+5.1	-0.055

NOAA-9	ΔI	ΔJ	ΘAH
Aoki	+1.07	+3.39	-0.10
Lloyd	+1.	+3.4	-0.08
Rochard	+1.7	+3.5	-0.09

a. ΔI is positive when it is necessary to move the HIRS IFOV from the nominal position along the track in the same direction as the satellite velocity vector (relative to the AVHRR image).

b. ΔJ is positive when it is necessary to move the HIRS IFOV from the nominal position across the track in the AVHRR scanning direction (relative to the AVHRR image).

c. ΘAH is positive on the following picture:

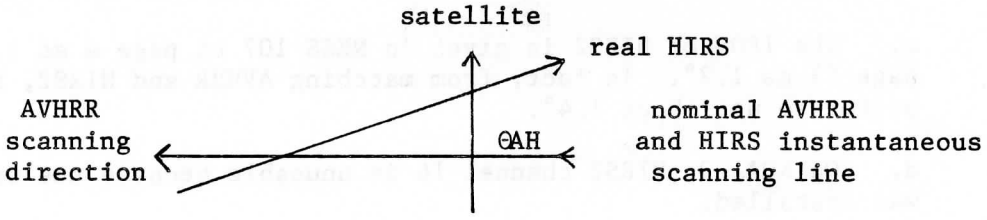

7. MSU INFORMATION

a. The MSU step time (NESS 107, p. 39, Table 4-7) is incorrectly given as 1.81sec. The correct value is 1.893sec.

b. For NOAA-7 channel 1, the correct value of d1 is 0.9844.

c. The MSU scan line start (NESS 107, p. 36) is incorrectly given as minor frame 257. The correct value is 275.

d. MSU3 of NOAA-7 seems warmer than MSU3 of NOAA-8 by about 2°C, but no explanations are available.

e. MSU3 of NOAA-9 appears to be losing gain. Space counts are increasing at a rate of one to five counts per day.

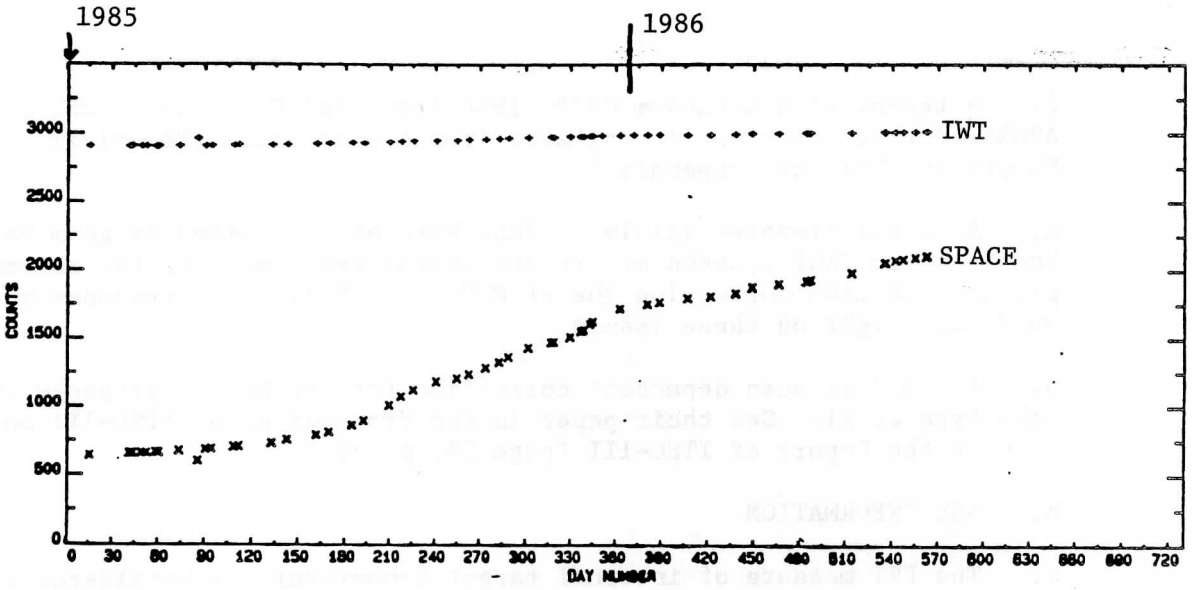

Fred Prata of Australia has suggested the following correction to INGMSU:

(i) Get numeric day of year and adjust CAVG (3,1) where CAVG (I,J) has I=1,4 for channel number and J=1,2 for space or IWT, as indicated for the three regions.

- Region 1: before 30 June 1985
  CAVG(3,1) = 650.+IDAY * 1.0
- Region 2: 1 July → 31 Dec 1985
  CAVG(3,1) = 250.+IDAY * 5.5
- Region 3: after 1 Jan 1986
  CAVG(3,1) = 1750.+IDAY * 2.1

(ii) A suggested code for this adjustment in INGMSU follows. Note this adjustment is appropriate only for NOAA-9 (you must test the satellite ID).

```
DO 280 NROWS = 1, 10000
          :
          :
IF(NROWS.GT.1) GO TO 130
CALL CALDAY (   )

IF (NYR.EQ.85) THEN
  IF(IDAY.LT.182) THEN
  A = 650.0
  G = 1.0
  ELSE
  A = -250.0
  G = 5.5
  ENDIF
ENDIF
IF (NYR.EQ.86) THEN
A = 1750.0
G = 2.1
ENDIF

CAVG(3,1) = A+IDAY * G
          :
          :
```

f. A technical memorandum CSIRO 1986 from Fred Prata about MSU and AVHRR picture matching is available from the author. (Technical Memorandum 86/1 and appendix.)

g. A letter prepared mainly by John Eyre of the United Kingdom has been sent to Paul Swanson at JPL concerning problems with the antenna pattern and limb correction the of MSU. Hopefully, the response will shed some light on these issues.

h. A residual scan dependent correction for the MSU is proposed by John Eyre et al. See their paper in the Proceedings of ITSC-III and also in the Report of ITSC-III (page 25, point 5).

8. SSU INFORMATION

a. The PRT measure of internal target temperature is considered to be precise and is calculated by (NESS 107, p. 50):

$$T(K) = \sum_{i=o}^{2} a_i \bar{X}^i$$

or $$T(K) = a_o + a_1 (\bar{X}) + a_2 (\bar{X})^2$$

where X is the averaged PRT data in counts and a_i are coefficients which vary depending on the model of SSU. Note that in NESS 83, page 48, it is necessary to correct -i to +i.

Satellite No.	Model No.	a_o	a_1	a_2
NOAA-6	F2	284.147	4.76×10^{-3}	6.35×10^{-9}
NOAA-7	F3	283.911	4.857×10^{-3}	0.0
NOAA-8	F6	285.288	4.817×10^{-3}	11.19×10^{-9}
NOAA-9	F5	284.249	4.889×10^{-3}	2.6×10^{-9}

It is necessary to introduce the appropriate values in <u>each</u> Appendix B for NOAA-6, 7, 8, 9.

b. Should the PRT fail or you suspect the measured value, then the two thermistors can be used. In this case:

$$T(K) = \frac{\sum_{i=0}^{3} b_i \bar{X}^i + \sum_{i=0}^{3} c_i \bar{Y}^i}{2}$$

where b and c are as given in NESS 107 Appendix B and are the same for all models. X and Y are as described in NESS 83 and NESS 107. The value of internal target temperature is then used to determine the radiance of the internal target, N_T. Space radiance N_s, is taken to be zero.

c. The technique for ramp calculation is given correctly in NESS 107, i.e.,

$$RAMP = \frac{8 \Sigma t s - \Sigma t \Sigma s}{8 \Sigma t^2 - (\Sigma t)^2}$$

However, the sample times in NESS 107 are wrong and should be as given in NESS 83, i.e.

Sample (s)	Time (t)
1	0.6 sec
2	1.0 sec
3	1.6 sec
4	2.0 sec
5	2.6 sec
6	3.0 sec
7	3.6 sec
8	4.0 sec

Note that for SSU3, the Bracknell computation has a bias of +0.5° with respect to the Lannion computation.

9. SATELLITE NAVIGATION AND PICTURE LOCATION

a. A report from F. W. Nagle is available in the Proceedings of ITSC-III and as NOAA Technical Memorandum NESDIS 16.

b. The improvement of TBUS Part IV is still under development in NOAA. News about improved TBUS message will be disseminated in the EBB when it is available.

c. CMS/Lannion has published a technical document entitled "Geographical Navigation of NOAA AVHRR Series Imagery" Satmos notes No. 2 using ARGOS parameters.

d. An international intercomparison of navigation software has been proposed at the AVHRR conference and probably will be conducted in early 1987.

10. ARCHIVAL FORMATS

a. As explained is the Appendix C of the Report on ITSC-III (pgs. 65-66), this topic should be further examined in 1987.

b. A description of the NOAA/NESDIS format is available in the "NOAA Polar Orbiter User's Guide", paper by K. B. Kidwell, and a description of the French Satmos format is available in the paper of P. Brunel et al., "Format description of the AVHRR-TOVS magnetic tapes produced by the SATMOS Service," C.M.S./Lannion (P. Brunel, CMS, BP147, 22302 Lannion, France).

11. EXTRACT FROM THE REPORT TO INTERNATIONAL RADIATION COMMISSION OF THE FIRST INTERNATIONAL AVHRR WORKSHOP

a. About navigation:

It is recommended that NOAA be asked to examine the question of incorporating the satellite orbital element information in the AVHRR data stream. If that is possible, it is important that information on roll, pitch and yaw should also be included.

It is recommended that NOAA be asked to examine the question of updating the satellite clock more frequently; in other words, to greatly improve the current one-second accuracy of the satellite time.

b. About archiving formats:

Dr. Guy Rochard of France has been asked to prepare a report on the current formats which are used throughout the world for archiving HRPT data.

Dr. John O'Callaghan of Australia has been asked to act as rapporteur to the AVHRR community on future developments in archival formats, and in particular to report on the recommendations coming out of Panel 2 of the CCDS which deals with the general question of satellite data formats. His address is:

Dr. J. F. O'Callaghan
CSIRONET,
GPO Box 1800
CANBERRA, ACT 2601

FUTURE NOAA POES SATELLITES AND SENSORS

James K. Sparkman, Jr.
NOAA, NESDIS, Systems Planning &
Development Staff, Washington, D.C.

At present, uncertainties concerning future funding leave us unsure what the future configuration will be of NOAA's Polar Orbiting Environmental Satellites (POES). Three systems are possible (Figure 2): (a) The present deployment of Morning and Afternoon satellites may continue; (b) Alternatively, a shortage of funds may force reduction of the Metsat fleet to deployment only of an Afternoon spacecraft; (c) A third possibility now under consideration would merge the operations of the NOAA environmental satellites with that of the EOSAT (Landsat) spacecraft.

NOAA's meteorological sensors would ride as paying passengers aboard the EOSAT satellites. However, there are incompatibilities between NOAA's sensors and those of EOSAT, notably between the AVHRR and HIRS, and the Landsat TM. TM is designed for a flight altitude of 700 km; AVHRR and HIRS expect an altitude of 850 km. Cost and time do not permit a redesign of either. Thus it is expected that if a Combined Mission is selected, carrying TM and Metsat instruments, the Morning spacecraft would fly at TM's altitude --and at a later time of day than preferred for meteorological remote sensing-- whereas the Afternoon spacecraft would orbit at the 850 km altitude of the present Advanced TIROS-N (ATN) spacecraft.

A last option (d) is planned for 1995 or later. It is NASA's Earth Observing System (EOS), called also "the Polar Platform." The first EOS mission presumably will be an Afternoon spacecraft, flying at NOAA's preferred altitude. A Morning spacecraft might be provided by NASA at a more distant date, or alternatively, might be supplied by other nations.

Figure 3, showing instruments to be carried aboard various of the optional systems, has been modified since presentation in Madison. This text follows the corrected version:

NOAA-H, I, J, K, L, and M are scheduled to carry an improved HIRS instrument called 2I. If NOAA-D flies in the time-slot shown, that is, after NOAA-H, it will carry the earlier HIRS as flow in -G and previous satellites. Hence the concept that -D (if flown) will carry an old model HIRS (but no older than -G's).

C1 and C2, the first Combined Mission satellites merging Landsat and Metsat operations, are scheduled to be repairable vehicles. Thus R1 is in fact C1,

after it has been recovered in space and refurbished.

Note that an uncertainty exists as to whether C2, R1 and R2 (et seq.) will carry HIRS instruments.

In Figure 4, the impact of the Combined Mission's lower Morning orbit is shown. While FOVs are smaller, so also are swath widths, to the detriment of both imaging and computation of low- to mid-latitude soundings.

Figures 5 - 7 show launch schedules for the options a, b, and c discussed above.

In Figure 8, changes in the DSB and HRPT services are shown for the present and next series of NOAA POES spacecraft. The reader may recall that, when this figure was shown at ITSC-III, TOVS data users urged that AMSU data, not HIRS data, be broadcast via the Beacon/TIP VHF channel. This might or might not be a wise strategy, since it would leave users without backup data if early models of AMSU hardware should fail. But either way, radio frequency specialists insist that AMSU data cannot be carried on the present TIP broadcasts. AMSU's data rate exceeds available bandwidth, it is explained.

Figure 9 through 13 show the heritage of experience leading to the AMSU design, and details concerning the operation of the new instrument. Figure 10 explains the entries listed in the subsequent figures. Filters for AMSU channels 5, 10-14 and 18-20 are "split-window" designs, in which energy is collected along the wings of the oxygen and water vapor resonant bands, to be compared with radiation sensed at the peak of the resonances.

Figure 14 shows the spectral channels for the present and future AVHRR designs. In AVHRR/3, Channel 3 contains filters for use in daylight and nighttime operations. In the combination instrument now considered for 1995 and later, a possibility exists that channels 1-3 might be replaced by channels for soundings, to permit deletion of the HIRS instrument, at that time. Note that resolution of the AMRIR may be improved to 500 m at nadir.

ITSC-III

NOAA-SPDS REPORT, AUG. 14, 1986

1. NOAA POLAR SATELLITES

2. AMSU

3. AVHRR

Figure 1

NOAA: POES FUTURE SYSTEMS

PRESENT SYSTEM	FUTURE SYSTEM OPTIONS
	a. AM PM AM PM ...
AM PM AM ...	b. PM PM PM PM ...
	c. AM(TM) PM AM(TM) ...
	d. 1995 OR LATER: EOS PM...(AM?)...AM...

OPTION c. DENOTES A COMBINED MISSION.

Figure 2

INSTRUMENTS: NOAA–G,M vs. COMB.MISSION

NOAA S/C:	G	H	D	I	J	K	L	M
~~HIRS–D~~			~~X~~					
HIRS/2	X	X'	x	X'	X'	X'	X'	X'
MSU	X	X	X	X	X			
SSU		X		X				
AMSU A/B						X	X	X
AVHRR	X	X	X	X	X	X*	X*	X*

COMB. MISSION:	C1	C2	R1	R2
HIRS/2	X	X ?	X ?	X ?
AMSU–A	X			
AMSU–A/B		X	X	X
AVHRR	X	X*	X*	X*

(X* DENOTES 5.5 CHANNEL AVHRR.)

(X' DENOTES HIRS MODEL 2I)

Figure 3

NOAA--G,M vs. COMB. MISSION

	NOAA--X		COMBINED		
	AM	PM	AM	PM	
ALT.	850	850	700	850	km
EQ.CRS.	0730	1330	0930/1030	1330	LOC.
HIRS FOV	17.4	17.4	14.3	17.4	km
SWATH	2240	2240	1845*	2240	km
AVHRR FOV	1	1	0.8	1	km
SWATH	2500	2500	2060*	2500	km

(* DENOTES COVERAGE GAPS AT LOW LATITUDES.)

Figure 4

NOAA POLAR LAUNCH SCHEDULE

(ONE SATELLITE SYSTEM)

(ALL PM ORBIT EXCEPT NOAA-G)

SATELLITE	LAUNCH DATE
NOAA-G	JUNE, 1986
NOAA-H	APRIL, 1987
NOAA-I	JUNE, 1988
NOAA-J	DEC., 1989
NOAA-K	JUNE, 1991
NOAA-L	DEC., 1992
NOAA-M	JUNE, 1994

Figure 5

NOAA POLAR LAUNCH SCHEDULE

(TWO SATELLITE SYSTEM)

SATELLITE	TIME	LAUNCH DATE
NOAA-G	AM	JUNE, 1986
NOAA-H	PM	FEB., 1987
NOAA-D	AM	MARCH, 1988
NOAA-I	PM	MARCH, 1989
NOAA-J	AM	MARCH, 1990
NOAA-K	PM	MARCH, 1991
NOAA-L	AM	MARCH, 1992
NOAA-M	PM	MARCH, 1993

Figure 6

NOAA POLAR LAUNCH SCHEDULE
(COMBINED MISSION SYSTEM)

SATELLITE	TIME	LAUNCH DATE
NOAA-G	AM	JUNE, 1986
NOAA-H	PM	DEC., 1986
NOAA-I	AM	JUNE, 1988
NOAA-J	PM	DEC., 1989
NOAA-COM	AM	APRIL, 1989
NOAA-COM	PM	APRIL, 1991
NOAA-REF	AM	OCT., 1992
NOAA-REF	PM	OCT., 1994

Figure 7

NOAA POES SATS: BROADCAST SERVICES

SERVICE	CURRENT	K,L,M (1990)
1. BEACON/TIP (DSB)	HIRS, MSU, SSU	HIRS (ONLY) (NOT AMSU)
2. HRPT	AVHRR, HIRS, ETC.	AMSU, AVHRR, HIRS, ETC.

(FREQUENCY, BANDWIDTH, AND MODE OF BROADCASTS DO NOT CHANGE, FOR BEACON OR HRPT.)

Figure 8

AMSU - LINEAGE

SATELLITE/DATE	IMAGER	SOUNDINGS	COMMENTS
		PMMR	
Nimbus 5/1972	ESMR		(1) 19.35 GHz
Nimbus 5/1972		NEMS	(5) 22, 31, 50-60
Nimbus 6/1975		SCAN	(5) 22, 31, 50-55
Nimbus 6/1975	ESMR		(1) 37
Nimbus 7/1978		SMMR	(5) 6.6, 10.7, 18, 21, 37
TIROS-N /1978		MSU	(4) 50-57
DMSP /1979-83		SSM/T	(7) 50-60
DMSP /1986	SSM/I		(4) 19, 22, 37, 85
(NOAA-K)/1990 (OMINSTAR 1,2)		AMSU	(20) 23 - 183

Figure 9

AMSU: ATMOS. ABSORPTION

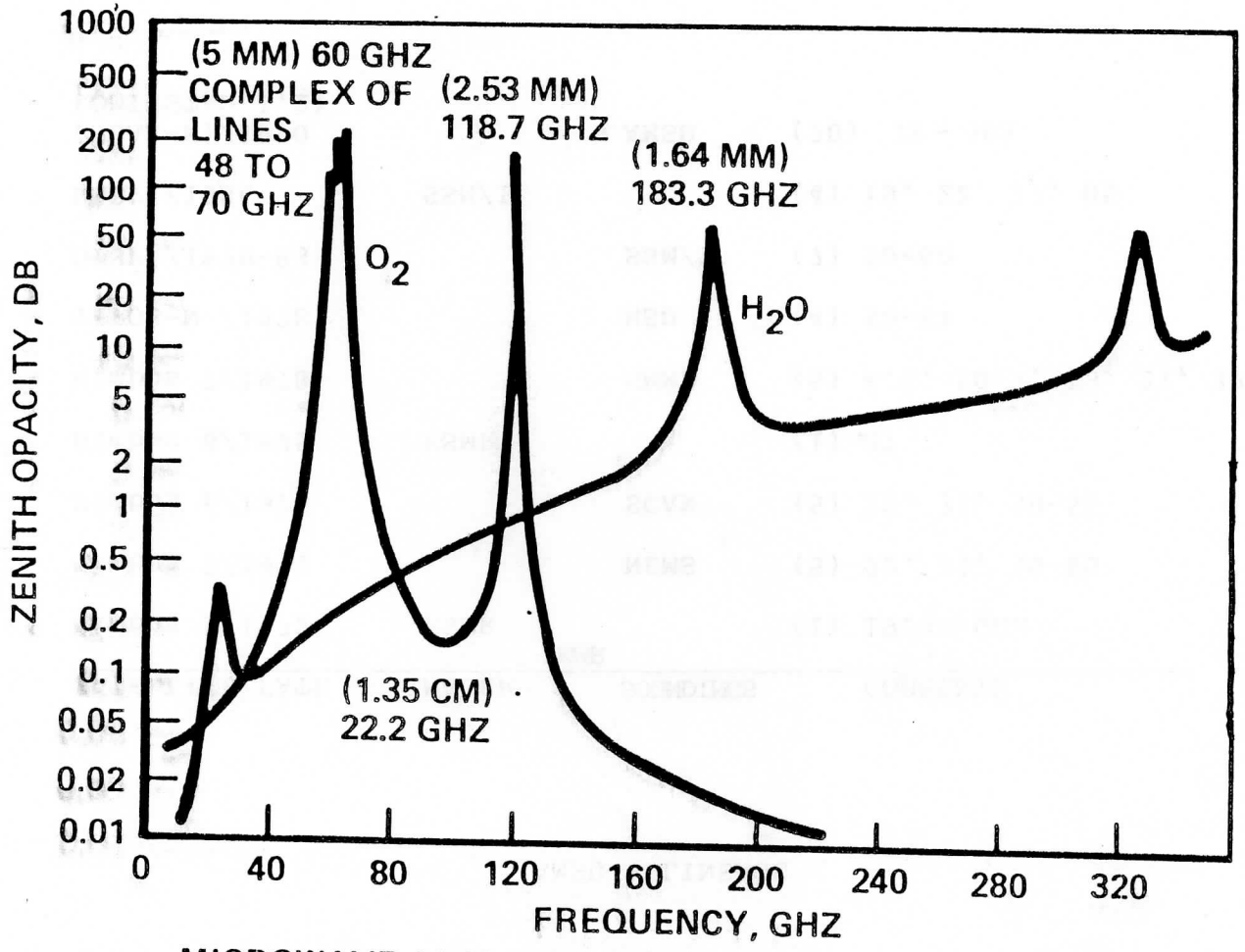

MICROWAVE ADSORPTION RESONANCES FOR O_2 AND H_2O

Figure 10

AMSU-A CHANNEL CHARACTERISTICS

CH NO.	CENTER FREQUENCY	BANDWIDTH (MHz)	TEMPERATURE SENSITIVITY (°K) NE T
1	23800 MHz	270	0.3
2	31400 MHz	180	0.3
3	50300 MHz	180	0.4
4	52800 MHz	400	0.25
5	53596 MHz $\pm$115 MHz	170	0.25
6	54400 MHz	400	0.25
7	54940 MHz	400	0.25
8	55500 MHz	330	0.25
9	57290.344 MHz $=f_{LO}$	330	0.25
10	f_{LO} $\pm$217 MHz	78	0.4
11	f_{LO} $\pm$322.2 $\pm$48 MHz	36	0.4
12	f_{LO} $\pm$322.2 $\pm$22 MHz	16	0.6
13	f_{LO} $\pm$322.2 $\pm$10 MHz	8	0.80
14	f_{LO} $\pm$322.2 $\pm$4.5 MHz	3	1.20
15	89.0 GHz	6000	0.5

Beam width of 3.3° gives a nadir FOV of 45 km

Figure 11

AMSU-B CHANNEL CHARACTERISTICS

CH NO. DESIGNATION	CENTER FREQUENCY (GHz)	MAXIMUM BANDWIDTH (MHz)	TEMPERATURE SENSITIVITY (K)
16	89.0	6000	0.60
17	157.0	4000	0.60
18	183.31±1.00	1000	0.60
19	183.31±3.00	2000	0.60
20	183.31±7.00	4000	0.60

Beam width of 1.1° gives a nadir FOV of 15 km.

Figure 12

AMSU: CHANNEL FACTORS

CHANNELS 5, 10–15, & 17–20 ARE SPLIT FRAME, AS SHOWN BELOW.

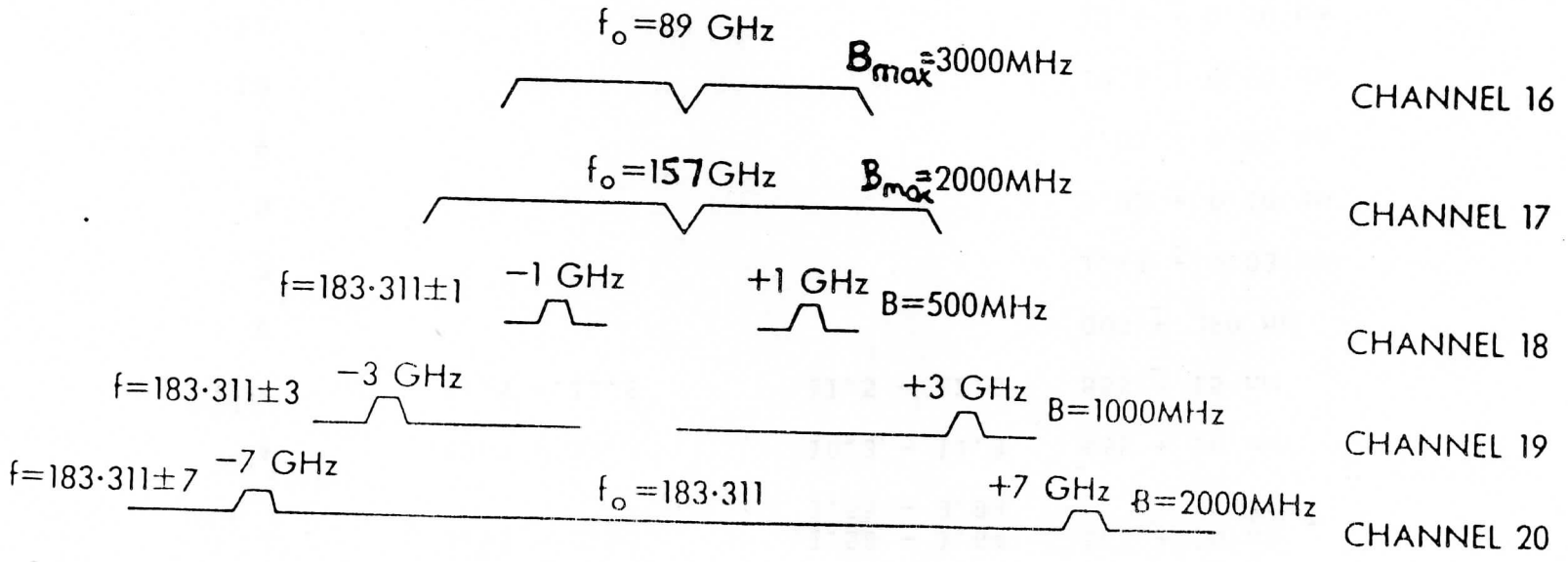

f_o=Local Oscillator B=Passband Bandwidth f=Centre Frequencies of Passband Centre

Figure 13

AVHRR CHANGES

CH NO.	AVHRR/2 Present (1986-90)	AVHRR/3 (1991-1995)	COMRI/AMRIR (1995--)
1	0.58-68	0.58 -0.68	443 ± 10 nm (50%)
2	0.725 - 1.10	0.84 - 0.87	500 ± 10 nm
3	3.55 - 3.93	1.58 - 1.64 3.55 - 3.93	565 ± 10 nm
4	10.3 - 11.3	10.3 - 11.3	665 ± 10 nm
5	11.5 - 12.5	11.5 - 12.5	855 ± 15 nm
6			800 ± 300 nm
7			1.61 ± 0.03 um
8			3.72 ± 0.10 um
9			4.01 ± 0.09 um
10			10.8 ± 0.50 um
11			12.0 ± 0.50 um
FOV	1 KM (nadir)	1 KM (nadir)	500M (Max)

In the COMIR/AMRIR, channels 1, 2 and 3 may be changed to channels for soundings, to replace the HIRS instrument. Channels 1-7 will have non-linear outputs, to expand sensitivity at low levels. Channel 6 will have commandable along-scan gain control, for day, night and near-terminator imaging.

Figure 14

SIMULTANEOUS RETRIEVAL OF TEMPERATURE AND RELATIVE HUMIDITY USING EMPIRICAL ORTHOGONAL FUNCTIONS

J. David Steenbergen, Brian T. Greaves and Tsoi-Ching Yip

Atmospheric Environment Service
Downsview, Ontario, Canada

1. INTRODUCTION

The retrieval of temperature and water vapour soundings from TOVS measurements is made more difficult because the temperature and water vapour information is interwoven in several sounding channels. To attack this problem, Smith et al. (1984) proposed a minimum-variance method for simultaneous retrieval of temperature and precipitable water. The concept was developed further by Smith et al. (1985) and Svensson (1985). An alternative formulation which included a statistical constraint was given by Fleming et al. (1986).

This paper describes a simple retrieval algorithm which uses empirical orthogonal functions (henceforth eof's) as basis functions for a simultaneous retrieval of temperature and water vapour as suggested by Smith et al. (1985). The formulation is adapted from the linear inversion method for a single unknown variable described by Twomey (1977). For reasons which will be explained later, relative humidity was chosen as the water vapour variable.

The central problem associated with a simultaneous retrieval appears to be properly accounting for the effects of changes in transmittance with temperature and water vapour concentration. We chose a conceptually simple (although computationally expensive) approach to this problem. Perturbations proportional to the temperature and relative humidity eof's were added to the guess profiles, the NESDIS radiative transfer model was used to compute transmittances and radiances from the perturbed profiles, and the derivatives of the radiances with respect to the eof coefficients were estimated by finite differences.

The algorithm was tested using a sample of closely collocated radiosonde and TOVS data over eastern North America. Because the algorithm does not yet include the effects of clouds, the data set was manually screened to select clear observations for comparison.

2. THE ALGORITHM

In this section vectors are identified by underlined lower case letters and matrices by underlined upper case letters. The unknown temperature and relative humidity profiles are expressed as the sum of a first guess and a perturbation in the usual manner

$$T(p) = T_o(p) + t(p) \tag{1}$$

$$H(p) = H_o(p) + h(p) \tag{2}$$

For each TOVS channel, the difference between the observed radiance and the radiance calculated from the first guess is

$$r(\nu) = R(\nu) - R_o(\nu) \tag{3}$$

All the TOVS channels with the exception of channels 9, 17 and 20 were used in the retrieval.

In order to scale the equations, the radiance difference for each channel is multiplied by the rate of change of brightness temperature with respect to radiance (evaluated at R_o) and divided by the root-mean-square difference between brightness temperatures computed from radiosonde measurements and collocated TOVS observations

$$g(\nu) = \frac{\partial T^*}{\partial R} \quad \varepsilon^{-1} \; r(\nu) \tag{4}$$

If the surface temperature is taken as being equal to the temperature of the pressure level closest to the surface, the scaled radiance differences can be written as a vector function of the temperature and relative humidity perturbation vectors

$$\underline{g} = \underline{g}\,(\underline{t},\underline{h}) \tag{5}$$

The temperature and relative humidity perturbations are expressed as a linear combination of empirical orthogonal functions

$$t(p) = b_1 \, \emptyset_1 \, (p) + b_2 \, \emptyset_2 \, (p) + \ldots \, b_J \, \emptyset_J \, (p) \tag{6}$$

$$h(p) = b_{J+1} \, \emptyset_{J+1} \, (p) + \ldots + b_{J+K} \, \emptyset_{J+K} \, (p) \tag{7}$$

where the first J eof's are computed from a covariance matrix of temperature only and the next K eof's are computed from a covariance matrix of relative humidity only.

The scaled radiance differences can now be written as a vector function of the eof coefficients

$$\underline{g} = \underline{g}\,(\underline{b}) \tag{8}$$

Linearizing about the first guess we have

$$\underline{g} = \underline{A}\,\underline{b} \tag{9}$$

where $\underline{A}$ is the Jacobian matrix of $\underline{g}\,(\underline{b})$. Following Twomey (1977) this equation is solved using as a constraint the quadratic form $\underline{b}^T\underline{L}^{-1}\underline{b}$ where $\underline{L}^{-1}$ is the matrix containing, on the diagonal, the inverses of the eigenvalues corresponding to each eigenfunction

$$\underline{b} = (\underline{A}^T\underline{A} + \gamma \, \underline{L}^{-1})^{-1} \; \underline{A}^T\underline{g} \tag{10}$$

Because each eigenvalue is equal to the mean square value of the corresponding coefficient, this constraint allows the coefficients of the eigenfunctions which explain the most variance to be large. However, there is a large penalty incurred if the coefficient of an eigenfunction which explains little variance in the dependent data set is large. When the eigenvalues of temperature and relative humidity are combined into one matrix, the constraint also has the effect of scaling the perturbations of temperature and relative humidity so that the radiance differences are partitioned between these perturbations in a statistically likely manner.

Once the eof coefficients are obtained using equation (10) the retrieved profiles can be computed simply from equations (6) and (7).

In order to account for non-linearity in the radiative transfer equation, equation (10) was applied twice. The guess profile for the first iteration was a mean profile. The matrix $\underline{A}$ was recomputed for the second iteration using the output of the first iteration as the base state. It should be noted that the profiles resulting from the second iteration are still linear combinations of the original eigenfunctions and that the constraint remains the same for each iteration.

The Jacobian matrix $\underline{A}$ was calculated using centred finite differences

$$\frac{\partial g_i}{\partial b_j} = (g_i(\underline{b}^+) - g_i(\underline{b}^-))/2\ \alpha \qquad (11)$$

where $\underline{b}^+ = (0,0,\ldots,\alpha,0,\ldots,0)^T$ and $\underline{b}^- = (0,0,\ldots,-\alpha,0,\ldots,0)^T$.

Equations (6), (7) and (2) were used to calculate a temperature and relative humidity profile corresponding to $\underline{b}^+$ and a set of profiles corresponding to $\underline{b}^-$. The NESDIS radiative transfer algorithms which are available from CIMMS were used to compute transmittances and radiances for each set of profiles. The radiances were then used to obtain $\underline{g}(\underline{b}^+)$ and $\underline{g}(\underline{b}^-)$ from equation (4). The size of the finite difference was chosen so that the maximum temperature perturbation at any level was approximately 5K and the maximum relative humidity perturbation at any level was approximately 20 percent. Occasionally on the second iteration applying the relative humidity perturbation caused the relative humidity to be less than zero or greater than 100 percent. When this occurred the value of α was reduced. When α reached a minimum value a one-sided finite difference was used instead of the two-sided one. In a few cases it was necessary to truncate the relative humidity profile above 40 kPa in order to calculate an approximate derivative.

Choice of Water Vapour Variable

Previous algorithms for simultaneous retrieval of temperature and water vapour have used either precipitable water (Smith et al., 1985;

Fleming et al., 1986) or the natural logarithm of mixing ratio (Svensson, 1985). However, several difficulties arise when mixing ratio is used as the water vapour variable in a minimum-variance scheme incorporating statistical information.

Figure 1 shows mixing ratio as a function of temperature for the 50-70 kPa layer for 00Z radiosondes over eastern North America (latitudes 30-60N, longitudes 55-115W) between 1 May and 21 May, 1984. Figure 2 is the corresponding scatter plot of relative humidity versus temperature. It may be seen that the range of mixing ratio near the warm end of the temperature range is about four times as large as that at the cold end of the temperature range. On the other hand, there is no obvious relationship between the range of relative humidity and the temperature. The same plots were done for the 30-40 kPa, 40-50 kPa, 70-85 kPa, and 85-100 kPa layers. In each case the mixing ratio varied at least four times as much near the warm end of the temperature range as near the cold end. If the statistical model which forms part of the retrieval scheme assumed that the mixing ratio variance is constant, the result would be systematic under-estimation of the water vapour variations in warm air masses and systematic over-estimation of the water vapour variations in cold air masses. Because of the strong temperature contrasts across fronts in the mid-latitudes, it is important for a retrieval scheme to take into account the large variations in saturation mixing ratio with temperature.

The correlations between relative humidity and temperature and between mixing ratio and temperature were calculated using the same radiosonde data as above. The results are shown in Table 1. Except for an association between warm temperatures and dry air (and the reverse) below 70 kPa, the relationship between layer mean temperature and relative humidity is very weak. The correlation between mixing ratio and temperature, on the other hand, is dominated by the increase in mean mixing ratio with temperature. Evidently little sacrifice of information is involved in treating the covariances of temperature and relative humidity separately.

TABLE 1

Correlations between Water Vapour and Temperature, 1 May-21 May, 1984

Layer (kPa)	Mixing Ratio vs. Temperature	Relative Humidity vs. Temperature
30 - 40	0.60	-0.45
40 - 50	0.59	-0.39
50 - 70	0.54	-0.17
70 - 85	0.51	-0.21
85 - 100	0.55	0.14

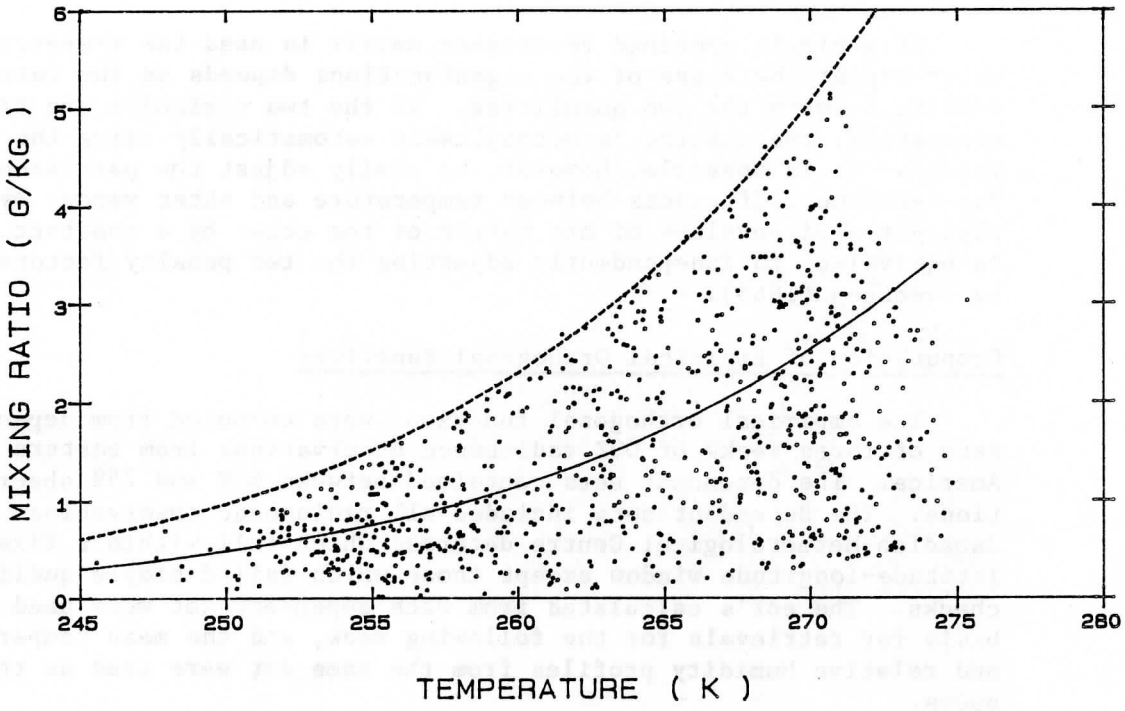

Figure 1. 50-70 kPa layer mean mixing ratio vs. temperature from May 01 to May 21, 1984 radiosondes. Curves show saturation mixing ratio (dashed) and mixing ratio corresponding to mean relative humidity (solid).

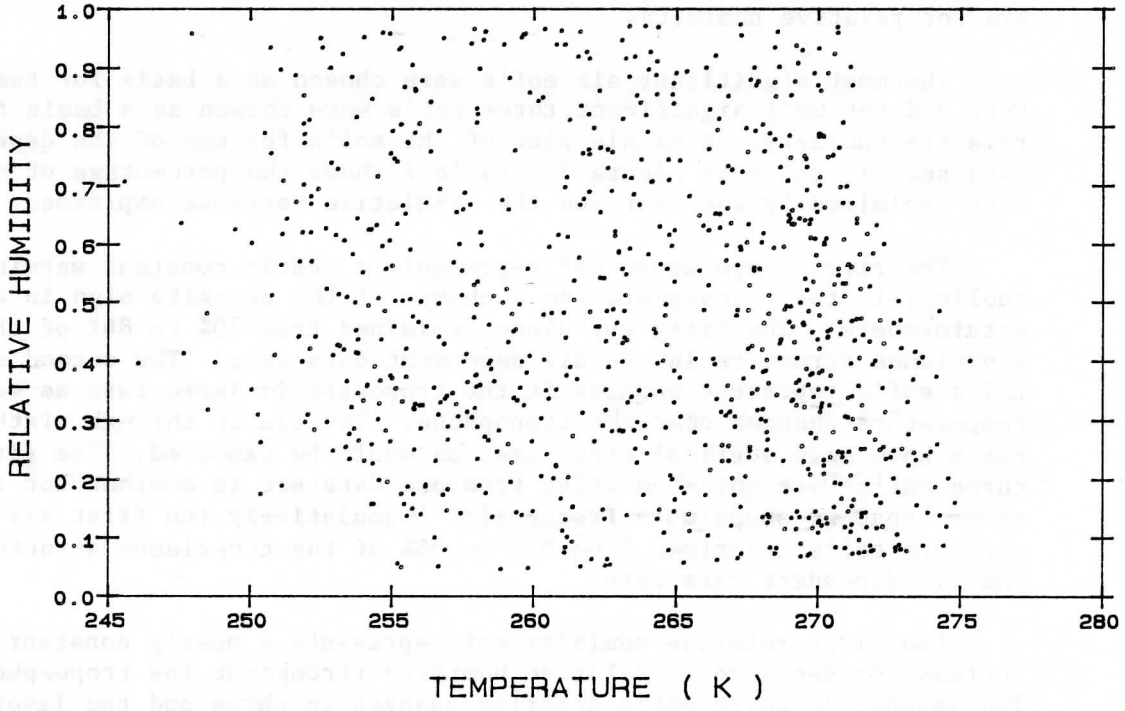

Figure 2. 50-70 kPa layer mean relative humidity vs. temperature from May 01 to May 21, 1984 radiosondes.

If a single combined covariance matrix is used for temperature and water vapour the shape of the eigenfunctions depends on the (arbitrary) scaling between the two quantities. If the two variables are treated separately, the scaling is accomplished automatically using the eigenvalues. It is possible, however, to easily adjust the partitioning of the radiance differences between temperature and water vapour by multiplying the eigenvalues of one matrix or the other by a constant. This is equivalent to independently adjusting the two penalty factors used by Svensson (1985).

Computation of Empirical Orthogonal Functions

The empirical orthogonal functions were computed from dependent sets of three weeks of 00Z radiosonde observations from eastern North America. The dependent sets contained between 579 and 759 observations. The dependent sets included all radiosonde observations on the Canadian Meteorological Centre database which fell within a fixed latitude-longitude window except those which failed simple quality checks. The eof's calculated from each dependent set were used as the basis for retrievals for the following week, and the mean temperature and relative humidity profiles from the same set were used as the first guess.

The eof's were obtained from the eigenvectors of separate covariance matrices of level temperatures and relative humidities computed from the radiosonde data. Covariances were computed for the standard NESDIS pressure levels (as used in the TOVS radiative transfer routines) between 100 kPa and 1 kPa for temperature, and 100 kPa and 30 kPa for relative humidity.

The most significant six eof's were chosen as a basis for temperature and the most significant three eof's were chosen as a basis for relative humidity. A sample plot of the eof's for one of the dependent data sets is shown in Figure 3. Table 2 shows the percentage of variance explained by each eof and the cumulative variance explained.

The first temperature eof represents a nearly constant warming (or cooling) in the troposphere and a change of the opposite sign in the stratosphere. The first eof alone explained from 70% to 86% of the covariance structure in the six dependent data sets. The second and third eof's represent changes in the tropospheric lapse rate as well as temperature changes near the tropopause. The fourth through sixth eof's have more vertical structure, as would be expected. The first three eof's were quite constant from one data set to another but the others changed shape more frequently. Cumulatively the first six temperature eof's described from 93% to 96% of the covariance structure in the six dependent data sets.

The first relative humidity eof represents a nearly constant increase or decrease in relative humidity throughout the troposphere. The second and third eof's describe changes in three and two layers respectively. The shape of the first three eof's remained nearly constant for all six dependent data sets but the order of importance

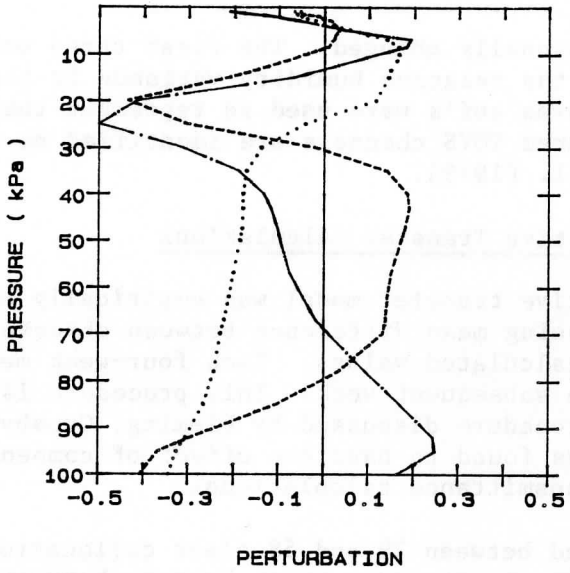

Figure 3a. First (dotted), second (dashed), and third (dash-dotted) temperature eigenvectors from April 10 to April 30, 1984 radiosondes.

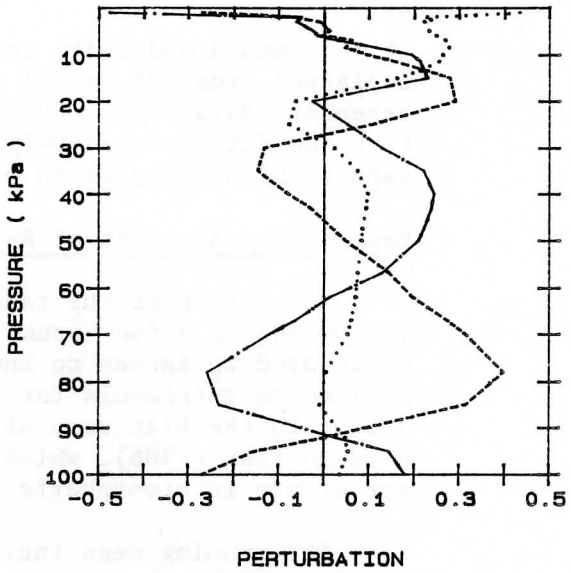

Figure 3b. Fourth (dotted), fifth (dashed), and sixth (dash-dotted) temperature eigenvectors from April 10 to April 30, 1984 radiosondes.

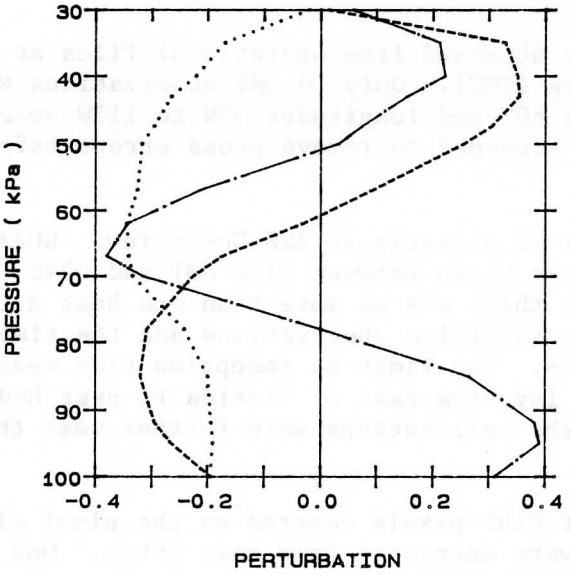

Figure 3c. First (dotted), second (dashed), and third (dash-dotted) relative humidity eigenvectors from April 10 to April 30, 1984 radiosondes.

Table 2. Variance explained by temperature (T) and relative humidity (RH) eof's 10-30 April 1984

EOF	Variance %	Cumulative %
T1	70.3	70.3
T2	9.4	79.7
T3	6.1	85.7
T4	3.8	89.5
T5	2.3	91.8
T6	1.6	93.4
RH1	40.4	40.4
RH2	25.3	65.8
RH3	11.5	77.3

of the second and third occasionally changed. The first three eof's explained from 70% to 77% of the relative humidity variance in the dependent data sets. Only three eof's were used to represent the relative humidity because only three TOVS channels are identified as water vapour channels by Smith et al. (1979).

Empirical Adjustment of Radiative Transfer Calculations

The output of the radiative transfer model was empirically adjusted by adding a four-week running mean difference between observed and calculated radiances to the calculated values. Each four-week mean was applied to retrievals for the subsequent week. This procedure is analogous to the bias removal procedure discussed by Fleming, Crosby, and Neuendorffer (1986), which was found to have the effect of compensating for errors in atmospheric transmittance calculations.

The running mean included between 29 and 58 clear collocations. The four week period was chosen to strike a rough balance between obtaining a statistically stable bias and tracking changes in the bias with time.

3. DATA

The retrieval algorithm was tested using collocated TOVS and radiosonde data over eastern North America during a six-week period from 1 May 1984 to 11 June 1984. An additional four weeks of data from 3 April 1984 to 30 April 1984 were used for generating eof's and empirical corrections to the radiative transfer model.

The radiosonde data were obtained from operational files at the Canadian Meteorological Centre (CMC). Only 00 GMT observations which fell between latitudes 30N to 60N and longitudes 55W to 115W were used. The radiosonde profiles were screened to remove gross errors before being used.

The TOVS data were received directly at AES Downsview. NOAA-8 orbits for which data reception began between 2300 GMT and 0040 GMT were used. This ensured that there was no more than one hour difference between the time of the satellite observations and the time when the radiosondes were at 30 kPa. The limit on reception time meant that most of the satellite tracks lay from east of Florida to near Hudson Bay. Consequently, none of the collocations were further west than 105W.

Three by three arrays of HIRS pixels centred on the pixel closest to each radiosonde location were extracted from each orbit. One set of brightness temperatures was obtained from each array by averaging the pixels for which the channel 8 brightness temperature was within 2K of the maximum value in the array. Arrays with less than three pixels satisfying this criterion were eliminated.

Because the eof algorithm does not yet contain cloud detection and correction routines, the HIRS data were manually screened to eliminate

clouds. The screening was based on visual examination of visible and infrared imagery. A total of 82 clear collocations were obtained from the six-week period.

4. RESULTS

Figure 4 shows the RMS differences between layer mean temperatures computed from the retrievals and those from the 82 collocated radiosondes. RMS differences are shown for both the first and the second iteration. Figure 5 shows the corresponding RMS differences for mixing ratio. Although there was a noticeable improvement in the temperature retrievals from the first iteration to the second, the mixing ratio differences began to increase below 85 kPa. In fact, for this layer the RMS mixing ratio differences on the second iteration were larger than they would have been if the original relative humidity guess had not been modified. Because of the importance of water vapour near the ground in driving convection and in contributing to total precipitable water, this was considered to be a serious deficiency.

To try to overcome this problem, we modified the constraint matrix L on the first iteration by dividing the eigenvalues corresponding to the three relative humidity eof's by ten. This had the effect of causing the first iteration to be mainly an adjustment of temperature. However, the mixing ratio was also changed since it was the relative humidity which remained nearly constant, and the adjustment to the temperature took into account this increase or decrease in mixing ratio. Figures 6 and 7 show the RMS differences for temperature and mixing ratio, after one and two iterations, which resulted when this adjustment was made. There was little difference in the temperature retrievals. The mixing ratio differences after two iterations were the same above 70 kPa, but there was a noticeable decrease in the RMS difference for 85-100 kPa.

This procedure was selected because the first guess in these retrievals was frequently a long way from the final solution, and because the dependence of the radiance measurements on relative humidity changes strongly with temperature. It can be seen from Figure (1) that if the temperature is adjusted holding the relative humidity constant, a reasonably good estimate of the mixing ratio is obtained. Once the temperature is closer to the final solution, better estimates of the dependence of the radiances on the relative humidity profile can be obtained. If a better first guess were used, it is possible that this step would not be required.

Effect of Surface Emissivity

Kornfield and Susskind (1977) showed that assuming the surface emissivity is unity may cause significant errors in temperature retrievals over land. Accordingly, the radiative transfer model used in the retrievals was modified to allow optional use of surface emissivities which differed from one. The contribution of radiation reflected from the surface was included following the procedure

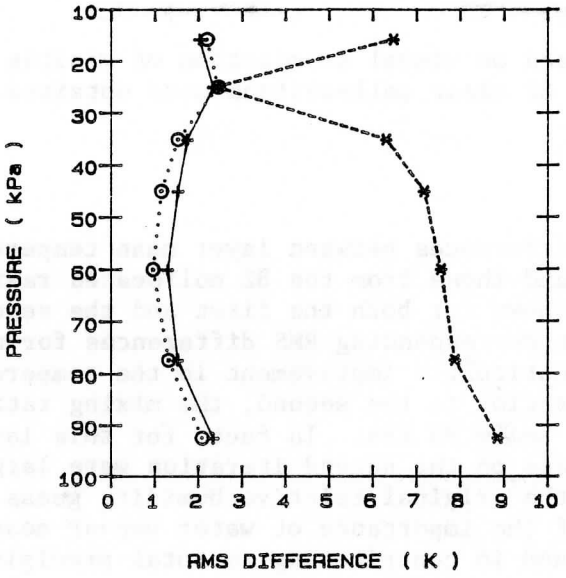

Figure 4. RMS differences for layer mean temperatures for one (solid) and two (dotted) iterations. Standard deviation of radiosonde temperatures (dashed) also shown.

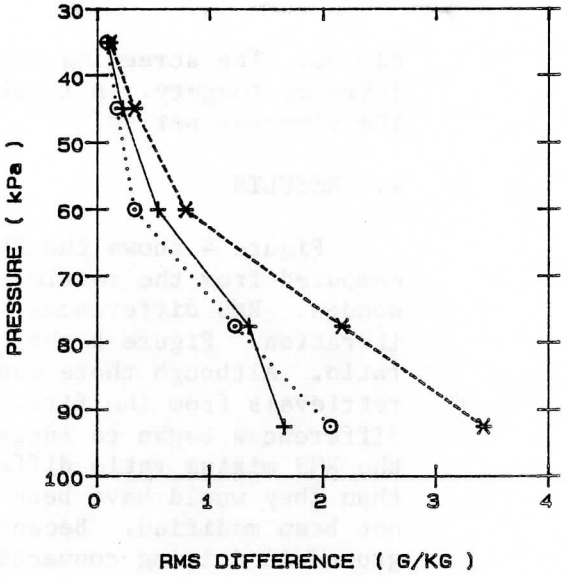

Figure 5. RMS differences for layer mean mixing ratios for one (solid) and two (dotted) iterations. Standard deviation of radiosonde mixing ratios (dashed) also shown.

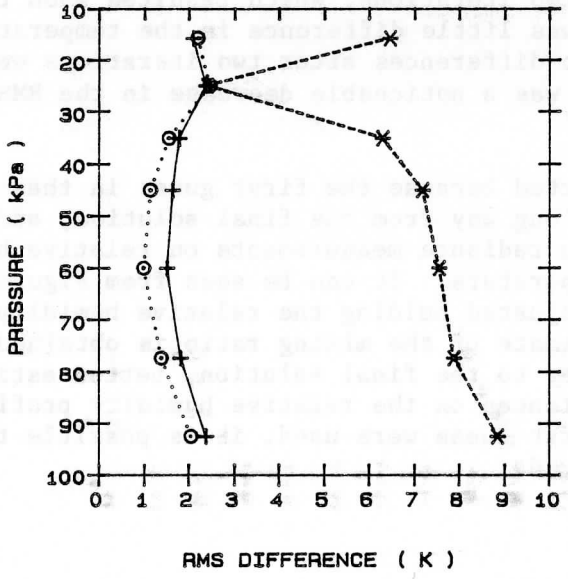

Figure 6. As in Figure 4 but with lower weight on relative humidity for first iteration.

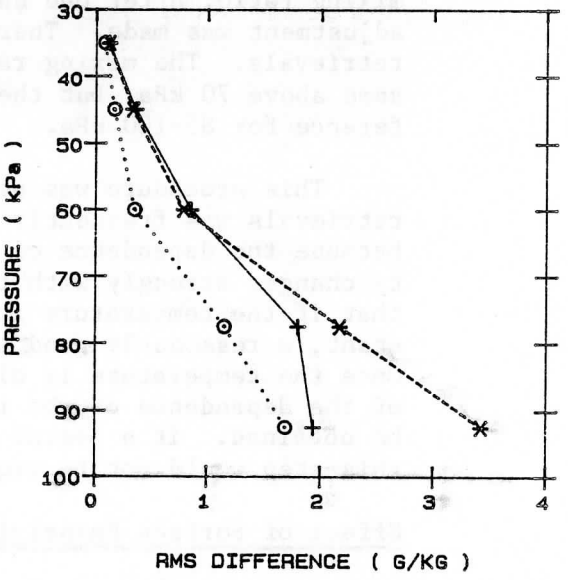

Figure 7. As in Figure 5 but with lower weight on relative humidity for first iteration.

described by Susskind et al. (1982). Because Susskind et al. did not include emissivity values for HIRS channels 10 to 12, we arbitrarily used the same values for those channels as for channels 13 to 17.

Radiances were computed using the 82 radiosonde profiles in the collocated data set with both unit and non-unit surface emissivities. Statistics of the differences between observed and computed brightness temperatures for both sets of calculations are shown in Figure 8.

As one would expect, there is no discernible effect on channels for which the weighting functions peak much above the surface (1 through 5, 11, 12, 15 and 16). The mean difference from observations is significantly reduced when non-unit emissivity is used for channels 8, 10, 13, 14, 18 and 19, which all peak at or near the surface. However, there is no significant reduction in the standard deviation of the differences for these channels. Consequently, one would expect that if an empirical bias adjustment was applied to the calculated radiances, the effect of the emissivity adjustment on retrievals would be small.

Figure 9 compares retrievals made assuming unit and non-unit emissivity. In both cases the radiance computations were adjusted using the procedure described in Section 2. It can be seen that there was a slight improvement in both temperature and water vapour retrievals when non-unit emissivity was used, and that the difference was largest near the surface (0.2 K and 0.3 g/kg for the 85-100 kPa layer).

Information Content of Water Vapour Retrievals

Figure 1 illustrates the strong correlation between temperature and mixing ratio that exists in the mid-latitudes. The North American radiosonde data which was studied indicates that this correlation is almost entirely attributable to the variation with temperature of the water vapour carrying capacity of the air. Consequently, a reasonably good estimate of the mixing ratio may be obtained if one knows the temperature profile and has an estimate of the climatological mean relative humidity.

In order to quantify the mixing ratio information carried by the temperature retrieval alone, we computed the mixing ratio profiles which would be obtained if the actual relative humidity retrievals were replaced by the first guess (i.e., the mean relative humidity profile computed from radiosondes for the previous three weeks). These mixing ratio profiles will be referred to as MEAN RH retrievals. Figure 10 compares the RMS mixing ratio differences from radiosondes for the retrievals shown in Figure 4 and the corresponding MEAN RH retrievals. Above 70 kPa the RMS differences for the MEAN RH retrievals were larger than the standard deviation of the radiosonde mixing ratios. In the 70-85 kPa layer the actual relative humidity retrievals carried significantly more information than the MEAN RH retrievals. However, in the 85-100 kPa layer the RMS differences for the MEAN RH retrievals and the

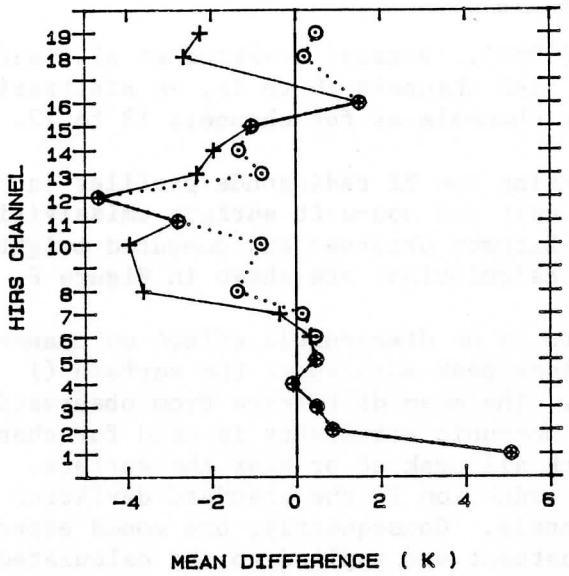

Figure 8a. Mean difference between computed and observed brightness temperatures for unit emissivity (solid) and non-unit emissivity (dotted).

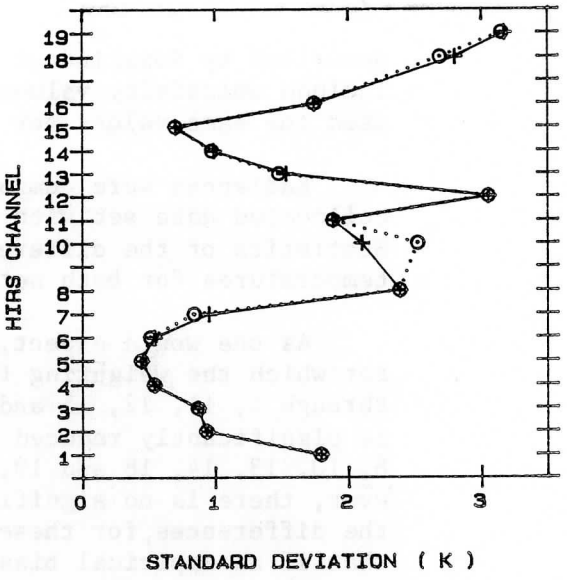

Figure 8b. Standard deviation of difference between computed and observed brightness temperatures for unit emissivity (solid) and non-unit emissivity (dotted).

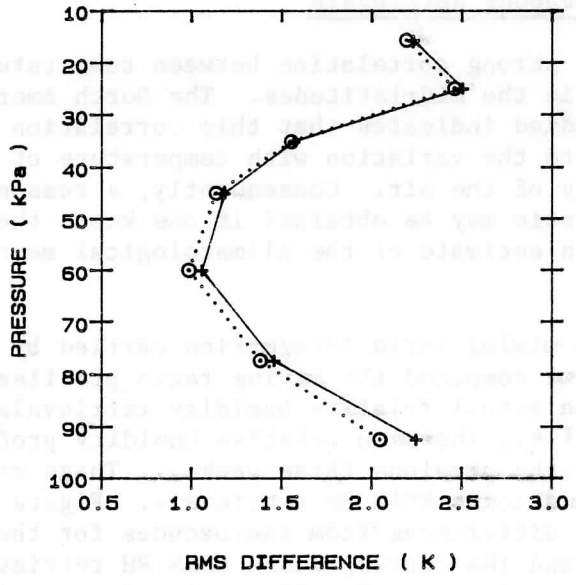

Figure 9a. RMS differences for layer mean temperatures for unit emissivity (solid) and non-unit emissivity (dotted).

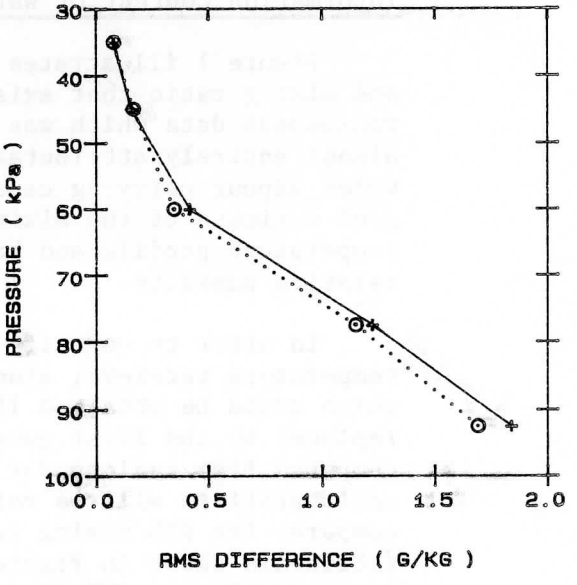

Figure 9b. RMS differences for layer mean mixing ratios for unit emissivity (solid) and non-unit emissivity (dotted).

actual retrievals were almost the same. The correlation between the retrieved relative humidity and the radiosonde relative humidity was calculated for each layer (Table 3). The 85-100 kPa correlation was near zero although the correlation was significant for each layer above 85 kPa. The differences between the retrieved relative humidity profiles and the radiosonde measurements are due to the combined effects of errors in both systems, differences between volume and point sampling, and variations in the atmosphere on scales smaller than the errors in collocation. Consequently, it may be that the retrievals actually contain information on 85-100 kPa relative humidity. However, using the collocated radiosondes it is not possible to distinguish between the simultaneous retrievals and retrievals containing no relative humidity information below 85 kPa. It should be noted that for the 85-100 kPa layer the mean square difference between the MEAN RH retrievals and the radiosonde mixing ratios was only 25% of the variance computed from the radiosondes.

It was shown by Hillger (1984) that radiance measurements in HIRS channel 10 (which is commonly identified as the lowest peaking water vapour sounding channel) are quite insensitive to low-level water vapour, and that in fact the sign of the dependency may change if a surface inversion is present. The same situation may occur if the

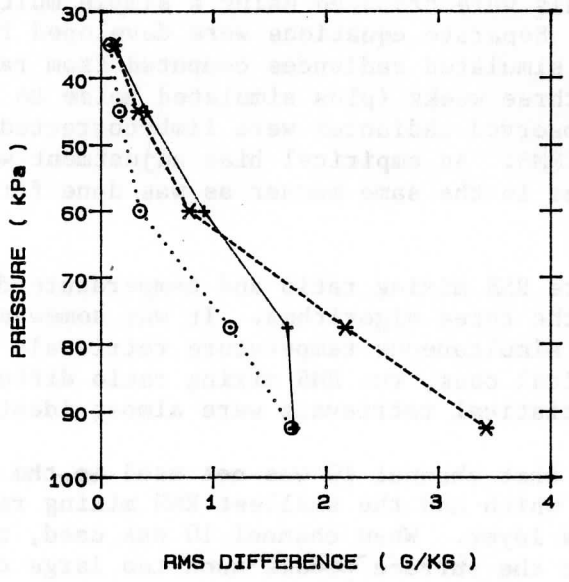

Figure 10. RMS differences for layer mean mixing ratios from simultaneous retrievals (dotted) and MEAN RH retrievals (solid). Standard deviation of radiosonde mixing ratios (dashed) also shown.

Table 3. Water vapour correlation between radiosondes and retrievals

Layer (kPa)	Mixing Ratio	Relative Humidity
30-40	0.78	0.45
40-50	0.90	0.59
50-70	0.90	0.76
70-85	0.88	0.41
85-100	0.90	0.10

surface emissivity in channel 10 is significantly less than one. In order to test the dependence of the retrievals on the channel 10 measurements the retrievals were re-run with channel 10 removed from the measurement vector. The result was a reduction in the RMS mixing ratio difference of 0.02 g/Kg in the 85-100 kPa layer. This negligible change indicates that if significant low-level water vapour information is contained in channel 10 it is not being exploited by the algorithm.

Comparison with Other Algorithms

Retrievals produced using the eof algorithm were compared with retrievals made using a non-linear iterative method and a statistical method.

The non-linear iterative method is based on algorithms described by Smith (1970), Chahine (1968), and Hillger (1984). The first guess profiles which were used with this method were produced by multi-linear regression using only MSU channels 2, 3 and 4 as predictors. Separate regression equations were used for each week's retrievals, based on MSU data simulated from radiosondes for the previous three weeks. Although the starting point for the method was the code available from CIMMS and described by Smith et al. (1984), there are a number of dissimilarities and the results cannot be considered to be necessarily representative of those which would have been obtained using the CIMMS method.

The statistical retrievals were produced using a simple multi-linear regression technique. Separate equations were developed for each week's retrievals using simulated radiances computed from radiosonde data for the previous three weeks (plus simulated noise to stabilize the retrievals). The observed radiances were limb-corrected using the routine available from CIMMS. An empirical bias adjustment was made to the computed radiances in the same manner as was done for the other two methods.

Figures 11 and 12 compare RMS mixing ratio and temperature differences from radiosondes for the three algorithms. It was somewhat surprising that although the simultaneous temperature retrievals were much superior to the statistical ones, the RMS mixing ratio differences for the simultaneous and statistical retrievals were almost identical.

It should also be noted that channel 10 was not used in the non-linear iterative retrievals, which had the smallest RMS mixing ratio differences in the 85-100 kPa layer. When channel 10 was used, the mixing ratio adjustments near the surface became much too large unless an arbitrary limit was introduced.

Retrieval of Tropopause Height

Tropopause heights were manually identified from tephigram plots of the retrievals and the collocated radiosondes. The standard WMO definition was used (i.e. the lowest level at which the lapse rate was less than 2K km^{-1}). The RMS difference between the radiosonde

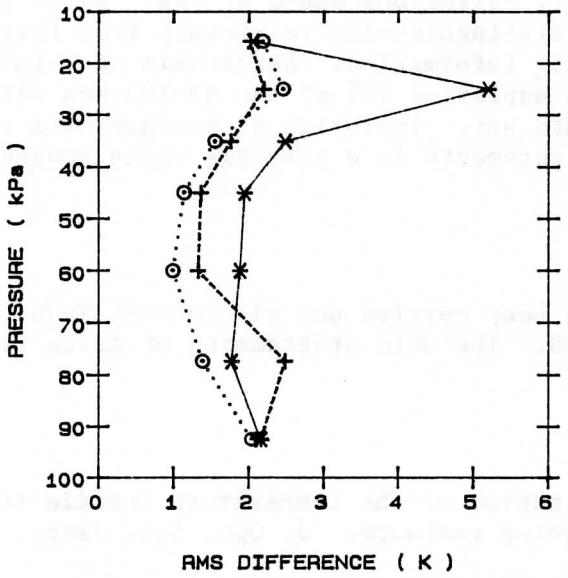

Figure 11. RMS differences for layer mean temperatures for simultaneous retrievals (dotted), non-linear iterative retrievals (dashed), and statistical retrievals (solid).

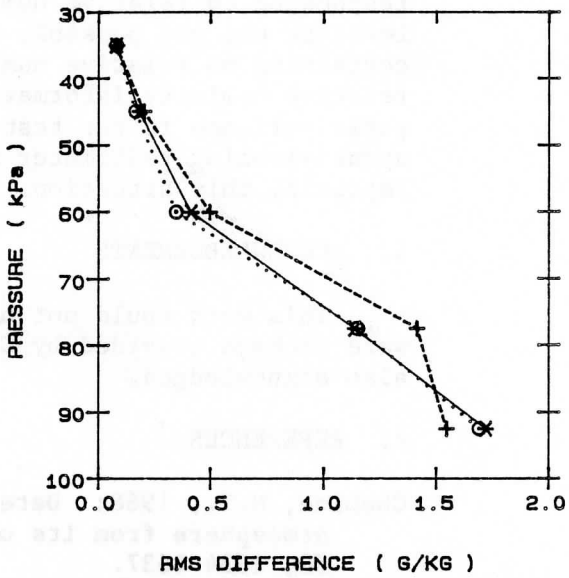

Figure 12. RMS differences for layer mean mixing ratios for simultaneous retrievals (dotted), non-linear iterative retrievals (dashed), and statistical retrievals (solid).

tropopause heights and the first guesses used in the corresponding retrievals was 62 hPa. The RMS difference between the radiosonde tropopause heights and the retrievals was 35 hPa, indicating that the retrievals were explaining 68% of the variance in the radiosonde tropopause height. The retrieved tropopause height was displaced by as much as 100 hPa from the first guess.

5. CONCLUSIONS

Although the algorithm was tested using manually screened data for only one season, the results appear to be promising. The RMS layer mean temperature difference from collocated radiosondes ranged from 1.0K for 50-70 kPa to 2.4K for 20-30 kPa. The algorithm was able to explain 68% of the variance of tropopause height in the collocated radiosondes. Iteration of the solution to account for non-linearity of the radiative transfer was shown to improve both the temperature and water vapour retrievals. The use of surface emissivities smaller than one (following Susskind et al. (1982)) resulted in a small improvement in retrievals of both quantities.

Comparison of the results with retrievals from which the relative humidity information had been removed showed that the algorithm was responding to relative humidity variations above 85 kPa. Below that level it was not possible to distinguish the retrievals from those containing no relative humidity information. Retrievals containing no relative humidity information explained 75% of the 85-100 kPa mixing ratio variance in our test data set. Inclusion of surface data or upward-looking radiometer measurements is a possible route toward improving this situation.

6. ACKNOWLEDGEMENTS

This work could not have been carried out without the TOVS software package provided by CIMMS. The able programming of Alvin Li is also acknowledged.

7. REFERENCES

Chahine, M.T., 1968: Determination of the temperature profile in an atmosphere from its outgoing radiance. J. Opt. Soc. Amer., **58**, 1634-1637.

Fleming, H.E., D.S. Crosby and A.C. Neuendorffer, 1986: Correction of satellite temperature retrieval errors due to errors in atmospheric transmittances. J. Climate Appl. Meteor. **25**, 869-882.

Fleming, H.E., M.D. Goldberg and D.S. Crosby, 1986: Minimum variance simultaneous retrieval of temperature and water vapor from satellite radiance measurements. Preprints, Second Conf. on Satellite Meteorology/Remote Sensing and Applications, Williamsburg, Amer. Meteor. Soc., 20-23.

Hillger, D.W., 1984: Spatial and temporal variations in mesoscale water vapor retrieved from TOVS infrared radiances in a nocturnal inversion situation. J. Climate Appl. Meteor., **23**, 704-723.

Kornfield, J., and J. Susskind, 1977: On the effect of surface emissivity on temperature retrievals. Mon. Wea. Rev., **105**, 1605-1608.

Smith, W.L., 1970: Iterative solution of the radiative transfer equation for the temperature and absorbing gas profile of an atmosphere. Appl. Opt., **9**, 1993-1999.

...., H.M. Woolf, C.M. Hayden and A.J. Schreiner, 1985: The simultaneous retrieval export package. Tech. Proc., Second International TOVS Study Conference, Igls, Austria, Cooperative Institute for Meteorological Satellite Studies, 224-253.

...., ..., ..., ..., and J.F. LeMarshall, 1984: The physical retrieval TOVS export package. Tech. Proc., First International TOVS Study Conference, Igls, Austria, Cooperative Institute for Meteorological Satellite Studies, 227-278.

...., ..., ..., D.Q. Wark and L.M. McMillin, 1979: The TIROS-N operational vertical sounder. Bull. Amer. Meteor. Soc., 60, 1177-1187.

Susskind, J., J. Rosenfield, D. Reuter and M.T. Chahine, 1982: The GLAS physical inversion method for analysis of HIRS2/MSU sounding data. NASA Tech. Mem. 84936, 101 pp.

Svensson, J., 1985: A nonlinear inversion method for derivation of temperature profiles from TOVS data. Tech. Proc., Second International TOVS Study Conference, Igls, Austria, Cooperative Institute for Meteorological Satellite Studies, 292-307.

Twomey, S., 1977: Introduction to the Mathematics of Inversion in Remote Sensing and Indirect Measurements, Elsevier Scientific, 139-144.

ESTIMATING THE CORRECT DEGREE OF SMOOTHING IN THE SIMULTANEOUS RETRIEVAL METHOD

Jan Svensson
The Swedish Meteorological and Hydrological Institute (SMHI)
Norrköping, Sweden

1. INTRODUCTION

The International TOVS Processing Package, version 3 (ITPP3), developed by the Cooperative Institute for Meteorological Satellite Studies (CIMSS), Madison, Wisconsin,has been implemented on the VAX 8600 computer system at SMHI. Test data were taken from the Meso-scale Analysis Area for PROMIS 600 at SMHI (appr. 54-61^{o}N, 6-28^{o}E), see Gustafsson and Törnevik (1984), during the period May 3-26, 1983. Fifteen satellite passages were processed. The same data have been used in the test of ITPP2, see Svensson (1984, 1985a). The test results for the temperature profiles are compared in Figure 1. This figure shows a significant improvement in ITPP3, especially for cloudy retrievals. The filtering programs, in ITPP2 and ITPP3 respectively, were used before comparison with radiosonde data. In ITPP2 24.8% of all soundings were rejected, while in ITPP3 only 8.2% were rejected. Another advantage is that ITPP3 seems to be faster. ITPP2 was implemented on a SPERRY 1122, which means that an exact comparison of execution times is difficult to do. The estimated CPU-time for one satellite passage is 9.5 minutes and estimated elapsed time is 19 minutes for ITPP3 on VAX 8600. One simple, but effective, modification of the program TOVRET in ITPP3 was done. The coefficients for HIRS radiative-transfer computations were stored in the virtual memory once and for all. In the original version the coefficients were reread every sounding. The I/O count in TOVRET was reduced with nearly 45% with our modification.

We will later implement the inversion method THAP, described by Svensson (1985a, 1985b) in ITPP3. The intention is to use the generalized cross-validation (GCV) in order to automatically select the regularization parameter. The GCV is more difficult to use in THAP than in the ordinary inversion method. Thus it seems reasonable to try to use the GCV in the ordinary inversion method first. In Section 2 we describe briefly the inversion method in ITPP3 and in Section 3 we describe the GCV. In section 4 we show some test results.

2. THE INVERSION METHOD IN ITPP3

The inversion method in ITPP3, also known as 'the simultaneous retrieval method', is described by Smith et al (1985). We shall here make a very short description of the method.

We start with an initial guess of the temperature and moisture profiles. We will then estimate a perturbation from the initial profiles. We have to solve the least-squares problem

$$\min_{\underset{\sim}{x}} \; || \underset{\approx}{A} \cdot \underset{\sim}{x} - \underset{\sim}{B} ||_2^2$$

where $\underset{\sim}{B}$ is a radiance vector, $\underset{\approx}{A}$ is a matrix calculated from the radiative transfer equation and $\underset{\sim}{x}$ is the perturbation vector to be found (more details are found in Smith et al (1985) or Svensson (1985 a, 1985 b). This least squares problem is ill-conditioned, that is taken the least-squares solution

$$\underset{\sim}{x} = (\underset{\approx}{A}^T \cdot \underset{\approx}{A})^{-1} \cdot \underset{\approx}{A}^T \cdot \underset{\sim}{B}$$

will give a physically unacceptable solution. If we add a regularization term

$$\underset{\sim}{x} = (\underset{\approx}{A}^T \cdot \underset{\approx}{A} + \lambda \cdot \underset{\approx}{I})^{-1} \cdot \underset{\approx}{A}^T \cdot \underset{\sim}{B} \qquad (1)$$

where λ is the regularization parameter and $\underset{\approx}{I}$ is the unit matrix, then we have a more well-conditioned problem with a physically acceptable solution. The parameter λ gives the degree of smoothing. If $\lambda \to 0$, then we will have the least-squares solution and if $\lambda \to \infty$, then we will have the initial profile as the solution.

The solution is received in two steps in ITPP3. In step 1 only the microwave channels and HIRS channels 1-3 and 11-12 are used. These channels are less affected by clouds, which means that they can be used for cloud correction of the other HIRS channels. In step 2 as many as nineteen different radiances are used. In step 1 the regularization parameter $\lambda = 1.0$ and in step 2, $\lambda = 0.1$ for clear retrievals and $\lambda = 1.0$ for cloudy retrievals. An automatic selection of λ would be preferable. Such an automatic selection would distinguish between good or bad initial guesses and between good or bad cloud corrections. The GCV is such an automatic method.

3. GENERALIZED CROSS-VALIDATION

The method of generalized cross-validation, described by Craven and Wahba (1979) and Golub et al (1979), determines the regularization parameter from the data, that is in our case from the radiances. The

parameter λ in (1) is determined as the minimizer of

$$V(\lambda) = || (\underset{\approx}{I} - \underset{\approx}{K}(\lambda) \cdot \underset{\sim}{B} ||_2^2 / (\text{trace } (\underset{\approx}{I} - \underset{\approx}{K}(\lambda)))^2$$

where

$$\underset{\approx}{K}(\lambda) = \underset{\approx}{A} (\underset{\approx}{A}^T \cdot \underset{\approx}{A} + \lambda \cdot \underset{\approx}{I})^{-1} \cdot \underset{\approx}{A}^T$$

We may calculate $V(\lambda)$ and $V'(\lambda)$ from the singular value decomposition of $\underset{\approx}{A}$, see Golub et al (1979) or from the bidiagonal decomposition, see Eldén (1984). We use the method of Eldén in the calculation of $V(\lambda)$ and use a golden section search, see Gill et al (1981), for the minima search. We prefer to make the minimization in a $\log(\lambda)$ scale as proposed by O'Sullivan and Wahba (1985).

The GCV gives a good estimation of the optimum λ when the errors in $\underset{\sim}{B}$ are uncorrelated with no bias. A Monte Carlo experiment with this assumption, using data from TOVS, is described by O'Sullivan and Wahba (1985).

4. TEST RESULTS

We have implemented the GCV algorithm in step 2 in the simultaneous retrieval method. In step 1 the regularization parameter is still fixed. The first attempt with GCV was rather discouraging. The values of λ were for some cases much less than 0.1 and for other cases much greater than 1.0. The RMS differences to the radiosonde data were more than 5^oC. We then limited the range of λ from 0.1 to 1.0. The RMS differences between satellite soundings and radiosondes are shown in Figure 2. This figure shows almost the same result for the soundings with fixed λ and those with λ decided by the GCV. The standard deviations between satellite soundings and radiosondes are shown in Figure 3. A small improvement when using the GCV is indicated for the cloudy retrievals.

One explanation of why we did not receive a more significant improvement of the satellite soundings, is that the assumption of uncorrelated errors with no bias is not fulfilled. We may suppose that there might be a bias, e g if the cloud algorithm fails to detect clouds for some situations, then we will have a negative bias. The cloud correction algorithm also makes the radiance errors correlated, because errors in the radiances used in step 1 will introduce errors in the cloud corrected radiances. A better understanding of the error statistics of the cloud corrected radiances would be valuable. The use of AVHRR for cloud correction might give a better agreement to the assumption of uncorrelated radiance errors with no bias.

It should be pointed out that the GCV is very inexpensive for such small least-squares problems like this one. The CPU time for the inversion method does not increase, when we added the GCV subroutines. The use of GCV seems encouraging, but more work must be done before it can be used in operational systems.

5. REFERENCES

Craven, P. and G. Wahba, 1979: Smoothing Noisy Data with Spline Functions: Estimating the Correct Degree of Smoothing by the Method of Generalized Cross-Validation. Numerische Mathematik, 31, 377-403.

Eldén, L., 1984: A note on the computation of the generalized cross-validation function for ill-conditioned least squares problems, BIT, 24, 467-472.

Gill, P.E., W. Murray and M.H. Wright, 1981: Practical Optimization, Academic Press, London.

Golub, G.H., M. Heath and G. Wahba, 1979: Generalized Cross-Validation as a Method for Choosing a Good Ridge Parameter. Technometrics, 21, 215-223.

Gustafsson, N. and H. Törnevik, 1984: Development of an Operational System for Very-Short-Range Forecasting (VSRF) at SMHI. Proceedings of the Second International Symposium on Nowcasting, Norrköping, Sweden, 3-7 September, 1984, 473-477.

O'Sullivan, F. and G. Wahba, 1985: A Cross Validated Bayesian Retrieval Algorithm for Nonlinear Remote Sensing Experiments. Journal of Computational Physics, 59, 441-455.

Smith, W.L., H.M. Woolf, C.M. Hayden and A.J. Schreiner, 1985: The simultaneous retrieval export package. Technical Proceedings of The Second International TOVS Study Conference, Igls, Austria, 18-22 February, 1985, 224-253.

Svensson, J., 1984: Temperature profile retrievals from TIROS Operational Vertical Sounder during the ONSAM-experiment. R & D notes 33, SMHI, Norrköping, Sweden, 13 pp.

Svensson, J., 1985a: Remote sensing of atmospheric temperature profiles by TIROS Operational Vertical Sounder, RMK 45, SMHI, Norrköping, Sweden, 61 pp.

Svensson, J, 1985b: Numerical treatment of an ill-posed problem in remote sensing of atmospheric temperature profiles, Report LiU-TEK-LIC-1985:23, Dept of Mathematics, Linköping University, 69 pp.

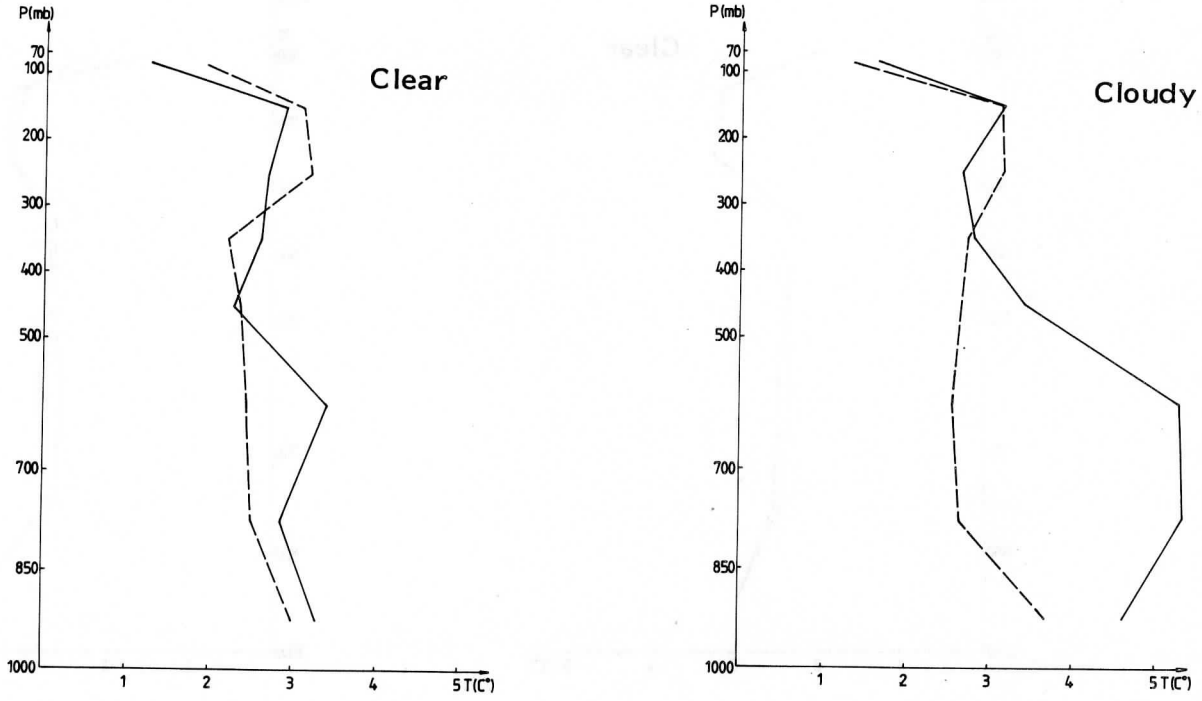

FIGURE 1. RMS differences in layer mean temperatures between satellite soundings and radiosondes launched in the Meso-scale Analysis Area.

——— = *satellite soundings from ITPP2 (104 clear retrievals, 34 cloudy retrievals)*

----- = *satellite soundings from ITPP3 (71 clear retrievals, 93 cloudy retrievals)*

First guess profile = climate.

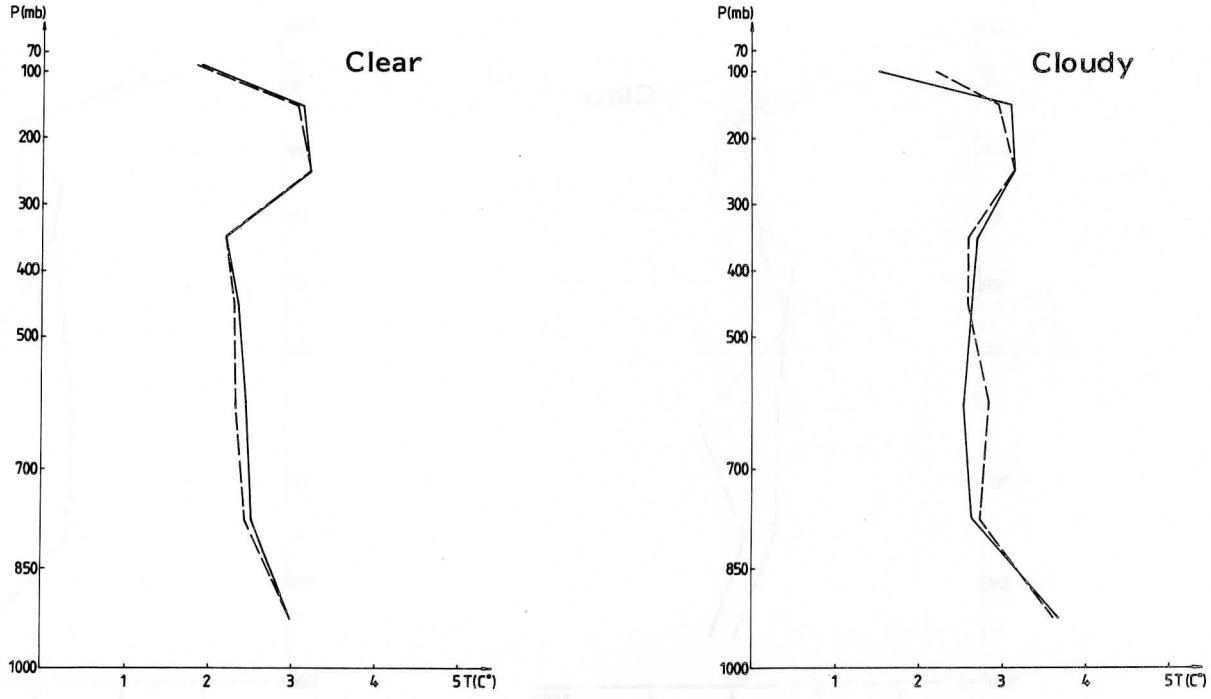

FIGURE 2. RMS differences in layer mean temperatures between satellite soundings and radiosondes launched in the Meso-scale Analysis Area.

——— = *satellite soundings from ITPP3, with fixed regularization parameter*
(71 clear retrievals, 93 cloudy retrievals)

----- = *satellite soundings from ITPP3, with regularization parameter determined by the method of generalized cross-validation*
(72 clear retrievals, 92 cloudy retrivals)

First guess profile = climate.

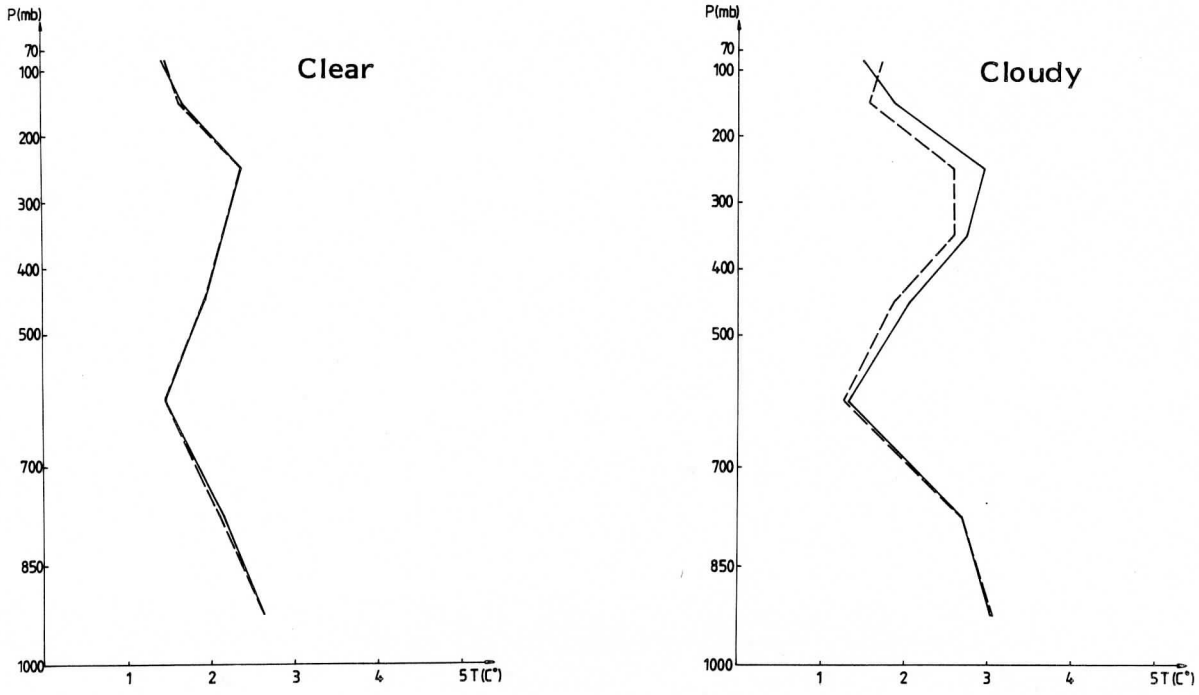

FIGURE 3. Standard deviation of differences in layer mean temperatures between satellite soundings and radiosondes launched in the Meso-scale Analysis Area.

——— = *satellite soundings from ITPP3, with fixed regularization parameter (71 clear retrievals, 93 cloudy retrievals)*

----- = *satellite soundings from ITPP3, with regularization parameter determined by the method of generalized cross-validation (72 clear retrievals, 92 cloudy retrievals)*

First guess profile = climate.

SYNTHETIC AND REAL DATA APPLICATIONS OF THE TYPICAL SHAPE FUNCTION SIMULTANEOUS PHYSICAL RETRIEVAL ALGORITHM

Michael J. Uddstrom

New Zealand Meteorological Service
Wellington, New Zealand

1. INTRODUCTION

Recently a number of important advances have been made in the specification of linear measurement models for the radiative transfer equation (Smith and Woolf, 1984; Smith *et al.* 1985; Fleming *et al.* 1986). However, because the retrieval problem is fundamentally ill-posed, additional ancillary data must always be supplied to retrieval estimators. The problem of the specification of the *a priori* first guess profile and retrieval constraints has been addressed by a number of authors, including Westwater *et al.* (1983), Uddstrom and Wark (1985), Chedin *et al.* (1985), Thompson *et al.* (1985), Wark (1986) and McMillin (1986). Each of these papers suggest different methods for determining first guess profiles, and in some cases retrieval constraints, which are independent of numerical weather prediction models, yet appropriate to the sounded atmosphere.

The purpose of this paper is to outline the characteristics of a physical simultaneous retrieval algorithm which utilises the method of Typical Shape Function (TSF) classification (Uddstrom and Wark, 1985; henceforth abbreviated UW). The advances made in both the selection of the first guess profile and constraints, and measurement specification models, are incorporated in this new algorithm. The essential element of TSF classification is that it enables the development of a non-linear retrieval scheme, without recourse to relaxation or iterative techniques. Instead, local domains in both radiance and retrieval parameter space are defined, in which the constituent atmospheres are in some sense linearly related. Within each TSF domain, linear retrieval methods may be applied without the usual consequences associated with the application of linear perturbation theory to strongly non-linear problems. In addition to providing a good estimate of the first guess profile, the TSF classification method also provides covariance constraints which define the "shape" of each TSF atmospheric class. This additional information is important and may be utilized in an appropriately specified retrieval algorithm.

The full TSF retrieval algorithm, which includes *a priori* temperature classification, radiance discrimination, cloud detection and correction, and simultaneous maximum *a posteriori* retrieval estimators, is applied to synthetic data and two NOAA 7 passes over the New Zealand region in July 1984. The TSF retrieval results are subjectively compared with operational NWP analyses, and output from the New Zealand Meteorological Service's operational retrieval scheme, which is a version of the NOAA NESDIS Development Laboratory - Cooperative Institute for Meteorological Satellite Studies (CIMSS) "Export" regression retrieval software.

Complete details of the TSF simultaneous retrieval algorithm are given in Uddstrom (1986).

2. TYPICAL SHAPE FUNCTION CLASSIFICATION

The theoretical basis of the TSF classification algorithm is described in UW. Here the TSF classification scheme has been applied to a Southern Hemisphere sample (including data from the Indian Ocean, Australian, Pacific, New Zealand and Antarctic regions) of 2181 July radiosonde profiles from the years 1981 to 1983. The classification region is defined by the temperatures at the 16 pressure levels bounded by the 50hPa and 500hPa levels of the NESDIS TOVS pressure coordinate system.

Although the the TSF classification algorithm is an unsupervised classifier, the number of classes or patterns detected in the *a priori* data must be specified, since the amount of structure resolved in the tropopause region is ultimately constrained by the indeterminancy of the radiance discrimination problem. Here 13 TSF classes are selected from the July data. Some characteristics of these TSF class samples are listed in Table 1 and the mean temperature profiles for all 13 classes are plotted in Fig 1.

3. RADIANCE DISCRIMINATION

A Bayesian discriminant function is used to specify the TSF *a priori* class constraints for a retrieval, given the observed radiance measurements (UW). For this function the ith discriminant length measure $g_i(\mathbf{r})$ is;

$$g_i(\mathbf{r}) = -\frac{d}{2}\log(2\pi) - \frac{1}{2}\log|\mathbf{S}_{r_i}| + \log(P(\omega_i)) - \frac{1}{2}(\mathbf{r}-\bar{\mathbf{r}}_i)^T\mathbf{S}_{r_i}^{-1}(\mathbf{r}-\bar{\mathbf{r}}_i) \qquad \ldots(1)$$

where $\mathbf{r}$ is the vector of discriminator channel measurements (dimension d), $P(\omega_i)$ the prior probability for the ith class, $\bar{\mathbf{r}}_i$ the mean radiance profile of the ith TSF class and $\mathbf{S}_{ri}$ the associated covariance matrix. The measurement errors are assumed to be unbiased. The posterior probability for each class, in terms of the discriminant function $g_i(\mathbf{r})$ is just;

$$p(\omega_i|\mathbf{r}) = \exp(g_i(\mathbf{r})) \,/\, \sum_{j=1}^{N} \exp(g_j(\mathbf{r})) \qquad \ldots(2)$$

for N TSF classes.

Radiance discrimination equations utilizing channels 1, 2, 4, 23, 5 and 6 have been applied to an independent sample of 500 noise-contaminated (as specified in Table 7) July profiles of known TSF class. Posterior probability distributions for two classes of correctly discriminated radiance measurements are displayed in Fig 2. In the case of class 34, which has a TSF quite different from all remaining TSFs, the posterior probability distribution is narrow with a mean close to 1.0. Conversely, in the case of the class 11 profiles, for which other classes have similar TSFs, the posterior probability distribution is rather broader and has a mean value somewhat less than 1.0. However, in both cases, the mean of the posterior distributions is very much larger than the prior probabilities, which are of the order of 1/13 (see Table 1).

The consequences of misclassifications can be addressed by considering the distributions of the radiance discriminated classifications for all the profiles belonging to some particular class. Included in Fig 2, for both of the classes for which posterior probability distributions are plotted, are histograms of the discriminated class populations for the respective TSF class samples. When the TSF class in question is not similar to any of the other classes, as in the case of class 34, there are few misclassifications. For those TSF classes which are related to other classes in that the differences in their TSFs are rather subtle, misclassifications do occur, as is evident from the class 11 results. None of these misclassifications should lead to serious retrieval errors.

The accuracy of the radiance discriminant inverse mapping function is dependent upon the number of *a priori* TSF classes, their differing vertical features and expected covariances, the vertical resolving power of the satellite radiometer measurement kernels, the measurement noise statistics, and the number and selection of channels used in formulating the discriminant equations. The discriminant function is

sensitive to measurement noise through the last term in equation (3), the Mahalanobis distance. This term compares the relationships between the various measurement channels, with the expected covariances of each TSF class. Small measurement errors can lead to large differences in the contribution from this term if the radiance covariance matrix is nearly singular. However, this noise sensitivity can be suppressed through the choice of discriminator channels which are reasonably vertically independent, since in this circumstance the radiance covariance matrix is better conditioned.

4. CLOUD DETECTION

The TSF class of an atmosphere may be determined with considerable skill from within the radiance domain of the observations by choosing a discriminant function which is well conditioned and does not make use of measurements that could be badly cloud contaminated. Combining the direct measurements with the *a priori* information enlarges the set of "measurements". Taken together, these measurements define the domain in which the observed atmosphere falls, and this information can be used in a cloud detection and clearing algorithm which does not invoke any assumptions about horizontal homogeneity in the temperature fields.

A linear regression model has been developed, whereby within a particular TSF class, those channels unaffected by clouds are used to predict the radiances of other channels which might be so affected. The model equations are derived from the TSF class radiance samples using an eigenvector expansion method. The predictors may be the stratospheric and high tropospheric HIRS channels, together with the three highest MSU channels, and the predictands are the lower tropospheric HIRS channels. Separate equations are derived for each TSF class, and for land and sea surfaces.

Scatter diagrams of the predictand results of this model, applied to the independent sample of 500 noise contaminated July profiles are given in Fig 3. The discriminant channels are 1, 2, 4, 23, 5 and 6 and the cloud detection predictor channels are 1, 2, 4, 23 and 22. Excluding channels 11 and 12, it is evident that the regression equations are of nearly uniform quality over the entire dynamic range of the independent sample, thus substantiating the assumption of linearity within each TSF domain. The largest errors occur for profiles at the low temperature end of the sample, and there are few outliers. Accordingly, once the TSF class of the observation has been determined, the presence of cloud contamination is easily detected. Cloud contaminated channels are declouded through substitution of the regression model predictand radiance temperatures for cloud affected measurements.

This TSF cloud detection and correction algorithm, like the psi method of Chedin and Scott (1983), has the advantage of not requiring horizontal homogeneity in paired temperature fields, and consequently should work equally well in baroclinic and barotropic situations.

5. RETRIEVAL ESTIMATOR SPECIFICATION

Formally, the linearized model of the measurement process is given by equation (3)

$$\mathbf{y} = \mathbf{A}\mathbf{x}' + \boldsymbol{\varepsilon} \qquad \ldots(3)$$

where

$$\mathbf{y} = \Delta\mathbf{T}^*$$

$$\mathbf{A} = [\mathbf{H}, \mathbf{K}, \mathbf{G}] \qquad \ldots(4)$$

$$\mathbf{x}' = [\Delta T_s, \Delta\mathbf{T}, \Delta\mathbf{U}]^T$$

and ΔT^* is the radiance temperature signal; **H**, **K** and **G** are respectively the surface temperature, temperature, and precipitable water kernels; and ΔT_s, ΔT and ΔU are the unknown perturbations of the surface temperature, temperature, and precipitable water profiles. Two different "simultaneous" measurement models for the radiative transfer equation have been developed. One is linear in terms of U(p), the precipitable water profile whilst, the other is linear in terms of log(U(p)) (see Uddstrom 1986). Both models can be used in the TSF retrieval estimator with the log(U(p)) model being more appropriate to specification of the water vapour channels and the U(p) model to the temperature sensing channels.

The TSF maximum *a posteriori* (henceforth MAP) retrieval estimator is formally identical to that of a simple (non-simultaneous) linearization model. The MAP estimator and covariance of the estimate are (from UW):-

$$\hat{\mathbf{x}}' = \mathbf{S}_{xk}\mathbf{A}^T (\mathbf{A}\mathbf{S}_{xk}\mathbf{A}^T + \mathbf{S}_e)^{-1}\mathbf{y}' \qquad ...(5)$$

$$\hat{\mathbf{S}}_{xk} = \mathbf{S}_{xk} - \mathbf{S}_{xk}\mathbf{A}^T (\mathbf{A}\mathbf{S}_{xk}\mathbf{A}^T + \mathbf{S}_e)^{-1} \mathbf{A}\mathbf{S}_{xk} \qquad ...(6)$$

where k refers to the TSF class and $\mathbf{S}_{xk}$ is the measurement error covariance matrix. However under the simultaneous specification, the constraint matrices $\mathbf{S}_{xk}$ include both covariances and cross-covariances for all three data types T_s, T(p) and U(p), i.e.,

$$\mathbf{S}_{xk} = E\left\{ \begin{bmatrix} \Delta T_s^T \Delta T_s & & \\ \Delta T^T \Delta T_s & \Delta T^T \Delta T & \\ \Delta U^T \Delta T_s & \Delta U^T \Delta T & \Delta U^T \Delta U \end{bmatrix} \right\} \qquad ...(7)$$

where E{.} is the expected value operator, and only the lower triangular matrix values are specified. In this way all *a priori* information is used in the retrieval procedure, both directly through the *a priori* means and their covariances, and indirectly via the cross-covariance relationships.

In practice, the MAP estimator is utilized in a sequential mode and the retrieval estimate and error covariance matrix of the estimate are updated as each new measurement is added. With this method, troublesome collinearities in either the measurements or the constraint matrices may be identified. The MAP retrieval equations in sequential form are:-

$$\hat{\mathbf{x}}_i' = \hat{\mathbf{S}}_{xk_{i-1}} \mathbf{a}_i^T ((\, y_i - \mathbf{a}_i \mathbf{x}_{i-1} \,) / (\, \mathbf{a}_i \hat{\mathbf{S}}_{xk_{i-1}} \mathbf{a}_i^T + \sigma_i^2 \,)) \qquad ...(8)$$

$$\hat{\mathbf{S}}_{xk_i} = \hat{\mathbf{S}}_{xk_{i-1}} - (\, \hat{\mathbf{S}}_{xk_{i-1}} \mathbf{a}_i^T \mathbf{a}_i \hat{\mathbf{S}}_{xk_{i-1}} \,) / (\, \mathbf{a}_i \hat{\mathbf{S}}_{xk_{i-1}} \mathbf{a}_i^T + \sigma_i^2 \,) \qquad ...(9)$$

where $\mathbf{x}_{k0}$ and $\mathbf{S}_{xk0}$ are the *a priori* TSF sample mean and constraint matrices. The susceptibility of these equations to data collinearities, measured or *a priori*, is determined by the bracketed term of equation (8). The radiance collinearities result because the measurements are not independent, but the *a priori* collinearities are a result of the dynamics which govern the atmosphere; the constraint covariances are non-zero. When the denominator of equation (8) is small relative to the signal the estimator equations may be nearly singular and the resulting retrieval unstable. With a sequential estimator this condition is easily detected. Should an instability arise, a smoothing parameter is applied to the estimator in order to adaptively condition the equations and reduce the effects of collinearities. The resulting retrieval is, of course, biased.

Another advantage of the sequential estimator relates to solving problems which while specified by linear models are known *a priori* to have a non-linear character, e.g., the interaction between the retrieved water vapour distribution and the temperature profile in the lower troposphere. In utilizing the retrieval estimator in a sequential mode it is possible to choose the order in which the observations are applied, with the most non-linear being used first. The resulting modified guess profiles are better approximations of the unknown profiles, and the more nearly linear observations may be used within the perturbation domains in which they are most applicable.

A full description of the linearized measurement model of the radiative transfer equation and specification of the simultaneous retrieval equations used here is given in Uddstrom (1986).

6. RETRIEVAL VALIDATION

Finally, the performance of the retrieval algorithm is characterised by examining the inverse mapping from measurement to parameter space for a set of measurements computed synthetically via a forward mapping from parameter to measurement space. Here the forward mapping function is the radiative transfer equation, and the inverse mapping function the radiance discrimination function followed by the TSF simultaneous, adaptively conditioned, MAP sequential retrieval estimator.

The sample of independent data on which this validation analysis is carried out is identical to that used to test the radiance discrimination and cloud detection algorithms. The accuracy of the retrieved profile samples (P profiles) will be represented by two parameters, namely the vertically averaged rms "error" (armse) over some specified height range defined by q layers (equation (10)),

$$\text{armse} = \frac{1}{q} \sum_{i=1}^{q} \sqrt{\frac{1}{P} \sum_{j=1}^{P} (\hat{x}_{ij} - x_{ij})^2} \qquad \ldots(10)$$

and the associated vertically averaged coefficient of determination, aR^2, (equation (11)),

$$aR^2 = \frac{1}{q} \sum_{i=1}^{q} \left(1 - \sum_{j=1}^{P} (\hat{x}_{ij} - x_{ij})^2 \Big/ \sum_{j=1}^{P} (x_{ij} - \bar{x}_{ij})^2 \right) \qquad \ldots(11)$$

(Kvalseth, 1985).

Noise contaminated synthetic measurements are used to indicate the susceptibility of the TSF retrieval algorithm to random measurement noise, but measurements from a "perfect" radiometer are employed to examine those features of the retrieval scheme which are not too sensitive to data noise. Some examples are different measurement model specification equations, the selection of the radiometer measurements used and the order in which they are applied, and errors arising from the radiance discrimination scheme.

Firstly consider retrieval results for "measurements" from a perfect radiometer. Complex multi-pass retrieval algorithms are possible since there is no requirement for either the measurement model or the channel selection to remain static between passes. Table 2 lists the retrieval error statistics for a selection of TSF MAP estimators.

Clearly, multi-pass estimators yield more accurate retrievals than single pass methods. Also, the advantages of using both linear and logarithmic precipitable water measurement models is demonstrated in the results labelled EN 3 and EN 4 (see Table 2). The largest improvements are evident in the water vapour retrievals. Addition of channel 11 measurements in the log(U(p)) model pass further improves the accuracy of the retrieval estimator. Comparing the error statistics for EN 5 and EN 6, it is apparent that there are important improvements in the water vapour retrievals and the accuracy of the temperature retrievals is not reduced. The channel 11 measurements enable better retrieval of the gradient of the precipitable water profiles, and hence more accurate mixing ratio profile retrievals.

The effect of radiance discrimination misclassifications on the TSF retrieval estimator results is demonstrated by the error statistics labelled EN 6 (radiance discrimination - DC) and EN 7 (perfect discrimination - TC). The rms error profiles for these two algorithms are plotted in Fig 4(a). There is a substantial improvement in the retrieval of the tropopause region with perfect discrimination, but the differences in the lower troposphere are small. Below 300hPa the temperature retrieval error (for DC) is little more than 1.0° C and the mixing ratio error is never more than 1.39 g/kg. The precipitable water rms error is always less than 0.16cm. The bias statistics in Fig 4(b) suggest that retrieval sample

biases are small at all levels and are similar for both TC and DC estimators.

The TSF MAP retrieval estimator provides an estimate of the accuracy of a retrieval (equation (9)), that is, the error covariance matrix of the estimate. Since this matrix is not diagonal the errors are correlated in the vertical. However, a simple although not precise estimate of the retrieval accuracy is afforded by the diagonal elements of this matrix, i.e., the variances of the estimate. The standard deviations of the sample error temperature and precipitable water estimates for the estimator of EN 6 are plotted in Figs 5(a) and 5(b). In this case, the estimated accuracy of the retrieval algorithm, over the whole sample, is close to the actual accuracy, and the vertical structure in the estimator error profile is similar to that in the "true" error profile. Fig 6 demonstrates the R^2 profiles for temperature, precipitable water and mixing ratio, and EN 6. It is most difficult to retrieve the gradient of the precipitable water profile in the height region where it changes most rapidly; i.e., between approximately 700 and 800hPa.

Finally, consider the retrieval algorithm error statistics for synthetic radiance measurements contaminated with Gaussian noise. Since the TSF retrieval algorithm is a two stage process - radiance discrimination followed by profile retrieval - there are two points at which data noise may affect the retrieval result. An incorrect TSF radiance classification could lead to a poor retrieval, as could noise sensitivity in the retrieval estimator.

The effect of measurement noise on the retrieval estimator can be isolated by comparing error statistics from two samples of retrievals where in each case perfect radiance discrimination is used followed by profile retrieval on samples of noise free and noise contaminated measurements. Results for the estimator of channel selection 5 (a four pass estimator (see Table 2); measurement models b,a,a,a), are presented in Table 3. Addition of noise to the measurements leads to only a small degradation in the performance of the retrieval estimator. The largest change in accuracy is for the mixing ratio retrievals. Apparently the TSF adaptively conditioned profile retrieval algorithm (as distinct from the radiance discrimination algorithm) is not particularly sensitive to measurement noise.

The susceptibility of the complete retrieval algorithm (including the radiance discrimination stage) to measurement noise is demonstrated by comparing the error statistics of retrieval samples generated from noise-free and noise-contaminated data. In these cases, the radiance discrimination algorithm is applied in order to determine the *a priori* TSF class of the sounded atmosphere. The errors due to misclassifications of the *a priori* TSF class arising from noise contamination of the radiance discrimination algorithm, and retrieval estimator noise sensitivity are accumulated and quantified by the sample error statistics. The results for three different retrieval estimators, applied to both noise-free and contaminated data, are given in Table 4. The same discrimination algorithm is used on both the noise-free and noise-contaminated radiance data.

For all three estimators, and the three profile types, there is a degradation in the accuracy of the retrieval algorithm when noise is added to the measurements. However the decrease in accuracy is not large, being of the order of 0.05°C per layer for temperature and 0.02 g/kg for water vapour mixing ratio. Considering the results of Tables 3 and 4 together it is clear that the radiance discrimination procedure is not particularly noise sensitive. The largest component of the error in the temperature retrievals arises from missclassification of the *a priori* TSF class due to the inherent indeterminancy of the discrimination problem.

The rms error profiles for one of these estimators, cs 5, for both noise-free and noise-contaminated measurements, are plotted in Fig 7. It is evident that the largest component of the difference in the error statistics arises from errors in retrieval of the tropopause region. The cause of such errors is missclassification of the *a priori* TSF class of the sounded atmosphere.

Some example retrievals from the TSF retrieval scheme and noise-contaminated data, are displayed in Fig 8. The only supplemental information used in these examples is the surface pressure. The retrieved profiles give accurate estimates of the temperature structure in the troposphere, especially in the region of the tropopause. Also, the retrieved dew point temperature profiles display a number of meteorological features of significance.

7. EXAMPLE NOAA 7 RETRIEVALS

The New Zealand Meteorological Service has a facility to receive HRPT data from TIROS-N polar orbiting weather satellites. The retrieval scheme presently in use is a version of the CIMSS regression software (Taylor, 1983). Owing to media storage overheads, the Meteorological Service does not archive radiance data. However, for a two week period in July 1984 some NOAA 7 satellite data were archived in support of the development of a new analysis algorithm. The stored data correspond to the final products from the regression software and are not the original TIROS Information Processor (TIP) data. Accordingly, the archived radiance data have been earth located, calibrated, corrected to nadir, adjusted for emissivity effects and corrected for solar radiation contamination, etc. Pre-processor and retrieval processor defined "bad" data have been removed. In this example, the TSF retrieval algorithms, which together incorporate: TSF *a priori* temperature classification, TSF cloud detection and correction, radiance discrimination, and retrieval by the TSF simultaneous adaptively conditioned MAP sequential estimators, are applied to two passes archived from this period. The purpose of this example is to give some indication of the type of results which might be expected from the TSF retrieval algorithms.

(a) Radiance temperature adjustments

The simulation results discussed in preceeding sections assume the TOVS transmittance functions are known accurately, and that the only errors present in the data are due to random measurement noise of mean zero. This assumption is in fact not correct (Fleming *et al.* 1983). The NESDIS provide transparency adjusting "gamma" correction parameters for transmittances computed by the fast transmittance model (Weinreb *et al.* 1981), but additional, "delta", radiance temperature corrections are required before computed and measured radiance temperatures can be brought into agreement. The delta corrections are generally computed from high quality samples of radiosonde and satellite colocations. Apparently, the delta values are not well known and are probably air mass dependent (Chedin and Scott, 1983).

The TSF retrieval equations were derived with delta values equal to zero; therefore, all measurements must be adjusted to equivalent "computed" radiance temperatures. Since no colocation data sample was available, the delta values have been estimated by another method. It is evident in Fig 1(a) that two of the TSF classes are associated with tropical atmospheres - classes 11 and 12 - with the second having the larger channel variances and, in both the temperature and radiance domains, the cooler surface. The variances of all channels for either of these classes is small, relative to all the other classes. These tropical classes define narrow peaks in the global spectrum of atmospheric radiances. An estimate of the delta values may be made by determining the differences between either or both of these radiance class mean vectors, and the mean of a sample of measured tropical radiances. From the two week archive of radiance data, mean radiance temperatures were computed for a sample constrained by the specifications that the measurements be cloud free (as defined by the CIMSS software), lie within nine IFOVs of nadir, and north of 21° S. The latter value was chosen so as to trade off sample size against the inclusion of non-tropical air, since the northern limit for HRPT data, received at Wellington, is near 17° S. Observations from both day and night time passes are included in the sample. The delta values are estimated from the class 12 synthetic radiance data since this class is assumed to be associated with the more southerly of the two tropical TSF classes. Table 5 lists the channel mean radiance temperatures and variances for class 12, the mean for the measured "tropical" radiance temperatures and their variances, the gamma values (supplied by the NESDIS) and the delta value estimates. The sample sizes are indicated.

The large delta value for channel 1 might result from the procedure used to extrapolate the radiosonde data to mesospheric heights, although the result for channel 2 does not substantiate this thesis. The channel 8 delta estimate may indicate a water vapour problem since the delta values for channels 18 and 19 (which are less sensitive to water vapour) are much smaller, although a residual component of reflected solar radiation may contaminate these channels. The correction for channel 16 is consistent with the computed transmittance being too transparent. Although the sample size for the measured data is 78, there are perhaps only 10 or so meteorologically independent observations, since

many of the sample measurements lie in the same air masses. Consequently these delta values and associated comments are necessarily tentative.

In the following example retrievals, the satellite measured radiance temperatures have been adjusted by the delta values given in Table 5. As a result of this approach those radiance measurements which are most sensitive to bias "noise", because they have the smallest signal, and their TSF classes the smallest hyper-volumes, are forced into agreement with the computed radiances. This strategy reduces the effect of bias errors which could result in serious misclassifications because of the sensitivity of the Mahalanobis term of the discriminant equations to data biases.

(b) Radiance discrimination and cloud detection

In the example discrimination classification of NOAA 7 radiance observations presented here, the radiance discriminator channels are 1, 2, 4, 23, 5 and 6, and TSF declouding predictor channels 1, 2, 4, 23 and 22. Channel 24 would be a useful addition to both the discrimination and declouding model equations, but because the weighting function is centered near 100hPa and has a high vertical resolution relative to channels 1 and 2, the information in this channel is quite sensitive to errors in both the gamma and delta correction parameters.

The results of TSF radiance discriminant classification to define a priori retrieval constraints for two July 1984 NOAA 7 passes over the New Zealand region are plotted in Fig 9. The associated AVHRR image for these same passes is presented in Fig 10. In Fig 9 the TSF class numbers, as defined in Fig 1, are printed for every third retrieval location, which is a 3 x 3 field of HIRS IFOVs, or when the TSF class changes. All classifications with posterior probabilities greater than 0.1 are plotted. It is evident that the progression in TSF class types from equatorial to polar regions is as might be expected. Also evident is the spatial consistency of the TSF classes in both the various airmass types and between orbits. Class 43 (double tropopause) *a priori* profiles are associated with surface low pressure features. In the anticyclone over New Zealand (see Fig 13) the selected TSF class has the expected 200hPa tropopause of the mid-latitude winter atmosphere. The transition to classes 41 and 21, which have lower mean tropopause heights (aproximately 250hPa) adjacent to the surface low near 40° S, is meteorologically realistic. The *a priori* retrieval constraint classifications are not zonal in nature, but appear to be related to different airmass types.

(c) TSF simultaneous physical retrievals for NOAA 7 passes

The radiance temperature observations, once discriminated to determine the *a priori* retrieval constraints, and declouded by the TSF stratified regression radiance prediction models, can be used in the TSF physical retrieval algorithm.

Table 6 indicates the channel selection used in the retrieval estimator. The HIRS shortwave window channels (18 and 19) are not used for day time passes since it is probable that these channels are contaminated by reflected solar radiation (Chedin and Scott, 1983). The size of the channel 16 delta correction suggests the possibility of some problem with this channel; accordingly it is not used in the retrieval algorithm. The measurement noise estimate applied in the retrieval algorithm to the information for any particular channel, is dependent upon whether the measurement has, or has not been, corrected for cloud contamination. The cloud-free measurement noise estimates together with the noise estimates of the declouding prediction equations, are given in Table 7.

The surface pressure assumed by the retrieval algorithm is set equal to the *a priori* TSF class value (see Table 1) except where the underlying surface is not at mean sea level in which case a new estimate for the surface pressure is computed. When the pressure at the surface is greater than 1000hPa the radiance temperatures are corrected for that part of the measured radiance which arises from the layer of atmosphere between 1000hPa and the surface. On the inclusion of each new measurement the above surface profile retrievals are checked for super-adiabatic lapse rates. However, the lapse rate between the surface and the lowest atmospheric retrieval level is permitted to be super-adiabatic since the satellite window channels measure the skin temperature. The gradient between the temperature of the underlying

surface and that a few meters above the surface can greatly exceed the dry adiabatic lapse rate (Taylor, 1973). No ancillary data are used by the retrieval algorithm other than the TSF *a priori* constraint information.

In Fig 11 a selection of TSF retrieval results for the two NOAA 7 passes is presented. Results from the Meteorological Service's operational regression retrieval software are given in Fig 12. The retrievals have been analysed onto a 41 x 29 grid with a Cressman analysis scheme. The sample sizes for both retrieval schemes are identical as are the locations of the retrieved profiles. The TSF retrievals have not been spatially filtered. Finally, in order to provide an almost independent assessment of the meteorological situation, the operational NWP analyses of surface pressure and 1000-500hPa thickness for the New Zealand region and times 0000 and 0600 GMT on 27/Jul/1984 are presented in Fig 13. GTS SATEM messages and a subset of the locally derived regression retrievals were used in constructing these analyses (which are on a much coarser grid than the satellite only analyses).

Considering the 1000-500hPa thickness fields first, it is evident that in broad detail the regression and TSF results are similar, with the exception of the trough in the TSF field near 45° S and 177° E. No strong bias is evident in either of the satellite-derived thickness fields relative to the NWP analyses. When considered in closer detail, the most noticable differences are in terms of the gradients in the main trough and ridge features. The TSF retrievals show stronger gradients than the regression retrievals - this observation is especially appropriate north of the cold pool near 175° W, and on the western edge of the ridge in the vicinity of 27° S and 153° E. During the period between the two passes there was considerable advection of warm air into the New Zealand region, which explains the apparent discontinuities in some thickness contours near the satellite pass boundaries. This advection is also evident in the 0000 and 0600 GMT analyses of Fig 13. The trough in the TSF retrievals at 177° E is difficult to explain. The AVHRR image indicates that there is low cloud generally in this region but does not reveal any significant trough related feature. Instead this trough might be evidence of a problem in the pre-processor limb correction algorithm since it occurs on the edge of the first pass.

In Fig 14, tephigrams of both regression and TSF retrievals are plotted for a selection of profiles from a cross-section along the trough axis and through the cold pool at 175° W. The retrieval locations are indicated on Fig 11(a). The results from the two retrieval algorithms show marked differences, especially in the tropopause region and near the surface. In particular it is evident that the regression temperature retrievals below 850hPa tend to have similar stability whereas the TSF retrievals display inversions as well as stable and dry adiabatic lapse rates in the boundary layer. The AVHRR imagery indicates convective activity is occurring along portions of this cross-section and therefore supports the low level vertical structure indicated in the TSF retrievals. With regard to the tropopause retrievals, the development in the TSF retrievals of a double tropopause structure in the vicinity of the cold pool and near the surface low at 165° W is reasonable, given the physical processes occurring. The 400hPa tropopause in the retrieval at 34.5° S near the centre of the trough is consistent with the 430hPa tropopause (an unexpectedly extreme value) measured by the Auckland (37° S, 175° E) 0000 GMT radiosonde on 26/Jul/84, when the trough was centred over Auckland. Further south along the trough axis the TSF retrieved tropopause rises to near 250hPa. The regression tropopause retrievals do not display structure of the type expected for this meteorological situation.

As might be expected from the preceding discussion, the 850hPa temperature and dewpoint temperatures, and the 500hPa temperature fields display some marked differences. From the 500hPa TSF temperature analysis it is evident that the trough in the TSF 1000-500hPa thickness analysis near 177° E is a low level feature since at 500hPa there is some evidence for a thermal ridge in this location. The presence of high cloud over the south of the South Island in the vicinity of this ridge is consistent with warm air advection aloft. The isotherms on the northern side of the cold pool feature are closely aligned with the lines of convection in the AVHRR image for both the regression and TSF retrievals, although the gradients are stronger for the TSF retrievals. At 850hPa, the gradients in the main trough are weaker for the TSF retrieval fields than they are for the regression fields, although the reverse is true for the ridge near 160° E. However, when the 850hPa dew point temperature fields are considered it is evident that the there is more structure in the TSF retrievals. Clearly the TSF retrievals are, in places, in error due to cloud contamination, especially in the cloud mass associated with the ridge in the region of 160° E. In the main trough, east of New Zealand, the TSF retrievals delineate clearly the moisture gradient between the open cell and adjacent area of subsidence (to the west). It is apparent

that for the regression algorithm the low level structure is contained principally in the temperature fields, with a flatter water vapour field, whereas, in this case, the reverse is true of the TSF retrieval results. This result is not unexpected since, unlike the regression scheme, the simultaneous retrieval algorithm utilizes the water vapour information in the temperature sensing channels directly, and therefore decouples the temperature and water vapour fields to a greater extent.

8. SUMMARY

Some of the characteristics of the TSF retrieval algorithm have been demonstrated for a winter case, and the results of a new type of TSF stratified, single field of view, cloud detection and clearing scheme presented.

Evidently the TSF simultaneous, adaptively conditioned, MAP retrieval estimator is, in so far as synthetic data experiments can prescribe, capable of producing accurate retrievals of temperature, precipitable water, and mixing ratio profiles. An additional advantage of the TSF retrieval algorithm is the specification of the expected accuracy of any particular retrieval, through recourse to the radiance discrimination posterior probability and the retrieval estimator error covariance matrix. Both pieces of information can be used by an optimum interpolation analysis algorithm.

In the case of the example satellite retrievals presented here, the TSF-retrieved 1000-500hPa analysed fields are similar, on the synoptic scale, to those produced from a regression retrieval scheme. However the gradients in the TSF results are greater than those for the regression scheme, and the TSF-retrieved profiles demonstrate greater variance than the equivalent regression retrievals. The differences between the TSF and regression retrievals would appear to be important and significant, but an objective analysis of the quality of individual TSF and regression retrievals must await full colocation and NWP analysis / forecast cycle experiments.

A number of problem areas can be identified for the TSF retrieval algorithm. The most important is the requirement for good estimates of the gamma transmittance, and delta radiance temperature correction parameters. The delta corrections should be calculated for each TSF *a priori* class. However once these problems, and those associated with various pre-retrieval processing algorithms, are resolved, it might be expected that the TSF retrieval accuracy will be close to that estimated from the validation analysis.

REFERENCES

Chedin, A. and N.A. Scott, 1983: Improved Initialization Inversion Procedure ("3I"). In *Technical proceedings of the first International TOVS Study Conference.* 14-79, 29 August-2 September, Igls, Austria, Pub CIMSS, University of Wisconsin.

Chedin, A., N.A. Scott, C. Waihiche and P. Moulinier, 1985: The Improved Initialisation Inversion Method: A high resolution physical method for temperature retrievals of the TIROS-N series. *J. Clim. Appl. Meteor.* **24**, 128-143.

Fleming, H.E., Crosby D.S. and A.C. Neuendorffer, 1983: Elimination of a major error component in satellite temperature retrievals. Preprint Volume, *Fifth Conference on Atmospheric Radiation,* October 31-4 November, Baltimore, Maryland.

Fleming, H.E., Goldberg M.D. and D.S. Crosby, 1986: Minimum variance simultaneous retrieval of temperature and water vapour from satellite radiance measurements. Preprint Volume, *Second Conference on Satellite Meteorology/Remote Sensing and Applications.* May 13-16, Williamsburg, Virginia.

Kvalseth, T.O., 1985: Cautionary note about R^2. *Amer. Stat.* 39, 279-285.

McMillin, L.M., 1986: The use of classification procedures to improve the accuracy of satellite soundings of temperature and moisture. Preprint Volume, *Second Conference on Satellite Meteorology/Remote Sensing and Applications.* May 13-16, Williamsburg, Virginia.

Smith, W.L and H.M. Woolf, 1984: Improved vertical soundings from an amalgamation of polar and geostationary radiance observations. In preprint volume to: *Conference on Satellite/Remote Sensing*

and Applications, June 25-29 1984, Clearwater Beach, Fla. Pub AMS.

Smith, W.L, H.M.Woolf, C.M.Hayden and A.J.Schreiner, 1985: The simultaneous retrieval export package. In *Technical proceedings of the second International TOVS Study Conference.* 224-253, February 18-22, Igls, Austria, Pub CIMSS, University of Wisconsin.

Taylor, B.F., 1973: The maritime convective layer in middle latitudes. 150pp, *PhD Thesis*, University of London

Taylor, B.F., 1983: The first International TOVS Study Conference case study report. In *Technical proceedings of the first International TOVS Study Conference.* 304-315, 29 August - 2 September, Igls, Austria, Pub CIMSS, University of Wisconsin.

Thompson, O.E., M.D. Goldberg and D.A. Dazlich, 1985: Pattern recognition in the satellite temperature retrieval problem. *J. Clim. Appl. Meteor.*, **24**, 30-48.

Uddstrom, M.J. and D.Q.Wark, 1985: A classification scheme for satellite temperature retrievals. *J. Climate Appl. Meteor.* **24**, 16-29.

Uddstrom, M.J., 1986: The retrieval of atmospheric profiles with Typical Shape Function simultaneous physical retrieval estimators. In preparation.

Wark, D.Q., 1986: Temperature profiles derived from a restricted range of solutions using satellite measurements. *Advances in Remote Sensing Retrieval Methods* (eds. A. Deepak, H. Fleming, and M. Chahine) A.Deepak Publishing, Hampton, Virginia, USA.

Weinreb, M.P., H.E.Fleming, L.M.McMillin and A.C.Neuendorffer, 1981: Transmittances for the TIROS operational vertical sounder. *NOAA Tech. Rep.* NESS 85, 60pp.

Westwater, E.R., M.T. Decker, A. Zachs and K.S. Gage, 1983: Ground- based remote sensing of temperature profiles by a combination of microwave radiometry and radar. *J. Clim. Appl. Meteor.*, **23**, 689-703.

TABLE 1: Characteristics of July TSF class samples.

Class name	Sample size	A priori probability	Trace (50hPa - 1000hPa) (K)	Mean sfc pressure* (hPa)
11	459	0.192	292.5	1010.1 (6.0)
12	412	0.173	298.3	1007.8 (13.9)
21	201	0.084	324.7	1012.9 (10.5)
22	116	0.049	456.2	1014.3 (12.9)
23	130	0.054	221.1	1015.4 (9.9)
24	146	0.061	514.7	1013.2 (10.5)
31	174	0.079	729.4	1006.7 (14.7)
32	71	0.030	1356.7	1002.5 (13.8)
33	66	0.028	2284.4	998.8 (15.1)
34	109	0.046	568.5	980.3 (10.7)
41	228	0.096	296.2	1011.4 (12.2)
42	125	0.052	463.5	1008.2 (15.1)
43	151	0.063	1124.7	1002.1 (13.9)

* Class standard deviation in brackets

TABLE 2: Multi-pass retrieval armse error statistics, (aR^2 in brackets) for indicated channel selections and measurement specification models. TC indicates perfect discrimination and DC indicates radiance discrimination. Sample size: 500.

EN'	Channel Selection*	Measurement models+	Temperature (100-1000hPa) K	Precipitable Water (500-1000hPa) cm	Mixing Ratio (500-1000hPa) g/kg
1	1 DC	a	1.4197 (0.9748)	0.1342 (0.9128)	0.9029 (0.8419)
2	2 DC	b,a	1.3522 (0.9765)	0.1062 (0.9453)	0.8645 (0.8590)
3	3 DC	a,a,a	1.2770 (0.9790)	0.1013 (0.9528)	0.8602 (0.8643)
4	3 DC	b,a,a	1.2676 (0.9794)	0.0983 (0.9547)	0.8323 (0.8709)
5	4 DC	b,a,a,a	1.2480 (0.9801)	0.0935 (0.9600)	0.8243 (0.8754)
6	5 DC	b,a,a,a	1.2466 (0.9800)	0.0866 (0.9649)	0.7934 (0.8835)
7	5 TC	b,a,a,a	1.1172 (0.9848)	0.0832 (0.9672)	0.7863 (0.8862)

' Estimator Number (i.e., EN) identifier as used in text.
+ Measurement model for each pass:- a : linear U(p); b : log(U(p))
* Channel selections and radiance discrimination algorithm used, where [.] defines a single pass
1 is: [18,12,10,1,2,3,4,5,6,7,8,16,15,14,13]
2 is: [18,12,10], [18,12,10,1,2,3,4,5,6,7,8,16,15,14,13]
3 is: cs 2, [18,12,10,1,2,3,4,5,6,7,8,16,15,14,13]
4 is: cs 3, [18,12,10,1,2,3,4,5,6,7,8,16,15,14,13]
5 is: [18,12,11,10], 3 x [18,12,10,1,2,3,4,5,6,7,8,16,15,14,13]

TABLE 3: Retrieval armse error statistics and aR^2 values for noise free and noise contaminated radiances. (TC, cs 5)

Noise	Temperature (100-1000hPa) K	Precipitable Water (500-1000hPa) cm	Mixing Ratio (500-1000hPa) g/kg
Yes	1.1493 (0.9838)	0.0898 (0.9668)	0.8154 (0.8801)
No	1.1172 (0.9848)	0.0832 (0.9672)	0.7863 (0.8862)

TABLE 4: Retrieval armse error statistics and aR^2 values for noise free and noise contaminated radiances. (DC)

Channel selection and models+	Noise*	Temperature (100-1000hPa) K	Precipitable Water (500-1000hPa) cm	Mixing Ratio (500-1000hPa) g/kg
1 a	yes	1.4590 (0.9729)	0.1360 (0.9119)	0.9211 (0.8359)
1 a	no	1.4197 (0.9748)	0.1342 (0.9128)	0.9029 (0.8419)
6 a,a,a,a	yes	1.3593 (0.9760)	0.0976 (0.9588)	0.8606 (0.8681)
6 a,a,a,a	no	1.2908 (0.9791)	0.0916 (0.9619)	0.8342 (0.8731)
5 b,a,a,a	yes	1.3006 (0.9776)	0.0912 (0.9639)	0.8092 (0.8785)
5 b,a,a,a	no	1.2466 (0.9800)	0.0866 (0.9649)	0.7934 (0.8835)

+ Channel selection and measurement models (see Table 9), and 6 is: [cs 1], [cs 1], [cs 1], [cs 1].
* Assumes 9 IFOVs for noise contaminated observations.

TABLE 5: Tropical atmosphere radiances, gamma transmittance adjustment and estimated delta radiance temperature adjustment values.

Channel No.	Class 12 Radiance temperatures (n=412) mean (K)	std dev	Measured Radiance temperatures (n=78) mean (K)	std dev	gamma	delta (K)
1	234.01	1.057	230.40	0.185	1.069	3.604
2	219.92	0.992	219.05	0.243	0.942	0.870
3	220.44	0.851	218.91	0.279	1.108	1.525
4	233.90	1.070	233.18	0.254	1.031	0.728
5	249.39	1.615	248.34	0.538	0.972	1.054
6	260.90	2.058	260.89	0.899	0.965	0.008
7	273.32	2.625	273.43	1.529	0.909	0.113
8	291.71	4.963	288.50	2.970	1.000	3.208
10	286.81	4.074	285.67	2.496	1.120	1.136
11	263.47	4.578	264.26	1.805	1.032	0.789
12	245.38	6.628	246.93	2.100	1.035	1.551
13	282.25	4.293	279.98	2.153	1.115	2.266
14	269.13	3.374	267.51	1.344	1.028	1.615
15	252.32	2.349	250.87	0.636	1.057	1.456
16	232.17	1.442	228.95	0.277	1.002	3.219
18	293.17	6.155	293.65	3.986	1.000	-0.488
19	293.12	5.883	293.70	2.817	1.000	-0.578
22	257.29	2.332	256.00	0.243	1.010	1.297
23	226.78	0.882	227.01	0.111	1.010	-0.231
24	209.10	1.784	209.90	0.256	1.070	-0.804

TABLE 6: NOAA 7 TSF retrieval channel and model specifications

Orbit time	TSF Retrieval Pass No.	PCW model	Channel selection
03GMT (day)	1	log	8,12,11,10
	2	lin	8,12,10,1,2,3,4,5,6,7,15,14,13
	3	lin	8,12,10,1,2,3,4,5,6,7,15,14,13
	4	lin	8,12,10,1,2,3,4,5,6,7,15,14,13

TABLE 7: Assumed noise characteristics for cloud free and TSF stratified regression declouded channels.

Channel Number	Measurement noise (K)	Declouding noise (K)
1	1.0	-
2	0.6	-
3	0.4	-
4	0.3	-
5	0.2	0.28
6	0.1	0.57
7	0.1	1.26
8	0.1	2.29
10	0.1	2.03
11	0.2	3.57
12	0.3	5.58
13	0.1	1.51
14	0.1	0.71
15	0.2	0.23
16	0.1	0.33
18	0.1	2.26
22	0.3	-
23	0.3	-
24	0.3	-

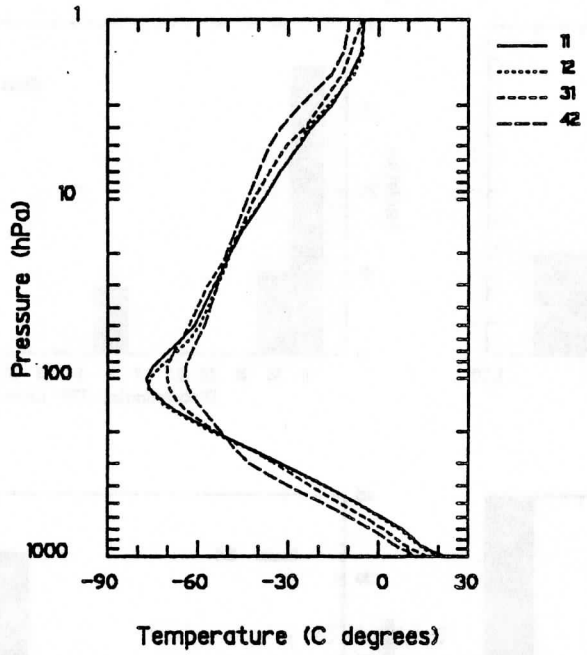

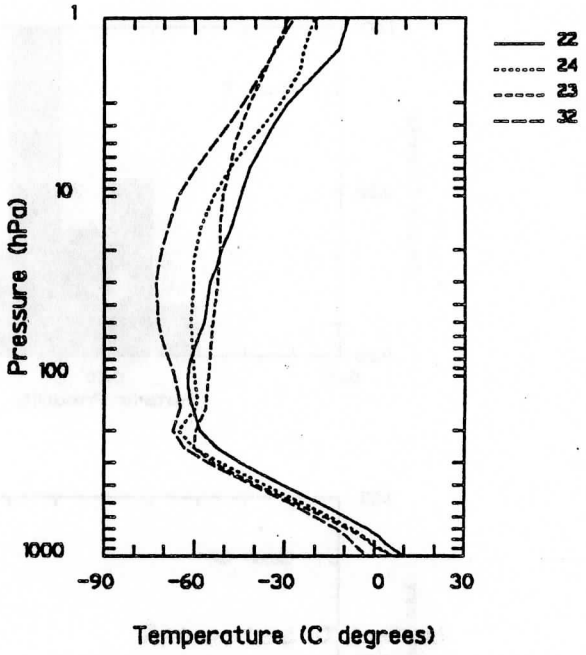

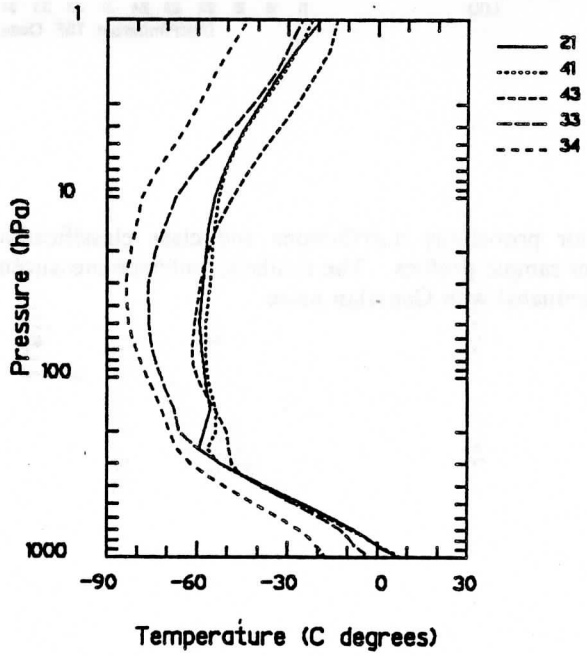

Fig 1. TSF class mean temperature profiles for July Southern hemisphere extrapolated radiosonde data. The class name identifiers are as given in table 1.

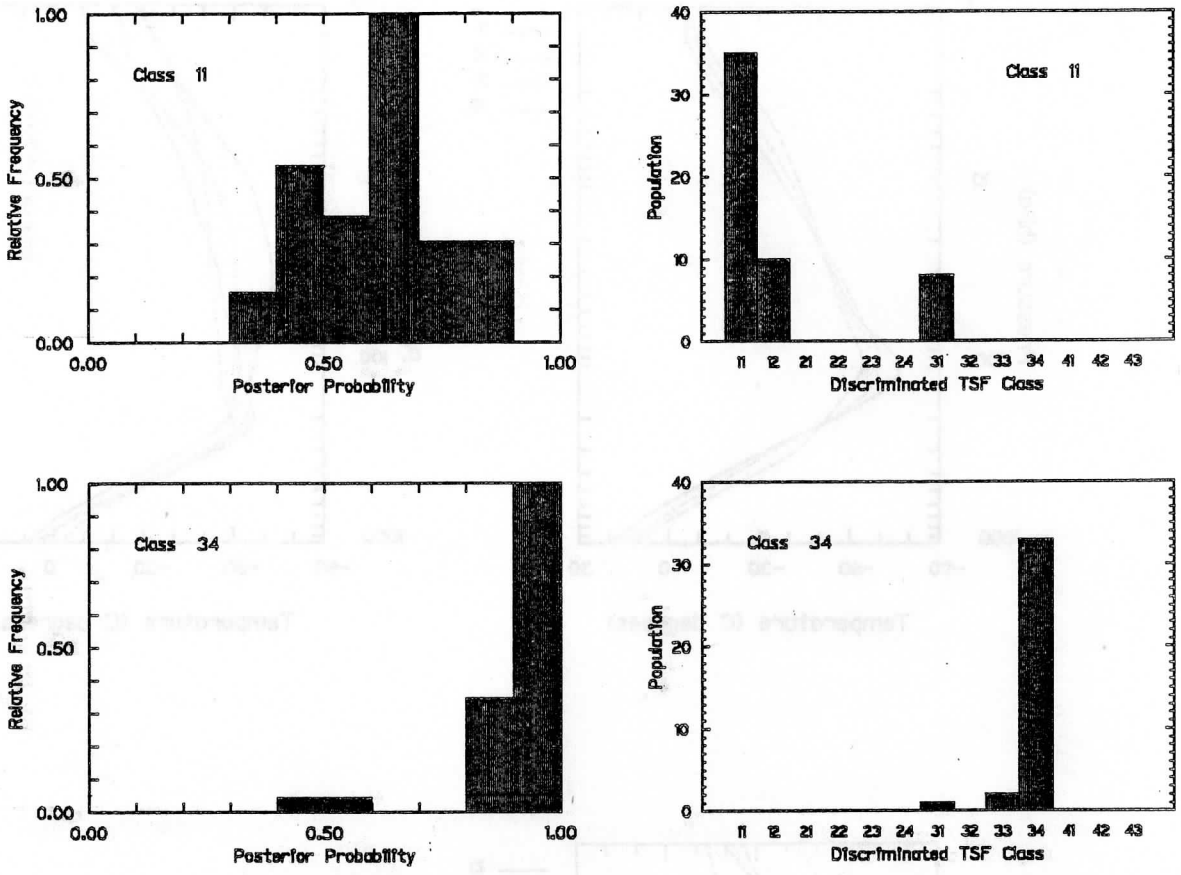

Fig 2. Radiance discriminant posterior probability distributions and class classification histograms for the TSF class 11 and 34 independent sample profiles. The synthetic radiance measurements used in the discrimination equations were contaminated with Gaussian noise.

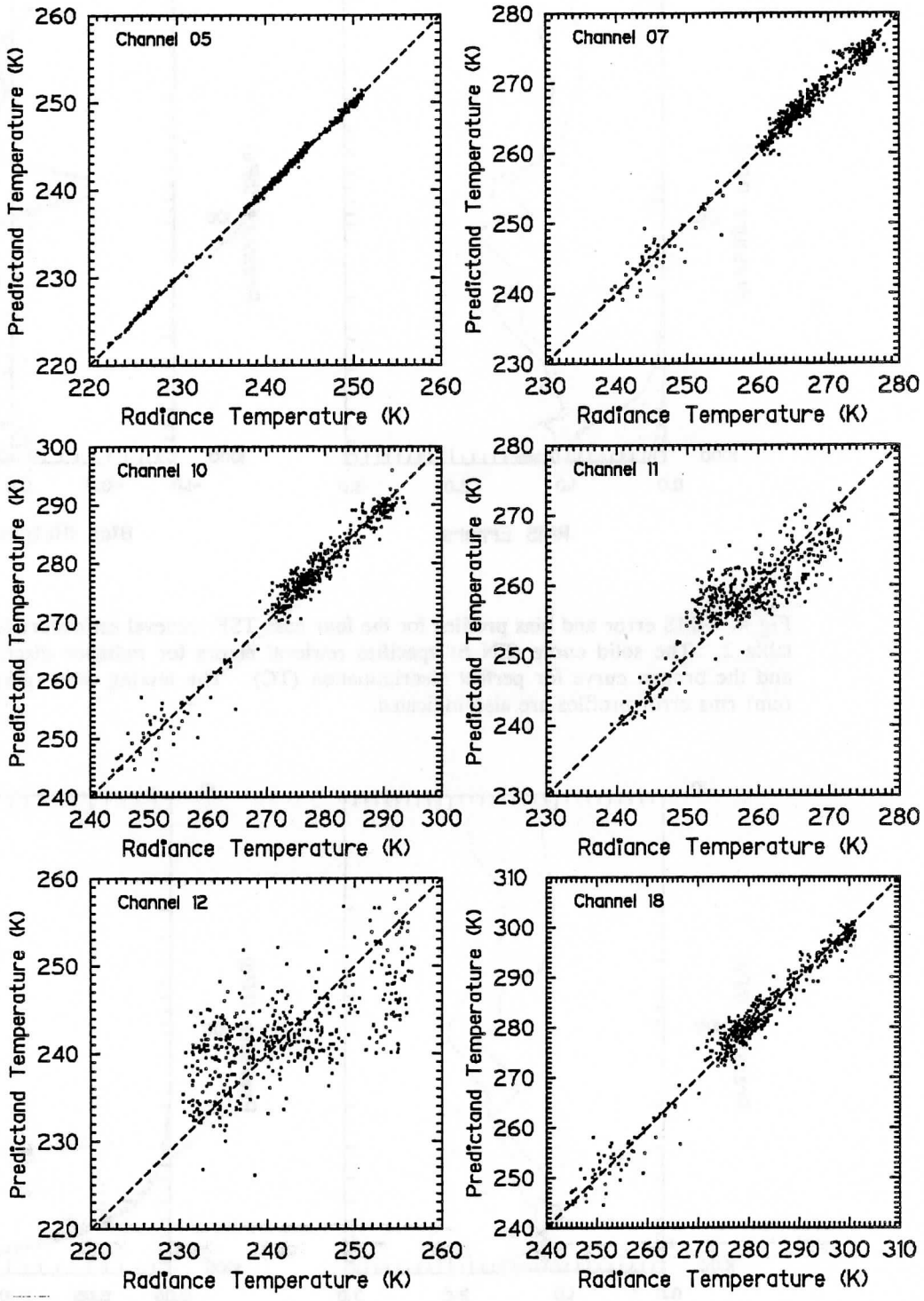

Fig 3. Scatter plots for the TSF cloud decontamination algorithm. The sample size is 500, divided into 13 TSF classes. The synthetic radiance measurements used in the discrimination classification were contaminated with Gaussian noise.

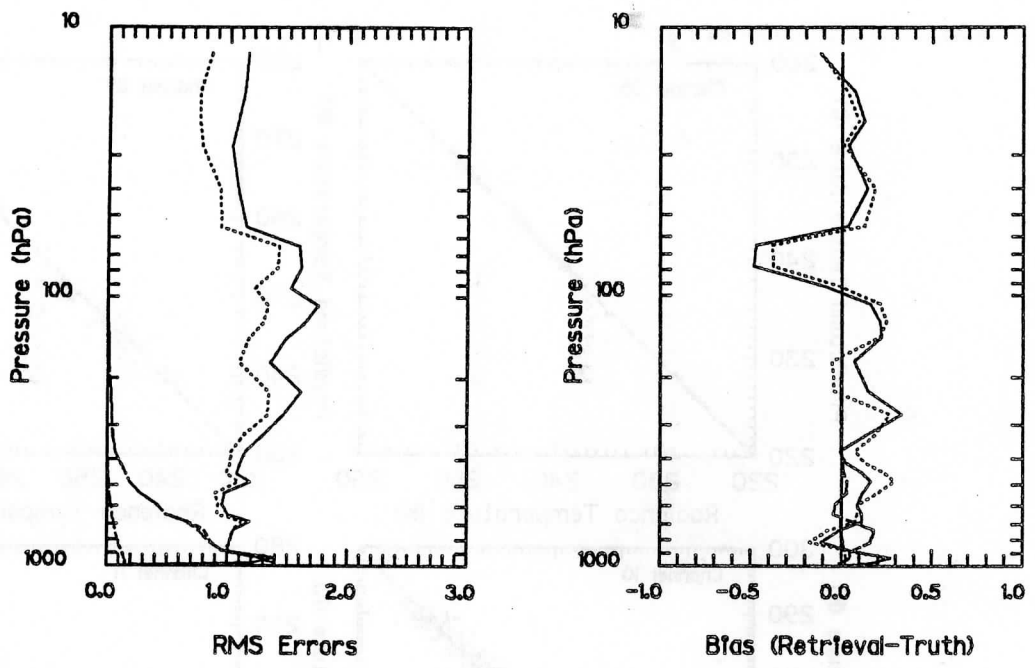

Fig 4. RMS error and bias profiles for the four pass TSF retrieval estimators labeled EN 6 and EN 7 in table 2. The solid curve (EN 6) specifies retrieval errors for radiance discrimination retrievals (DC) and the broken curve for perfect discrimination (TC). The mixing ratio (g/kg) and precipitable water (cm) rms error profiles are also indicated.

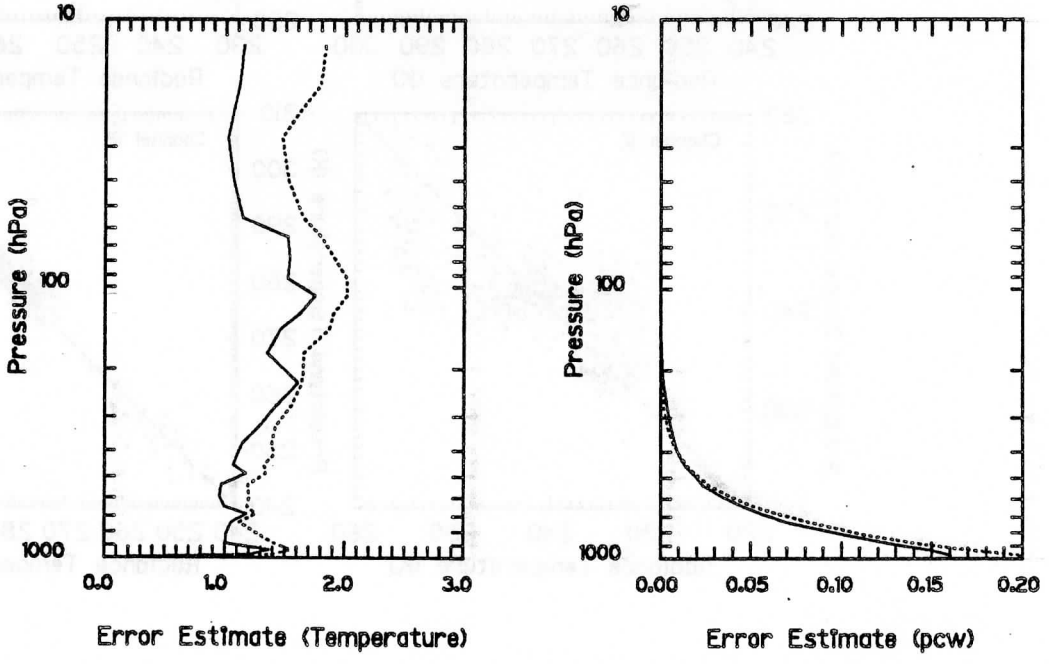

Fig 5. TSF MAP estimated error profiles for temperature and precipitable water (cm) for the TSF retrieval estimator labeled EN 6 in table 2. The solid curves indicate the "true" rms error profiles and the broken curves the estimator error profiles.

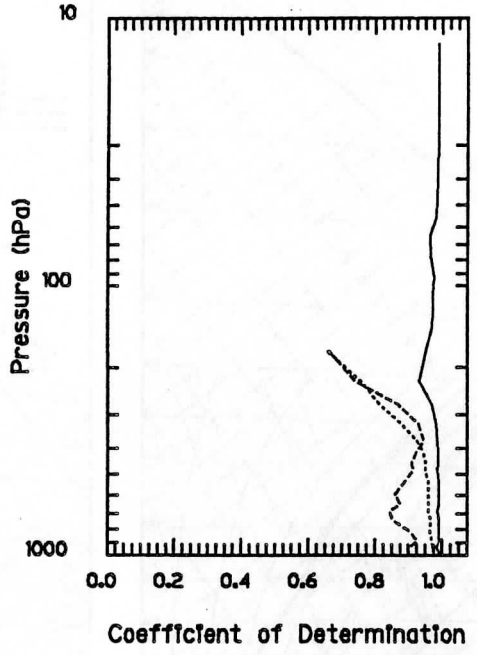

Fig 6. R^2 profiles for EN 6 TSF retrievals. The solid curve refers to temperature, the dotted curve to precipitable water and the dashed curve to mixing ratio.

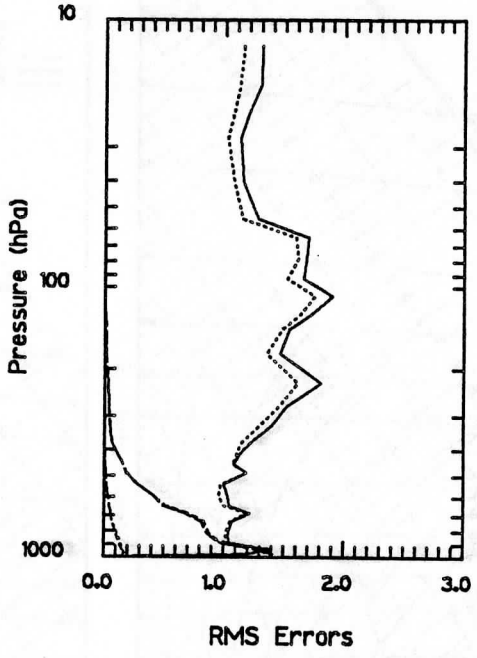

Fig 7. RMS error curves for the TSF retrieval algorithm for noise free and noise contaminated synthetic measurements. A four pass estimator has been used in both cases with cs 5 (see table 4). The solid curve refers to the results for the noise contaminated measurements and the dotted curve for the noise free measurements. Mixing ratio (g/kg) and precipitable water (cm) error profiles are also given.

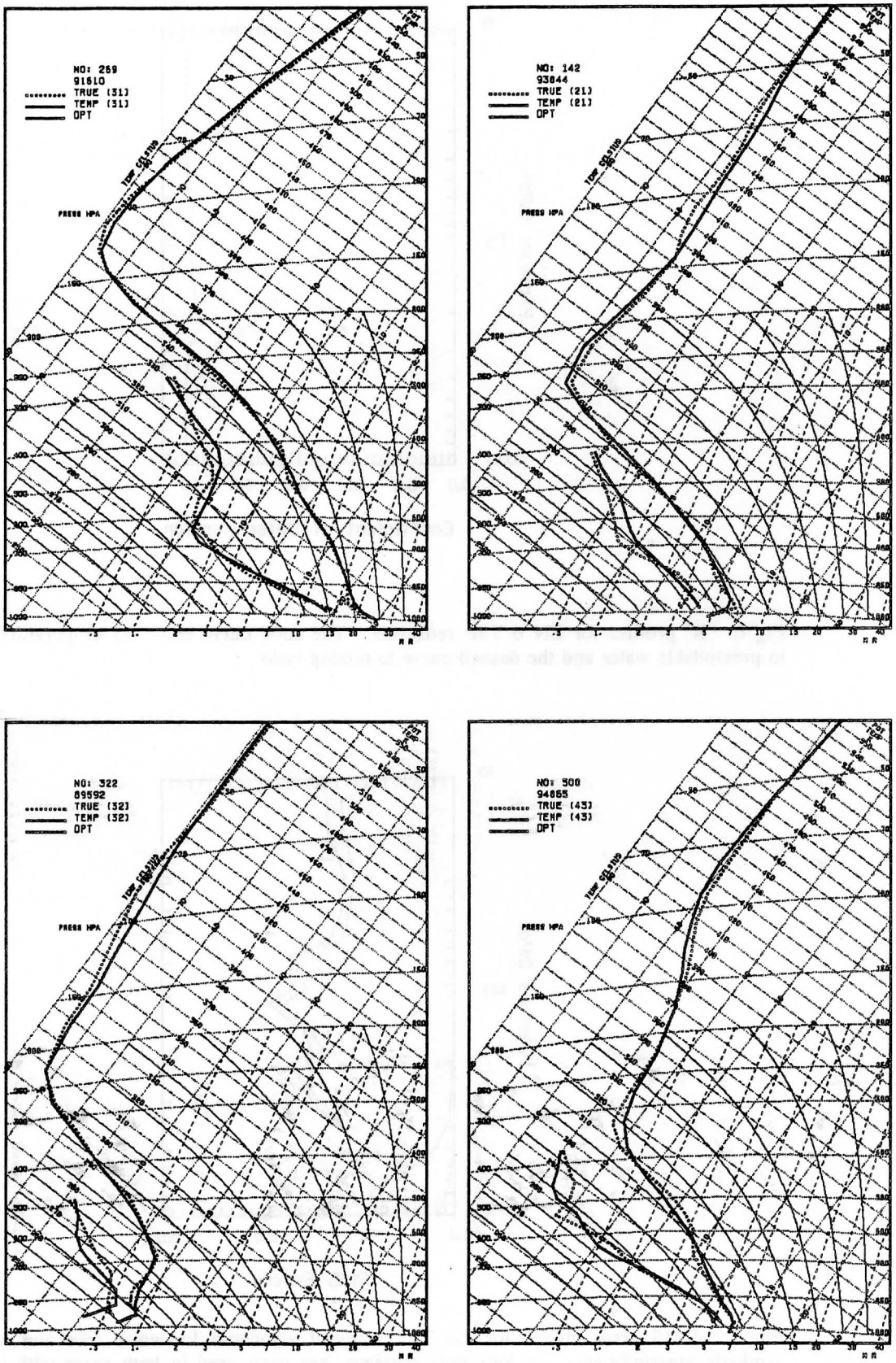

Fig 8. Tephigram plots of temperature and dew point temperture for four representative synthetic data retrievals. The true profiles are the dashed curves and the solid curves the TSF retrieved profiles. The TSF retrieval estimator utilized cs 5 data and the radiance temperature measurements were contaminated with Gaussian noise.

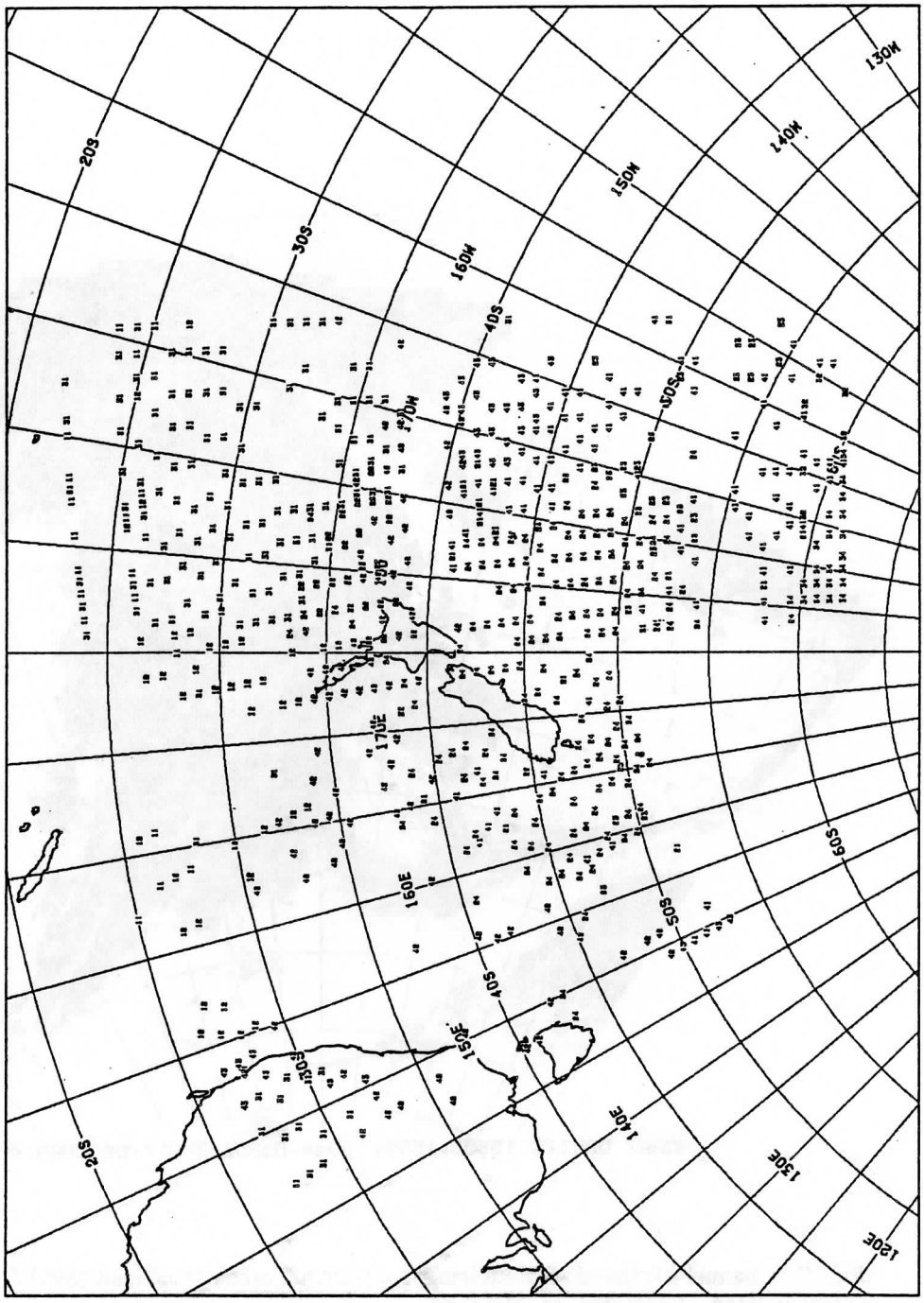

Fig 9. Radiance discrimination classes for NOAA 7 orbits 15950 and 15951. The class identifiers refer to figure 1 and table 1. The discrimination function utilized channels 1, 2, 4, 23, 5 and 6 and the declouding algorithm, channels 1, 2, 4, 23 and 22.

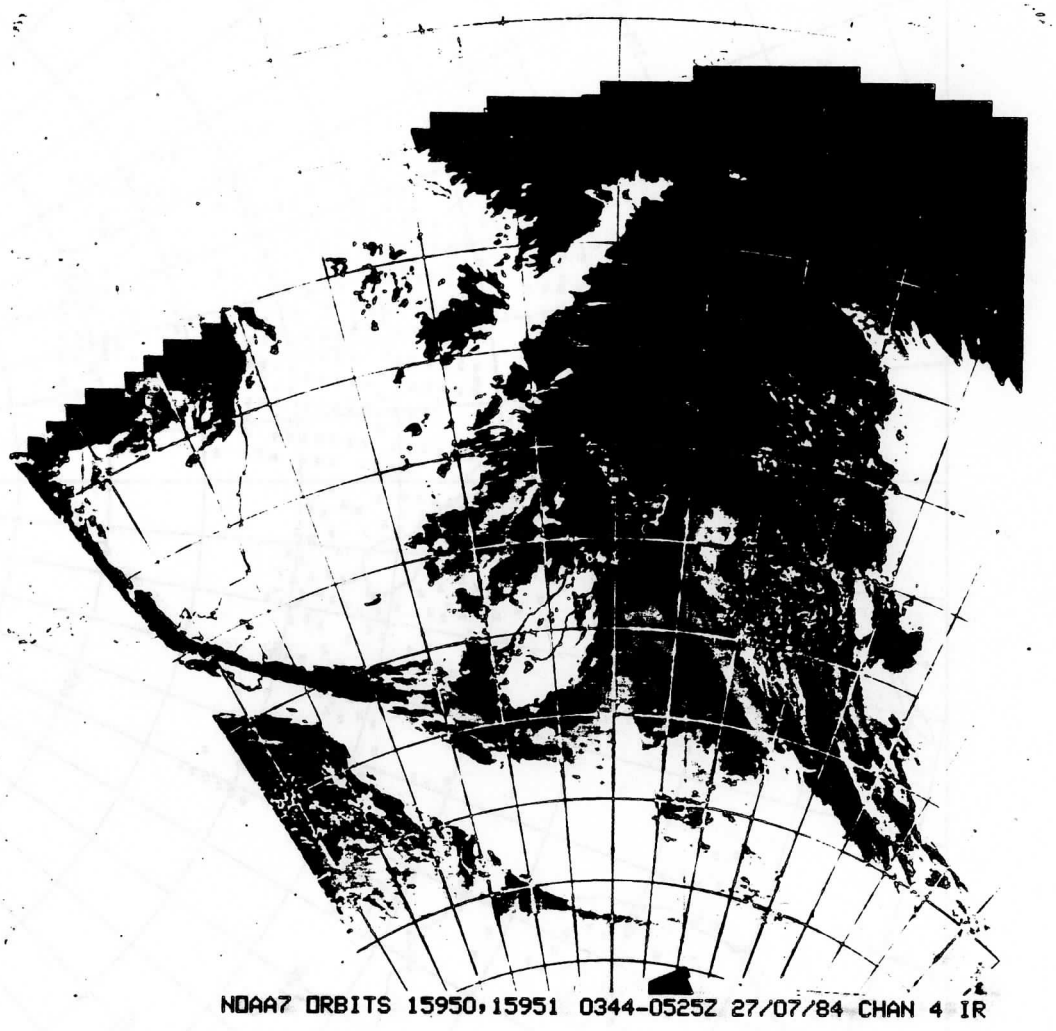

Fig 10. Channel 4 infrared AVHRR image for NOAA 7 orbits 15950 and 15951. The time span of the two passes is 0344 - 0525GMT on 27/Jul/84.

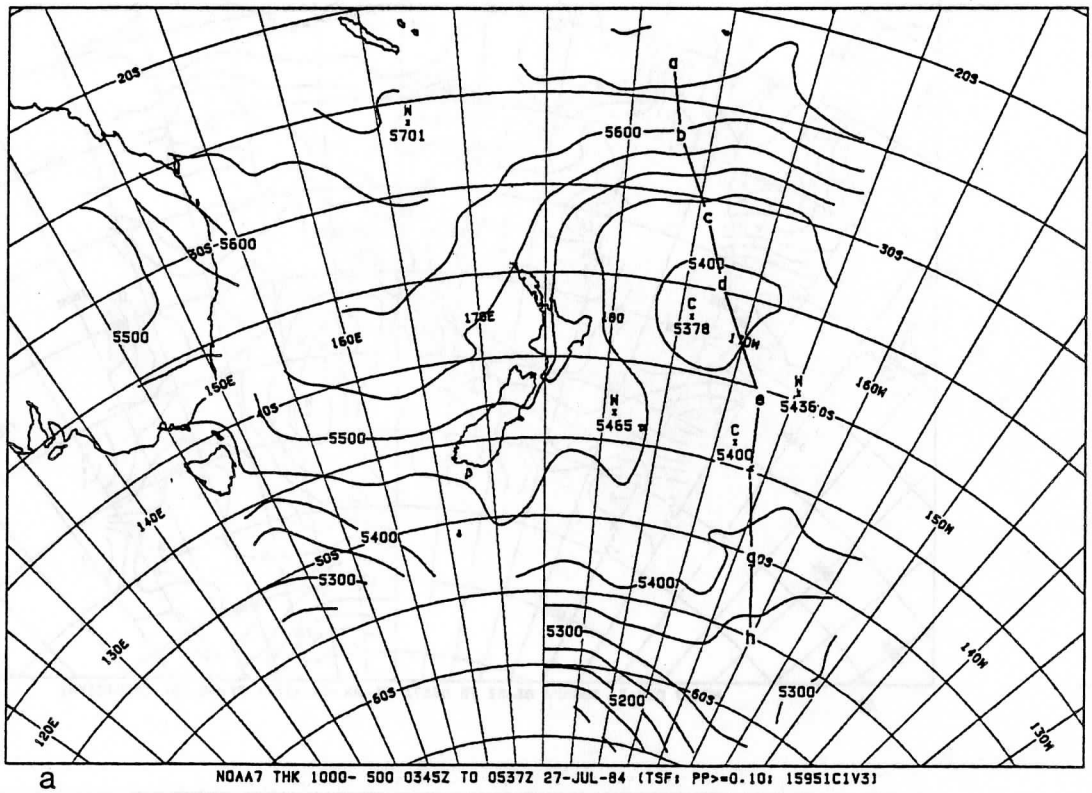

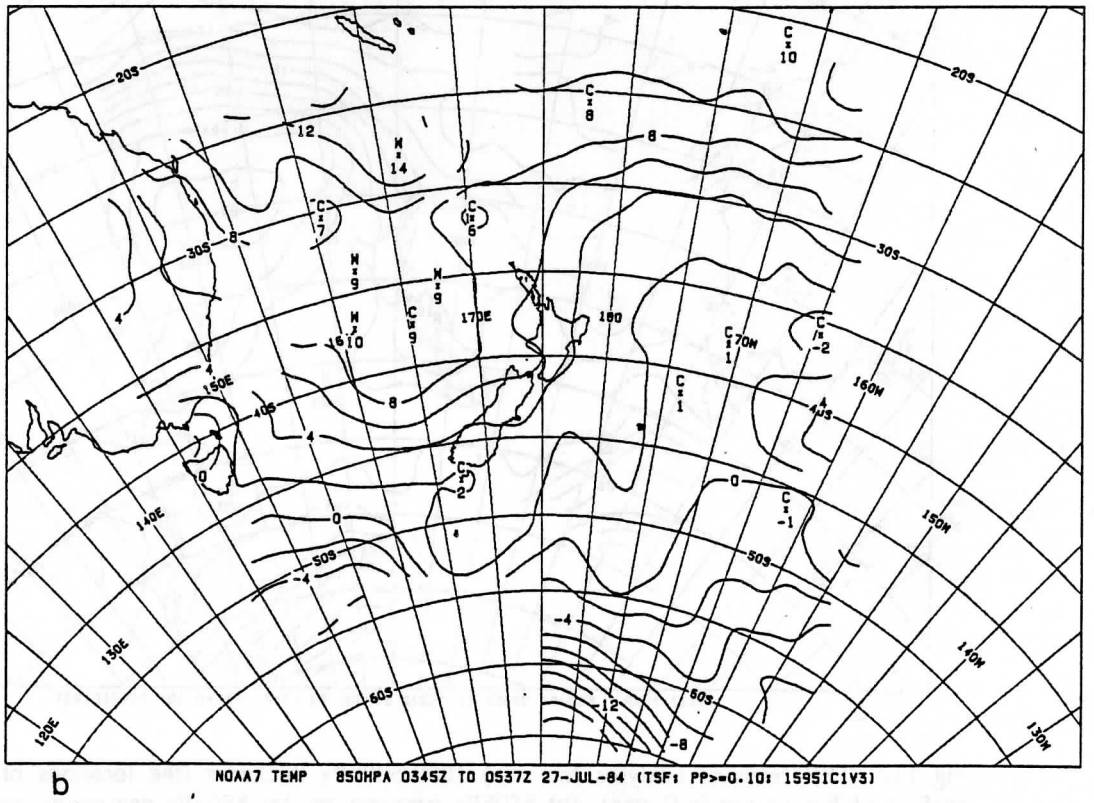

Fig 11. TSF retrieval analyses for; (a) 1000-500hPa thickness (the locations of the cross-section profiles of Fig 14 are indicated), (b) 850hPa temperature, (c) 850hPa dew point temperature, and (d) 500hPa temperature fields, for NOAA 7 orbits 15950 and 15951.

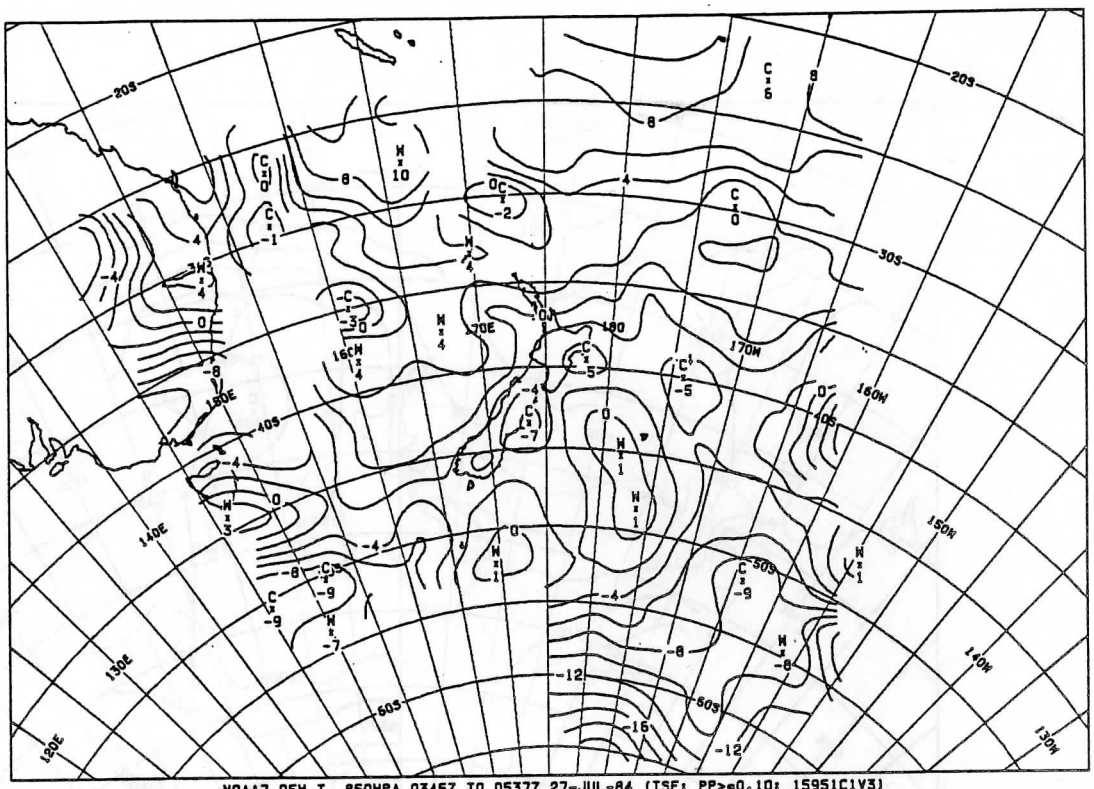

c

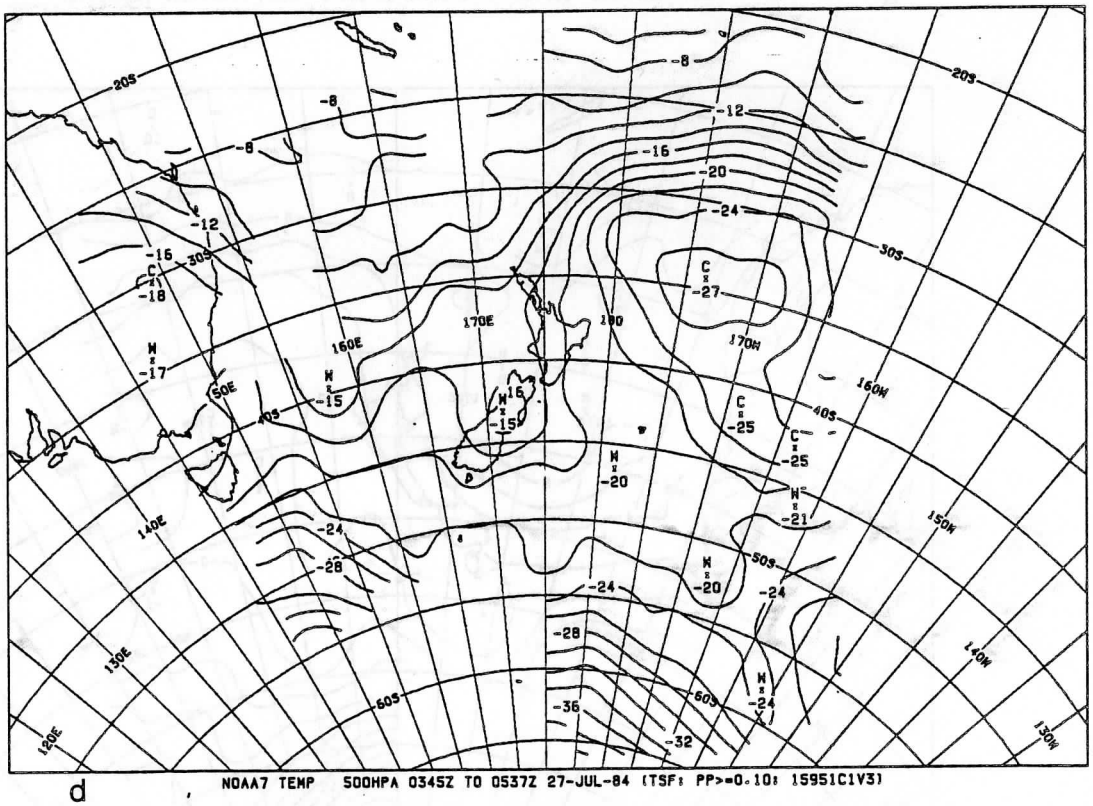

d

Fig 11. TSF retrieval analyses for; (a) 1000-500hPa thickness (the locations of the cross-section profiles of Fig 14 are indicated), (b) 850hPa temperature, (c) 850hPa dew point temperature, and (d) 500hPa temperature fields, for NOAA 7 orbits 15950 and 15951.

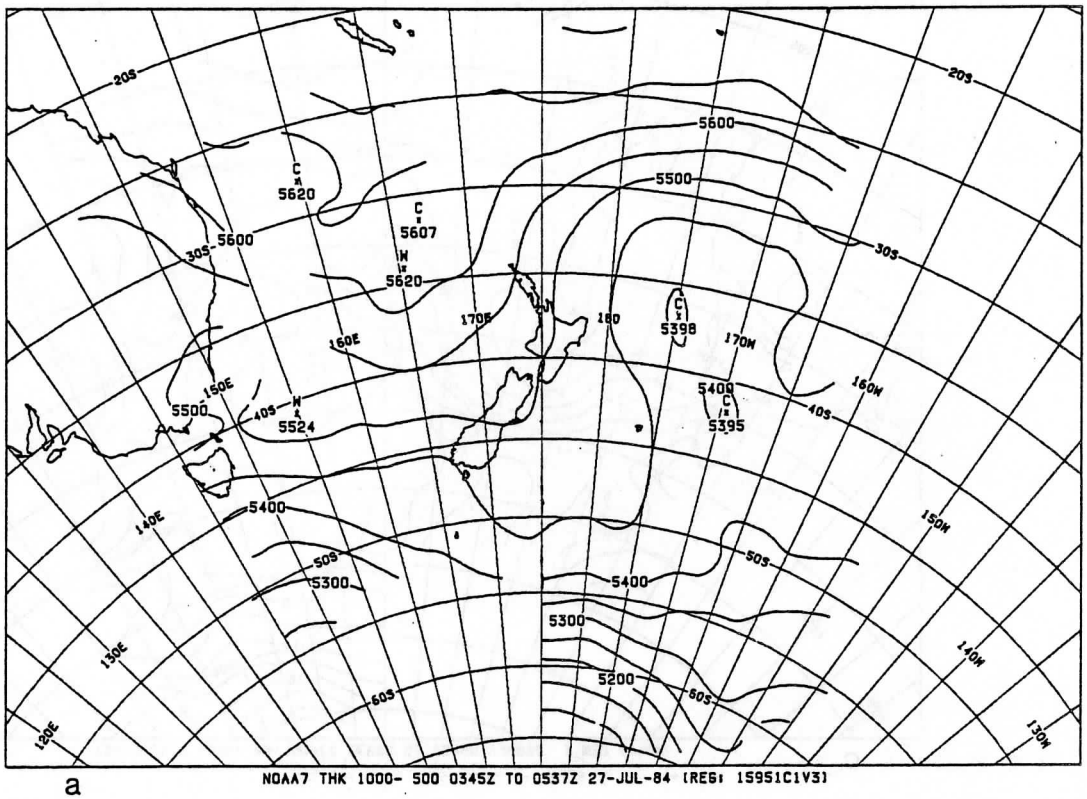

a

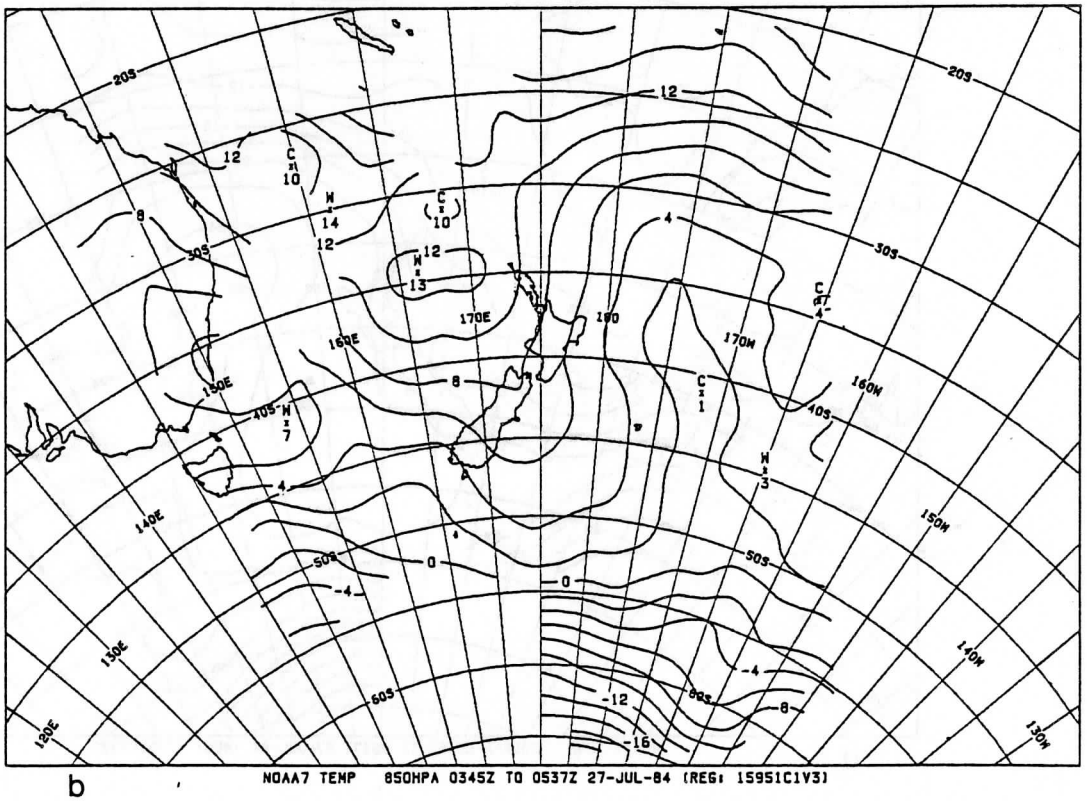

b

Fig 12. Regression retrieval analyses for; (a) 1000-500hPa thickness, (b) 850hPa temperature, (c) 850hPa dew point temperature, and (d) 500hPa temperature fields, for NOAA 7 orbits 15950 and 15951.

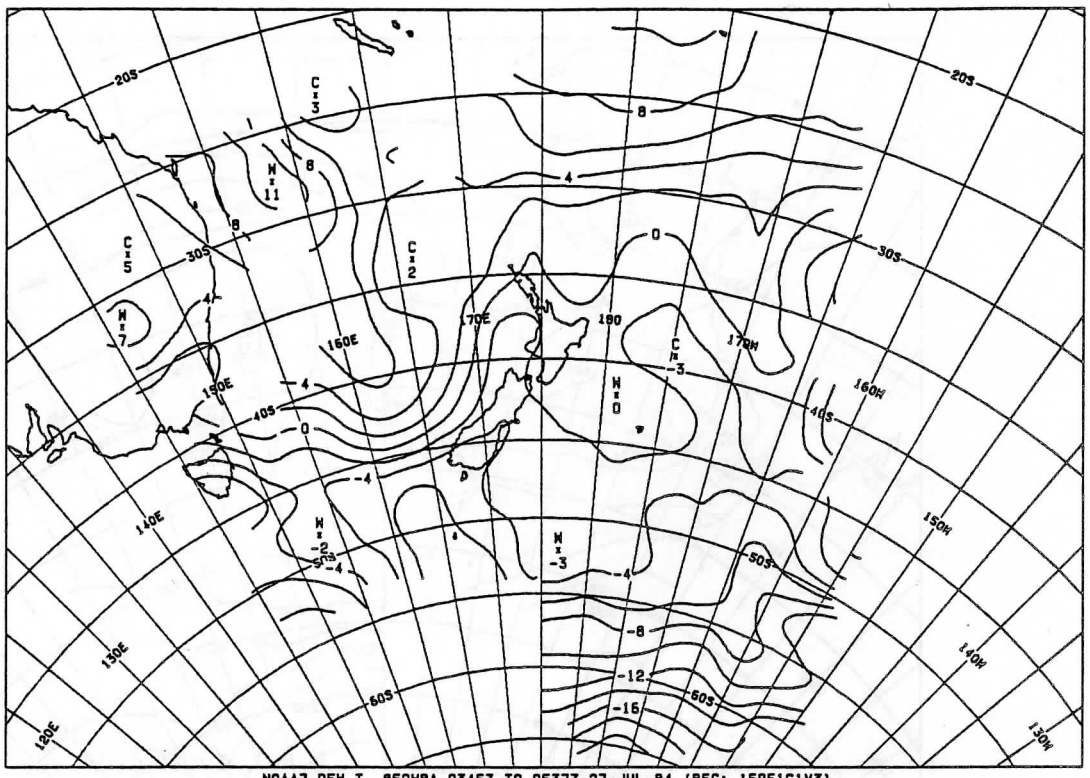

c

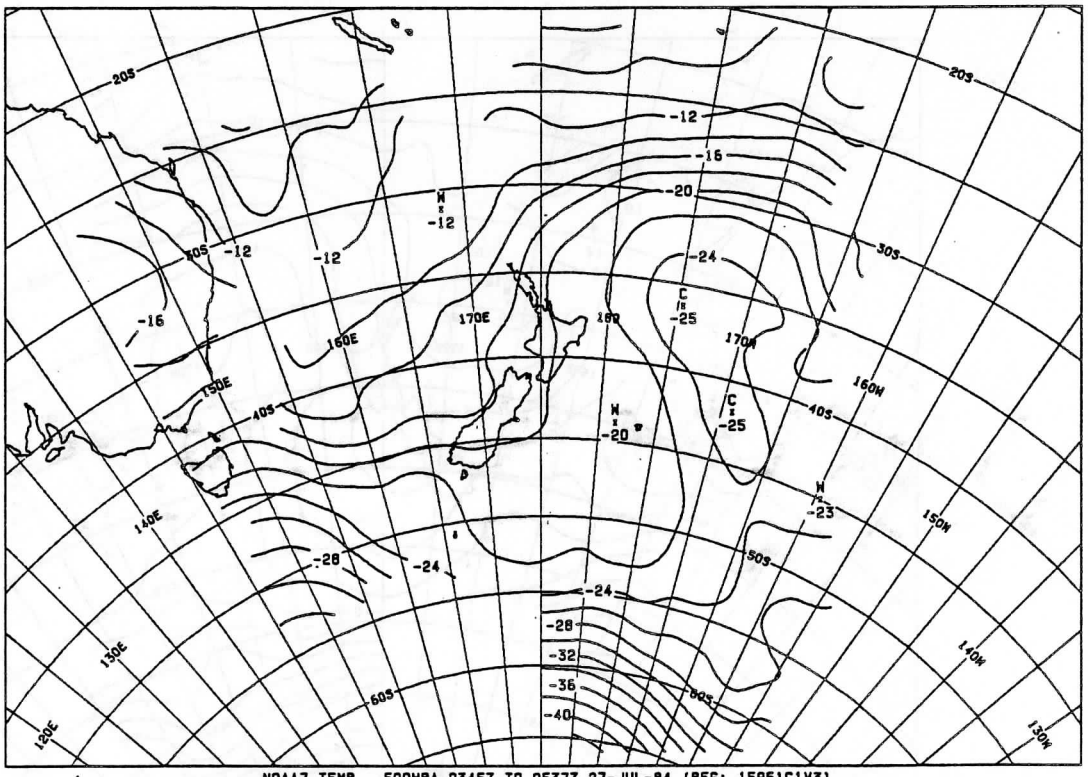

d

Fig 12. Regression retrieval analyses for; (a) 1000-500hPa thickness, (b) 850hPa temperature, (c) 850hPa dew point temperature, and (d) 500hPa temperature fields, for NOAA 7 orbits 15950 and 15951.

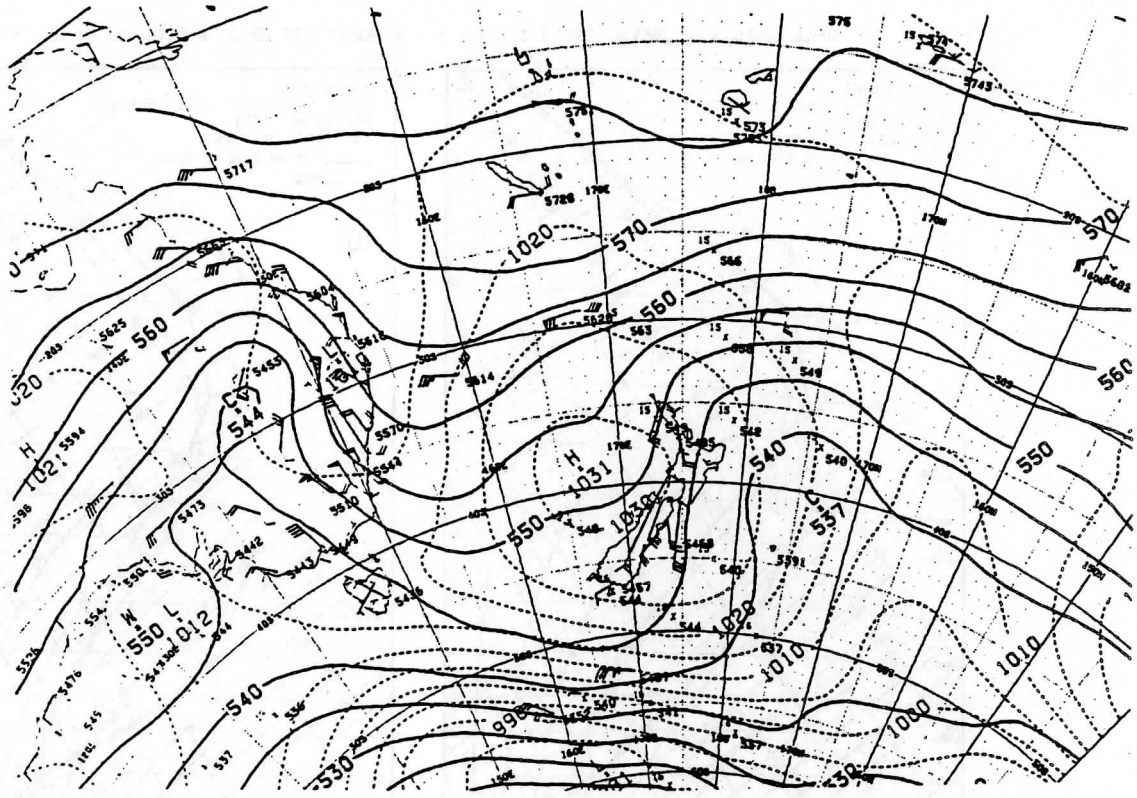

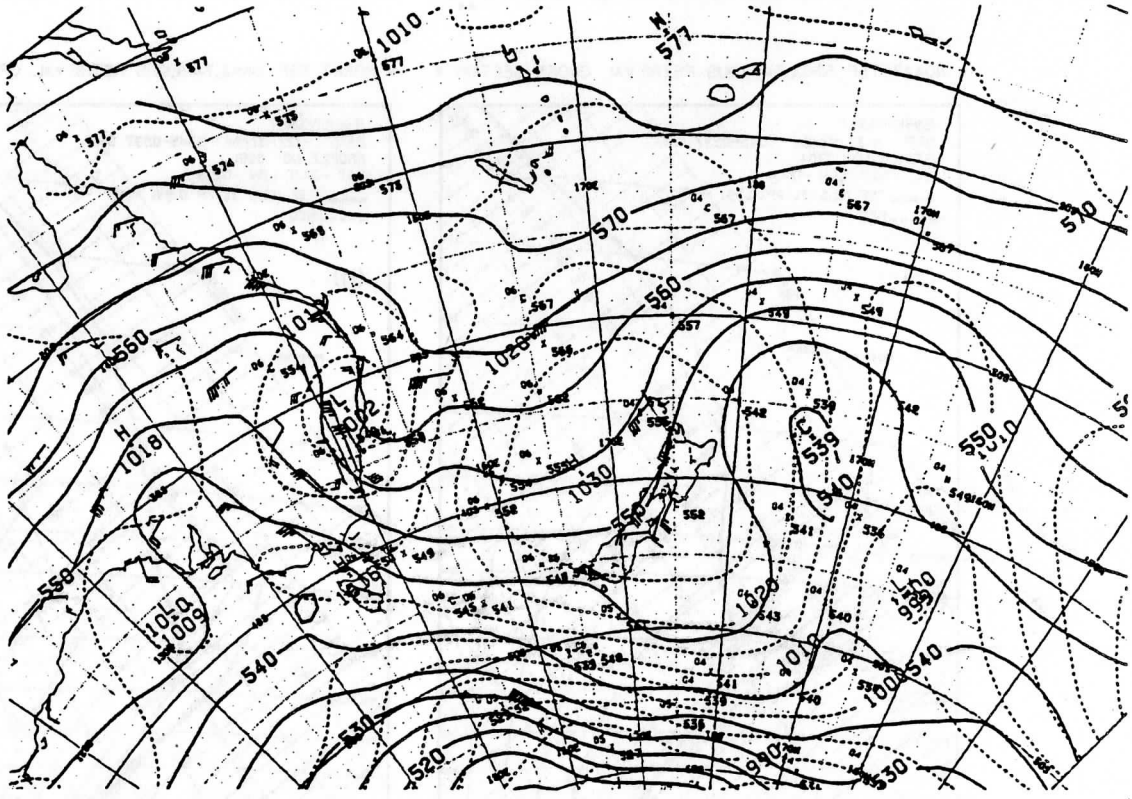

Fig 13. NWP analyses of 1000-500hPa thickness (solid curves) and surface pressure (dashed curves) fields at 0000 (a) and 0600 GMT (b) 27/Jul/84. Subsets of the GTS SATEM (marked by a cross) and locally derived SATEM observations are indicated (c refers to a clear retrieval, * to a cloudy retrieval, and M to a microwave only retrieval).

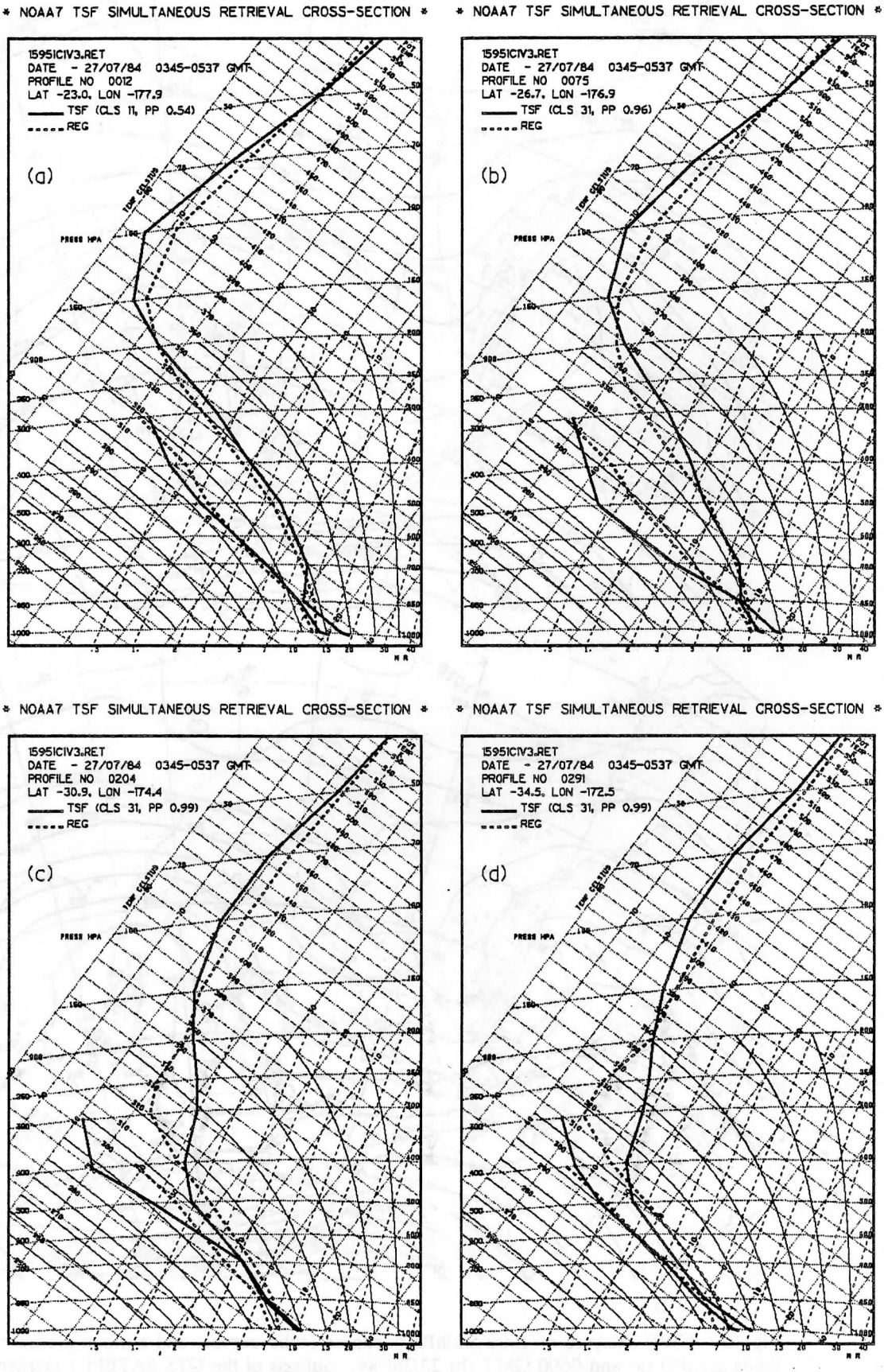

Fig 14. Tephigrams of TSF (solid curves) and Regression (dashed curves) retrievals for the cross-section indicated in figure 11(a).

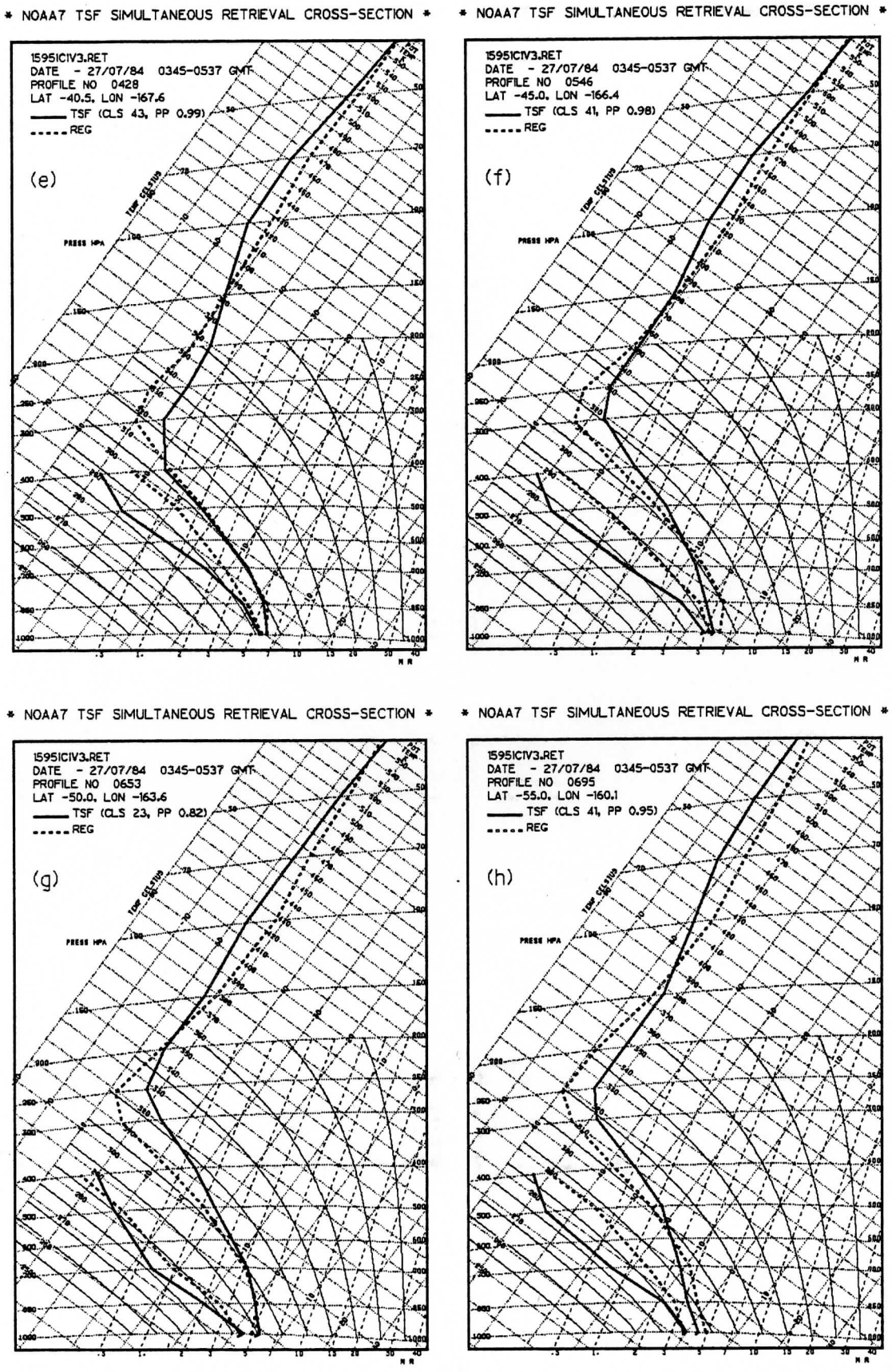

Fig 14. Tephigrams of TSF (solid curves) and Regression (dashed curves) retrievals for the cross-section indicated in figure 11(a).

VALIDATING A TOVS CLOUD CLEARING SCHEME USING AVHRR DATA

P.D.Watts and J.R.Eyre

Meteorological Office Unit,
Robert Hooke Institute for Cooperative Atmospheric Research,
Clarendon Laboratory, Oxford, U.K.

1. INTRODUCTION

A new cloud clearing scheme is undergoing operational trials in the Local Area Sounding System of the U.K. Meteorological Office. Prior to these trials a sensitive method of validation of the cloud clearing of HIRS (High-resolution Infra-red Radiation Sounder) radiances was devised using AVHRR (Advanced Very High Resolution Radiometer) data. With this method of validation, the performance of the new cloud clearing can be compared with that of the existing scheme. Many interesting features of cloud clearing infra-red radiances become apparent when an accurate "ground truth" is available; normally the error characteristics of the cleared radiances are obscured by larger errors inherent in the validation system. The new cloud clearing scheme and the operational scheme which it is intended to replace are only described briefly here. A summary of the approach used in the new scheme is given by Eyre et al. (1985) and full descriptions of both schemes are available elsewhere (Eyre and Watts 1986, Watts 1985). The Local Area Sounding System is described by Eyre (1984).

2. NEW AND OLD CLOUD CLEARING SCHEMES

The new cloud clearing scheme (NCCS) is intended to improve upon and replace the version currently operational in the Local Area Sounding System (LASS). Hereafter in this paper any reference to "LASS" will be to the cloud clearing part of the operational scheme rather than to the processing suite as a whole.

NCCS is based on LASS and uses the same basic cloud detection mechanism. The Microwave Sounding Unit channel 2 (MSU-2) brightness temperature is estimated from HIRS brightness temperatures and compared to the measured value. If the two values are the same, to within a certain limit, the field of view (FOV) is assumed to be clear of cloud. A higher value in the measured brightness temperature indicates the presence of cloud. If this is the case, then an attempt is made to account for the effect of the cloud on the radiances using the adjacent field of view or N* method (Smith 1968). If this fails (for a variety of reasons), then, in the LASS scheme, the FOV is abandoned as too cloudy. At this stage the LASS cloud clearing is

essentially finished. In NCCS, if the N* method fails, linear combinations of the MSU channels (unaffected by cloud) are used to obtain estimates of the clear HIRS radiances. The coefficients for this process are obtained by multiple linear regression on theoretically computed TOVS brightness temperatures derived from a large set of radiosonde profiles. In NCCS, this cloud detection and correction is carried out on all FOVs rather than on only every second line and second FOV as in LASS. In this way NCCS establishes a complete field of HIRS and MSU data whereas the result of LASS is an intermittent field of data with large gaps in very cloudy areas. The "MSU regression" route in NCCS produces large areas of HIRS data which have locally correlated errors. The problem is sufficiently acute that an analysis scheme is included to estimate this error and subsequently account for it. In NCCS we consider that better estimates of the brightness temperatures are obtained by smoothing the field to a certain degree, i.e. by locally combining estimates. To do this optimally we require estimates of the errors in the brightness temperatures and a part of NCCS performs this estimation.

In summary, NCCS and LASS use the same cloud detection and correction mechanisms except in very cloudy areas where NCCS obtains clear HIRS values from the MSU. NCCS attempts to retain the full information content of the data by clearing on every FOV and includes a filter to use these data optimally. For more details on both schemes the above references should be consulted. The validation exercise reported here examines the following aspects of NCCS: its performance relative to LASS, the error characteristics of the various cloud clearing routes, and the behaviour of the filter and of the scheme for analysis of the bias in estimates obtained by the "MSU regression" route. regression bias analysis.

3. VALIDATION SCHEME USING AVHRR DATA

3.1 Rationale

It is possible to use AVHRR data to validate a TOVS cloud clearing scheme because AVHRR has infra-red channels (4 and 5) in the same (11μm) window region as HIRS channel 8. The latter can be readily synthesised from the former. Providing that the two instruments can be collocated to a sufficient accuracy (about 1 km) and that cloud contamination of AVHRR data can be identified with a high degree of certainty (about 1% error in detection of contaminated pixels), an estimate of the clear value of HIRS channel 8 can be obtained. One drawback of such a method is that relatively large amounts of AVHRR data have to be processed to validate a single pass of HIRS data, and the method is therefore only practicable for a limited number of passes. However, a large variety of cloud conditions are normally met within a single pass, thus providing a reasonably wide test of the scheme. Secondly, only HIRS window

channels can be synthesised from AVHRR and so the performance of the cloud clearing scheme for other channels remains untested. This is only a minor problem since HIRS window channels are the most sensitive to cloud effects. However, there are dangers in a scheme highlighting only one channel, and it may be over-sensitive to errors which would be negligible in most other channels. Finally, it is only where there are clear AVHRR pixels that a synthesised HIRS channel 8 can be obtained so that the method fails in very cloudy areas. This problem is unavoidable and is probably the only serious drawback in this method of validation.

An alternative and more conventional method is to use collocated radiosondes and to compute the radiances expected from the observed profiles. This has the advantages that all HIRS channels can be checked and there is no restriction to partly clear areas. However deficiencies in the radiative transfer model used, lack of surface temperature information in the sonde report and the space and time tolerances of the collocation criterion all introduce differences which will tend to mask the cloud clearing errors one is trying to observe. Retrieved temperature profiles can be compared (e.g. McMillin and Dean, 1982) but at the expense of introducing retrieval errors which can be more damaging to the comparison (Eyre and Watts 1986, Eyre 1987). It will be shown that a HIRS 8 value synthesised from AVHRR is accurate to about 0.3 K and therefore an order of magnitude better than that which might be expected from radiosonde collocations. It is also significantly less than typical cloud clearing errors (2-5 K) so that it provides an effective "ground truth" and thus allows quantitative conclusions to be drawn that would otherwise be impossible.

A significant advantage in using AVHRR is in the density of collocations available; a typical pass allows 50-70% of the HIRS FOVs to be validated. This is a very useful feature, as an important assumption of NCCS is that radiance fields can be expected to be horizontally consistent. Exactly how consistent (in channel 8) and how successfully the filter achieves this consistency can be seen using the AVHRR.

In summary, although the validation only applies directly to channel 8 and in regions with some clear areas, the high accuracy and density of collocations more than compensate for the drawbacks. The accuracy allows quantitative checks to be made on the cloud-cleared radiances and on the error estimates, and the high density allows detailed effects of the filter to be monitored.

3.2 Method

Details of the method of validation are given in Eyre and Watts (1986) but the main points and some supporting evidence for its validity are given here. The HIRS FOV is collocated with the AVHRR to

within 1 km (Aoki 1983: Lloyd et al. 1985) and the AVHRR pixels associated with each HIRS FOV are thus identified. Cloud contaminated pixels are identified using the scheme described by Saunders (1986), employing AVHRR channels 1, 2, 4 and 5 during the day and channels 3, 4 and 5 at night. AVHRR channels 4 and 5 and HIRS channel 8 all lie in the 11μm window region with the AVHRR channels lying either side of the HIRS; Figure 1 shows the spectral response functions of the three channels. Thus, values of AVHRR channels 4 and 5 averaged over the HIRS FOV can be used to estimate HIRS channel 8 (using a regression relation). Figure 2 shows the HIRS 8 value derived from AVHRR (hereafter called AVHRR"8") plotted against the measured HIRS 8 brightness temperature for all FOVs of a pass before cloud clearing, i.e. both AVHRR and HIRS data are cloud contaminated. The fit can be seen to be good, giving a bias of 0.2 K and a standard deviation of 0.3 K. The validation scheme utilises our ability to identify contaminated AVHRR pixels in order to average over the remaining clear pixels to obtain an AVHRR"8" which is an estimate of the clear HIRS 8. The accuracy of the clear AVHRR"8" is unlikely to be better than the figures quoted above, and may be degraded somewhat by residual contamination of the AVHRR. However, the cloud detection scheme was designed to find clear pixels and the number of cloudy pixels admitted is found to be very small. In fact, the number of clear pixels is usually underestimated. In summary we can expect the AVHRR"8" clear value to be no more than 0.4-0.5 K from the truth. By comparison, typical cloud clearing errors in HIRS 8 are around 2-5 K.

Figures 3a and 3b summarise the method for part of a pass of data (25 January 1986 at 1307Z). Figure 3a is AVHRR channel 2 (near infra-red) with collocated HIRS footprints overlaid. Figure 3b is the "cloud mask" and is grey or black for the pixels considered cloudy by the AVHRR detection scheme. The numbers above the ellipses give the AVHRR"8" values derived for the clear portion remaining (in tenths of a degree with the leading figure omitted, e.g. 784 = 278.4 K). Notice that no value is present for totally cloudy HIRS FOVs.

The symbols within the ellipses indicate the route by which NCCS obtained clear radiances. In brief, "." indicates that the FOV was judged clear, "*" indicates cloud clearance by the N* method and, apart from residual contamination checks "A" and "#", all other symbols indicate failure of the N* method for one of a variety of reasons (see Eyre and Watts 1986, or Watts 1985).

3.3 Histograms and statistics

Clear radiances are produced by both LASS and NCCS, and the resulting HIRS 8 value may be compared with the AVHRR"8". An instructive way to examine the differences is in the form of histograms. Figure 4 is an example of such a histogram for the NCCS scheme, and we now describe the notation in this and subsequent histograms. Positive values represent AVHRR"8" warm with respect to

HIRS 8. There are 1170 collocations with a standard deviation (S.D.) of 3.7 K and a bias of 1.6 K. In view of the accuracy of AVHRR"8" as a measure of the clear HIRS 8 temperature these differences may be regarded practically as errors in the cloud cleared HIRS 8 values. On each histogram a value of "P.E." is given. This is the mean value of the error estimated by the NCCS scheme itself and used in the sequential estimation filter. The above collocations may be split advantageously into subsets of the whole. Firstly the set of FOVs where LASS obtained clear radiances is selected in order to compare the relative performance of the two schemes. Other obvious subsets are the cloud clearing routes - clear, N* and MSU regression - with the further separation into land and sea areas also instructive.

4. SOME RESULTS

4.1 Comparison of NCCS with LASS

Figure 5a is the histogram of errors obtained with LASS for a pass at 1319Z on 16 April 1985. 154 collocations were obtained with a standard deviation of 3.5 K and a bias (HIRS cold) of 1.1 K. Over the same FOVs, Figures 5b and 5c show the errors obtained with NCCS at the pre- and post-filtered stages respectively. The standard deviations and biases are seen to be substantially lower than the LASS results. The filtering stage does not have a large impact in this case, reducing the standard deviation by only 0.2 K. Figures 6a and 6b are the error histograms for all NCCS collocations for the same pass, for pre- and post-filtered stages respectively. With cloudier situations included, the filter can be seen to be more effective, reducing the standard deviation by 1.0 K. The final standard deviation and bias of 3.0 and 0.4 K respectively are both lower than the results for LASS over its limited set. In general we may expect NCCS errors for all collocations to be larger than NCCS errors for the limited LASS set, since the former will include cloudier areas. However, in this case the performance is not greatly degraded over all FOVs.

In conclusion, NCCS performs better than LASS with respect to both standard deviation and bias of errors. Many more clear radiances are produced with NCCS in cloudier areas but they remain of a standard comparable to or better than LASS.

4.2 Error characteristics

The histogram in Figure 4 of unfiltered NCCS errors shows a spread of errors. It is very instructive to split the statistics into types of clearance and, in some cases, into land and sea areas. The typical error characteristics then become apparent.

Figure 7 is a histogram of the FOVs determined clear by NCCS from the same pass (1307Z, 25 January 1986) for both land and sea areas. There is a large peak value almost at zero difference which represents the genuine clear FOVs. At larger values of AVHRR"8"-HIRS 8 there is a decreasing "tail" of contaminated FOVs that have been passed as clear. The number in the "tail" at more than 2.0 K difference is quite large. This result was obtained with the improved NCCS, incorporating visible threshold and low cloud checks described in section 4.4. The length of the tail is related to any bias present in the estimated MSU-2 value used in the cloud detection (see Watts 1985 Appendix E). A warm bias in this value creates a longer tail. A cold bias would tend to remove the tail but increasingly at the expense of losing genuine clear FOVs. An attempt has been to identify and correct for a damaging warm bias in the estimated MSU-2 values and this is described in section 4.4. The above results, with a relatively short tail, were obtained after this bias correction had been applied.

The predicted errors for the clear FOVs are obtained from a knowledge of the limb-correction and radiometric errors and from the likely amounts of cloud missed because of the uncertainty in the estimated MSU-2 (Watts 1985 Appendix A). The resulting mean value of 2.0 K for this pass is close enough to the actual mean errors to have an appropriate effect in the filter.

Disregarding the very small number of "clear" FOVs which appear too warm (probably due to contamination in AVHRR), the error characteristics of "clear" FOVs are an edge at zero error with a tail of increasing cold error. The filter currently weights according to error variance, i.e. it assumes a normal distribution of errors with zero mean. The above error characteristics suggest a more suitable estimator should be used.

Figure 8 is the histogram of errors for "N*" FOVs for the same pass. The distribution of errors can be seen to be more nearly normal than that of the "clear" FOVs. The mean error is also reasonably near zero. Thus error characteristics of "N*" FOVs are well suited to the filter currently in NCCS. The error estimated for an N* clearance is calculated from expected errors in all the quantities used in its derivation and some assumptions about the correlation of these quantities. The average predicted value comes out far too high at 14.7 K compared to the actual mean value of 2.8 K. The result is that these FOVs get too little weight in the filter and some investigation of these predicted errors is described in section 4.4(f).

HIRS estimation by regression on MSU data is the third route to a set of clear radiances. Figures 9a and 9b are histograms of the MSU regression route for the same pass for land and sea FOVs respectively. As expected from a regression relation, locally consistent biases are apparent. The sea FOVs are particularly strongly biased by an average 8 K (HIRS cold) on this occasion. The standard deviations, however,

are reasonably small (around 2 K) and should represent the expected error in the filter if the bias correction part of the scheme is fully successful. The value of 6.2 K for the mean predicted error is simply the expected error from the regression and takes no account of the bias correction having removed part of it. However, we think it prudent to allow such a high value to remain because even after the bias correction the smaller errors remaining are likely to be locally correlated and therefore damaging if these data are weighted too heavily.

4.3 The effect of the filter

We have already shown in section 4.1 that the filter in NCCS is useful to some extent and now describe its behaviour in more detail. Figures 10a, 10b and 10c are histograms for all FOVs (for the same pass) for NCCS before filtering, after the bias correction has been made to the MSU regressions and after filtering respectively. It can be seen that the MSU bias correction is responsible for a large drop in the overall standard deviation (and bias), larger in fact than the filtering of the brightness temperature field. This is a common result mainly because "MSU regressions" constitute a large proportion of the clearances and because they are often badly biased. Because of the greater degree of genuine variation in brightness temperature over the land than over the sea filtering is less effective in the former case. Inspection of the histograms shows that the filter tends to remove outliers but fails to tighten the main peak. In general, when true variations in a field become equal in magnitude to the errors or noise which we are trying to remove, filtering improvements will be limited to removing "rogue data". The different characteristics of land and sea are accounted for by filtering less strongly over land (see section 4.4).

"Clear" FOVs have the lowest expected error and are usually the most accurate clearances in the field. They therefore usually supply other FOVs with information rather than receive it. Consequently, where they are inaccurate with a long cold "tail", not only can they be damaged themselves, but they can also damage other FOVs through the filtering process. The effect of the filter is to produce a peak in the new histogram towards the "centre of mass" of the tail in the unfiltered "clear" histogram. The standard deviation is reduced but there is also a detrimental effect on other FOVs.

"N*" FOVs, with normally distributed unbiased errors, are treated by the filter in a simple manner. They tend to remain unbiased and improve in accuracy. "N*" FOVs are used in the bias correction of "MSU regression" FOVs and their lack of bias is an important advantage here.

"MSU regression" FOVs have also quite normally distributed errors though commonly about a large bias. In an ideal case, the bias correction (which is performed through a filtering procedure) removes the bias and reduces the standard deviation. The filter then only has a minor effect on these FOVs because much of the information from adjacent "clear" and "N*" FOVs has gone into the bias correction. The bias correction to the "MSU regression" FOVs tends to be worst when it is based on neighbouring, supposedly "clear" FOVs which are in fact too cold.

In summary, the filter is shown to be very useful in reducing errors in channel 8 brightness temperatures (and therefore by implication in all other channels). There are two parts to the filter: the MSU regression bias correction and the filtering of the final fields. The bias correction is very important for channel 8 but may become less so for channels with higher peaking weighting functions, for which the regression relation between the HIRS and MSU is stronger. The brightness temperature filter works well over the sea and less well over the land where genuine variations are larger. For channels peaking higher than HIRS 8 we may expect that genuine variations in the field will become much less than the cloud-clearing noise and thus the filter should be still more effective. A danger of the filter is that it not only allows good unbiased information to be used optimally but it also allows biased information to corrupt the good. The cold tail for "clear" FOVs is an example and efforts should be (and have been) made to reduce it.

4.4 Improvements made to NCCS

This section describes changes made recently to NCCS mainly as a result of findings from the validation exercises.

(a) Filtering strengths.

Detailed inspection of images like Figure 3a reveal that clear FOVs can be contaminated by adjacent FOVs that lie over a different surface and which therefore have different temperatures. Coastlines are obvious examples of adjacent areas of genuinely different characteristic temperatures. Clearly we should not filter so strongly across what are known land-sea boundaries and what are therefore likely to be areas of high radiance gradient. The filtering strength is reduced by the proportion $(1 - \tau_i)$, where τ_i is the total atmospheric transmission in channel i, whenever adjacent FOVs straddle a coastline. Consequently for channels which do not sense the surface, the filtering is unchanged and for window channels the change is the greatest. The same arguments apply when filtering the bias estimate for the "MSU regression" route, and a significant part of the gain in accuracy is due to avoiding corruption to the MSU bias field rather than the to the temperature field directly.

It was noted in section 2.1 that sea and land areas have notably different characteristic variations in brightness temperature. In view of this the filtering strength is reduced over land in order not to smooth genuine features. The appropriate filtering parameter has been estimated from cleared fields of AVHRR"8" for land and sea separately and used likewise in the filter.

Improvements to error statistics with these modifications were small: 0.1 K in standard deviation and bias at most with, again, most of this coming from an improved estimate of the bias field for the "MSU regression" route.

(b) HIRS 20 albedo check

Residual contamination of "clear" FOVs is potentially very damaging on both other FOVs and on the bias field. During daytime passes, use may be made of visible channel HIRS 20. McMillin and Dean (1982) describe the use of HIRS 20 for cloud detection whereby an upper limit (threshold) for clear FOVs is set. Their threshold is stored in an historical data set updated whenever a particular earth location is found definitely clear. In NCCS a simpler approach has been adopted initially, whereby a gross threshold is set empirically after inspection of images like Figure 3a. It is set rather high so that it can detect FOVs that appear at the end of the cold "tail" but does not remove good data at the peak. Substantial errors in HIRS 8 have been avoided by use of this check. However, many FOVs are not trapped because a constant gross threshold cannot be tightened without risk of losing a lot of data. A more dynamic threshold which allows a more stringent test is being developed.

(c) Low cloud test

A well established cloud detection method with AVHRR data is a threshold on the channel 3 (3.7μm) minus channel 4 (11μm) difference (see Eyre et al. 1984). The method relies upon differing emissivities of water cloud at the two wavelengths to supply a difference in the measured brightness temperatures. It is particularly useful because low cloud often avoids other detection mechanisms (e.g. spatial coherence and infra-red thresholds). It also often avoids the estimated MSU-2 detection test because the MSU-2 weighting function is small near the surface. Following the approach used with AVHRR data, we use HIRS channels 8 (11μm) and 18 (3.7μm) and set a threshold of 2.0 K to be used at night only (since during the day solar reflection in the 3.7μm channels renders the method useless). The method is not nearly as effective within a TOVS system as it is with AVHRR data since the HIRS FOVs, being larger, are more often only partially cloud filled. Relatively few FOVs are detected by the technique but it is very fast and will be effective in a situation where large areas of low cloud are accompanied by a failure of the MSU-2 detection system due, for example, to regression biases.

(d) Other inter-channel regressions

A further attempt at residual cloud detection has been made using a technique again following AVHRR techniques and McMillin and Dean (1982). It utilises the different behaviour of the Planck function at the different wavelengths present in HIRS data. A partially cloud filled FOV will give, for channels with identical weighting functions, a higher brightness temperature in the longwave than in the shortwave because the rate of change of radiance with temperature is higher at shorter wavelengths (see, for example, Saunders 1986). Such a pair of identical channels does not exist within the TOVS system but we can take a shortwave channel, say HIRS 14, and synthesise its longwave analogue with a linear combination of channels 1-12. Typical errors in a regression relation of this sort are about 0.5 K or less. The cloud test takes an estimate of HIRS 14 from channels 1-12, whenever the FOV is supposed clear, and compares this with the measured value. If it differs by more than, say, twice the regression residual error then the FOV may be assumed to contain cloud. In practice the test is found to be rather less sensitive than the MSU-2 system and fails to identify any cloud missed by the latter.

(e) Warm biases in estimated MSU-2 values

Section 4.2 describes the problem of a warm bias in the estimated MSU-2 values used in the cloud detection. Essentially, if the estimated MSU-2 value is too high in clear FOVs then some cloudy FOVs will escape detection. This is clearly seen in Figure 11a (pass at 1307Z, 25 January 1986) over the Mediterranean. The numbers above the ellipses are (in tenths of a degree) the differences between measured and estimated MSU-2 values. This quantity has to reach a value of about +7 (= 0.7 K, the typical residual error in estimating MSU-2) before we can say with confidence that cloud is present. Figure 11a shows estimated MSU-2 values up to 2.5 K too warm in "clear" FOVs leading to a great deal of missed cloud and inaccurate values in "N*" FOVs. It would be profitable to analyse the bias, in a similar manner to the MSU-regression bias, before cloud clearing the data. If the bias estimate were reasonably accurate it would considerably improve the cloud detection.

An approach has been adopted which can currently deal only with warm biases. The only way estimated MSU-2 can be greater than measured MSU-2 is when there is both a bias error in the estimated value and little or no cloud in the FOV. The analysis is done in the following manner. The pass is divided into boxes (of about 7x7 FOVs) and a search is made of all the FOVs within a box. From the negative measured-minus-estimated MSU-2 differences, we save the one with warmest value in HIRS 8, assuming that this gives the "clearest" FOV. After examining the whole pass, the field is filtered in the normal manner to give the analysed bias. NCCS is then run normally but with the bias estimates at each FOV added to the estimated MSU-2 values. Figure 11b is equivalent to Figure 11a but with the bias correction

applied. Clear areas now have almost zero measured-minus-estimated MSU-2 differences. Detection of low cloud or small amounts of cloud is improved and N* clearances are more frequent. The impact on the pass at 1307Z on 25 January 1986, with its large biases, is substantial; the number of "clear" FOVs is halved reducing the cold "tail". The number of successful "N*" FOVs is doubled and a substantial cold bias is removed. Biases for all validated FOVs drop from 2.8 K cold to 0.4 K warm. The bias analysis scheme worked so well in this case because the biases were large and consistent. It is not expected that it will normally be so dramatic. Certainly, an extension to allow analysis of cold biases is desirable but much more difficult, since values of estimated MSU-2 which are too cold are obtained from cloud as well as from estimation errors.

Inspection of estimated MSU-2 values for other cases reveals no large biases of either sign although they may generally be expected to be present with a magnitude of the order of the residual error in the regression (about 0.7 K).

(f) Estimated errors in "N*" FOVs

NCCS uses an algorithm to calculate the expected error in an N* cleared radiance, given expected errors in the radiances used in the N* equation, in N* itself and expected correlations between these errors (see Watts 1985). However, errors in N* clearance may be dominated by the cloud field failing to satisfy the required conditions. With the AVHRR data we can test the error algorithm explicitly, comparing the estimated error with the actual error obtained from the validation. Results show a lack of any significant correlation between estimated and actual N* errors and we find this is a characteristic regardless of the correlations assumed in the estimation. This suggests errors in N* clearances are dominated by inappropriate cloud conditions and that amplification of radiometric and preprocessing noise by the N* algorithm contributes only a small part. Therefore, a complicated calculation of expected error is not justified and it seems reasonable to use an average expected error for "N*" FOVs as well as for "clear" and "MSU regression" FOVs.

5. SUMMARY

The availability of AVHRR data coincident with TOVS data permits detailed exploration and sensitive validation of the performance of a HIRS cloud-clearing scheme. We have used AVHRR data to demonstrate the improvement of the new cloud-clearing scheme (NCCS) over its predecessor, to assess the error characteristics and remaining weaknesses of the NCCS, and to make improvements to NCCS to alleviate some of the problems found.

ACKNOWLEDGMENTS

We thank our colleagues John Barnett, Philippa Lloyd and Roger Saunders for contributions to and helpful comments on this work.

REFERENCES

Aoki T.
Clear radiance retrieval of HIRS channels with the use of AVHRR data.
Tech. Proc. 1st Int. TOVS Study Conf.; 29 Aug - 2 Sept 1983; Igls, Austria; CIMSS Report, 1-9 (1984).

Eyre J.R.
High-resolution temperature retrievals at the U.K. Meteorological Office.
Tech. Proc. 1st Int. TOVS Study Conf.; 29 August - 2 Sept 1983; Igls, Austria; CIMSS Report, 94-100 (1984).

Eyre J.R.
On systematic errors in satellite sounding products and their climatological mean values.
Accepted for publication in Quart.J.Roy.Met.Soc. (1987).

Eyre J.R., Brownscombe J.L. and Allam R.J.
Detection of fog at night using AVHRR imagery.
Meteorological Magazine, 113, 266-271 (1984).

Eyre J.R. and Watts P.D.
A sequential estimation approach to cloud-clearing for satellite temperature sounding.
Submitted to Quart.J.Roy.Met.Soc. (1986).

Eyre J.R., Watts P.D., Turner J. and Lorenc A.C.
Research and development on TOVS retrievals in the U.K.
Tech. Proc. 2nd Int. TOVS Study Conf.; 18-22 February 1985; Igls, Austria; CIMSS Report, 58-74 (1985).

Lloyd P.E., Barnett J.J. and Eyre J.R.
Investigations of AVHRR data to improve TOVS retrievals.
Tech. Proc. 2nd Int. TOVS Study Conf.; 18-22 February 1985; Igls, Austria; CIMSS Report, 162-176 (1985).

McMillin L.M. and Dean C.
Evaluation of a new operational technique for producing clear radiances.
J. Appl. Meteor., 12, 1005-1014 (1982).

Saunders R.W.
An automated scheme for the removal of cloud contamination from AVHRR radiances over western Europe.
Int. J. Remote Sensing, 7, 867-886 (1986).

Smith W.L.
An improved method for calculating tropospheric temperature and moisture from satellite radiometer measurements.
Mon. Wea. Rev., 96, 387-396 (1968).

Watts P.D.
An improved TOVS cloud clearing scheme -- preliminary report.
Met. Office internal report, Met.O.19 Branch Memo 81 (1985).

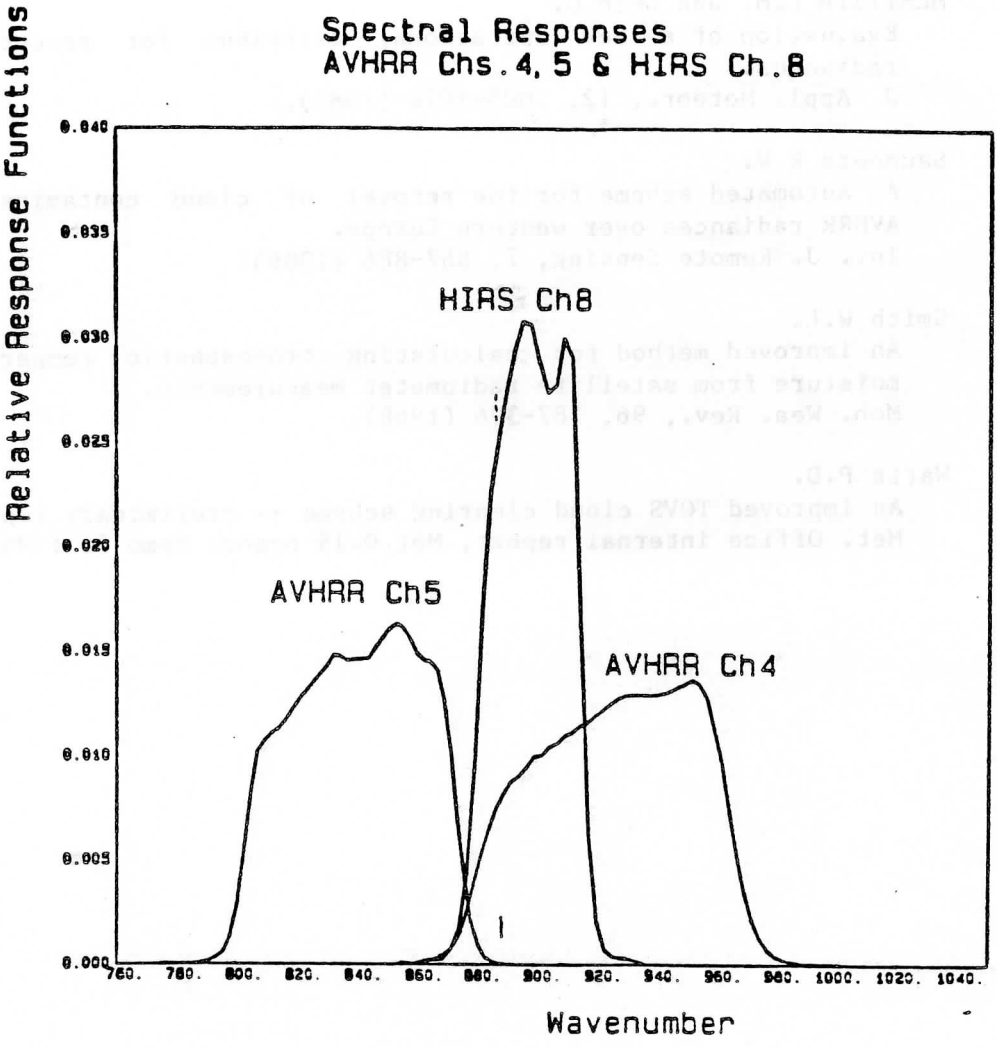

Fig. 1 Filter profiles for HIRS channel 8 and AVHRR channels 4 and 5 on NOAA-7.

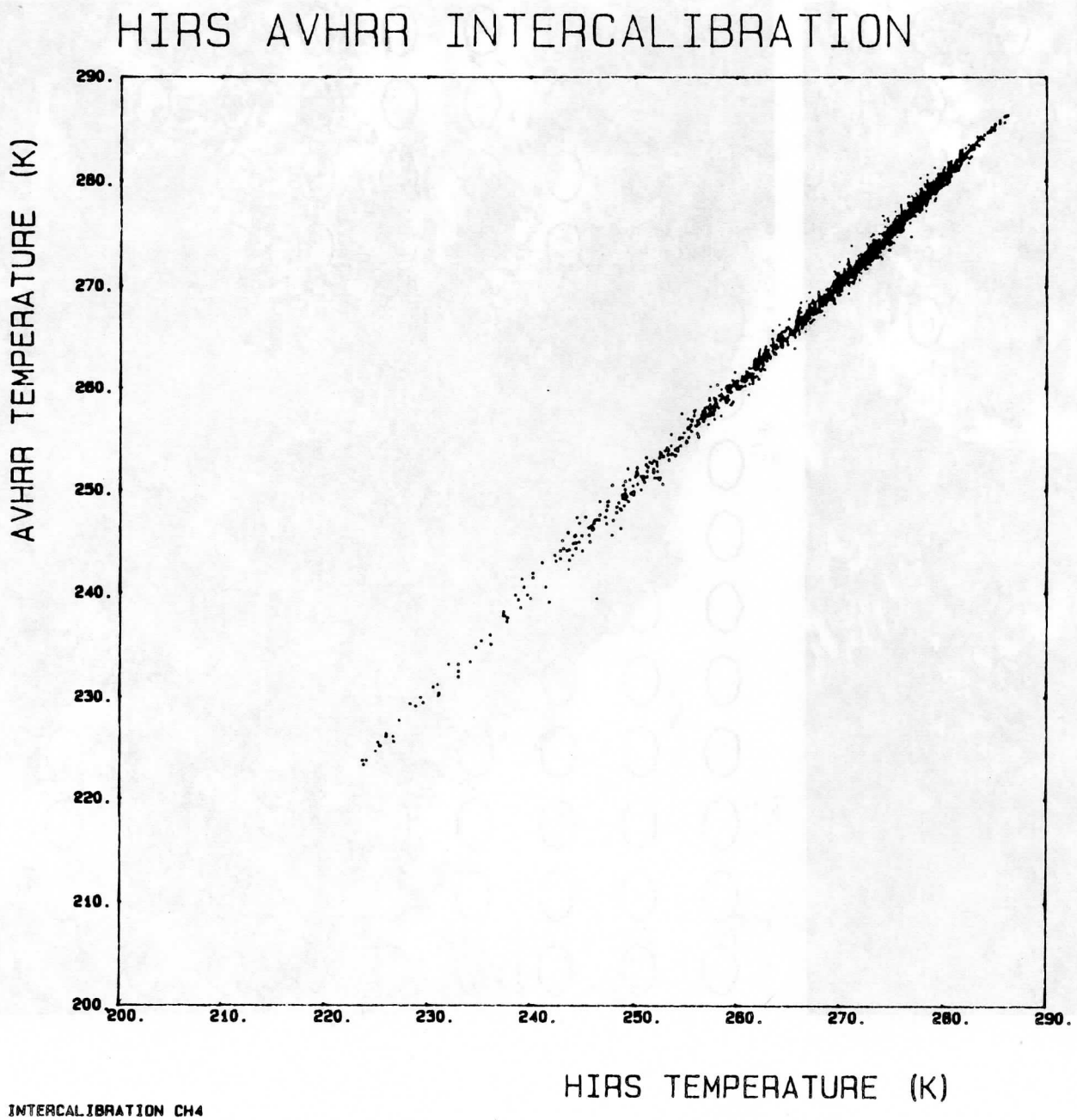

Figure 2

Illustrating the degree of agreement obtained between AVHRR"8" and HIRS 8 brightness temperatures (before cloud clearing)

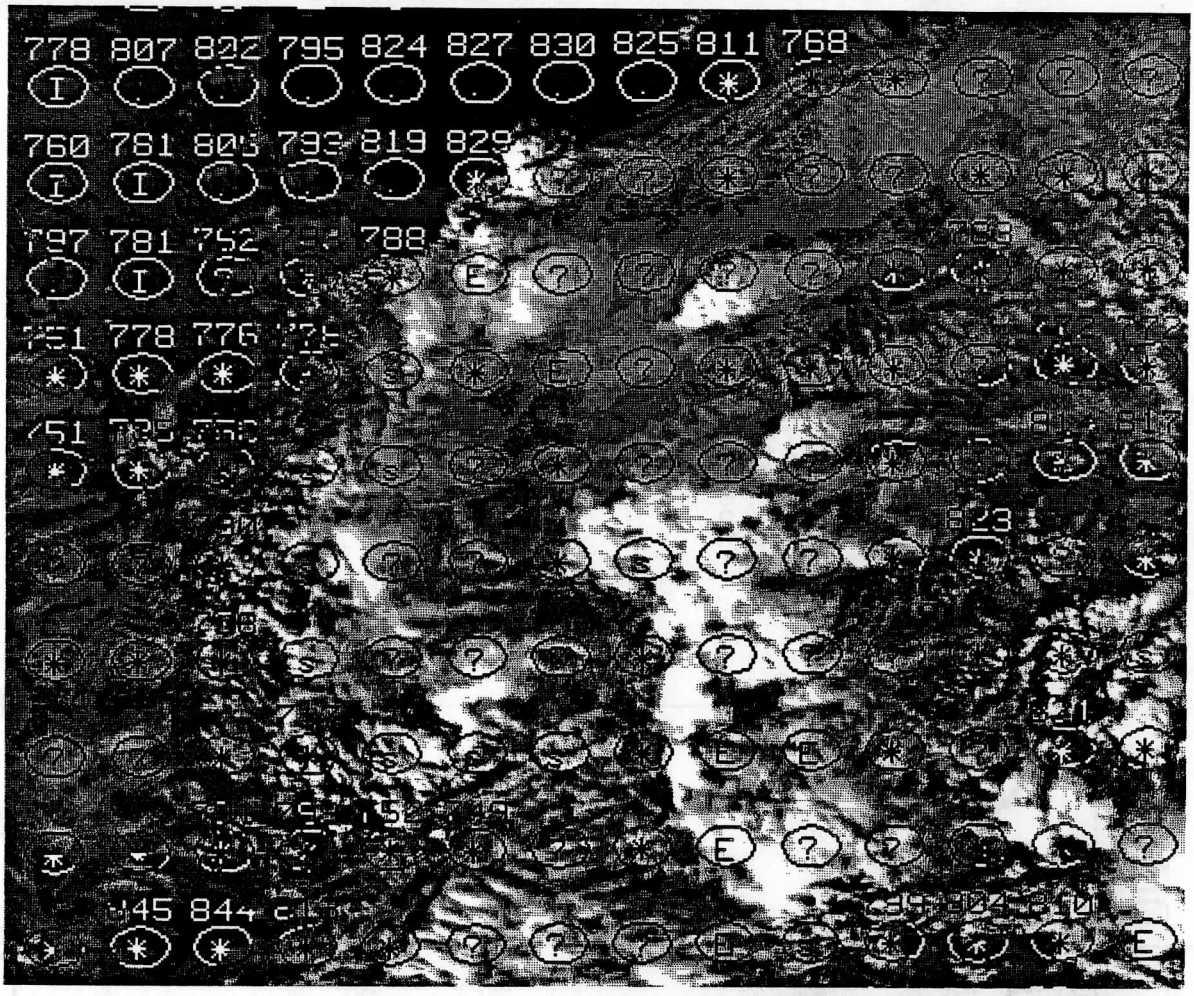

Figure

see tex

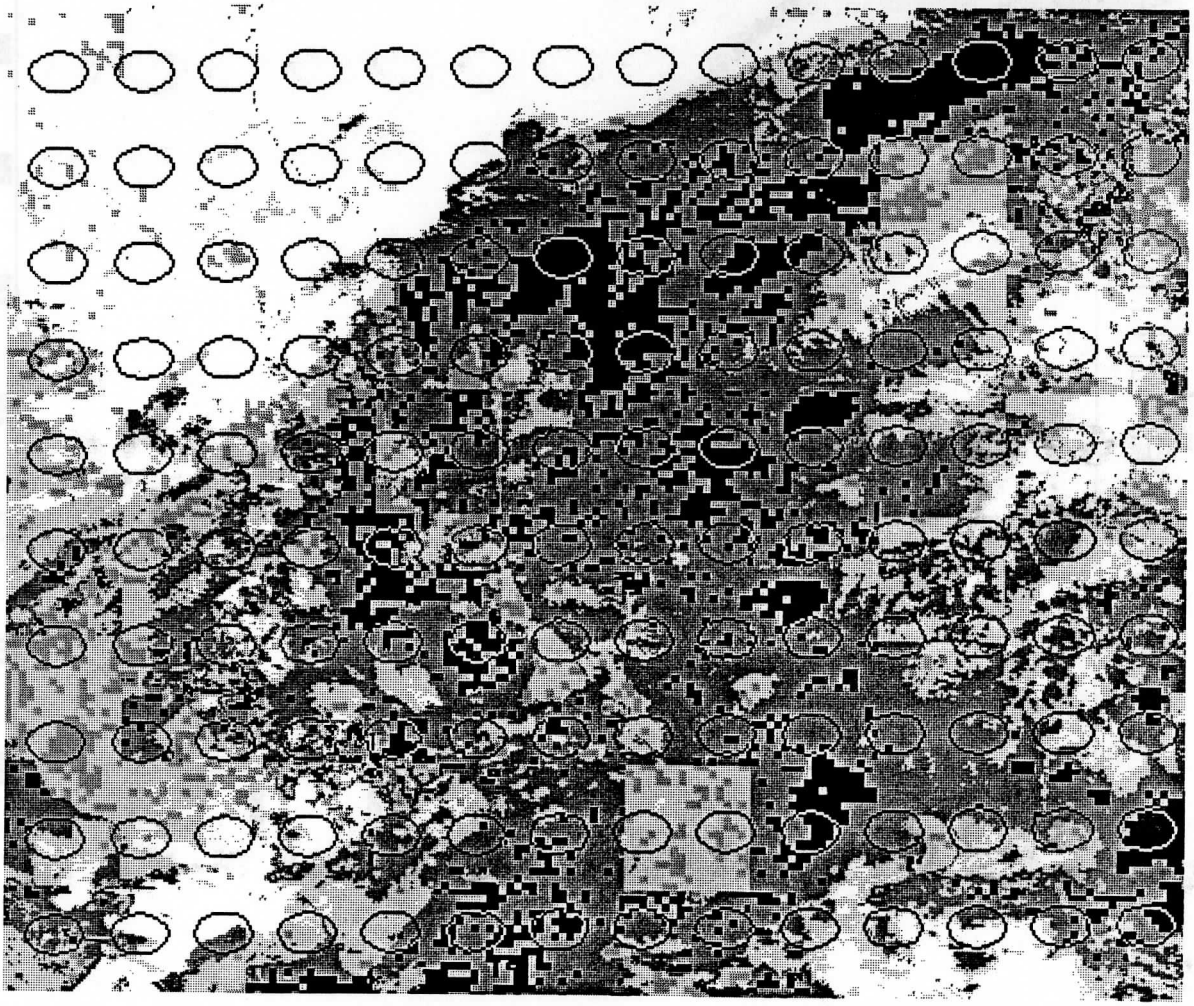

Figure

see tex

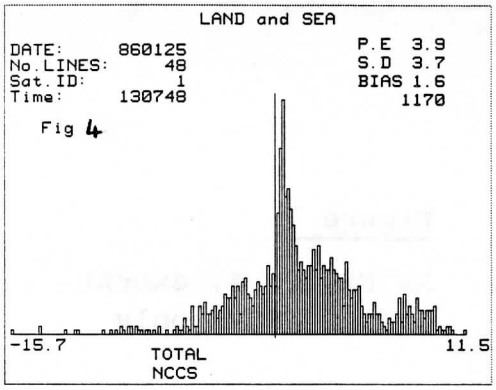

Figure 4

Histogram of AVHRR"8" minus HIRS 8 brightness temperature.
NOAA-9. 25 January 1986. 1307Z.
All FOVs on which AVHRR"8" values available.
See text for further explanation.
Data from NCCS pre-filtering.

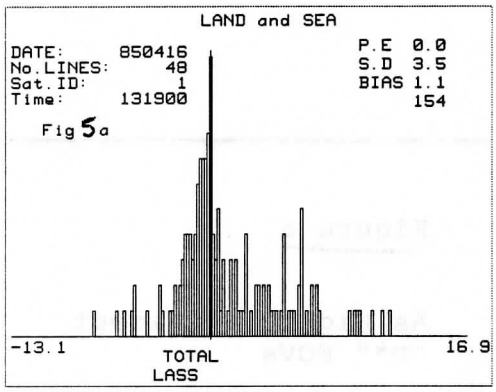

Figure 5a

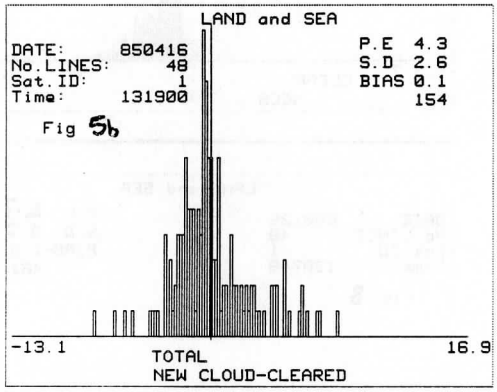

Figure 5b

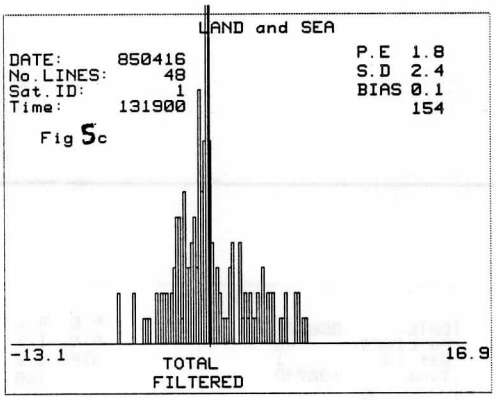

Figure 5c

As Figure 4, except for 16 April 1985 at 1319Z, and for

(a) LASS,
(b) NCCS pre-filtered and
(c) NCCS post-filtered,

all for only those FOVs on which LASS values available.

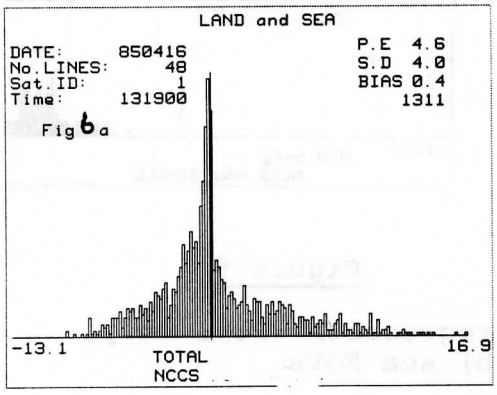

Figure 6a

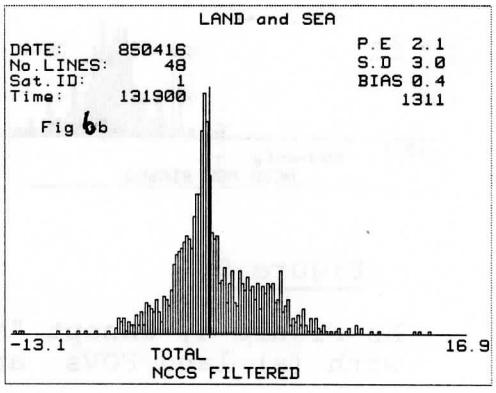

Figure 6b

As Figure 5, except for all FOVs on which NCCS values available with (a) pre-filtered and (b) post-filtered.

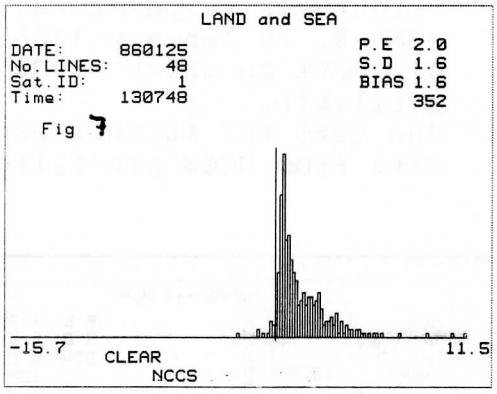

Figure 7

As Figure 4, except "clear" FOVs only

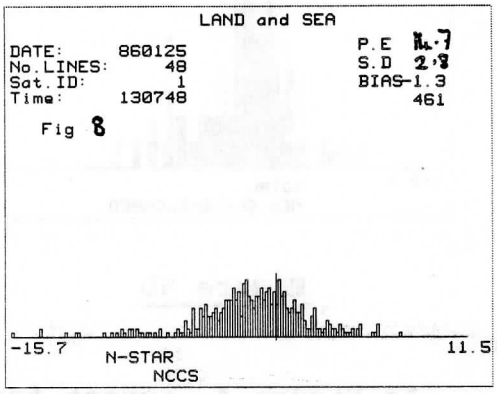

Figure 8

As Figure 4, except "N*" FOVs

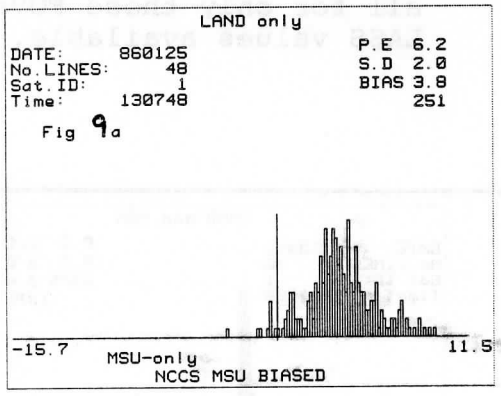

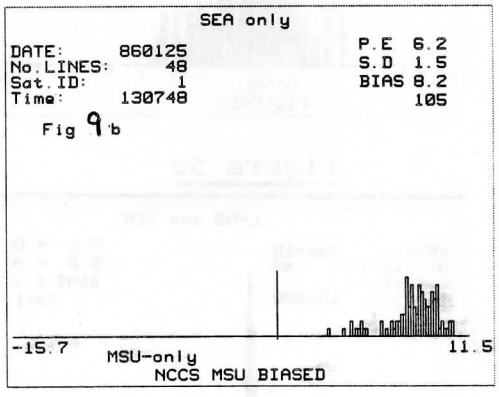

Figure 9a

Figure 9b

As Figure 4, except "MSU regression" FOVs only, with (a) land FOVs and (b) sea FOVs

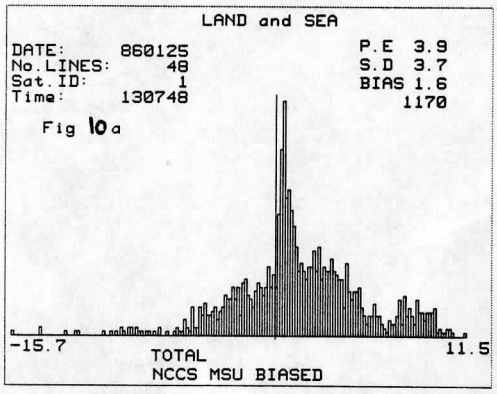

Figure 10a

As Figure 4

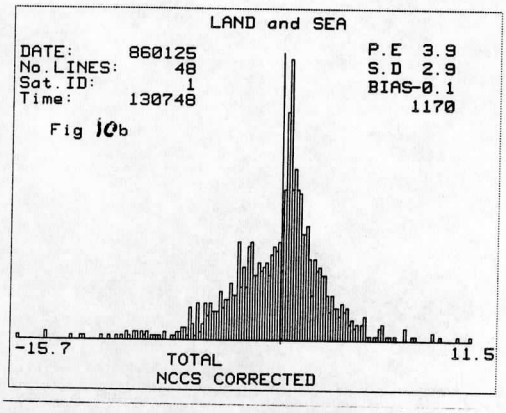

Figure 10b

As figure 4, except after bias correction of "MSU regression" FOVs

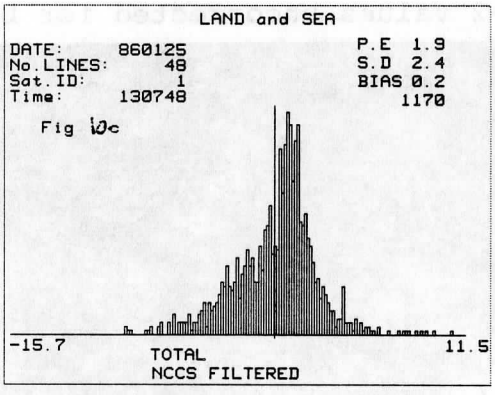

Figure 10c

As figure 4, except post-filtering

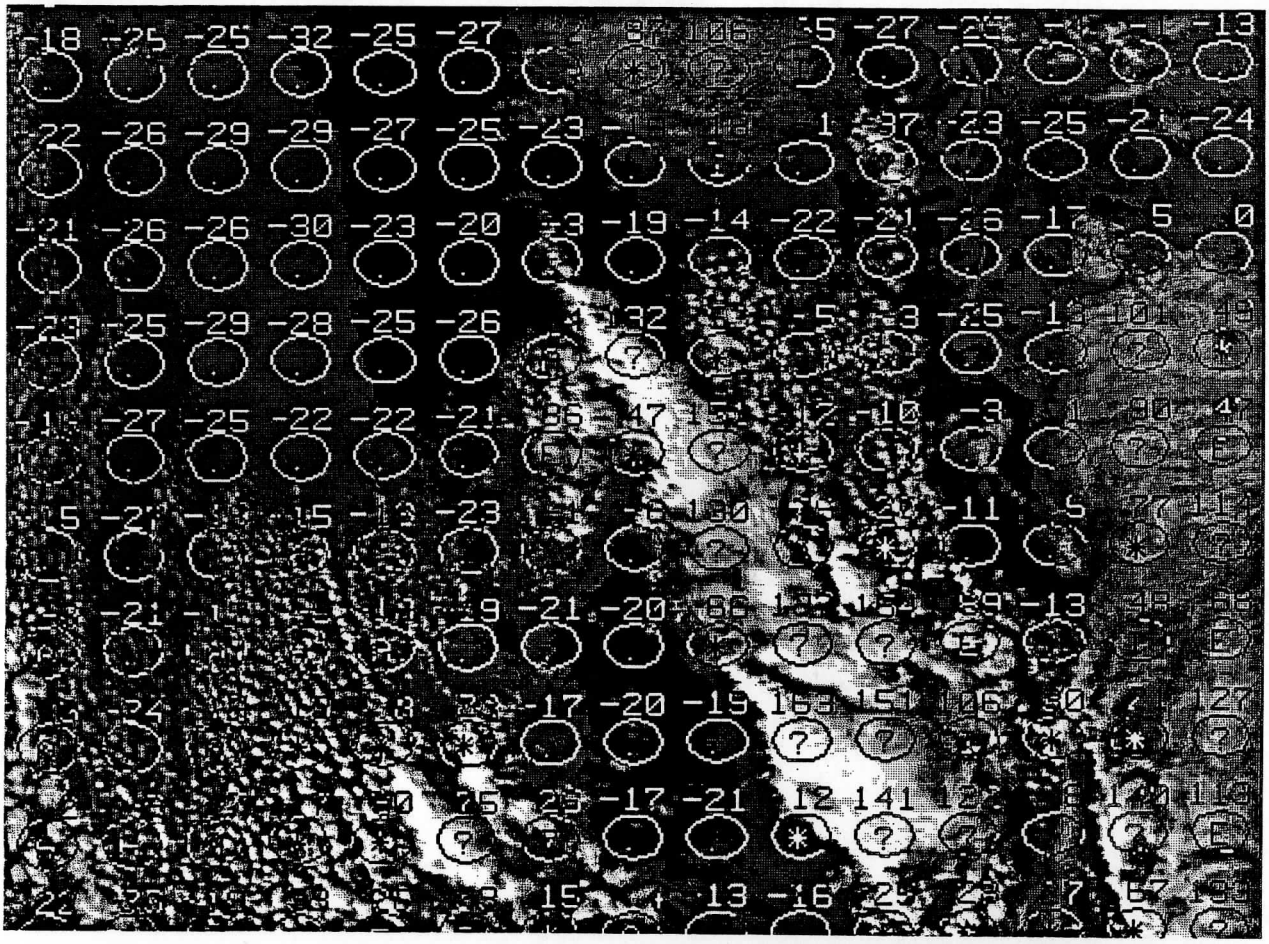

Figure 11a Estimated MSU-2 values uncorrected for bias

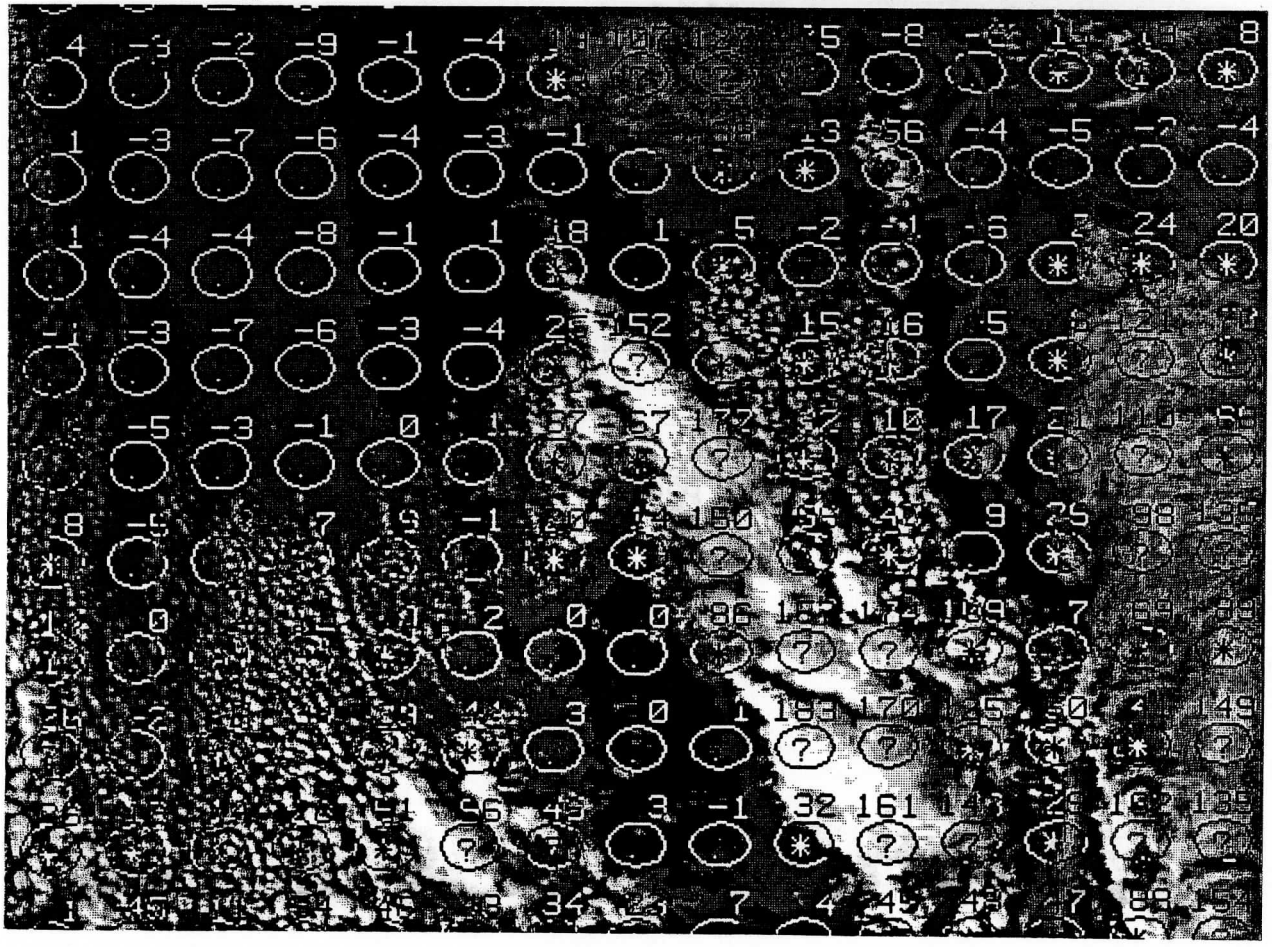

Figure 11b Estimated MSU-2 values corrected for bias

A PRELIMINARY STUDY OF TOVS RETRIEVAL IN TAIWAN, R.O.C.

T-C. Yen, H-J. S. Wang

Meteorological Satellite Groud Station
Central Weather Bureau
Taipei, Taiwan
Republic of China

1. INTRODUCTION

The sounding retrievals from TOVS data of TIROS-N / NOAA series satellites have been studied for many years. Many retrieval methods have been used such as statistical regression, minimum information, iteration, physical. (McMillin et. al., 1973; Smith & Woolf, 1976; Smith et. al., 1979; Smith et. al., 1983.) It had been proved that the sounding retrieval from TOVS data provide useful and valuable meteorological information, especially in data-sparse regions. (Phillips, et. al., 1979).

An HRPT ground station was established at Taiwan, R.O.C., in January 1981. The AVHRR data is used to monitor the typhoon during summer time and the meso-scale convective system during Mei-Yu season in cooperate with the images from Japan's GMS satellite. AVHRR data have also been studied to estimate the sea surface temperature around Taiwan by multi-channel method (Hong et. al., 1985). Due to lack of observation in the West Pacific Ocean, the sounding retrieval from the TOVS data seems to be very helpful for weather analysis of typhoon and meso-scale convective system around Taiwan. TOVS data processing have been studied in the last three years (Yen & Wang, 1986). In the following section some result from TOVS data processing will be presented.

2. TOVS DATA RETRIEVAL

During the past three years, a procedure of preprocess of TOVS data was implemented on PDP-11/70 of the Meteorological Satellite Ground Station of Central Weather Bureau, Republic of China. The procedure include the extraction of TIP data from HRPT data, the extraction of HIRS/2 and MSU data from TIP data, the calibration and navigation of HIRS/2 and MSU data, the preparation of HIRS/2 and MSU data for sounding retrieval, and the brightness temperature image display on the COMTAL Vision One / 20 image processing system. The sounding retrieval by the regression method had also been tried.

In the beginning of this year, we obtained the International TOVS Retrieval Package (ITRP) of VAX version from the Cooperative Institute for Meteorological Satellite Studies. We have made some modification to implement it on our PDP-11/70. This package uses a physical retrieval algorithm to produce temperature and moisture profile from a 3 x 3 array of HIRS

radiances and spatially interpolated MSU observations. The algorithm solves the true profile from an initial guess profile. We use only the latitude and time interpolated profile from ten standard atmosphere as the initial guess profile. The surface data we use are estimated from the initial guess profile and topography. The transmittance is calculated according to the method of Weinreb et. al. (1981).

3. RESULT AND DISCUSSION

After the package being implemented, we selected the data of NOAA-9 in 19Z JUNE 4, 1986 and 18Z JUNE 5, 1986 as an experiment. During that period there were several meso-scale convective system occured in south China and Taiwan area. Intensive observations from several radiosonde stations had been made those could provide data for concurrent profile comparison.

Figure 1 shows the root mean square difference between the TOVS retrieval temperature profile and radiosoned observational temperature profile within 1.5 degree latitude. The result is quite good at 300mb but with somewhat larger difference near surface and 150mb.

Figure 2 shows the thickness of 1000-500mb of the radiosonde observation from 12Z JUNE 4, 1986 to 00Z JUNE 6, 1986. Figure 3 shows the TOVS retrieval thickness of 1000-500mb at 19Z JUNE 4, 1986 and 18Z JUNE 5, 1986. It is quite well in the East China Sea, but bad in the west of the path and Japan. The cold core in Korea is consistent. The warm ridge is a little stronger in TOVS retrieval. Warm core in the southern China where the meso-scale convective system can also be seen in the TOVS retrieval but more complicate.

4. CONCLUSION

It can be seen from the result that the spatial resolution of TOVS retrieval is better than the conventional data. Although the accuracy of retrieval sounding is not good enough, it could still provide some detail information in the ocean area. There are still many things we can do to improve the retrieval, such as the refinement of initial guess profile, addition of the surface observational data, improvement of the retrieval technique. The improvement in TOVS retrieval will make it possible to have better analysis for meso-scale convective system and typhoon.

ACKNOWLEDGE:

We thank the Cooperative Institute for Meteorological Satellite Studies for generously providing us the International TOVS Retrieval Package.

REFERECE:

Hong, L-C., T-C. Yen, E-W. Chiou, and S-J. Chen, 1985: The Study of Relations between Mullet Catch and Sea Surface Temperature Using MSS and Meteorological Satellite Data. Remote Sensing, No. 5, p. 27-47. (in Chinese)

Lauritson, L., G. J. Nelson, and F. W. Porto, 1979: Data extraction and calibration of TIROS-N/NOAA radiometers. U.S. Department of Commerce, National Oceanic and Atmospheric Administration, National Earth Satellite Service, Washington, D.C., NOAA Technical Memorandum NESS 107, 73 pp.

McMillin, L. M., D. Q. Wark, J. A. Siomkajlo, P. G. Abel, A. Werbowetzki, L. A. Lauritson, J. A. Pritchard, D. S. Crosby, H. M. Woolf, R. C. Luebbe, M. P. Weinreb, H. E. Fleming, F. E. Bittner, and C. M. Hayden, 1973: Satellite infrared soundings from NOAA Spacecraft. U.S. Department of Commerce, National Oceanic and Atmospheric Administration, National Environmental Satellite Service, Washington, D.C., NOAA Technical Report NESS 65, 112 pp.

Phillips, N. A., L. M. McMillin, D. Wark, and A. Gruber, 1979: An evaluation of early operational temperature soundings from TIROS-N. Bulletin of the American Meteorological Society, 60, p. 1188-1197.

Smith, W.L., and H.M. Woolf, 1976: The use of eigenvectors of statistical covariance matrices for interpreting satellite sounding radiometer observations. Journal of Atmospheric Science, 35(7), p. 1127-1140.

Smith, W.L., H.M. Woolf, C.M. Hayden, D.Q. Wark, and L.M. McMillin, 1979: The TIROS-N operational vertical sounder. Bulletin of the American Meteorological Society, 60, p. 1177-1187.

Smith, W.L., H.M. Woolf, C.M. Hayden, A.J. Schreiner, and J.F. LeMarshall, 1983: The Physical Retrieval TOVS Export Package. The Technical proceeding of First International TOVS Study Conference, p. 227-256

Smith, W.L., H.M. Woolf, C.M. Hayden and A.J. Schreiner, 1985: The Simultaneous Retrieval Export Package. The Technical Proceeding of Second International TOVS Study Conference. p. 224-253

Weinreb, M.P., H.E. Fleming, L.M. McMillin and A.C. Neuendorffer, 1981: Transmittances for the TIROS Operational Vertical Sounder. NOAA Technical Report NESS 85, 60 pp.

Werbowetzki, A., 1981: Atmospheric Sounding User's Guide. NOAA Technical Report NESS 83, 82 pp.

Yen, T-C. and H-J. S. Wang, 1986: Study of TOVS Data Calibration and Navigation. Central Weather Bureau Research Report No. 135. 21 pp.(in Chinese)

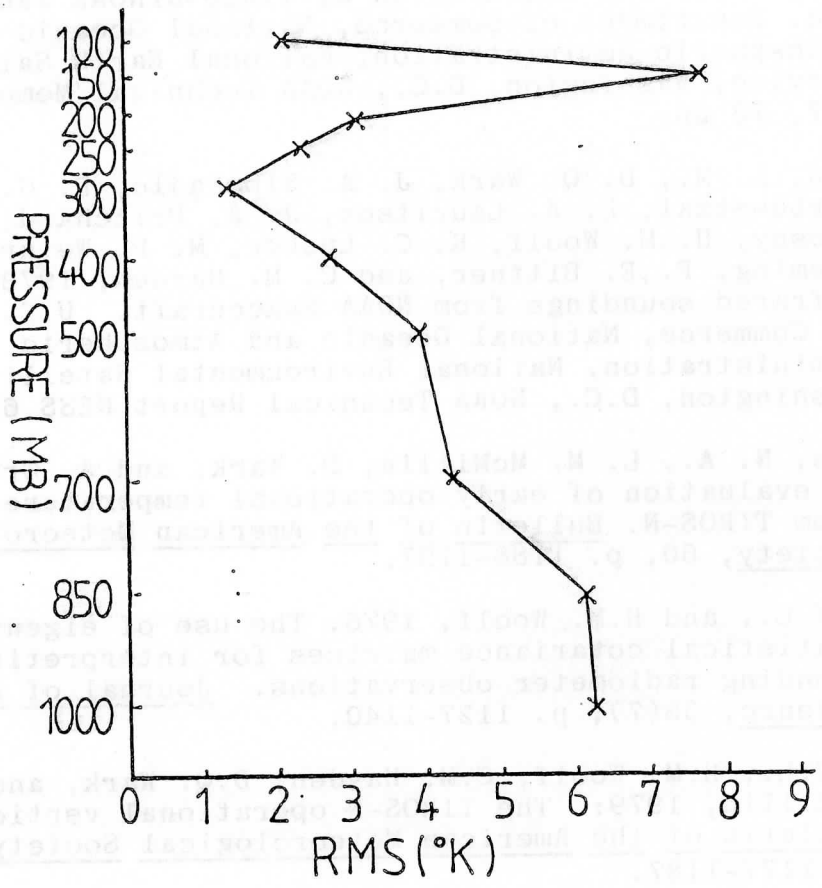

Fig 1. The root mean square difference of TOVS temperature profile and radiosonde temperature profile

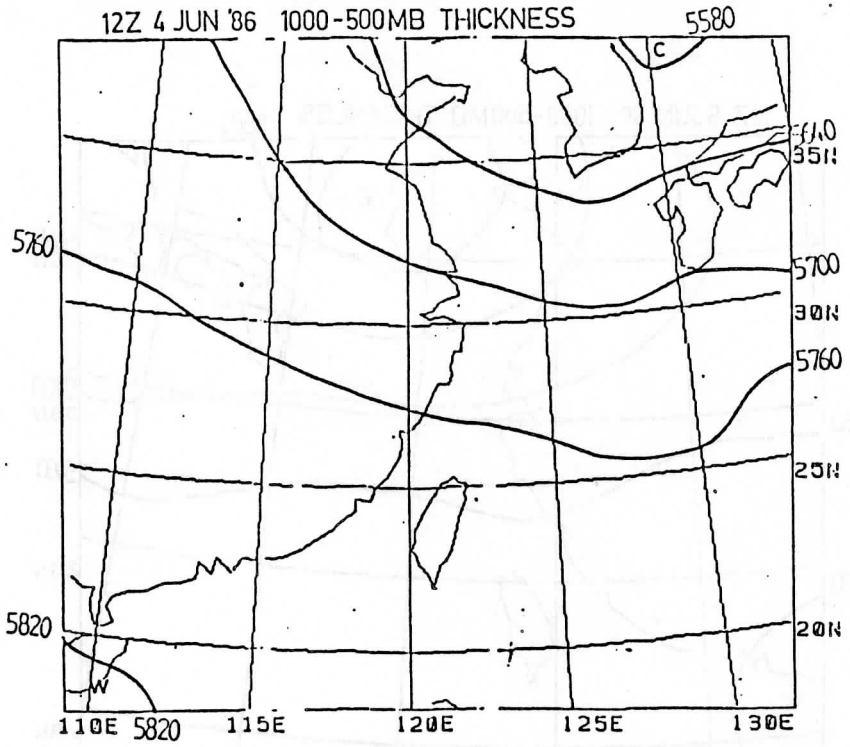

Fig 2 (a). Analysis of 1000-500mb geopotential thickness from radiosonde 12Z JUNE 4, 1986

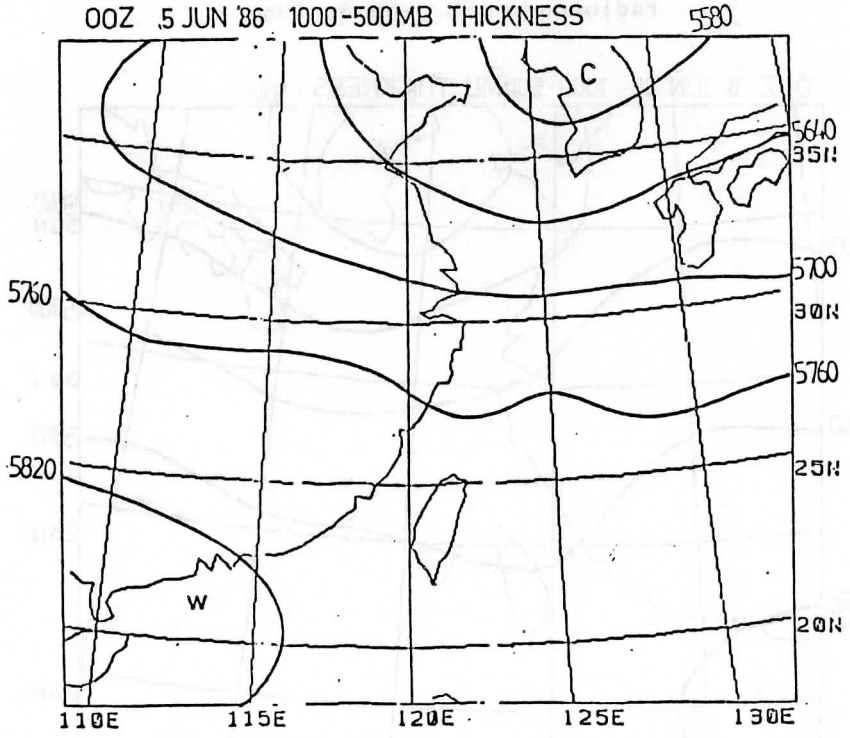

Fig 2 (b). Analysis of 1000-500mb geopotential thickness from radiosonde 00Z JUNE 5, 1986

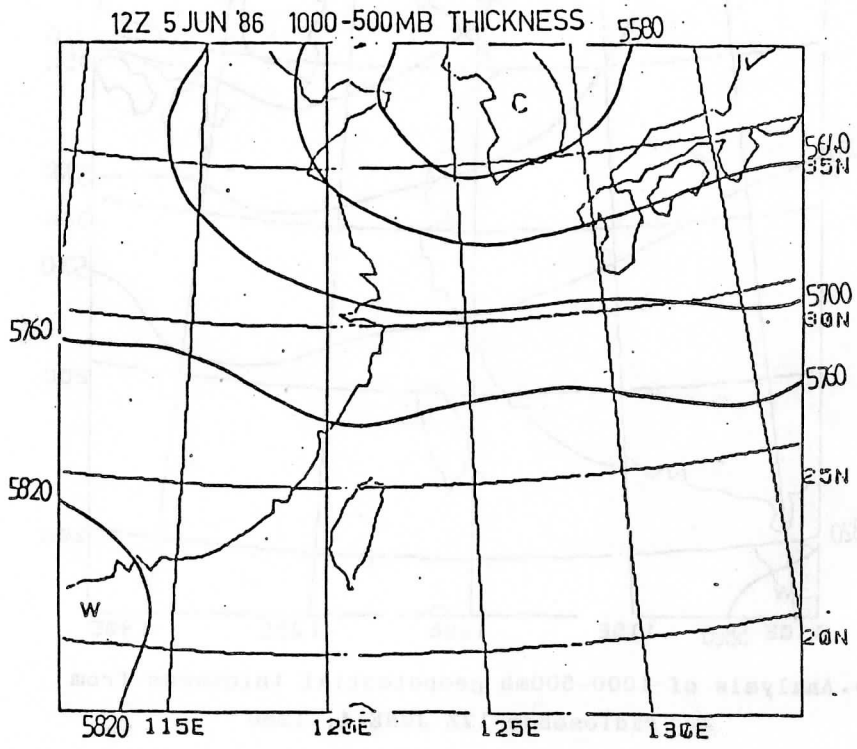

Fig 2 (c). Analysis of 1000-500mb geopotential thickness from radiosonde 12Z JUNE 5, 1986

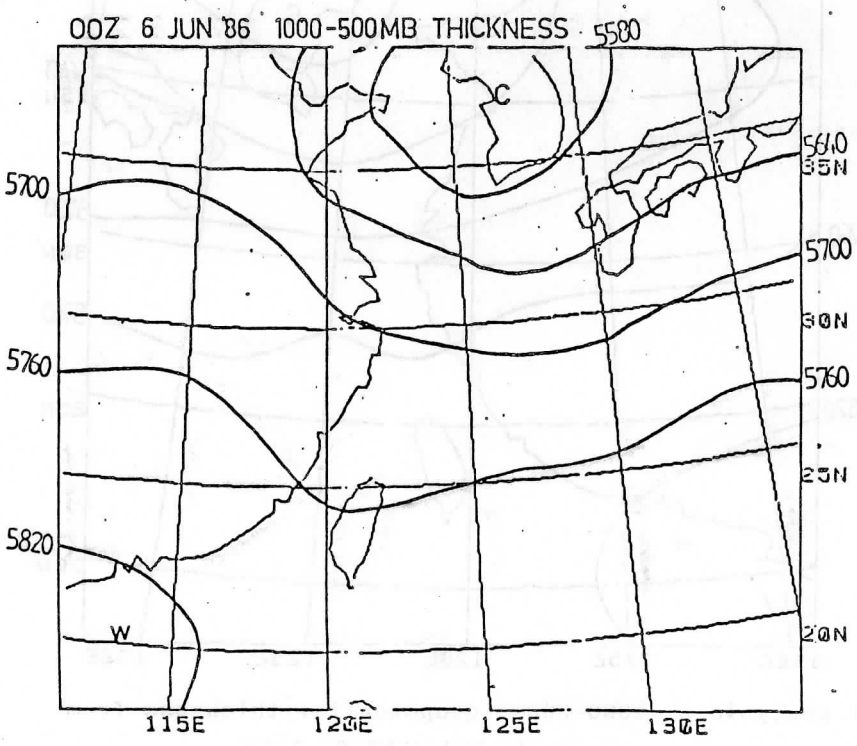

Fig 2 (d). Analysis of 1000-500mb geopotential thickness from radiosonde 00Z JUNE 6, 1986

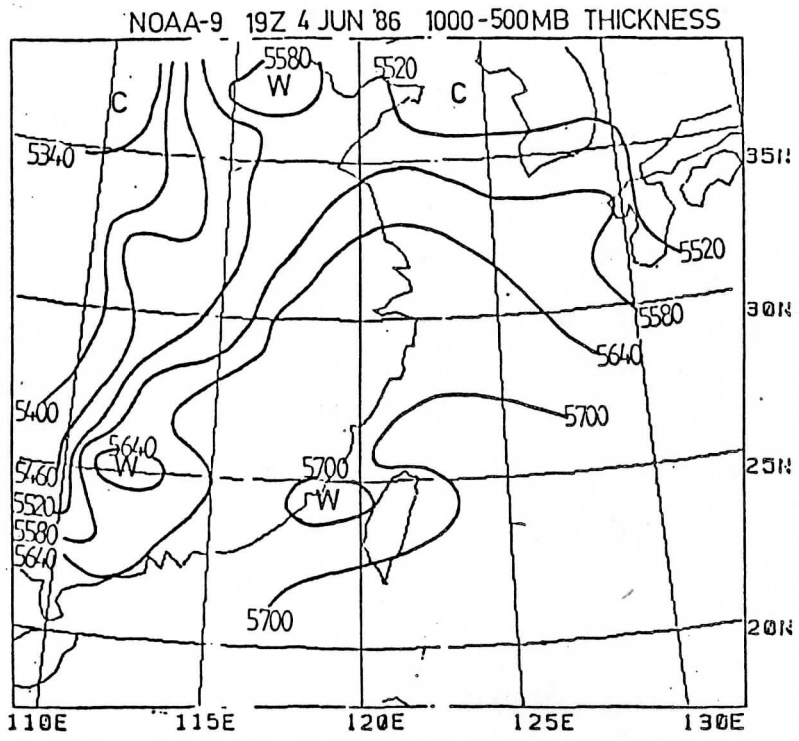

Fig 3 (a). Analysis of 1000-500mb geopotential thickness from TOVS retrieval 19Z JUNE 4, 1986

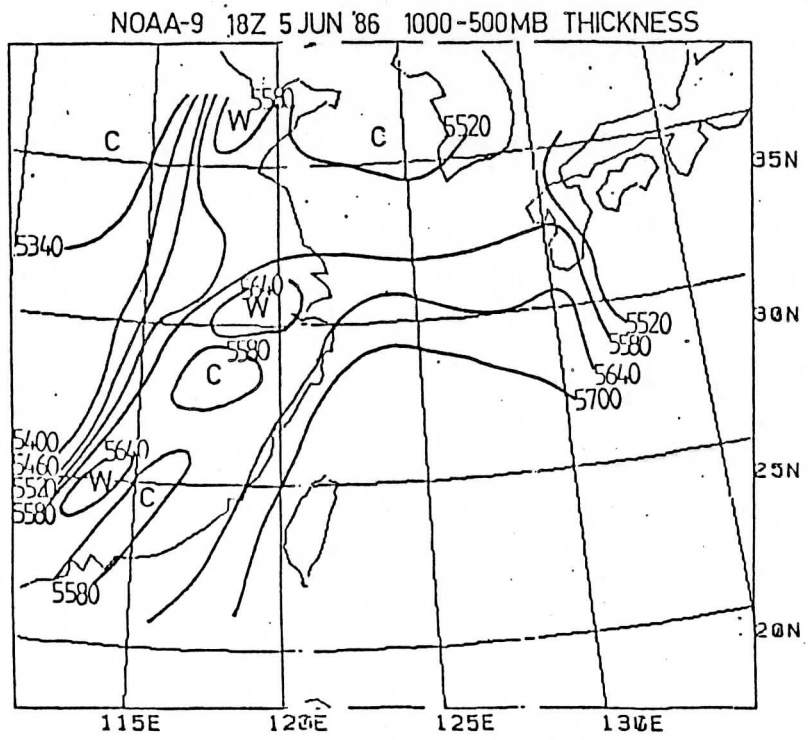

Fig 3 (b). Analysis of 1000-500mb geopotential thickness from TOVS retrieval 18Z JUNE 5, 1986

PROGRESS ON THE BASELINE UPPER AIR NETWORK

Frederick Zbar
NOAA/National Weather Service
Silver Spring, Maryland

1. BACKGROUND

The concept for an upper air baseline network arose at the first meeting of the International TOVS Study Conference at Igls, Austria during September 1983. The concept centers on improving satellite calibrations from ground based observations. The WMO Commission for Basic Systems (CBS) decided, at the Extraordinary Session at Hamburg, FRG during October 1985, that a feasibility study should be undertaken.

The goal of this study is to determine whether satellite soundings can be improved measurably by a BUAN, and to determine the optimum characteristics of the network. In a preliminary study (prepared by J. Le Marshall (Australia) on secondment to the WMO Secretariat in August 1985), it was noted that there are two principal reasons for establishing a BUAN: (1) to provide high quality, intercalibrated, and at times contemporaneous, set of radiosonde and rawinsonde sounding data for verifying and optimizing the quality and utility of satellite temperature and moisture vertical sounding data, and (2) to provide a standard which would be the basis for obtaining uniformly high quality data throughout the global upper-air sounding programme.

2. FEASIBILITY STUDY

The United States agreed to formulate a plan, carry out studies for a six month period, and report to the WMO. The NWS and NESDIS have formed a committee of experts who have been tasked with (1) identifying the organizational components, (2) developing a feasibility study plan, (3) operating the baseline network, and (4) evaluating its usefulness. The study plan has been drafted and is being reviewed prior to requesting the WMO to enlist the support of international members. The plan envisions a six month evaluation which would be conducted during 1987.

The first draft of the study plan identifies a set of candidate stations to participate in the BUAN program. These are shown in Figures 1 and 2. The plan further delineates the operational requirements of the baseline stations and describes the NESDIS/NMC network evaluations. A tentative milestone schedule is also set forth (Figures 3 and 4).

BASELINE NETWORK UPPER AIR PROGRAM
CANDIDATE STATIONS

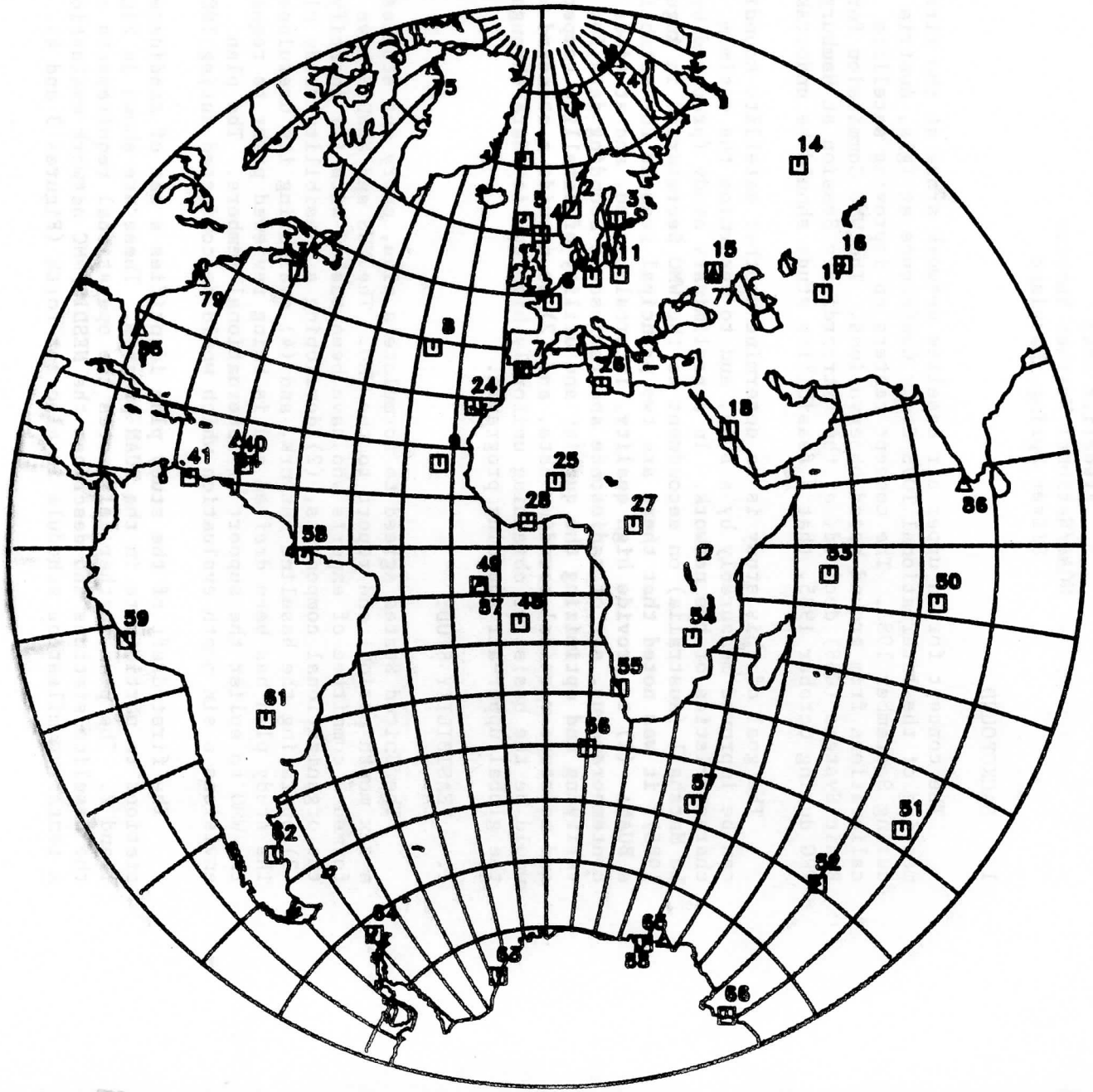

BASELINE NETWORK UPPER AIR PROGRAM
CANDIDATE STATIONS

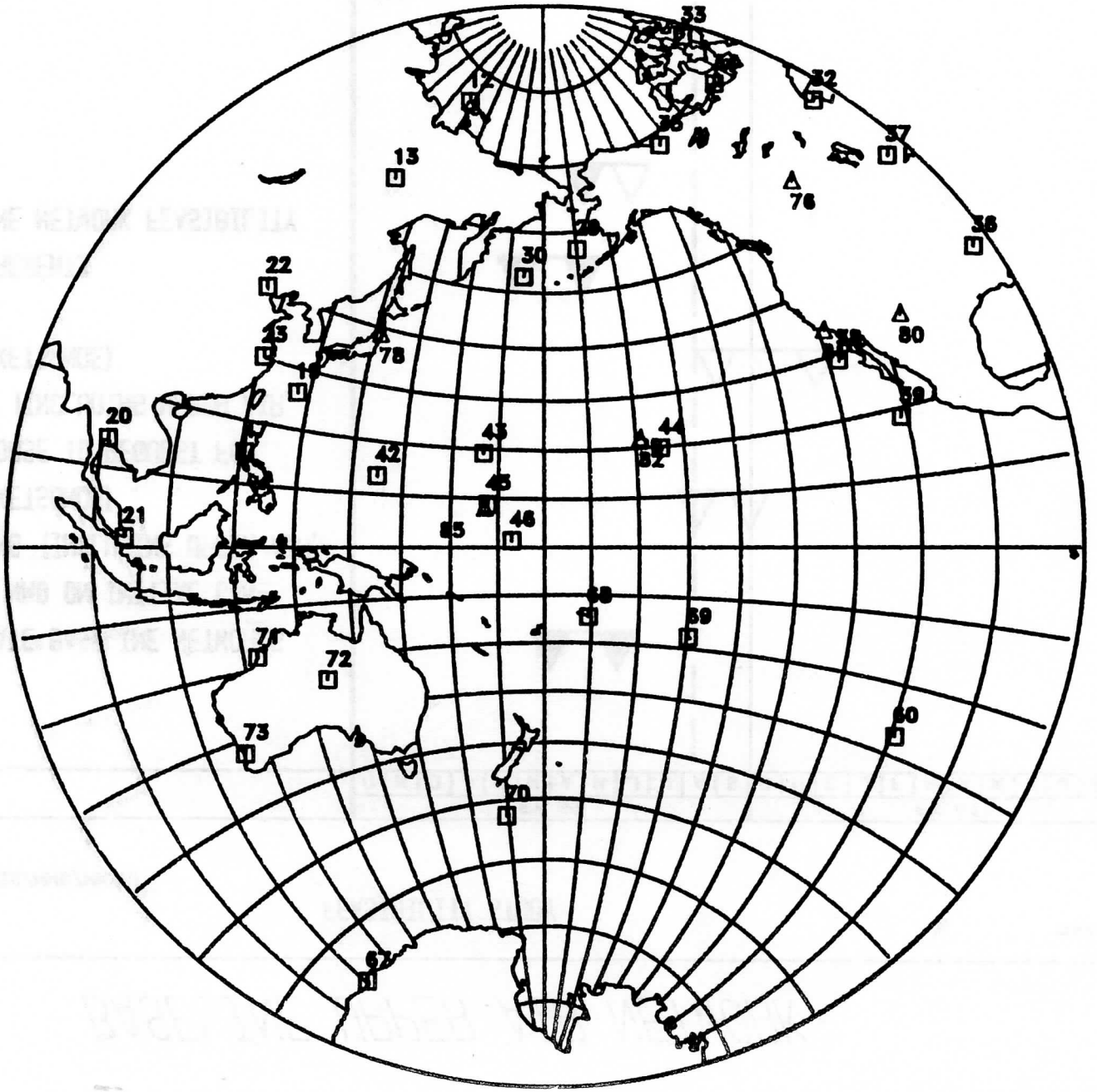

BASELINE UPPER AIR NETWORK

8-11-86

FEASIBILITY STUDY

REQUIREMENTS (NESDIS/NMC/NWSH)

MILESTONES MAJOR ACTION
NETWORK DESIGN:
IDENTIFY CANDIDATE BASELINE NETWORKS
COORDINATE WITH WMO ON INITIAL CANDIDATE STATIONS (INCLUDING UPPER AIR, ASAP, AND ROCKETSONDE)
WMO MEMBER RESPONSE TO REQUEST FOR PARTICIPATION (INCLUDING UPPER AIR, ASAP, AND ROCKETSONDE)
BASELINE PLAN:
IDENTIFY REQUIREMENTS
DEVELOP BASELINE NETWORK FEASIBILITY STUDY PLAN

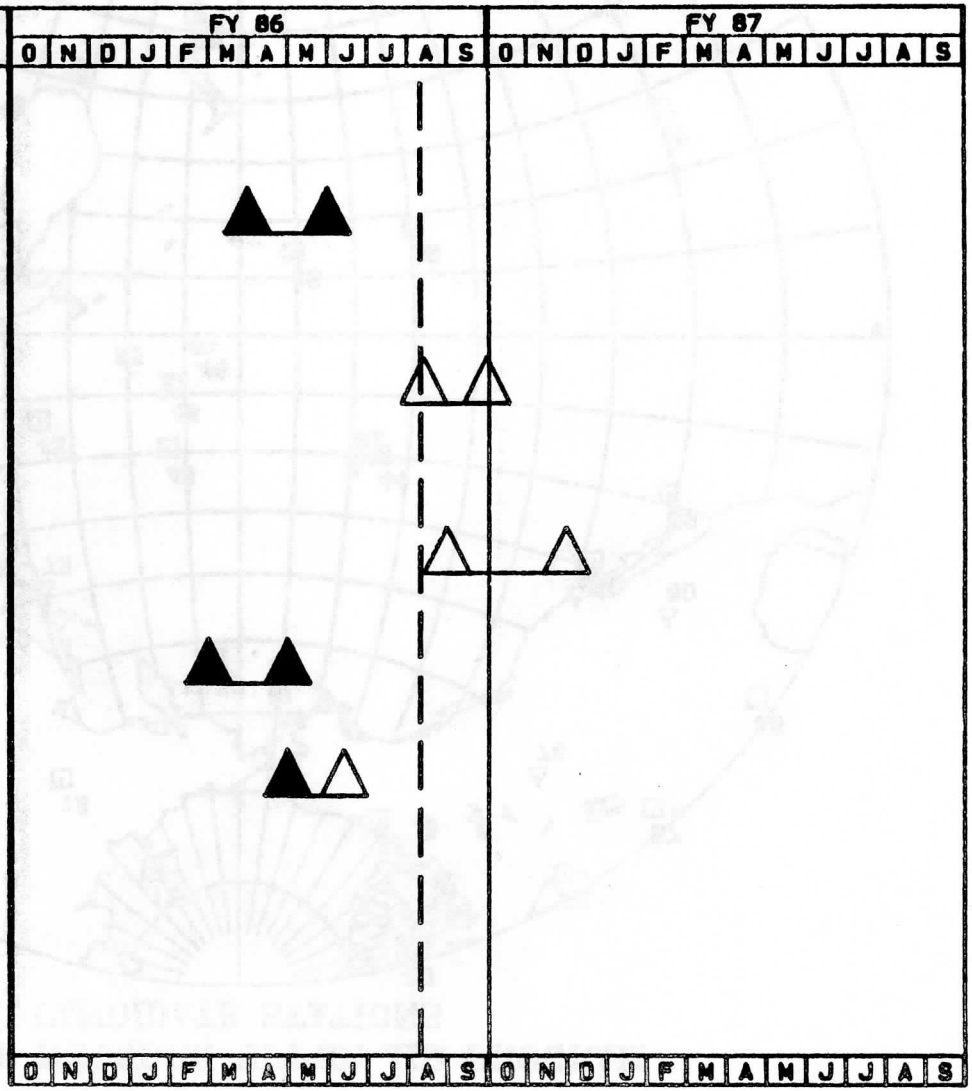

BASELINE UPPER AIR NETWORK

8-11-86

FEASIBILITY STUDY

EVALUATIONS AND REPORTS (NESDIS/NMC)

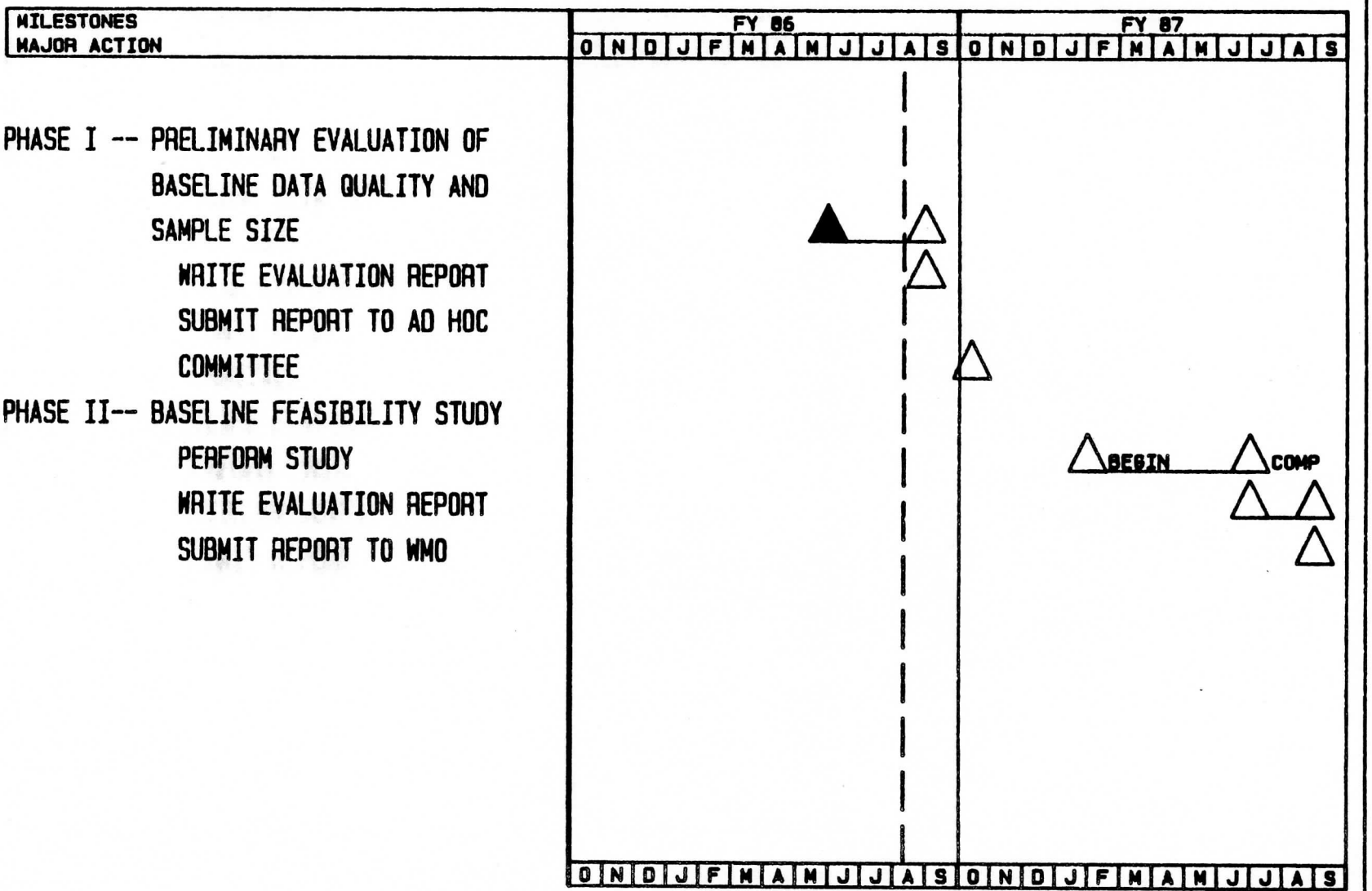

IBM PC PACKAGE FOR TOVS PROCESSING AND DISPLAY

Fengxian Zhou and Yanni Qu
System Development Laboratory
Institute of Atmospheric Physics, Academia Sinica
Beijing, People's Republic of China

ABSTRACT

An IBM PC package for TOVS data ingestion, preprocessing retrieval and display is available now. This package is based on previous work done by CIMSS and SSEC scientists. Our major effort was concentrated on TIP data ingestion and retrieval display software.

1. INTRODUCTION

As noted in the Report on ITSC-II in Igls, Austria in 1985, there is a need of low cost workstation to process the direct readout TOVS data. The IBM PC computer is well suited to do this job. Programs and subroutines of the ITPP have been down-loaded from the SSEC IBM 4381 to an IBM PC/XT and TOVS retrievals have been made on it. The simultaneous physical retrieval algorithm was sped up on the IBM PC/AT and several display programs were developed.

2. SOFTWARE AND HARDWARE DEVELOPMENT

The low cost workstation is of interest to many international communities. For example, China needs satellite soundings for input into mesoscale numerical models for very short range forecasting. An effort was started March 1986 at the System Development Laboratory, Institute of Atmospheric Physics (IAP), Chinese Academy of Sciences, Beijing, China, to build hardware for direct TIP data ingestion between the satellite receiving system and IBM PC/AT. In the meantime, PC TOVS software from the ITPP including main programs and subroutines were modified to fit the PC environment. The major changes were made on the ingestion program "PRETIP' and related subroutines such as "GETMNF', 'UMMFC', 'SCTIM', and 'HISCNT'. The most important modification substitute 'MVBYT2' for 'MVBYTE' in the PC system, because INTEGER*2 is used quite often in the PC programs. Some corrections were made on 'TOVDRI' to eliminate an error in subroutine 'INGHIR'. From 'PRELOC' down to 'TOVRT2' there were no changes. Figure 1 is the flow chart of TOVS data processing. It takes about 40 minutes to finish ingestion and preprocessing of one orbit and each retrieval requires about 50 seconds.

3. A SAMPLE CASE

Due to the high bit rate, errors still occur in the direct raw TIP data received from the IAP HRPT station. The case presented here is transferred from the data recorded by HP1000 computer's tape driver located at Satellite Meteorological Center in Beijing. It is a NOAA-9 orbit over the area covering northeastern China and Korea on 5 July 1986 from 18:25 GMT to 18:33 GMT. The raw TIP data was loaded on to the IBM 4331 and then transferred to the IBM PC/AT through the emulator at

IAP. For unknown reasons, there are no MSU data on the tape, so all steps regarding MSU data processing are skipped.

After preprocessing, the menu program 'TOVSDEMO' can be followed to calculate the retrievals and to display the results as Fig. 2.

Figures 3 and 4 are examples of the satellite soundings. For comparison, the radiosonde data over same area are also presented in Figures 5 and 6. The time difference between the two data sets is about 18 hours. It should be mentioned here that the TOVS retrievals have not been edited and the radiosonde data are not complete (no data is shown over the USSR and Korea). So it is hard to judge how good the retrievals are. The purpose of our work is to contribute to a workable TOVS PC software package, that can be improved and optimized by international colleagues later.

The program to display TOVS imagery works as follows: 'LCTOVS' creates the 'TOVSMAP.BIN' file from the 'TOVSND.BIN' file, and then 'LLTOVS' displays six TOVS images.

4. CONCLUSION

The low cost workstation is important and valuable for several reasons. First, the hardware equipment (IBM PC/XT or PC/AT) is affordable for most countries and can be integrated with a HRPT or DBS station. Second, the software is easy to learn and operate. Third, thru the PC more meteorologists will be able to use quantative satellite data and gain experience in applications. The remaining problem to be solved is how to speed up the retrievals without sacrificing accuracy for the real-time users.

Hardware and software development for polar-orbiting satellite data processing and dislay will be continued in China, because there are more than 20 weather stations equipped with an HRPT receiving system and satellite soundings would be valuable over Tibet plateau and southeast China Sea.

The TOVS IBM PC package presented here is based on software developments at the Cooperative Institute of Meteorological Satellite Studies, University of Wisconsin-Madison. We very much appreciate the contributions from H. Woolf, R. Dedecker and H. B. Howell.

02/TOVS3/22

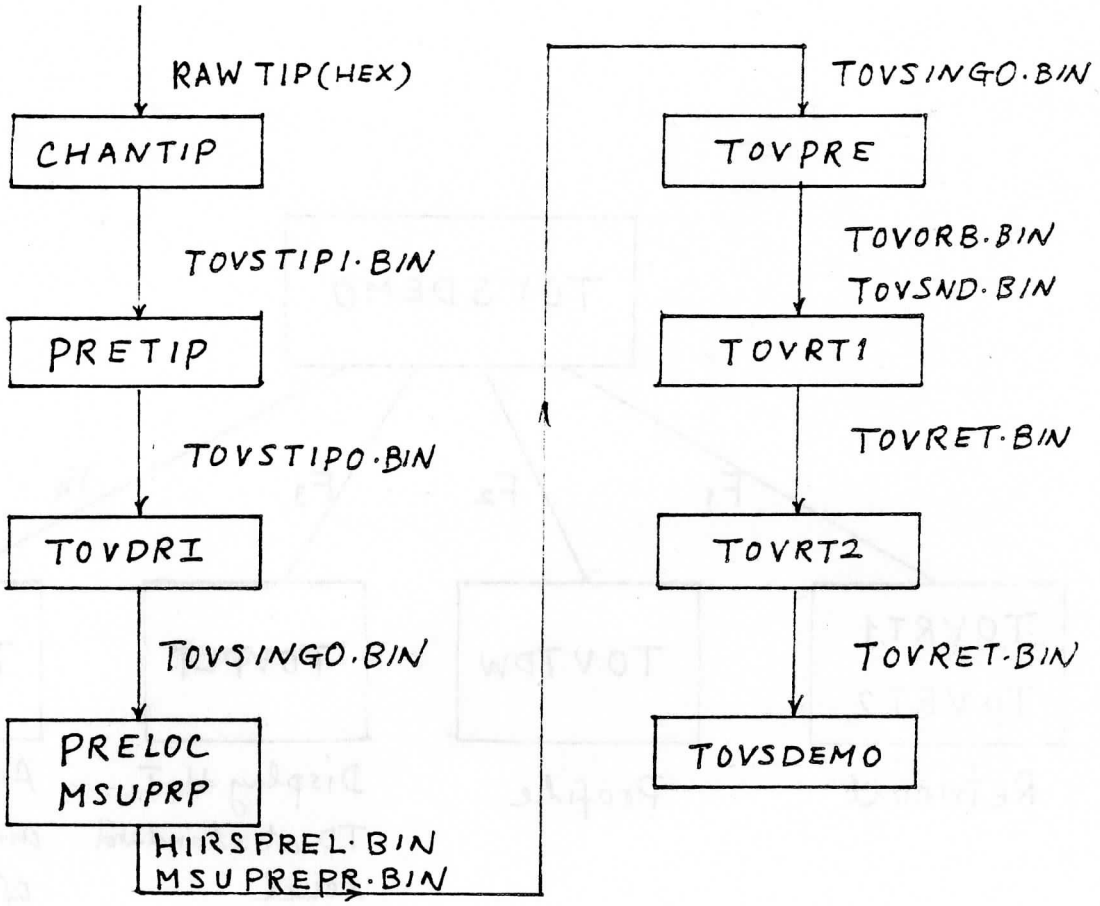

Fig. 1: Procedures of TOVS data processing.

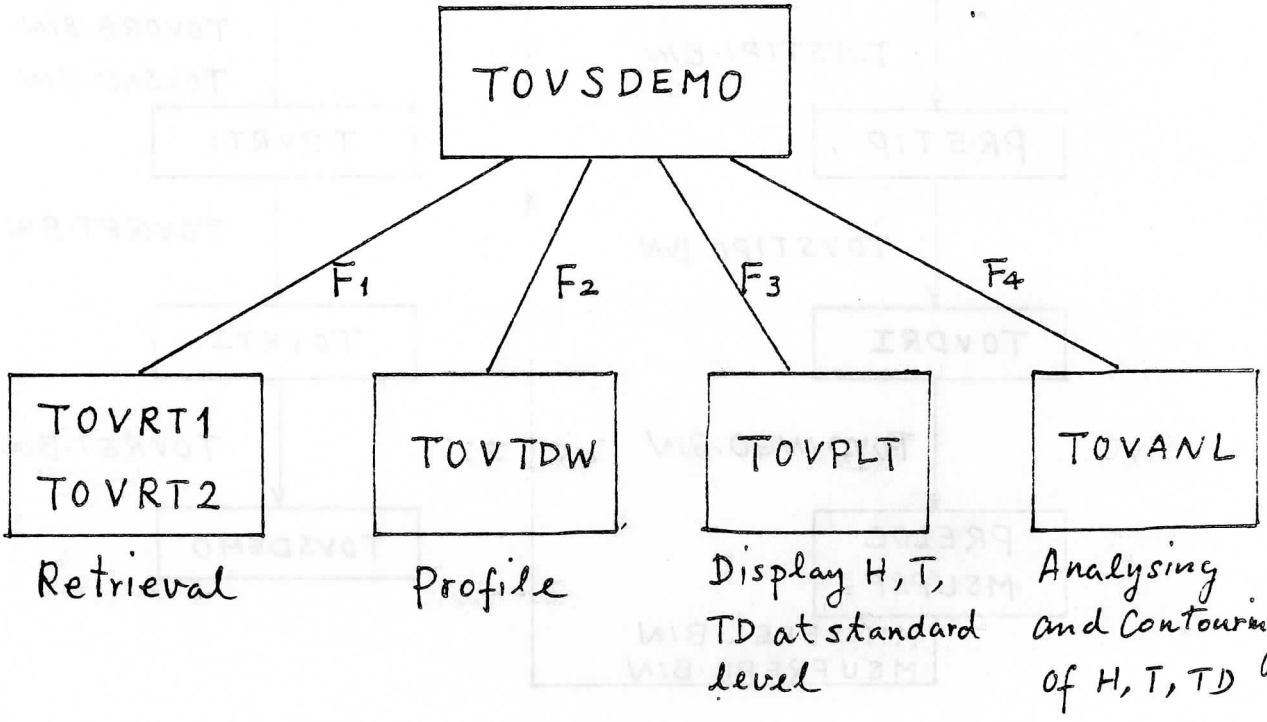

Fig. 2: Display package.

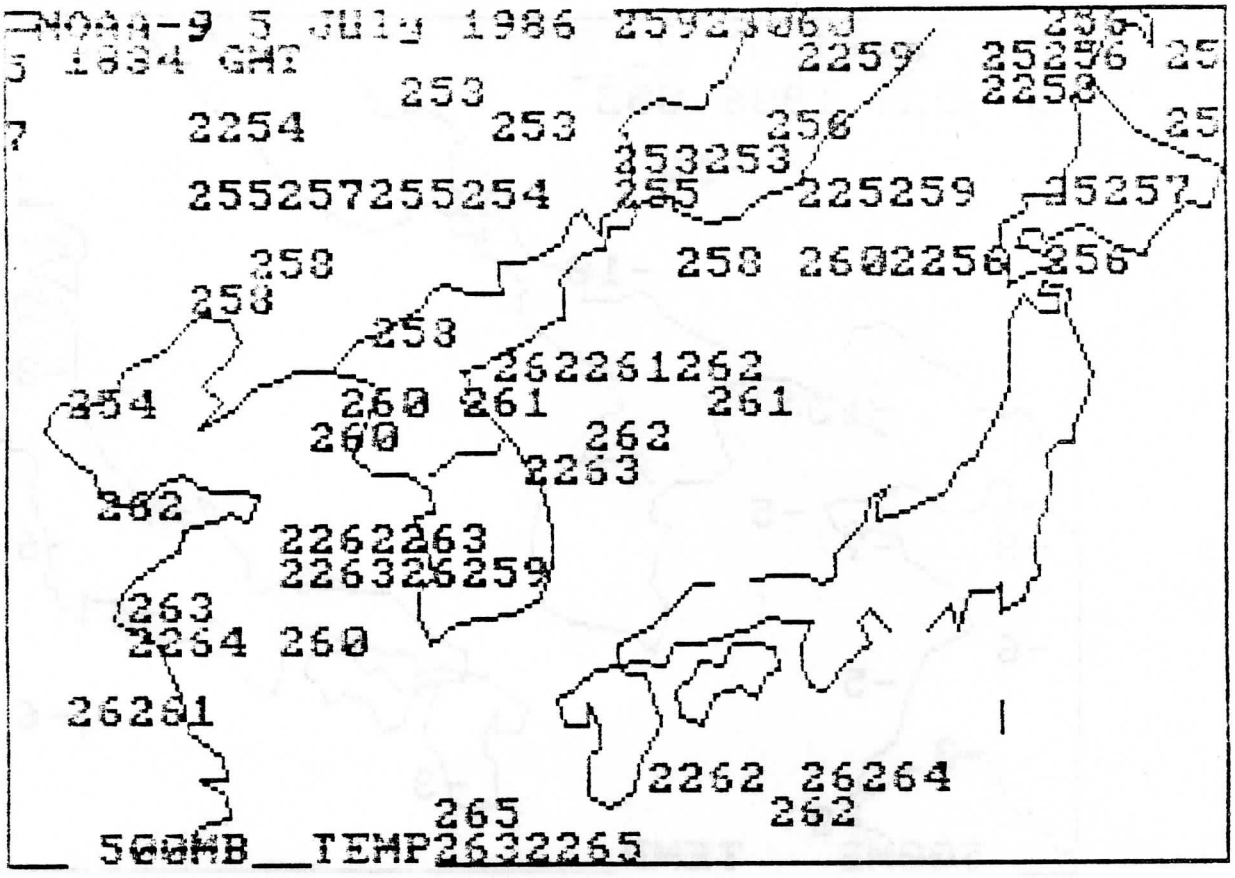

Figure 3

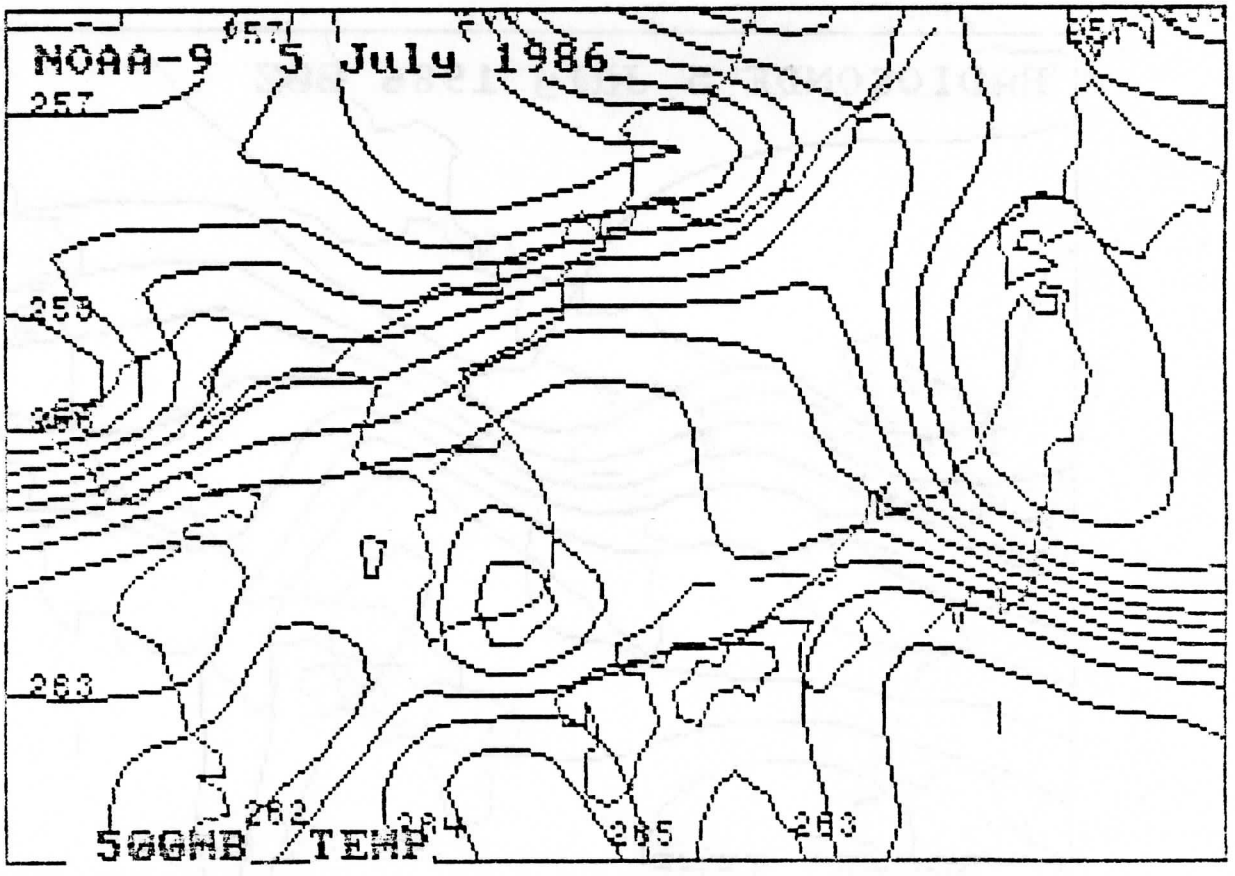

Figure 4

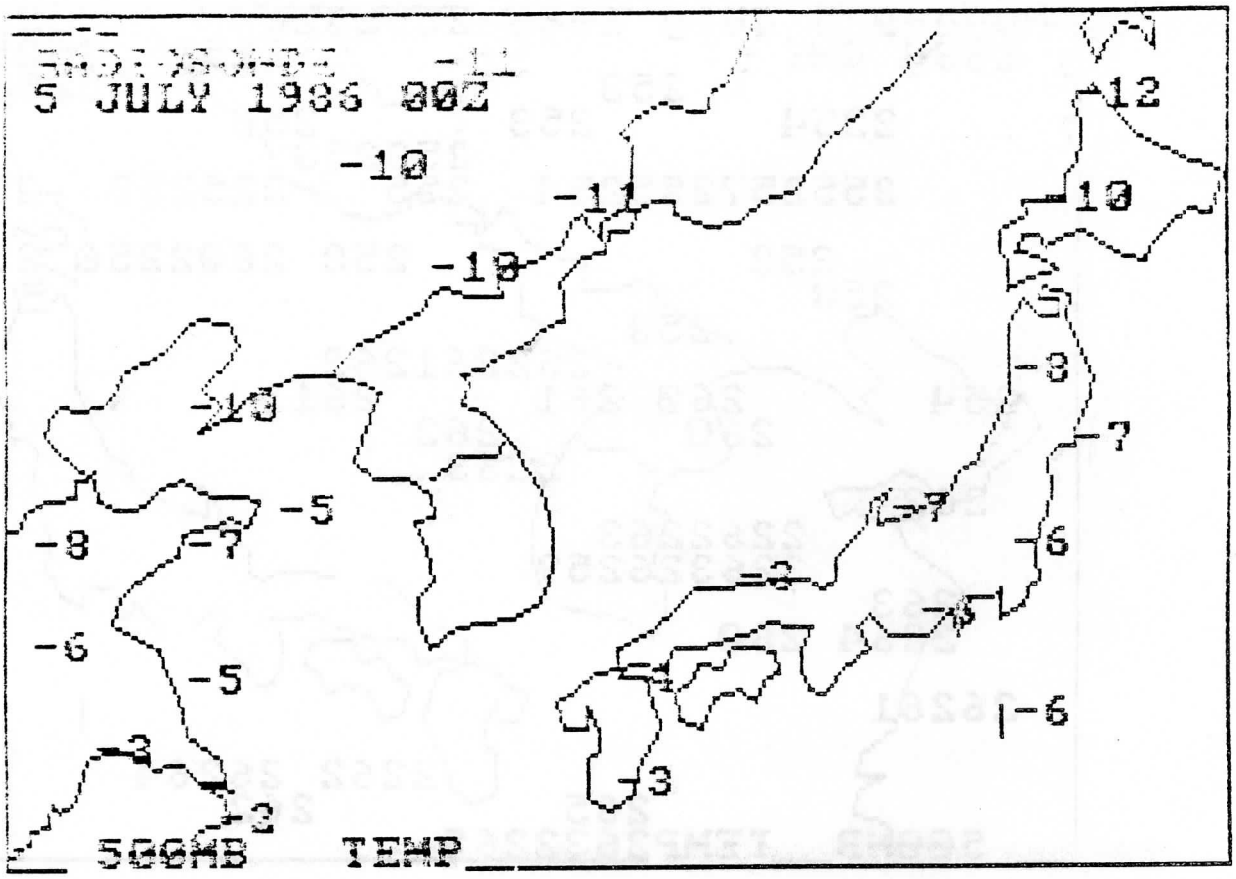

Figure 5

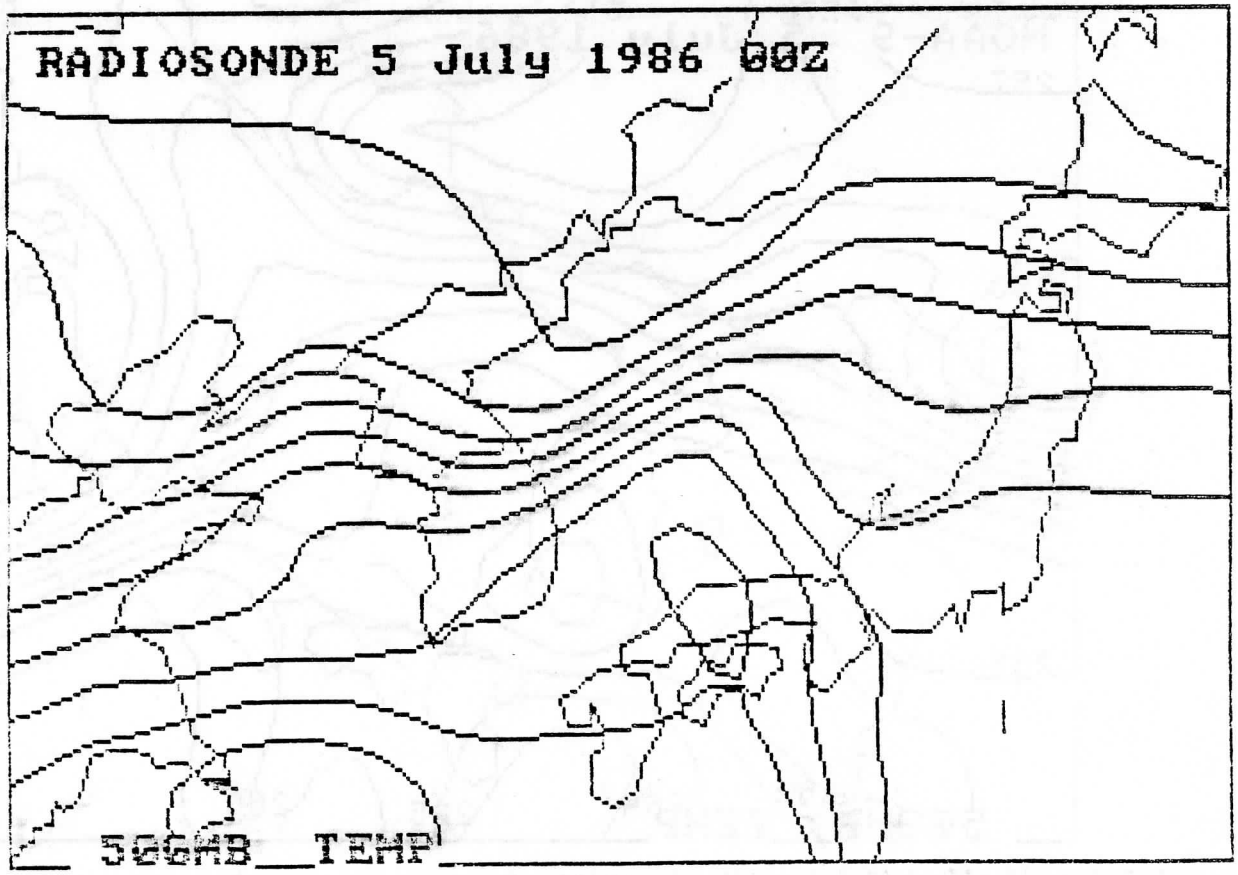

Figure 6

ADDITIONAL PAPERS RELEVANT TO ITSC-III

INTERACTIVE PROCESSING OF SATELLITE RADIANCE MEASUREMENTS

Thomas Achtor

Cooperative Institute for Meteorological Satellite Studies
Space Science and Engineering Center
University of Wisconsin-Madison

Harold Woolf

NOAA/NESDIS Systems Design and Applications Branch
Madison, Wisconsin

Harold Maurer

NASA/Goddard Space Flight Center
Greenbelt, Maryland

Frank Huang

Science Systems and Applications, Inc.
Greenbelt, Maryland

1. INTRODUCTION

This paper discusses the installation of an interactive videographic computer system at the Space Research and Remote Sensing Organization (SPARRSO) in Dhaka, Bangladesh. Additionally, the installation of the International TOVS Processing Package (ITPP) software, which enables the processing of NOAA polar orbiting satellite radiance measurements, provides SPARRSO with meteorological information on surface fields and atmospheric structure in the South Asia region.

2. INSTALLATION OF SPARRSO SYSTEM

2.1 Participants

Under the sponsorship of the U.S. Agency for International Development (USAID), NASA was contracted to implement the Agro/Climatic Environmental Monitoring Project (ACEMP) at the SPARRSO in Dhaka, Bangladesh. The project mission is to provide the means for remote sensing research leading to applications in disaster alert and other physical science problems. NASA provided management, staff and technical support, and the facilities of the Goddard Space Flight Center for system assembly and testing. Science Systems and Applications, Inc. (SSAI), the primary subcontractor, was involved in system design, assembly, training of Bangladesh technicians and on site installation in Bangladesh. The Louisiana State University's (LSU) coastal studies program provided training for Bangladesh scientists in applications of the Advanced Very High Resolution Radiometer (AVHRR) on the NOAA polar orbiting satellites to problems in agriculture, fisheries, and hydrology.

The Cooperative Institute for Meteorological Satellite Studies (CIMSS) at the University of Wisconsin-Madison was contracted to install the ITPP on the ACEMP system, train SPARRSO employees in its operation, and teach Bangladesh scientists research and operational applications of the data.

The SPARRSO sent nine employees to the U.S. for ten months of training during 1984-1985. Among the group were three hardware specialists, three computer programmers and three scientists. The group spent most of their time at Goddard, receiving instruction in system design, maintainance and operation. The group also visited LSU to receive training in AVHRR applications. The three scientists visited the University of Wisconsin-Madison to familiarize themselves with the ITPP and observe research and operations-related work using satellite derived information.

2.2 ACEMP System

The system designed for SPARRSO is intended to provide extensive data processing capabilities. The main functions of the system are for image display and interpretation, interactive use with a data base to allow imagery and graphics of derived calculations to be displayed simultaneously, and graphics creation for hard copy output. Twin (identical) systems were provided to insure greater reliability and user access. The system hardware includes:

1) 2 VAX 11/750 computers with 6 mbytes central memory,
2) 2 IIS model 575 image processors
3) 2 DEC RA81 456 mbyte disks

4) 2 DEC model TU78 magnetic tape drives
5) 2 Printronix printers
6) 1 Trilog color printer
7) 1 Matrix recording device
8) 1 Optronix microdensitometer

A computer compatible environment had to be created for the system at SPARRSO. Equipment installed included air conditioning, dehumidification and dust removal systems for the computer rooms, and a generator and uninterruptable power supply to insure continuous power for the system. Finally, the ACEMP included the installation of ten remotely located data collection platforms and one marine buoy. The river based platforms provide water level monitoring for flood control, and meteorological measurements of temperature, humidity, pressure, wind and precipitation. The data collected from these platforms is available for use on the SPARRSO/ACEMP System.

2.3 SPARRSO Objectives

The SPARRSO in Dhaka, Bangladesh evolved in the early 1970's in response to the need for more timely disaster warnings. The SPARRSO charter establishes research objectives in remote sensing applications to meteorology, oceanography, hydrology, agriculture, fisheries and coastal zone management. Few areas of the world are harder hit by floods from heavy monsoon or tropical cyclone rains. Also, heavy rains in the Himalayas produce frequent floods downstream in Bangladesh. The confluence of three major rivers in central Bangladesh has created a large river delta region which is very fertile, but prone to extensive flooding. In addition to the flood problem, a branch of the upper tropospheric westerlies, which is diverted south of the Himalayas during the winter and spring months, brings disturbances which can produce severe local storms, including tornadoes. The high population density and the difficulty of rapid evacuation in this water rich region makes timely forecasts and warnings of great importance.

3. INTERNATIONAL TOVS PROCESSING PACKAGE (ITPP)

The ITPP (formerly known as the TOVS Export Package) grew out of the efforts of participants in the First International TOVS Study Conference (Smith et al., 1983). The initial algorithms were developed by the NOAA/NESDIS Systems Design and Applications Laboratory on the Man-computer Interactive Data Access System (McIDAS) at the Space Science and Engineering Center, University of Wisconsin-Madison. The ITPP contains software for establishing a local/regional system for processing TOVS sounding data from the Tiros-N/NOAA series of polar orbiting spacecraft. Using the software and supporting data in the ITPP, raw radiance data is ingested directly from antenna readout or magnetic tape into the host cpu, calibrated, navigated and formatted for input into the temperature and moisture profiling algorithm (Nelson, 1985). A simultaneous, one-step direct physical solution to the radiative transfer equation has been incorporated into the ITPP to calculate atmospheric temperature and moisture profiles and other derived meteorological products (Smith et al., 1985).

4. APPLICATIONS OF THE ITPP IN BANGLADESH

The meteorological desires of SPARRSO include the ability to diagnose tropical cyclone intensity and movement, improved knowledge of monsoon dynamics, intensities and depression movement, and forecasting of potential severe local storms, including tornadoes. The utilization of ITPP products, and a software library of meteorological product generation and graphics display programs provides SPARRSO with the capability to investigate these topics.

4.1 Product Generation and Editing

The simultaneous, one-step physical retrieval algorithm in the ITPP utilizes a 3 x 3 TOVS field of view matrix (80 km resolution) to generate meteorological information. The algorithm calculates temperature and dewpoint values at 50 mb increments from radiance measurements. Additionally, geopotential heights for these levels are calculated from a surface pressure field and mean layer temperatures. Values for the total column precipitable water vapor and the total stratospheric ozone are also obtained. To this point the raw data reception, structuring, and calculation techniques can be totally automated. However, from this point the interaction of a meteorologist with the data is important. Since the radiance to space can be effected by atmospheric water vapor and liquid droplets, careful editing of the data is necessary to elimate those retrievals contaminated by attenuated radiances. The editing is accomplished by graphically displaying temperature and moisture fields over satellite imagery and screening for data that looks affected. The technique requires the ability to operate an interactive videographic computer and the meteorological knowledge to determine which data are affected. Interactive screening techniques and software to implement them were initially developed on the McIDAS. The software was made available to the SPARRSO, and the techniques taught in classroom and hands-on training. The Fig. 1 satellite image shows a major tropical cyclone in the Bay of Bengal on 23 May 1985.

Figure 1.

The graphics overlay shows the unedited and edited satellite retrieval locations in the region. The extensive cloudiness over the Bay of Bengal necessitated the editing of a rather large number of retrievals. However, the large number of remaining retrievals provides high quality atmospheric information in a region where almost no data is routinely available.

4.2 Final Products

The generation of final meteorological products for interpretation and display is of great importance for operational and research studies. Software available on McIDAS provides for the calculation of numerous derived fields, with a variety of display techniques (Suomi et al., 1982). For example, Fig. 2 shows contours of 500-250 mb geopotential thickness, derived from satellite information, over the tropical cyclone. The upper tropospheric warm core of the cyclone is indicated by the contours. Products such as this allow forecasters and research scientists to study the spatial and temporal evolution of the atmosphere, requesting the fields they want to see and combining graphics with imagery to uniquely fit their needs. The future development of software for scientific calulation and graphics display at SPARRSO will permit scientists there to utilize the interactive nature of the VAX/IIS system to its fullest extent.

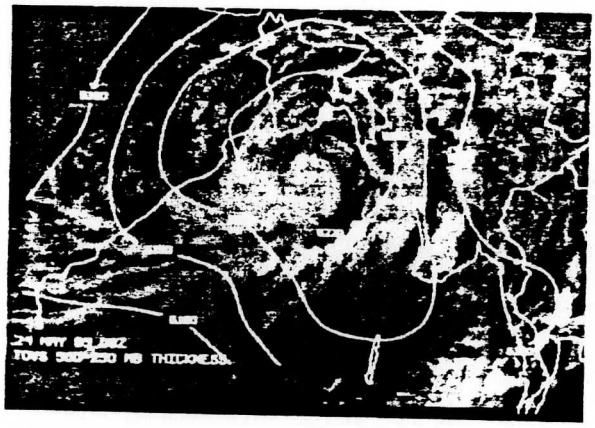

Figure 2.

5. SUMMARY

An interactive videographic display computer was installed at the SPARRSO in Dhaka, Bangladesh during 1985. The USAID sponsored project combined efforts of the federal government, the private sector and the university community. A summary of the project is provided, as well as a discussion of an interactive application of the system. A videotape will be shown at the conference to elaborate on the applications of an interactive videographic computer to satellite meteorology.

6. REFERENCES

Nelson, J., 1985: Documentation of the TOVS Bangladesh Data Processing Software. CIMSS Report.

Smith, W. L., H. M. Woolf, C. M. Hayden, A. J. Schreiner, and J. M. LeMarshall, 1983: The physical retrieval TOVS export package. Presented at the First International TOVS Study Conference, Igls, Austria, August, 1983.

Smith, W. L., H. M. Woolf, C. M. Hayden, A. J. Schreiner, 1985: The simultaneous retrieval export package. Submitted to J. Atmos. and Ocean Tech.

Suomi, V. E., R. Fox, S. Limaye and W. L. Smith, 1982: McIDAS III: A modern interactive data access and analysis system. JCAM, 22, No. 5, May, 1985.

WMO ISSUES FOR DISCUSSION

J. Giraytys
World Meteorological Organization
Geneva, SWITZERLAND

1. Baseline Upper Air Network

1.1 Background

The First International TOVS Study Conference (ITOVS-I), 29 August - 2 September 1983, recommended the establishment of an independent baseline sounding capability from radiosondes (recommendation 10, page 6, Final Report). ITOVS-II (18 - 22 February 1985) gave strong support to the concept of a baseline upper air network (conclusion 5, page 3, Final Report). The WMO Executive Council XXXVII (1985) invited the President of CBS in consultation with the Secretary-General to complete the definition of a baseline network (Paras 3.1.32 - 3.1.35, General Summary, EC-XXXVII).

1.2 A preliminary Study on the definition of the Baseline Upper Air Network (B/UAN) was prepared by J. Le Marshall (Australia) on secondment to the WMO Secretariat in August 1985. The study notes that there are two principal reasons for establishing a B/UAN:

(a) To provide high quality, intercalibrated, and at times contemporaneous, set of radiosonde and rawinsonde sounding data for verifying and optimizing the quality and utility of satellite temperature and moisture vertical sounding data, and

(b) To provide a standard which would be the basis for obtaining uniformly high quality data throughout the global upper-air sounding programme.

1.3 The Extra-ordinary session of the Commission for Basic Systems held in 1985 (CBS/Ext(85) agreed that there should be an evaluation effort prior to full-scale implementation of the baseline upper-air network. The USA agreed to formulate the plan for such an evaluation and to carry out some studies. A proposal for the evaluation is expected to be available at ITOVS-III.

1.4 The ITOVS-III may wish to:

(a) Consider what data are needed from a baseline upper air network in view of the recent changes in satellite retrieval techniques, and

(b) Make recommendations on what steps can be taken to provide the level and quality of that radiosonde data which may be required.

(WWW/2097)

2. Radiosonde Intercomparisons

2.1 The Commission for Instruments and Methods of Observation (CIMO) established a Working Group on Upper Air Data Compatibility, which has organized an intercomparison of radiosondes. The intercomparison took place in two phases: (1) June/July 1984 at Beaufort Park, Berkshire, UK and (2) February/March 1985 at Wallops Is, Virginia, USA. In Phase II, for example, Australia, Finland, India, USA and the UK took part. In total for phase II, 102 balloons were successfully flown, each carrying at least five different instruments.

2.2 Interim reports of these intercomparisons are available (see attached). The final report on both phases is expected to be available at the time of TOVS-III.

2.3 The TOVS-III may wish:

(a) To discuss the results of these intercomparisons in the context of the impact on satellite retrievals, and

(b) To make recommendations on how such data from intercomparisons might be used to improve the quality of satellite sounding data.

3. Operational World Weather Watch Systems Evaluations - North Atlantic (OWSE-NA)

3.1 The OWSE-NA was formulated for two purposes:

(a) to evaluate the operational performance of a composite network of current and new observing systems, and

(b) to draw conclusions which can be used to assist in the further implementation of the WWW.

3.2 The strategy is to actually put in service a composite system incorporating new and existing technologies. Then, over a finite period, to examine systematically the performance of the composite and the value of the resultant data. The operational phase is from 1 January 1987 to 31 December 1988. The build-up phase began in 1985.

3.3 Two broad sets of results are expected:

(a) those dealing with the operational performance of the systems (data availability, maintenance, etc.), and

(b) those concerned with the scientific evaluation of the value of the data (eg, in analyses).

3.4 The plan for the scientific evaluations calls for four categories of activities:

(a) preparation of statistics based on monitoring (error rates, data quality, error statistics vis-à-vis other systems, etc.)

(WWW/2097)

(b) parallel runs to examine the impact of various combinations of systems on the analyses. These will be done at several centres (eg, the European Center for Medium Range Weather Forecasting, UK, Germany, Federal Republic of, and Netherlands have all agreed to participate)

(c) Case studies, which could include forecast products as well as analyses, and

(d) National studies, eg examining the impact on providing specialized marine forecasts. (Both the USA and Netherlands have expressed interest in the latter.)

3.5 A Scientific Evaluation Group (SEG) has been established to organize these evaluations and to assemble the results. Mr. Andrew Gilchrist (UK) is the chairman. The final version of the evaluation plan is in preparation.

3.6 In support of the OWSE-NA, some 12 countries and organizations have agreed to provide substantial increases in the data base over the North Atlantic (roughly between 10° and 65°N and from Europe to N. America). For example, 10-12 ASAP ships will be implemented taking radiosonde observations twice daily, some 75-80 drifting buoys will be launched during the two year period, and upwards of 100 merchant ships will be equipped with satellite transmission capabilities.

3.7 The increase in surface and upper air marine data for the OWSE-NA offers the possibility to examine in detail the impact of these data on satellite retrievals. Such evaluations had been proposed by both ITOVS-I (eg recommendation 13, page 6) and ITOVS-II (eg recommendations 2 and 10). Certain evaluations of this nature will be carried out by several of the main centres and their results likely will be of interest to the ITOVS. In addition, the ITOVS may wish to consider:

(a) proposing to the several centres involved with the OWSE-NA, questions relating to satellite retrievals which could be investigated,

(b) what IOVS participants might do to assist centres in their evaluations of satellite retrievals,

4. World Climate Research Programme (WCRP)

4.1 The WCRP is a jointly sponsored programme of the WMO and the International Council of Scientific Unions (ICSU). There are three main objectives (streams) in the work which covers the period 1985-1995:

(a) to establish the physical basis for the prediction of weather anomalies for time scales up to one to two months,

(b) to predict the variations in global climate over periods up to several years, and

(c) to characterize variations of climate over periods up to several decades and to assess the potential response of climate to either natural or man-made influences.

(WWW/2097)

4.2 The Joint Scientific Committee notes in the first WCRP Implementation Plan that with respect to atmospheric data the success of the programme will depend in important ways on the maintenance and upgrading of the present WWW, on the development and implementation of new observing systems and on making provision for processing and analyzing the vast quantities of data that will result. In the discussion of the WWW systems, the WCRP Implementation Plan points out that "the WCRP would benefit directly from any advance made in the performance of the WWW, --- such as --- improved satellite instruments and information retrieval algorithms."

4.3 The ITOVS-III may wish to:

(a) summarize for the WCRP the status of the current capabilities of the TOVS,

(b) indicate what additional work is required to make more useful the data from current satellites or those to be launched in the next 3-5 years,

(c) indicate what prospects there are for improved instruments in the next generation of satellites, and

(d) propose what kinds of studies and/or research is needed to investigate the uses of satellite data in climate programmes.

(WWW/2097)

MULTIVARIATE ANALYSES OF ALPEX SATELLITE RETRIEVALS

W. P. Menzel,[1] G. A. Mills,[3] A. J. Schreiner,[2]
C. M. Hayden,[1] and W. L. Smith[2]

[1]NOAA/NESDIS Systems Design and Applications Branch
Madison, Wisconsin, U.S.A.

[2]Cooperative Institute for Meteorological Satellite Studies
Madison, Wisconsin, U.S.A.

[3]Bureau of Meteorology Research Centre
Melbourne, Victoria, Australia

October 1985

ABSTRACT

A comparison of analyses of high resolution temperature and humidity profiles retrieved from polar orbiting sounding satellites and in situ profile data gathered during the ALPEX Intensive Observing Period is presented. The retrieval technique is the simultaneous physical solution for temperature and water vapor profiles. The analysis scheme is multivariate. The moisture analysis is compared with Meteosat water vapor images to investigate the horizontal resolving power of the satellite sounding data acquired during ALPEX. This study demonstrates that the TOVS data contain moisture information of good quality at high horizontal resolution that should impact numerical forecasts positively.

1. Introduction

The data gathered during the Alpine Experiment (ALPEX) has received considerable attention from the International TOVS Study Conference in its study of the quality and applicability of satellite derived temperature and moisture profiles for operational use (Menzel, 1983 and Menzel, 1985). The ALPEX has been used as a test bed for evaluation and improvement of various inversion algorithms and more recently several analysis schemes. This paper reports on the results that have been realized with the direct physical retrieval that solves for temperature and water vapor simultaneously (Smith et al., 1985). Moisture fields show considerable structure that is partially verified by conventional observations and Meteosat imagery. In addition, a multivariate analysis (Mills and Callan, 1985) has been run on the TOVS satellite retrievals for two consecutive days, 0300 GMT on 4 March and 5 March 1982. Improvements over the traditional Barnes analysis are realized by allowing the geopotential thickness fields from adjacent pressure levels to interact and through the objective editing capability in the multivariate analysis.

This work was done on the Man-computer Interactive Data Access System (McIDAS) at the University of Wisconsin.

2. Simultaneous Physical Retrieval Method

Simultaneous retrieval of the temperature and water vapor solutions is described in detail elsewhere (Smith et al., 1985). Briefly, the radiative transfer equation is written in perturbation form with respect to an estimated or mean atmospheric condition. The temperature and moisture perturbations are represented as a linear expansion of basis functions that are profile weighting functions of the radiative transfer equation. From a set of TOVS spectral radiance observations which are sensitive to both temperature and moisture profiles, a least squares solution in matrix form is then sought.

The main advantage of the simultaneous retrieval method is that the temperature and water vapor profiles and the surface skin temperature are determined simultaneously using all the radiance information available. The interdependence of water vapor radiance observations upon temperature, and of several of the carbon dioxide channel radiance observations used for temperature profiling upon the water vapor concentration, is thus addressed directly. Also, the dependence of the radiance observations on surface emissions is accounted for in the simultaneous solution by the inclusion of surface temperature as an unknown. Since a single matrix inversion is required for the specification of all parameters, the solution is computationally efficient. Finally, but significantly, ancillary observations of temperature and/or moisture from surface sensors or aircraft, for example, can be readily incorporated in the solution.

The processing of the ALPEX TOVS data presented here starts with the specification of an initial profile including surface observations, if available. The initial profile is obtained through the use of regression coefficients based on real radiances matched to radiosonde observations. These coefficients are those derived operationally by NESDIS during the ALPEX.

MSU and HIRS radiances are processed at 75 km resolution (3 x 3 array of HIRS FOVs) as described in an earlier report (Smith et al., 1983); MSU data are interpolated to each HIRS FOV. These data are used in a two step procedure to generate an initial estimate, to determine cloud contamination, and to produce a final solution of temperature and moisture as follows.

In the first step, the stratospheric HIRS brightness temperatures (channels 1-3), the MSU brightness temperatures (MSU 2-4) and the middle and upper tropospheric HIRS water vapor channels (HIRS 11 and 12) are used to derive a first estimate of the temperature and moisture profile at the sounding location. This channel selection assures that the estimate should be relatively free of error due to cloud attenuation. The weighting functions for HIRS-1 and MSU 2-4 are utilized as the basis functions for temperature and the HIRS 7 and 12 weighting functions are used as the basis functions for water vapor in the initial retrieval. Once the first estimate of the temperature and water vapor profile is achieved, the height and amount of any cloud affecting the infrared observations are determined by the CO_2 absorption technique (Menzel et al., 1983). The mixing ratio profile and the infrared transmittance are adjusted based on cloud amount.

In the second step, the cloud affected channels are screened for contamination. The screening may cause the rejection of either short or longwave channels (but not both). Also, if cloud is detected, the influence of these channels is reduced below the cloud level. The weighting functions for HIRS 1, 3, 7 and MSU 2-4 are used as the temperature profile basis functions, and those for HIRS 7, 11, and 12 are used as the water vapor profile basis functions. Since as many as 19 different spectral radiance observations are used to determine the coefficients for the nine basis functions, the system of equations to be inverted is heavily overdetermined, thereby stabilizing the solution.

3. Multivariate Analysis

The three-dimensional objective analysis scheme uses a combination of the successive correction method (SCM) of Cressman (1959) and a three-dimensional version of the fields by information blending (FIB) technique of Holl and Mendenhall (1971). The FIB system is based on the objective analysis techniques using the calculus of variations which were described by Sasaki (1958, 1970). The primary difference with regard to the scheme on which it was based (Seaman et al., 1977) is that it uses the FIB technique in an explicitly three-dimensional manner when deriving geopotentials; vertical coupling is incorporated into the variational blending of this system.

Ten pressure levels are analyzed in the vertical (1000, 850, 700, 500, 400, 300, 250, 200, 150 and 100 mb). Output fields include geopotential, temperature, dewpoint, wind components, and mean sea level pressure. The analysis sequence proceeds as follows:

a. An SCM analysis of mean sea level pressure (MSLP) is performed, and a consistent 1000 mb geopotential field derived. This provides a reference level for subsequent geopotential analyses.

b. SCM analyses of 1000-250 mb thicknesses using scalar observations, and of 250 mb geopotential gradient using vector (i.e., wind) observations are made. Using the 1000 mb geopotential from (a), and the thickness and gradient analyses, a FIB procedure is carried out to define the 1000-250 mb thickness. This step defines the values of geopotential height at 1000 and 250 mb, while allowing the relatively dense geopotential gradient information expected near the tropopause from cloud vector winds and aircraft reports to affect the analyses in the middle troposphere.

c. Individual layer SCM thickness analyses are performed, together with geopotential gradient SCM analyses at each level, using respectively scalar and vector observations. Then at each analysis level in turn, an FIB procedure is used to blend the geopotential thicknesses of the layers immediately above and immediately below the level in question, together with the gradient analyses at that level, to define the geopotential at each level. The procedure is carried out iteratively in the vertical, after the manner of Lewis (1972) with the upper (250 mb) and lower (1000 mb) geopotentials fixed, to couple the geopotentials at all intermediate levels. An analogous procedure is used to define the geopotentials above 250 mb.

d. SCM analyses of temperature are produced with first-guess fields derived hydrostatically from the analyzed geopotential fields.

e. Moisture fields are specified by SCM analyses of dewpoint depression, in combination with the analyzed temperature fields. An elliptical influence function oriented with semi-major axes perpendicular to the gradient is used to define sharp moisture gradients.

f. Using the gradient wind equation, first-guess fields for SCM analyses of horizontal wind components are derived from the analyzed geopotentials. A two-dimensional FIB procedure is then used to derive a streamfunction from the analyzed wind components at each level. This streamfunction can be used for prognosis model initiation.

While there is no specific coupling between the temperature and the wind fields, the geopotential analyses, which are based on both mass and wind information, influence the temperature and stream-function fields as first guesses and, consequently, produce a substantial degree of consistency between these two fields. Full details of the analysis scheme can be found in Mills and Callan, 1985.

For the two case studies presented here, the ECMWF analysis was used as a first guess for the multivariate analysis. The multivariate analysis (with grid spacing of 67 km) then incorporated the TOVS retrievals (processed at 75 km resolution).

4. Comparison of Different Analyses

The two consecutive NOAA-7 passes over the ALPEX region on 4 March 1982 (at 0215 GMT and 0357 GMT) were processed using the simultaneous physical retrieval method (as described in Section 2). Figure 1a shows the TOVS infrared window image from the two overpasses. Figure 1b indicates the locations of the satellite retrievals. Good coverage with almost uniform density is shown.

The multivariate analysis was performed on the satellite retrievals using the ECMWF analysis from three hours earlier as an initial guess. Figure 2a shows the 500 mb height field from the ECMWF analysis. The corresponding TOVS data and the multivariate analysis are shown in Figure 2b. The TOVS data generally lower the heights over the western half of the domain, but maintain the cutoff low in the southeastern corner. This is consistent with the trend expected for a deepening trough. The multivariate analysis appears to fit the data quite well, allowing for some smoothing inherent in the three-dimensional blending of geopotentials at all levels even in the absence of any wind data.

Figure 2c shows a comparison of the multivariate and the Barnes analyses (Barnes, 1973) of the same 500 mb height field. The Barnes analysis was designed for rapid, univariate single level analysis while the multivariate three-dimensional analysis was designed to provide balanced fields for numerical weather prediction model initialization. Therefore, the multivariate analysis does reduce the goodness of the single level fit to benefit the whole

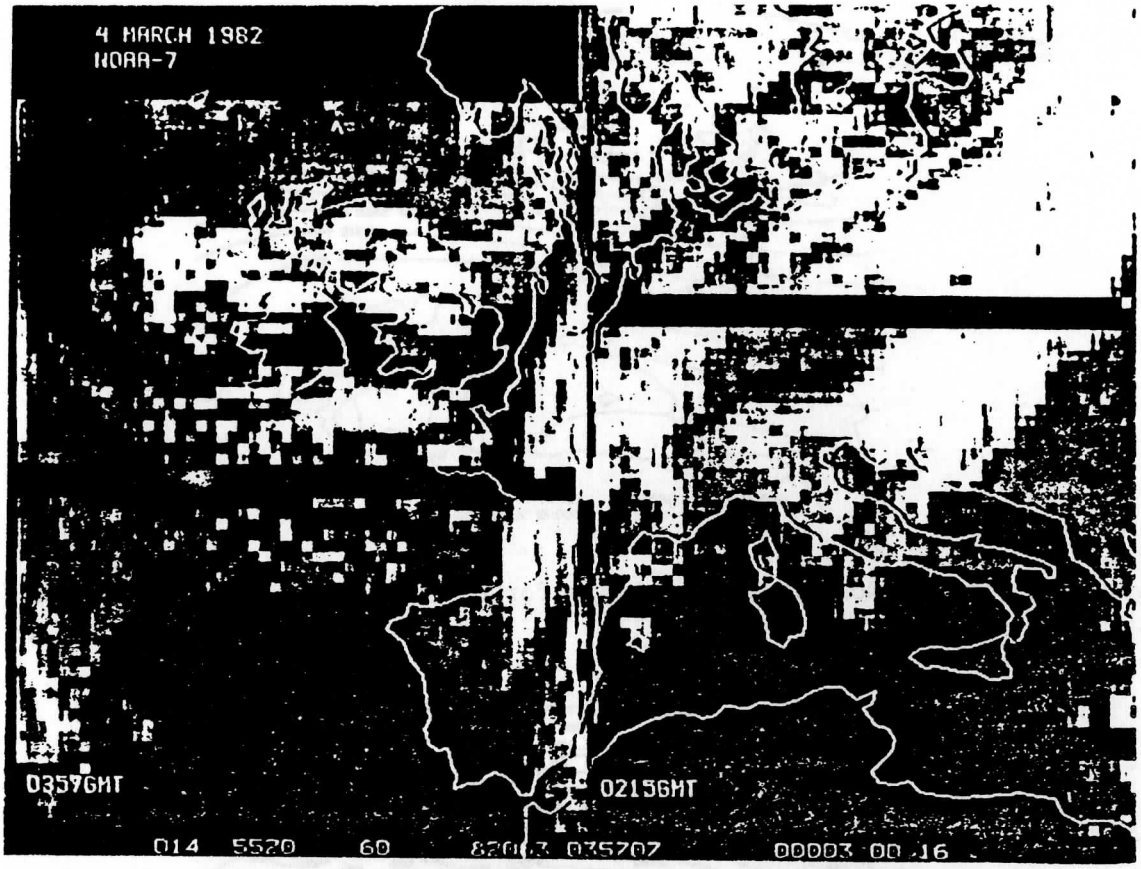

Figure 1a: A composite of the infrared window images from the 215 GMT and the 357 GMT 4 March 1982 NOAA-7 passes over the Alpex region.

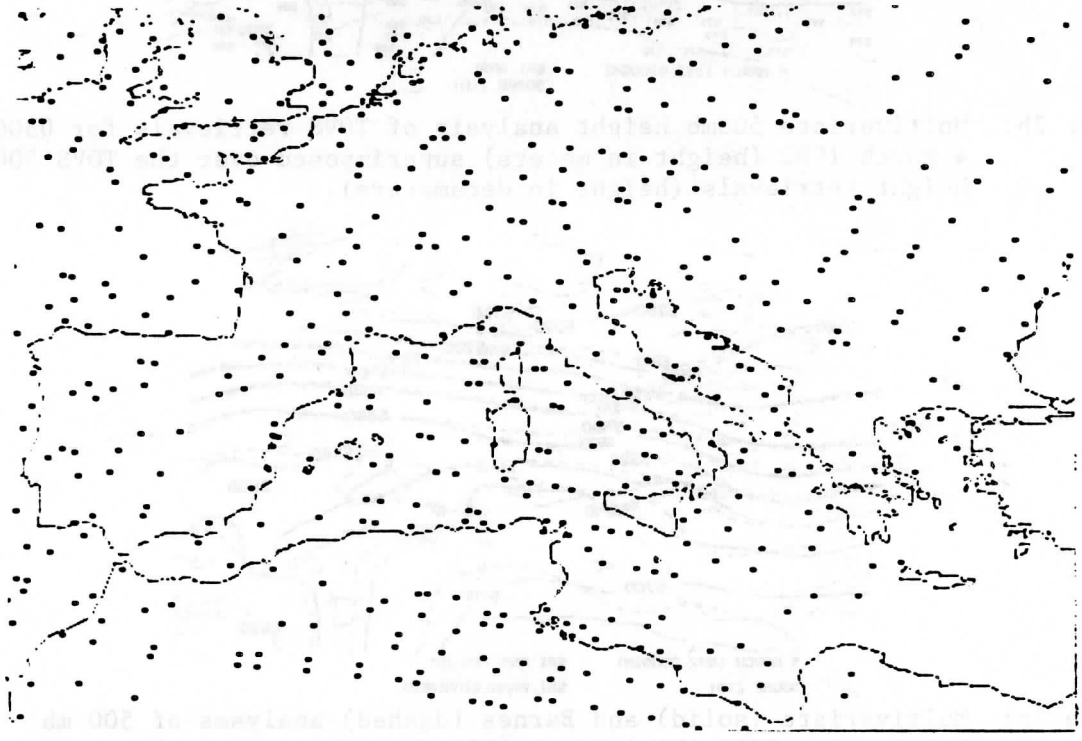

Figure 1b: Locations of the TOVS retrievals.

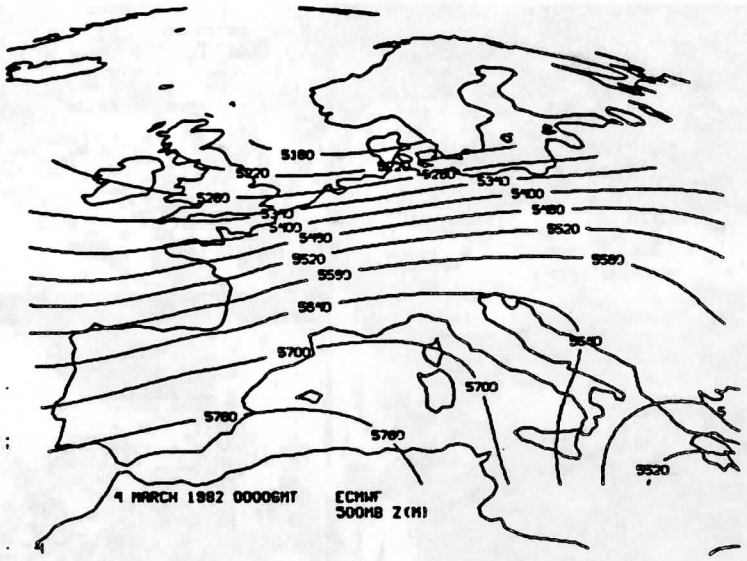

Figure 2a: ECMWF 500mb height analysis for 0000 GMT 4 March 1982 (height in meters).

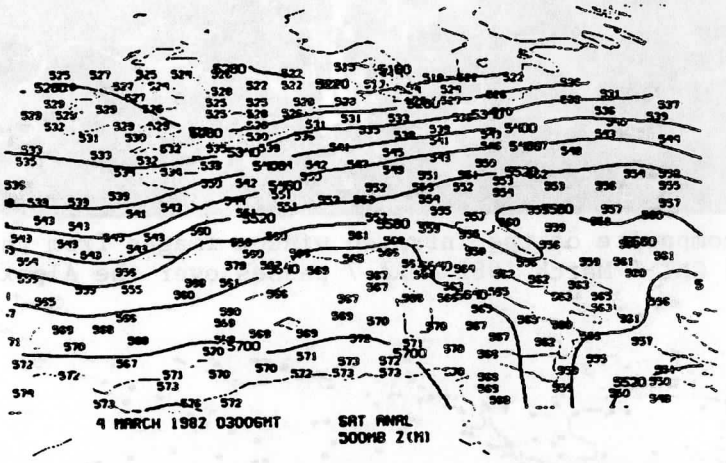

Figure 2b: Multivariate 500mb height analysis of TOVS retrievals for 0300 GMT 4 March 1982 (height in meters) superimposed over the TOVS 500mb height retrievals (height in decameters).

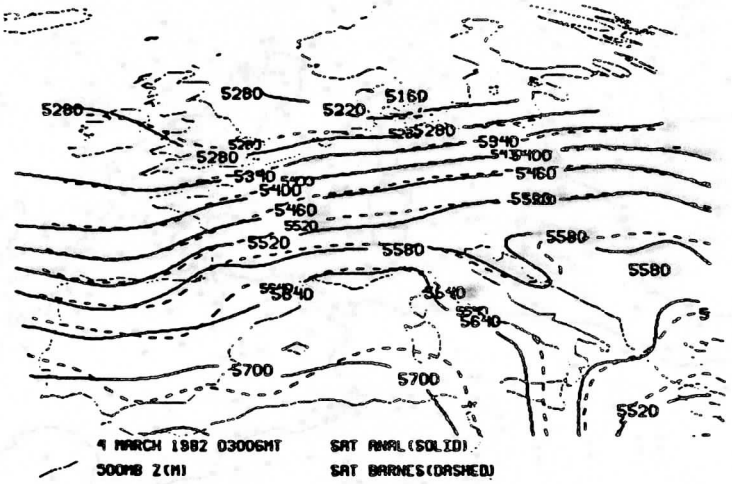

Figure 2c: Multivariate (solid) and Barnes (dashed) analyses of 500 mb heights for 0300 GMT 4 March 1982 (height in meters).

data set. The general agreement between the two is quite good, especially in the western region. This can be attributed to some degree to the good quality and density of the TOVS retrievals. The differences are (a) over the Yugoslavian coast where the multivariate analysis has a sharper contour detail, (b) over the Pyrenees where the 5640 meter contour is shifted (the five passes of the SCM analysis have rejected the 568 and 579 decameter data points, thus eliminating the small scale ridge in the Barnes analysis), and (c) over the southern Spanish coast in the 5700 meter contour (a similar effect as just mentioned). Dell'Osso showed similar details in his work by reducing the grid spacing of the ECMWF forecast model to 37 km (Dell'Osso, 1984).

Incorporation of the high horizontal resolution TOVS data into the multivariate analysis has produced a credible height field. However, the benefits of higher horizontal resolution are much greater for fields such as dewpoint temperature where large local gradients are apt to occur. The next section addresses this.

5. Moisture Results

After comparing geostationary sounding data with a special network of radiosondes, it has been found that the simultaneous direct physical retrieval offers improved determination of moisture profiles and better delineation of moisture patterns than the previous iterative schemes (Jedlovec, 1985). Comparison of some TOVS derived moisture profiles for 0300 GMT 4 March 1982 with colocated radiosonde observations from three hours earlier support the notion that good quality moisture profile information is available. Figure 3a shows a skew T plot with a moist below, dry aloft comparison over west Great Britain and Figure 3b shows a nearly saturated comparison over southern France. The dewpoint temperatures track each other within 3°C.

The field of 500 mb dew point temperatures of Figure 4a indicates the good delineation of moisture patterns possible; the multivariate analysis of this moisture data, shown in Figure 4b, highlights the moist and dry contours for easy identification. The major features defined are (a) a sharp moisture gradient down the northern European coast and across the Bay of Biscay into Spain; and (b) a dry tongue across England and into the Baltic Sea.

The moisture structure across Europe evident in the multivariate analysis of the TOVS data is well matched by similar features in a simultaneous Meteosat 6.7 micron water vapor image shown in Figure 4c. Moist areas are found in both Figure 4b (250°K contours) and Figure 4c (bright areas in image) over southeastern Spain, southern France, and northern Yugoslavia. The dry pockets of Figure 4b (230-235°K contours) over England, the Baltic Sea and northern Italy are corroborated by Figure 4c (dark areas in image).

The ECMWF analysis of dewpoint temperature at 500 mb for 0000 GMT 4 March 1982 is shown in Figure 4d. The match with the Meteosat image (Figure 4c) is clearly not as good; similar small scale moisture features are not present.

A deficiency of the multivariate analysis of the TOVS data is witnessed in the lack of intensity in the dry air over the Bay of Biscay. The satellite retrievals of Figure 4a would support a dewpoint temperature dryer by 10°C.

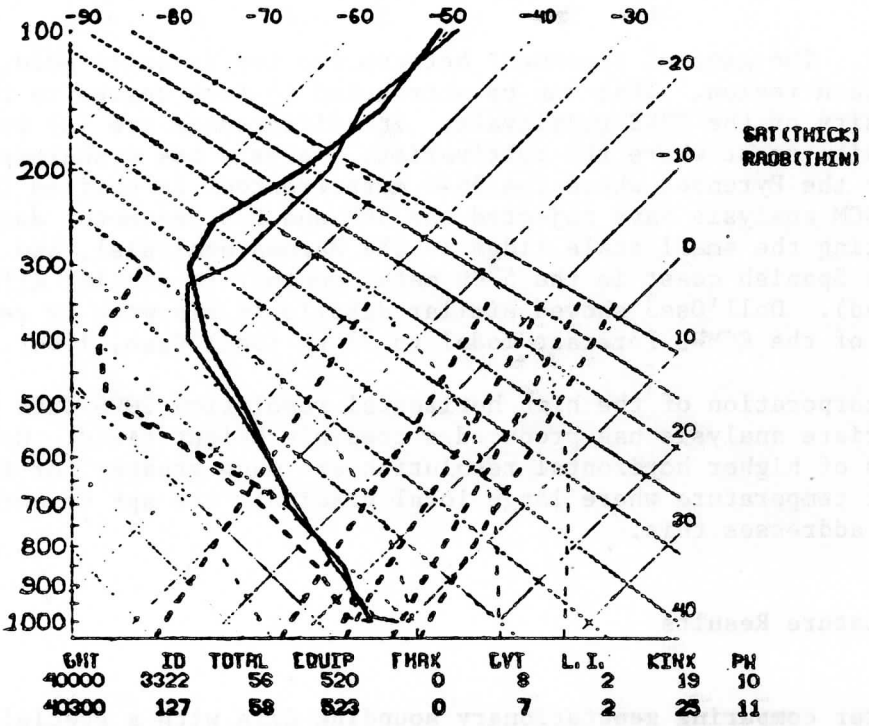

Figure 3a: Comparison of TOVS at 0357 GMT temperature and dewpoint temperature profiles (thick) with corresponding radiosonde at 0000 GMT observation (thin) over Great Britain on 4 March 1982.

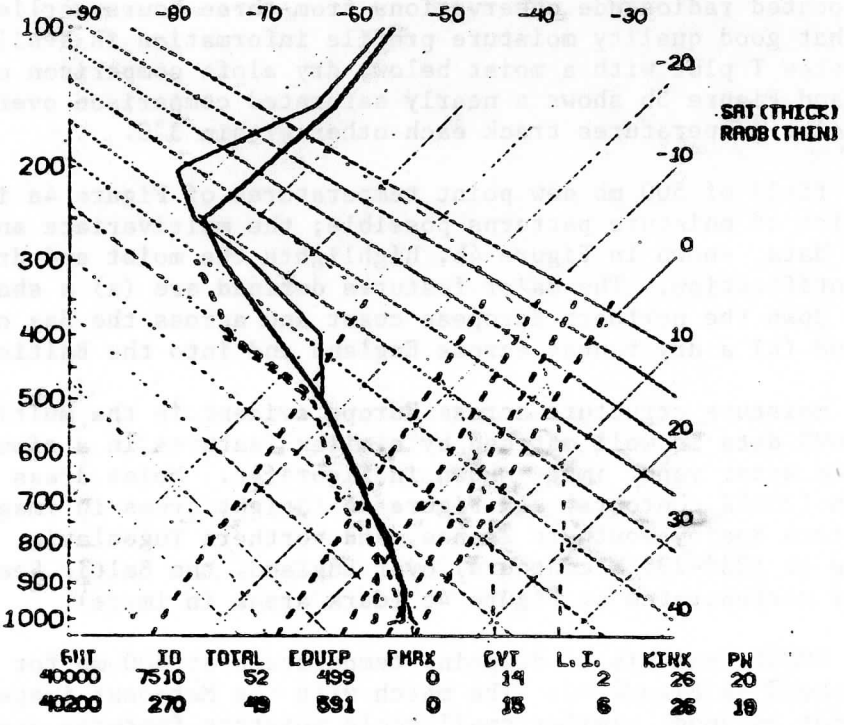

Figure 3b: Comparison of TOVS at 0215 GMT temperature and dewpoint temperature profiles (thick) with corresponding radiosonde at 000 GMT observation (thin) over southern France and 4 March 1982.

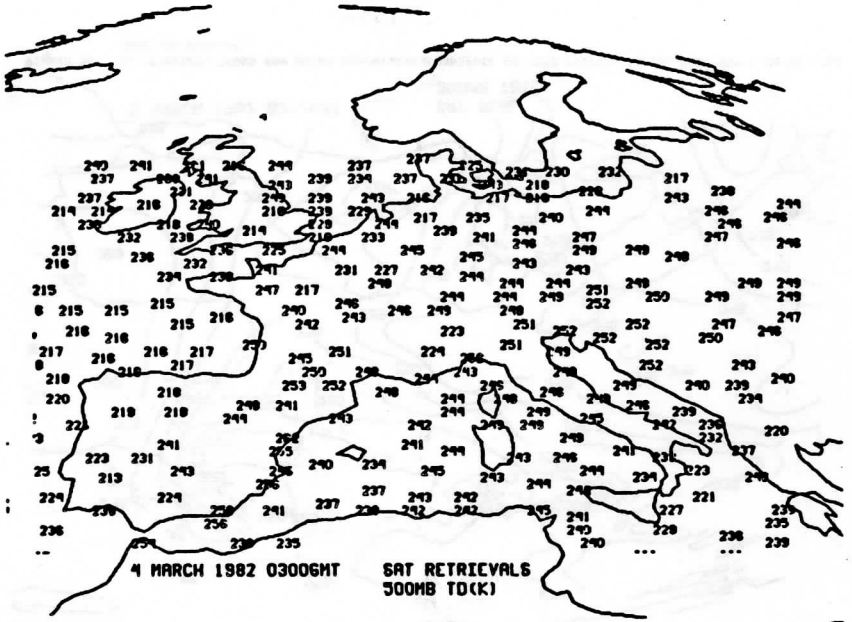

Figure 4a: TOVS retrievals of 500mb dew point temperatures for 0300 GMT 4 March 1982 (degrees Kelvin).

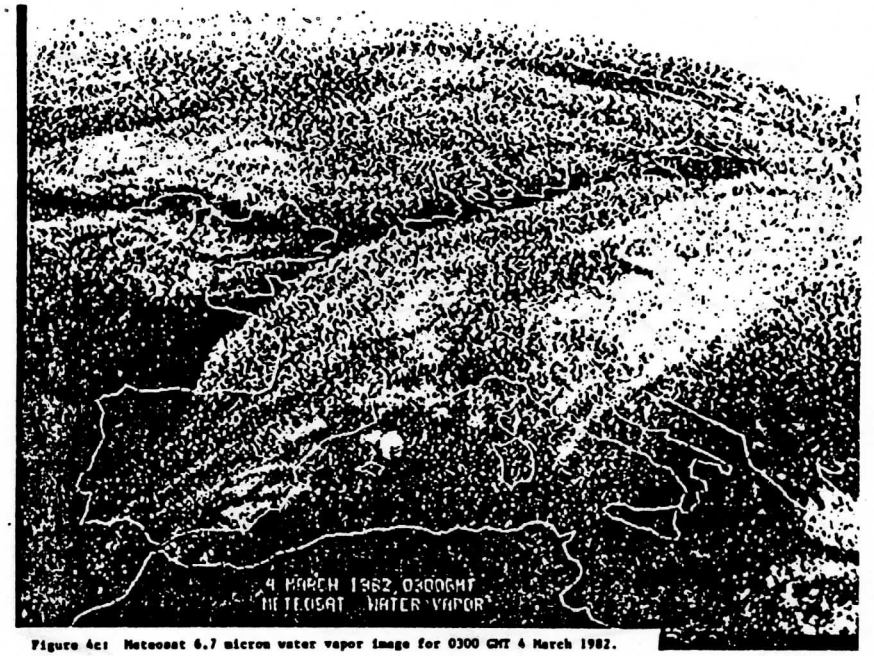

Figure 4c: Meteosat 6.7 micron water vapor image for 0300 GMT 4 March 1982.

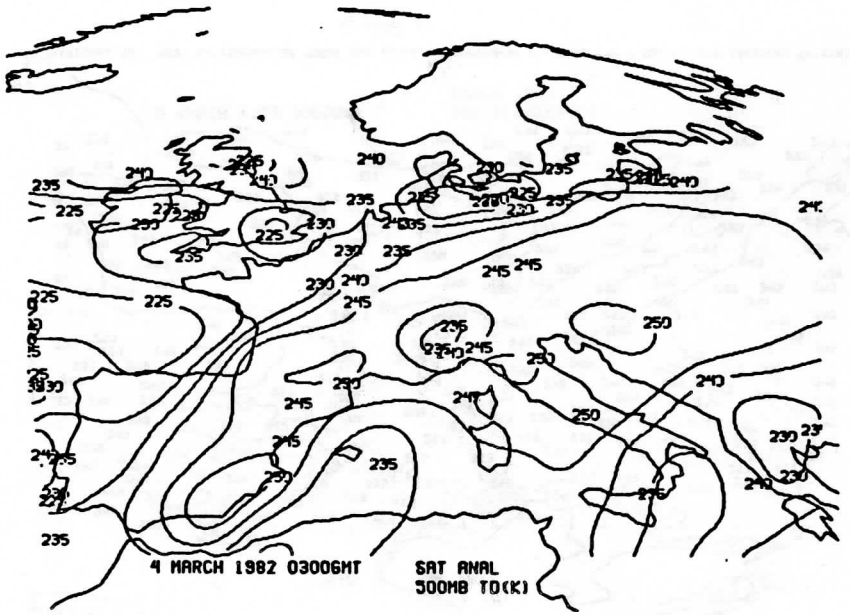

Figure 4b: Multivariate 500mb dew point temperature analysis of TOVS retrievals for 0300 GMT 4 March 1982 (degrees Kelvin).

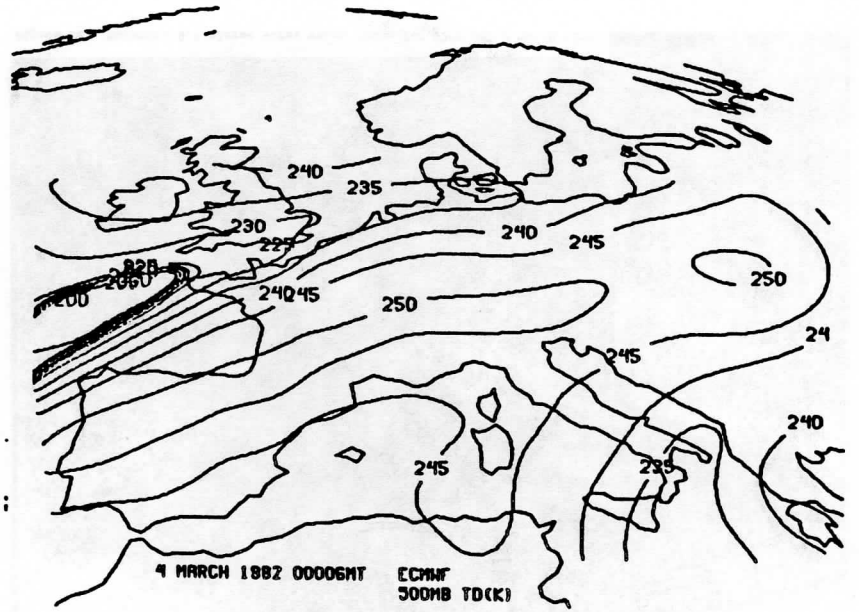

Figure 4d: ECMWF 500mb dewpoint temperature analysis for 0000 GMT 4 March 1982 (degrees Kelvin).

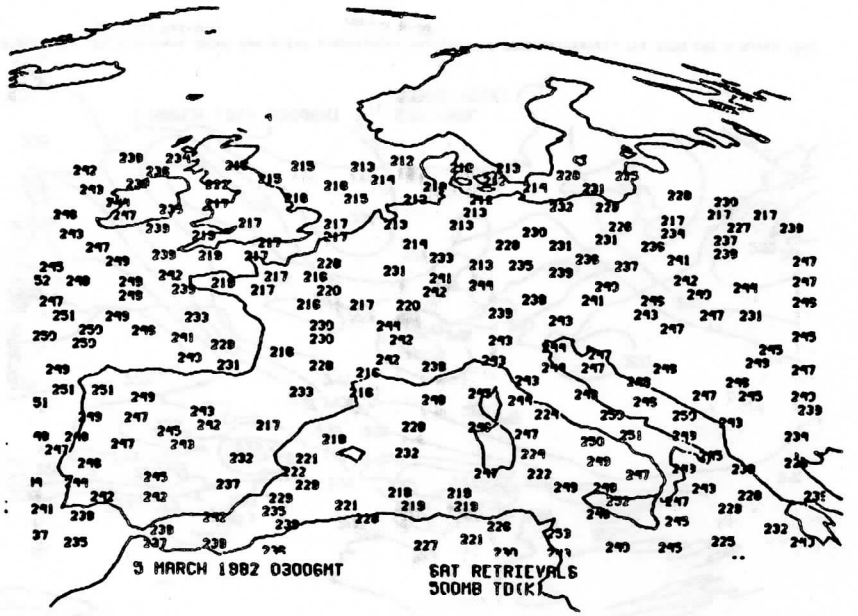

Figure 5a: TOVS retrievals of 500mb dew point temperatures for 0300 GMT 5 March 1982 (degrees Kelvin).

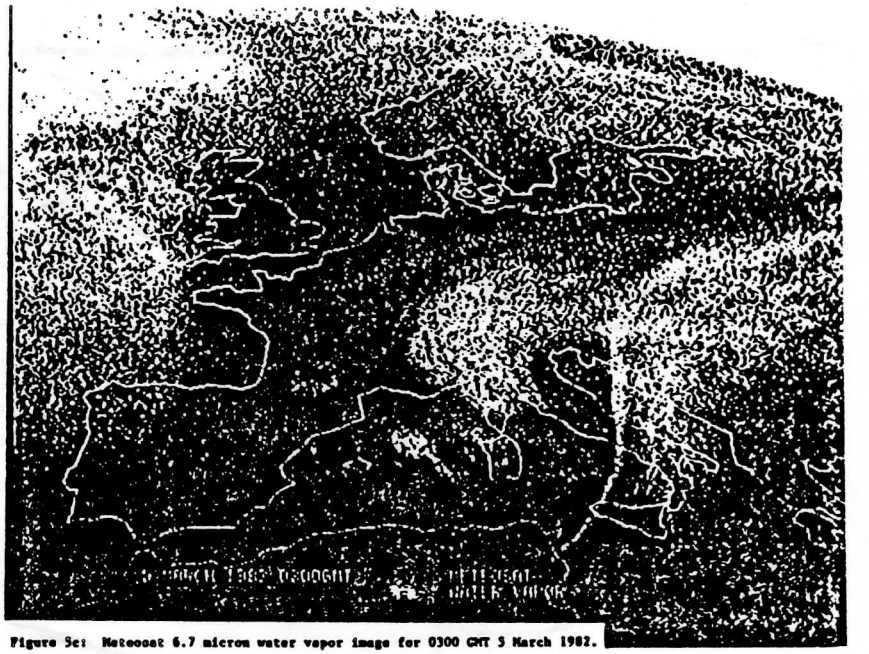

Figure 5c: Meteosat 6.7 micron water vapor image for 0300 GMT 5 March 1982.

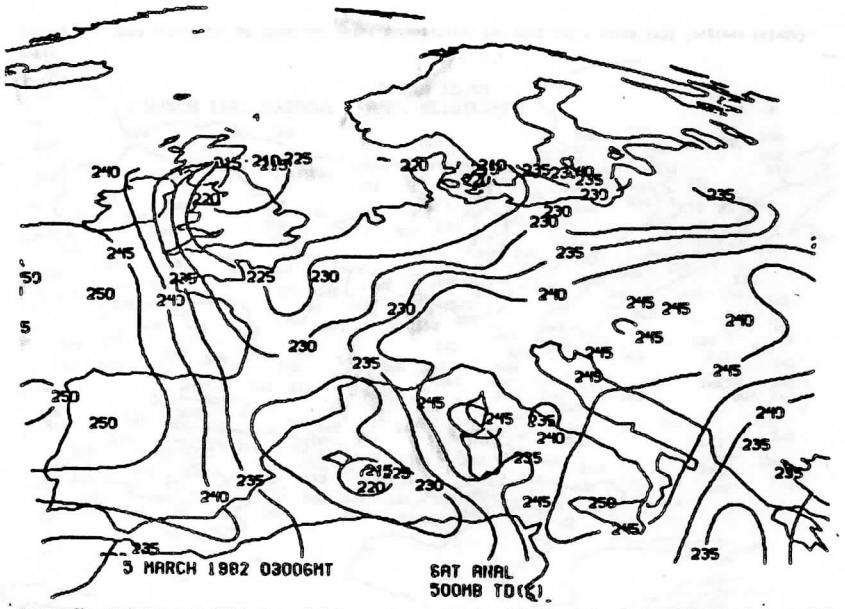

Figure 5b: Multivariate 500mb dew point temperature analysis of TOVS retrievals for 0300 GMT 5 March 1982 (degrees Kelvin).

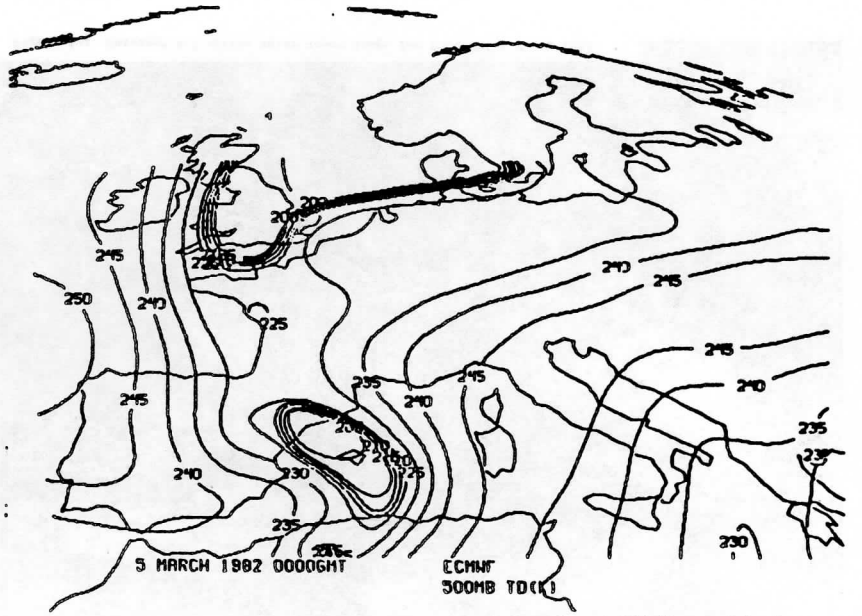

Figure 5d: ECMWF 500mb dewpoint temperature analysis for 0000 GMT 5 March 1982 (degrees Kelvin).

The lack of intensity appears to be caused by an unfortunate interaction between the guess field gradient (the intense dry slot in the ECMWF analysis) and the multivariate analysis.

In Figure 5, the four panels show the corresponding information for one day later on 5 March 1982. The same good agreement exists in the moisture patterns displayed on the 500 mb dewpoint temperature multivariate analysis and the simultaneous Meteosat water vapor image.

The multivariate analysis of the TOVS temperature and moisture has produced fields with large local gradients that show good agreement with the Meteosat water vapor images. Additional comparisons with the special ALPEX sounding data are planned to further verify these features.

6. Conclusion

The TOVS retrievals demonstrate significant detail in the moisture fields at scales not available in the conventional radiosonde network. The multivariate analysis of the data preserves the local variations of moisture while preparing the data for forecast modelling. Numerical Weather Prediction impact studies with the TOVS data are planned using the CIMSS data assimilation system.

02/WPM5/02

References

Barnes, S. L., 1973: Mesoscale objective analysis using weighted time-series observations. NOAA Tech. Memo. ERL NESSL-62, National Severe Storms Laboratory, 1313 Halley Circle, Norman, OK 73069, 60 pp.

Cressman, G., 1959: An operational objective analysis system. Mon. Wea. Rev., 87, 367-374.

Dell'Osso, L., 1984: High resolution experiments with the ECMWF model: a case study. Mon. Wea. Rev., 112, 1853-1883.

Holl, M. M., and B. R. Mendenhall, 1971: Fields by information blending, sea level pressure version. Project Rep. M167. Meteorology International, Monterey, CA, $$$pp.

Jedlovec, G. J., 1985: Private communication.

Lewis, J. J., 1972: An operational upper air analysis using the variational method. Tellus, 24, 514-530.

Menzel, W. P., W. L. Smith and T. R. Stewart, 1983: Improved cloud motion wind vector and altitude assignment using VAS. J. Climate Appl. Meteor., 22, 377-384.

Menzel, W. P. (editor), 1983: The Technical Proceedings of the First International TOVS Study Conference, Igls, Austria, 29 August - 2 September 1983. CIMSS publication.

Menzel, W. P. (editor), 1985: The Technical Proceedings of the Second International TOVS Study Conference, Igls, Austria, 18-22 February 1985. A CIMSS publication.

Mills, G. A. and G. M. Callan, 1985: A mesoscale data assimilation system for quasi-real time use in the McIDAS environment. CIMSS Technical Report.

Sasaki, Y., 1958: An objective analysis based on the variational method. J. Meteor. Soc. Japan, 36, 77-88.

Sasaki, Y., 1970: Some basic formalisms in numerical variational analysis. Mon. Wea. Rev., 98, 875-910.

Seaman, R. S., R. L. Falconer and J. Brown, 1977: Application of a variational blending technique to numerical analysis in the Australian Region. Aust. Meteor. Mag., 25, 3-23.

Smith, W. L., H. M. Woolf, C. M. Hayden, A. J. Schreiner, and J. M. LeMarshall, 1983: The physical retrieval TOVS export package. The Technical Proceedings of the First International TOVS Study Conference, Igls, Austria, 29 August - 2 September 1983. A CIMSS publication.

Smith, W. L., H. M. Woolf, C. M. Hayden, and A. J. Schreiner, 1985: The Simultaneous Retrieval Export Package. The Technical Proceedings of the Second TOVS Study Conference. A CIMSS publication.

REPORT OF PHASE 2 OF THE CIMO INTERNATIONAL RADIOSONDE COMPARISON CONDUCTED FROM WALLOPS ISLAND, VIRGINIA, U.S.A.

Francis J. Schmidlin
Observational Science Branch
NASA GSFC/Wallops Flight Facility
Wallops Island, Virginia 23337, U.S.A.

and

F. G. Finger
Anaysis and Information Branch
Climate Analysis Center, NMC
World Weather Building
Camp Springs, Maryland 20233, U.S.A.

ABSTRACT

The WMO/CIMO International Radiosonde Comparison has been held in two phases, during which a number of operational instruments, used globally were compared. Phase 1 took place at the UK Meteorological Office Facility in Beaufort Park, UK, during June/July 1984, and Phase 2 at the National Aeronautics and Space Administration Facility in Wallops Island, Virginia, during February/March 1985.

This report describes a number of aspects of Phase 2, including the procedures used for launching large balloons carrying several radiosondes, the data processing system, and some preliminary results of the comparison. The employment of high-precision tracking radar for the Wallops test provides an additional, independent standard.

Recommendations for merging the data sets from both phases of the experiment are given, in addition to possible operational use of the results by analysis centers.

1. INTRODUCTION

The second phase of the World Meteorological Organization's Commission on Instruments and Methods of Observation (WMO/CIMO) International Radiosonde Intercomparison was hosted in the United States (US) by the National Aeronautics nautics and Space Administration (NASA) at its Wallops Island, Virginia, facility during February and March 1985. The selection of the Wallops Island facility was an excellent choice because it provided the unique advantage of the high precision tracking radars located there for tracking each balloon released. These radars added a considerably larger dimension to the intercomparison because of the independent height and wind data subsequently made available for comparison purposes.

The Organizing Committee on the International Radiosonde Intercomparison agreed that the comparison should be held in two parts. The first part, or Phase 1, was to be held in the United Kingdom (UK) during June and July 1984, and Phase 2 at NASA's Wallops Island facility during February and March 1985. Both phases were successfully completed on time.

An important consideration when comparing radiosonde observations made at different times and at different locations is how to relate the separate results. The Organizing Committee considered it important, even necessary, that at least two identical radiosonde types be included in Phases 1 and 2. To fulfill this need, it was planned that the radiosondes of Finland and the United States would be flown in the UK and in the US. These radiosondes provided the "transfer standard" or link between the measurements obtained in Phases 1 and 2.

Phase 2 participants were Australia, Finland, India, United Kingdom, and the United States. Early in the comparison the UK Meteorological Office offered to provide 40-60 GRAW M60 radiosondes for comparison since these instruments are used by the UK.

2. OPERATIONAL PROCEDURES

To carry out Phase 2, each participant was required to provide their own ground equipment, radiosondes, manpower, and other resources (such as transportation costs) unique to their needs. Wallops, as the host site, provided the necessary expendables; such as balloons and inflation gas, electric power, manpower for balloon inflation and release, radar tracking, work space and housekeeping, data handling (initial data reduction was the participants' responsibility), and arranged for customs assistance and other accommodations.

It was required that the radiosondes measure the same atmospheric volume at the same time. To do this the radiosondes of each balloon flight had to be flown on the same platform. This potentially limited the number of sondes that could be flown at the same time, since the weight to be lifted had to meet the balloon's capability to lift it. Since only four countries indicated their willingness to participate at Wallops this did not present an insurmountable problem. A cross-shaped platform was constructed out of lightweight styrofoam simply because of the need to keep the total package weight below the limit required by Federal Aviation Administration regulations. This platform was frangible and did not have sharp surfaces so that if an unlikely accidential encounter with aircraft did occur it would not cause damage. The sondes, by being located at the ends of the cross members did not create flow nor radio frequency interference with each other. The plastic cross-frame instrument rig weighed 640 grams. The balloon, made of natural rubber, was manufactured by Totex and weighed 3000 grams. The suspended weight of the radar corner reflector, parachute, instruments, string, etc., nominally weighed 4500 grams. The average burst altitude of the Totex 3000 gram balloons was approximately 32 km.

The first test of the individual radiosonde systems took place on February 6. The first joint test of all radiosondes took place on February 7. This test was successful and provided the first data set of the intercomparisons. High winds presented a balloon release problem on February 8 and 9.

One release was termed a failure after the instruments crashed into the side of a building. The high winds also caused the styrofoam cross-frame platforms to break which placed the sondes undesirably close to each other during the flight. The weakness in the platform was corrected and no further problem occurred.

Wallops releases two routine radiosondes a day at 0000 UT and 1200 UT. To avoid radio frequency interference (see Table 1 for the radio frequencies used by each participant) between the routine and intercomparison radiosondes the first intercomparison balloon was released after the completion of the routine morning radiosonde and the data from the US radiosonde were used in the evening in place of the routine observation. The morning launch time was nominally established as 1345 UT. This was followed every three hours with another intercomparison balloon, i.e., at 1645 UT, 1945 UT, and 2245 UT. All reduced data, except Indian data, were transmitted to the NASA computer using direct transmission capability. The Indian data were manually keyed into the same computer.

TABLE 1

	R/S Type	Frequency MHz	
		Nominal	Used During Phase 2
Australia	Philips-TMC RS4 MK3	403	403.5
Finland	Vaisala RS80-15M	403	406.6
	RS80-15P	403	405.0
India	India Meteo Dept. MK-III	403	398
United Kingdom	Graw M60	28	28
United States	Viz Model 1392	1680	1650
	Routine 0000 UT and 1200 UT	403	403

The number of balloons released during Phase 2 was 103. Only one release was a total failure so that 102 balloons (each carrying at least five instruments) were successfully released. It is important to note that a recommendation of the organizing committee (1) was for a minimum number of flights of 72 balloons reaching the 50 hPa level. Table 2 summarizes the radiosonde pairs obtained at four pressure levels for the permutations of the 5 instruments compared. It must be kept in mind that the testing of the GRAW M60 radiosonde by the UK was added after the intercomparison began and only 44 instruments were flown. This, therefore, gave a smaller number of pairs when the UK instrument is included in the pair. Table 2 shows that the organizing committee recommendation was adequately met.

Each balloon released from Wallops was radar tracked by a precision C-band radar. The radar data were sampled at one-per-second and stored on magnetic tape. This quantity of information is more than adequate to fix the position of the radiosonde instruments and provide quality wind information and precise altitude. Although the procedures to be followed for the final analysis have not yet been adopted, consideration must be given to the method to be used to reduce wind data. For example, the United States procedure with the GMD

TABLE 2

	Number of Pairs			
	Pressure Level - hPa			
Radiosonde Pairs	50	20	10	7
Australia - US	94	87	50	18
Finland - US	97	82	60	48
India - US	79	58	48	11
UK - US	40	33	24	20
Finland - Australia	94	77	50	18
India - Australia	79	58	48	11
UK - Australia	40	33	24	18
India - Australia	79	58	48	11
UK - Finland	40	33	24	20
UK - India	40	33	24	11

tracking system is to calculate a 4-minute layer wind, i.e., displacement (in direction and speed) between two position points, four minutes apart, is used. This is an interative procedure that is updated each minute. The Vaisala system used by Finland, is the MicroCora Omega NAVAID technique. In this case the eight Omega transmitting sites send a signal every 10 seconds. The information is then integrated over 4 minutes and iterated every 10 seconds. The DigiCora Omega system uses a two and one-half minute integration of the same signals. Thus, three different procedures were followed to produce wind information. This suggests that the radar information should be treated in the same manner in order to properly compare the winds obtained from the radiosonde systems.

3. PRELIMINARY COMPARISON OF LINK RADIOSONDE PAIRS

Preliminary comparisons between the instruments of Finland and the United States are presented for Phase 1 and 2. Because the highest solar angle reached in Phase 2 at Wallops Island during the observation period (February 4 - March 15) would be ~40 degrees it was decided that comparisons would be made at the same solar angle during Phase 1 in the UK. Zenith angles of 36-43 degrees were reached at Wallops Island during the 1700 UT release. Similar angles were reached in Phase 1 at 0800 and 1600 UT. The test results for temperature differences at constant pressure levels for all day and night data are given in Figure 1.

It is clear from Figure 1 that the Phase 1 temperature differences (shown by the dots) between Finland and the US are mostly negative at pressures between 1000 and 30 hPa. The US radiosonde temperatures are seen to be colder than

Finland's at the 20-, 15-, and 10-hPa levels. Significant is the 1.5°C difference at 10 hPa. This difference may arise from Finland making corrections to their temperature measurements while the US does not. The Phase 2 temperature differences (shown by the crosses) are similar to Phase 1 below 70 hPa but the US temperatures are noted to be warmer than Finland's temperatures above, except at the 10 hPa surface where the US, once again, becomes colder. These two data sets from identical instruments measuring in Phases 1 and 2 appear to disagree. The important question to ask is whether the solar angles were the same? It is already known that they were not.

The data of Figure 2, for solar angles near 40° above the horizon, agree fairly well. The Phase 1 differences at 1600 UT show good agreement with Phase 2 differences at 1700 UT up to 10 hPa. This agreement, while preliminary, infers that the original purpose of including two radiosonde types to link Phase 1 data with Phase 2 data was well founded (at least for temperature).

Nighttime comparisons, shown in Figure 3, also agree well and reinforce the information provided by Figure 2. The interesting aspect of the nighttime and daytime differences is the direction of the differences and magnitudes, respectively. For example, at night the US VIZ radiosonde using a white rod thermistor measures about 2°C colder than the bead thermistor of the Vaisala radiosonde; during the day the VIZ temperatures increase to be about 1-1.5°C warmer than Vaisala temperatures up to the 15 hPa level where they reverse their trend. Further examination of the Finland-United States data differences is required.

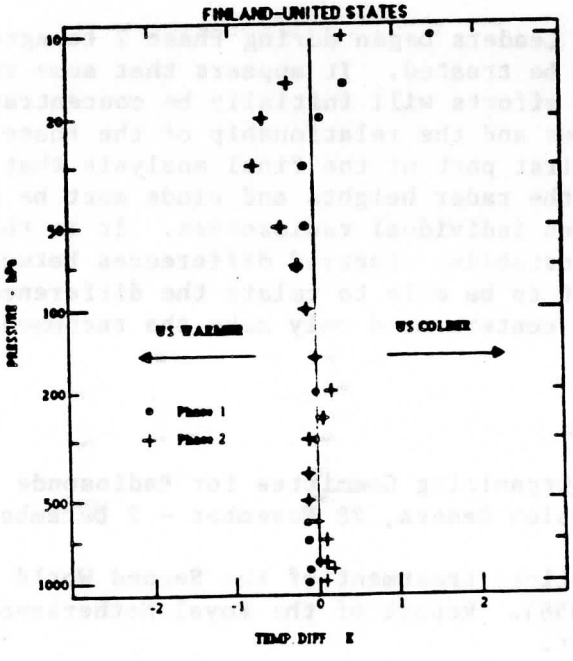

Fig. 1. All day and night data from Phases 1 and 2 showing temperature differences between Finland and US radiosondes.

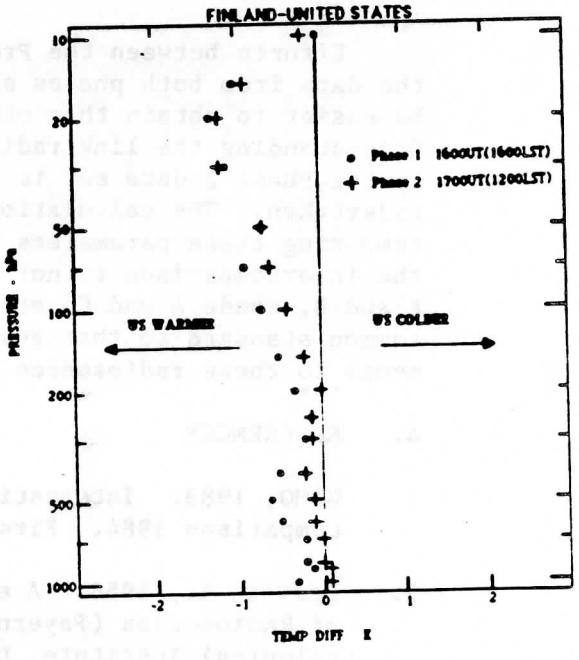

Fig. 2. Temperature differences between Finland and US radiosondes when solar angle is ~40°.

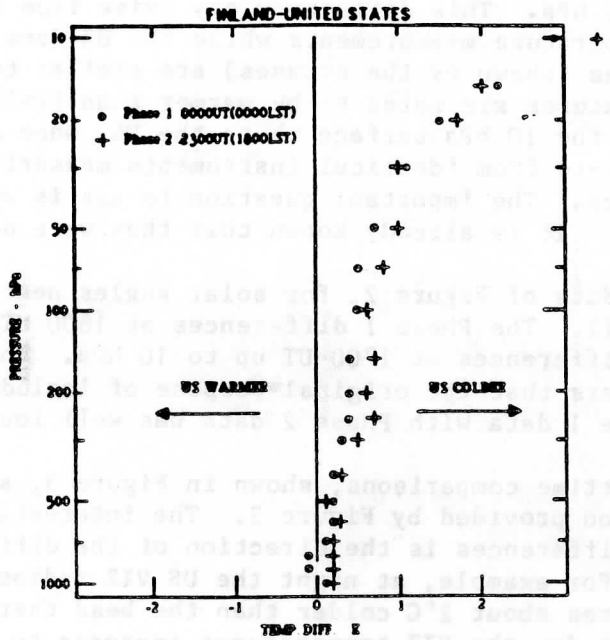

Fig. 3. Temperature differences between Finland and US radiosondes at night.

4. SUMMARY

Efforts between the Project Leaders began during Phase 2 to agree on how the data from both phases should be treated. It appears that some results will be easier to obtain than others; efforts will initially be concentrated there. Understanding the link radiosondes and the relationship of the Phase 1 data set to the Phase 2 data set is the first part of the final analysis that must be undertaken. The calculation of the radar heights and winds must be done before comparing these parameters between individual radiosondes. It is the goal of the intercomparison to not only establish observed differences between sonde A and B, sonde A and C, etc., but to be able to relate the differences to some common standard so that analysis centers need only make the recommended adjustments to these radiosondes.

4. REFERENCES

1. CIMO, 1983: International Organizing Committee for Radiosonde Intercomparison 1984. First Session Geneva, 28 November - 2 December 1983.

2. Delver, A., 1956: A statistical treatment of the Second World Comparison of Radiosondes (Payerne, 1956). Report of the Royal Netherlands Meteorological Institute, De Bilt.

3. Hooper, A. H., 1975: Volume I: Studies on Radiosonde Performance. In, Upper-Air Sounding Studies. WMO Technical Note No. 140. Geneva, Switzerland.

4. Richner, H., and P. D. Phillips, 1982: The Radiosonde Intercomparison SONDEX Spring 1981, Payerne. Pageoph, Vol. 120, pp. 851-1198.

COMPARISONS OF RELATIVE HUMIDITY MEASUREMENTS FROM PHASE I OF THE WMO INTERNATIONAL RADIOSONDE COMPARISON

J. Nash, M. Kitchen, and J.F. Ponting

U.K. Meteorological Office.

1. Introduction

Simultaneous relative humidity (R.H.) measurements from five different radiosonde types were obtained during the first phase of the WMO International Radiosonde Comparison (CIMORSEX) which took place at the United Kingdom (U.K.) Meteorological Office Experimental Site, Beaufort Park near Bracknell during June and July 1984. Details of the relative humidity sensors and their mountings on the five radiosonde types are presented in Table 1 and Fig. 1 respectively. The time constants of response (taken as the time required to indicate 63 per cent of a step change in R.H.) which are cited in Table 1 are taken from the manufacturer's specifications.

Table 1 Relative humidity sensors

Team	Radiosonde	R.H. Sensor	Time constant (at 1000hPa, 25 C)	Interval between readings
Finland	Vaisala RS80-15N	thin film capacitor	1s	1s
F.R.Germany	Graw G78C	carbon hygristor	<2s	6s
U.K.	RS3	goldbeaters skin	6s	4s
U.S.A	VIZ 1392	carbon hygristor	<2s	15s
Beukers Lab.	Micros 1524-511	carbon hygristor	<2s	4s

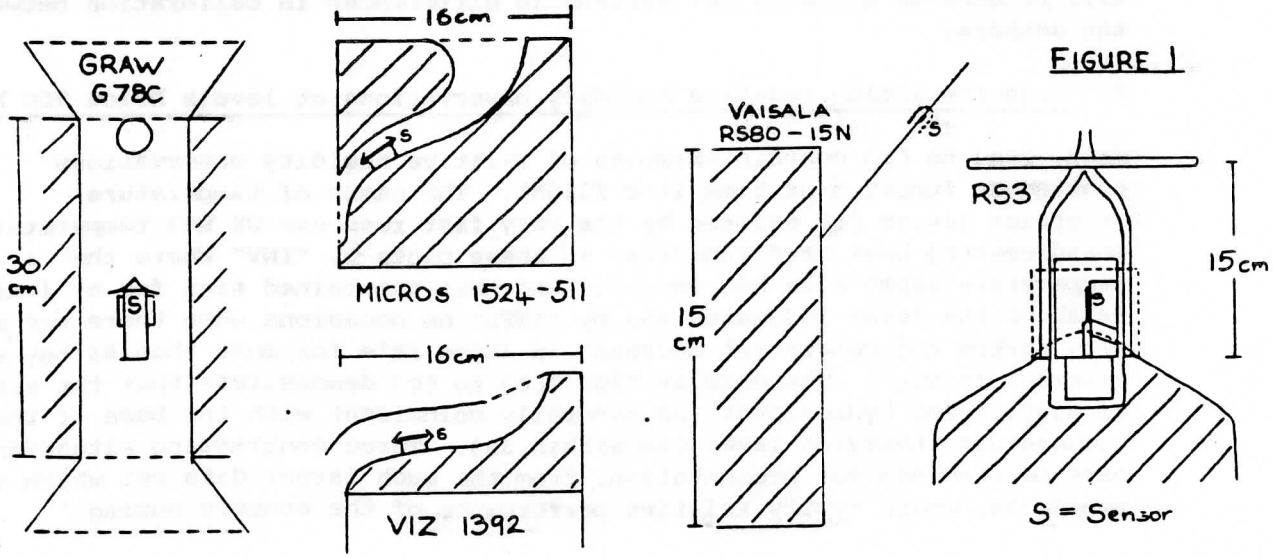

FIGURE 1

In the remainder of this paper the thinfilm capacitor of the Vaisala radiosonde will be referred to by its trade name of Humicap. The carbon hygristors of all three radiosonde types were obtained from the same source, VIZ Manufacturing Co. The intervals between readings which are cited in Table 1 are the smallest at which data could be output from the respective ground stations as operated during CIMORSEX. In most cases the intervals refer to data which have not been subjected to the smoothing and quality control procedures which are normally applied to operational output. The one exception to this is the West German output which was smoothed with a running mean over 12s, the effects of which can be readily seen by comparison with the other hygristor measurements in eg Fig. 2(a).

In the majority of multiple radiosonde flights performed in CIMORSEX all five radiosondes were suspended at a similar level from a bamboo cross which provided a spacing in the horizontal between the sondes of about 2m. Accurate timing of data samples is critical when comparing measurements by very fast response humidity sensors, particularly given the rapid changes in humidity which occur in the vertical in typical British summertime conditions. Finnish, American and British measurements were synchronised to better than $\pm$1s thoughout a flight by direct control of the ground stations by a central clock. Timing in the West German and Beukers ground stations was manually initiated and subsequent quality control procedures (using matching of fine structure temperature measurements by the different radiosonde types) has reduced timing errors to less than $\pm$3s. On other occasions, when three of the five radiosondes were flown $\bar{2}$0m beneath the other two, clock pulses to the ground stations of the lower sondes were delayed by 4 s to compensate for the displacement in the vertical and no further adjustments were found to be necessary. A typical ascent rate for the balloons in CIMORSEX was 5.5 ms^{-1}.

The weather during CIMORSEX was typical of a British summer, with surface temperatures ranging between +8 and +26 C overall. Only three of the 100 multiple flights were actually launched when it was raining, but a large number of ascents passed through low, medium or high cloud.

In this paper, high resolution relative humidity data will be used to examine the relative time responses of the sensors, and the samples taken at one minute intervals (which constitute the official CIMORSEX data set) will be used to quantify the systematic differences in calibration between the sensors.

2. High resolution relative humidity observations at levels below 700 hPa

Figs. 2(a) to (c) contain examples of relative humidity observations plotted as function of time into flight. The bases of temperature inversion layers (as defined by the very fast response UK RS3 temperature measurements) have been indicated in these plots by "INV" where the temperature lapse rate has reversed and then maintained sign for at least 6s above the level indicated and by "INFL" on occasions when there was a very marked and consistent decrease in lapse rate for more than 6s but no reversal in sign. The data in Figs 2(a) to (c) demonstrate that the start of significant hydrolapses was generally coincident with the base of the temperature inversion layer (to within 3s). Three contrasting situations have been chosen for presentation, from the much larger data set which is available, which typify relative performance of the sensors during

CIMORSEX. The key in Fig 2a is common to all figs 2a-3b. The USA measurements are plotted as individual points because of the relatively large gaps in the data record. (Table 1).

Fig 2(a)

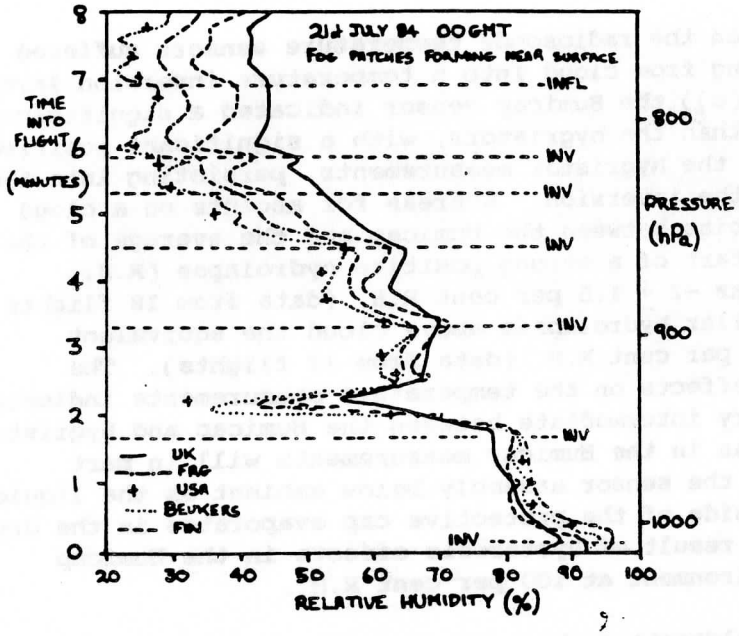

Fig 2(b)

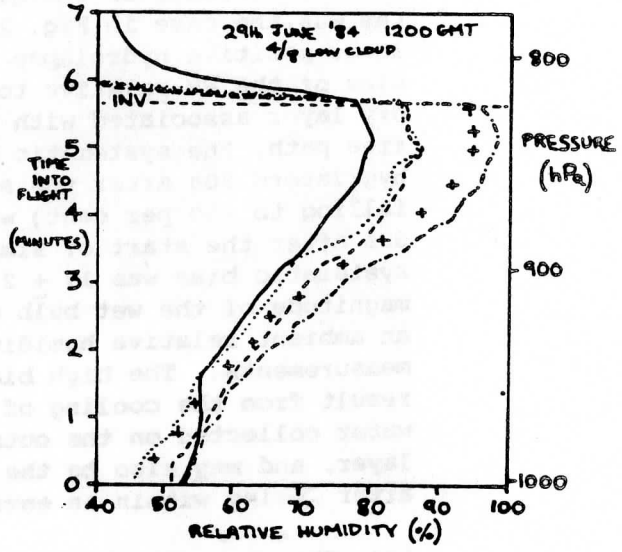

Fig 2(c)

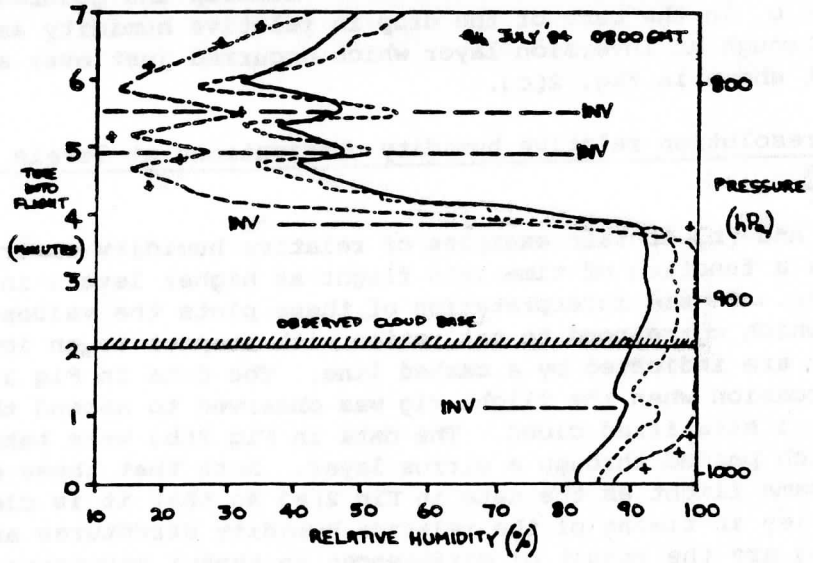

The following performance characteristics have been noted:

(a) At levels below 700 hPa the detailed vertical structures in relative humidity profiles measured by Humicap and hygristor sensors in cloud-free ascent paths are in close agreement (once allowance is made for calibration bias between individual sensors, e.g. at the dry end of the R.H. scale in Fig 2(a) and at the wet end of the R.H. scale in Fig. 2(b).

(b) On those occasions when the radiosonde temperature sensors suffered wet bulb effects on emerging from cloud into a temperature inversion layer (as was the case in Fig. 2(c)) the Humicap sensor indicated a significantly lower positive hydrolapse than the hygristors, with a significant positive bias of the RH relative to the hygristor measurements, persisting into the dry layer associated with the inversion. Whereas for ascents on a cloud free path, the systematic bias between the Humicap and the average of the hygristors 30s after the start of a strong positive hydrolapse (R.H. falling to <50 per cent) was -2 ± 1.5 per cent R.H. (data from 18 flights), 30s after the start of similar hydrolapses above cloud the equivalent systematic bias was 17 ± 2 per cent R.H. (data from 13 flights). The magnitude of the wet bulb effects on the temperature measurements indicated an ambient relative humidity intermediate between the Humicap and hygristor measurements. The high bias in the Humicap measurements will in part result from the cooling of the sensor assembly below ambient as the liquid water collected on the outside of the protective cap evaporates in the dry layer, and may also be the result of hysteresis effects in the Humicap after being within an environment at 100 per cent R.H..

(c) The response of the goldbeaters skin sensor is obviously much slower than that of the Humicap and hygristor sensors. There was little consistency in its response on passing into and out of clouds and inversion layers at levels below 700 hPa. Time constant values ranged from 10 to 36s with a typical average value of about 20s.

(d) In ascents into and through low cloud the hygristors often indicated less vertical humidity structure than the Humicap and goldbeaters skin sensors, e.g. in the case of the drop in relative humidity associated with passage through an inversion layer which occurred just over a minute into the flight shown in Fig. 2(c).

3. High resolution relative humidity observations at levels between 600 and 250hPa

Figs 3(a) and (b) contain examples of relative humidity observations plotted as a function of time into flight at higher levels in the troposphere. To aid interpretation of these plots the values of relative humidity which correspond to sat ration with respect to an ice surface at a given time are indicated by a dashed line. The data in Fig 3(a) are taken from an occasion when the flight rig was observed to ascend through a medium level stratified cloud. The data in Fig 3(b) were taken on an ascent which passed through a cirrus layer. Note that these data are taken from the same flight as the data in Fig 2(a) so that it is clear that the discrepancies in timing of the relative humidity structures around 300 hPa in Fig 3(b) are the result of differences in sensor responses and not timing initiation errors.

Fig 3(a)

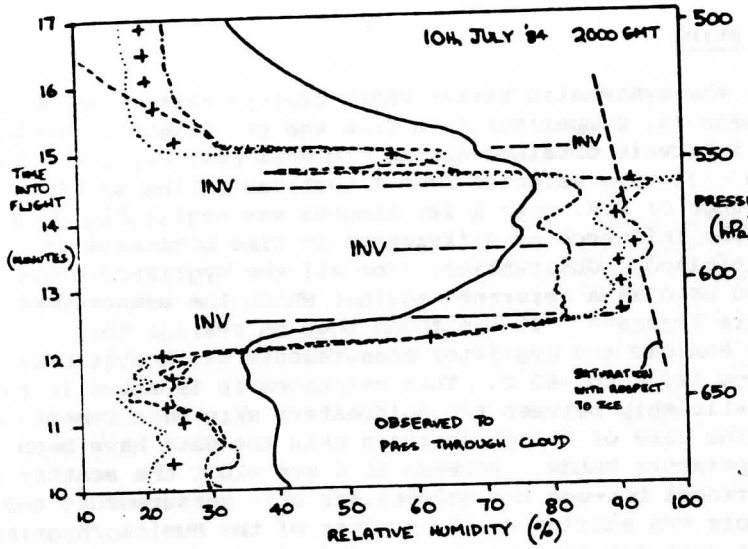

Fig 3(b)

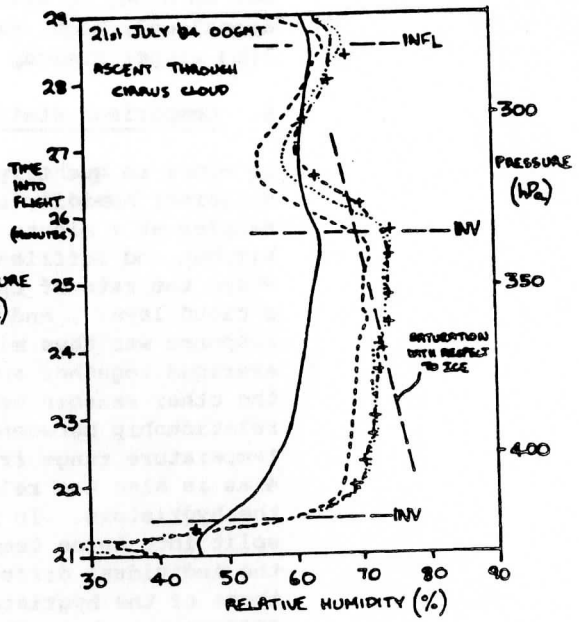

As at lower levels, the plots shown here were chosen from a larger data set, from which the following conclusions can be drawn:-

(a) It is only at levels above 350 hPa that discrepancies in the timing of structure in the vertical R.H. profiles begin to appear between the Humicap and hygristor measurements. At the tropopause in Fig. 3(b) (at 280 hPa) the maximum in relative humidity observed by the hygristors and goldbeaters skin sensor occurs 15s after that indicated by the Humicap sensor (with the maximum indicated by the Humicap coincident with the measured tropopause). Thus the Humicap sensor appears better suited to measurements at the highest levels. Of the three hygristor sondes the Beukers, on average, produces R.H. profiles closest to those measured by the Humicap sensor close to the tropopause.

(b) The time constant of response of the goldbeaters skin sensor degrades rapidly at the upper levels with a typical time constant of response of just over 1 minute at 500 hPa and about 5 minutes at 300 hPa. Thus the operational procedure of ceasing to report UK RS3 R.H. measurements at temperatures below −40 C is clearly justified. A similar operational procedure is adopted by the Americans, but the data in Fig 3 suggest that this is a somewhat stringent restriction on the carbon hygristor measurements. It has been shown in Nash, Stancombe and McGovern (3) that the Humicap sensor has a time constant of response of just over 1 minute at 300 hPa (temperature about -45 C), degrading to about 5 minutes at levels above 200 hPa. It is thus suggested that 200 hPa would be a more appropriate cut-off level for operational relative humidity measurements by Humicap and hygristor sensors in summertime conditions.

(c) As at the lower levels, the Humicap measurements at the wet end of the R.H. scale are systematically lower than the hygristor measurements. In Fig. 3(a) the hygristor measurements are judged to be closest to the truth

but on other occasions it was observed that hygristor measurements appeared anomalously high, particularly after passing through deep cloud. In Fig. 3(b) either Humicap or hygristor measurements could be correct.

5. Comparison statistics

In order to quantify the systematic biases which clearly exist between the different humidity sensors, comparison data from the raw relative humidity samples at 1 minute intervals obtained during CIMORSEX (see Nash, Ponting, Kitchen and Jeffries (2)) were selected from situations during an ascent where the rate of change of R.H. over a few minutes was negligible, e.g. in a cloud layer., and the influence of differences in time constants of response was thus minimised. Observations from all the hygristors were averaged together and used as a reference against which the measurements of the other sensors were assessed. It was found that on average the relationship between Humicap and hygristor measurements was stable over the temperature range from +20 C to -40 C. This relationship is shown in Fig. 4 as is also the relationship between the goldbeaters skin measurements and the hygristors. In the case of the goldbeaters skin the data have been split into three temperature bands. Between 20 C and -20 C the scatter of the individual differences between the goldbeaters skin measurements and those of the hygristors was similar to the scatter of the Humicap/hygristor differences about the best fit line shown, the individual data points rarely being >10% R.H. from the lines. However, at temperatures between -20 and -40 C the scatter between the goldbeaters skin and hygristor measurements doubled and fitting of any curve apart from a straight line to the data was not justified.

At the dry end of the R.H. scale the Humicap sensor shows a tendency to read lower humidities than the hygristors. This is attributed to the known insensitivity of the carbon hygristors in this range which is the reason why in American operational products relative humidities less than 20 per cent are not quantified.

At the wet end of the scale the data confirm that the Humicap and goldbeaters skin measurements have a negative offset in low level cloud and support the previous comparison results in Nash (1) where comparison was made with a hair hygrometer sensor operating in rainy conditions.

The systematic difference in relative humidity measured by the Humicap and hygristor sensors at the wet end of the R.H. scale (i.e. R.H. greater than 90 per cent as measured by the hygristors) was found to be greatest in day time observations when the ascent did not pass through low cloud. The increase in the offset of daytime Humicap (and goldbeaters skin)

Fig 4

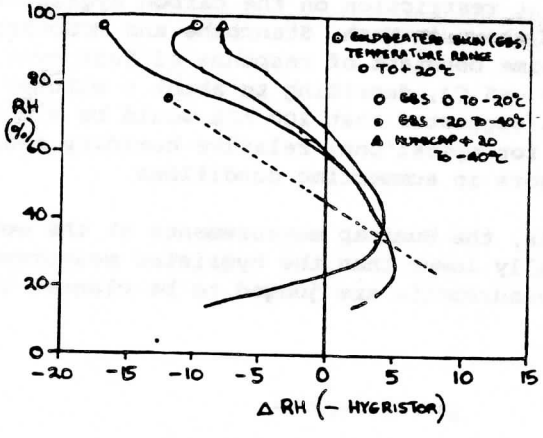

Fig 5

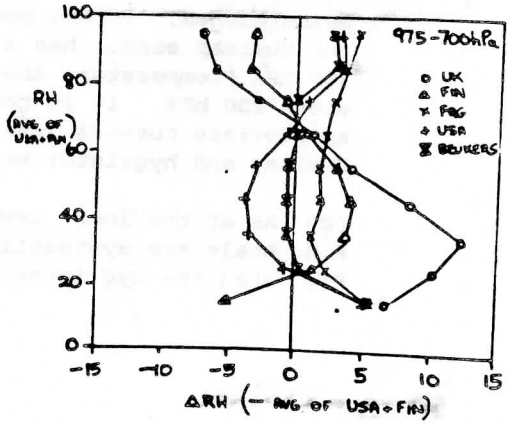

measurements relative to the hygristor measurements in cloud free ascents compared with the average offset derived from ascents in all conditions at all times of day was about 5 per cent R.H. (drier).

The relative performance of all the different radiosonde types can be seen in Fig 5 where all the flight data obtained in CIMORSEX between 975 and 700 hPa have been used to generate mean differences between the humidity data of each radiosonde type and the average of the American and Finnish measurements with RH data split into 10 per cent bands. In this data the effects of the inferior time constant of the goldbeaters skin sensor have produced a larger positive bias relative to the three hygristors than was present in Fig 4. The relationships between the Humicap and hygristor measurements in Fig 5 are compatible with those in Fig 4. The high reproducibility associated with the individual sensor measurements, particularly at the wet end of the R.H. scale is evidenced by the low standard deviation (less than 4 per cent) in the differences between the measurements of the different radiosonde types. Differences relative to the American measurements have the highest standard deviations (not illustrated here) and this degradation is attributed to interpolation errors in derivation of R.H. during the 15s intervals in which RH data are not being transmitted by the American sonde (see Table 1).

6. Summary

The CIMORSEX relative humidity measurements demonstrated that in general the time constants of response of the Humicap and carbon hygristor sensors were similar. The measurements by these sensors were of high precision and thus should be amenable to correction for systematic biases where appropriate. To what extent the systematic biases identified here were specific to atmospheric conditions experienced at CIMORSEX will not be apparent until the results from the second phase of the International Radiosonde Comparison at Wallops Island are available.

The external mounting of the relative humidity sensor on the Vaisala radiosonde leads to superior response over the duct-mounted hygristors at levels close to the tropopause, but appears to render the measurements more susceptible to sensor assembly cooling (wet bulb effects) or heating (solar heating) errors than the measurements of radiosondes with internally mounted sensors.

The sampling rate of the American radiosonde is inadequate for those users who are interested in accurate measurements of hydrolapses in the lower troposphere. The goldbeaters skin sensor of the UK RS3 was inferior in most respects to the Humicap and carbon hygristor sensors.

References

1. Nash, J. 1984 Multiple Flight Radiosonde Comparisons Proceedings of TECEMO 84 Noorwijkhewhouk, Netherlands.

2. Nash, J., Ponting, J.F. Kitchen, M., and Jeffries, P.H. 1984 Intercomparison statistics from Phase 1 of the WMO international Radiosonde Intercomparison (CIMORSEX), O.S.M. 29, Meteorological Office, Bracknell.

Nash, J., Stancombe J., 1985 and McGovern, J.C.

Twin flight measurements, UK RS3 and Vaisala RS 80. OSM 30, Meteorological Office, Bracknell.